MUSME 2011
4 th International Symposium on Multibody Systems and Mechatronics

EDITORIAL
UNIVERSITAT POLITÈCNICA DE VALÈNCIA

This editorial is member of the UNE, which guarantees the diffusion and commercialization of its publications at national and international level.

First edition 2011

Print: Diazotec S.A.

Depósito Legal: V-3478-2011
Ref. editorial: 2655

Printed in Spain

FINAL PROGRAM FOR THE 4TH INTERNATIONAL SYMPOSIUM ON MULTIBODY SYSTEMS AND MECHATRONICS (MUSME 2011)

TIME	Nº	TUERSDAY 25th October 2011
9:00-10:00		**REGISTRATION**
10:00-11:00		OPENING ACT
		SESSION 1: ROBOTS AND MICROMACHINES **Chairman: Pietro Fanghella**
11:00-11:30	1	INVERSE AND FORWARD DYNAMICS OF THE BIPED PASIBOT Eduardo Corral , Jesús Meneses and Juan Carlos García Prada
11:30-12:00	2	ROBOT TRAJECTORY PLANNING USING CUBIC B-SPLINES IN JOINT SPACE Werley Rocherter Borges Ferreira, João Carlos Mendes Carvalho
12:00-12:30	3	OMNIBOLA: A SPHERICAL ROBOT Mariano Jaimez, Juan A. Cabrera, Juan J. Castillo and Francisco García
12:30-13:00	4	WIRELESS TELEOPERATED OF A ROBOTIC MANIPULATOR BASED IN IMU SENSOR AND CONTROL ANTHROPOMORPHIC MOVEMENT Alejandro Jofré Moreno and Diego Álvarez Villegas
13:00-13:30	5	A TOPOLOGY SEARCH FOR A NEW LARM LEG MECHANISM Tao Li and Marco Ceccarelli
13:30-15:00		LUNCH
		SESSION 2: DYNAMICS OF MULTIBODY SYSTEMS I **Chairman: Javier Cuadrado**
15:30-16:00	6	EXPONENTIAL INTEGRATION SCHEMES IN MULTIBODY DYNAMICS Javier Ros, Xabier Iriarte, Roberto Yoldi and Jorge Ángeles
16:00-16:30	7	MULTIBODY MODELLING OF A HIGH SPEED ROUTING SYSTEM FOR AUTOMATED LETTER HANDLING Pietro Fanghella and Andrea Sintich
16:30-17:00	8	COMPARISON OF METHODS TO DETERMINE GROUND REACTIONS DURING THE DOUBLE SUPPORT PHASE OF GAIT Urbano Lugrís, Jairo Carlín, Rosa Pàmies-Vilà and Javier Cuadrado
17:00-17:30		COFFE BREAK
17:30-18:00	9	INVERSE DYNAMICS SIMULATION OF HUMAN MULTIBODY DYNAMICS García-Vallejo, Daniel and Schiehlen, Werner
18:00-18:30	10	DYNAMIC ANALYSIS OF A FIVE-BAR LINKAGE MECHANISM IN TRACTION Arinola B. Ajayi
18:30-19:00	11	DYNAMICS MODELING OF THE SAAB SEAEYE COUGAR ROV Alessandro Cammarata, Mario Musumeci and Rosario Sinatra

TIME	Nº	WEDNESDAY 26TH OCTOBER 2011
		SESSION 3: DYNAMICS OF MULTIBODY SYSTEMS II AND EXPERIMENTAL VALIDATIONS **Chairman: Werner Schiehlen**
9:00-9:30	12	NEWTON-EULER FORMULATION OF A PAN-TILT GIMBAL José A. Colín-V, Carlos S. López-C, Moisés G. Arroyo-C and José A. Romero-N
9:30-10:00	13	ANALYSIS OF WEAR IN GUIDE BEARINGS FOR PNEUMATIC ACTUATORS AND NEW SOLUTIONS FOR LONGER SERVICE LIFE Guido Belforte, Andrea Manuello Bertetto, Luigi Mazza and Pier Francesco Orrù
10:00-10:30	14	CONTROL SYSTEM AND DATA ACQUISITION FOR A RECIPROCATING COMPRESSORS FRICTION TEST STAND Luigi Mazza, Andrea Trivella and Roberto Grassi
10:30-11:00	15	A HYDRAULIC SHAKE TABLE FOR VIBRATION TESTING: MODEL PARAMETERS ESTIMATION AND VALIDATION Giandomenico Di Massa, Stefano Pagano, Salvatore Strano and Francesco Timpone
11:00-11:20		COFFE BREAK
		SESSION 4: SIMULATION PROCEDURES **Chairman: Carlos Munares**
11:20-11:45	16	AN EXPERIMENTAL VALIDATION OF COLLISION FREE TRAJECTORIES FOR PARALLEL MANIPULATORS G. Carbone , F. Gómez-Bravo and O. Selvi
11:45-12:10	17	COMPUTER SIMULATIONS OF THE COAL WAGON LABORATORY EXCITATION AND INFLUENCE OF THE SWEEP LOAD TEST PARAMETER Pavel Polach and Michal Hajžman
12:10-12:35	18	TRAJECTORY GENERATION THROUGH THE EVOLUTION OF THE OPTIMAL PATH Francisco Rubio, Francisco Valero and Josep Ll. Suñer
12:35-13:00	19	EFFECT OF COOPERATIVE WORK IN OBJECT TRANSPORTATION BY MULTY-AGENT SYSTEMS IN KNOWN ENVIRONMENTS Renato Miyagusuku, Jorge Paredes, Santiago Cortijo and José Oliden
13:00-13:45		QUICK LUNCH
13:45-17:00		VISIT TO FORD ´S CAR ASSEMBLY AND ENGINE PLANT

TIME	Nº	THURSDAY 27TH OCTOBER 2011
		SESSION 5: MECHATRONICS **Chairman: Javier Ros**
9:00-9:30	20	HUMAN COMPUTER INTERFACE BASED ON HAND TRACKING Pedro Achanccaray, Cristian Muñoz, Luis Rojas and Ricardo Rodriguez
9:30-10:00	21	ON THE BIOMECHANICAL DESIGN OF STANCE CONTROL KNEE ANKLE FOOT ORTHOSIS (SCKAFO) Pedro Moreira, Pedro Ramôa, Luís F. Silva and Paulo Flores
10:00-10:30	22	DEVELOPMENT OF A CONTROL SYSTEM FOR MODELLING A 5MW WIND TURBINE AND CORRELATION BETWEEN DIFFERENT EXISTING CODES José Manuel Yepes Rodriguez and Dr. Omar Aït-Salem Duque
10:30-11:00	23	MECHATRONICS DEVELOPMENT AND DYNAMIC CONTROL OF A 3 DOF PARALLEL MANIPULATOR Marina Vallés, Miguel Díaz-Rodríguez, Ángel Valera , Vicente Mata and Álvaro Page
11:00-11:30		COFFE BREAK
		SESSION 6: MECHATRONICS AND KINEMATICS I **Chairman: Manfred Husty**
11:30-12:00	24	FLEXIBLE PNEUMATIC ACTUATION FOR BLOOD PRESSURE RECOVERY Andrea Manuello Bertetto, Silvia Meili, Alberto Concu and Antonio Crisafulli
12:00-12:30	25	OBJECT ORIENTED MODELING FOR WALKING MACHINES Mauricio Alba, Juan Carlos García Prada and Cristina Castejon
12:30-13:00	26	COMPARISON OF DIFFERENTS METHODS TO CALCULATE COMPLIANT DISPLACEMENTS OF MULTIBODY SYSTEMS Rogério Sales Gonçalves and João Carlos Mendes Carvalho
13:00-13:30	27	NUMBER SYNTHESIS OF METAMORPHIC MECHANISMS USING SUBGRAPH CONSTRAINTS Martín Pucheta, Agostino Butti, Valerio Tamellini, Alberto Cardona and Luca Ghezzi
13:30-15:00		LUNCH
		SESSION 7: MECHATRONICS AND KINEMATICS II **Chairman: João Carlos Mendes Carvalho**
15:30-16:00	28	DYNAMICS OF SENSITIVE EQUIPMENTS ON WRS ISOLATORS Giandomenico Di Massa, Stefano Pagano, Ernesto Rocca and Salvatore Strano
16:00-16:30	29	OPTIMAL DIMENSIONAL SYNTHESIS OF LINKAGES USING EXACT JACOBIAN DETERMINATION IN SQP ALGORITHM Ramon Sancibrian, Ana de Juan, Angel Sedano, Pablo Garcia, Miguel Iglesias, Fernando Viadero and Alfonso Fernandez
16:30-17:00	30	ASSEMBLY MODE CHANGE OF SPHERICAL 3-RUPUR PARALLEL MANIPULATOR Mónica Urízar and Manfred L. Husty
17:00-17:30		COFFE BREAK
17:30-18:00	31	FAILURE IN THE FRONT SUSPENSION MECHANISM. MITSUBISHI L-200 CASE Carlos Munares
18:00-18:30	32	MODELING AND CONTROL OF A BIPED ROBOT BASED ON THE CAPTURE OF HUMAN MOVEMENT PATTERNS Elvis O. Jara, Cristian Cisneros, Edison Alfaro and José Oliden
18:30-19:00	33	UNIFIED THEORY OF FIELDS IN SWARM BASED OPTIMIZATION METHODS Alexandr Stefek
19:00-20:00		SCIENTIFIC COMMITTEE MEETING
21:00-24:00		CONFERENCE DINNER

TIME	Nº	FRIDAY 28TH OCTOBER 2011
		SESSION 8: STUDENT SESSION **Chairman: Carlos Lopez Cajún**
9:00-9:20	34	THE ORIGINAL DOUBLE-GOLDBERG 6R LINKAGE AND ITS BIFURCATION ANALYSIS Chaoyang SONG and Yan CHEN
9:20-9:40	35	INVERSE AND DIRECT KINEMATICS OF AN UNDERWATER PARALLEL ROBOT Hector A. Moreno, Roque Saltaren, Eugenio Yime and Isela Carrera
9:40-10:00	36	ON THE INFLUENCE OF ANTI-ROLL STIFFNESS ON VEHICLE STABILITY AND PROPOSAL OF AN INNOVATIVE SEMI-ACTIVE MAGNETORHEOLOGICAL FLUID ANTI-ROLL BAR Flavio Farroni, Daniele Giordano, Michele Russo, Mario Terzo and Francesco Timpone
10:00-10:20	37	A HISTORY OF ARTIFICIAL HANDS Ettore D'Aliesio and Marco Ceccarelli
10:20-10:40	38	A DYNAMIC ANALYSIS OF THE ROBOT CAPAMAN (CASSINO PARALLEL MANIPULATOR) AS SOLAR TRACKER Elisabet Jiménez, Marco Ceccarelli and Giuseppe Carbone
10:40-11:00		COFFE BREAK
11:00-14:00		VISIT TO THE HISTORICAL CENTRE OF VALENCIA
14:00-16:00		LUNCH

Contents

Proceedings of MUSME 2011, the International Symposium
on Multibody Systems and Mechatronics
Valencia, Spain, 25-28 October 2011

INVERSE AND FORWARD DYNAMICS OF THE BIPED PASIBOT.

Eduardo Corral [*], Jesús Meneses [†] and Juan Carlos García Prada [†]

[*] Universidad Carlos III de Madrid. Dpt. Ingeniería Mecánica. MAQLAB groupe. Av. De la Universidad S/N, 30, 28911 Leganes, Spain.

e-mail: e.corral@ing.uc3m.es,
web page: http://www.uc3m.es

Keywords: Legged walking, bipod robots, mechanisms, Dynamics.

Abstract.

This paper presents a one degree-of-freedom (DOF) biped robot with one actuator that gives a torque to the crank. The mechanical design, walking kinematics and dynamics of this biped are presented.

The kinematics of PASIBOT is first studied, then the inverse and forward dynamical problems are presented in a matrix form, in such a way that sliding and overturning can be taken into account. Forward dynamics allows us to deal with starting torque calculations, and several singular conditions related to it are discussed.

The results of this paper can be of great help in the design, optimization and control of such devices.

1 INTRODUCTION

Nowadays, humanoid robots are formed by a large number of actuators, used to control the large degrees of freedom (DOF) they have [1]. On the other hand, one of the most drawbacks in humanoids is the weight and the power consumption. In the majority of them, around 30% of the total weight is due to the actuators and wires, and more than 25% is due to the reduction systems coupled [2]. For this reason, our work is focused on the design of new mechanisms and kinematic chains which, maintaining the robot capabilities, require smaller number of actuators. This would reduce the robot mass and hence, its power consumption and total cost. In the last years, different research groups have developed robots based on passive walking techniques [3], [4].

In this article, we present a human size biped, called PASIBOT, with low DOF, which represents a qualitative improvement in the service robotic field [5].

The 1-DOF biped robot studied in this article (see Fig. (1)) consist of a torque engine that is connected to a called hip base by two legs.

The innovative design has been carried out with the combination of classical mechanisms (Peaucellier, Watt, pantograph [6], etc.). This prototype is based on the one designed and built at the Laboratory of Robotics and Mechatronics in Cassino (LARM) [6], following the philosophy of low cost [7]. A similar leg design has also been used in a four legs walking chair [8].

The proposed mechanism is an arrangement of links in planar movement that has only one DOF. In this manuscript, the planar kinematics and dynamics analysis of PASIBOT is presented. The study is performed from a theoretical point of view, and aims to obtain the linear and angular position coordinates, velocities and accelerations for all links, as well as all the forces and torques between links including motor torque, for any time in the course of one step. The expressions have been implemented in MATLAB® code, and the corresponding results have been used in the design and construction of a real prototype, and they are being used in movement control tasks.

2 TOPOLOGICAL DESCRIPTION OF PASIBOT

In fig.(1), a virtual model and a photograph of the first prototype of PASIBOT, built at MAQLAB group, Universidad Carlos III de Madrid, are presented. Thanks of that prototype some researches could be tested.

Fig. (1): the biped robot PASIBOT. Left: a virtual model. Right: the real prototype.

PASIBOT is a 1-DOF planar mechanical system which consists of two identically actuated legs with one degree-of-freedom that is activated by one torque engine. The mechanism of both legs is the same and that can be divided into three essential subassemblies or "sub-mechanisms", each of them having a particular function:

1.- Quasi-straight line generator mechanism (Chebyshev)
2.- Amplifier mechanism (pantograph)
3.- Stability extension and foot (parallelogram extensions).

In , the coupling Chebyshev-pantograph mechanism is shown, together with two trajectories tracked by the points of interest. Chebyshev mechanism transfers the motor rotational movement at its crank into a continuous cyclical trajectory, which is composed by a curved section and a quasi-straight one, at the end of its connecting rod (point C in Fig. (2)). This point is then linked to a pantograph mechanism in such a way that its free end (point E in Fig. (2)) executes a trajectory that is inverted and amplified with respect to that described above. The ratio of magnification of the pantograph depends on the dimension of its bars; for the design presented in this work, this ratio is two.

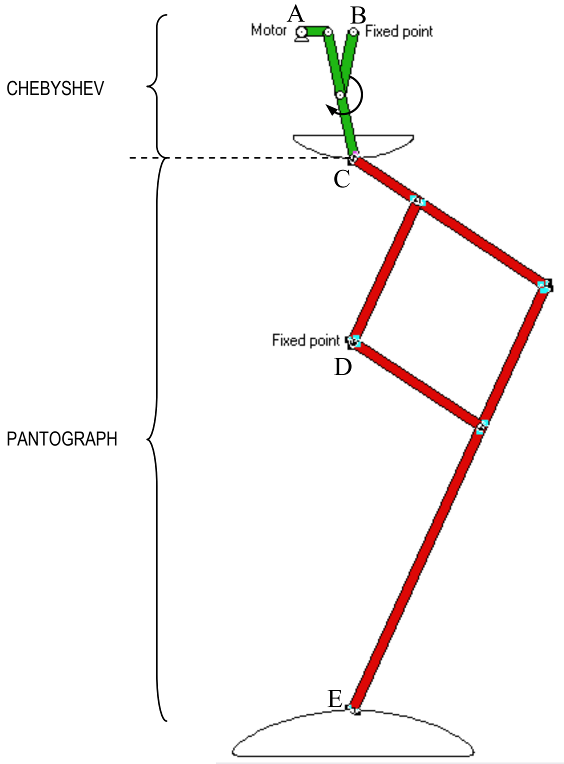

Fig. (2): Coupling Chebyshev-Pantograph mechanism with the corresponding trajectories of interest

The relative positions of points A, B and D in Fig. (), are fixed at the member called "hip", shown in **Fig. (2)**. The hip also carries a slot (see Fig. ()) which is the base of the stabilization system: a set of links arranged in parallelograms with the two longest bars of the pantograph. This stability extension guarantees the parallelism between the supporting foot and the stabilizing bar, which end slides along the slot at the hip. The first approach is to align the slot with the linear section of the Chebyshev trajectory, in such a way that the supporting foot remains also parallel to the slot.

To provide the opposite leg with the proper movement, the corresponding crank is phased out π rad (see Fig. (3)) in the same motor axis. In fact, both cranks take part of the same rigid element.

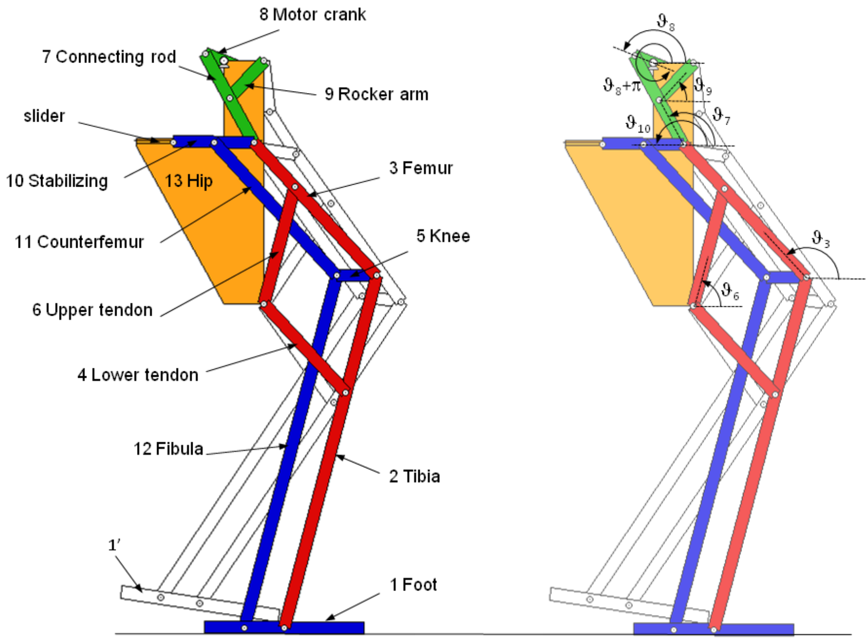

Fig. (2): Sub-mechanisms of PASIBOT. (A) Nomenclature and numeration for the supporting leg. (B) angular positions for the links. The members of the opposite leg will be referred to using primes. Chebyshev sub-mechanism: links 7, 8 and 9; Pantograph sub-mechanism: links 2, 3, 4 and 6. Stability extension sub-mechanism: links 1, 5, 10, 11 and 12.

As can be seen in Fig.(3), each link has been numerated and named, using prime (x') for the links belonging to the flying leg, to distinguish from those belonging to the supporting leg. Each leg has 12 links, but since the motor crank (link number 8) is shared with both legs (hence, there is no link number 8'), the number of links for PASIBOT, including the single hip (link number 13), is 24.

3 KINEMATICS OF PASIBOT

The kinematical study presented here is related to one PASIBOT's step, having one of its feet (the supporting foot) always in contact with a horizontal surface (x axis). Taking into account this, the PASIBOT is a planar mechanism with one DOF, so we can refer the angular positions of any link, to the angular position of the motor crank (θ_8):

$$\theta_i = \theta_i(\theta_8),\ i=1,2,\ldots 1',2',\ldots \quad (1)$$

Then, the x,y coordinates for its centre of mass (COM), can be easily expressed with respect to that angle:

$$x_i = x_i(\theta_8);\ y_i = y_i(\theta_8),\ i=1,2,\ldots 1',2',\ldots \quad (2)$$

Furthermore, if the time dependent function for the motor crank angle is known, those coordinates can also be expressed as time dependent functions. The corresponding angular velocities and accelerations, as well as the centre of mass linear velocities and accelerations are obtained by taking the first and second derivatives of functions in Eq. (1) and Eq. (2).

Actually, the biped kinematics is based on three close loop kinematic chains (one for each submechanism described above) which lead to the following three equations systems (The link lengths have been particularized for the designed PASIBOT, and normalized to the crank length, so that $l_8=1$, as the resulting angles are independent of the scale):

1.- CHEBYSHEV CHAIN (formed by links number 7, 8, 9 and 13)

In a Chevyshev mechanism, the distance between motor crank and rocker arm fixed points (A and B in Fig. (, respectively) is $2\cdot l_8$, the rocker arm length is $2.5\cdot l_8$, the connecting rod length is $5\cdot l_8$, and the rocker arm and connecting rod are joined at the middle point of the latter. Taking into account these lengths, the Chebyshev close loop kinematic chain provides (see **Fig. (**4):

$$2.5e^{i\vartheta_7} - 2.5e^{i\vartheta_9} - e^{i\vartheta_8} + 2 = 0 \tag{3}$$

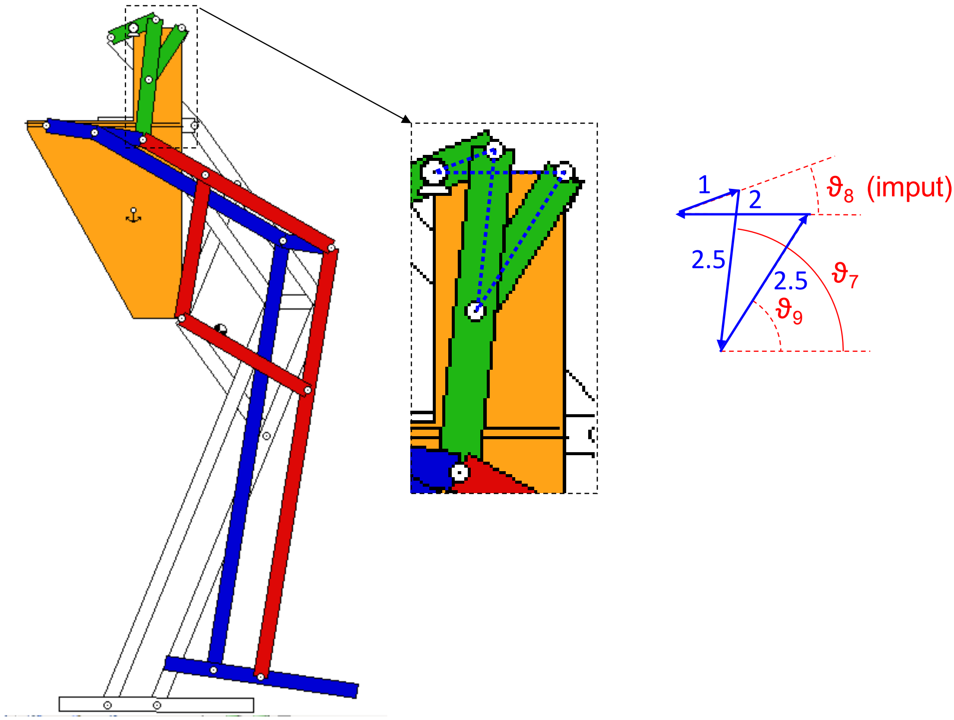

Fig. (4): Chevyshev chain (lengths in units of l_8)

In Eq. (3) to Eq. (5), both projections (vertical and horizontal) for each close loop equation are written in a compact form following the Euler's formula, were i is the imaginary unit.

2.- PANTOGRAPH CHAIN (formed by links number 9, 7, 3, 6 and 13)

In our model, the tendons length is $6\cdot l_8$, whereas the distance between the connecting rod-femur and upper tendon-femur joints is $3\cdot l_8$, and the distance between rocker arm-hip and upper tendon-hip joints (points B and D respectively) is $12\cdot l_8$, so the pantograph close loop kinematic chain provides (see **Fig. (3)**:

$$6e^{i\vartheta_6} + 3e^{i\vartheta_3} + 2.5\left(e^{i\vartheta_7} + e^{i\vartheta_9}\right) - 12i = 0 \tag{4}$$

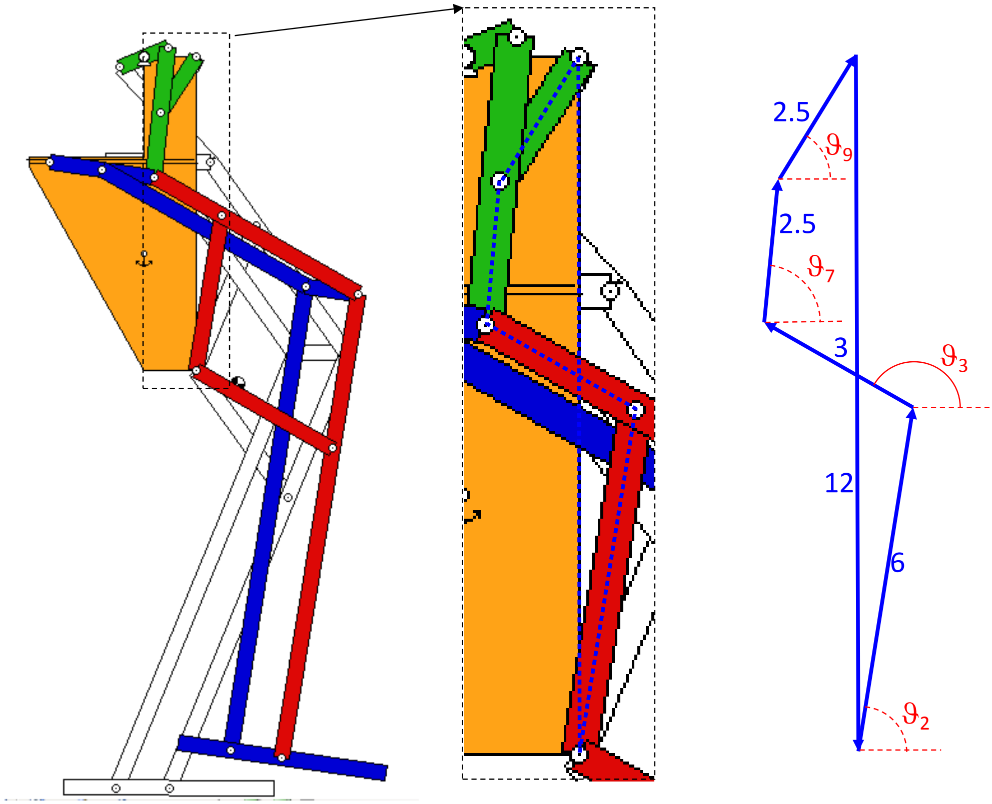

Fig. (3): Pantograph chain (lengths in units of l_8)

3.- STABILITY CHAIN (formed by links number 8, 7, 10 and 13)

In our model, the stabilizing link length is $4.2 \cdot l_8$. Note that, in order to align the slot with the linear section of the Chebyshev trajectory, the vertical distance between the motor crank joint and the slot at the hip must be equal to $4 \cdot l_8$. Calling x the horizontal projection distance between the motor crank joint and the end of the stabilizing link, the stability close loop kinematic chain provides (see **Fig. (4)**):

$$4.2e^{i\vartheta_{10}} - 5e^{i\vartheta_7} + e^{i\vartheta_8} - x + 4i = 0 \tag{5}$$

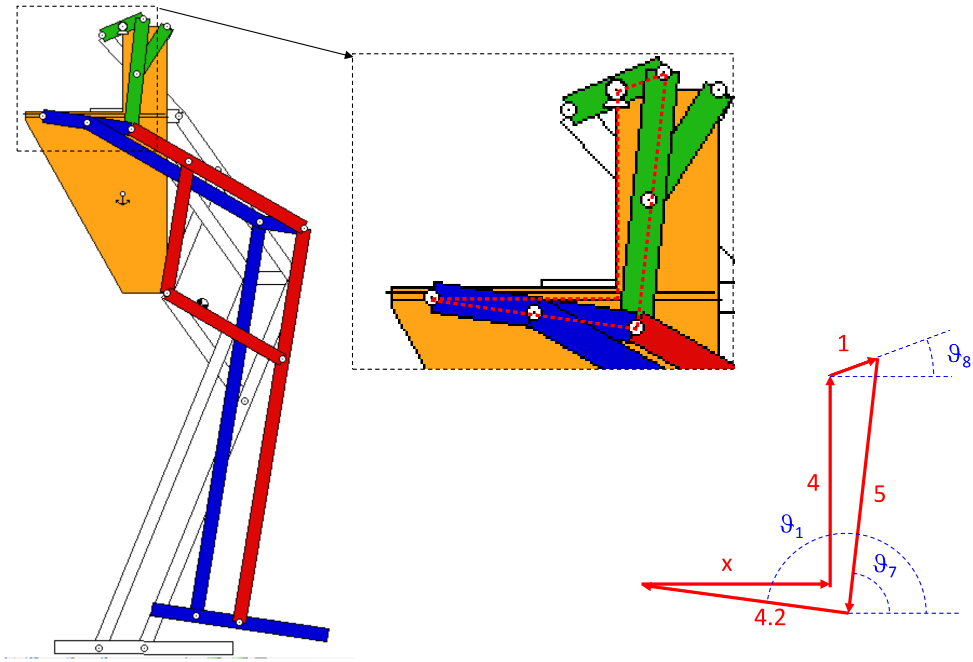

Fig. (4): Stabilization chain (lengths in units of l_8)

As stated below, these equations determine the angles for all the links as functions of that for the motor crank, ϑ_8, which is also a function of time.

Solving the equations system (3), the following expressions for the connecting rod and rocker arm angles are found:

$$\begin{cases} \vartheta_7 = a\cos\left[\dfrac{-4\cdot\cos^2\vartheta_8 + 13\cdot\cos\vartheta_8 - 10 + \mathrm{sen}\vartheta_8\cdot\sqrt{-16\cdot\cos^2\vartheta_8 - 60\cdot\cos\vartheta_8 + 100}}{25 - 20\cdot\cos\vartheta_8}\right] \\ \vartheta_9 = a\cos\left[\dfrac{-4\cdot\cos^2\vartheta_8 + 13\cdot\cos\vartheta_8 - 10 - \mathrm{sen}\vartheta_8\cdot\sqrt{-16\cdot\cos^2\vartheta_8 - 60\cdot\cos\vartheta_8 + 100}}{-25 + 20\cdot\cos\vartheta_8}\right] \end{cases} \tag{6}$$

From equation (4), the femur and tibia angles are found as functions of the previous ones:

$$\begin{cases} \vartheta_6 = a\cos\left[\dfrac{(2.5\cdot(\cos\vartheta_7 + \cos\vartheta_9)\cdot(-27 - A) - 2.5\cdot(\mathrm{sen}\vartheta_7 + \mathrm{sen}\vartheta_9 - 12)\cdot\sqrt{144\cdot A - (-27 - A)^2}}{12\cdot A}\right] \\ \vartheta_3 = a\cos\left[\dfrac{(2.5\cdot\cos\vartheta_7 + \cos\vartheta_9)\cdot(27 - A) + 2.5\cdot(\mathrm{sen}\vartheta_7 + \mathrm{sen}\vartheta_9) - 12)\cdot\sqrt{36\cdot A - (27 - A)^2}}{6\cdot A}\right] \end{cases} \tag{7}$$

Where:

$$A = (2.5\cdot(\cos\vartheta_7 + \cos\vartheta_9))^2 + (2.5\cdot\mathrm{sen}\vartheta_7 + \mathrm{sen}\vartheta_9) - 12)^2$$

Finally, the equation (5) gives the solution for the stabilizing angle:

$$\vartheta_{10} = a\sin\left(\frac{5 \cdot sen\vartheta_7 - sen\vartheta_8 - 4}{4.2}\right) \quad (8)$$

As can be seen in Fig. (2), the rest of the angles involved are identical to one of the given ones in the expressions Eq. (6) to Eq. (8), in particular:

$$\begin{aligned} \vartheta_1 &= \vartheta_5 = \vartheta_{10} \\ \vartheta_{12} &= \vartheta_4 = \vartheta_3 \\ \vartheta_2 &= \vartheta_{13} = \vartheta_6 \end{aligned} \quad (9)$$

For the links belonging to the opposite leg, we apply a phase out of π radians on ϑ_8:

$$\vartheta_{i'}(\vartheta_8) = \vartheta_i(\vartheta_8 + \pi) \quad (10)$$

All these angles have been calculated using a reference system fixed at the hip, the x-axis direction being defined by the points A and B in fig. (1). In order to apply the second Newton's law, all the kinematic values must be referenced to an inertial system. An inertial system can be placed at the ground (or at the supporting foot, link number 1 in Fig. (2), as no relative motion between this link and the ground is considered). The corresponding base change is described in Eq. (11):

$$\vartheta_i^{ground} = \vartheta_i^{hip} - \vartheta_1^{hip} \quad (11)$$

Where $\vartheta_i^{\ ground}$ is the angle of the i-link related to the ground system, and $\vartheta_i^{\ hip}$ is corresponding one related to the reference system fixed at the hip.

Once the angles are determined in the new reference system, the positions of the center of mass for all the links are easily obtained. Then, by time differentiating once and twice, the angular velocity and acceleration respectively for any link, as well as the linear velocity and acceleration of its center of mass are found.

In summary, the planar kinematics of PASIBOT is solved. As an application, all the kinematical values for one step of PASIBOT have been calculated, considering a motor crank constant angular velocity, ω_8:

$$\vartheta_8(t) = \omega_8 \cdot t \quad (12)$$

4 DYNAMICS OF PASIBOT

The dynamical magnitudes involved in the complete mechanical study of PASIBOT are the weight of every link, $m_i \cdot g$, the motor torque, T_8, and all the forces between links, f_{ji} (exerted by link j on link i). All those kinematical and dynamical magnitudes are represented in **Fig. (5)**, for a general link i.

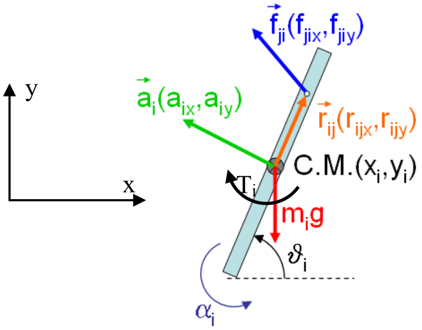

Fig. (5): Dynamical entities for a general link i

4.1 Inverse dynamics

The inputs for the inverse dynamical problem are the previously calculated kinematic magnitudes for every link, that is to say, its angular acceleration, α_i, and its center of mass acceleration, (a_{ix}, a_{iy}).

For any link, i, the dynamical equations for the motion of the center of mass and for the rotation of the rigid body, using the action-reaction Newton's law to reduce the number of unknown forces, are exposed in equation (13):

$$\left.\begin{array}{l}\sum \vec{F}_{on\,i} = m_i \vec{a}_i \\ \vec{f}_{ij} = -\vec{f}_{ji} \\ \sum T_{on\,i} = I_i \alpha\end{array}\right\} \Rightarrow \left\{\begin{array}{l}\sum\limits_{j<i} f_{ji_x} - \sum\limits_{k>i} f_{ik_x} = m_i a_{ix} \\ \sum\limits_{j<i} f_{ji_y} - \sum\limits_{k>i} f_{ik_y} = m_i g + m_i a_{iy} \\ T_i + \sum\limits_{j<i}\left(r_{ij_x} f_{ji_y} - r_{ij_y} f_{ji_x}\right) - \sum\limits_{k>i}\left(r_{ik_x} f_{ik_y} - r_{ik_y} f_{ik_x}\right) = I_i \alpha_i\end{array}\right.$$

$$i = 2,3,\ldots,13,1',2'\ldots,7',9',\ldots,12' \qquad (13)$$

Since there are 23 links (excluding the supporting foot) and there are three equations for each link, the system describing the dynamics of the whole mechanism consists of 69 linear equations. The linear equation system (equation 13) is expressed in a matrix form (equation 14), and then solved via matrix inversion, with a MATLAB® code.

$$\begin{bmatrix} a_{11} & a_{12} & \cdots & \\ a_{21} & a_{22} & \cdots & \\ \vdots & \vdots & \ddots & \vdots \\ & & \cdots & \end{bmatrix} \cdot \begin{bmatrix} f_{12_x} \\ f_{12_y} \\ \vdots \\ T_8 \\ \vdots \end{bmatrix} = \begin{bmatrix} m_2 a_{2_x} \\ m_2 g + m_2 a_{2_y} \\ I_2 \alpha_2 \\ \vdots \end{bmatrix}$$

$$[A(\text{coefficient})] \cdot [F(\text{force})] = [I(\text{inertia})]$$

$$\Downarrow$$

$$[F] = [A]^{-1} \cdot [I] \tag{14}$$

4.2 Forward dynamics

The forward dynamical problem involves finding the position and kinematics of the system corresponding to a given set of input forces and torques applied on. For the given mechanism, the inputs forces and torques are known, and the kinematics of the robot is to be found. If we consider, in addition, that the support foot can slid, x_1 varies and the biped becomes a 2DOF dynamical system, as the x coordinate of all the links increases in x_1.

Then, the linear COM and angular velocities and accelerations of all the links can be expressed as:

$$\begin{aligned}
\dot{x}_i &= \frac{dx_i}{dx_1}\dot{x}_1 + \frac{dx_i}{d\theta_8}\dot{\theta}_8 = \dot{x}_1 + \frac{dx_i(\theta_8)}{d\theta_8}\dot{\theta}_8 = \dot{x}_1 + x'_i(\theta_8)\dot{\theta}_8 \\
\ddot{x}_i &= \ddot{x}_1 + \frac{d^2x_i(\theta_8)}{d\theta_8{}^2}\dot{\theta}_8{}^2 + \frac{dx_i(\theta_8)}{d\theta_8}\ddot{\theta}_8 = \ddot{x}_1 + x''_i(\theta_8)\dot{\theta}^2{}_8 + x'_i(\theta_8)\ddot{\theta}_8 \\
\dot{y}_i &= \frac{dy_i}{d\theta_8}\dot{\theta}_8 = y'_i(\theta_8)\dot{\theta}_8 \\
\ddot{y}_i &= \frac{d^2y_i(\theta_8)}{d\theta_8{}^2}\dot{\theta}_8{}^2 + \frac{dy_i(\theta_8)}{d\theta_8}\ddot{\theta}_8 = y''_i(\theta_8)\dot{\theta}^2{}_8 + y'_i(\theta_8)\ddot{\theta}_8 \\
\dot{\theta}_i &= \frac{d\theta_i}{d\theta_8}\dot{\theta}_8 = \theta'_i(\theta_8)\dot{\theta}_8 \\
\ddot{\theta}_i &= \frac{d^2\theta_i(\theta_8)}{d\theta_8{}^2}\dot{\theta}_8{}^2 + \frac{d\theta_i(\theta_8)}{d\theta_8}\ddot{\theta}_8 = \theta''_i(\theta_8)\dot{\theta}^2{}_8 + y\theta'_i(\theta_8)\ddot{\theta}_8
\end{aligned} \tag{15}$$

where $x'_i(\theta_8)$, $x''_i(\theta_8)$, $y'_i(\theta_8)$,$y''_i(\theta_8)$,$\theta'_i(\theta_8)$,$\theta''_i(\theta_8)$, are the first and second derivative of the variables in function of θ_8, that can be approximate to:

$$\begin{cases} \vartheta'_i(\vartheta_8) = \dfrac{1}{\Delta\vartheta_8}\left(\vartheta_i(\vartheta_8 + \Delta\vartheta_8) - \vartheta_i(\vartheta_8)\right) \\ \vartheta''_i(\vartheta_8) = \dfrac{1}{(\Delta\vartheta_8)^2}\left(\vartheta_i(\vartheta_8 + 2\cdot\Delta\vartheta_8) - 2\cdot\vartheta_i(\vartheta_8 + \Delta\vartheta_8) + \vartheta_i(\vartheta_8)\right) \end{cases}$$

$$\begin{cases} y_i'(\vartheta_8) = \dfrac{1}{\Delta\vartheta_8}\left(y_i(\vartheta_8 + \Delta\vartheta_8) - y_i(\vartheta_8)\right) \\ y_i''(\vartheta_8) = \dfrac{1}{(\Delta\vartheta_8)^2}\left(y_i(\vartheta_8 + 2\cdot\Delta\vartheta_8) - 2\cdot y_i(\vartheta_8 + \Delta\vartheta_8) + y_i(\vartheta_8)\right) \end{cases}$$

$$\begin{cases} x_i'(\vartheta_8) = \dfrac{1}{\Delta\vartheta_8}\left(x_i(\vartheta_8 + \Delta\vartheta_8) - x_i(\vartheta_8)\right) \\ x_i''(\vartheta_8) = \dfrac{1}{(\Delta\vartheta_8)^2}\left(x_i(\vartheta_8 + 2\cdot\Delta\vartheta_8) - 2\cdot x_i(\vartheta_8 + \Delta\vartheta_8) + x_i(\vartheta_8)\right) \end{cases}$$

(16)

Now, the Newton equations for all the links COM, and the torque dynamical equations lead to the following system:

$$\begin{cases} \sum\limits_{j<i} f_{ji_x} - \sum\limits_{k>i} f_{ik_x} - m_i\ddot{x}_1 - m_i x_i^{pf}{}'(\vartheta_8)\ddot{\vartheta}_8 = m_i x_i^{pf}{}''(\vartheta_8)\dot{\vartheta}_8^{\,2} \\ \sum\limits_{j<i} f_{ji_y} - \sum\limits_{k>i} f_{ik_y} - m_i y_i'(\vartheta_8)\ddot{\vartheta}_8 = m_i g + m_i y_i''(\vartheta_8)\dot{\vartheta}_8^{\,2} \\ \sum\limits_{j<i} T_{ji} - \sum\limits_{k>i} T_{ik} + \sum\limits_{j<i}\left(r_{ij_x} f_{ji_y} - r_{ij_y} f_{ji_x}\right) - \sum\limits_{k>i}\left(r_{ik_x} f_{ik_y} - r_{ik_y} f_{ik_x}\right) - I_i\vartheta_i'(\vartheta_8)\ddot{\vartheta}_8 = I_i\vartheta_i''(\vartheta_8)\dot{\vartheta}_8^{\,2} \end{cases}$$

(17)

Or in the matrix form:

$$\left[\begin{array}{cccccc:c} a_{11} & a_{12} & \cdots & a_{1,73} & 0 & & -m_1 \\ a_{21} & a_{22} & \cdots & a_{2,73} & 0 & & 0 \\ a_{31} & a_{32} & \cdots & a_{3,73} & -m_2 x_2^{pf}{}'(\vartheta_8) & & -m_2 \\ a_{41} & a_{42} & \cdots & a_{4,73} & -m_2 y_2'(\vartheta_8) & & 0 \\ a_{51} & a_{52} & \cdots & a_{5,73} & -I_2\vartheta_2'(\vartheta_8) & & 0 \\ \vdots & \vdots & \ddots & \vdots & \vdots & & \vdots \\ \cdots & \cdots & \cdots & \cdots & -I_8 & & 0 \\ \vdots & \vdots & \vdots & \ddots & \vdots & & \vdots \\ a_{74,1} & a_{74,2} & \cdots & a_{74,73} & -I_{13'}\vartheta_{13'}(\vartheta_8) & & 0 \\ \hdashline & & & & & & \end{array}\right] \cdot \begin{bmatrix} f_{01x} \\ f_{01y} \\ f_{12x} \\ f_{12y} \\ \vdots \\ . \\ f_{10',12'y} \\ \ddot{\vartheta}_8 \end{bmatrix} = \begin{bmatrix} 0 \\ m_1 g \\ m_2 x_2^{pf}{}''(\vartheta_8)\dot{\vartheta}_8^{\,2} \\ m_2 g + m_2 y_2''(\vartheta_8)\dot{\vartheta}_8^{\,2} \\ I_2\vartheta_2''(\vartheta_8)\dot{\vartheta}_8^{\,2} \\ \vdots \\ T_{8,14} \\ \vdots \\ . \end{bmatrix}$$

$$[A(\text{coefficients})]\cdot\left[F(\text{strength}, \ddot{\vartheta}_8, \ddot{x}_1)\right] = [I(\text{inertial})] \Rightarrow [F] = [A]^{-1}\cdot[I]$$

(18)

The dynamics for the whole footstep is obtained by time iteration over the equation system (18). The inputs of this system are the motor torque, T_8, and quantities that can be approximately obtained, for each time step, from equations (16).

5 NUMERICAL RESULTS

The kinematical and dynamical equations have been implemented in a MATLAB code in order to obtain solutions (position, velocities, acceleration, as well as forces and torques) depending of a set of parameters (link dimensions, masses, and densities, motor angular velocity) entered by the user. This code is being integrated into the movement control task.

As the first result, the program implemented in MATLAB®, has helped us to choose the suitable actuators and transmission systems, from the crank torque. This code will allow us to obtain in a fast way all the dynamic and kinematical parameters of interest for control and optimization tasks.

The main advantage of the developed program is that it let us perform fast modifications, making easier the final robot design by selecting new materials, choosing actuators and reduction devices, or even applying any type of optimization process.

As an example of the capacities of the program, some results are presented. **Fig. (6)** shows the actuator torque in the crank (link number 8) related to time, for different values of the motor angular velocity, ω_8.

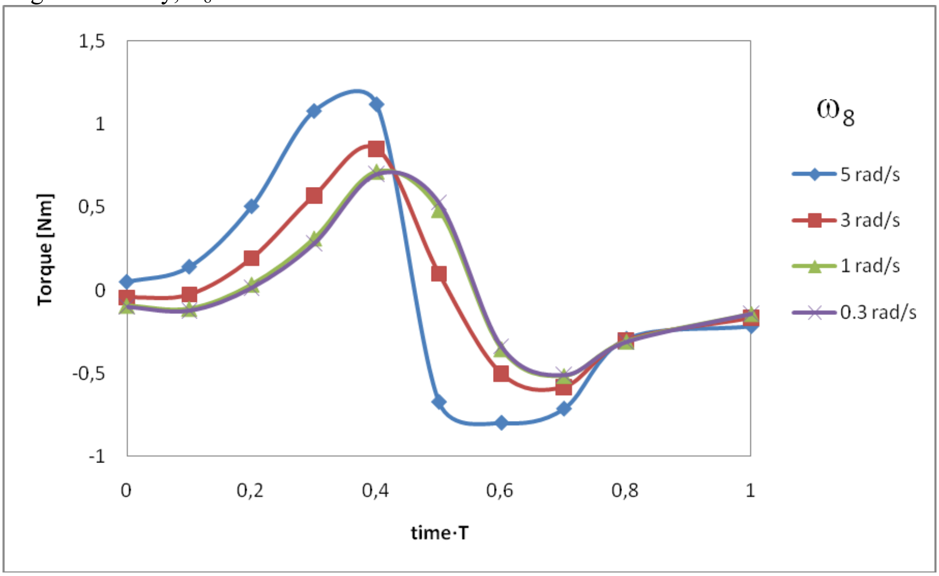

Fig. (6): Actuator torque for different crank velocities. T is the semi-period for the rotation of the motor crank, that is, the time for one PASIBOT's step

Another interesting result concerns the motor torque required when the robot load increases (when different actuators, transmissions, batteries, wires, etc. are included in the robot hip). In **Fig. (7)** the crank torque is represented again, but for different loads (5, 10 and 15 Kg) added to the hip.

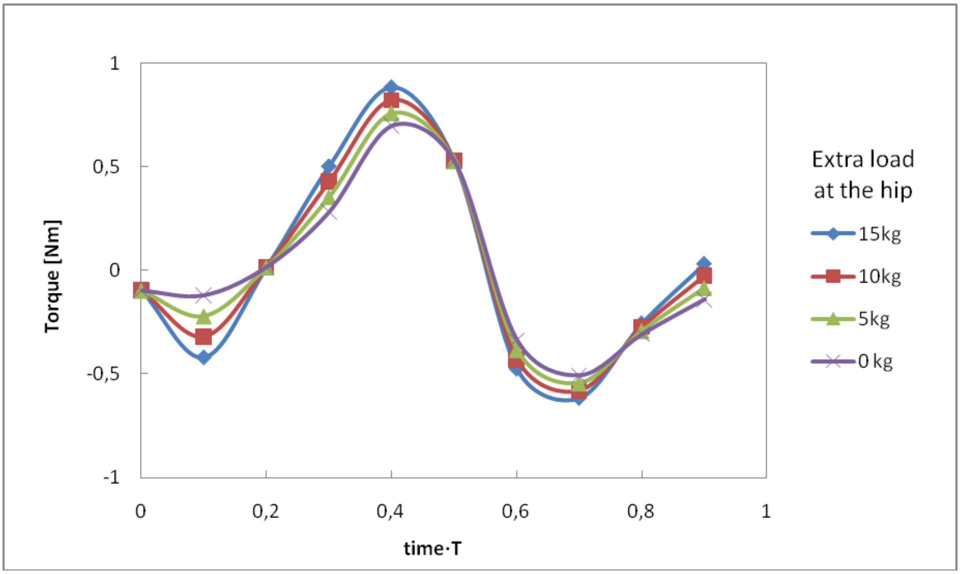

Fig. (7): Actuator torque for different hip extra loads

The graph in **Fig. (7)** shows that the required motor torque depends slightly on the added load. This is because the hip remains at almost the same level in a course of a step. Nevertheless, since the robot begins from the rest position, the differences between the required torques are significant only over the first period of the step. In fact, in the stationary walking state, practically all the motor torque is spent raising alternatively the flying leg, while the supporting leg sustains the rest of the weight -that of the hip, mainly- in such a way that the hip centre of mass moves almost horizontally at constant speed.

But direct dynamics is particularly valuable in transient regime calculations, answering questions like ¿which is the minimum applied motor torque PASIBOT needs to carry out a step (or begin walking) from rest? That is shown in **Fig. (8)**, indicating that the torque above which the biped is able to begin walking is 0.84Nm (below this value, it has not enough power to take a step). Actually, the presented dynamics provides a tool to calculate the movement of the PASIBOT when any variable torque is applied to the crank.

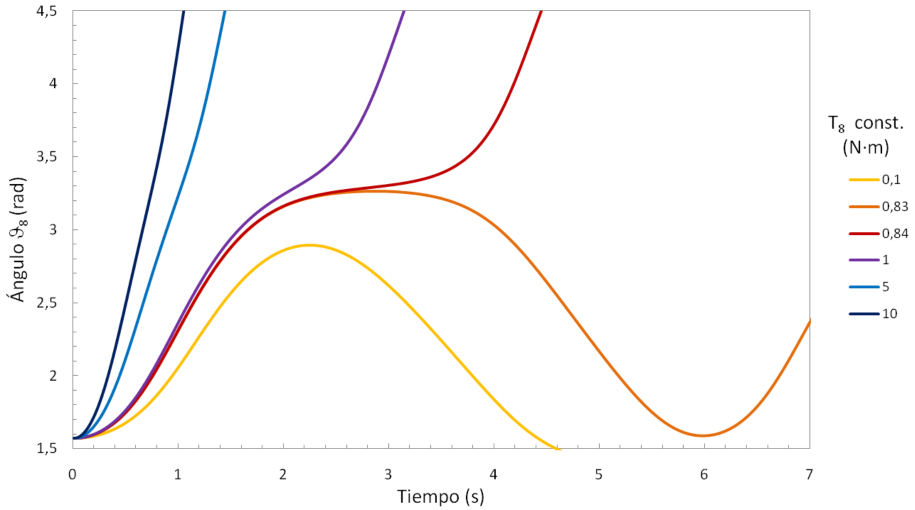

Fig. (8): movement of the PASIBOT for different (constant) torques

6 CONCLUSIONS

A prototype of a quasi-passive biped called PASIBOT has been presented. The mobility of the presented robot is depending only on one link that is actuated by a conventional electrical motor. Kinematical and dynamical (inverse and forward) expressions for a PASIBOT gait have been obtained. A program code has been developed to get parametric solutions from these expressions.

Thank to the proposed code for resolving forward dynamics, it is possible to calculate the initial torque required for the biped to walk, or how the robot moves after a specific time-dependent torque and/or external forces.

The kinematic part of the program has been validated by comparison with other commercial software. The developed code has been used to study the PASIBOT behavior before its construction, reducing the complexity in the design process; it is also to be used in control tasks for the real prototype walking. Forward dynamics would give more useful information than inverse dynamics in those kinds of tasks.

With respect to the presented numerical results, we can highlight the dependency of the load at the hip and the rotational input speed in the actuator torque, which let us to study the most suitable actuator for the movement requirements.

ACKNOWLEDGEMENTS

The authors wish to thank the Spanish Government for financing provided through the MCYT project DPI-2006-15443-C02-02 , and the LARM laboratory, specially professors Ceccarelli and Ottaviano for their suggestions in the design process of PASIBOT.

REFERENCES

[1] Yu Ogura; Hiroyuki Aikawa; Kazushi Shimomura; Hun-ok Lim; Atsuo Takanishi. “Development of a New Humanoid Robot WABIAN-2”. Proceedings IEEE International Conference on Robotics and Automation, pp 76-81, Florida, May 2006.

[2] Hirose, M; Ogawa, K. “Honda humanoid robots development”. Philosophical Transactions of the royal society A-Mathematical physical and engineering Sciences. Vol.: 365, Issue: 1850, Pages: 11-19, January 15, 2007.

[3] Masato H.; Kennichi O. “Honda Humanoid Robots Development“. Philosophical Transactions of the Royal Socierty A, Series A, (Mathematical, Physical and Engineering Sciences), vol. 365, num. 1850, pp 11-19, 2007.

[4] Akachi K.; Kaneko K.; Kanehira N. “Development of Humanoid Robot HRP-3P”. Proceeding 5th IEEE-RAS International Conference on Humanoid Robots,pp. 50-55, London 2005.

[5] Maqlab Research Group (University Carlos III de Madrid) web site: http://maqlab.uc3m.es/proyectos/pasibot/pasibot.htm (last visit: june 2011)

[6] Tavolieri C., Ottaviano E., Ceccarelli M., Di Rienzo A., “Analysis and Design of a 1-DOF Leg for Walking Machines”, Proceedings of RAAD’06, 15th International Workshop on Robotics in Alpe-Adria-Danube Region, Balantonfured, CD Proceedings, 2006.

[7] Castejón C., Carbone G., García-Prada J.C., Ceccarelli M. “A Multi-Objective optimization of a robotic arm for service tasks”. Strojniški vestnik - Journal of Mechanical Engineering, volume 56, number 5, May 2010, pp. 316-329

[8] Y. Hu, H. Nakamura, Y. Takeda, M. Higuchi, K. Sugimoto, “Development of a Power Assist System of a Walking Chair Based on Human Arm Characteristics” Journal of Advanced Mechanical Design, Systems and Manufacturing. Vol. 1. nº 1. 141-154. 2007.

Proceedings of MUSME 2011, the International Symposium
on Multibody Systems and Mechatronics
Valencia, Spain, 25-28 October 2011

ROBOT TRAJECTORY PLANNING USING CUBIC B-SPLINES IN JOINT SPACE

Werley Rocherter Borges Ferreira*, João Carlos Mendes Carvalho†
School of Mechanical Engineering
Federal University of Uberlandia, Campus Santa Monica, 38400-902 Uberlandia, Brasil
* e-mail: wrbferreira@mestrado.ufu.br
† e-mail: jcmendes@mecanica.ufu.br

Keywords: B-spline, trajectory planning, robotics, curve approximation.

Abstract. *Industrial robots and several researches for optimization of trajectory planning use cubic splines for defining the path function. This is due to its second derivative is set to zero at each end points obtaining a simple system to calculate its coefficients. Nevertheless, a spline is constructed from all points that define the curve. Then, changing one point changes the entire curve. B-spline curves have a local control i.e., if a point is changed only its nearest neighbor region is modified. Then, this paper addresses a trajectory planning using cubic B-spline. Results show that using the time parameterization proportional to the chord length the obtained curve can be predictable. Simulations for a 6 d.o.f. serial robot show the behavior of the end effector trajectory as well the joint ones.*

1 INTRODUCTION

Robots has been used in several industrial applications such as in assembly and disassembly processes, packing, painting, tool and object handling, and so on. A large number of these robotic applications involve repetitive processes and then a proper trajectory planning has an important role in the robotic process.

A trajectory planning problem consists of finding a relationship between time and space and that can be studied based on a desired motion to perform a specific task [1]. Basically a trajectory planning means planning the end effector path to perform a specific task preventing collisions in a minimal time. Others objectives can be considered to avoid undesirable effects such as vibrations and wear of mechanical components, to design the system by choosing and sizing the actuators and transmission devices, reducing errors during the motion execution, optimizing the performances of the system and others.

A time optimization in an industrial process is directly related to high-velocity production, which is also applied for a robotic system. Then, minimizing a robotic process the robot must operate at high velocities at all points along the programmed path and on an optimum trajectory. Important research activities to obtain optimum trajectories have been carried out through algorithms for minimizing the traveling time like presented by [2], [3], [4], [5], [6], [7], [8], [9] and [10]. However, the problem is not so simple to solve because the optimization problem involves several constraints like joint velocities, accelerations and jerks, power consumption, input torque/force constraints, manipulator dynamics, maximum actuators torques and so on [11]. Then, the planning of the robot trajectory is very important, principally when it operates at high velocities [12].

In general the end effector path is defined by a set of via points, to perform the desired task, where a curve can be obtained by interpolation or approximation methods. The interpolation method consists in obtaining a polynomial curve that pass through the points, while on the approximation the curve passes near the points. Planning the path on time the trajectory can be obtained.

The trajectory can be done by point-to-point motion or by a continuous motion. In the continuous motion the robot end effector traces a continuous trajectory along a curve. The curve can be done by a geometric function and both the end effector position and orientation should be defined along the trajectory [13]. The continuous trajectory is used in tasks such as laser cutting and sealant applications.

In the point-to-point motion the robot end effector moves from an initial pose to a final pose, the velocities and accelerations at the ends are zero and the described trajectory between points is not important. Then, it can be applied when no obstacles exist and are commonly used in pick-and-place operations for material handling and spot welding. This kind of motion can also be done when the robot should describe a specific path avoiding obstacles and/or passing through an important position. In this case one should have as many points as necessary for a good definition of the path. The robot stops at each intermediate point.

Both trajectories can be planned in joint space or in task space. In general the task space is defined in Cartesian space. When the trajectory planning is done in the task space the inverse kinematics must be solved and, if the planning is done in the joint space the end effector behavior must be analyzed because it cannot describe the desired trajectory. In both cases the robot trajectory should be as smooth as possible in order to avoid abrupt changes in position, velocities and accelerations.

As the motion control acts on actuators level, the trajectory planning can be analyzed in joint space. Then, firstly an adequate number of points are used to define the desired trajectory in the task space, usually using Cartesian coordinates. Then, from the inverse kinematics the correspondent joint coordinates are obtained for each point. Finally, each set of joint coordinates should be used by an approximation and/or interpolation method to obtain a smooth trajectory [14].

For pick-and-place operations several techniques are available for planning the desired movement, each of them with peculiar characteristics such as initial and final positions, velocities, accelerations, jerk, duration and so on, like presented by [1], [15], [16] and [17], in general using a function defined between the initial and final points.

When the trajectory is defined by a set of points P_i, the interpolation problem consists in obtaining a polynomial $S(\tau) = \sum_{j=0}^{n} a_j \tau^j$, whose coefficients a_j can be obtained by solving a system with $(n+1)$ linear equations and $(n+1)$ unknowns, satisfying the boundary conditions. As higher is the number of points P_i as higher is the degree n of the polynomial, since to obtain a polynomial of degree n, $n+1$ points are needed.

The polynomial interpolation is not recommended for a high number of points because the process has high computational cost for solving the system to obtain the a_j coefficients. In addition, the obtained high order polynomial has an inadequate profile for robotic trajectories, presenting abrupt variations between points.

One alternative consists in dividing the set of points in sub-set of points, where low order polynomials can be obtained for each sub-set of points. The final curve is a composed curve by a set of particular polynomials which are connected between them at its extremities, subject to adequate boundary conditions that, for robotics trajectories, corresponds to smooth continuity. This procedure is called as piecewise polynomial interpolation (or piecewise polynomial approximation) which each curve segment is represented by a function. Although there exists the continuity at the connection points, the differentiation continuity is not guarantee.

The piecewise polynomial interpolation is the base for obtaining splines, B-splines and NURBS (Non-Uniform Rational B-Spline) curves. A order $(p+1)$ spline with knots u_i $(i=0, \dots, n)$ is a piecewise polynomial of order $(p+1)$, and has continuous derivatives up to order $p-1$. For example, a cubic spline has order four and is constructed of piecewise cubic polynomials which pass through a set of control points. The cubic spline is commonly used for planning trajectories because if the second derivative of each polynomial is set to zero at the end points, the system becomes a simple tridiagonal system which can be solved easily to obtain the coefficients of the polynomial. This spline is called “natural cubic spline”.

The spline is then a continuous piecewise polynomial that is constructed based on all control points of the curve. A change in any point causes the change in the entire curve. This behavior is, in general, inappropriate for interactive curve fitting. In Figure 1 is shown this behavior for a cubic spline where control point P_4 is changed. One can see that changing only one point the entire curve is changed.

In order to overcome this problem, one can use B-spline curves that implements the local control of the curve, i.e., changes in control points propagate only to the nearest neighbor, according to their order of continuity. In general, for a $(p+1)$ order B-spline the curve is changed over the $\pm(p+1)/2$ spans as can see on Fig. 2. One can see in Fig. 2 that changing point P_4 only its nearest regions were changed. B-spline is, in reality, a curve fitting by approximation because the generated curve does not pass on the control points like in spline curves. If it is necessary pass the curve through the control points, an interpolation can be done by obtaining new control points from the known data points [18], [19], [20].

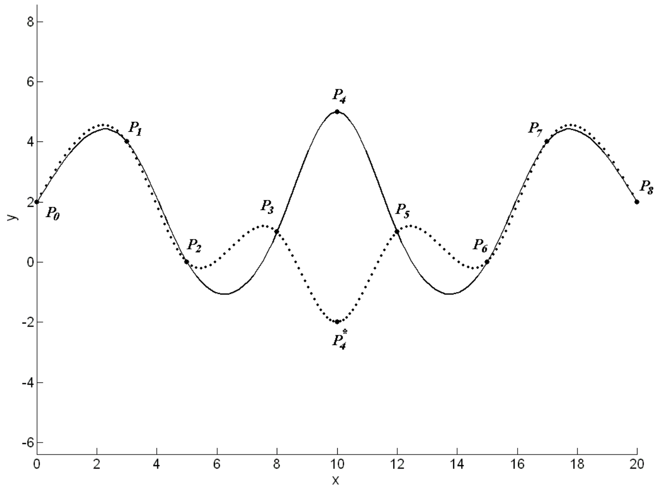

Figure 1: Behavior of a cubic spline curve for changing a control point.

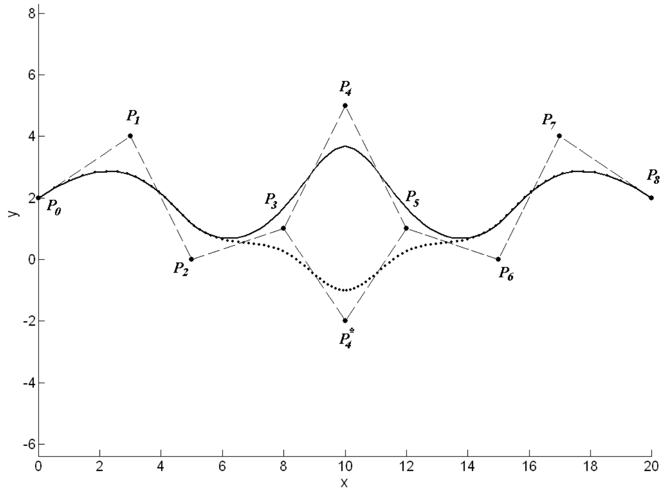

Figure 2: Behavior of a cubic B-spline curve for changing a control point.

The local control of B-apline curves is an important characteristic for applying in robot planning trajectories in view of avoiding obstacles. In this paper is presented the first step of a robotic trajectory planning using a cubic B-spline curve, i.e., the analysis of the trajectory without considering the robot dynamics. The methodology is applied to a 6 d.o.f serial robot. Using B-spline curves the robot motion is predictable both using the task space as the joint space. For that, an introduction to B-spline curves is presented and, in order to apply the methodology to an industrial robot, its kinematics model is presented and finally simulations are presented.

2 B-SPLINE INTERPOLATION AND CUBIC B-SPLINE

Authors like Piegl & Tiller [18] De Boor [19] and Rogers [20] define a B-spline as a spline that implements the local control of the curve, in such a way that changes in control points propagates only to the nearest points according the order of the continuity. The continuity, or smoothness, is associated to parametric curves and surfaces and can be geometric continuity and parametric continuity. For details of continuity conditions and types see [18], [19] and [20].

An important characteristic of B-spline is that the curve is within the convex hull of the control polygon, i.e., the convex polygon defined by the control polygon vertices that defines each curve segments. This means that it is possible to predict the curve behavior.

The flexibility of B-spline basis functions lead to the flexibility of the B-spline curves. Then, several types of control handles can be used to modify the shape of a B-spline curve such as changing the type of knot vector and hence basis function-periodic uniform, open uniform or non uniform; changing the order $(p+1)$ of the basis function; changing the number and position of the control polygon vertices; using multiple polygon vertices and using multiple knot values in the knot vector [20].

In this paper the basis functions $N_{i,p}(u)$ are defined by the Cox-de Boor recursion formulas. As shown in [18], let $U=\{u_0,...,u_m\}$ be a nondecreasing sequence of real numbers i.e., $u_i<u_{i+1}$, $i = 0,1,...,(m-1)$, where u_i are called *knots* and U the *knot vector*. The *i-th* B-spline basis function of p-degree (order $p+1$), denoted by $N_{i,p}(u)$, is defined as

$$N_{i,0}(u) = \begin{cases} 1 \; if \; u_i \le u \le u_{i+1} \\ 0 \quad otherwise \end{cases} \tag{1}$$

$$N_{i,p}(u) = \frac{u-u_i}{u_{i+p}-u_i} N_{i,p-1}(u) + \frac{u_{i+p+1}-u}{u_{i+p+1}-u_{i+1}} N_{i+1,p-1}(u) \tag{2}$$

Then, known the basis function and for a set of points P_i ($i = 0,..., n$) the B-spline curve is defined as

$$C(u) = \sum_{i=0}^{n} N_{i,p}(u) P_i \tag{3}$$

In this case the curve does not pass through the control points. However, if it is necessary, one can obtain new control points and a new knot vector from the data points.

If a set of points $\{Q_k\}$, $k = 0,..., n$, is known one can to obtain a B-spline curve from them. If for each Q_k of the curve there is a corresponding knot $\bar{u}_k$, and a knot vector $U = \{u_0,..., u_m\}$ can be chosen to obtain the basis function. Then, a system composed by $(n+1)(n+1)$ equations can be solved:

$$Q_k = C(\bar{u}_k) = \sum_{i=1}^{n} N_{i,p}(\bar{u}_k)\, P_i \tag{4}$$

Where the control points P_i are the $(n+1)$ unknowns.

Since the values of $\bar{u}_k$ and U affect the shape and parameterization of the curve, an adequate choice should be done. Basically there are three common methods for chosen the $\bar{u}_k$. The usual method that gives a good parameterization is by the chord length and that is used here.

Let d the total chord length given by

$$d = \sum_{k=1}^{n} |Q_k - Q_{k-1}| \tag{5}$$

Then, $\bar{u}_k$ can be obtained proportionally to the chord length as

$$\begin{aligned} \bar{u}_0 &= 0 & \bar{u}_n &= 1 \\ \bar{u}_k &= \bar{u}_{k-1} + \frac{|Q_k - Q_{k-1}|}{d} & k &= 1, \dots, n-1 \end{aligned} \tag{6}$$

Then, the knot vector should be obtained in order to calculate the basis function. The most appropriated method is the technique of averaging because the knots reflect the distribution of $\bar{u}_k$. The averaging technique is given as

$$\begin{aligned} u_0 = \dots = u_p &= 0 & u_{m-p} = \dots = u_m &= 1 \\ u_{j+p} &= \frac{1}{p} \sum_{i=j}^{j+p-1} \bar{u}_i & j &= 1, \dots, n-p \end{aligned} \tag{7}$$

From the knot vector the basis function can be obtained and the control points can be calculated from Eq. (4).

For a cubic B-spline, $p=3$. Then, if a control point is changed, the curve regions that are changed is composed by four curve segments, two before the control point and two after.

3 KINEMATIC MODEL FOR A 6 D.OF. SERIAL ROBOT

The trajectory planning using cubic B-spline has been applied to a 6 d.o.f. serial robot. Its kinematic model was described using homogeneous matrices from reference frames attached to the robot as sketched in Fig. 3, [21]. Both the direct and inverse kinematics had been obtained in analytical form. The end effector orientation is given by (z,x,z) Euler angles θ, φ and ψ.

The direct kinematics is given by

$$T_{07} = \begin{bmatrix} u_x & v_x & w_x & x_0 \\ u_y & v_y & w_y & y_0 \\ u_z & v_z & w_z & z_0 \\ 0 & 0 & 0 & 1 \end{bmatrix} \tag{8}$$

Where,

$$x_0 = sq_1\{-c(q_2+q_3)[cq_5(a_6+a_7)+a_4+a_5]+s(q_2+q_3)a_3+sq_2a_2-a_1\}+sq_5(a_6 + a_7)[cq_1sq_4+cq_4sq_1s(q_2+q_3)] \tag{9}$$

$$y_0 = cq_1\{c(q_2+q_3)[cq_5(a_6+a_7)+a_4+a_5]-s(q_2+q_3)a_3-sq_2a_2+a_1\}+sq_5(a_6 + a_7)[sq_1sq_4-cq_4cq_1s(q_2+q_3)] \tag{10}$$

$$z_0 = s(q_2+q_3)[cq_5(a_6+a_7)+a_4+a_5]+c(q_2+q_3)[cq_4sq_5(a_6+a_7)+a_3]cq_2a_2+h_1 \tag{11}$$

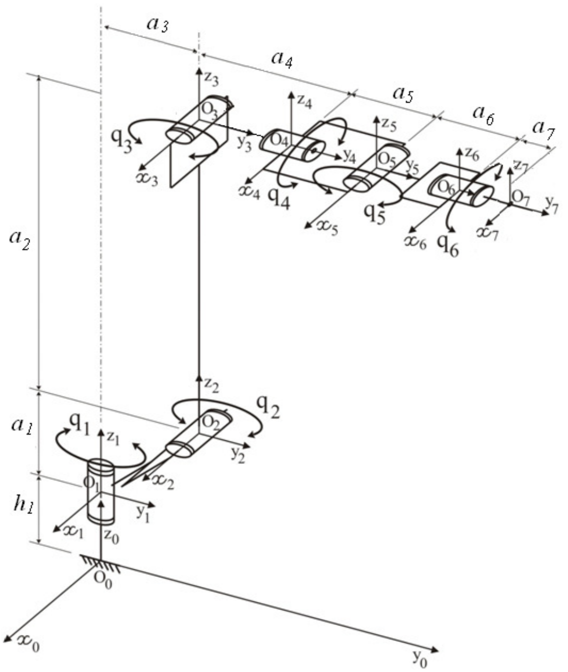

Figure 3: Sketch of the 6 d.o.f. serial robot and its parameters.

$$u_x = c(\varphi)c(\psi) - s(\varphi)c(\theta)s(\psi) \qquad u_y = s(\varphi)c(\psi) + c(\varphi)c(\theta)s(\psi) \qquad u_z = s(\theta)c(\psi)$$
$$v_x = -c(\varphi)s(\psi) - s(\varphi)c(\theta)c(\psi) \qquad v_y = s(\varphi)s(\psi) + c(\varphi)c(\theta)c(\psi) \qquad v_z = s(\theta)c(\psi)$$
$$w_x = s(\varphi)s(\theta) \qquad w_y = -c(\varphi)s(\theta) \qquad w_y = c(\theta) \tag{12}$$

The inverse kinematics is written as

$$q_1 = atan2\left[v_x(a_6+a_7) - x_0, y_0 - v_y(a_6+a_7)\right] \tag{13}$$

$$q_2 = atan2[\frac{-B \pm \sqrt{B^2 - 4AC}}{2AC}, k_2\frac{-B \pm \sqrt{B^2 - 4AC}}{2AC} - k] \tag{14}$$

$$q_3 = atan2\left\{\left[(a_4 + a_5)\frac{Na_3 + M(a_4 + a_5)}{{a_3}^2 + (a_4 + a_5)^2} - M\right]/a_3, \frac{Na_3 + M(a_4 + a_5)}{{a_3}^2 + (a_4 + a_5)^2}\right\} \tag{15}$$

$$q_4 = atan2\left[v_x c q_1 + v_y s q_1, v_x s q_1 s(q_2 + q_3) + v_y s q_1 c(q_2 + q_3) + v_z c(q_2 + q_3)\right] \tag{16}$$

$$\begin{cases} sq_5 = [cq_1 sq_4 - sq_1 cq_4 s(q_2 + q_3)]v_x + [sq_1 sq_4 - cq_1 cq_4 s(q_2 + q_3)]v_y + [cq_4 c(q_2 + q_3)]v_z \\ cq_5 = -sq_1 c(q_3 - q_2)v_x + cq_1 c(q_2 + q_3)v_y + s(q_2 + q_3)v_z \end{cases} \tag{17}$$

$$q_5 = atan2(sq_5, cq_5) \tag{18}$$

$$\begin{cases} sq_6 = [cq_1cq_4 - sq_1sq_4s(q_2+q_3)]w_x + [sq_1cq_4 + cq_1sq_4s(q_2+q_3)]w_y - sq_4c(q_3-q_2)w_z \\ cq_6 = [cq_1cq_4 - sq_1sq_4s(q_2+q_3)]u_x + [sq_1cq_4 + cq_1sq_4s(q_2+q_3)]u_y - sq_4c(q_3-q_2)u_z \end{cases} \tag{19}$$

$$q_6 = atan2(sq_6, cq_6) \tag{20}$$

Where

$$k_1 = -x_0sq_1 + y_0cq_1 - a_1 - (a_6+a_7)\left[v_ycq_1 - v_xsq_1\right]$$

$$k_2 = z_0 - h_1 + v_z(a_6+a_7)$$

$$k = \left[(a_4+a_5)^2 - a_2{}^2 + a_3{}^2 - \left(k_1{}^2 + k_2{}^2\right)\right]/-2a_2$$

$$A = k_1{}^2 + k_2{}^2 \qquad B = -2kk_2 \qquad C = k^2 - k_1{}^2$$

$$M = k_1cq_2 + k_2sq_2 \qquad N = k_1sq_2 + k_2cq_2 - a_2 \tag{21}$$

And q_j ($j = 1,...,6$) are the joint coordinates; $s\alpha = sin(\alpha)$; $c\alpha = cos(\alpha)$; $h_1 = 450\ mm$; $a_1 = 150\ mm$, $a_2 = 570\ mm$, $a_3 = 155\ mm$, $a_4 = 178\ mm$, $a_5 = 462\ mm$, $a_6 = 95\ mm$ and $a_7 = 20\ mm$.

4 PLANNING CUBIC B-SPLINE TRAJECTORY IN JOINT SPACE

The control of a robot motion is done at its joints and the planned curve from joint interpolation/approximation, function of time, is used as a set-point for controller. Then, each coordinate joint is associated to its time motion forming a ordered pair (t_i, q_j^i).

Let a trajectory defined by $n+1$ points Q_i ($i = 0,...,n$), in the task space. A cubic B-spline curve can be used to obtain the trajectory. As cited before the best parameterization is based on the chord length and is used in this analysis. Simulations showed that an uniform time parameterization produces a not adequate curve since it produces a non predictable behavior.

In order to verify the behavior of the planned curve in joint space, a curve in task space was defined from known points and using a cubic B-spline. From the known set of points that defines the desired end effector path and using the inverse kinematic the correspondent joint coordinates were calculated. These corresponding joint coordinates had been used to obtain a cubic B-spline in joint space. Using the direct kinematics the new end effector trajectory was obtained. Both end effector trajectory can be evaluated.

For parameterization the time is proportional to chord length in the same way that $\bar{u}_k$. From vector $\bar{U} = [\bar{u}_0, \dots, \bar{u}_k]$, the time is written as function of total motion time T as

$$t = T.\bar{U} = T[\bar{u}_0, \dots, \bar{u}_k] \tag{22}$$

In Figure 4 is presented an example for a planar trajectory defined by the known points Q_0(550,500,200), Q_1(700,520,200), Q_2(850,590,200), Q_3(900,590,200), Q_4(950,700,200), Q_5(980,730,200) and Q_6(1000, 800, 200). The continuous line represents the desired trajectory planned using cubic B-spline in task space and, in dashed line, the planned trajectory using cubic B-spline in joint space. One can note the similarity between curves. In Figure 5 the error between curves is presented.

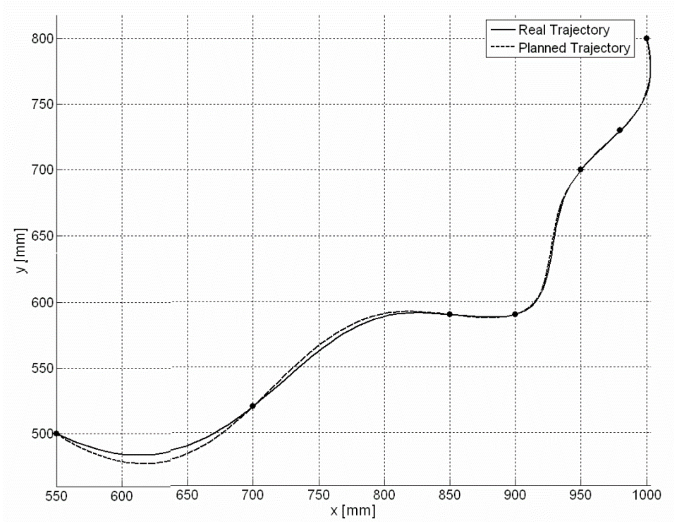

Figure 4: Trajectory planning using a cubic B-spline and time parameterization as function of length's chord.

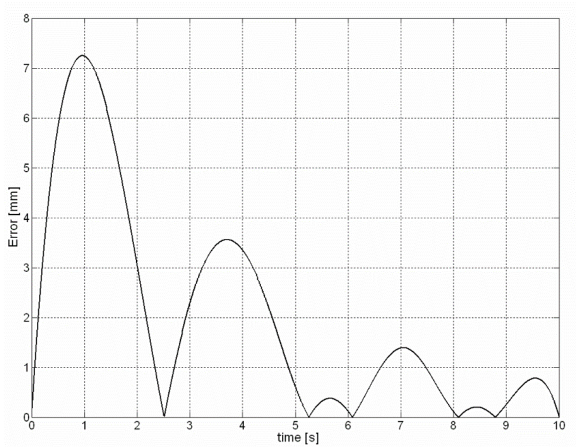

Figure 5: Error between the planned trajectories in joint and task space.

The methodology can be also used for a tridimensional trajectory as presented in Fig. 6 for points Q_0(400, 430, 252), Q_1(460, 400, 252), Q_2(520, 430, 276), Q_3(535, 490, 303), Q_4(490, 640, 354), Q_5(655, 655, 393), Q_6(760, 730, 444) and Q_7(850, 640, 426). The continuous line represents the desired trajectory planned using cubic B-spline in task space and, in dashed line, the planned trajectory using cubic B-spline in joint space. The error between both trajectories is presented in Fig. 7.

In Figure 8 are shown the behavior of each robot joint. One can see that each joint presents a smooth trajectory, following the end effector trajectory.

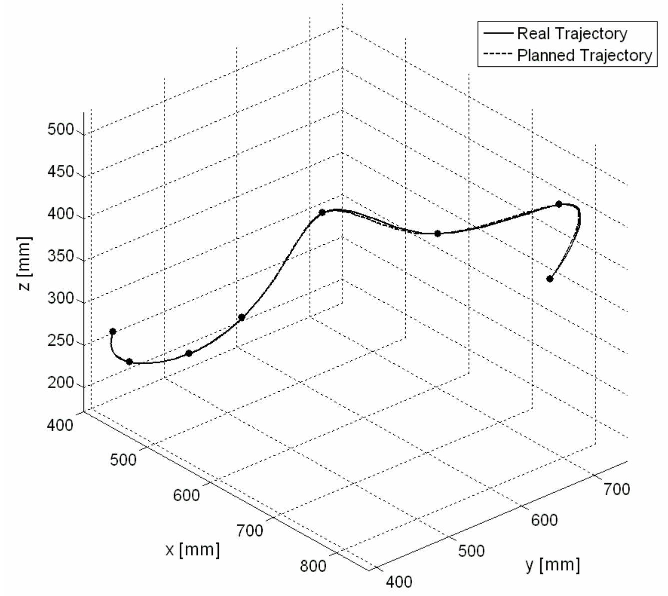

Figure 6: Tridimensional trajectory.

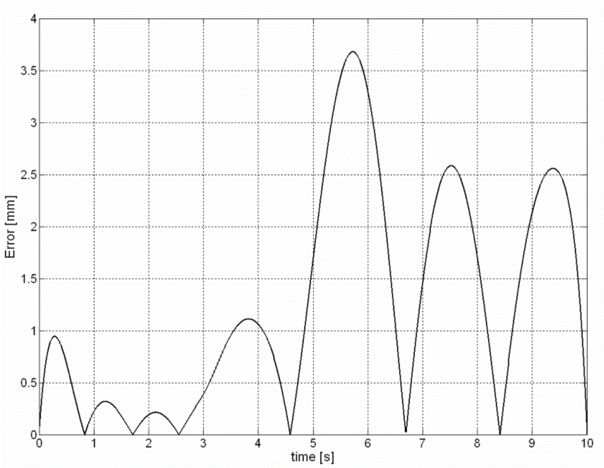

Figure 7: Error between the planned trajectories in joint and task space for tridimensional trajectory.

The error can be reduced by adding new points in defining the trajectory.

Similar analysis had been made for end effector orientation. Specifically for the presented examples the end effector was considered at vertical direction and pointing up. In all case the end effector remained at the same orientation. New analysis should be made in order to verify if orientation behavior is similar to the trajectory.

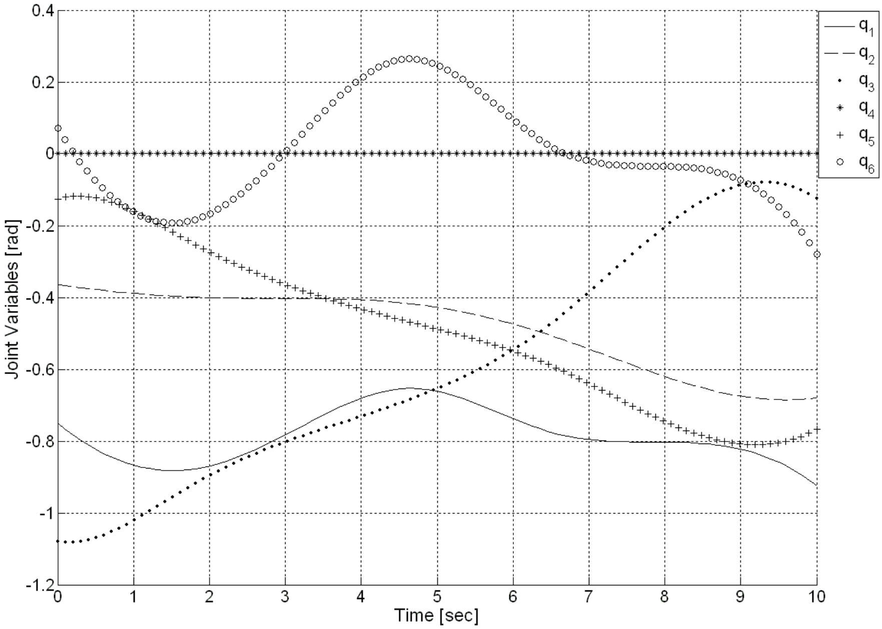

Figure 8: Trajectory of robot joint.

5 CONCLUSIONS

In this paper a trajectory planning using cubic B-spline curves had been presented. B-spline curves differ from usual spline curves in such way one can modify only a part of the curve, unlike the spline if one point is changed, the total curve is changed too. On B-spline curves one promotes only a local change.

Due to its convex hull propriety the behavior of the B-spline curve is predictable since its parameterization is done as a function of chord length as shown in presented examples. Although simulations for analysis of the end effector orientation had been done, maintaining it as defined along the trajectory, new analysis are necessary for a conclusion about its behavior.

In the presented analysis it was considered that actuators have the necessary power/torque and the control system can track the signal to promote the robot motion.

The obtained curve is smooth, without oscillations, what does not happen with a high order polynomial used for a trajectory planning defined by several points.

Using an adequate time parameterization a planned trajectory in joint space can be obtained quite similar to a trajectory defined in task space. Using a time parameterization as function of chord length one can eliminate the unpredictability of the movement, which is guaranteed by the convex hull propriety.

The next step of this study the robot dynamic characteristics will be considered in order to analyze the robot behavior.

ACKNOWLEDGEMENTS

Authors thanks CNPq and FAPEMIG for financial support for this project.

REFERENCES

[1] L. Biagiotti, C. Melchiorri. *Trajectory Planning for Automatic Machines and Robots.* Springer-Verlag, Berlin, 2008.

[2] J. Zhao, S.X. Bai. Load Distribuition and Joint Trajectory Planning of Coordinated Manipulation for Two Redundant Robots. *Mechanism and Machine Theory*, vol. 34, 1155-1170, 1999.

[3] C.G. Johnson, D. Marsh. Modelling Robot Manipulators with Multivariate B-Splines. *International Journal Robotica*, vol. 17, nº 3, 239-247, 1999.

[4] F.C. Park, J. Kim, J.E. Bobrow. Algorithms for Dynamics –Based Robot Motion Optimization. *Proceedings of 10th World Congress on the Theory of Machines and Mechanics - IFToMM*, Oulu, 1216-1221, 1999.

[5] Y.K. Choi, J.H. Park, H.S. Kim, J.H. Kim. Optimal Trajectory Planning and Sliding Mode Control for Robots Using Evolution Strategy. *International Journal Robotica*, vol. 18, nº 4, 423-428, 2000.

[6] S.F.P. Saramago,V. Steffen Jr. Trajectory Modeling of Robots Manipulators in the Presence of Obstacles. *Journal of Optimization Theory and Applications*, Kluwer Academic, vol. 110, nº 1, pp. 17-34, 2001.

[7] S.F.P. Saramago, M. Ceccarelli. An Optimum Robot Path Planning with Payload Constraints. *International Journal Robotica*, vol. 20, 395-404, 2002.

[8] S.F.P. Saramago, M.Ceccarelli. Effect of Some Numerical Parameters on a Path Planning of Robots Taking Into Account Actuating Energy. *Mechanism and Machine Theory*, vol. 39, nº 3, 247-270, 2004.

[9] P.J. Oliveira, S.F.P. Saramago, J.C.M. Carvalho, G. Carbone, M. Ceccarelli. An optimum path planning for Cassino Parallel Manipulator by using inverse dynamics. *Robotica (Cambridge)*, vol. 26, 229 – 239, 2007.

[10] R.R. Santos, S.F.P. Saramago, V. Steffen Jr. Optimal Task Placement of a Serial Robot Manipulator for Manipulability and Mechanical Power Optimization. *Intelligent Information Management*. , vol.2 , 512 – 525, 2010.

[11] F. Kim, S. Kim, S. Kim, D. Kim. A Practical Approach for Minimum-Time Trajectory Planning for Industrial Robots. *Industrial Robot*. v. 37, nº 1, 51-61, 2010.

[12] F. Rubio. The simultaneous algorithm and the best interpolation function for trajectory planning. *Industrial Robot*, vol. 37, nº 5, 441–451, 2010.

[13] S. Macfarlane. On-Line Smooth Trajectory Planning for Manipulators. *M.Sc. Thesis*, The University of British Columbia, Columbia Britânica, Canadá, 2001.

[14] T. G. Zheng, L. Feng, W. Y. Chao. Real-time Accurate Hand Path Tracking and Joint Trajectory Planning for Industrial Robots. *Journal of Central South University of Technology*, vol. 9, nº 3, 191-196, 2002.

[15] W.A. Wolovich. *Robotics: Basic Analysis and Design*, Holt, Rinehart and Winston, New York, 1985.

[16] Y.C. Chen. Solving Robot Trajectory Planning Problems with Uniform Cubic B-Splines. *Optimal Control Applications & Methods*, vol. 12, 247-262, 1991.

[17] Angeles, J. (1997). Fundamentals of Robotic Mechanical Systems: Theory, Methods, and Algorithms. Springer-Verlag, New York.

[18] L. Piegl, W. Tiller. The Nurbs Book. Springer, New York, USA, 1997.

[19] C. de Boor. *A Pratical Guide to Spline*. Springer, New York, USA, 2000.

[20] D. F. Rogers. *An Introduction to NURBS*. Morgan Kaufmann Publishers, San Diego, USA, 2001.

[21] L. W. Tsai. *Robot Analysis*. John Wiley, USA, 1999.

Proceedings of MUSME 2011, the International Symposium
on Multibody Systems and Mechatronics
Valencia, Spain, 25-28 October 2011

OMNIBOLA: A SPHERICAL ROBOT

Mariano Jaimez*, Juan A. Cabrera*, Juan J. Castillo* and Francisco García*

* Department of Mechanical Engineering
University of Málaga, Doctor Ortiz Ramos s/n, 29071 Málaga, Spain
e-mail: marianojt@uma.es,
web page: http://www.uma.es

Keywords: Spherical robot, dynamic model.

Abstract. *A spherical robot called Omnibola is introduced and analysed in this paper. Some advantages of this kind of robots compared with typical wheeled robots are described. Its geometry and its features are presented, emphasizing on those which make it different from other ball-shaped robots. A mathematical model has been developed in order to have a tool to study our robot dynamics. We carried out some experiments to confirm model results are similar to experimental results observed in the real robot.*

1 INTRODUCTION

Mobile robot research is a booming area of investigation, which takes its bases from mechanics, electronics and automation. Mobile robots find many applications in modern society. There are also many geometric configurations they may adopt. Some of them are aerial robots that adopt forms similar to airplanes or helicopters. Similarly, robots that can navigate over and under water have been developed. However, the most common are those that move over land. A wide and detailed classification of them is described by Siegwart and Nourbakhsh [1]. Within this classification, some use wheels in contact with the ground to move, others have legs or limbs that allow them to walk or run, and others feature more original solutions than before. Spherical robots are an example of them. As shown by Armour et al. [2], their perks are many. The most important ones are presented as follows:

- Spherical robots, due to their geometry, cannot overturn. Therefore, they are ideal for reconnaissance or inspection.

- They do not have limbs which can hang on certain obstacles.

- They are omnidirectional. In general, they can move in any direction on plane surface, so it is easier to avoid obstacles or to find feasible routes.

- All devices in the robot are usually enclosed in a type of spherical shell, so they are protected from direct impacts and corrosion.

They also have some disadvantages, such as the difficulty to overcome obstacles, or the complexity of their kinematics and dynamics.

In recent years, research centers around the world have built and analyzed spherical robots based on different operating principles [2][3]. Here a few are presented:

- Some spherical robots [4][5] base their motion on the conservation of angular momentum. They fix the position of the center of mass at the geometric center of the sphere and control their movement by regulating the movement of some rotors attached to them internally.

- Others move the center of mass of the robot to generate motion [6]. They use mobile masses whose position is regulated to achieve the desired motion.

- Some incorporate an internal mechanism that rotates freely within a spherical shell [7][8][9]. The mechanism generates and transmits motion to the case by non-holonomic constraints. To do this, the mechanism should move its center of gravity. In this case, the displacement of the center of gravity generates robot motion indirectly.

- There are examples of robots that attach a shaft to the outer case and cause the case to rotate around the axis [10][11]. In this case, the robot is spherical but not omnidirectional.

- Finally, we find different configurations of robots that are not exactly spherical, but they are similar in shape and behavior to them. For example, Brown et al. [12] describes an ellipsoidal robot that uses gyroscopic effect to stabilize and control its movement. Gheorghe et al. [13] present a robot with many telescopic legs that takes on a roughly spherical shape. This robot varies the length of its legs to generate movement.

The solution adopted in our department is included in the third classification. The structure of the Omnibola © is similar to the robots contained in that classification, but there are important differences in the design of the internal mechanism. These differences are discussed in the following section.

The script that we follow in this article is as follows. Section 2 describes in detail the geometry of our robot. In Section 3, its behavior is modeled mathematically. In section 4 experimental results are compared with those obtained by the mathematical model. In Section 5 conclusions and future lines of our work are summarised.

2 ROBOT DESIGN

In this section we analyze and describe the geometric configuration of our robot, and each of the component parts. As already mentioned at the end of Section 1, our robot is composed of:

• A spherical shell: whose exterior is in contact with the ground and with the external environment. The mechanism is in the interior part as described below.

• The internal mechanism: which integrates power supply, motors and all electronic devices that allow joint operation. This internal mechanism rotates inside the case, and interacts with it through a two-wheel drive.

To clarify the disposition of each of the elements in the internal mechanism, Figure 1 is attached:

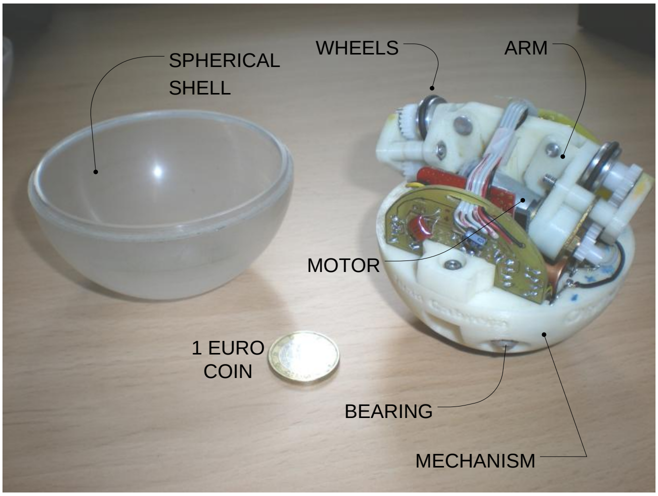

Figure 1.- Physical description of Omnibola© robot

The outer shell consists of two hemispheres that are screwed together. Figure 1 only shows the internal mechanism since it is the most complex to describe. The robot has two wheels in contact which transmit motion from the mechanism to the outer shell. If both wheels have the same speed, the robot moves in a straight line, and if their speeds are different, the robot describes a curved path. Omnibola© uses two DC motors. Each one moves to one of the wheels, so they work independently. The base of the internal mechanism places the most weight at the bottom of the robot, to improve stability. Four 1.5 V batteries are integrated inside the base and feed the engines, and a counterweight is located at the bottom of it. The arms contain the engines, transmission and wheels. They are attached to a joint with the mechanism base. To ensure contact between wheels and chassis, a spring is incorporated between the arms and the base of the internal mechanism, although in Figure 1 it cannot be observed.

Figure 2 illustrates schematically what the Omnibola © is like:

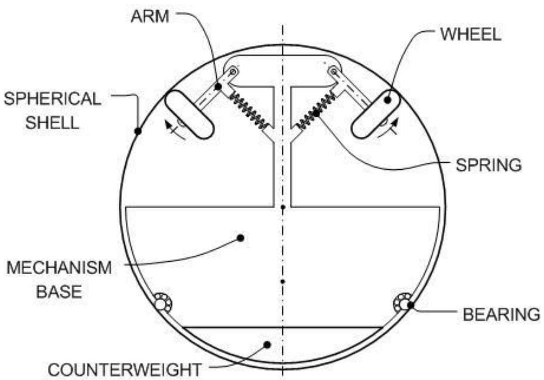

Figure 2.- Top perspective of the robot

The main difference between our robot and other spherical robots that use a similar configuration is that the center of gravity is located as low as possible, but the drive wheels are on top. These wheels always keep contact with the shell. If the internal mechanism overturns, it will be able to return to its stable state. In other words, if an external disturbance causes the point of contact between wheels and shell to be at the bottom of the robot, a voltage could be applied to recover stable configuration. Furthermore, if there is no external block, the gravity force will move the robot back to its stable position by itself. Figure 3 shows these kinds of behavior.

Consequently, our robot is statically stable and can always recover its orientation. Thanks to its geometry, the Omnibola © robot could be very useful in exploration and inspection missions in which omnidirectionality is important. An example would be the inspection of pipelines.

It is important to note that the power of the motors is controlled by remote control and that our robot has a diameter of 0.08 m, and a weight of 0.5 kg. It can reach speeds of up to 0.8 m / s. Due to its small size, is not able to overcome obstacles, unless these are very small.

In the future, the design of a new larger version of the robot is planned, which can move on rough surfaces and overcome larger obstacles.

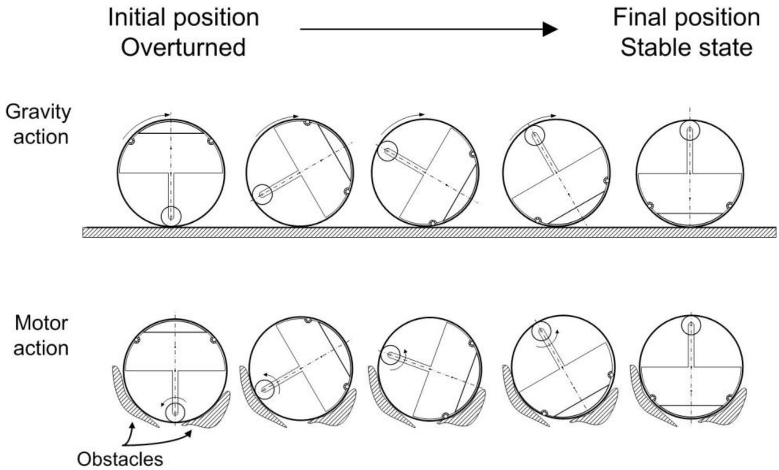

Figure 3.- Recovering from overturn when the robot is free (upper sequence) and when the robot is blocked (lower sequence)

3 ROBOT MODELING

In this section, we present and describe the equations which govern the behavior of the robot. At first, we define the reference systems we use in our study. We consider a still XYZ reference system with respect to which the motion of the robot is described. We also consider a xyz reference system attached to the internal mechanism that moves solidly with it. Finally, we use a x'y'z' reference system associated to the outer shell, but which is not fixed to it. This reference system will always have its origin at the geometric center of the sphere. The x'y' plane will always remain parallel to the XY plane of the still reference and the x' axis will always point in the direction of the robot's advance. This coordinate system is defined this way to simplify the mathematical formulation of the problem. Figure 4 helps to clarify the explanation:

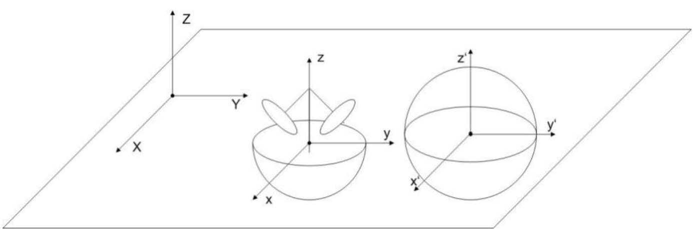

Figure 4.- Reference systems used in the mathematical model

After defining the coordinate references, the laws of Newton - Euler are applied to both bodies to study dynamic motion in mobile axes. Dynamic equilibrium of our system is considered, and therefore we include the acceleration terms as inertia forces, according to the principle of D'Alembert. The Tait – Bryan angles are used to know the internal mechanism orientation at each instant of time. The three rotations of this orientation method are summarized below. We apply a rotation around the Z axis to get the X1Y1Z1 system. This rotation is called yaw (Ψ), and is shown in Figure 5:

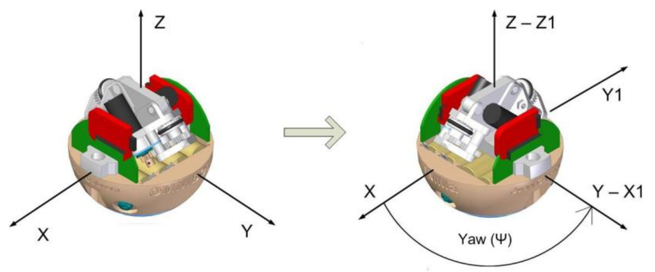

Figure 5.- First rotation. Yaw angle

Yaw marks the advance direction of our robot. Then we apply a second rotation around the Y1 axis and X2Y2Z2 system is obtained. This rotation is called pitch (ξ) and represents a forward and backward swing. It is shown in Figure 6:

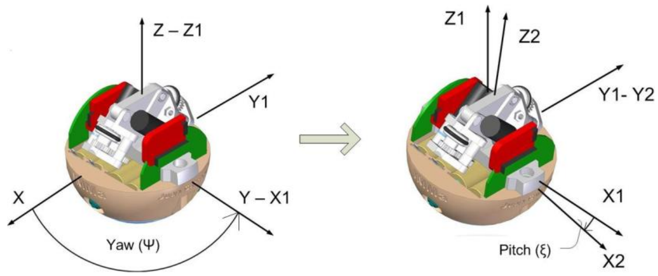

Figure 6.- Second rotation. Pitch angle

Finally, the mechanism is rotated around the X2 axis to obtain the final xyz coordinate system. This rotation is called roll (θ) and is shown in Figure 7:

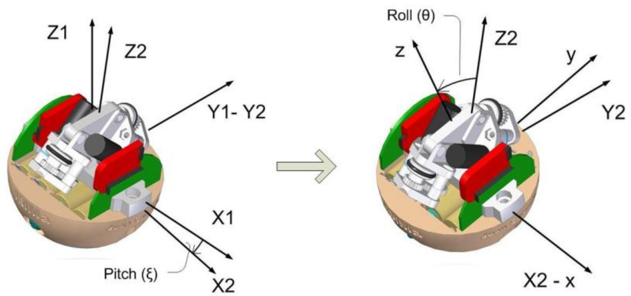

Figure 7.- Third rotation. Roll angle

Roll (θ) represents a lateral oscillation in the mechanism with respect to its direction of movement.

Once we have described the reference systems and the angles used to determine the orientation of our robot, we can raise the study of forces and moments applied to both the internal mechanism and the spherical shell. The schedule of forces and moments that serves as the basis for the construction of the mathematical model of the robot is attached. Figure 8 shows the scheme for the internal mechanism:

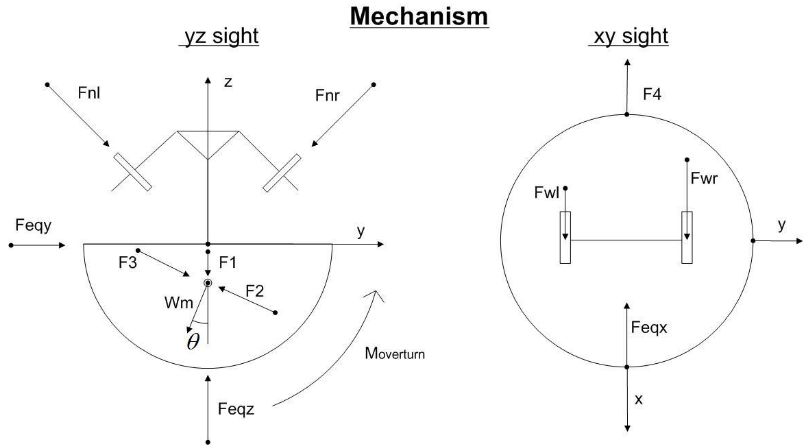

Figure 8.- Scheme of forces and torques in the internal mechanism

And Figure 9 shows the force schedule of the Shell:

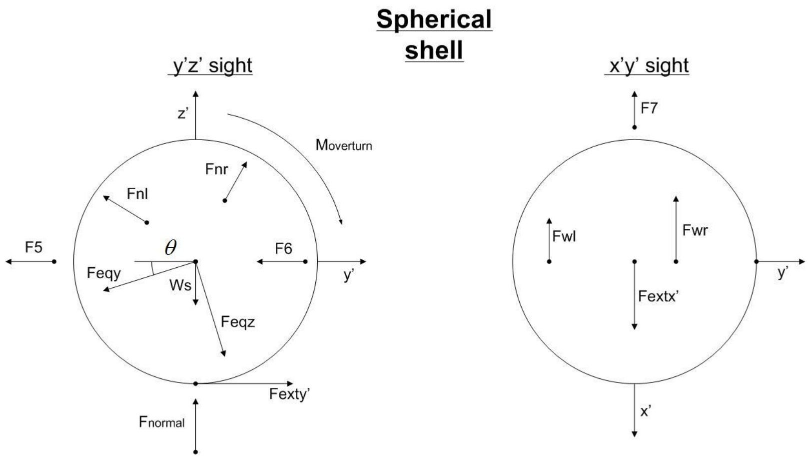

Figure 9.- Scheme of forces and torques in the spherical shell

Keep in mind that, for clarity of the drawing, it is considered that the mechanism has a positive roll angle and a zero pitch angle. Also, consider that the mechanism scheme is shown in xyz axes and the shell one is shown in x'y'z' axes.

From this scheme, we can apply the necessary equations to model our robot. The meaning of all terms displayed in Figure 8 and Figure 9 as well as those that will be presented in subsequent equations is explained in Table I.

SYMBOL	*MEANING*
F_{nl}, F_{nr}	Normal forces between wheels and shell
F_{wl}, F_{wr}	Motive forces between wheels and shell
$F_{eqx}, F_{eqy}, F_{eqz}$	Components of the "equivalent force". This force is used to model the bearing interaction between mechanism and shell
$M_{overturn}$	It models the overturn torque which exists between shell and mechanism due to the transverse force generated by the wheels in the yz plane
$F_i \ (i = 1,2 \ldots 7)$	Inner forces related with linear and normal acelerations
$F_{extx'}, F_{exty'}$	Ground forces acting in the shell
W_m, W_s	Mechanism and sphere weights
g	Gravity acceleration
F_{normal}	Normal force acting in the shell
$\varphi_x, \varphi_y, \varphi_z$	Mechanism angular velocity with respect to XYZ, described in the xyz reference
$\omega_x, \omega_y, \omega_z$	Sphere angular velocity with respect to XYZ, described in the x'y'z' reference
M_m, M_s	Mechanism and sphere masses
I_{mx}, I_{my}, I_{mz}	Mechanism moments of inertia with respect to the xyz reference
I_s	Sphere moment of inertia with respect to the x'y'z' origin
R_{se}, R_{si}	Outer and inner radius of the shell
D_{contz}	Distance between the contact point of wheels and the z axis
D_{conty}	Distance between the contact point of wheels and the y axis
R_r	Motive wheel radius
δ	Angle between the planes containing the wheels and the z axis
D_{cscm}	Distance between geometric center of the sphere and center of mass of the mechanism

Table 1.- Nomenclature, physical magnitudes

Some of these explained parameters are geometrical magnitudes. They are represented in Figure 10 so as to improve clarity about what they mean.

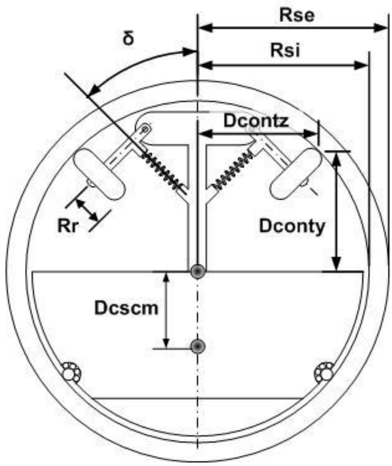

Figure 10.- Geometric parameters of the robot

It is necessary to indicate the expression of all the forces F_i $(i = 1,2 \dots 7)$ in terms of kinematic and dynamic parameters of robot motion:

$$F_1 = M_m \left(\varphi_x^{\,2} + \varphi_y^{\,2}\right) D_{cscm} \qquad (1)$$

$$F_2 = M_m \ \omega_y \ R_s \ \dot{\Psi} \qquad (2)$$

$$F_3 = M_m \ R_s \ \dot{\omega}_x \qquad (3)$$

$$F_4 = M_m \ R_s \ \dot{\omega}_y \qquad (4)$$

$$F_5 = M_s \ \omega_y \ R_s \ \dot{\Psi} \qquad (5)$$

$$F_6 = M_s \ R_s \ \dot{\omega}_x \qquad (6)$$

$$F_7 = M_s \ R_s \ \dot{\omega}_y \qquad (7)$$

All dynamical and geometrical variables have already been described. From here onwards, the equations which govern the behavior of the system are listed below.

$$F_{eqx} = F_{wl} + F_{wr} + M_m \ g \cos(\theta) sin(\xi) \qquad (8)$$

$$F_{eqy} = M_m \ g \ sin(\theta)\cos(\xi) + M_m \ \omega_y \ R_{se} \ \dot{\Psi} \cos(\theta) \qquad (9)$$

$$F_{eqz} = M_m \ g \cos(\theta)\cos(\xi) + (F_{nl} + F_{nr})\cos(\delta) +$$

$$+ M_m \left(\varphi_x^{\,2} + \varphi_y^{\,2}\right) D_{cscm} - \left| M_m \ \omega_y \ R_{se} \ \dot{\Psi} \ sin(\theta) \right| \qquad (10)$$

To apply the Euler equations to the mechanism we consider that the reference system xyz is closely linked to it. In this case, the Euler equations adopt the format shown as follows:

$$M_x = I_{mx}\ \dot{\varphi}_x + \varphi_y\ \varphi_z \left(I_{mz} - I_{my}\right) \qquad (11)$$

$$M_y = I_{my}\ \dot{\varphi}_y + \varphi_z\ \varphi_x \left(I_{mx} - I_{mz}\right) \qquad (12)$$

$$M_z = I_{mz}\ \dot{\varphi}_z + \varphi_x\ \varphi_y \left(I_{my} - I_{mx}\right) \qquad (13)$$

Where M_x, M_y, M_z are the resulting torques applied on each axis of the mechanism. Substituting the real forces and torques affecting the mechanism, we obtain:

$$\frac{d\varphi_x}{dt} = \frac{1}{I_{mx}}\Big[M_{overturn} - M_m\ g\cos\left(\xi\right)\ sin\left(\theta\right) D_{cscg}$$

$$-M_m\ \omega_y\ R_{se}\ \dot{\Psi}\ D_{cscg}\cos\left(\theta\right) - \varphi_y\varphi_z(I_{mz} - I_{my})\Big] \qquad (14)$$

$$\frac{d\varphi_y}{dt} = \frac{1}{I_{my}}\Big[\left(F_{wl} + F_{wr}\right)D_{conty}\ - M_m\ g\cos\left(\theta\right)\ sin\left(\xi\right)D_{cscg}$$

$$+M_m\ \dot{\omega}_y\ R_{se}\cos\left(\xi\right)D_{cscg}\ - \varphi_z\varphi_x\left(I_{mx} - I_{mz}\right)\Big] \qquad (15)$$

$$\frac{d\varphi_z}{dt} = \frac{1}{I_{mz}}\Big[\left(F_{wl} - F_{wr}\right)D_{contz}\Big] \qquad (16)$$

The Newton equations are applied only in the x’ and y’ axes for the spherical shell:

$$F_{extx'} = F_{eqx}\cos\left(\xi\right) + F_{eqz}\cos\left(\theta\right)sin\left(\xi\right) - F_{eqy}\sin\left(\theta\right)sin\left(\xi\right) + \left(F_{wl} + F_{wr}\right)\cos\left(\xi\right)$$

$$-sin\left(\xi\right)\Big[\ F_{nl}\cos\left(\delta+\theta\right) + F_{nr}\cos\left(\delta-\theta\right)\Big] - (M_s + M_m)\ R_{se}\ \dot{\omega}_y \qquad (17)$$

$$F_{exty'} = M_s\ \omega_y\ R_{se}\ \dot{\Psi} + \left(M_s + M_m\right)R_{se}\ \dot{\omega}_x + F_{nl}\cos\left(\xi\right)\ \sin\left(\delta+\theta\right) - F_{nr}\cos\left(\xi\right)\ sin\left(\delta-\theta\right)$$

$$-F_{eqz}\ sin\left(\theta\right)\cos\left(\xi\right) + F_{eqy}\cos\left(\theta\right)\cos\left(\xi\right) \qquad (18)$$

In z' they are not applied as they would only obtain the normal floor force which is not useful in our study.

To study the Euler law in the shell we must first remember how the x'y'z' coordinate system is defined. Taking into account what is said at the beginning of this section, this coordinate system is not fixed to the case. It is a system whose z' axis is always parallel to the Z axis of the absolute coordinate system, and, moreover, the x' axis always points in the direction of movement of the robot. Therefore, the angular speed of the shell coordinate system with respect to XYZ is precisely the yaw speed (Ψ). As a result, the general equations applied to the case have the following format:

$$\begin{pmatrix} M_{x'} \\ M_{y'} \\ M_{z'} \end{pmatrix} = \begin{pmatrix} I_{x'}\ \dot{\omega}_x \\ I_{y'}\ \dot{\omega}_y \\ I_{z'}\ \dot{\omega}_z \end{pmatrix} + \begin{bmatrix} i & j & k \\ 0 & 0 & \dot{\Psi} \\ I_{x'}\ \omega_x & I_{y'}\ \omega_y & I_{z'}\ \omega_z \end{bmatrix}$$

$$= \begin{pmatrix} I_{x'}\ \dot{\omega}_x - I_{y'}\ \omega_y\ \dot{\Psi} \\ I_{y'}\ \dot{\omega}_y + I_{x'}\ \omega_x\ \dot{\Psi} \\ I_{z'}\ \dot{\omega}_z \end{pmatrix} \qquad (19)$$

Where $M_{x\prime}, M_{y\prime}, M_{z\prime}$ are the resulting torques which act on each axis of the sphere. If we substitute the real terms, the final equations are as follows:

$$I_s\ \dot{\omega}_x = -M_{overturn}\cos(\xi) + F_{exty'}\ R_{se} + I_s\ \omega_y \dot{\Psi} \qquad (20)$$

$$I_s\ \dot{\omega}_y = R_{se}\ F_{extx'} - F_{wl} R_{si}\cos(\delta+\theta) - F_{wr} R_{si}\cos(\delta-\theta) - \dot{\Psi}\, I_s\ \omega_x \qquad (21)$$

$$I_s\ \dot{\omega}_z = F_{wr}\ R_{si}\ sin(\delta-\theta)\cos(\xi) - F_{wl}\ R_{si}\ sin(\delta+\theta)\cos(\xi) + M_{overturn}\ sin(\xi) \qquad (22)$$

Equations for calculating the yaw speed (Ψ), roll speed (θ) and pitch speed (ξ) are obtained by applying the three rotations discussed at the beginning of this section. With them, we know the orientation of the robot from the $\varphi_x, \varphi_y, \varphi_z$ velocities:

$$\dot{\Psi} = \varphi_y \frac{sin\ (\theta)}{\cos\ (\xi)} + \varphi_z \frac{cos\ (\theta)}{cos\ (\xi)} \qquad (23)$$

$$\dot{\xi} = \varphi_y \cos(\theta) - \varphi_z\, sin(\theta) \qquad (24)$$

$$\dot{\theta} = \varphi_x + \varphi_y\ sin(\theta)\tan(\xi) + \varphi_z \cos(\theta)\tan(\xi) \qquad (25)$$

By integrating these magnitudes, we know the yaw, pitch and roll angles respectively.

Equations (26) and (27) represent the operation curves of DC motors, although the motor speed has been replaced by kinematic parameters of the robot. In them, the ω_{ref} term depends on the input voltage of each motor (V_{motor}) and is derived from its technical characteristics.

The η magnitude represents the efficiency of the transmission from the motor to the wheels and Z is the reduction ratio between wheel and motor.

$$F_{wr} = -1{,}18 \cdot 10^{-6} \frac{\eta\, Z^2}{R_r} \left[\frac{R_{si}}{R_r} \left[\left(\omega_y - \dot{\xi}\right) \cos\left(\delta - \theta\right) - \left(\omega_z - \dot{\Psi}\right) sin\left(\delta - \theta\right) \right] - \omega_{ref,\ wr} \right] \quad (26)$$

$$F_{wl} = -1{,}18 \cdot 10^{-6} \frac{\eta\, Z^2}{R_r} \left[\frac{R_{si}}{R_r} \left[\left(\omega_y - \dot{\xi}\right) \cos\left(\delta + \theta\right) + \left(\omega_z - \dot{\Psi}\right) sin\left(\delta + \theta\right) \right] - \omega_{ref,\ wl} \right] \quad (27)$$

$$\omega_{ref,\ w} = 10.59\ V_{motor} \quad (28)$$

Equation (29) serves to make mechanism rotation and shell rotation compatible in the perpendicular direction to the drive wheels. It is an approximate non – slipping constraint:

$$\dot{\omega}_x \cong \dot{\theta} \qquad (29)$$

Finally, we discuss the main simplifications taken into account when formulating the above set of equations:

- We assume that there is no slippage between the casing and the ground or through the drive wheels and case.
- We believe that the center of mass of the mechanism is located exactly on the z axis.
- We consider that the mechanism is symmetrical with respect to the xz and yz planes.
- We do not take into account dissipative or friction effects.
- We do not consider the electromechanical dynamics of the motor, i.e., it is assumed that they react instantly.

As the equations are built, the model becomes invalid if pitch (ξ) and roll (θ) angles take high values at the same time. It is due to how we have made wheel speed and shell rotation compatible [equations (26), (27) and (29)]. Furthermore, equations used to calculate yaw (Ψ), pitch (ξ) and roll (θ) speeds are singular if the inclination is π / 2. In the real robot, these conditions hardly ever occur and, hence, our model is useful to simulate almost any type of movement.

4 EXPERIMENTAL RESULTS

Before using the model as a tool to study and improve the Omnibola ©, we must first verify that the results it offers are similar to those that we observe experimentally. In particular, to carry out the validation of the model, we utilize a commercial system of motion analysis called “Vicon Nexus”. This includes four infrared cameras with associated hardware and software for its use and control. The operation of the entire system is as follows:

- The infrared reflectors (markers) are placed inside the robot.

- Cameras emit infrared radiation, which is reflected on the markers of the robot and is again captured by the cameras.

- Using triangulation algorithms, the system is capable of knowing the position of the robot in space.

- The system operates at a frequency of 100 Hz, and, thus, it is able to follow any movement performed by the robot.

Reflectors are placed inside the spherical shell, fixed to the mechanism. Figure 11 shows how reflectors are located on the mechanism.

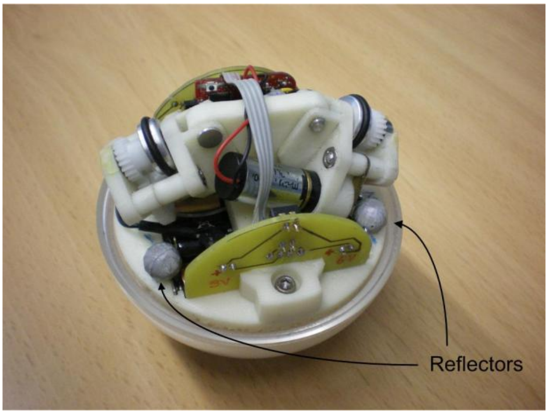

Figure 11.- Reflectors location on the internal mechanism

As the mechanism moves inside the shell, which is not absolutely transparent, detecting reflectors is complex. In order to achieve this, we use more than one reflector to make the system redundant. Moreover, cameras have to be located near the robot and this reduces the spatial measurement range considerably. Figure 12 represents the measurement system and the motion range.

According to these characteristics, the experiment which is the easiest to perform is recording motion in a stationary curve as, in this case, the area of movement is limited and small. As in the case of a stationary curve the power for both engines is constant and measurable, we can simulate the same movement with the model, taking into account those values of input voltage. In the end, we compare the results to see the validity of the model.

We have conducted two experiments with different rotation directions and different speeds. The results obtained are shown below. For clarity, let’s assume that the movement parts from the origin of coordinates. Figure 13 shows the results when the voltage of the right engine is 1.8 V and the voltage of the left engine is 3.8 V.

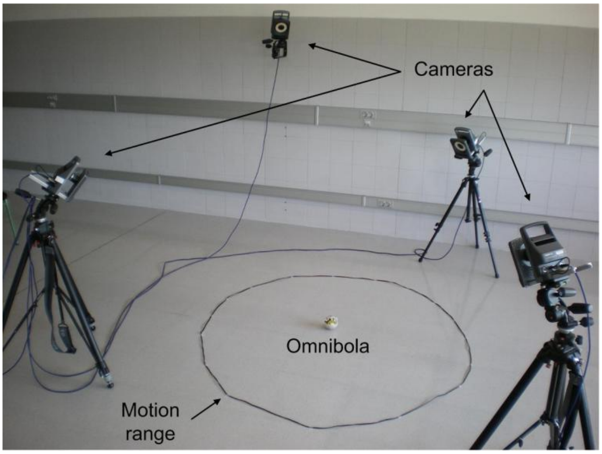

Figure 12.- Measurement system, Omnibola© and motion range

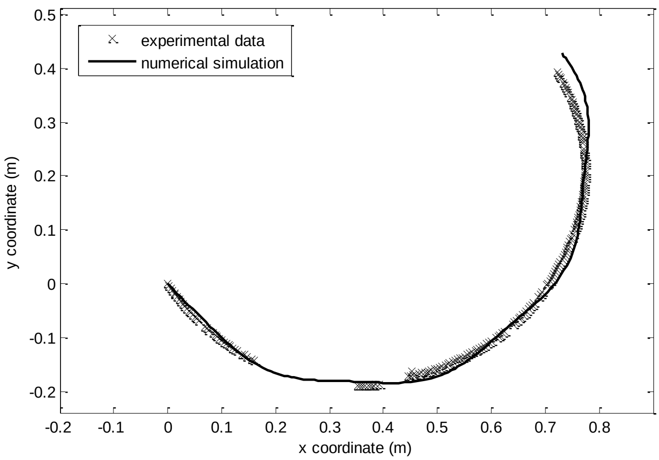

Figure 13.- Trajectory described by the robot in the first experiment

It can be seen that it describes a counterclockwise curve. Figure 14 shows the results when the voltage of the right engine is 5.2 V and the voltage of the left engine is 1.2 V.

In this case, the curve is described clockwise, as expected. As previously mentioned, due to the situation of the markers, sometimes cameras cannot find any of them and, consequently, we can appreciate layout areas with very few experimental measurements. It can be seen that the real path and the path we obtain with the model results are quite similar.

On the other hand, there are some differences between the solution obtained with our model and data measured experimentally. We can see that the model solution is more oscillatory than the real solution, as the path followed by the simulation is not perfectly circular. It is the internal mechanism which swings laterally (roll) and causes this effect.

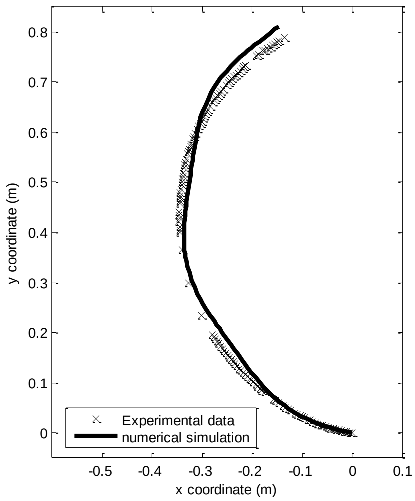

Figure 14.- Trajectory described by the robot in the second experiment

To show this effect, the difference between the simulated trajectory and the path followed by the robot is plotted in Figure 15. For the sake of clarity, the error is considered to be positive when the experimental measurement is in the inner part of the simulated trajectory and negative in the opposite case.

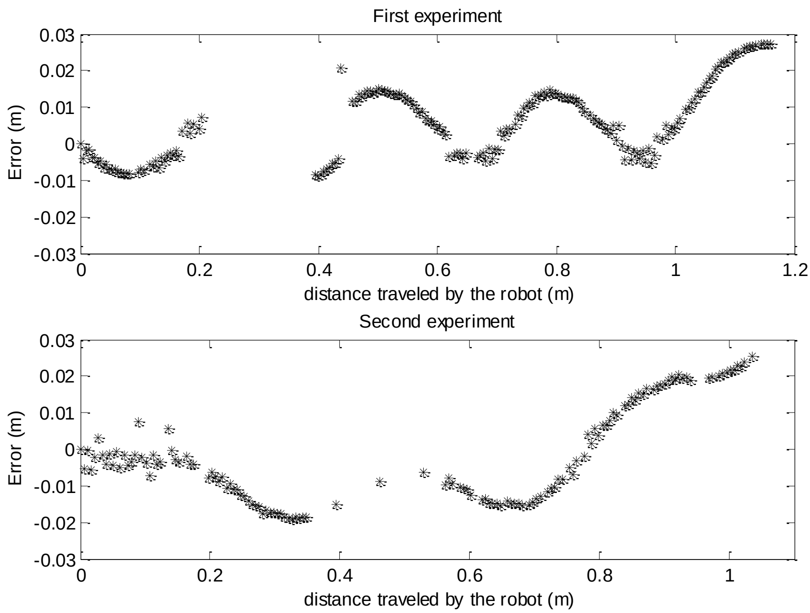

Figure 15.- Difference between measured and simulated paths followed by the robot

Moreover, although it cannot be appreciated in the graphics, the actual speed of the robot and the speed according to the model differ slightly. In the first case, the robot uses 2.7 seconds to perform the track whereas, according to the model, it would use 3 seconds. In the second case, the robot uses 1.85 seconds whereas, regarding the model, it would need a time of 2 seconds to describe the trajectory.

As specified in the previous section, the model assumes that there is no slippage between the case and the floor. The veracity of this hypothesis depends on the friction acting between both surfaces. When the floor is polished the friction is low and we can appreciate slippage in some movement phases. Slippage can be rejected when moving on a rough surface. Dynamically, slippage has been proven to destabilize the robot's movement.

In view of the results, the model describes the behavior of our robot quite well. The small differences found are due to physical defects in the robot, inaccuracies in the modeling, error accumulation in the simulation due to the numerical approach and errors made by the motion analysis system.

5 CONCLUSION

We have briefly presented the main characteristics of a spherical robot, and several physical configurations that it can adopt. We have designed and built a spherical robot based on our own knowledge and on experience transmitted by those research centers which have done it previously. We have described in detail the physical layout and operation of our robot. A complex mathematical model based on Newton – Euler laws has been developed to analyze the robot's behavior. Finally, experiments have been conducted to compare the actual motion with the one predicted by the model, and it has been noticed that the results are quite good. In the future, we intend to build a larger robot which can overcome obstacles and move over more rugged terrain. In order to prevent slippage, its outer surface may be cover with a thin layer of rough plastic. Furthermore, a control algorithm will be physically implemented and new goals will be set, such as tracking predefined trajectories autonomously.

REFERENCES

[1] Siegwart, R., Nourbakhsh, I.R. *Introduction to Autonomous Mobile Robots*. The MIT press, 2004.

[2] Armour, R. H., Vincent, J.F. *Rolling in Nature and Robotics: A Review*. ScienceDirect, Journal of Bionic Engineering 3, pp 195 – 208, 2006.

[3] Ylikorpi, T., Suomela, J. *Ball – Shaped Robots*. In H. Zhang (ed.), *Climbing & Walking Robots, Towards New Applications*. pp 235 – 256, Viena, Itech Education and Publishing, 2007

[4] Bhattacharya, S., Agrawal, S. K. *Spherical Rolling Robot: A Design and Motion Planning Studies*. IEEE transactions on Robotics and Automation, Vol. 16 (6), pp 835 – 839, 2000.

[5] Joshi, V. A., Banavar, R. N., Hippalgaonkar, R. *Design and analysis of a spherical mobile robot*. Mechanism and machine theory, 45, pp 835 – 839, 2010.

[6] Mukherjee, R., Minor, M. A., Pukrushpan, J.T. *Simple Motion Planning Strategies for Spherobot: A Spherical Mobile Robot*. In Proceedings 38th Conference on Decision & Control, Phoenix, Arizona, December 1999.

[7] Halme, A. H., Suomela, J., Schönberg, T., Wang, Y. *A Spherical Mobile Micro – Robot for Scientific Applications*. In 4th ESA Workshop on Advanced Space Technologies for Robot Applications, Noordwijk, The Netherlands, pp 1-7, 1996.

[8] Bicchi, A., Balluchi, A., Prattichizzo, D., Gorelli, A. *Introducing the "Sphericle": an Experimental Testbed for Research and Teaching in Nonholonomy*. In Proceedings of the IEEE International Conference on Robotics and Automation, Albuquerque, USA. Vol. 3. pp. 2620-2625, 1997.

[9] Alves, J., Dias, J. *Design and control of a spherical mobile robot*. In Proceedings of the Institution of Mechanical Engineers. Part I: Journal of Systems and Control Engineering. Vol. 217 (6). pp 457 – 467, 2003

[10] Michaud, F., Caron, S. *Roball, the Rolling Robot*. In Autonomous Robots, Vol. 12 (2), pp 211 – 222, 2002.

[11] Laplante, J., Masson, P., Michaud, F. *Analytical longitudinal and lateral models of a spherical rolling robot*. Technical Report, Department of Electrical Engineering and Computer Engineering, 2007.

[12] Brown, H. B. Jr., Xu, Y. *A Single – Wheel, Gyroscopically Stabilized Robot*. In IEEE Robotics and Automation Magazine. Vol. 4. pp. 39 – 44, 1997.

[13] Gheorghe, V., Udrea, C., Alexndrescu, N., Duminica, D. *Design of a Rolling Robot with Telescopic legs, able to displace itself on irregular surfaces*. The Romanian Review Precision Mechanics, Optics & Mechatronics. Vol 18 (34). pp 139 – 144, 2008.

Proceedings of MUSME 2011, the International Symposium
on Multibody Systems and Mechatronics
Valencia, Spain, 25-28 October 2011

WIRELESS TELEOPERATED OF A ROBOTIC MANIPULATOR BASED IN IMU SENSOR AND CONTROL ANTHROPOMORPHIC MOVEMENT

Alejandro Jofré Moreno[1], Diego Álvarez Villegas[2]
Escuela de ingeniería en Mecatrónica
Universidad de Talca, Camino los Niches s/n, Curicó, Chile
[1] Alejandro.jofre.m@gmail.com
[2] ing.dalvarez@gmail.com

Keywords: Robotics, Teleoperation, IMU, Arduino, Bluetooth, Labview

Abstract. This paper presents the development of a teleoperation system for an anthropomorphic robotic manipulator. The system's design considerations allow for an intuitive operation, which simultaneously reduces learning time and provides control with higher degrees of freedom than a conventional control (teach pendant). This feature is achieved by the control being based on the operator's arm, and then the system being adjusted to extrapolate these movements to the robot. The structure of the text is presented first in the conceptual development of the project. Then the process of physical construction is described, which involves the IMU sensor and data processing via microcontroller and PC. Later on we describe the control software that controls the system based on Labview and Processing /Wiring (C). Finally we present the development of experimental tests with an educational robot Scorbot ER-V for the control of two position axes.

1 INTRODUCTION

Currently, it is an increasingly important element in the Industry to have maximum security standards for workers whatever their field of action. In this context, the project seeks to solve this problem by designing a system for remote control; a system known in the Industry as Teleoperation. This system consists of a robotic arm devoted to the handling of objects which under certain circumstances might put human beings' physical integrity under risk, for example, radioactive waste, Biohazard, explosives, etc. The operator is positioned at a safe distance from the action and he is able to command the movements of the robotic arm through an interface as intuitive as possible (anthropomorphic moving).

Exist a great number of project of teleoperation systems currently being investigated, we take a look at two interesting projects. First we find the project entitled "A Human Arm Mimicking with 5-DOF Controlled by Lab VIEW" from Islamic University of Gaza, Palestine. This is a teleoperation system based on mechanical detection of the operator's movements. In the second case we examine the project entitled "Teleoperation of a 5-DOF Robotic Arm Using a Microsoft Kinect Sensor" from Minnesota University, which controls the robotic arm by means of a motion capture using the Kinect sensor.

In this project the central device is used as a sensor called IMU (Inertial Measurement Unit), which is a widely used component in aerospace systems (planes, ferries, satellites) but are also very flexible in their other fields of application. This sensor is basically a combination of accelerometers and gyroscopes, which can be found in very compact and easy-to-connect formats, besides being relatively cheap.

2 MATHEMATICS MODELING OF A KINEMATICS HUMAN ARM

The study of human body's kinematic structure is relevant to a good control system design. In this context, scientific literature mentions several models, being some more complex than others, but ultimately it is assumed that a good approximation is a movement of 6 degrees of freedom, 3 for the wrist base position, and 3 expressing wrist orientation in space (Moeslund, Granum. 2001).

The spatial positioning of the wrist base is mainly based on the muscle force exerted on the arm's tendons, which are generated by angular movements of the joints (pivots). Although in reality there are more degrees of redundant freedom, we will state that a position will be modeled as follows: two angular movements at the shoulder base plus an angular elbow movement as shown in Figure 1.

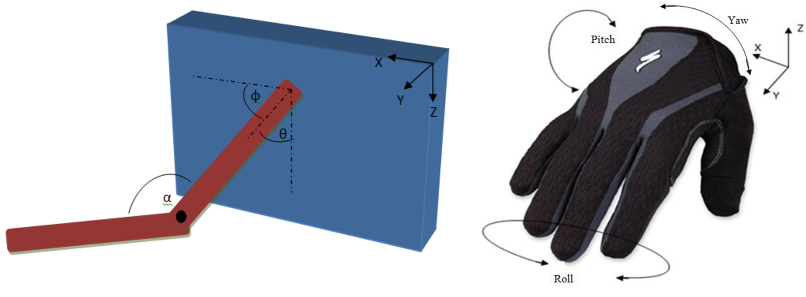

Figure 1: Variable position coordinate system (a) coordinate system variables angle (b).

The human arm has restrictive movements such as bending the arm behind the elbow, which are limits that restrict movement, and that are also important to define. Next, the results of these angular constraints are presented, defined as general average since each person has variable structural characteristics in this regard.

	θ	φ	α
Minimum	-135°	-135°	45°
Maximum	45°	100°	180°

Table 1: Limited range of motion of angles pertaining to the shoulder and elbow. (Moeslund, Granum. 2001).

Aside from the angles in which the arm movement works, it is important to define the relationship between this variable and time, i.e. the angular velocity. These values depend on the activity that human beings do, but the maxim value is $400\,{}^{deg}/_{s}$. As for the maximum acceleration, it is estimated that humans can vary their angular speed from minimum to maximum in one tenth of a second, or about $4000\,{}^{deg}/_{s^2}$, (Moeslund, Granum. 2001).

3 CONCEPTUAL SOLUTION

The solution draft is shown in Figure 2, which dissects the components of both hardware and necessary software to carry out the project.

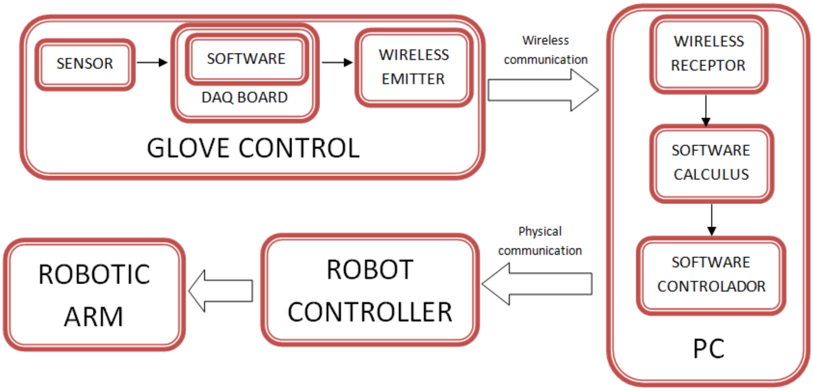

Figure 2: Conceptual scheme of the project solution.

The diagram shows the total project specification. However, in this opportunity, (first stage of the project) the control design for angles φ y θ.

The algorithm is the following:

1. The operator movement signals are captured by the IMU sensor. The giroscopes will measure the angular velocity $\dot{\theta}$ and $\dot{\varphi}$, referring to the shoulder base. The accelerometers will measure through the programming of an inclinometer, which is the angular position of the hand related to the Earth's gravitational axis.
2. The signals are received in analog form by the microcontroller's ADC, in which signals were digitized to a suitable sampling rate and stored in the buffer.

3. These modified signals are sent to the WT11 Bluetooth module for their transmission, and sent in a defined format or protocol for writing / reading.
4. On the PC, signals are received first from another Bluetooth module connected to an available USB port.
5. Subsequently, the information will be processed in the PC software programmed in Labview, which will calculate the position and the issuance of commands to the robotic arm.
6. The information will be transmitted via RS232 serial port in ASCII code, which must be in the format specified by the robot controller.
7. The robot will be updating the calculated hand position times per second times per second. Then, the command to move the robot to the indicated position will be executed in each update.

In this case, the educational robot Scorbot ER-V was used as a test. Command communication is done through ACL language, characteristic of these robots.

4 MECHATRONICS DEVELOPMENT

The project has been decided to be carried out in stages, which involve in each advance a confirmation of a research floor. At this stage of construction, all the necessary hardware is prepared in order to carry out the project as indicated by the conceptual solution, except for the control of the angle α (elbow) as described in Figure 1. In terms of software, we will have a confirmation of the proper signal collection and transmission obtained by the installed sensors. The position calculation process will be done by using θ and φ shoulder-related angles as variables. The missing variable α is assumed as a fixed parameter at 180°. The emission of commands towards the robot is arranged according to the algorithms and syntax provided by the ACL language.

4.1 Mechanical

In mechanical terms, the mobile system is quite simple; first define the support of the electronics. First is the neoprene glove on top of which is a Velcro surface, wherein positioning the IMU sensor cover, and then there is a bracelet you must designed especially for this project, and on top of which there is a velcro again but this time to cover the microcontroller as shown in Figure 3.

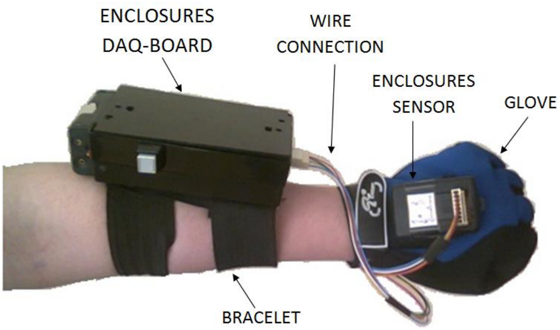

Figure 3: Scheme of control devices for control.

4.2 Electronics

The physical implementation of the system requires the development of support systems and connections for the proper coupling of systems and to ensure a good flow of information.

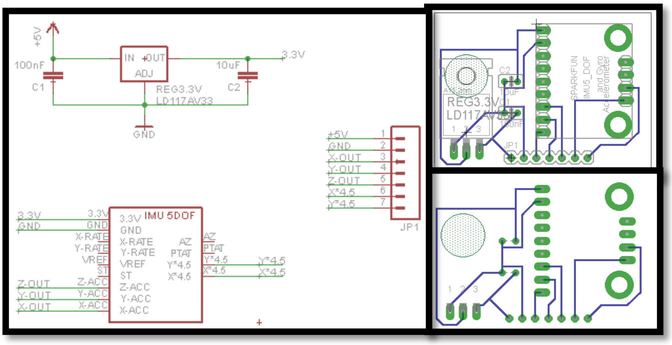

Figure 4: Electrical connection and sensor board PCB

Figure 5: Electronic overview of the mobile part.

Electrical connections consist primarily of the following monitoring:

1. First define two AA batteries of 1.5 V for each mobile system power supplies (gloves).
2. Then you get the signal energy to the arduino board which regulates the voltage internally, this plate is removed from a signal of 5 V to power the board voltage regulator to 3.3 V for the subsequent board power IMU.
3. The signals measured by the sensor travel to ports of the microcontroller ADC (see Table 2). Through a Category 5 UTP cable and slim connectors on each deck.
4. Following this continues in the electronics section of the PC, where the bluetooth module connects to the USB port of PC, and then exit the PC is connected to the robot controller via RS-232 communication available (USB-serial or serial-serial).

4.3 Software

The calculation processes are carried out in two sections "DAQ software" and "PC Software", which transform the measured signals from sensors, and will be gradually transformed into that needed positional data to eventually be sent to the robotic manipulator. This latter will execute the corresponding movements.

Software of the board (DAQ): Its main function is to command the microcontroller (AVR ATmega168) immersed in Arduino board, for it to use its analog to digital converter (ADC) in order to digitize the signals coming from the sensors (IMU). DAQ software programming was made with Arduino IDE (version 0017), whose programming Processing / Wiring facilitates the code syntax run on the board, since it is based on the application and integrated development AVR. The list of digitized signals is presented in Table 2.

Pin	ADC0	ADC1	ADC2	ADC3	ADC4
Signal	Acel X	Acel Y	Acel Z	Gyro θ	Gyro φ
Final Measurement	Inclination (Pitch, Roll, Yaw)			Angle θ	Angle φ

Table 2: Classification of signals and their connection to the ports of Microcontroller.

The second process to set through this software corresponds to the transmission of information from the microcontroller to the Bluetooth module (WT11). This will be done through the UART (Universal Asynchronous Receiver transmitter) Microcontroller. This device integrated into the microcontroller allows encapsulation of previously stored data by the ADC, which are also stored in the microcontroller's buffer. Sending data is done serially via a standard format called 8N1, which contains 8 data bits, no parity bit and 1 stop bit. The data transmission rate corresponds to a communication of 9600 baud per second, which can be easily modified if required. The previously described parameters are mentioned as the standard 9600/8N1.

PC Software: This is composed of 4 main processes to be performed:

1. Receiving data from the Bluetooth module connected to the USB port of PC.
2. Filtering data received in order to obtain a distortion-free curve and represent reality in a better way.
3. Position and rotation angle calculating process from the signals received by sensors (acceleration and angular velocity)
4. Sending the order of action to the robotic manipulator with proper position argument calculated.

This is the core element regarding information processing. This item consists of scheduling algorithms that allow us to handle the signal processing and calculations.

For reception of data from the glove the Labview VISA module is used (National Instruments, 2010), with which the reception is configured through the USB port where the Bluetooth module is connected. The communication parameters are those mentioned above.

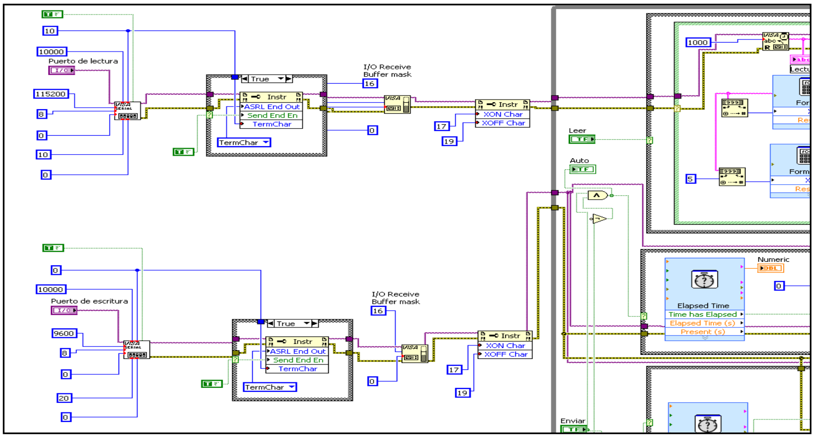

Figure 6: Scheduling algorithm, port handling section I/O

After receiving the information from the control globe, it is necessary to have a filtering algorithm, which is extremely necessary for the proper receipt of data from the sensor, decreasing in this way noise signals in order to get a signal clear for handling. In this way we get signals “cleaner” signals with which you can work with motion values closer to reality. Noise signals are mainly electromagnetic in nature and dependent mainly on the physical environment of project implementation (Fernandez, 2009).

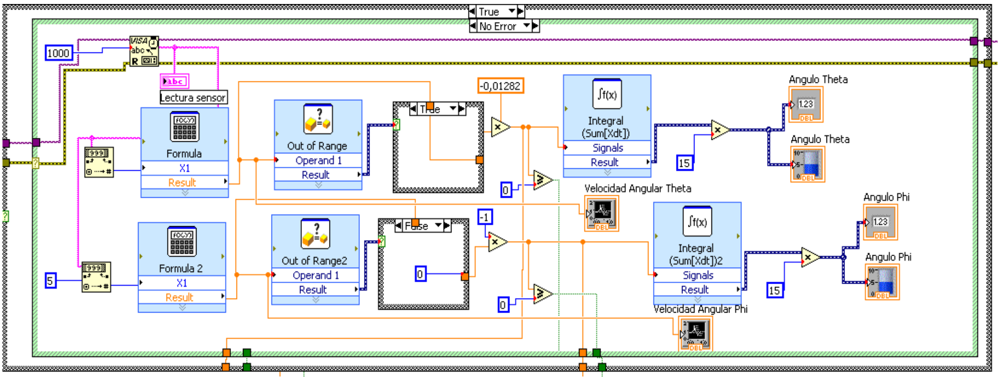

Figure 7: Scheduling algorithm, filter and calculation of angular position.

To calculate the glove position and rotation from the measurements of acceleration and angular velocity sensor made by the 5 DOF IMU we must rely primarily on numerical integration algorithms and arithmetic adjustments. The first corresponds to spatial position variables (X, Y, Z) for the base of the hand; the calculation is done assuming the fully extended arm which is defined by a constant radius from the shoulder base pivoting respect the wrist. Then through variable polar coordinates with angle variables $(\dot{\theta}, \dot{\varphi})$ and constant R, we get the position as follows:

First, a filter is defined on the central oscillation band (ripple offset), so any module value of a magnitude greater than an ε value is taken into account, while if the value is in the band it will then be replaced by 0, as shown in expression (1).

$$\begin{aligned} \dot{\theta} > |\epsilon| &\rightarrow \hat{\dot{\theta}} = \dot{\theta} \\ \dot{\theta} < |\epsilon| &\rightarrow \hat{\dot{\theta}} = 0 \end{aligned} \tag{1}$$

The following relevant operation is the integration of the new signal ($\hat{\dot{\theta}}$) to thus obtain the position, as shown in expression (2).

$$\theta = A \cdot \int \hat{\dot{\theta}}\ dt + C \tag{2}$$

The integration constant C and adjustment multiple shall be added by adjusting the data obtained in the integration and the reality of the movements obtained from the first test performed. It is also necessary to compensate for the accumulation of error during calculation, in addition to defining the integration process step size, which must typically be a magnitude order smaller than the higher signal frequency oscillations (shorter period).

The final stage of programming is to configure the sending signals from the PC software to control the robot cabinet that we teleoperate. In order to do this we must send the calculated angular position value, and attach it as an argument to a command word, which belongs to the robot programming language. While command-taxis can vary from robot brands, in general what is needed is a constant update of a variable position, and to instantly execute a movement to the position stored in the variable (Intelitek. 2003).

4.4 HMI (Human-machine Interface)

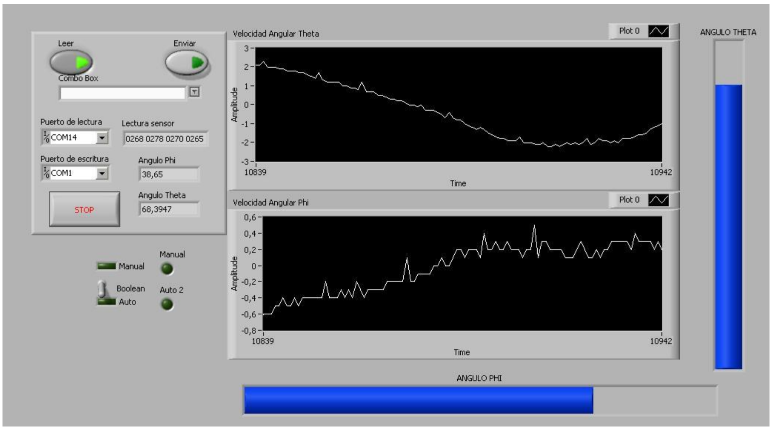

Figure 8: Appearance of Human-Machine Interface (HMI)

The human-machine graphic interface has the look shown in Figure 9. The purpose of this is to show the system operator to certain variables that could be useful, i.e.: sensor graphic, calculated position graphic, operation mode, etc. There are also buttons for system configuration, such as read / write operation mode, communication ports, operation mode manual / automatic of the robot.

5 RESULTS

Once the modular construction process and communication testing is concluded, the next step is the integration of all mechanical, electronic and software subsystems in order to check the overall system performance. There are two testing levels, the first consisting of the accuracy level in the calculation made by the PC software, which can be checked with the system without the need for connectivity to the robot. This is undoubtedly the most important validation of the system created. The second level consists of a validation of correspondence between the movement of the human arm and then the actual position carried out by the robot. This latter type of evidence depends exclusively on the type and model of the robot you are controlling via the remote control system. In this case (Scorbot ER-V) has no control system in real time. The response time of the robot did not meet the full range of operating speed of a human arm, but in a limited range between $30\,{}^{deg}/_{s}$ and $40\,{}^{deg}/_{s}$ or so. In this sense, the experimental results for individual and simultaneous angle (φ and θ) control and simultaneous control are presented.

The validation test was carried out as it follows, the starting point was defined by a fixed mark in the space, then exercises were conducted by positioning the operator's hand, with 10 total swings 90 degrees in 30 seconds, and then the stop was made at the same point of departure. The result tabulation for each test is shown below.

N° Test	Deflected angle θ	Deflected angle φ
1	-7°	-5,5°
2	-4.2°	8
3	-6°	2,3
4	1,9°	2,6
5	3,2°	1,3
6	6,8°	-4,8
7	-1,1°	-1,1
8	-1,2°	0,6
9	-2,2°	4
10	-0,8°	3,8
Average	3,44°	3,4
Standard deviation	2,41	2,29
Max	7	8
Min	0,8	0,6

Table 3: Test results of test for θ and φ axes, individually

Average calculus, Standard Deviation, Minimum and Maximum, are made on the absolute value of the deflection angles.

For simultaneous motion testing 10 800mm diameter circular movements approximately at arm's full length were performed. These are the results

N° Test	Deflected angle θ	Deflected angle φ
1	-12	-2,8
2	5,4	11
3	-4	10,3
4	2,2	4,8
5	17,3	1,6
6	7,8	-2,7
7	-2,3	-5,5
8	-12,4	3,9
9	-12,9	-3,2
10	-4	4,1
Average	8,3	4,99
Standard deviation	5,2	3,1
Max	17,3	11
Min	2,2	1,6

Table 4: Test results of test for θ and φ axes, simultaneously

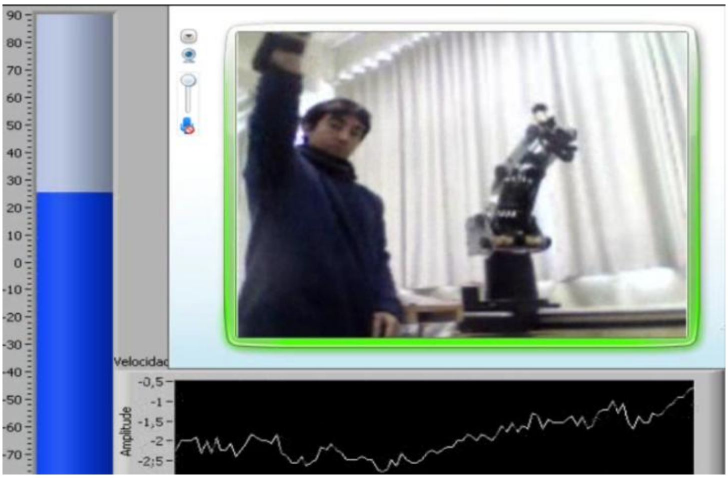

Figure 9: Charting test trials

6 UPCOMING WORKS

The next stage of this project consists of programming the software to calculate the variables Pitch, Roll and Jaw, which indicate the inclination angle of the wrist compared to the gravitational force. This will be done by creating a gravitational inclinometer based on accelerometers, which gives us the desired variables.

After this improvement, this teleoperation system is integrated to an industrial manipulator robot, which can provide better characteristics regarding the flow of information (sampling time), allowing us to have faster movement, besides they can be updated in real time , making the system more dynamic and clear.

7 CONCLUSIONS

• The IMU sensor technology may be appropriate to create even more accurate and versatile teleoperation systems. These sensors allow measurements in a small physical employment space, which increases the portability and compactness of the mobile system and that is definitely one of the main features teleoperation seeks.

• The completion of this project (2 nd stage) involves an undeniable need, if more realistic conclusions are wanted, for the usefulness of this teleoperation design in the industry. The results of the first stage we can conclude that there is a good design concept, but it requires full finishing in order to understand whether the control synergy between all the degrees of freedom is a good response.

REFERENCES

[1] Thomas b. Moeslund, Erik Granum. Pose estimation of a human arm using kinematic constraints. Aalborg University, Denmark,2001

[2] Mario Alberto Fernández Fernández. Advanced control-optimal control and robust. Class notes, Universidad de Talca, 2009

[3] LabVIEW VISA Tutorial, National Instrument, retrieved March 15, 2010, from http://www.ni.com/support/visa/vintro.pdf

[4] LabVIEW Tutorial Manual, National Instrument, retrieved March 15, 2010, from http://www.ni.com/pdf/manuals/320998a.pdf

[5] User Manual Scorbot ER-V Plus. Catalog No. 100016 Rev. C, Intelitek Inc. 2003.

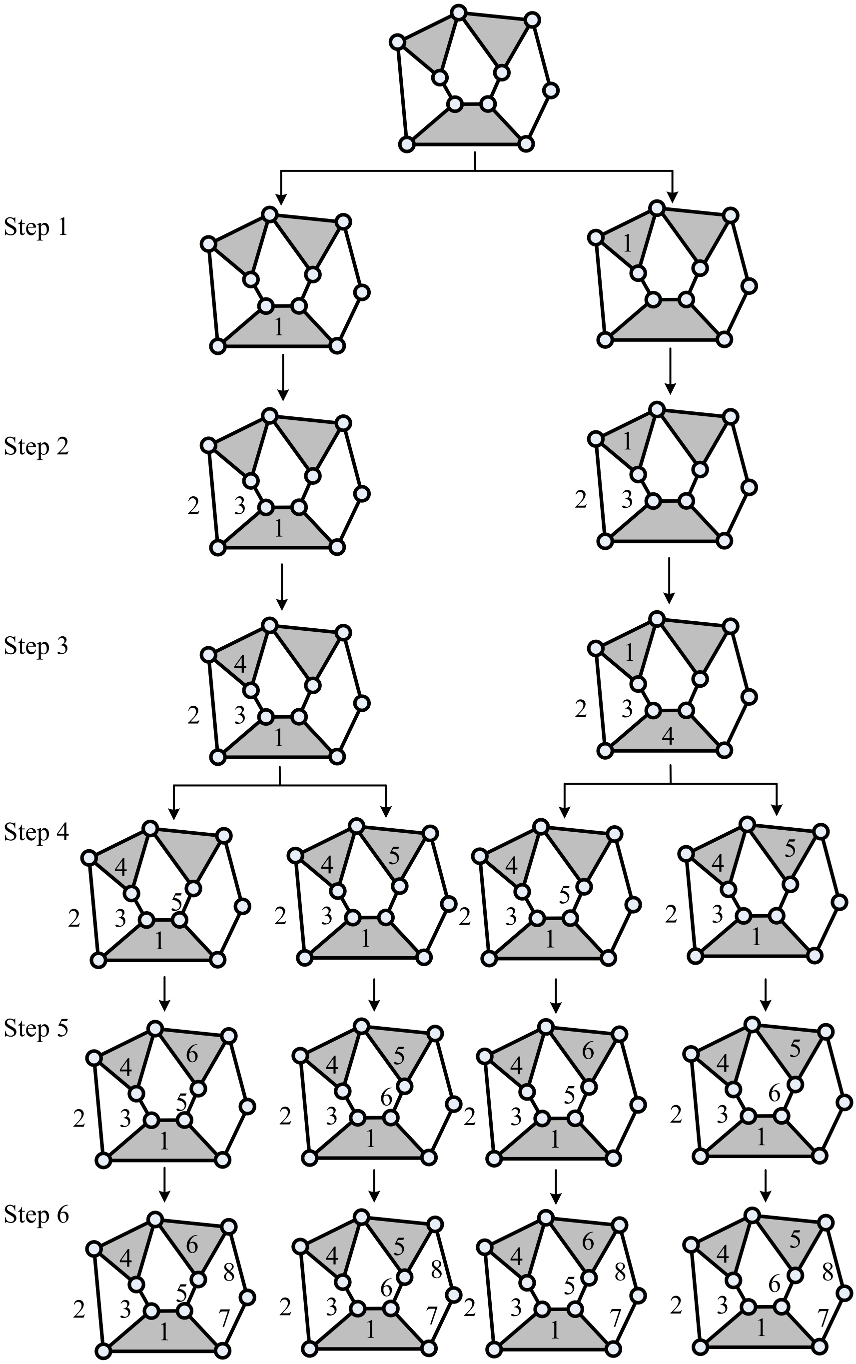

Figure 10: Specification procedure for generalized kinematic chain in Fig. (5e) for LARM leg mechanism

3.5 A particulization procedure

Once feasible specialized chains are obtained, they can be particularized into their corresponding mechanical devices by means of skeleton drawings. Graphically, particularization is the reverse process of generalization, and it can be done by applying the generalizing rules in reverse order. Fig. (11) shows the atlas of designs for the atlas of feasible specialized chains shown in Fig. (6) to Fig. (10). As shown in the atlas, Fig. (11e) is the one shown in Fig. (2).

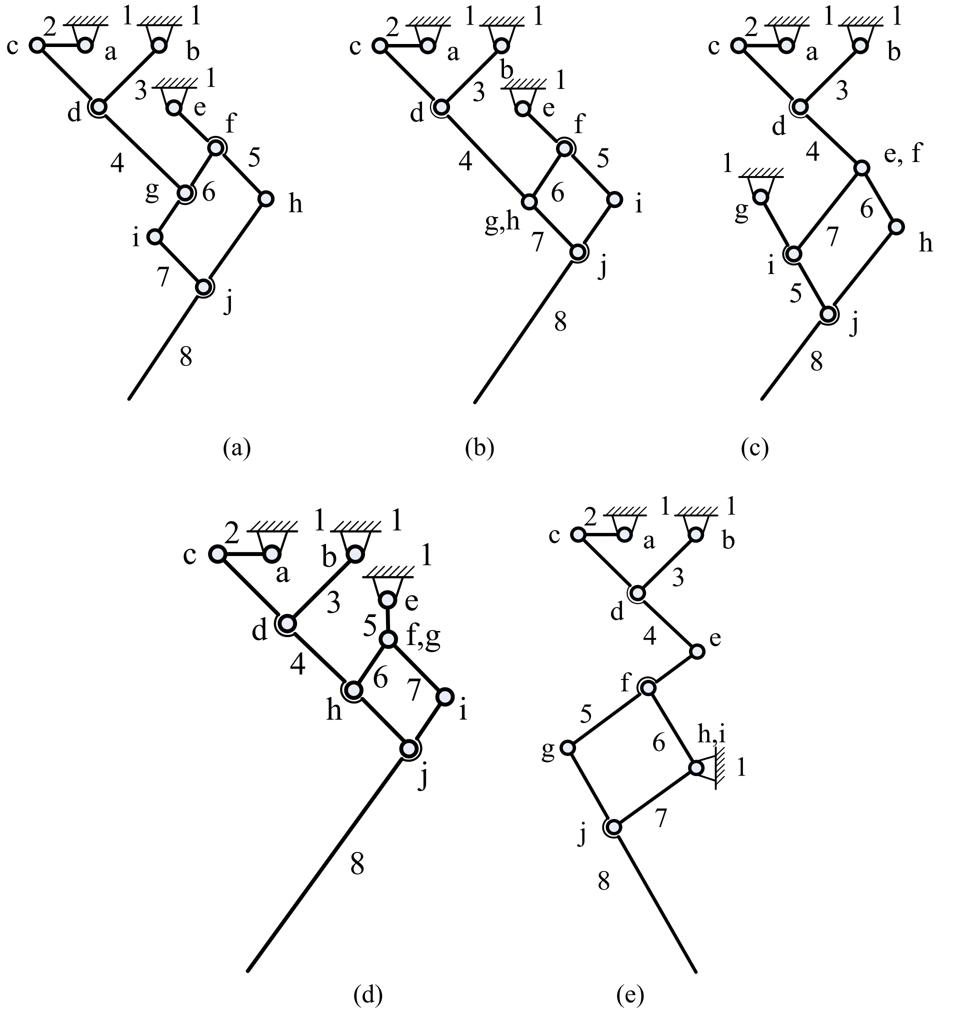

Figure 11: Atlas of designs for the leg mechanism

3.6 An atlas of new designs

The last step of this methodology is to identify all existing designs from the atlas of designs. Then, those that haven't been identified as existing designs are new designs, which are shown in Fig. (11a), Fig. (11c), and Fig. (11d).

In LARM designs, mechanisms of Fig. (11b) and Fig. (11e) have been already experienced.

Once the atlas of new designs is obtained, it is feasible to implement the optimal design procedure of the proposed design solution.

4 CONCLUSIONS

This paper presents a topology search for a new leg mechanism as based on an existing LARM leg mechanism. In order to implement this search, a procedure has been introduced and adopted with the aim of achieving an optimal design. Several new topology leg mechanisms have been found after a practical procedure of this methodology.

New design solutions obtained by this creative methodology provide comparison study between them. Then a best design solution can be found with the desired design specifications.

ACKNOWLEDGMENT

The first author acknowledges Chinese Scholarship Council (CSC) and Institute of Advanced Manufacturing Technology (IAMT) of Chinese Academy of Science (CAS) for supporting his PhD study and research at LARM in the University of Cassino in Italy from the year 2010 to 2012.

REFERENCES

[1] M. Hirose, Y. Haikawa, T. Takenaka, and K, Hirai, Development of Humanoid Robot ASIMO, Proc. IEEE/RSJ Int. Conference on Intelligent Robots and Systems, Workshop2, Oct. 29, 2001.

[2] K. Kaneko, F. Kanehiro, M. Morisawa, K. Miura, and S. N. S. Kajita, Cybernetic human hrp-4c, in Humanoids, pp.7–14, 2009.

[3] M. Ceccarelli and G. Carbone, A new leg design with parallel mechanism architecture, AIM 2009 IEEE/ASME International Conference on Advanced Intelligent Mechatronics 14-17 July 2009, pp 1447-1452.

[4] G. Carbone, M. Ceccarelli, Legged Robotic Systems, Cutting Edge Robotics ARS Scientific Book, Wien, pp. 553-576, 2005.

[5] S. Yoshiaki, W. Ryujin, and A. Chiaki, Intelligent ASIMO: system overview and integration. Proceeding of the IEEE/RSJ International Conference on Intelligent Robots and Systems, EPFL, Switzerland September 30-October 4: 2478-2483, 2002

[6] K. Kaneko, F. Kanechiro, S. Kajita, et al. Humanoid robot HRP-2. Proceeding of the 2004 IEEE International Conference on Robotics and Automation, New Orleans, USA, April 26-May 1: 1083-1090, 2004

[7] A.M.M. Omer, Y. Ogura, H. Kondo, et al. Development of a humanoid robot having 2-DOF waist and 2-DOF trunk. Proceeding of the 2005 5th IEEE-RAS International Conference on Humanoid Robots, Tsukuba, Japan, December 5-7: 333-338, 2005

[8] S.M. Song, K.J. Waldron, Machines that walk-the adaptive suspension vehicle, Cambridge MA: The MIT Press, 1989.

[9] H. Funabashi, M. Horie, H. Tachiya, et al, A synthesis of robotic pantograph mechanisms based on working spaces and static characteristics charts, JSME International journal Series III, 34(2)., 1991.

[10] W.B. Shieh, L.W. Tsai, and S. Azarm, Design and optimization of a one-degree-of-freedom six-bar leg mechanism for a walking machine. Journal of Robotic systems, 14(12): 871-880, 1997.

[11] C. Lanni, M. Ceccarelli, E. Ottaviano and G. Figliolini, Actuating mechanisms for pantograph legs: structures and characteristics, Tenth world congress on the theory of machines and mechanisms, Oulu, Finland, June 20-24, 1999, Vol.3, pp.1196-1201.

[12] E. Ottaviano, C. Lanni, M. Ceccarelli, Numerical and Experimental Analysis of a Pantograph-Leg with a Fully-Rotative Actuating Mechanism, Proceedings of the 11th World Congress in Mechanism and Machine Science, August 18–21, 2003, Tianjin, China, pp.1537-154.

[13] M. Ceccarelli, G. Carbone, E. Ottaviano and C. Lanni, Leg designs for walking machines at LARM in Cassino, Robotica mobile per esplorazione lunare Unmanned, 1-2, June, Roma Italy, 2009 pp. 5-15.

[14] M. Ceccarelli, M., Figliolini, G., Lanni, C., Ottaviano, E., A Study of Feasibility for Rickshaw Type Mobile Robot, IEEE International Conference on Industrial Electronics, Control and Instrumentation, Nagoya, 2000, paper MT9-MRC-2.

[15] C. Liang, M. Ceccarelli, and Y. Takeda, Operation analysis of a one-DOF pantograph leg mechanism. CD Proceedings of the 17th International Workshop on Robotics in Alpe-Adria-Danube Region, RAAD'2008, Ancona, n. 50, 2008.

[16] H.S. Yan, Creative design of mechanical devices. Singapore: Springer, 1998.

Proceedings of MUSME 2011, the International Symposium
on Multibody Systems and Mechatronics
Valencia, Spain, 25-28 October 2011

A TOPOLOGY SEARCH FOR A NEW LARM LEG MECHANISM

Tao Li[*], Marco Ceccarelli[†]

[*] LARM: Laboratory of Robotics and Mechatronics, DiMSAT
University of Cassino, Via Di Biasio 43, 03043 Cassino (Fr), Italy
e-mail: taoli@unicas.it
web page: http://webuser.unicas.it/weblarm/larmindex.htm

[†] LARM: Laboratory of Robotics and Mechatronics, DiMSAT
University of Cassino, Via Di Biasio 43, 03043 Cassino (Fr), Italy
e-mail: ceccarelli@unicas.it

Keywords: Topology Search, Leg Mechanism, Biped Robot.

Abstract. *Most biped robots, which have leg mechanisms with three actuating motors at the hip, knee and ankle joints, have such drawbacks as the control system is very complex and difficult, the cost is large, and electronics hardware and sophisticated control algorithms are also needed at the same time. While leg mechanisms with reduced DOF (degree of freedom) have advantages such as low-cost and easy-operation because fewer motors are used. Such biped robots are similar to the costly biped robots in the sense that they can offer the capacities to develop and improve new biped walking algorithms, and they are more affordable.*

Design works of robot leg with Chebyshev mechanism have been carried out in the past several years at LARM (Laboratory of Robotics and Mechatronics). By Using Chebyshev mechanism, these legs can have the ability of generating a suitable curve at the foot point of the leg, which is an effective way to reduce the complexity of control.

This paper presents a topology search for a new leg mechanism based on an existing LARM leg mechanism, which is composed of Chebyshev mechanism and pantograph mechanism. In order to implement this search, a procedure of a methodology has been introduced and adopted. Several new topological leg mechanisms have been found after a practical application of the proposed methodology.

1 INTRODUCTION

In recent years, research works on biped robots have been addressed great interest by corporations [1], institutes [2] and universities [3]. This is largely because legged locomotion has many advantages, such as high efficiency and excellent suitability in people's day life environment, like ascending or descending stairs, overcoming obstacles, and changing directions.

In the domain of legged robot, a leg mechanism will determine not only the degrees of freedom of a robot, but also actuation system efficiency and its control strategy. Therefore, leg mechanisms are fundamental for design and operation issues of a biped walking robot [4].

Most of the existing biped robots have leg mechanisms with three actuating motors at the hip, knee and ankle joints. This kind of leg mechanism shows anthropomorphic motion capability. But they have also drawbacks, such as the control system design is very complex and difficult, the cost is large, and electronics hardware and sophisticated control algorithms are also needed at the same time. In addition, they are not energy efficient because of the "Back-driven" effect and heavy masses of motors with gear boxes [5-7].

On the other hand, leg mechanisms with reduced DOF (degree of freedom) have advantages such as low-cost and easy-operation because fewer motors are used [8-10]. Such biped robots are similar to the costly biped robots in the sense that they can offer the capacities to develop and improve new biped walking algorithms, and they are more affordable.

In the past several years at LARM, one research line is devoted to the design of linkage leg mechanism. Several leg mechanisms have been developed and built [11-13]. Most of these leg mechanisms are consist of Chebyshev mechanism and pantograph mechanism. Using Chebyshev mechanism and pantograph mechanism can make these leg mechanisms have the ability of generating a suitable curve at the foot point of the leg, which is an effective way to reduce the complexity of control.

In this paper, combination of Chebyshev mechanism and pantograph mechanism are still supposed to be a basal construction of a leg mechanism as has been done at LARM before. A topology search for a new leg mechanism based on one LARM leg mechanism has been carried out. A methodology has been introduced and adopted to obtain new results.

2 A PROCEDURE FOR TOPOLOGY SEARCH

In order to find out the best combination of Chebyshev mechanism and pantograph mechanism as a leg mechanism, a creative design methodology based on the concept of generation and specialization can be adopted as outlined in [16]. A specific procedure can be proposed as shown in Fig. (1). It mainly consists of 6 steps as:

Step 1. To find out all the existing design solutions that can fully satisfy the required design specifications; and conclude the topological characteristics of these existing designs.

Step 2. To select one of these existing solutions; then to transform it into its corresponding generalized chain, according to the rules of generalization.

Step 3. Based on the algorithm of number synthesis presented in [16], to synthesize an atlas of generalized chains that have the same members and joints as the generalized chain obtained in Step 2.

Step 4. By using a suitable algorithm of specialization, assign members and kinematic joints to each generalized chain generated in Step 3 in order to obtain the atlas of all the feasible specialized chains that satisfy the design specifications and constraints.

Step 5. Particularize each feasible specialized chain obtained in Step 4 into its corresponding schematic format of mechanical device, to have the atlas of mechanical devices.

Step 6. Identify existing designs from the atlas of designs, to have the atlas of new designs.

Detailed explanation of the algorithms needed in these steps will be introduced in section 3.

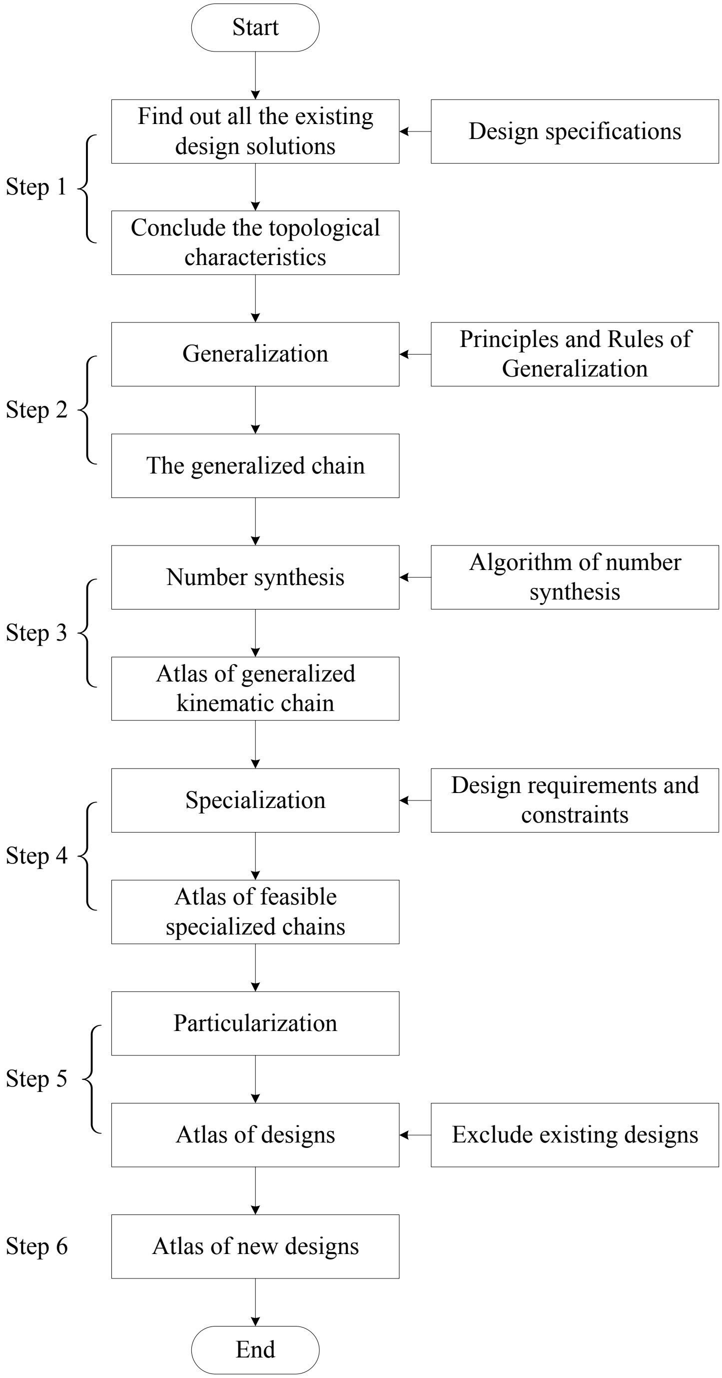

Figure 1: A flowchart for a creative design procedure

3 A PRACTICAL PROCEDURE FOR NEW LEG DESIGN

The proposed creative design procedure in Fig. (1) has been developed and applied to determine a new optimal design for a new LARM biped robot with low-cost easy-operation features. Implementation of the procedure has been carried out through detailed steps proposed in section 2 with desired specifications, principles and rules, requirements and constraints, and algorithms, which contain design requirements, principle and rules of generalization, design requirement and constraints, and algorithm of number synthesis.

3.1 An existing solution

The LARM single DOF leg mechanism is composed of a Chebyshev four-bar linkage ABCDE and a pantograph mechanism EFGHJ, as shown in Fig. (2).

The Chebyshev mechanism ABCDE is the input driving mechanism, and it is used to generate a suitable ovoid curve for the point E, in which AC is a crank, BD is a rocker, and CDE is a coupler. Joint at pivot point B is fixed on the frame of the mechanism. The pantograph mechanism EFGHJK is used as the leg mechanism, and it is used to amplify the input trajectory of point E into output trajectory with the same shape at point K. The amplify ratio of the pantograph mechanism depends on the length of bar GJ and bar JK.

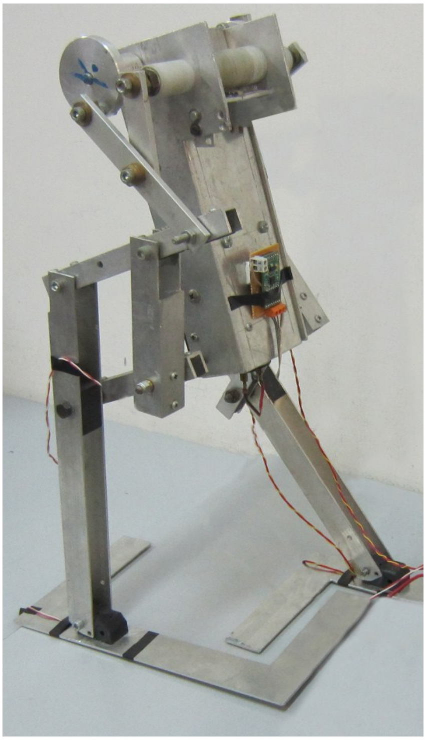

(a)

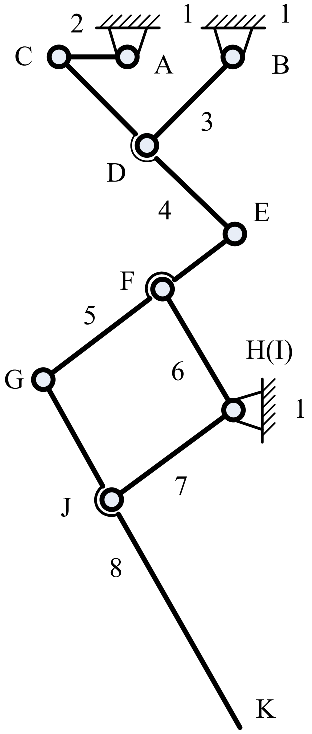

(b)

Figure 2: An existing design of leg mechanism composed of Chebyshev mechanism and pantograph mechanism: (a) a prototype; (b) a kinematic scheme (1 the frame link; 2 the input link; 3 rocker a; 4 the transmission link a; 5 the transmission link b; 6 rocker b; 7 rocker c; 8 the output link)

The reason that the mechanism in Fig. (2) can be chosen as a leg mechanism is that it has just one DOF, which make it with low-cost and easy-operation design features. Furthermore, the mechanism can generate a curve at the extremity of the leg which is suitable for human-like walking. The aim here is to find out all the topological structures of this mechanism with the aim of achieving an optimal design.

At the beginning of a conceptual phase for creating mechanical devices, only basic specifications regarding topological structures are of major concern. Design specifications of the leg mechanism can be considered as:

(1) It has a Chebyshev four-bar linkage working as an input mechanism;

(2) It has a pantograph mechanism for amplifying and outputting the curve generated by the input Chebyshev mechanism;

In addition, topological characteristics of this leg mechanism can be outlined as:

(1) It consists of 8 links and 10 joints;

(2) It has one frame link (1), one crank (2), three rockers (3, 6, and 7), two transmission links (4 and 5), and one output link (8);

(3) It has 10 revolute joints (A, B, C, D, E, F, G, H, I, and J);

(4) It is a one-DOF mechanism;

A topology matrix, M_T, of the mechanism can be defined as

$$M_T = \begin{bmatrix} 1 & R & R & 0 & 0 & R & R & 0 \\ R & 2 & 0 & R & 0 & 0 & 0 & 0 \\ R & 0 & 3 & R & 0 & 0 & 0 & 0 \\ 0 & R & R & 4 & R & 0 & 0 & 0 \\ 0 & 0 & 0 & R & 5 & R & 0 & R \\ R & 0 & 0 & 0 & R & 6 & 0 & 0 \\ R & 0 & 0 & 0 & 0 & 0 & 7 & R \\ 0 & 0 & 0 & 0 & R & 0 & R & 8 \end{bmatrix} \tag{1}$$

in which 1, 2, 3, 4, 5, 6, 7, and 8 are the components of the mechanism. R represents the revolute joints and it appears at the point of intersection of row i (i=1, 2… 8) and column j (i=1, 2… 8) means that link i and j are connecting to each other by a revolute joints.

M_T is the topology matrix of those mechanisms, which have the same topological structure [16]. It represents the number of links that a mechanism has; and also represents the type of joints between links that are connecting to each other.

3.2 A generalization procedure

The purpose of a generalization is to transform a mechanism involving various types of members and joints into a generalized kinematic chain with only generalized links and generalized joints. A generalized joint is a joint in general; it can be a revolute joint, a prismatic joint, a pin-in-slot joint, a spherical joint, a helical joint, or others. A generalized link is a link with generalized joints; it can be a binary link, a ternary link, a quaternary link, etc. Therefore, through the process of generalization, an existing design can be generalized into the corresponding generalized kinematic chain, [16].

Generalization is based on generalization principles and rules. Generalizing principles and rules are:

(1) Every kinematic joint between links of the mechanical device must be generalized into generalized kinematic revolute joints;

(2) Every link of the mechanical device must be generalized into generalized link;

(3) Mechanical device has to be in conformity with its generalized kinematic chain; topology structure should bring into correspondence with the links and joints;

(4) The DOF of the generalized kinematic chain should be the same as the mechanical device.

According to the concept of the generalization, all joints are generalized into generalized joints, and all links are generalized into generalized links. As shown in Fig. (2), all the joints are revolute joints; and five links are binary links (2, 3, 6, 7, and 8), two are ternary links (4 and 5) and one is quaternary link (1).

The generalized chain of this leg mechanism is shown in Fig. (3), and it is a (8, 10) generalized kinematic chain, in which 8 and 10 mean there are 8 links and 10 joints in the leg mechanism, respectively. Link 1 represents the frame link, which is connecting to link 2 (the input crank of the mechanism), 3 (the rocker of Chebyshev mechanism), 6 and 7 (two rocker of the pantograph mechanism) by revolute joints; link 4 is the output link of Chebyshev mechanism, which is connecting to link 2, 3, and 5 (the input link of pantograph mechanism) by revolute joints; link 8 is the output link of pantograph mechanism, which is connecting to 5 and 7 also by revolute joints.

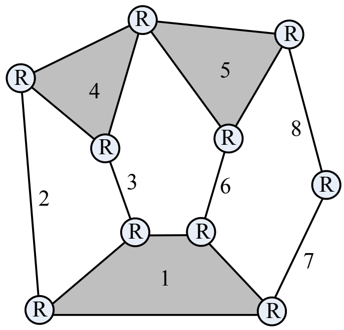

Figure 3: A generalized chain for LARM leg mechanism in Fig. (2)

3.3 Kinematic number synthesis

The atlas of generalized kinematic chains is obtained as based on the concepts of generalization and number synthesis. Then, based on an algorithm for number synthesis, all possible generalized kinematic chains with the same numbers of members and joints as the original generalized kinematic chain can be obtained.

Two basic algorithms of number synthesis are based on link assortment and graph theory, respectively. Link assortment of a generalized chain means the number and type of its links. Detailed explanation of link assortment can be found in [16]. By using number synthesis of a link assortment with M links and N joints, one can obtain the atlas of (M, N) generalized chains. One specified link assortment can have more than one types of structure. However, the procedure must comply with these constraints:

(1) Every link must be used to make the chain connected;

(2) Every kinematic joint must be used to make the chain closed;

(3) There should not be a link separated from the others;

(4) One joint should only be connected between two links to make the chain only has simple kinematic joints;

(5) Two links should not be connected by more than two joints.

Graph theory has been used since the 1960's. Some basic definitions of graph theory, such as graph and block, along with the procedure for number synthesis based on graph theory and hypergraphs theory can be found in [16].

Then through the algorithm of number synthesis, the atlases of the generalized kinematic chains with eight links and ten joints are generated. As result, 16 topological generalized kinematic chains as in Fig. (4) are obtained for the leg mechanism in Fig. (2).

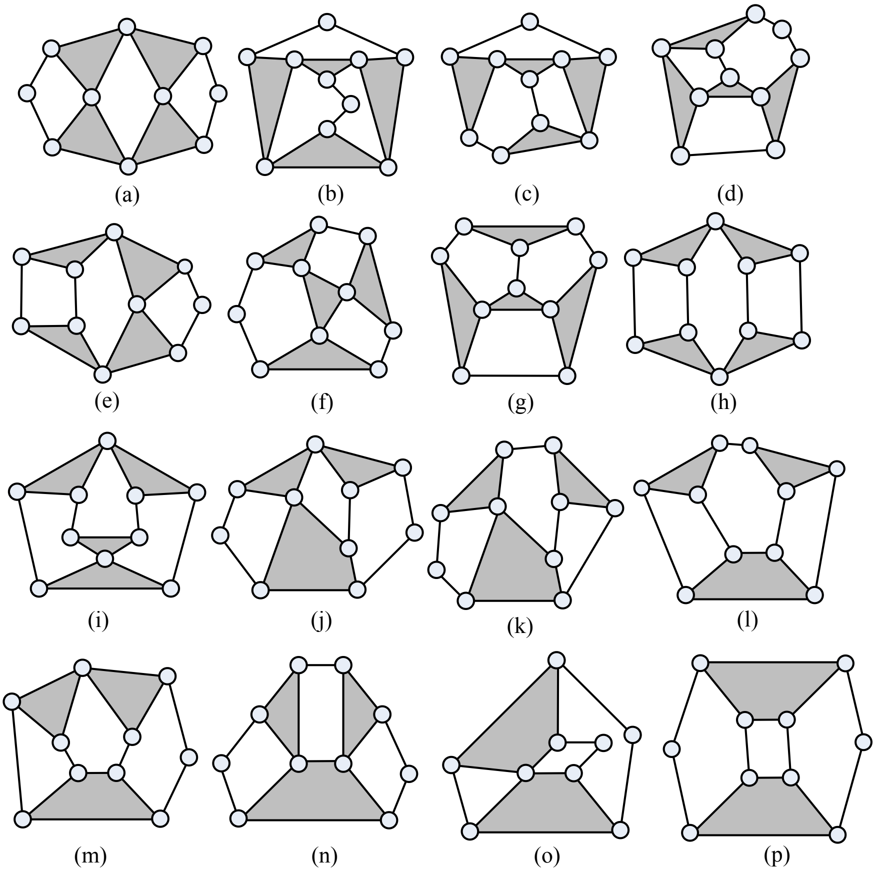

Figure 4: Atlas of 8-link and 10-joint generalized kinematic chains

3.4 A specialization procedure

Specialization is the process of assigning specific types of members and joints in the available atlas of generalized kinematic chains, subject to the concluded design constraints. Through specialization, a generalized kinematic chain is transformed into a specialized chain. A specialized chain subject to design constraints is called a feasible specialized chain, [16]. Therefore, the atlas of the feasible specialized chains can be generated through a process of specialization.

Thus, before the implementation of specialization, it is necessary to give out the design requirements and constraints of the leg mechanism. Design requirements and constraints can be outlined according to design specifications and topology characteristics that are described in section 3.1 as following:

(1) There must be a Chebyshev mechanism;

(2) There must be a pantograph mechanism;

Equivalent requirements and constraints including but not limited to:

(1) The frame must be a multiple link with at least three joints;

(2) There must be at least 2 binary links connecting to the frame;

(3) There must be at least 1 ternary links not connecting to the frame but connecting to those two binary links;

(4) There must be at least 3 links connecting to the frame;

(5) There must be 4 links forming a closed chain.

According to these conditions, some kinematic chains which are not feasible are excluded from the atlas of Fig. (4). Atlas of feasible generalized kinematic chains can be determined as shown in Fig. (5).

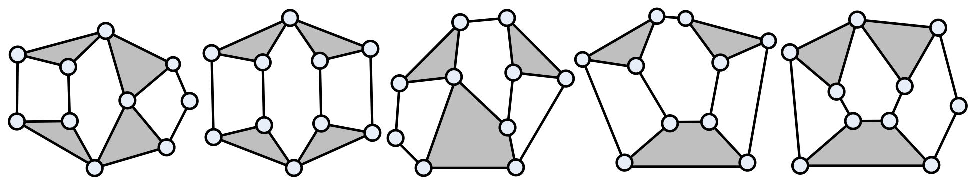

(a) (b) (c) (d) (e)

Figure 5: Atlas of feasible generalized kinematic chains from Fig. (4)

All feasible specialized chains subject to the concluded design requirements and constraints can be identified through the following steps:

1. Assign frame link 1;
2. Assign input link 2;
3. Assign link 3;
4. Assign link 4;
5. Assign link 5;
6. Assign rocker 6;
7. Assign rocker 7;
8. Assign the output link 8.

These steps must be implemented to each feasible generalized kinematic chain in Fig. (5).

For Fig. (5a), the process can be applied through the following steps:

1. Assign frame link 1

Since there must be a multiple link as frame and the frame must connect to two binary links, for the generalized kinematic chain shown in Fig. (5a), the assignment of the ground link generates one result. Therefore, one specialized chain with the frame link is generated as shown in Fig. (6).

2. Assign input link 2 and 3

Since there must be two binary links connecting to the frame, after the frame is specified, link 2 can be specified. As similar to the assignment of link 2, link 3 can be assigned as shown in Fig. (6).

3. Assign link 4

Since link 4 must not connect to the frame link and must connect to two binary links, it can be assigned as shown in Fig. (6).

4. Assign links 5

Since link 5, 6, 7, and 8 must form a closed chain, links 5 can be assigned accordingly.

5. Assign links 6

Since link 5, 6, 7, and 8 must form a closed chain, links 6 can be assigned accordingly as in Fig. (6).

6. Assign links 7 and 8

Links 7 and 8 can be assigned from remaining links as shown in Fig. (6).

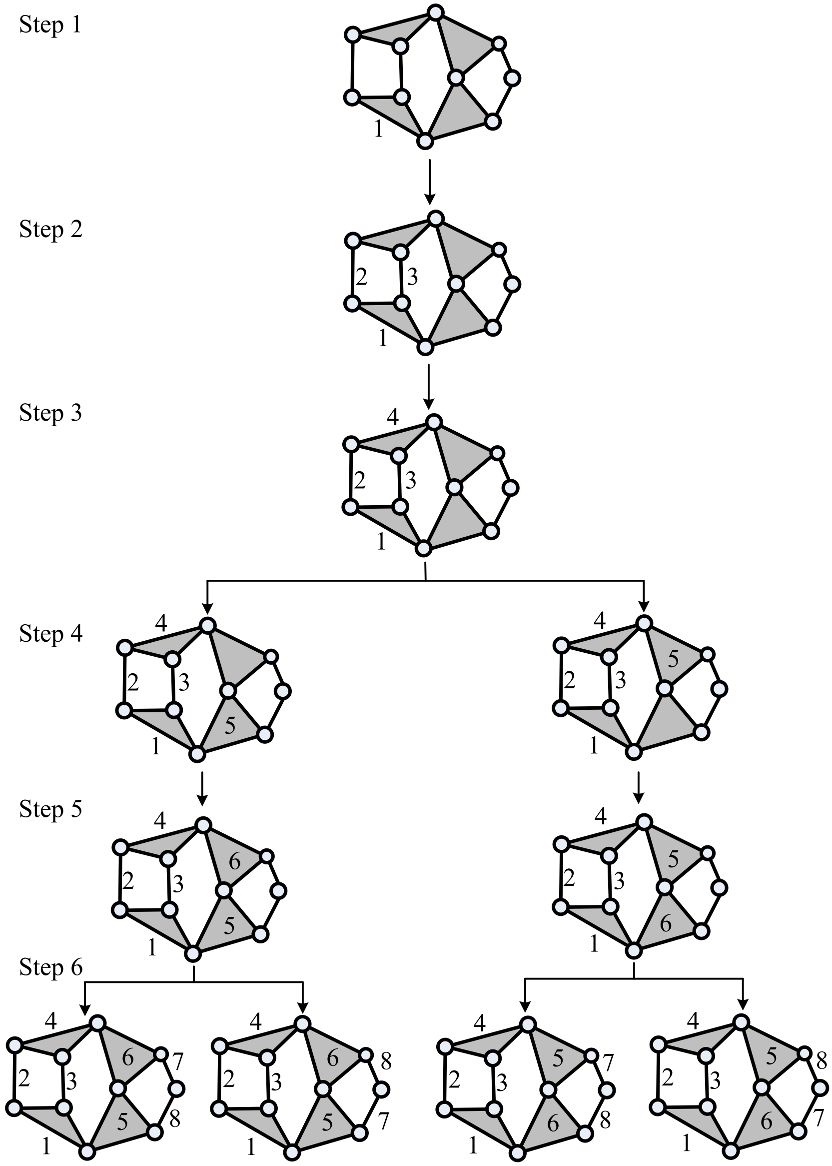

Figure 6: Specification procedure for generalized kinematic chain in Fig. (5a) for LARM leg mechanism

Similar steps have been given to the others shown in Fig. (5b), Fig. (5c), Fig. (5d), and Fig. (5e). Results are shown in Fig. (7), Fig. (8), Fig. (9), and Fig. (10), respectively.

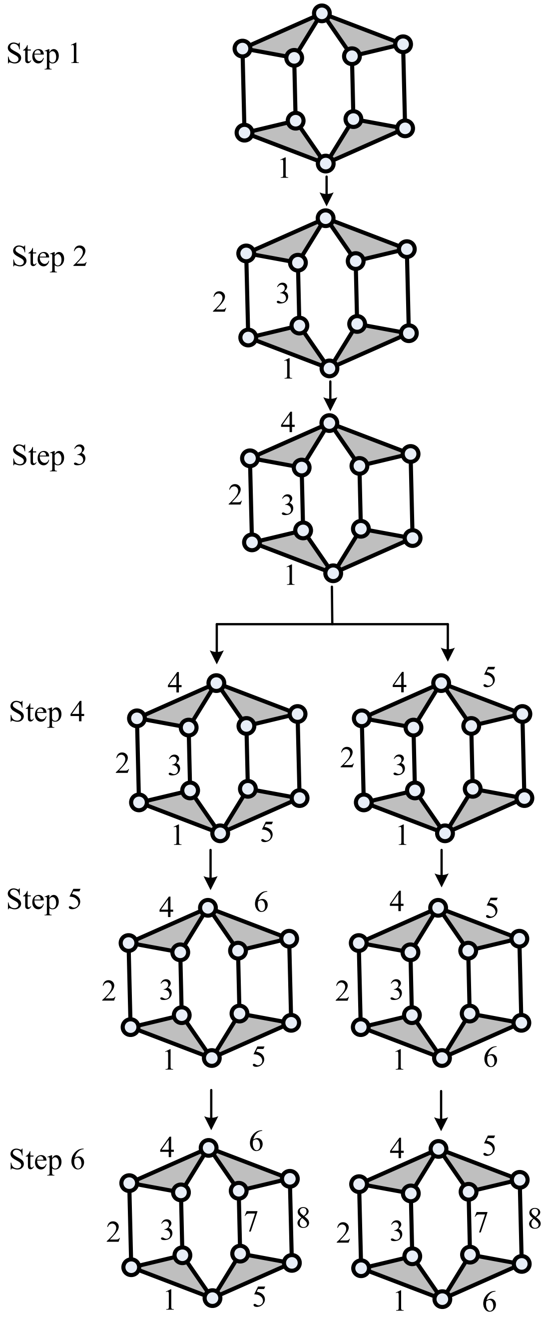

Figure 7: Specification procedure for generalized kinematic chain in Fig. (5b) for LARM leg mechanism

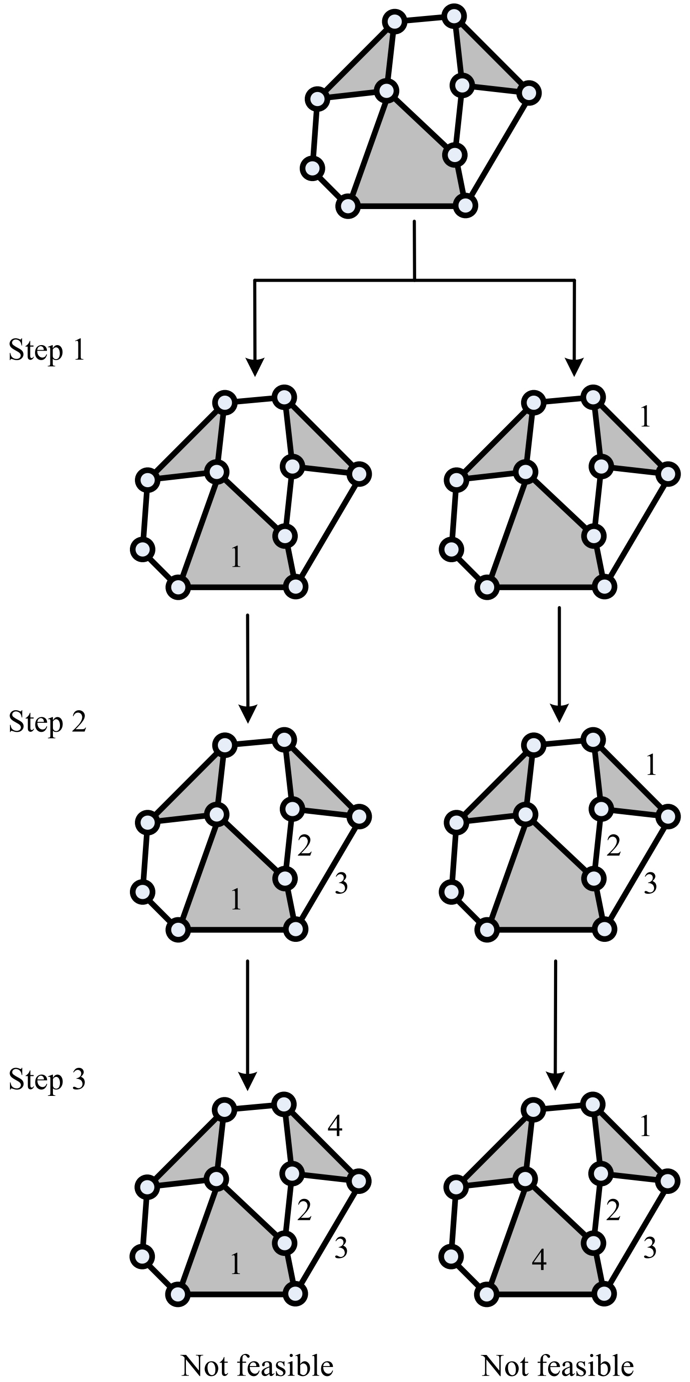

Figure 8: Specification procedure for generalized kinematic chain in Fig. (5c) for LARM leg mechanism

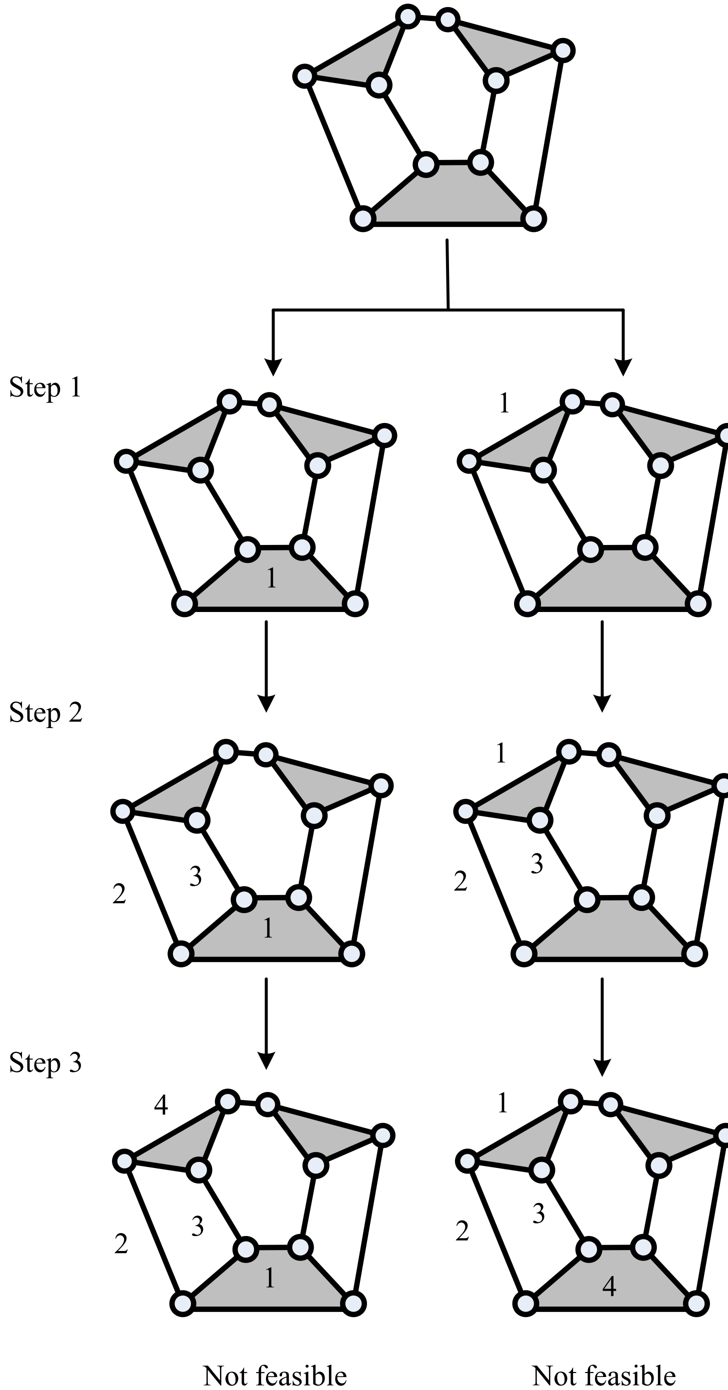

Figure 9: Specification procedure for generalized kinematic chain in Fig. (5d) for LARM leg mechanism

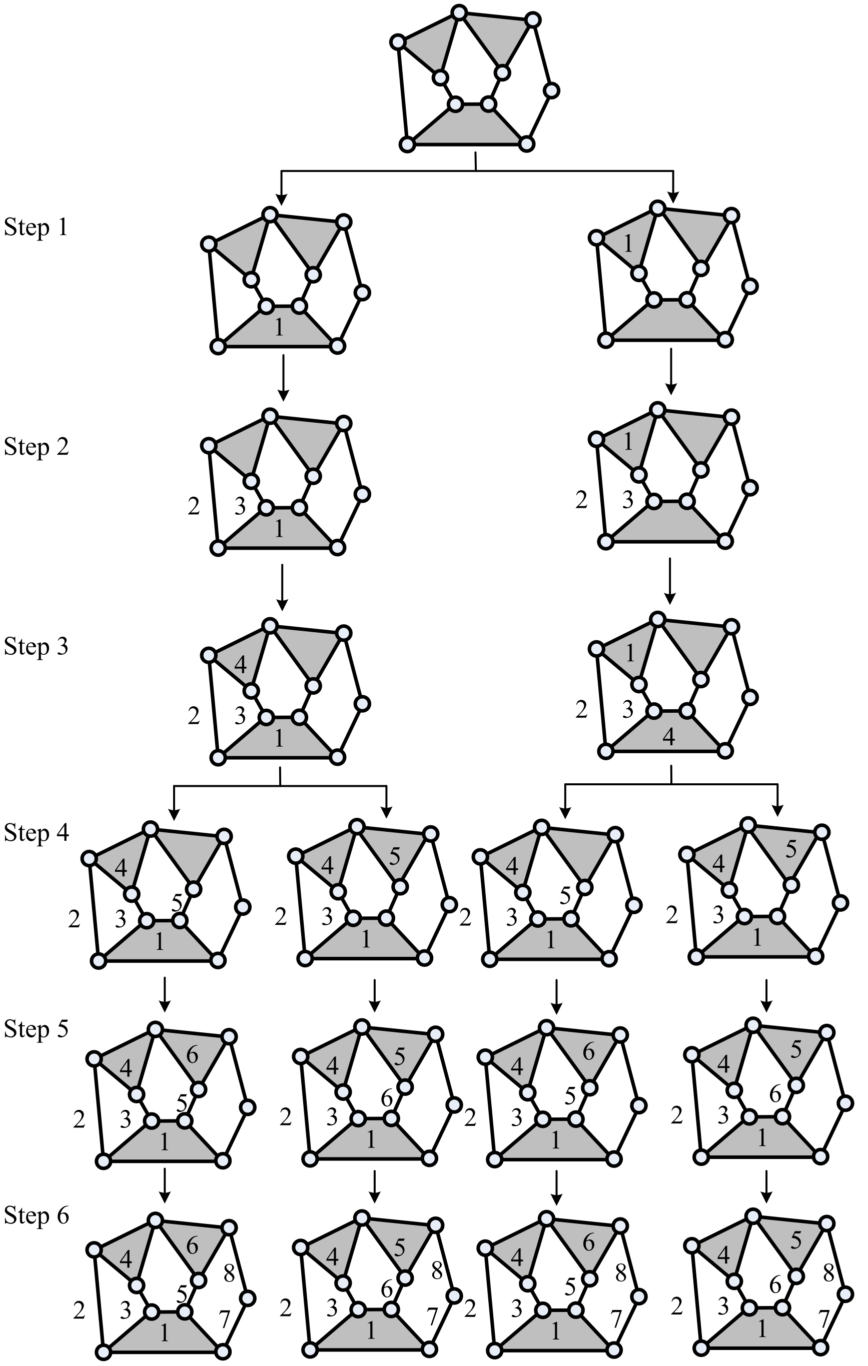

Figure 10: Specification procedure for generalized kinematic chain in Fig. (5e) for LARM leg mechanism

3.5 A particulization procedure

Once feasible specialized chains are obtained, they can be particularized into their corresponding mechanical devices by means of skeleton drawings. Graphically, particularization is the reverse process of generalization, and it can be done by applying the generalizing rules in reverse order. Fig. (11) shows the atlas of designs for the atlas of feasible specialized chains shown in Fig. (6) to Fig. (10). As shown in the atlas, Fig. (11e) is the one shown in Fig. (2).

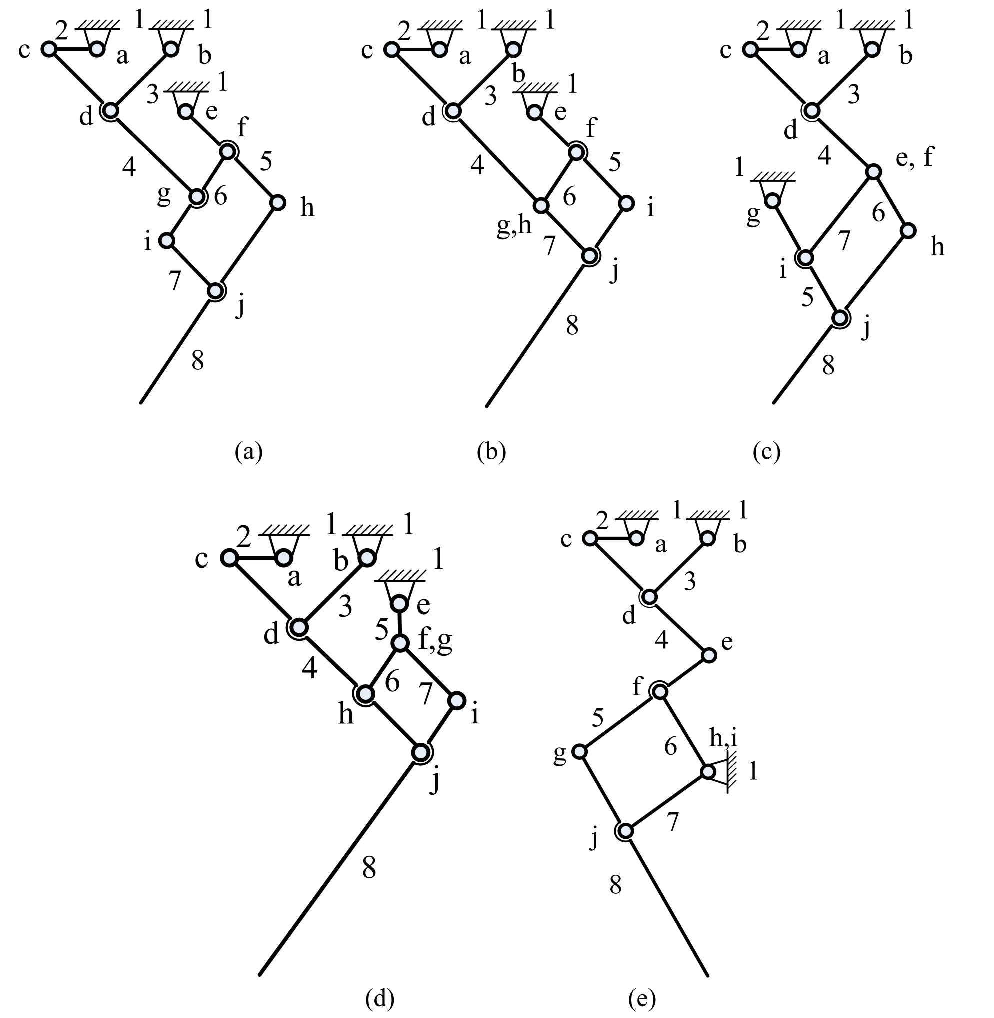

Figure 11: Atlas of designs for the leg mechanism

3.6 An atlas of new designs

The last step of this methodology is to identify all existing designs from the atlas of designs. Then, those that haven't been identified as existing designs are new designs, which are shown in Fig. (11a), Fig. (11c), and Fig. (11d).

In LARM designs, mechanisms of Fig. (11b) and Fig. (11e) have been already experienced.

Once the atlas of new designs is obtained, it is feasible to implement the optimal design procedure of the proposed design solution.

4 CONCLUSIONS

This paper presents a topology search for a new leg mechanism as based on an existing LARM leg mechanism. In order to implement this search, a procedure has been introduced and adopted with the aim of achieving an optimal design. Several new topology leg mechanisms have been found after a practical procedure of this methodology.

New design solutions obtained by this creative methodology provide comparison study between them. Then a best design solution can be found with the desired design specifications.

ACKNOWLEDGMENT

The first author acknowledges Chinese Scholarship Council (CSC) and Institute of Advanced Manufacturing Technology (IAMT) of Chinese Academy of Science (CAS) for supporting his PhD study and research at LARM in the University of Cassino in Italy from the year 2010 to 2012.

REFERENCES

[1] M. Hirose, Y. Haikawa, T. Takenaka, and K, Hirai, Development of Humanoid Robot ASIMO, Proc. IEEE/RSJ Int. Conference on Intelligent Robots and Systems, Workshop2, Oct. 29, 2001.

[2] K. Kaneko, F. Kanehiro, M. Morisawa, K. Miura, and S. N. S. Kajita, Cybernetic human hrp-4c, in Humanoids, pp.7–14, 2009.

[3] M. Ceccarelli and G. Carbone, A new leg design with parallel mechanism architecture, AIM 2009 IEEE/ASME International Conference on Advanced Intelligent Mechatronics 14-17 July 2009, pp 1447-1452.

[4] G. Carbone, M. Ceccarelli, Legged Robotic Systems, Cutting Edge Robotics ARS Scientific Book, Wien, pp. 553-576, 2005.

[5] S. Yoshiaki, W. Ryujin, and A. Chiaki, Intelligent ASIMO: system overview and integration. Proceeding of the IEEE/RSJ International Conference on Intelligent Robots and Systems, EPFL, Switzerland September 30-October 4: 2478-2483, 2002

[6] K. Kaneko, F. Kanechiro, S. Kajita, et al. Humanoid robot HRP-2. Proceeding of the 2004 IEEE International Conference on Robotics and Automation, New Orleans, USA, April 26-May 1: 1083-1090, 2004

[7] A.M.M. Omer, Y. Ogura, H. Kondo, et al. Development of a humanoid robot having 2-DOF waist and 2-DOF trunk. Proceeding of the 2005 5th IEEE-RAS International Conference on Humanoid Robots, Tsukuba, Japan, December 5-7: 333-338, 2005

[8] S.M. Song, K.J. Waldron, Machines that walk-the adaptive suspension vehicle, Cambridge MA: The MIT Press, 1989.

[9] H. Funabashi, M. Horie, H. Tachiya, et al, A synthesis of robotic pantograph mechanisms based on working spaces and static characteristics charts, JSME International journal Series III, 34(2)., 1991.

[10] W.B. Shieh, L.W. Tsai, and S. Azarm, Design and optimization of a one-degree-of-freedom six-bar leg mechanism for a walking machine. Journal of Robotic systems, 14(12): 871-880, 1997.

[11] C. Lanni, M. Ceccarelli, E. Ottaviano and G. Figliolini, Actuating mechanisms for pantograph legs: structures and characteristics, Tenth world congress on the theory of machines and mechanisms, Oulu, Finland, June 20-24, 1999, Vol.3, pp.1196-1201.

[12] E. Ottaviano, C. Lanni, M. Ceccarelli, Numerical and Experimental Analysis of a Pantograph-Leg with a Fully-Rotative Actuating Mechanism, Proceedings of the 11th World Congress in Mechanism and Machine Science, August 18–21, 2003, Tianjin, China, pp.1537-154.

[13] M. Ceccarelli, G. Carbone, E. Ottaviano and C. Lanni, Leg designs for walking machines at LARM in Cassino, Robotica mobile per esplorazione lunare Unmanned, 1-2, June, Roma Italy, 2009 pp. 5-15.

[14] M. Ceccarelli, M., Figliolini, G., Lanni, C., Ottaviano, E., A Study of Feasibility for Rickshaw Type Mobile Robot, IEEE International Conference on Industrial Electronics, Control and Instrumentation, Nagoya, 2000, paper MT9-MRC-2.

[15] C. Liang, M. Ceccarelli, and Y. Takeda, Operation analysis of a one-DOF pantograph leg mechanism. CD Proceedings of the 17th International Workshop on Robotics in Alpe-Adria-Danube Region, RAAD'2008, Ancona, n. 50, 2008.

[16] H.S. Yan, Creative design of mechanical devices. Singapore: Springer, 1998.

Proceedings of MUSME 2011, the International Symposium
on Multibody Systems and Mechatronics
Valencia, Spain, 25–28 October 2011

EXPONENTIAL INTEGRATION SCHEMES IN MULTIBODY DYNAMICS

Javier Ros*, Xabier Iriarte*, Roberto Yoldi* and Jorge Ángeles†

*Mechanical, Energetics and Materials Engineering Department
Public University of Navarre, Campus Arrosadia s/n, 31006 Pamplona, Spain
e-mail: [jros,xabier.iriarte,roberto.yoldi]@unavarra.es,
web page: http://www.imac.unavarra.es

†Department of Mechanical Engineering & Centre for Intelligent Machines,
McGill University, Montreal, Quebec, H3A 2K6, Canada
e-mail: angeles@cim.mcgill.ca

Keywords: Exponential, Exponetially f tted, Integration scheme, Zero and First Order Hold, Precise integration method, Multibody, Nonlinear dynamic system.

Abstract. *Exponential integrators are certainly not new, but despite their good properties they seem to be absent in the multibody dynamics literature. This article introduces the concept and proposes a formulation for the use of such a kind of integrators in the context of multibody dynamics. The exposition has been focused to the linear system control theory to make the ideas more simplistic an accessible to the multibody community. From control theory it is known that discretizations based on the N-th Order Hold (NOH) can be set up for the numerical integration of a LTI system. The resulting integration schemes are the so called exponential schemes. This representation readily leads to the extension of the N-th order hold discretization to multibody systems, that is to exponential multi-step and Runge-Kutta methods. In order to apply this discretizations to the case of multibody dynamics it is proposed to reshaped the model of the multibody system so that its appearance is that of a linear system: First, the model is expressed as the linearized model of the system but with a forcing term that additionally contains all the nonlinearities, then it is written in terms of a set of independent velocities, and finally expressed in the form of a first-order differential equation. The proposed method with a Zero OH discretization is demonstrated for a simplistic nonlinear mechanical system. The simulations demonstrate the outstanding characteristics of the proposed scheme. Due to nonlinearity, the stability of the discretized multibody system cannot strictly be claimed to be that of the continuous system, although this will be true in the limit when the discretization step goes to zero. Simulation examples show that the proposed schemes outperform explicit integration schemes of the same order. The proposed schemes seem very interesting for a number of relevant applications, like control, Hardware in the Loop (HiL) systems, haptics, flexible multibody dynamics, identification, etc.*

1 Introduction

For a general Linear Time Invariant (LTI) system of the form

$$\dot{\mathbf{x}}(t) = \mathbf{A}\mathbf{x}(t) + \mathbf{B}\mathbf{u}(t), \quad \mathbf{x}(0) = \mathbf{x}_0, \quad \mathbf{x} \in \mathbb{Z} \tag{1}$$

it time response is known to be

$$\mathbf{x}(t) = e^{\mathbf{A}(t-t_0)}\mathbf{x}(t_0) + \int_{t_0}^{t} e^{\mathbf{A}(t-\tau)}\mathbf{B}\mathbf{u}(\tau)d\tau, \tag{2}$$

see for example [1] or [2]. The solution involves the sum of the impulse response of the system to the initial conditions –homogeneous solution–, and the convolution integral of the forcing term with the impulse response of the system –non-homogeneous–.

In the control engineering context, the equations of linear systems have been discretized since the start of the digital computer era as a requirement for the computer implementation of controllers and f lters [2]. These discretizations, also called recurrence relations, can be used to perform an exact integral –up to the numerical precision– of the system equations. This idea has been taken advantage of long time ago to develop integrators for continuous systems [4].

Integration schemes for nonlinear systems based on this idea has been proposed as soon as 1959, see [18], [19], and have a long history [21], [22], [24], [25], [26], [28], [32]. Apparently they have been independently rediscovered many times –including us– [6], [7], [8], [9], [10], [11], [15]. For a review of several methods see [24].

These integrators are known to outperform conventional integrators when applied to linearly stiff systems. They are known under different names, most frequently as *Exponential* or *Exponentially fitted* schemes, although some rediscoverers name it differently, *Time Precise*, *Precise*,... integrators.

Schemes of different orders, including multi-step [19], [22] [34], [21] and Runge–Kutta type [23], [26] [28] generalizations has as well been proposed. More specialized integrators, conservative, geometric structure-preserving,... [30], [29], [27], can be found in the literature.

The exponential schemes require the computation of the exponential of the Jacobian matrix or matrix functions of the Jacobian involving the exponential, [12], [13], [16]. For small systems of ODEs this method has been used with success, but until the the 1980's it was considered impractical for large systems due to the diff culties in computing these functions in a reliable and economical way. The Krylov-subspaces approximation technique [17] has made the matrix exponential computation feasible. Nevertheless it seems that there is still a lot of research in this direction [14].

In this article it is explained how deal with such a kind of integrators in the context of multibody dynamics.

In section 2 Zero and First OH based explicit/implicit exact exponential discretizations for a general linear system are presented. Exponential multi-step or Runge-Kutta discretizations are brief y introduced as a natural N-th order hold extensions of the previously introduced discretizations.

In section 3, A-stability is demonstrated for the exponential schemes. The stability of classical f rst and second order schemes is analyzed as well. Also, classical non-exponential integrators are seen to be approximations of the exponential schemes in which the exponential matrix computation is approximated in different ways.

In section 4 it is explained the way in which the exponential integrators can be applied to the case of multibody systems. To that end it is proposed to reshape the dynamic equations so that their appearance is that of a linear system: First, the model is expressed as the linearized model of the system but with a forcing term that additionally contains all the nonlinearities, then it is written in terms of a set of independent velocities, and f nally expressed as f rst-order differential equation.

Section 5, it is explained how exponential schemes can be used in the case of multibody dynamics.

In section 6, comparisons of the performance of f rst order classical integrator against the proposed ZOH exponential integrators are presented an discussed.

Finally, in section 7, the conclusions and ideas presented in this article are summarized.

The proposed method with a Zero OH discretization is demonstrated for a simplistic nonlinear mechanical system. The simulations demonstrate the good characteristics of the proposed scheme. Due to nonlinearity, the stability of the discretized multibody system cannot strictly be claimed to be that of the continuous system, although this will be true in the limit when the discretization step goes to zero. Simulation examples show that the proposed scheme outperforms in comparison explicit integration schemes of the same order. The proposed schemes seem very interesting for a number of relevant applications like, control, Hardware in the Loop (HiL), haptics, f exible multibody dynamics, etc.

2 N-th Order Hold based exact discretization of a LTI system

If we consider a ZOH on the system input $\mathbf{u}$,

$$\mathbf{u}(t) = \mathbf{u}(kT), \quad kT \leq t \leq (k+1)T, \quad k \in \mathbb{Z}, \tag{3}$$

the discrete system response of the continuous system 1 is

$$\mathbf{x}[k+1] = e^{\mathbf{A}T}\mathbf{x}[k] + \left(\int_0^T e^{\mathbf{A}\eta} d\eta\right)\mathbf{B}\mathbf{u}[k]. \tag{4}$$

Noting that,

$$\int_0^T e^{\mathbf{A}\eta} d\eta = \mathbf{A}^{-1}(e^{\mathbf{A}T} - \mathbf{1}) \equiv \mathbf{F_0}, \tag{5}$$

where $\mathbf{1}$ is the identity matrix, the ZOH discretization of a LTI system can be expressed as

$$\mathbf{x}[k+1] = \mathbf{A}_d\mathbf{x}[k] + \mathbf{B}_d\mathbf{u}[k], \tag{6}$$

where

$$\mathbf{A}_d = e^{\mathbf{A}T} \tag{7}$$

$$\mathbf{B}_d = \mathbf{F}_0\mathbf{B} \tag{8}$$

2.1 First and Higher Order Hold based exact discretizations

Higher Order Hold discretizations are introduced to obtain more accurate discrete representations of the continuous system 1. For example, assuming a First Order Hold (FOH) on the system input $\mathbf{u}$,

$$\mathbf{u}(t) = \mathbf{u}(kT) + \frac{\mathbf{u}((k+1)T) - \mathbf{u}(kT)}{T}(t - kT), \quad kT \leq t \leq (k+1)T, \quad k \in \mathbb{Z}, \tag{9}$$

the time response is

$$\mathbf{x}[k+1] = e^{\mathbf{A}T}\mathbf{x}[k] + \int_0^T e^{\mathbf{A}\eta}\mathbf{B}\mathbf{u}[k]d\eta + \int_0^T e^{\mathbf{A}\eta}\mathbf{B}\frac{\mathbf{u}[k+1]-\mathbf{u}[k]}{T}\eta d\eta. \tag{10}$$

Noting that

$$\int_0^T e^{\mathbf{A}\eta}\eta d\eta = T\mathbf{A}^{-1}e^{\mathbf{A}T} - \mathbf{A}^{-2}(e^{\mathbf{A}T} - \mathbf{I}) \equiv \mathbf{F}_1 \tag{11}$$

the time response of the system can f nally be expressed as,

$$\mathbf{x}[k+1] = \mathbf{A}_d\mathbf{x}[k] + {}^0\mathbf{B}_d\mathbf{u}[k] + {}^1\mathbf{B}_d\mathbf{u}[k+1], \tag{12}$$

where

$$\begin{aligned} \mathbf{A}_d &= e^{\mathbf{A}T} && (13)\\ \mathbf{B}_d &= (\mathbf{F}_0 - \frac{\mathbf{F}_1}{T})\mathbf{B} && (14)\\ {}^1\mathbf{B}_d &= \frac{\mathbf{F}_1}{T}\mathbf{B}. && (15) \end{aligned}$$

The proposed FOH can be said to be *implicit* in the sense that it needs information about $\mathbf{u}$ in the future, i.e., ($[k+1]$). This is not a problem when integrating a system, based on a known input. In some instances, as the ones that may arise in control, Hardware in the Loop (HiL) systems, or haptics, this cannot be the case, and then an explicit FOH discretization can be used instead. In this case,

$$\mathbf{u}(t) = \mathbf{u}(kT) + \frac{\mathbf{u}(kT) - \mathbf{u}((k-1)T)}{T}(t - kT), kT \leq t \leq (k+1)T, k \in \mathcal{N}. \tag{16}$$

Analogously, FOH discretization can also be made implicit. Consider for example

$$\mathbf{u}(t) = \mathbf{u}((k+1)T), \quad kT \leq t \leq (k+1)T, \quad k \in \mathcal{N}, \tag{17}$$

Higher Order Holds The previous ideas can be readily extended to obtain Higher Order Hold discretizations. For example, as in the previous derivations, based on the analytical solution (2), exponential multi-step and Runge-Kutta methods, can obtained from

$$\mathbf{x}[k+1] = e^{\mathbf{A}T}\mathbf{x}[k] + \left(\int_0^T e^{\mathbf{A}\eta}\mathbf{B}\mathbf{u}(\eta)d\eta\right). \tag{18}$$

To that end the previous integral is approximated giving to

$$\mathbf{u}(t), \quad kT \leq t \leq (k+1)T, \quad k \in \mathbb{Z}, \tag{19}$$

the particular polynomial form corresponding to the desired method.

3 Discretization Stability

It is known that the eigenvalues of matrix $\mathbf{A}$ and $\mathbf{A}_d$ determine the stability of the corresponding system [2] :

- The linear continuous-time system (1) is a) asymptotically stable if the eigenvalues of $\mathbf{A}$ lie in the left half of the complex plane; b) marginally stable if none of the eigenvalues of $\mathbf{A}$ lies in the right half of the complex plane, but at least one vanishes; and c) asymptotically unstable if at least one eigenvalue of $\mathbf{A}$ lies in the right half of the complex plane.

- The linear discrete-time system (6) is a) stable if the eigenvalues of $\mathbf{A}_d$ lie inside the unit circle centered at the origin of the complex plane; b) marginally stable if none of the eigenvalues of $\mathbf{A}_d$ lies outside the unit circle centered at the origin of the complex plane, but at least one lies on the unit circle; and c) unstable if at least one eigenvalue of $\mathbf{A}_d$ lies outside the unit circle.

Now, let us assume that system (1) is stable; in this case, all the eigenvalues of $\mathbf{A}$ have a negative real part. If $\lambda_i = u + jv$ denotes the ith eigenvalue of $\mathbf{A}$, then the ith eigenvalue of $\mathbf{A}_d$ is $\lambda_{d,i}$, which is given by

$$\lambda_{di} = e^{(u+jv)T} = e^{uT}(\cos vT + j \sin vT)$$

Now, since $u < 0$, $0 < e^{uT} < 1$, and hence, $\lambda_{d,i}$ lies within the unit circle centered at the origin of the complex plane, and the discrete-time system derived from its continuous counterpart is stable. Similar arguments apply to the marginally stable and unstable cases.

That is, *the stability properties of the continuous-time and discrete-time systems correspond with each other and are independent of the sampling period T.*

It can be said that the discretization maps the complex continuous left and right s–plane into the interior and exterior of the complex unit circle on the discrete z–plane, respectively:

$$\lambda_i \xrightarrow{e^{AT}} \lambda_{d,i} = e^{\lambda_i T}. \tag{20}$$

This is a very important characteristic for a discretization. For example, a HiL simulation could become unstable when the real system is not. This would somehow limit the applicability of the HiL setup. Most discretization schemes make the stability of the discretized system to differ from that of the continuous system. The stability of the discretized system becomes dependent on T, and the system becomes more unstable the bigger the T.

3.1 Stability of other discretizations

Euler The Explicit/Implicit Euler discretization scheme gives the following discrete systems

$$\text{Explicit} \quad : \quad \mathbf{x}[k+1] = (\mathbf{1} + T\mathbf{A})\mathbf{x}[k] = \mathbf{V}(\mathbf{1} + T\mathbf{\Lambda})\mathbf{V}^T\mathbf{x}[k] \tag{21}$$

$$\text{Implicit} \quad : \quad \mathbf{x}[k+1] = (\mathbf{1} - T\mathbf{A})^{-1}\mathbf{x}[k] = \mathbf{V}(\mathbf{1} - T\mathbf{\Lambda})^{-1}\mathbf{V}^T\mathbf{x}[k], \tag{22}$$

(we are omitting the forcing term) that are stable if

$$\text{Explicit} \quad : \quad \Rightarrow 1 + T\lambda_i < 1 \; \forall i \tag{23}$$

$$\text{Implicit} \quad : \quad \Rightarrow 1 - T\lambda_i > 1 \; \forall i. \tag{24}$$

Obviously the stability of these dicretizations is dependent on T. These schemes can be understood as N-th Order Hold schemes, in which the exponential matrix gets approximated as

$$\text{Explicit} \quad : \quad e^{\mathbf{A}T} \approx (\mathbf{1} + \mathbf{A}T) \tag{25}$$

$$\text{Implicit} \quad : \quad e^{\mathbf{A}T} = \left(e^{-\mathbf{A}T}\right)^{-1} \approx (\mathbf{1} - \mathbf{A}T)^{-1}. \tag{26}$$

Trapezoidal It is interesting to note that the bilinear transform, or Tustin transform [2, 3], that approximates the exponential matrix as

$$e^{\mathbf{A}T} \approx \left(\mathbf{1} + \frac{1}{2}\mathbf{A}T\right)\left(\mathbf{1} - \frac{1}{2}\mathbf{A}T\right)^{-1}, \tag{27}$$

produces a discretization that has also the same stability properties as those of the associated linear system. Looking at the mapping

$$\lambda_i \xrightarrow{(\mathbf{1}+\frac{1}{2}\mathbf{A}T)(\mathbf{1}-\frac{1}{2}\mathbf{A}T)^{-1}} \lambda_{d,i} = \frac{1+\frac{1}{2}\lambda_i T}{1-\frac{1}{2}\lambda_i T} \tag{28}$$

it is apparent that, in this case, the discretization maps the complex continuous left (right) s–plane into the interior(exterior) of complex unit circle on the discrete z–plane. Note that (making $\lambda_i = \sigma + j\omega$)

$$\left|\frac{(1+\frac{1}{2}(\sigma + j\omega)T)}{(1-\frac{1}{2}(\sigma + j\omega)T)}\right| = \frac{(1+\sigma)^2 + \omega^2}{(1-\sigma)^2 + \omega^2}. \tag{29}$$

As a consequence

$$if \quad \sigma = 0 \Rightarrow \lambda_i \longrightarrow \lambda_{d,i} \quad with \quad |\lambda_{d,i}|^2 = 1 \tag{30}$$

$$if \quad \sigma < 0 \Rightarrow \lambda_i \longrightarrow \lambda_{d,i} \quad with \quad |\lambda_{d,i}|^2 < 1 \tag{31}$$

$$if \quad \sigma > 0 \Rightarrow \lambda_i \longrightarrow \lambda_{d,i} \quad with \quad |\lambda_{d,i}|^2 > 1 \tag{32}$$

If the bilinear approximation, Eq. (27), is used in the FOH discretization, Eq. (12), to substitute the exponential, then the trapezoidal rule,

$$(\mathbf{1} - \frac{1}{2}\mathbf{A}T)x[k+1] = (\mathbf{1} + \frac{1}{2}\mathbf{A}T)x[k] + \frac{1}{2}\mathbf{B}T(u[k+1] + u[k]) \tag{33}$$

is obtained.

4 Linear-like reshaping of the multibody system model equations

In this section a procedure is proposed to reshape the nonlinear model of a multibody system so that its outlook is that of a linear system, but without changing it. Here there are several procedures to follow: Linear-like reshaping on dependent coordinates with Lagrange multipliers, dependent coordinates without multipliers, or formulation on independent coordinates. For brevity only the last case will be dealt with.

First the model is expressed as the linearized version of the system, but with an augmented forcing term that contains all the nonlinearities. Then, it is written in terms of a set of independent velocities. Finally it is reshaped, so that it takes the form of a f rst order differential equation. The procedure proposed is somehow based on a variation of the linearization procedure described in [5].

Consider a multibody system parameterized by the set of dependent generalized coordinates $\mathbf{q}$. and he input to the system denoted by the vector of generalized forces $\boldsymbol{\tau}$.

Let $\mathbf{g}(\mathbf{q}, \dot{\mathbf{q}}, \ddot{\mathbf{q}}, \boldsymbol{\tau}) = \mathbf{0}$ be the vector of dynamic equations, where $\mathbf{q}$, $\dot{\mathbf{q}}$, $\ddot{\mathbf{q}}$ are the vectors of dependent generalized coordinates, velocities and accelerations, and $\boldsymbol{\tau}$ is the vector of external forces/moments applied to the robot. The linearized dynamic equations are derived as the f rst order Taylor expansion of the dynamic equations in terms of $\mathbf{q}^* = [\mathbf{q}^T\, \dot{\mathbf{q}}^T\, \ddot{\mathbf{q}}^T\, \boldsymbol{\tau}^T]^T$, around $\mathbf{q}_0^* = [\mathbf{q}_0^T\, \dot{\mathbf{q}}_0^T\, \ddot{\mathbf{q}}_0^T\, \boldsymbol{\tau}_0^T]^T$:

$$\mathbf{g}(\mathbf{q}^*) = \mathbf{g}(\mathbf{q}_0^*) + \left.\frac{\partial \mathbf{g}(\mathbf{q}^*)}{\partial \mathbf{q}^*}\right|_{\mathbf{q}_0^*} \Delta\mathbf{q}^* + \mathbf{O}\left(|\Delta\mathbf{q}^*|^2\right) \tag{34}$$

This equation can be expressed in a linear-like form:

$$\mathbf{M}\Delta\ddot{\mathbf{q}} + \mathbf{C}\Delta\dot{\mathbf{q}} + \mathbf{K}\Delta\mathbf{q} + \mathbf{g}_{\boldsymbol{\tau}}(\mathbf{q}_0^*)\Delta\boldsymbol{\tau} = \mathbf{f}^{nl} \tag{35}$$

where $\mathbf{g}_{\boldsymbol{\tau}}(\mathbf{q}_0^*)$ is the external forces/torques transmission matrix, $\mathbf{K} \equiv \mathbf{g}_{\mathbf{q}}(\mathbf{q}_0^*)$ is the stiffness matrix, $\mathbf{C} \equiv \mathbf{g}_{\dot{\mathbf{q}}}(\mathbf{q}_0^*)$ is the damping matrix, and $\mathbf{M} \equiv \mathbf{g}_{\ddot{\mathbf{q}}}(\mathbf{q}_0^*)$, is the mass matrix. Note that in the linearized problem the variables are $\Delta\mathbf{q}^* = \mathbf{q}^* - \mathbf{q}_0^*$.

The term $\mathbf{f}^{nl}$,

$$\mathbf{f}^{nl} = -\mathbf{g}(\mathbf{q}_0^*) + \mathbf{O}(|\Delta\mathbf{q}^*|)^2 = -(\mathbf{g}(\mathbf{q}^*) - \frac{\partial \mathbf{g}(\mathbf{q}^*)}{\partial \mathbf{q}^*}\Delta\mathbf{q}^*) \tag{36}$$

contains all the nonlinear contributions on the dynamics of the system.

In order to reshape the model according to (1), the linearized model should f rst be expressed in terms of a set of independent linearized coordinates. Suppose that the set of coordinates $\mathbf{q} = [\mathbf{d}^T\, \mathbf{z}^T]^T$, where $\mathbf{z}$ is an arbitrary set of independent coordinates, and $\mathbf{d}$ are the remaining coordinates.

Next, the geometric constraint equations can be approximated by $\boldsymbol{\Phi} \approx \boldsymbol{\Phi}(\mathbf{q}_0) + \boldsymbol{\Phi}_{\mathbf{q}}(\mathbf{q}_0)\Delta\mathbf{q} = \mathbf{0}$. For brevity it is assumed that the constraints are scleronomic, $\boldsymbol{\Phi}(\mathbf{q}_0) = \mathbf{0}$. A set of generalized independent differential pseudo-coordinates $\Delta\mathbf{z}$ can be def ned as

$$\Delta\mathbf{q} = \mathbf{R}\Delta\mathbf{z} \tag{37}$$

where $\mathbf{R}$ has independent columns that span the space orthogonal to the row space of $\boldsymbol{\Phi}_{\mathbf{q}}$, so that $\mathbf{R}^T\boldsymbol{\Phi}_{\mathbf{q}} = \mathbf{0}$.

Frequently, in the case of non-holonomic systems, the previous transformation if obtained by partitioning the vector of coordinates into arbitrarily choosed sets of independent and dependent coordinates, as $\Delta\mathbf{q} = [\Delta\mathbf{d}^T\, \Delta\mathbf{z}^T]^T$, and the Jacobian as $\boldsymbol{\Phi}_{\mathbf{q}} = [\boldsymbol{\Phi}_{\mathbf{d}}\, \boldsymbol{\Phi}_{\mathbf{z}}]$, it is possible to write

$$\Delta\mathbf{d} = -\boldsymbol{\Phi}_{\mathbf{d}}(\mathbf{q}_0)^{-1}\boldsymbol{\Phi}_{\mathbf{z}}(\mathbf{q}_0)\Delta\mathbf{z}. \tag{38}$$

Moreover, the generalized coordinates $\Delta\mathbf{q}$ can be expressed in terms of $\Delta\mathbf{z}$ as.

$$\Delta\mathbf{q} = \mathbf{R}\Delta\mathbf{z}, \tag{39}$$

where

$$\mathbf{R} = \begin{bmatrix} -\boldsymbol{\Phi}_{\mathbf{d}}(\mathbf{q}_0)^{-1}\boldsymbol{\Phi}_{\mathbf{z}}(\mathbf{q}_0) \\ \mathbf{1} \end{bmatrix}. \tag{40}$$

The linear-like dynamic equations expressed in terms of the independent coordinates ($\Delta\mathbf{z}$), can be derived from the previously obtained linear-like dynamic equations as[1]:

$$\mathbf{R}^T\mathbf{M}\mathbf{R}\Delta\ddot{\mathbf{z}} + \mathbf{R}^T\mathbf{C}\mathbf{R}\Delta\dot{\mathbf{z}} + \mathbf{R}^T\mathbf{K}\mathbf{R}\Delta\mathbf{z} + \mathbf{R}^T\mathbf{g}_{\boldsymbol{\tau}}\Delta\boldsymbol{\tau} = \mathbf{R}^T\mathbf{f}^{nl} \tag{41}$$

where the matrices are evaluated at $[\mathbf{q}_0\,\dot{\mathbf{q}}_0\,\ddot{\mathbf{q}}_0^T\,\boldsymbol{\tau}_0^T]$. It is important to note that in the particular case of multibody systems, $\ddot{\mathbf{q}}_0 = \mathbf{0}$ and $\boldsymbol{\tau}_0 = \mathbf{0}$, as the equations are linear in $\ddot{\mathbf{q}}$ and $\boldsymbol{\tau}$. This fact will be used in the following section 5 in order to simplify various expressions. Also, note that $\mathbf{q}_0$, $\dot{\mathbf{q}}_0$, and $\ddot{\mathbf{q}}_0$ must be compatible with the kinematic restrictions. Care should be taken so that $\mathbf{q}_0$ and $\dot{\mathbf{q}}_0$ are consistent with the actual assembly of the mechanism.

Finally, the coeff cient matrices of the standard state space form,

$$\dot{\mathbf{x}}(t) = \mathbf{A}(t)\mathbf{x}(t) + \mathbf{B}(t)\mathbf{u}(t) \tag{42}$$

are obtained by identifying $\mathbf{x} \equiv [\Delta\dot{\mathbf{z}}^T\ \Delta\mathbf{z}^T]^T$ and $\mathbf{u} \equiv [\boldsymbol{\tau}^T, \mathbf{f}^{nl^T}]^T$, as:

$$\begin{aligned}
\mathbf{A} &= \begin{bmatrix} -(\mathbf{R}^T\mathbf{M}\mathbf{R})^{-1}\mathbf{R}^T\mathbf{C}\mathbf{R} & -(\mathbf{R}^T\mathbf{M}\mathbf{R})^{-1}\mathbf{R}^T\mathbf{K}\mathbf{R} \\ \mathbf{1} & \mathbf{O} \end{bmatrix} \\
\mathbf{B} &= \begin{bmatrix} -(\mathbf{R}^T\mathbf{M}\mathbf{R})^{-1}\mathbf{R}^T\mathbf{g}_{\boldsymbol{\tau}} & (\mathbf{R}^T\mathbf{M}\mathbf{R})^{-1}\mathbf{R}^T \\ \mathbf{O} & \mathbf{O} \end{bmatrix}.
\end{aligned}$$

It should be noted that matrices $\mathbf{A}$ and $\mathbf{B}$, are no longer constant, but position dependent.

5 N-th Order Hold discretization of a multibody system

From the analysis of Sec. 2 it follows that the system obtained in the previous section can be discretized using a ZOH as[2]:

$$\mathbf{x}[k+1] - \mathbf{x}[l] = \mathbf{A}_d[l](\mathbf{x}[k] - \mathbf{x}[l]) + \mathbf{B}_d[l,k]\mathbf{u}[k], \tag{43}$$

where l ($l \le k$) is the time step used to do the linearization, and

$$\mathbf{A}_d[l] = e^{\mathbf{A}[l]T} \tag{44}$$

$$\mathbf{B}_d[l,k] = \mathbf{F}_0[l]\mathbf{B}[k]. \tag{45}$$

Matrices $\mathbf{A}[l]$ and $\mathbf{B}[k]$ are the ones def ned in Sec. 4.

The previous scheme can be used in different ways. For example,

- For a system that behaves close to linear it can be convenient to choose $l = 0$, i. e.,

  $$\mathbf{x}[k+1] = \mathbf{x}[0] + \mathbf{A}_d[0](\mathbf{x}[k] - \mathbf{x}[0]) + \mathbf{B}_d[0,k]\mathbf{u}[k], \tag{46}$$

  as this will reduce importantly the computational work needed. $l = 0$ can be also understood to be a linearization point, whether or not the trajectory pases through it.

- For a system behaving quite nonlinearly, it can be interesting to update the exponential matrix computation at each step, in which case $l = k$

  $$\mathbf{x}[k+1] = \mathbf{x}[k] + \mathbf{B}_d[k,k]\mathbf{u}[k], \tag{47}$$

- Obviously in-between situations can be considered, which allows one to adjust the computational requirements to those of the simulation at hand.

[1]Here it is assumed $\mathbf{R} = \mathbf{cte}$, then each time that the linearization point is going to be changed, we should go before from $\Delta\mathbf{z} \Rightarrow \Delta\mathbf{q} \Rightarrow \mathbf{q}$ and after the new linearization from $\mathbf{q} \Rightarrow \Delta\mathbf{q} \Rightarrow \Delta\mathbf{z}$, the same procedure should be followed with $\dot{\mathbf{q}}\,\Delta\dot{\mathbf{q}}\,\Delta\dot{\mathbf{z}}$. This is not the only possible way to proceed, although it is frequently the most convenient.

[2]note that $\mathbf{u}[l]$ disappears because $\boldsymbol{\tau}_0 = \mathbf{0}$ in multibody dynamics

5.1 First and Higher Order Hold discretization of a multibody system

From the analysis of Sec. 2.1 it follows that the system obtained in the previous section can be discretized using a FOH as:

$$\mathbf{x}[k+1]-\mathbf{x}[l]=\mathbf{A}_d[l](\mathbf{x}[k]-\mathbf{x}[l])+{}^0\mathbf{B}_d[l,k]\mathbf{u}[k]+{}^1\mathbf{B}_d[l,k+1]\mathbf{u}[k+1], \qquad (48)$$

where l ($l \le k$) is the time step used to do the linearization, and

$$\mathbf{A}_d[l] \;=\; e^{\mathbf{A}[l]T} \qquad (49)$$

$${}^0\mathbf{B}_d[l,k] \;=\; (\mathbf{F}_0[l]-\frac{\mathbf{F}_1[l]}{T})\mathbf{B}[k] \qquad (50)$$

$${}^1\mathbf{B}_d[l,k+1] \;=\; \frac{\mathbf{F}_1[l]}{T}\mathbf{B}[k+1] \qquad (51)$$

Obviously, depending on the degree of nonlinearity of the simulation, the same considerations about the choice of linearizing point l, made in the preceding section, can be done.

Higher Order Holds It is obvious how to extend the previous discretization schemes for the case of arbitrary N-th OH discretizations. The only remark, to the considerations being done in Sec. 2.1, is that the polynomial approximation would be applied to $\mathbf{B}(\eta)\mathbf{u}(\eta)$ instead of only to $\mathbf{u}(\eta)$.

Also, the way in which the N-th OH discretizations can be modif ed to substitute the exponential matrix with, for example, the bilinear transform –trapezoidal rule– or any other approximations like the ones associated with Explicit/Implicit Euler schemes, seen in Sec. (3.1), that might be considered interesting for a particular application.

6 Application Examples

For comparison purposes direct dynamic simulation of a simple pendulum with the following dynamic equation

$$l\,\ddot{\theta}+g\,\sin(\theta)=0 \qquad (52)$$

is considered. Two different initial conditions are considered,

1. $\theta=\pi/18$, so that the pendulum behaves close to a linear system.

2. $\theta=\pi-\pi/36$, so that the system is exhibits clear nonlinear behavior.

At the conference presentation results for a more elaborate, flexible multibody system will be presented.

The results are obtained using three different discretization schemes:

1. Euler Explicit

$$\mathbf{x}[k+1]=\mathbf{x}[k]+\mathbf{A}[k]\mathbf{x}[k]T+\mathbf{B}[k]\mathbf{u}[k]T \qquad (53)$$

where

$$\mathbf{x}[k]=\begin{bmatrix}\dot{\theta}\\ \theta\end{bmatrix} \quad , \quad \mathbf{u}[k]=\mathbf{f}^{nl}[k] \qquad (54)$$

$$\mathbf{A}=\begin{bmatrix}-M^{-1}C & -M^{-1}\,K\\ 1 & 0\end{bmatrix} \quad \mathbf{B}=\begin{bmatrix}M^{-1}\\ 0\end{bmatrix} \qquad (55)$$

with

$$\mathbf{R} = [1] \quad \mathbf{M} = [l] \quad \mathbf{C} = [0] \quad \mathbf{K} = [g\ \cos(x_2)]\, \mathbf{f}^{nl} = [-g\ (\sin(x_2) - \cos(x_2)\ x_2] \tag{56}$$

2. ZOH with linearization around a f xed point.

$$\mathbf{x}[k+1] = e^{\mathbf{A}[k]T}\mathbf{x}[k] + \mathbf{A}^{-1}[k](e^{\mathbf{A}[k]T} - I)\mathbf{B}[k]\mathbf{f}^{nl}[k] \tag{57}$$

where $\mathbf{A}$ and $\mathbf{B}$ def ned as before, with

$$\mathbf{R} = [1] \quad \mathbf{M} = [l] \quad \mathbf{C} = [0] \quad \mathbf{K} = [g\ \cos(0)]\, \mathbf{f}^{nl} = [-g\ (\sin(x_2) - \cos(0)\ x_2] \tag{58}$$

3. ZOH with linearization at each new integration step.

$$\mathbf{x}[k+1] = e^{\mathbf{A}[k]T}\mathbf{x}[k] + \mathbf{A}^{-1}[k](e^{\mathbf{A}[k]T} - I)\mathbf{B}[k]\mathbf{f}^{nl}[k] \tag{59}$$

where $\mathbf{A}$ and $\mathbf{B}$ def ned as before, with

$$\mathbf{R} = [1] \quad \mathbf{M} = [l] \quad \mathbf{C} = [0] \quad \mathbf{K} = [g\ \cos(x_2)]\, \mathbf{f}^{nl} = [-g\ (\sin(x_2) - \cos(x_2)\ x_2] \tag{60}$$

Simulation with a close to Linear behavior:

Figures 1, 2 and 3 show the results of the pendulum example simulation for initial conditions $\theta_0 = 20\pi/180$, $\dot{\theta}_0 = 0$ (close to linear simulation). For comparison purposes each of the plots contain the simulations with $T = 0.01$ and 0.001.

Figure 1, depicts the results of the simulation using a standard Explicit Euler Method. Obviously the behavior can not be claimed to be good.

Figure 2, depicts the results of the simulation using the proposed ZOH based exponential integrator with only a initial evaluation, at $t = t_0$, of the $\mathbf{A}$ and $e^{\mathbf{A}T}$ functions. The results clearly reveal that the method outperforms the Euler method, non-exponential related classical integrator.

Figure 3, depicts the results of the simulation using the proposed ZOH based exponential integrator with evaluation of the $\mathbf{A}$ and $e^{\mathbf{A}T}$ functions at every time step. This method is known in the literature as *Exponentially Fitted Euler*, or simply *Exponential Euler* method. For these close to linear simulation, the expensive reshaping at each time step does not produce any signif cant advantage in comparison with single reshaping at equilibrium point version.

The advantages of this will become evident in the case of the far from linear simulations.

Simulation with a marked nonlinear behavior:

Figures 4, 5 and 6 show the results of the pendulum example simulation for initial conditions $\theta_0 = \pi - 5\pi/180$, $\dot{\theta}_0 = 0$ (far from linear simulation). For comparison purposes each of the plots contain the simulations with $T = 0.01$ and 0.001.

Figure 4, depicts the results of the simulation using a standard Explicit Euler Method. Obviously the performance is still much worse than the one in the more linear situation depicted in 1.

Figure 5, depicts the results of the simulation using the proposed ZOH based exponential integrator with only a initial evaluation, at $t = t_0$, of the $\mathbf{A}$ and $e^{\mathbf{A}T}$ functions. The results

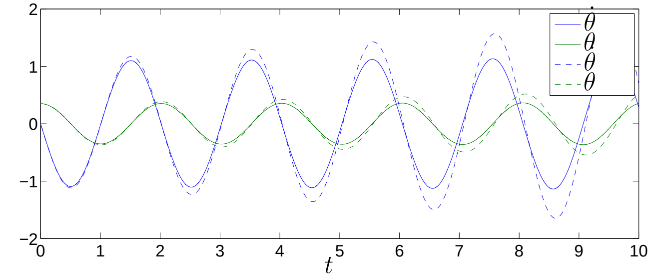

Figure 1: Euler Explicit. $\theta_0 = 20\pi/180$. "–" $T = 0.001s$, "– –" $T = 0.01s$.

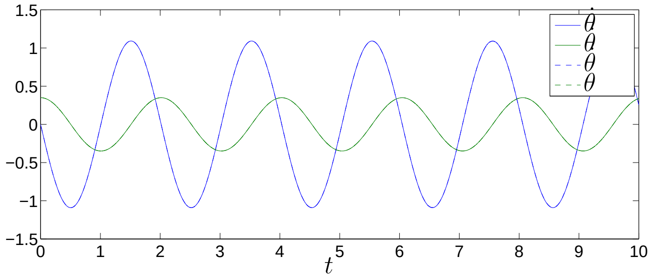

Figure 2: ZOH Linearized at $l = 0$. $\theta_0 = 20\pi/180$. "–" $T = 0.001s$, "– –" $T = 0.01s$.

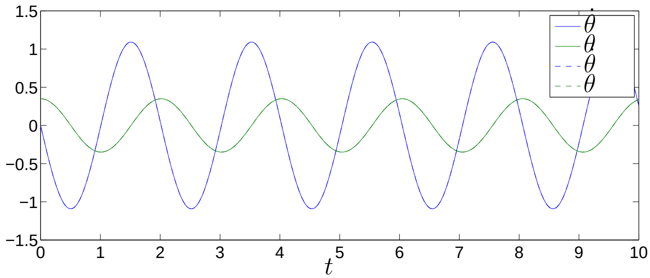

Figure 3: ZOH Linearized at $l = k$. $\theta_0 = 20\pi/180$. "–" $T = 0.001s$, "– –" $T = 0.01s$.

clearly reveal that a single reshaping around the equilibrium point is not enough in this case. Nevertheless, the performance is better than in the case of the classical explicit Euler method.

Figure 6, depicts the results of the simulation using the proposed ZOH based *Exponential Euler* method. It is clear that reevaluation of $\mathbf{A}$ and $e^{\mathbf{A}T}$ at every time step is needed.

Even for this simplistic example, the exponential Euler method outperforms, the single evaluation ZOH and Explicit Euler methods.

7 Conclusions

This work has been started with a review of the state of the art of exponential type integrators. It have been reported the extremely good properties that the literature confers to these methods. Surprisingly no references at all to these methods have been found in the multibody dynamics literature. This was the motivation of this work.

In order simplify the introduction of the exponential integrator concept to the multibody community, it is presented as a natural result of the linear system control theory. First and second

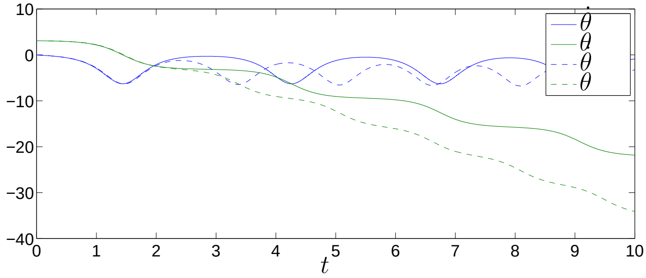

Figure 4: Euler Explicit. $\theta_0 = \pi - 5\pi/180$. "–" $T = 0.001s$, "– –" $T = 0.01s$.

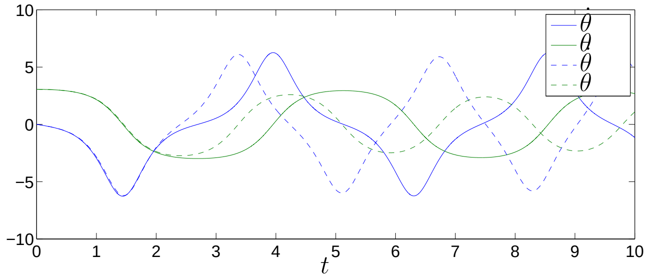

Figure 5: ZOH Linearized at $l = 0$. $\theta_0 = \pi - 5\pi/180$. "–" $T = 0.001s$, "– –" $T = 0.01s$.

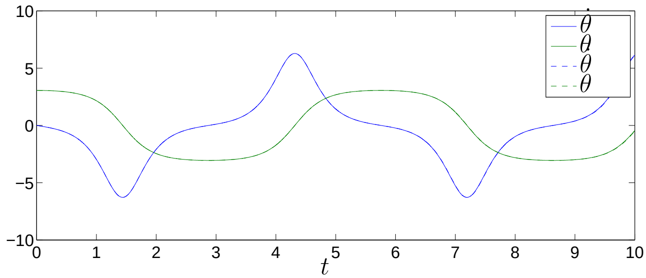

Figure 6: ZOH Linearized at $l = k$. $\theta_0 = \pi - 5\pi/180$. "–" $T = 0.001s$, "– –" $T = 0.01s$.

order accurate explicit and implicit exponential integrators have been derived. Their relation to the explicit and implicit Euler methods and with the trapezoidal rule has been formally established through the intervention of different degree approximations to the exponential matrix. Stability of these exponential methods and its non-exponential counterparts has been analyzed and compared. It has brief y explained how easily exponential integrators of the multi-step and Runge-Kutta families can be derived.

The ideas presented allow to understand from a physical point of view why exponential integrators outperform their classical non-exponential counterparts.

A methodology to use this kind of integrators in the context of general multibody systems has been proposed, and some others suggested. In addition, it is proposed that the method can be used with adjustable linear-like reshaping frequency, depending on the particular needs of the case studied.

Finally, a simplistic example exhibiting the good performance of the simplest exponential integrator, in comparison with its non-exponential counterpart has been demonstrated. Close to linear physical situations can take advantage of the eff ciency of discretization with a low frequency of linear reshaping of the model. For far from linear situations, the linear reshaping has to be performed more frequently. In every situation analyzed exponential integrators outperform their non-exponential counterparts.

It is claimed that exponential integrators should f nd their way into the multibody dynamics discipline.

REFERENCES

[1] Hespanha,J.P. Linear System Theory. Princeton university press, 2009. ISBN 0691140219.

[2] Karl J. Åström , Björn Wittenmark. Computer-Controlled Systems: Theory and Design (3rd Edition). *Prentice Hall*, 1997. ISBN-10: 0133148998

[3] A.V. Oppenheim and R. Schafer, Discrete-Time Signal Processing, *Prentice Hall, Upper Saddle River, NJ,* 1989.

[4] Jon M. Smith. Mathematical Modeling and Digital Simulation for Engineers and Scientists. *Wiley-Interscience*. 2 Sub edition. 1987. ISBN 0471085995.

[5] A. G. Lynch and M. J. Vanderploeg. A Symbolic Formulation for Linearization of Multibody Equations of Motion. *Journal of Mechanical Design*, **117**, 441–445, 1995.

[6] Zichen Deng, Yu-i Zhao. Precise Integration Method for Nonlinear Dynamic Equation. *International Journal of Nonlinear Sciences and Numerical Simulation*, **2**, 371–374, 2001.

[7] Zi-chen, Deng Wan-xie, Zhong. Time precise integration method for constrained nonlinear control system. *Applied Mathematics and Mechanics*. Shanghai University, in copublication with Springer. **23**, 1, 18–25, 2002.

[8] Deng Zichen, Wang Xiaorong, Zhao Yuli. Precise control for vibration of rigid-f exible mechanical arm, *Mechanics Research Communications*, **30**, 2, 135-141, 2003

[9] Zhang Suying, Deng Zichen. An improved precise integration method for nonlinear dynamic system. *Mechanics Research Communications*, **30**, 1, 33–38, 2003.

[10] Zhong Wan-Xie, On precise integration method, *Journal of Computational and Applied Mathematics*, Proceedings of the International Symposium on Computational Mathematics and Applications, **163**, 1, 59–78, 2004.

[11] Suying Zhang, Zichen Deng, Wencheng Li, A precise Runge-Kutta integration and its application for solving nonlinear dynamical systems, *Applied Mathematics and Computation*, **184**, 2, 496–502, 2007.

[12] C. Moler and C. Van Loan. Nineteen dubious ways to compute the exponential of a matrix. *SIAM Review*, 20 801–836, 1978.

[13] Moler, C. and van Loan, C. "Nineteen Dubious Ways to Compute the Exponential of a Matrix, Twenty-Five Years Later." *SIAM Rev.* **45**, 3-49, 2003.

[14] A. H. Al-Mohy and N. J. Higham. Computing the action of the matrix exponential, with application to exponential integrators. *SIAM J. SCI. COMPUT.*, **33**, 2, 488-511, 2011.

[15] F. Aluff -Pentini, V. De Fonzo and V. Parisi. A novel algorithm for the numerical integration of systems of ordinary differential equations arising in chemical problems. *Journal of Mathematical Chemistry* **33**, 1, 2003.

[16] G.H. Golub and C.F. van Loan. Matrix computations. The Johns Hopkins University Press,. Baltimore, 3rd edition edition, 1996.

[17] Y. Saad, Analysis of some Krylov subspace approximations to the matrix exponential operator, SIAM J. Numer. Anal. 29 (1992) 209-228.

[18] S. C. R. Dennis. The numerical integration of ordinary differential equations possessing exponential type solutions. *Mathematical Proceedings of the Cambridge Philosophical Society*, **56**, 240–246, 1960.

[19] J. Certaine. The solution of ordinary differential equations with large time constants, *Math. Meth. Dig. Comp.*. 129–132, 1960.

[20] David A. Pope. An exponential method of numerical integration of ordinary differential equations. *Commun. ACM*, **6**, 8, 491–493, 1963.

[21] S. Nørsett, An A-stable modif cation of the Adams-Bashforth methods. *Lecture Notes in Mathematics* 109 , 214–219, 1969.

[22] J. Verwer, On generalized linear multistep methods with zero-parasitic roots and an adaptive principal root. *Numer. Math.* 27 , 143–155, 1977.

[23] A. Friedli, *Lecture Notes in Mathematics*, 631:214, 1978.

[24] M. Hochbruck, C. Lubich and H. Selhofer. Exponential integrators for large systems of differential equations. *SIAM J. Sci. Comput.*, **19** 5, 1552–1574, 1998.

[25] G. Beylkin, J. M. Keiser and L. Vozovoi, A new class of time discretization schemes for the solution of nonlinear PDEs. *J. Comp. Phys.* 147, 362–387, 1998.

[26] S. Cox and P. Matthews, Exponential time differencing for stiff systems. *J. Comp. Phys.* 176, 430–455, 2002.

[27] O. Kotovych & J. C. Bowman, J. Phys. A.: Math. Gen., 35:7849, 2002.

[28] M. Hochbruck and A. Ostermann, Explicit exponential Runge-Kutta methods for semilinear parabolic problems, SIAM J. Numer. Anal. 43, 1069–1090, 2005.

[29] B. A. Shadwick, J. C. Bowman, & P. J. Morrison, SIAM J. Appl. Math., 59:1112, 1999.

[30] J. C. Bowman, B. A. Shadwick, & P. J. Morrison, "Exactly conservative integrators," in 15th IMACS World Congress on Scientif c Computation, Modelling and Applied Mathematics, edited by A. Sydow, volume 2, pp. 595–600, Berlin, 1997, Wissenschaft & Technik.

[31] An Exactly Conservative Integrator for the n-Body Problem, O. Kotovych and J. C. Bowman, *J. Phys. A: Math. Gen.*,**35**, 7849–7863, 2002.

[32] J. C. Bowman. Structure-Preserving and Exponential Discretizations of Initial-Value Problems. *Canadian Applied Mathematics Quarterly*, **14**, 223–237 (2006).

[33] Koch, C., and Segev, I., Eds. Methods in Neuronal Modeling, From Ions to Networks, second ed. Series on Computational Neuroscience. *The MIT Press*, Cambridge, Massachusetts, London, England, 1998.

[34] E. F. Sarkany and W. Liniger. Exponential Fitting of Matricial Multistep Methods for Ordinary Differential Equations. *Mathematics of Computation*, **28**, 128 1035–1052. 1974

Proceedings of MUSME 2011, the International Symposium
on Multibody Systems and Mechatronics
Valencia, Spain, 25-28 October 2011

MULTIBODY MODELLING OF A HIGH SPEED ROUTING SYSTEM FOR AUTOMATED LETTER HANDLING

Pietro Fanghella[*], Andrea Sintich[†]

[*] Department of Mechanics and Design of Machines
University of Genoa, via Opera pia 15a, 16145 Genova, Italy
e-mail: pietro.fanghella@unige.it
web page: http://www.dimec.unige.it

[†] ROSSOCARBON S.r.l.
Via Lungo Sciusa 4/4, 17024 Finale Ligure, SV, Italy
e-mail: andrea.sintich@rossocarbon.it
web page: http://www.rossocarbon.it

Keywords: multibody dynamics, mail handling, letters, flexible bodies, flexible body contacts.

Abstract. *The paper presents a complex multibody model developed to simulate the interaction among letters, a routing system and a storage box in a high performance transport system for the automated mail handling. The general features of the system and the goals of the modelling activity are first outlined. Then approaches adopted to represent the flexibility of letters (large elastic displacements) and their interaction in term of multiple contacts with the transport line, the switch geometry and storage mailbox are discussed. Model validation and simulation results for various system configurations and working conditions are discussed and compared with actual working conditions in the real system.*

1 INTRODUCTION

This paper presents the development, testing and use of a complex multibody model for the simulation of a mechanism for routing letters used in a high performance machine for automated mail handling. To introduce the topic, Fig. (1) shows a picture, taken with a high speed camera, of the considered mechanism in action: an electro-mechanical switch in its open position detours a letter, from a transport line to a desired destination box. As shown in next section, a complete system may comprise up to hundreds of switches and boxes, so the design and optimization of the basic group is of great interest.

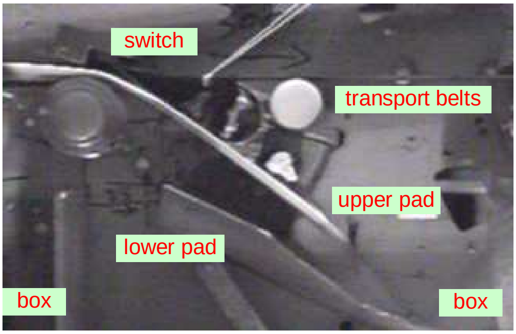

Figure 1: Picture of a letter entering the box.

In general, the considered problem has a very complex dynamics, involving the fast, gross motion of one or more flexible bodies subject to large elastic displacements (the letters) under the effect of multiple contacts with their surrounding environment and between them.

In absence of different approaches, the development of advancement solutions for this kind of machines has been usually based on the classical approach comprising expert engineers conceiving new design solutions, building physical prototypes and then long phases of testing to refine the design and the prototypes and a final fine tuning of the system to be delivered.

As a general trend, in all fields of engineering, this kind of development process is being sped up by a more in depth design-simulate-refine phase that has proved to be able to reduce development costs and time-to-market of new or revamped systems. Here the problem of adopting a virtual prototyping approach to minimize the testing effort on the real prototypes is constituted by the very complex dynamic behaviour of the handled objects - the letters.

So key goals of the research are: to evaluate the feasibility of adopting a simulation approach, i.e., the effort required to develop multibody models representative of the real dynamics of the system; to validate model responses in comparison to those of the real system; once (and if) obtained reasonably well behaved models, a third goal is evaluate the models as tools to validate the goodness of the current design and explore alternatives for better ones.

In is worth remembering that the large range in the letter dimensions, thickness, weight and, in general, mechanical characteristics such as stiffness, type of envelope paper, allowed by Mail Services specifications creates many variants to be verified both in real and virtual prototyping and testing. So, for example, computation times required to carry out a typical dynamic simulation compared with the time required to carry out a test on the physical prototype may become a critical factor in the choice of the development approach for new solutions.

As far as we know, scientific literature regarding this topic is very limited: beyond two references on destacking mechanisms, one design oriented [1], the second discussing multibody simulation, but with letters modelled as rigid bodies [2], no scientific literature about physical letter handling has been found. In some cases, control logics are considered, but without any reference to the physical behaviour of system components [3]. Accordingly, as far as we know, this is the first contribution regarding the development of flexible body - multibody models applied to this field.

The paper is structured as follows: in next Section, a general outline of the considered system is provided. The mapping of the real system to a multibody model has required a certain effort and is discussed in Sections 3-5. In reality, the choice on how to implement the models has been carried out by considering simultaneously all the critical aspects of both the real system and the multibody tool adopted for the simulations. For the reasons previously discussed, a great effort has been devoted to the goal of obtaining computationally efficient models. In Section 3, the basic characteristics of the adopted contact model are outlined. In Section 4, the letter model is presented and then in Section 5 the model of the transport line, of the pads and of the box are discussed. Model validation and some simulation results are examined in Section 6.

2 SYSTEM DESCRIPTION

The switching & storing subsystem considered in the present paper is a key component of a more complex system for dealing with the final stages of letter dispatching (Fig. (2)).

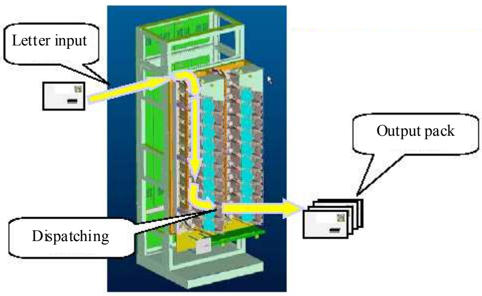

Figure 2: Letter dispatching system.

The system receives in input a flow of (already recognized) letters and it routes them to output boxes, for example according to criteria based on final destination location.

The letters are transported by a system of flat belts and directed to their destination boxes by a set of electro-mechanical switches.

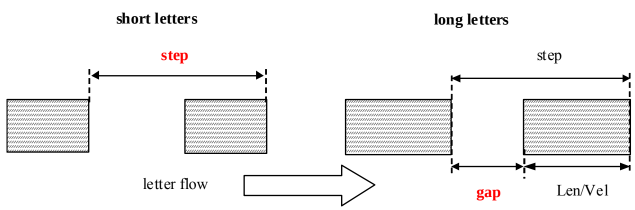

Figure 3: Geometry of letter flow.

Commutation time for such switches can be obtained by considering letter minimum and maximum allowed lengths (respectively 126 and 270 mm), transport speed (about 4-5 m/s) and required throughput (40-45 kletters/h). The worst case occurs when a long letter is transported, as, to maintain the required flow, its tail has the minimum gap from the head of the following letter (Fig. (3)): as the "step" distance between two subsequent letters is determined by required flow rate, the minimum value of gap occurs with a long letter, and determines switch open/close cycle time (less than 0.1 s).

Fig. (4) and Fig. (5) show a perspective and a lateral views of the considered subsystem. Its main elements are: transport system constituted by upper and lower belts along with their rollers, the electromechanical switch and the box with the lower and upper pads; both such pads are hinged to the box frame and are able to move, passively, in order to adapt the space between them to the amount of contained letters. In particular the upper pad presses the letter stack in order to favour the insertion of next letters directed to the box. The cut in the lower pad is for ergonomic purposes, to ease the pinch and lateral extraction action of the letter stack by the postman or by a robot.

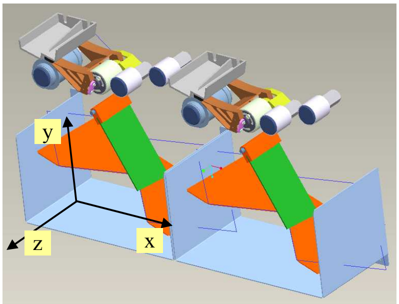

Figure 4: Geometry of the switching & storing subsystem.

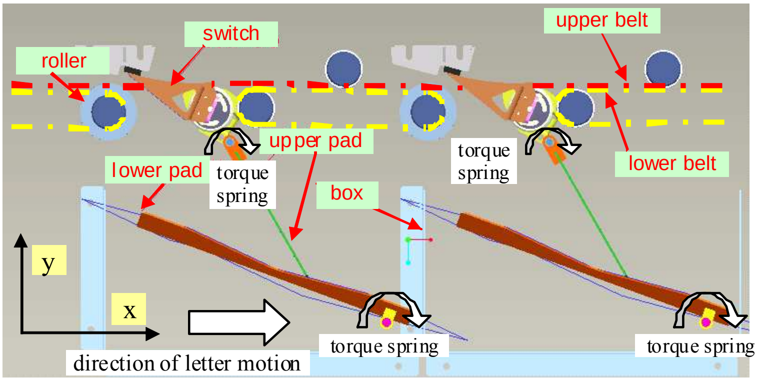

Figure 5: Lateral view of the transport, switching & storing subsystem.

The functioning scheme of the system is relatively simple. All switches are normally kept closed (in Fig. (5) they are drawn in the open position) to form together with the belts a continuous transport line for the letter flow; when a letter is immediately before its destination box, the switch is opened and the letter is routed into the box. Before the next letter head reaches the switch tip, the switch must be perfectly closed again.

What makes the system design challenging are the tough requirements in terms of throughput, reliability of transport and routing, and system availability.

The study presented in this paper is specifically aimed at analyzing the dynamic behaviour of the letters during their routing to a box, by an open switch. Fig. (1), taken with a high speed camera on the real system, shows a typical situation. The letter, hitting the lower surface of the open switch, is deflected and its head directed to the inside of the box. The box is presently empty, so the lower pad is in its upper position, in direct contact with the upper pad (not clearly visible in the picture); in the following, the letter slips between the two pads, it hits the left vertical wall of the box and, after some residual motion, it halts.

3 ELEMENTARY CONTACT MODELS

The representation of unilateral contacts of objects subject to collisions involve two basic aspects: a) the definition of the geometry of the objects, and b) the model of the dynamic interaction of the two objects when in contact (normal force, friction, dissipative effects).

Regarding the first aspect, the chosen multibody code supports several solutions to define contact geometries. Among them, two basic type of contacts have been chosen:

- point-point contact, in which the contact geometries are both spheres;
- point-segment contact, in which the two geometries in contact have distinct shapes: one is a sphere, the other is a surface obtained from a planar curve formed by a set of line segments and arcs of circumferences, either extruded in the direction orthogonal to the sketching plane or revolved along an axis belonging to such a plane.

The advantages of these representations are that they allow a closed form, analytical detection of geometry interferences, that they provide a well established and efficient solution also for the computation of interaction forces [4-5] and that any number of contacts between the same two objects can be established; they all work in parallel, providing the tool for representing complex relations among interacting bodies with high computational efficiency.

As discussed in next Sections, this is a key characteristics massively used to set up the presented model. On the other side, the main disadvantage of this approach is that complex geometries must be approximated by a large numbers of elementary contact components (large modelling effort).

Regarding the force model, this kind of contact component supports a non-linear, visco-elastic model, with friction. Dissipative effects in the normal direction are obtained by simulating a sort of hysteretic effect whose amplitude is based on the value of the restitution coefficient [5]. Static tangential friction is modelled in an approximated way non allowing exact stiction representation; in the present case, this is not a relevant limitation as the main goal of the study regards the dynamic interaction of the letters, in motion, with the switch and box geometries. No relevant stiction phenomena are present in considered system.

4 MODEL OF LETTERS

Contrary to previous studies regarding similar topisc [2], here, as shown in Fig. (1), to represent the behaviour of the considered system, a model of letters comprising their flexibility is required. For their representation, the chosen solver supports the classical approach based on modal superposition [6, 7]. Accordingly, the position $\mathbf{r}_i$ of a point $\mathbf{P}_i$ on a flexible body is obtained as the sum of its position in the undeformed state $\mathbf{r}+\mathbf{s}_{i0}$ plus the elastic displacement obtained as a linear combination of modes $\mathbf{\Phi}_i$ times modal coordinates $\mathbf{u}$:

$$\mathbf{r}_i(t)=\mathbf{r}(t)+\mathbf{s}_i=\mathbf{r}(t)+\mathbf{s}_{i0}+\sum_{j=1}^{\text{n\_modes}}\mathbf{\Phi}_{ij}u_j(t) \qquad (1)$$

The advantages of this approach are that it is well supported by software tools, that to prepare data regarding the structural properties of flexible bodies is relatively easy by using FEM codes, and that, being the model usually based on a limited number of modes, it is computationally more efficient than models based, for example, on direct nodal representations. On the other hand, a well known limitation of the modal superposition as used in Eq. (1) is that it only allows a linearized, first order approximation of the flexible behaviour of objects. Therefore, higher order effects such as large elastic deformations and displacements, buckling, stress stiffening and others are not modelled by adopting a direct modal based approach. Here, the most relevant higher order effect is related to the large bending deformations of the letters (Fig. (1)). Moreover, such effects are not uniformly distributed, but occur in limited, time varying, regions of the letters body, as the letter hits the switch and flexes toward the box.

The approach adopted here to overcome the limitations of basic modal superposition is a specific form of "sub-structuring“ techniques [7] allowing large geometric displacements. Such approach is particularly suited for the representation of the nonlinear effects related to flexibility found in the studied system. The general idea of this sub-structuring method is:

- the complete flexible object is divided into a set of smaller bodies, according to criteria based on the type of nonlinear effects to be represented;
- the structural model of each elementary body is obtained in the classical way adopted in case of modal superposition, via, for example, an unconstrained FEM modal analysis and various static analyses [6, 7];
- the complete object is composed, in the multibody environment, as a collection of flexible bodies, one for each elementary body; proper relative constraint conditions must be applied in the multibody model on the boundary nodes of the elementary bodies in order to properly form the complete object.

4.1 One letter

Since one of the goals of the model is to represent the variety of geometric and mass characteristics of allowed letters, a parametric model of a generic letter has been developed. Although the geometry of a single letter is very simple (a rectangle of length *lu_lett* , width *la_lett* and thickness *sp_lett)*, the complete parameterization of both FEM and multibody models for all the elementary bodies used to represent a single (parametric) letter is a non-trivial task. Moreover, it is to be noted that, in order to avoid undesired transitory effects, the starting position of each elementary flexible body in the multibody model should correspond to a (parametric) equilibrium position for such body.

After a few trials, it has been decided that an acceptable compromise between model complexity and model accuracy is achieved by dividing each letter into six elementary identical bodies. Fig. (6) shows the main characteristics of a letter model: six elementary flexible bodies are attached in sequence, through a set of boundary nodes.

The FEM model of elementary flexible bodies is implemented and solved in Ansys. Since the large flexible rotations of the complete letter are obtained by composing small rotations of elementary flexible bodies, it is mandatory to select FEM elements with nodal d.o.f. comprising rotations (6 d.o.f. nodes). So, the mesh of the FEM models is formed by shell elements. By observing the real machine, it is clearly noted that the flexibility of the letters affects their behaviour mainly trough elastic displacements in the x-y plane (Fig. (1)), so, to reduce model complexity, the FEM model is restricted to allow to nodal coordinates only 3 d.o.f (x, y, rotz). Fig. (7) shows the results of FEM models: the first two mode shapes of an elementary body are shown. Since it is unlikely that the deformed shape of a single (complete) letter had more than 13 nodes, only the first two modes of elementary bodies have been included in the letter model. In this way, each letter has 12 elastic d.o.f., with displacements constrained in its local x-y plane, plus six d.o.f. allowing large motions of the complete letter in 3d space.

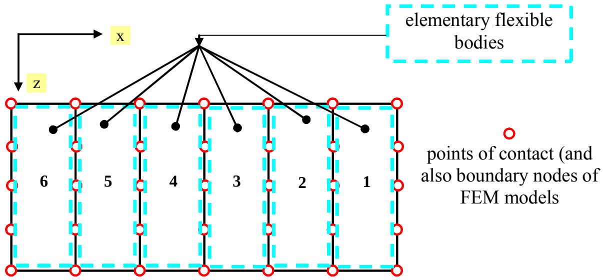

Figure 6: Substructured model of letter.

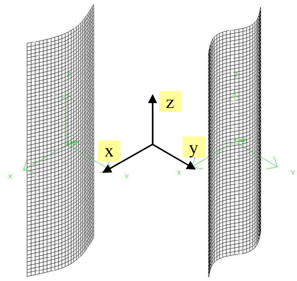

Figure 7: Modal shapes of elementary flexible bodies.

Due to the unconventional nature of simulated objects, a relevant and difficult task of the modelling activity is the determination of physical parameters of letters (mass, stiffness and damping). The density of a "pressed" letter (no air inside the envelope) is assumed to be equal to that of paper: this choice applies reasonably well to the considered problem as the letters are transported by the pressed upper and lower belts (Fig. (5)) that, in turn, keep the envelope squeezed.

The parameter used to define letter stiffness is the Young modulus set in the FEM model for the material of shell elements defining the structural model of elementary flexible bodies. Reminding that, as a relevant example, a letter is a stack of probably folded sheets of paper contained in an glued envelope, it can be concluded that the analytical determination of letter stiffness is a very complex, probably impossible, task. Moreover, due to the sub-structuring approach adopted, the relation between elementary body material properties and complete letter bending characteristics is very complex. Therefore an experimental and simulation approach has been adopted to tune this important parameter. As a reference methodology, a standard about experimental determination of bending characteristics of paper and board has been adopted [8]. To meet experimental data and model characteristics, a clamped model of a complete letter is defined (Fig. (8-a)Figure 8). Due to the parametric nature of the developed letter model, such model is easily adapted to several different letter dimensions. The tuning of Young modulus has been obtained by comparing static deflections of the free tip of real and model letters, for various dimensions, thickness and types of letters. Obviously, short postcards, made of one sheet of board (thickness between 0.5 and 1 mm), are found to have much higher Young modulus than lightweight letters containing, for example, a few sheets of air-mail paper.

Table 1 shows the values of estimated Young moduli for different types of letters. By setting such values in the elementary flexible bodies, the deflection of clamped simulated letters are reasonably close to the behaviour of real letters. It is worth noting that real letters show a highly variable behaviour, due, for example, to their intrinsic nonlinearity (internal friction among sheets, evenly distributed bending curvature, formation of wrinkles, air humidity, and so on). Nevertheless, as shown in Section 6 , the model of letters set up with the presented approach has demonstrated a behaviour significantly close to that of real letters.

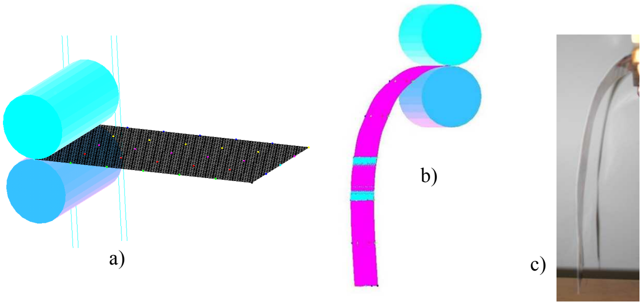

Figure 8: Test model of full letter for physical parameter determination.

letter dimensions (l*w) [mm]	thickness [mm]	Young modulus N/m^2	static deflection of free end [mm]	modal damping z_m
220×110	1	$2E9$	7	5
250×110	1	$5E8$	50	5
150×104	0.5	$1E10$	1,4	10

Table 1: Stiffness and damping data for sample letters.

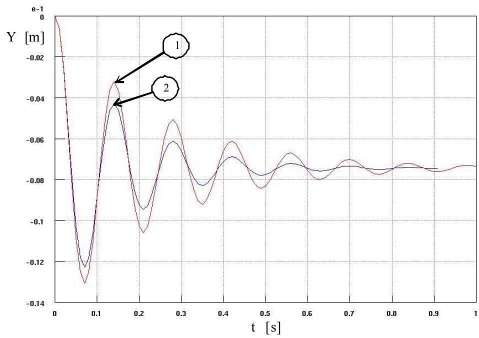

Figure 9: Simulation results for clamped letter model under gravity load.

According to the chosen approach, the parameter used to control the internal damping in the letter models is the modal damping, associated with each elastic d.o.f. Again, in this case, the correspondence between modal damping values and oscillatory behaviour of complete letters is very complex, so simulation and comparison with real letter characteristics has been the method adopted to set up such parameters. Fig. (9) shows the transitory of a clamped letter under gravity load, for two different values of modal damping z_m (2 and 10), assumed equal for all modes. Curve 1 shows a high value of the settling time (more than 1s), while Curve 2 has a behaviour closer to that a the real letter, so, in this case, the higher value of modal damping is assumed. It is to be noted that the selected value for z_m is much higher than usual values used in case of underdamped flexible bodies ($0<z_m<1$), and that, at the same time, the complete letter has an evidently underdamped behaviour. This is due to the substructuring approach that by joining several bodies into a unique object makes each modal coordinate see a reduced mass much higher than the modal mass of the elementary flexible body, thereby, de facto, reducing the actual damping coefficient applied to it.

Finally, Fig. (8-b) shows the deflected model, under gravity load, of a very soft letter (low values of thickness and material Young modulus) analyzed to verify the capacity of the substructured model to deal with geometrical nonlinearities. Compared with a real object (Fig. (8-c)), the result of simulation confirms the correctness of the selected modelling approach.

4.2 Interaction between letters

To model the interaction between two letters, here named letter 1 and letter 2, the first, for example, already in the box, the second entering it and, therefore, hitting the first, it is necessary to define a high number of point-segment contacts. To limit the number of such contacts, instead of six, one for each flex body, only 3 "planes" are defined on letter 1, each fixed to the centre an odd elementary flexible body (Fig. (10-a)). For each of such planes, contact relations with several points fixed to the nodes of flex bodies of letter 2 (Fig. (10-b) and Fig. (6)) are defined. This results in a large number of elementary contacts for each pair of letters in possible collision and justifies the need of adopting a simple but very efficient model for the definition of contact geometries.

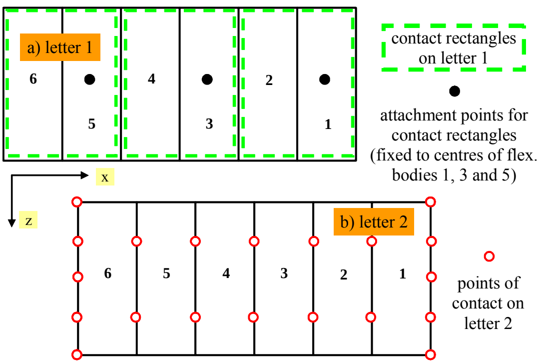

Figure 10:Point-segment contacts between letter 1 and letter 2.

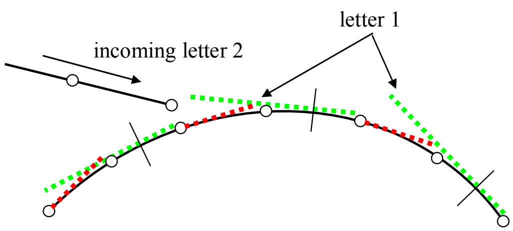

Figure 11: Countermeasures for polygonal effect.

To avoid the polygonal effect caused by the use of only three planes on letter 1 (green lines in Fig. (11)), a second inclined segment is attached to each even segment body (red line segments). If letter 1 is approximately straight, the red segments are covered by the green ones, and they do not make any effect; if, as in Fig. (11), the letter is bent, they help letter 2 head to float on letter 1 upper surface. Other relevant cases, such as letter 2 below letter 1 or letters with large differences in length require other refinements in the contact definitions, some of them emerging after observing wrong or unrealistic simulation results. A more detailed analysis can be found in [9].

5 MODEL OF HANDLING SYSTEM

The two main components constituting the group devoted to route the incoming letters are (Fig. (5)):

- the transport system, formed by the pair of opposite lower and upper belts
- the switch and the box with its upper and lower pads, both able to rotate around hinges fixed to the box frame.

5.1 Transport system

Modelling directly two opposite flat belts in continuous contact with deformable flat objects is very difficult as any visco-elatic model based on Hertzian representation becomes singular. Therefore, an approach similar to that adopted for contacts between letters is adopted. The continuous belts are substituted by a discretized set of spheres in point-segment contacts with lower and upper flat surfaces fixed to flexible bodies (Fig. (12)). All spheres are put in rotation around axes parallel to the system absolute z axis, at an angular velocity that impose the correct translation velocity to letters (4 to 4.5 m/s). Similarly to the real system, the intrinsic compliance of the adopted contact model allows the passage, between tangent spheres, of letters of different thicknesses, so the same transport model can be used in all considered cases. In the real system, the coating of transport belts ensures a high friction with the letters, and, in the model, the transport forces necessary, for example, to make the letter advance when they hit the switch, are obtained by a high friction coefficient between spheres and flat surfaces. The width of the flat belts is modelled by putting four in parallel spheres distributed along the z direction on each rotation axis. Also in this case, the chosen solution requires a high number of elementary contacts, but all defined in term of simple elements. A reasonably fine level of discretization (Fig. (12)) ensures that during transport the letters do not bend or oscillate in the vertical direction.

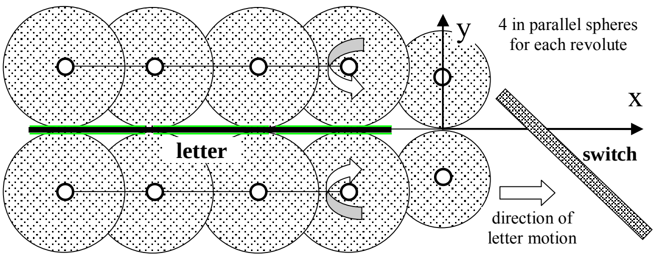

Figure 12: Schema of the model of transport line.

The last two series of spheres before the switch have the exact diameter of the actual rollers plus belt thickness (Fig. (5)), the correct position relative to the switch and box and a higher contact stiffness. In this way, it is imposed that letter bending phase in the model is subject to conditions close to those found in the real system.

5.2 Switch and box

Also the switch model takes advantage of the geometric elements fixed to the flexible bodies forming the letter. In Fig. (13) it is shown a the real and model geometries of a switch with straight profile, along with other elements introduced to improve model efficacy.

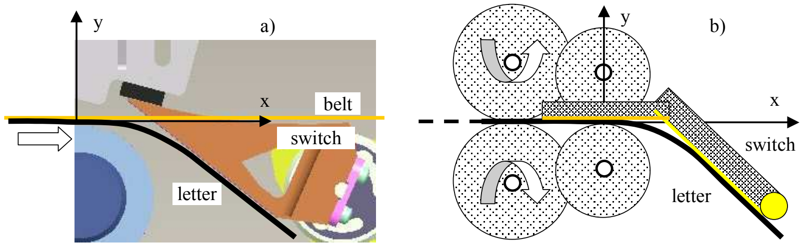

Figure 13: Schema of the contact model of switch.

In the model, the switch is treated as already open, so its geometry is considered as fixed to the absolute reference system. The contacts between the switch and the letters are defined in the following way:

- contacts between the points fixed to flexible bodies (Fig. (10-b)) and the lower surface of switch (yellow line in Fig. (13-b));
- to avoid artificial oscillations of letters when a group of such point terminates the contact with the switch, contacts between flat surfaces on letters (Fig. (10-a)) with spheres located along the z axis at the base of the switch (yellow circle in Fig. (13-b)).

Moreover, to better avoid the discretization effects introduced by the model of transport line in the critical zone of letter bending, contacts between a flat surface, fixed and frictionless, simulating the presence of the upper belt (orange line in Fig. (13)), and the points fixed to flexible bodies are established.

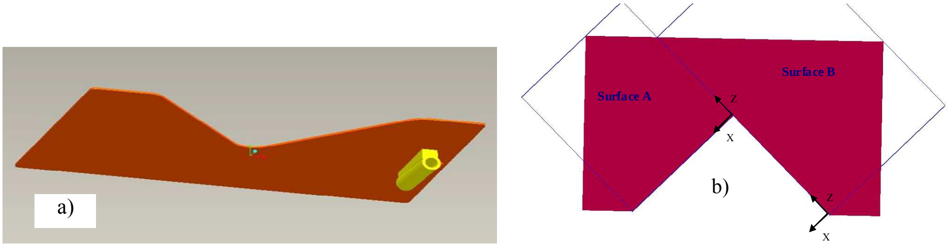

Figure 14: Body geometry and contact model of the lower pad.

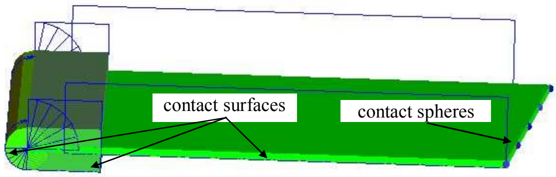

Figure 15: Body geometry and contact model of the upper pad.

The most relevant elements of the box are the upper and lower pads, hinged to the box frame. When the box is empty, they are kept in contact by two torsion springs acting on the two hinges (Fig. (5)). As more and more letters are routed to the box (Fig. (16)), the two pads are forced to rotate in opposite directions to enlarge box internal volume; at the same time, they continue to exert a certain pressure on the letter stack, so avoiding the unwanted casual falling of letters out of the box and keeping compressed the stacked letters. For both pads, torsion springs characteristics are chosen as a compromise between the necessity of allowing the insertion of new letters arriving into the box (soft springs) and the need to keep the letter stack under pressure (stiff springs) [9]. Fig. (14) shows the geometry of the lower pad (Fig. (14)-a) and its contact surfaces, “Surface A” and “Surface B” (Fig. (14)-b). Such flat surfaces are related by contact elements to the spheres fixed to the letter flexible bodies. Fig. (15) represents the upper pad geometry: its surfaces (identified by blue lines in figure) are related with letter spheres while the (blue) contact spheres on the rear edge of the pad are in contact with the flat rectangles on the letters.

6 CASE STUDIES AND RESULTS

Due to the complexity of dynamics of the considered physical system, the presented model, after an initial development phase, required a trial and error fine tuning phase during which several unrealistic results have been corrected. The availability of macro data on real machine performance and characteristics (transport speed, throughput and letter physical properties), along with shots taken with a high speed camera during letter motion allow a good level of model validation. Fig. (16) shows a typical comparison situation between images of a real letter and their simulated counterparts. The obtained agreement is satisfactory.

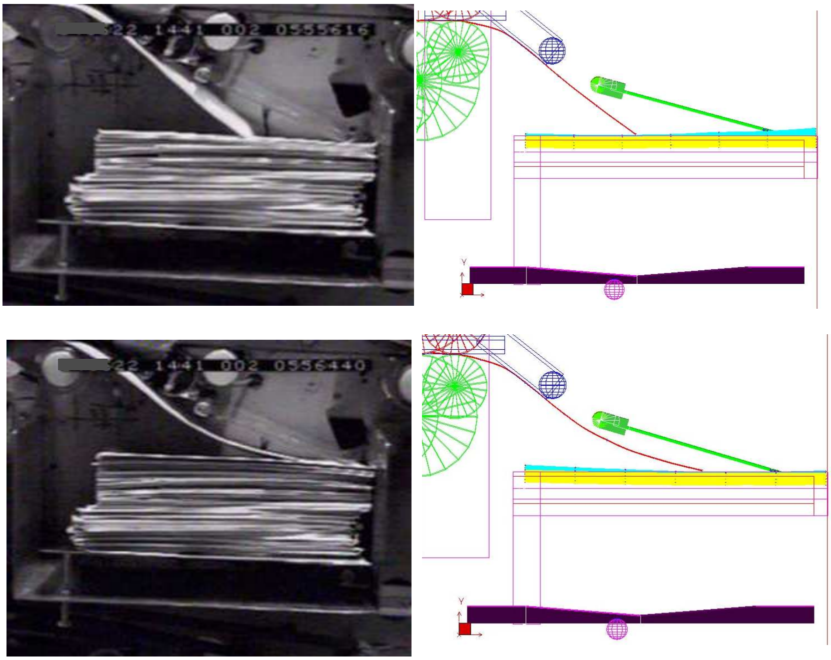

Figure 16: Comparison of behaviour of real and simulated systems.

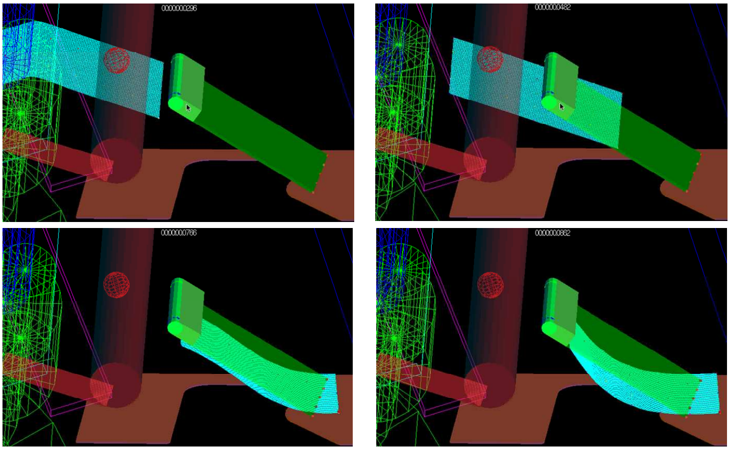

Figure 17: Routing of a short and stiff letter into the box (switch geometry is transparent).

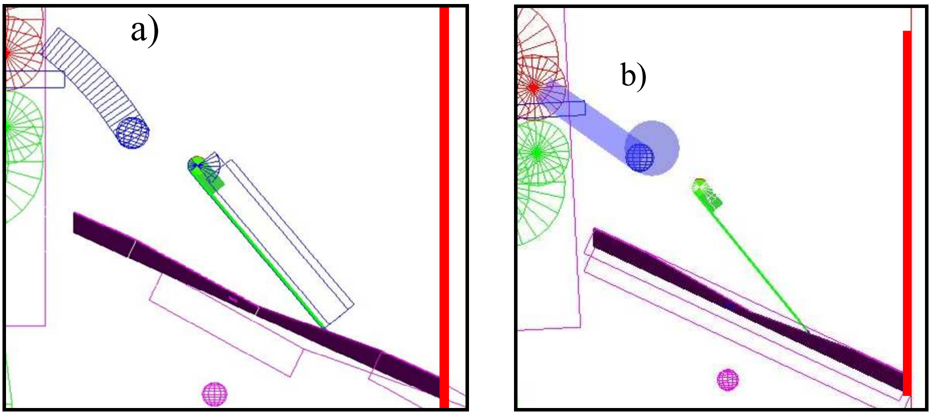

Figure 18: Different solutions for the switch geometry.

Once the model is validated, it can be used to test several different design alternatives. A few of them are discussed in the following.

Fig. (17) shows the insertion into the box of a short and stiff letter: here it is assumed that the box is empty, and the goal of the simulation is to verify that the postcard enters the box without hitting the large cut in the lower pad. Such an event is undesired as it could cause improper positioning of the letter into the box and the jamming or falling of following letters.

By comparing the new lower-pad design in Fig. (17) with the original one shown in Fig. (14), it is evident that, for the new design, the front edge of the letter lands on the pad very close the cut edge, making the chances to have a hit, in the new configuration, higher than in the original geometry. On the other hand a wider cut in the lower pad would make easier the grabbing of the letter stack by the postman, rendering the new design more ergonomic for letter extraction from the box. Simulation results with various letter geometries show that the new design, although slightly more risky, is acceptable.

As a second example of use of the model as a design tool, Fig. (18) shows two different geometries for the switch shape. Solution a) tends to route the letter tip toward a more vertical direction, thereby reducing the velocity of the letter when it hits the end surface of the box (red vertical line). This decreases the kinetic energy of the letter and the chances of a significant bounce back after the collision. On the other hand, solution b) tends to impose an almost straight trajectory to the letter during its entering the box, so the letter hits the end wall at higher velocity. One goal of this comparison is explained by Fig. (19): in some cases, a box may become partially full of short letters on top of long letters (simulated by pink shapes in Fig. (19-b)) and a new letter entering the box, instead of landing on the horizontal upper surface of previous letter, may hit the vertical side of the letter stack, producing an undesired jamming of the box and, in some cases, of the complete machine. This is a very unwelcome event as a "worm" of thousands of letters moving at high speed (4-5 m/s) stops almost instantaneously, normally causing massive letter falling and disordering.

Plots in Fig. (20) show different trajectories of tips of various letters entering the box, case a) with curved switch geometry, case b) with the straight one. The difference between the two cases is notable being of 20-30 mm in x direction in proximity of the possible zone of collision with previous short letters.

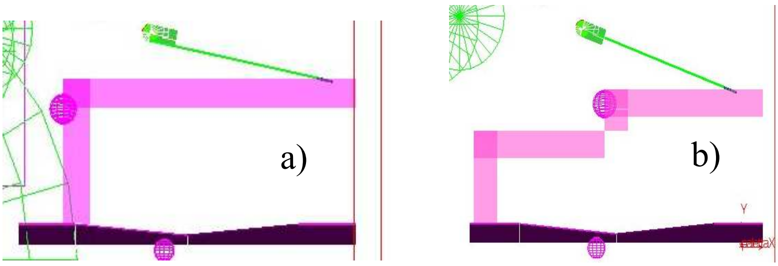

Figure 19: Different conditions of box filling status.

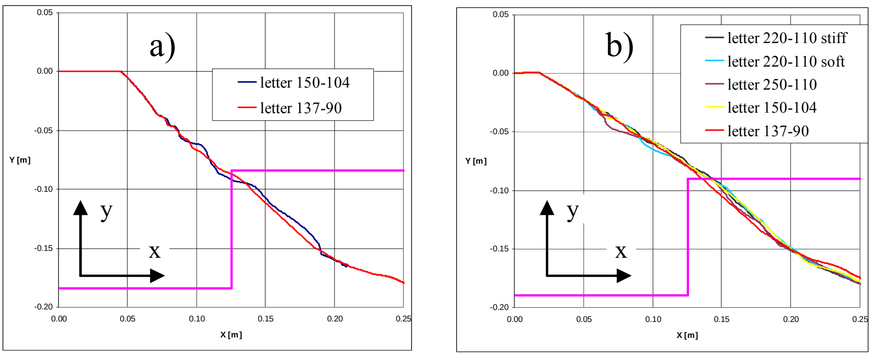

Figure 20: Different trajectories of letter tips (pink line: box "C" status).

Finally, Fig. (21) and Fig. (22) show two different simulations containing three moving letters. The frames shown in both Figures regard the event of a long, soft letter (the second of three in the transport line) entering the box guided by the straight (21) and curved (22) switches. In both cases the mailbox is modeled to simulate the presence of a previous stack of short letters (pink shapes); in the second simulation, the short letters are supposed to be lying on top of a stack of longer letters, but this difference is not relevant for the effect considered here. During the first part of both simulations (not shown in figures) the first letter in the transport line (the blue one) already entered the box, and in the initial frames (a) of both Figures such letter lies, at rest, on top of the simulated letter stack. As the second incoming letter hits previous one, the two cases follow different paths: in the first simulation, the straight shape of the switch makes the tip of the incoming letter hit the upper surface of the previous one close to the vertical edge of the letter stack. Due to the position of the collision point and to the contribution of the upper pad that balances the blue letter, the incoming letter slides on top of the previous one, correctly entering the box (frames c and d). In the second simulation (Fig. (22)), the incoming letter hits the previous one farther from the letter stack, making both letters bend; as shown in frames c and d, in this second case, the incoming letter does not enter correctly the box, most likely causing, in the real system, a malfunction condition.

As evidenced in the last frames of Fig. (22), the adopted model for the letters is fully capable to represent nonlinear, large displacement, buckling effects, together with multiple contacts between deformed letters with their surrounding environment. For example, in frame d, the red letter is beginning to bend due to the axial compression force exerted on it by the pushing force of the transport line; also, the same frame shows the largely bent blue letter lifting the upper pad.

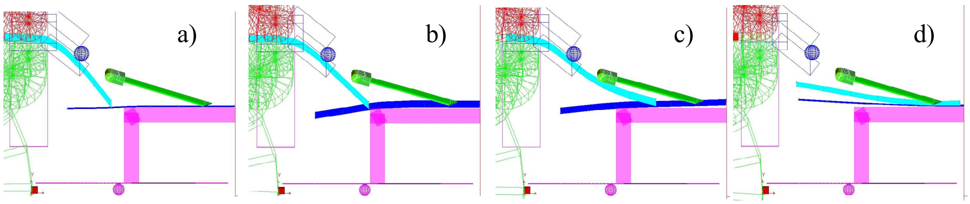

Figure 21: Long, soft letter entering a partially full box (switch with straight geometry).

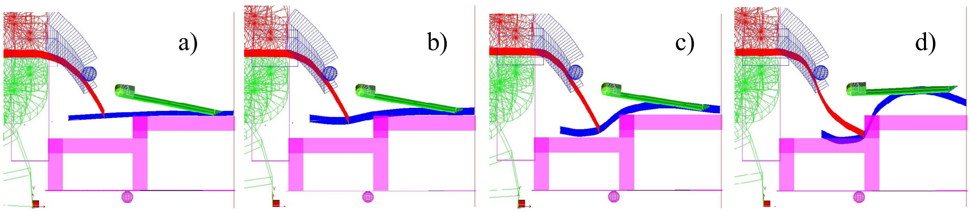

Figure 22: Long, soft letter jamming into a partially full box (switch with curved geometry)

7 FINAL CONSIDERATIONS

The paper has presented the main features, the validation and some results of a complex multibody model simulating the motion of letters in a routing mechanism. For a model with three letters, the representation of the letter-letter and letter-environment contact relations has required the definition of more than two thousand elementary point-segment contact components. The continuous attention to the tuning of the model for computational efficiency has allowed us to obtain a model running in less than 500s (cpu time) on a mid-range PC, for a complete routing of the three letters (0.5s simulated time). So, regarding the questions posed at the beginning of the paper about the feasibility of the presented approach, it can be concluded that: a) it produces results that are representative of the real behaviour of the system and that can be usefully applied to develop and virtually test new design alternatives; b) the computational effort required to run the large number of simulations required to test design alternatives for several different letter characteristics is compatible with the design activity; c) a critical point is the very large effort required to develop the first models, or to apply significant variations to the topology and geometry of existing ones.

REFERENCES

[1] G. Hipwell, K. Jones. Improving the performance of the NP4000 letter sorting machine through better destacking - a study on 'in service' development. Proceedings of the 1996 IEE Colloquium on Mechatronics in Automated Handling. London, UK, May 16, 1996.

[2] P. Fanghella, B. Borasca, C. Galletti. Modelling and Simulation of a Singling-Out Mechanism for Automated Mail Handling. Proceedings of the International Symposium on Multibody Systems and Mechatronics MUSME 2005, Uberlândia, Brazil, March 6-9, 2005.

[3] A. Tarau, B. De Schutter, H. Hellendoorn, Throughput optimization of automated flats sorting machines. Proceedings of the 17th World Congress, International Federation of Automatic Control, vol. 17, n° 1, 2008.

[4] E. J. Haug, S. C. Wu, and S. M. Yang. Dynamics of Mechanical Systems with Coulomb Friction, Stiction, Impact and Constraint Addition-Deletion - I Theory. *Mechanism and Machine Theory*, Vol. 21, n° 5, 401-406, 1986.

[5] DADS Contact Modelling Guide - Rel. 9.6. LMS International, Leuven - Belgium, 2004.

[6] P. Fanghella, C. Galletti, G. Torre. An Explicit Independent-Coordinate Formulation for the Equations of Motion of Flexible Multibody Systems. *Mechanism and Machine Theory*, vol. 38, n° 5, 417-437, 2003.

[7] S. C.Wu, E. J. Haug. Geometric Non-linear Substructuring for Dynamics of Flexible Mechanical Systems. *International Journal for Numerical Methods in Engineering*, vol. 26, 2211–2226, 1988.

[8] UNI 9070:1994. Paper and board - Determination of resistance to bending, (in Italian) 1994.

[9] A. Sintich. Development and Solution of Multibody Models for the Performance Analysis of a Mail Handling Mechanism. MS Thesis (in Italian), DIMEC, University of Genoa, 2004.

Proceedings of MUSME 2011, the International Symposium
on Multibody Systems and Mechatronics
Valencia, Spain, 25-28 October 2011

COMPARISON OF METHODS TO DETERMINE GROUND REACTIONS DURING THE DOUBLE SUPPORT PHASE OF GAIT

Urbano Lugrís*, Jairo Carlín*, Rosa Pàmies-Vilà† and Javier Cuadrado*

* Laboratory of Mechanical Engineering
University of La Coruña, Mendizabal s/n, 15403 Ferrol, Spain
e-mails: ulugris@udc.es, jairo.carlin@udc.es, javicuad@cdf.udc.es
web page: http://lim.ii.udc.es

† Department of Mechanical Engineering
Polytechnic University of Cataluña, Diagonal 647, 08028 Barcelona, Spain
e-mail: rosa.pamies@upc.edu

Keywords: Gait, ground reactions, force contact model, double support, stochastic optimization.

Abstract. *There is a growing interest in predicting the gait motion of real subjects under virtual conditions, e.g. to anticipate the result of surgery or to help in the design of prosthetic/orthotic devices. To this end, the motion parameters can be considered as the design parameters of an optimization problem. In this context, determination of the joint efforts for a given motion is a required step for the subsequent evaluation of cost function and constraints, but force plates will not exist. In the double support phase of gait, the ground reaction forces include twelve unknowns, rendering the inverse dynamics problem indeterminate if no force plate data is available. In this paper, several methods for solving the inverse dynamics of the human gait during the double support phase, with and without using force plates, are presented and compared.*

1 INTRODUCTION

A great effort has been done by the biomechanics community to analyze the gait of real subjects [1]. Usually, the procedure starts with the capture of the subject's motion by means of an optical system, and the measurement of the ground reactions through force plates. Then, the obtained positions of a number of markers serve to calculate the histories of the coordinates defining a computer model of the subject. These data are processed to minimize the errors and differentiated to yield the histories of the coordinates at velocity and acceleration level. At this point, the equations of motion of the model are set in some way (forward or inverse dynamics) and the muscle forces that produce the joint efforts are estimated through optimization techniques due to their redundant nature. It can be said that today this whole process has reached a high degree of maturity, although the obtained values of the muscular forces are not always reliable. The results of this kind of analyses are a good help for medical applications.

However, in the last years, the biomechanics community is attempting to go one step further: the prediction of the gait motion of real subjects under virtual conditions [2-4]. If this problem was successfully solved, it would be extremely useful for the medical world, e.g. to anticipate the result of surgery or to help in the design of prosthetic/orthotic devices.

Multibody dynamics is a suitable tool to address the mentioned challenge. In fact, the dynamic behavior of many complex machines has been simulated for a long time thanks to this discipline, by stating and solving the so-called forward dynamics problem. The human body can be also considered a multibody system and, hence, its motion can, in principle, be simulated in the same way. There is, however, a key difference between the simulation of machines and the simulation of the human body: in the latter case, the inputs to the system, i.e. the motor actions, are the result of the neuro-muscular actuation and, hence, they are unknown. Consequently, forward dynamics cannot be applied as in man-made machines. Instead, two approaches can basically be followed: a) to state an optimization problem, so as to find the most likely motion or muscular forces according to some objective function under the corresponding constraints; b) to replicate the neuro-muscular system by means of an intelligent algorithm [5], like the smart drivers do in the automotive case. Up to now, the multibody community has chosen the first approach, as closer to its experience in mechanical problems.

The present work is part of a project aimed to simulate the gait motion of incomplete spinal cord injured subjects wearing active orthoses. The objective is to simulate the gait of real and specific patients when wearing orthoses that have not even been built. This is expected to serve for the design or adaptation and testing of subject-tailored orthoses in the computer, so that disturbance to patients is minimized.

To solve this problem, the plan is to follow the optimization approach indicated above. The design variables will be either the parameters defining the motion of the patient or the parameters defining the excitations of his muscles, while the objective function will be the total metabolic cost, whose calculation requires the histories of muscular forces to be known [6].

In the first case (motion parameters as design variables), the calculation of the muscular forces requires the joint efforts to be previously determined, which is not possible unless the ground reactions are obtained for the motion defined by the current value of the design variables. This last problem, i.e. to obtain the ground reactions for a given motion, is not such when only one foot is in contact with the ground, but its solution becomes undetermined during the double support phase. When actual captured motions are analyzed, the mentioned indeterminacy is overcome by the measurement of ground reactions by means of force plates, as explained at the beginning of this Introduction. However, force plates do not exist for the virtual motions generated during the optimization procedure. Therefore, the problem here is to calculate the ground reactions for a given motion, both during the single and double support phases, without making use of measurements coming from the force plates.

In the second case (excitation parameters as design variables), the muscular forces are straightforwardly obtained from the excitations defined by the current value of the design variables. However, a force contact model is required for the foot-ground contact, in order to obtain the motion resulting from the excitations by means of forward dynamics.

The problem of determining the ground reactions for a given motion when force plates are not available has previously been addressed by other authors. For example, Ren et al. [7] introduce the concept of Smooth Transition Assumption (STA), which basically consists of adjusting a smooth function for the double support phase between the uniquely determined values of the ground reaction components of the single support phase. However, this approach may not be applicable when the duration of the double support phase represents a relevant part of the full gait period, as in some cases of pathological gait. Therefore, an alternative solution is proposed in this paper, which serves for the problems arisen in the two optimization options considered in the previous paragraphs. Given the motion, the inverse dynamics allows for the calculation of the resultant ground reaction forces and moments during the whole period. Then, the parameters of a force contact model in both feet are considered as the design parameters of an optimization process. The objective function to be minimized is defined as the difference between the ground reactions obtained through inverse dynamics and the ground reactions yielded by the force contact model. Moreover, a null value of the reaction is imposed to each foot when it is not contacting the ground. The proposed method is applied to the captured motion of a real healthy subject, and the resulting ground reactions are compared with those measured by force plates, in order to assess their accuracy.

The proposed method shows some similarities with the work by Millard et al. [4], who address the problem of obtaining a foot-ground contact model that may be used within a predictive optimization scheme based on forward dynamics analyses. However, these authors define a planar model, not a 3D one, and try to tune the contact model parameters to reproduce the normal and tangential forces, but do not consider the reaction moments. Moreover, they measure the real contact forces by means of force plates instead of calculating them from the captured motion through an inverse dynamics analysis, which is consistent with the objective they were pursuing.

The paper is organized as follows. Section 2 describes the experiment, the measurements carried out, the computational model of the subject, the applied signal processing, and the inverse dynamics formulation. Section 3 explains the different solutions for the double stance problem. Section 4 shows the obtained results and their discussion. Finally, Section 5 gathers the conclusions of the work.

2 EXPERIMENT, MEASUREMENTS, MODEL, SIGNAL PROCESSING, AND FORMULATION.

A healthy adult male of age 37, mass 74 kg and height 180 cm, has been dressed with a special suit where 37 passive reflective markers have been attached, as illustrated in Fig. (1a). For the experiment, the subject walks on a walkway with two embedded AMTI AccuGait force plates, located in such a way that each plate measures the ground reactions of one foot during a gait cycle. The motion is captured by an optical system composed by 12 Natural Point OptiTrack FLEX:V100 cameras and its software, which provides the 3D trajectories of the markers.

A 3D computational model of the subject has been developed in mixed (natural + relative) coordinates. The model, shown in Fig. (1b) possesses 18 bodies and 57 degrees of freedom, and it is defined by 228 dependent coordinates. Unlike the 3D models proposed by several authors [2, 3], the present model does not use the Head-Arms-Trunk (HAT) simplification. The reason is that it is expected that the upper limbs play a relevant role in the gait of incomplete spinal cord injured subjects, who are the final target of the project. All the body segments are connected by spherical joints in the model, so as to circumvent the problem of determining the rotation axes. Each foot is defined by means of two segments. Following the picture in Fig. (1b), the coordinates of the system are composed by the three Cartesian coordinates of all the points at the spherical joints plus the points at the centers of mass of the five distal segments (head, hands and forefeet), the three Cartesian components of two orthogonal unit vectors at each body (red and green vectors in Fig. (1b)), the three angles that define the pelvis orientation with respect to the inertial frame, and the 51 (3x17) angles that define the relative orientation of each body with respect to the previous one in the open chain system with base in the pelvis.

The geometric parameters of the model are obtained, for the lower limbs, by applying correlation equations from a reduced set of measurements taken on the subject and, for the upper part of the body, by scaling table data according to the mass and height of the subject. Regarding the inertial parameters, they are obtained, for the lower limbs, by a correction, based on data coming from densitometry if available, of the method already indicated for the geometric parameters; for the upper part of the body, the scaling method is used again, but a second scaling is applied in order to adjust the total mass of the subject.

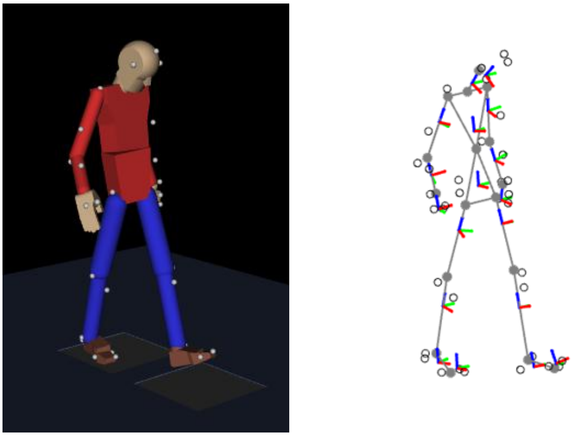

Figure 1: (a) Markers location; (b) Computational model.

To reduce the noise due to the motion capture process, the Singular Spectrum Analysis (SSA) filter is applied to the position histories of the markers, which are then used to calculate the histories of the model natural coordinates by means of simple algebraic relations. The values of these coordinates at each instant of time are not kinematically consistent due to the inherent errors of the motion capture process. Therefore, the kinematic consistency of the natural coordinates at position level is imposed, at each instant of time, by means of the following augmented Lagrangian minimization process [8],

$$\begin{gathered}\left(\mathbf{W}+\mathbf{\Phi}_{\mathbf{q}}^{\mathrm{T}}\alpha\mathbf{\Phi}_{\mathbf{q}}\right)\Delta\mathbf{q}_{i+1}=-\mathbf{W}\left(\mathbf{q}_i-\mathbf{q}^*\right)-\mathbf{\Phi}_{\mathbf{q}}^{\mathrm{T}}\left(\alpha\mathbf{\Phi}+\boldsymbol{\lambda}_i\right)\\ \boldsymbol{\lambda}_{i+1}=\boldsymbol{\lambda}_i+\alpha\mathbf{\Phi}\quad;\quad i=1,2,\ldots\end{gathered}\tag{1}$$

where $\mathbf{q}^*$ is the vector of the inconsistent natural coordinates, $\Delta\mathbf{q}_{i+1}=\mathbf{q}_{i+1}-\mathbf{q}_i$, $\mathbf{\Phi}$ is the vector of kinematic constraint equations, $\mathbf{\Phi}_{\mathbf{q}}$ is the corresponding Jacobian matrix, $\boldsymbol{\lambda}$ is the vector of Lagrange multipliers, α is the penalty factor, and $\mathbf{W}$ is a weighting matrix that allows to assign different weights to the different coordinates according to their expected errors.

From the consistent values of the natural coordinates, a set of independent coordinates $\mathbf{z}$ is calculated: the three Cartesian coordinates of the spherical joint connecting pelvis and torso, along with the three x, y, z rotation angles with respect to the fixed global axes, are used to define the pelvis position and orientation, while the joint relative coordinates are used to define the remaining bodies of the model in a tree-like structure.

Prior to differentiate the histories of the independent coordinates $\mathbf{z}$, the SSA filter is applied to them in order to reduce the noise introduced by the kinematic consistency. Then, the Newmark's integrator expressions are used to numerically differentiate the filtered position histories so as to obtain the corresponding velocity and acceleration histories [8].

Once the histories of the independent coordinates $\mathbf{z}$, and their derivatives, $\dot{\mathbf{z}}$ and $\ddot{\mathbf{z}}$, have been obtained, the inverse dynamics problem is solved by means of the velocity transformation formulation known as matrix-R [9], which provides the motor efforts required to generate the motion. However, since such motor efforts are obtained as an external force and torque acting on the pelvis and the corresponding internal joint torques, they are not the true ground reaction force and torque and the true joint torques, as long as the true external force and torque must be applied at the foot or feet contacting the ground, not at the pelvis. Anyway, a simple linear relation can be established between the two sets of motor efforts: it is obtained by equating the vector of generalized forces due to the set of force and torques with the pelvis as base body, and the vector of generalized forces due to the force/forces and torques with the foot/feet as base body/bodies.

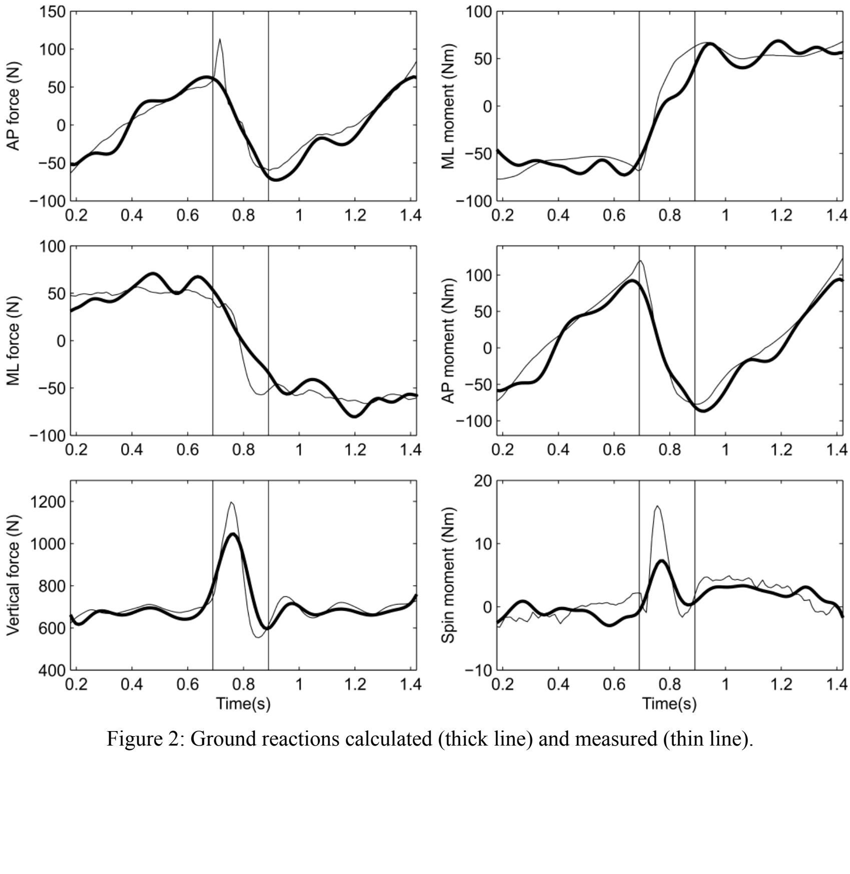

Figure 2: Ground reactions calculated (thick line) and measured (thin line).

Fig. (2) shows the correlation between the ground reaction force and moment components calculated and measured. The reaction force and moment components coming from both plates have been added and the results plotted, so that they can be compared with the same terms obtained from inverse dynamics. The plots start at the toe-off of the right foot and finish at the heel-strike of the same foot. The two vertical lines delimitate the double-support phase, in which the inverse dynamics can only provide the addition of the force and moment components due to both feet. However, during the single support phase, the inverse dynamics provides the force and moment at the contacting foot.

3 SOLUTION OF THE DOUBLE STANCE PROBLEM

3.1 Using reactions from force plates

The most common way to calculate the joint torques during a gait cycle including double support is to measure the ground reaction forces and moments by means of force plates. Then, these measured reactions can be used as the inputs of an inverse dynamics problem. This is the only solution when only the lower limbs are considered in the study: the Newton-Euler equations can be solved from the feet to the hips, and no knowledge about what happens with the upper part of the body is needed.

In case the whole body is considered, a resultant reaction vector **R**, which includes the three components of both the external reaction force and moment, can be obtained by solving the inverse dynamics problem stated in Section 2. This resultant reaction will not coincide with that measured at the force plates, $\mathbf{R}_F$, due to the errors accumulated in the estimation of the body segment parameters and the motion capture, and the measurement error of the force plates themselves. This means that the inverse dynamics results are inconsistent with the force plate measurements. However, these force plate measurements can still be used as an input for the solution of the double support problem, since their shapes contain information about how the total reaction is transferred from the trailing foot to the leading foot. A solution to this problem would be to combine the results from inverse dynamics with the measured reactions in a least square sense [10], but this would modify the resulting motion. In order to preserve the kinematics, a simpler alternative method is here presented.

The residual between the reactions obtained from inverse dynamics and those measured by force plates, $\boldsymbol{\varepsilon}=\mathbf{R}-\mathbf{R}_F$, can be split and added to each of the force plate reactions to make their resultant consistent with the inverse dynamics, thus assuming that all the residual comes from errors in the reaction measurement. In order to avoid discontinuities at heel strike and toe off, the correction is split between both force plates by using a linearly varying function κ:

$$\begin{aligned} \mathbf{R}_1(t) &= \mathbf{R}_{F1}(t) + \kappa(t)\boldsymbol{\varepsilon}(t) \\ \mathbf{R}_2(t) &= \mathbf{R}_{F2}(t) + \left[1-\kappa(t)\right]\boldsymbol{\varepsilon}(t) \end{aligned} \tag{2}$$

where $\mathbf{R}_1$ and $\mathbf{R}_2$ are the reactions at the trailing and leading foot respectively, and $\mathbf{R}_{F1}$ and $\mathbf{R}_{F2}$ are they force plate counterparts. This leads to a set of reactions at each foot that is close to the force plate results, but keeping the consistency with inverse dynamics. This means that the force plate information is used only for approximating the transition of the reactions, instead of as an input of the inverse dynamics problem.

3.2 The smooth transition assumption (STA)

In case no force plate data is available, the ground reaction forces and moments at each foot can be determined by using a reasonable transition criterion. An example of this type of procedures is the *smooth transition assumption* (STA), proposed by Ren et al. [7]. This algorithm is based on the assumption that the reaction forces and moments at the trailing foot decay according to a certain law along the double support phase. The method uses two shape functions $f_x(t)$ and $f(t)$ that approximate the shape of the reactions at the trailing foot during the double support phase, by using a combination of exponential and linear functions whose parameters are obtained by trial and error. The first function, f_x, is used for the anteroposterior reaction force, whereas the second function, f, is used to model the shape of the remaining five components. Thus, the anteroposterior reaction force R_{1x} is obtained as:

$$R_{1x}\left(t\right)=f_x\left(t\right)R_{1x}\left(t_{HS}\right) \tag{3}$$

where f_x is a function whose value is 1 at the heel strike of the leading foot, and 0 at the toe off of the trailing foot, and t_{HS} is the time instant at the heel strike of the leading foot, i.e. the end of the single support phase.

For the remaining five components of the ground reaction the procedure is the same, but using the second smoothing function f and the value of the corresponding component at heel strike. In order for the smoothing function to correctly mimic the decay of the reaction moments, the reaction forces must be considered as applied at the respective centers of gravity of each foot. Once the reactions along the support phase are estimated for the trailing foot, their counterparts at the leading foot are the result of forcing the resultant to be equivalent to the total reaction **R** given by the inverse dynamics.

3.3 Force contact model with optimization

Using an assumed transition curve to determine the reaction sharing in the absence of force plates can be a good approximation in normal gait applications. However, the STA and similar methods are based on the assumption that the double support phase is short in comparison to the cycle period, and that the reactions at toe off behave in a certain way, which has been previously observed from normal gait measurements. In pathological gait, neither of these assumptions is true, since, on the one hand, the double support phase may be even longer than the swing phase, and, on the other hand, the force transfer between both feet is unknown. A possible way to obtain the ground reaction forces at each foot from inverse dynamics can be the usage of a foot-ground contact model.

To model the foot-ground contact, a point force model that provides the contact force as function of the indentation between the two contacting surfaces is used. The total contact force is divided into the normal and tangential components. The normal component follows the model proposed by Lankarani and Nikravesh [11], while the tangential component is the bristle-type model proposed by Dopico et al. [12]. The corresponding parameters are design variables of the optimization process. The foot surface is approximated by several spheres, whose positions and radii are also design variables of the optimization process.

The objective is to adjust the position and size of the spheres and the contact force parameters, so that the ground reactions provided by the inverse dynamics are reproduced by the contact model. During the single-support phase, the contacting foot is responsible for providing the ground reaction force and torque obtained from inverse dynamics. However, during the double-support phase, both feet contribute to produce the total ground reaction force and torque obtained from inverse dynamics.

Therefore, the optimization problem is stated as follows: find the force contact parameters and the position and size of the spheres approximating the feet surfaces, so that the error between the ground reaction force and torque components provided by the inverse dynamics and the contact model is minimized. Upper and lower boundaries are set for each design variable. Moreover, a null value of the reaction is imposed to each foot when it is not contacting the ground. The introduction of this last constraint requires the transition times between single and double support to be determined, which has been done by using the force plate data. In case no force plate data were available, a method based on kinematics, such as the *Foot Velocity Algorithm* (FVA) [13], could be used for that purpose.

Figure 3: Feet models during the optimization process: right foot (blue solid line); left foot (blue dashed line).

To speed-up the optimization process, only the models of the two feet are used for each function evaluation, as illustrated in Fig. (3). Indeed, since the motions of the feet are known and the forces introduced by the contact model only depend on the indentation histories, dealing with the whole human body model is not required. The picture in Fig. (3) is a projection on the sagittal plane of the 3D feet models. For each foot, the red reference frames are rigidly connected to the heel and toe segments respectively: three spheres belong to the hindfoot and the fourth one is part of the forefoot.

The evolutive optimization method known as *Covariance Matrix Adaptation Evolution Strategy* (CMA-ES) [14] has been applied. A Matlab function containing the implementation of the algorithm has been downloaded from www.lri.fr/~hansen/. Being an evolutive optimization method, it does not require that function evaluations are sequentially executed, thus enabling the process to be parallelized. Consequently, the CMA-ES function is prepared to simultaneously send several sets of design variables (arranged as columns in a matrix) for their respective values of the objective function to be calculated. A Matlab function has been developed by the authors that receives a matrix with as many columns (sets of design variables) as available parallel processors, and returns a row vector with the corresponding values of the objective function. This function makes use of the *Parallel Computing Toolbox* through the *parfor* statement, in order to perform the multiple function evaluations in parallel. Each function evaluation is carried out by a Fortran code packed into a MEX-file, that calculates the ground reactions due to the contact model and obtains the error with respect to the inverse dynamics results.

The method described so far is a general approach. However, to begin with, a simpler version has been implemented in this work. Four spheres have been considered for each foot. The design variables are the following five parameters for each sphere: x and y local position of the sphere center for a given z (blue vectors in Fig. (1b)), sphere radius r, stiffness K and restitution coefficient c_e of the Lankarani-Nikravesh normal contact force model [11]. This makes a total of 40 design variables. Regarding the objective function, only the RMS errors due to the discrepancies between the normal force and the longitudinal and lateral moments provided by inverse dynamics and the force contact model are taken into account, this being equivalent to adjust the normal force and the center of pressure. All the three mentioned terms of the objective function are affected by weighting factors (1, 5, 5), in order to balance their different scales. The null value reaction at each foot when it is not contacting the ground is imposed by returning a Not-a-Number (NaN) value of the objective function when this condition is violated, as required by the CMA-ES algorithm.

4 RESULTS AND DISCUSSION

Fig. (4) shows the force plate reactions, modified according to the procedure described in Section 3.1 (FPm), versus their unmodified counterparts (FP). The *x*, *y* and *z* axes correspond to the anteroposterior, mediolateral and vertical directions respectively. In Fig. (5), the results obtained by applying the STA are displayed, and compared to the same reference. It can be observed that the STA approximates the reactions of the trailing foot (toe-off) better than those at the leading foot, which is something to be expected due to the nature of the method. Sharing the residual between force plates and inverse dynamics among both feet (FPm) yields worse results than STA at the trailing foot, but the overall results are better, since the maximum error is bounded by the residual ε.

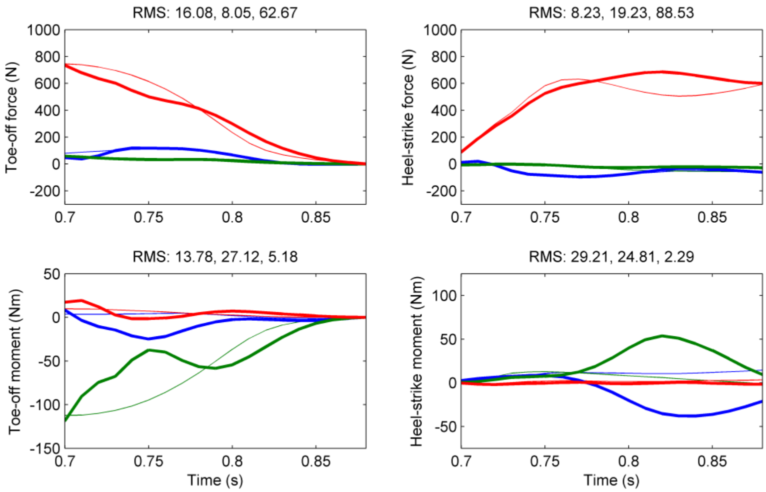

Figure 4: Ground reaction components: FPm (thick lines) vs. FP (thin lines); *x* component (blue), *y* component (green), *z* component (red).

The results obtained from the contact model (CM) are shown in Fig. (6). Fig. (6a) plots the total normal contact force provided by inverse dynamics (ID), the two normal contact forces yielded by the contact models of the feet, their addition, and the normal contact forces measured by the force plates during the experiment. The plots start at the toe-off of the right foot and finish at the heel-strike of the same foot. The grey area delimitates the double-support phase, in which the inverse dynamics can only provide the addition of the normal forces due to both feet. Fig. (6b) plots the mediolateral and anteroposterior moments provided by the contact model and the inverse dynamics.

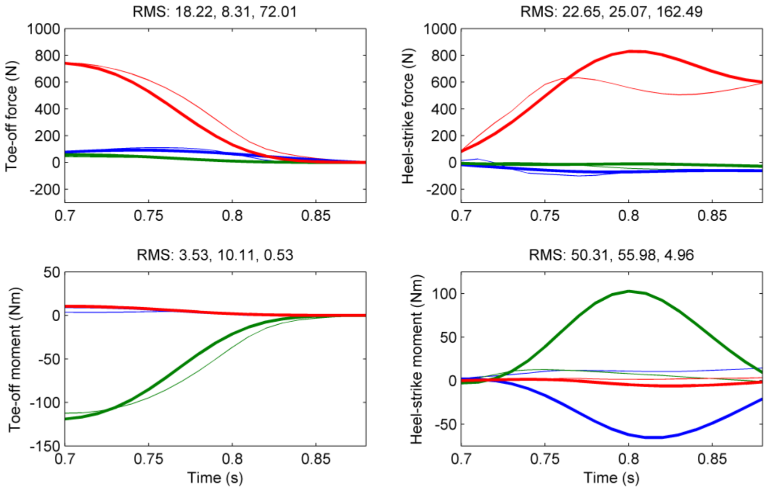

Figure 5: Ground reaction components: STA (thick lines) vs. FP (thin lines); *x* component (blue), *y* component (green), *z* component (red).

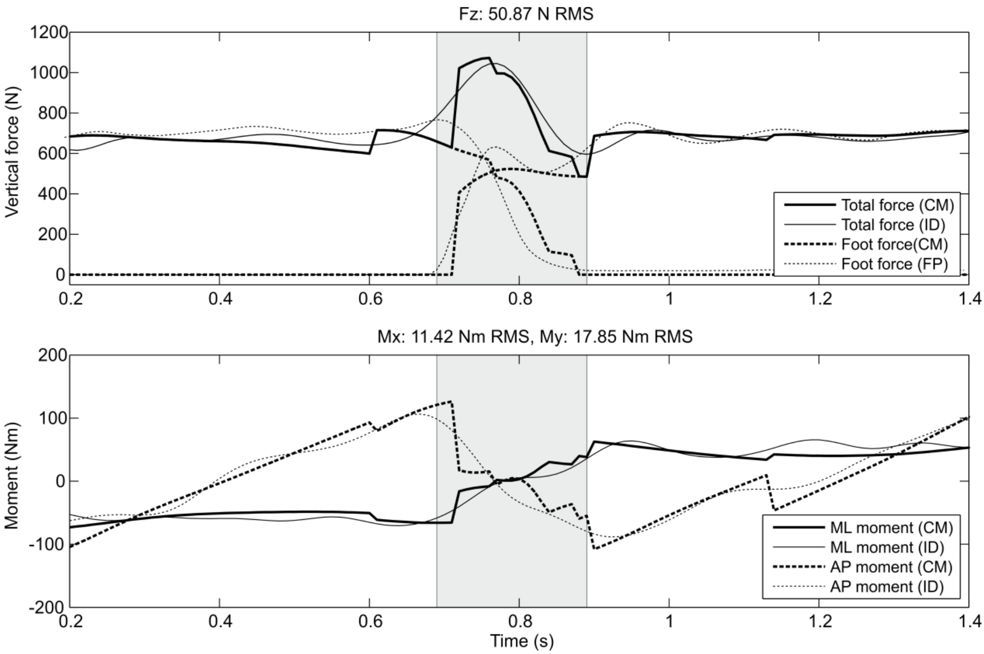

Figure 6: Comparison among ground reactions from inverse dynamics (ID), contact model (CM) and force plates (FP): a) vertical force; b) horizontal moments.

It can be seen that the total normal force obtained from inverse dynamics is well reproduced by the total normal force obtained as the addition of the normal forces provided by the feet due to the optimized contact model. Moreover, the normal force at each foot measured by the force plates during the experiment is well adjusted too by the normal force at each foot due to the optimized contact model. On the other hand, an acceptable agreement is also observed between ID and CM for the two horizontal components of the reaction moment.

In Fig. (7), the results of matching the CM forces to the inverse dynamics by sharing the residual (CMm) are displayed. The results obtained for the vertical force and its corresponding moments are, in terms of maximum RMS error, better than those obtained by the STA.

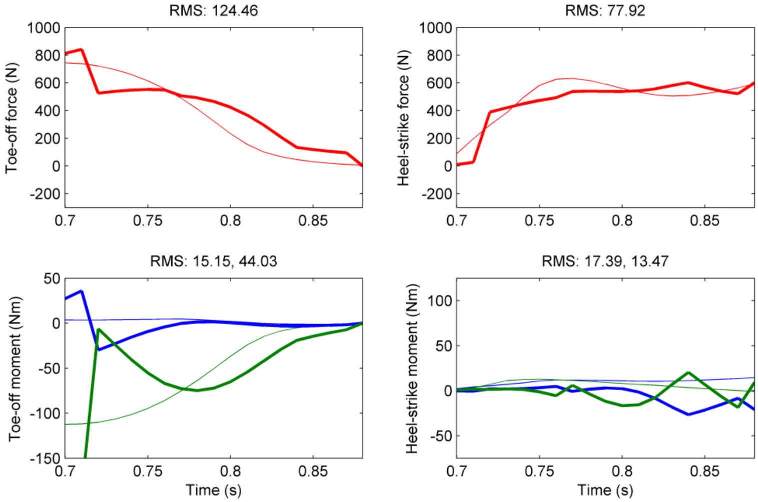

Figure 7: Ground reaction components: CMm (thick lines) vs. FP (thin lines); *x* component (blue), *y* component (green), *z* component (red).

It must be said that modeling the foot as two segments proved to be relevant: a single-segment foot model was also tested but it led to notably higher errors.

The discontinuities shown by the force and moments yielded by the contact model are presumably due to the fact that the motion is imposed. This, along with the fact that the time-step used by the motion capture system (10 ms) is rather large for contact problems, means that a contact sphere might undergo sudden indentation increments from one time-step to another. Moreover, no mechanism has been provided in order to handle the variation of stiffness depending on the number of active spheres. Other possible cause is the notable error in the captured positions of the markers at the feet, which further amplifies the mentioned problem.

Regarding efficiency, the optimization process that led to the presented results took a wall-clock time of around 14 seconds on an Intel Core i7 950 computer, and roughly required 12,000 function evaluations, being these figures representative of the general trend observed during the study.

At the view of the results and the computational effort required by this optimization process, it is clear that the proposed method is not suitable to be applied at each iteration of a predictive optimization process having the motion as design variables, as long as the required computation times would be too high. Instead, it seems more reasonable to use this technique to obtain a foot contact model that could be applied on a predictive optimization process, having either the motion or the excitations as design variables. In such a context, it would be expected that the observed discontinuities in the reactions produced by the contact model vanished: in the first case, the optimizer would move away from motions causing discontinuities, due to their high metabolic cost; in the second case, forward dynamics would be run at each function evaluation, thus yielding a smooth profile of the contact reactions.

For the use of the method in the abovementioned way, it would be advisable to set the same model for both feet. However, this has not been done in the present work, since the excessive inaccuracy in marker location led to non-satisfactory results. Therefore, more attention should be paid to marker location (especially in the feet) in the experiment. Also, it would be recommendable to carry out experiments at different gait speeds, as in [4], in order to adjust the model to all of them, or to seek a relationship between the contact model parameters and the gait speed. Finally, the method should be extended to the general case, including tangential contact forces, although this objective might need to be approached in a different way.

5 CONCLUSIONS

The solution of the double support problem during gait, i.e. the determination of ground reactions from a given motion without the help of force plates, allows estimating the joint efforts that generated the motion. The difficulty of the problem comes from the ground reactions indeterminacy that occurs during the double support phase of gait. In this paper, different methods for solving the double stance problem in human gait have been presented and compared. Apart from the use of force plate measurements, two methods that do not use force plate information are addressed, namely the smooth transition assumption and the use of a foot-ground contact model.

Basically, the idea in the latter approach is to seek the parameters of a force contact model that produce the same reaction forces and moments than those estimated from inverse dynamics. In this work, only the contact surface and normal force parameters have been considered as design variables, being the normal reaction force and the horizontal components of the reaction moment the magnitudes whose error has been minimized.

The proposed force-based approach has shown a good correlation with measurements taken from force plates, and the computational times required have been kept moderated (some seconds). Therefore, it could serve to generate foot-ground contact models to be used within optimization processes aimed at predicting the motion of real subjects under virtual conditions. This kind of tool would be of great help to anticipate the result of surgery or to help in the design of prosthetic/orthotic devices. However, for such an application, further work should be done in the future, especially in the direction of eliminating the force and moment discontinuities.

It should be noted that the method is not intended for identifying the actual parameters of the foot-ground contact, since that would require a much more precise measurement of the foot motion during support phase.

ACKNOWLEDGEMENTS

This work is supported by the Spanish Ministry of Science and Innovation under the project DPI2009-13438-C03, the support is gratefully acknowledged. The help from Alvaro Noriega, from University of Oviedo, in the selection of the optimization algorithm is also greatly acknowledged.

REFERENCES

[1] J. Ambrosio, A. Kecskemethy. Multibody dynamics of biomechanical models for human motion via optimization. In: Garcia Orden JC, Goicolea JM, Cuadrado J, editors.

Multibody Dynamics: Computational Methods and Applications, Springer, Dordrecht, 245–272, 2007.

[2] F. C. Anderson, M. G. Pandy. Dynamic optimization of human walking. *J. of Biomechanical Engineering*, vol. 123, 381–390, 2001.

[3] M. Ackermann, W. Schiehlen. Dynamic analysis of human gait disorder and metabolical cost estimation. *Archive of Applied Mechanics*, vol. 75, 569–594, 2006.

[4] M. Millard, J. McPhee, E. Kubica. Multi-step forward dynamic gait simulation. In: Bottasso CL, editor. *Multibody Dynamics: Computational Methods and Applications*, Springer, 25–43, 2009.

[5] A. Murai, K. Yamane, Y. Nakamura. Modeling and identification of human neuromusculoskeletal network based on biomechanical property of muscle. Proc. of the 30th Annual International IEEE EMBS Conference, Vancouver, Canada, 2008.

[6] B. R. Umberger, K. G. M. Gerritsen, P. E. Martin. A model of human muscle energy expenditure. *Computer Methods in Biomechanics and Biomedical Engineering*, vol. 6, 99–111, 2003.

[7] L. Ren, R. K. Jones, D. Howard. Whole body inverse dynamics over a complete gait cycle based only on measured kinematics. *Journal of Biomechanics*, vol. 41, 2750–2759, 2008.

[8] F. J. Alonso, J. Cuadrado, U. Lugris, P. Pintado. A compact smoothing-differentiation and projection approach for the kinematic data consistency of biomechanical systems. *Multibody System Dynamics*, vol 24, 67–80, 2010.

[9] J. Garcia de Jalon, E. Bayo. *Kinematic and dynamic simulation of multibody systems – the real-time challenge–*, Springer–Verlag, New York, 1994.

[10] A. Kuo. A least-squares estimation approach to improving the precision of inverse dynamics computations, *Journal of Biomechanical Engineering*, vol. 120, 148–159, 1998.

[11] H. M. Lankarani, P. E. Nikravesh. A contact force model with hysteresis damping for impact analysis of multibody systems. *Journal of Mechanical Design*, vol. 112, 369–376, 1990.

[12] D. Dopico, A. Luaces, M. Gonzalez, J. Cuadrado. Dealing with multiple contacts in a human-in-the-loop application. *Multibody System Dynamics*, vol. 25, 167–183, 2011.

[13] C. M. O'Connor, S. K. Thorpe, M. J. O'Malley, C. L. Vaughan. Automatic detection of gait events using kinematic data, *Gait and Posture*, vol. 25, 469–474, 2007.

[14] N. Hansen. The CMA evolution strategy: a comparing review. In: Lozano JA, Larrañaga P, Inza I, Bengoetxea E, editors. *Towards a new evolutionary computation. Advances in estimation of distribution algorithms*, Springer, 75–102, 2006.

Proceedings of MUSME 2011, the International Symposium
on Multibody Systems and Mechatronics
Valencia, Spain, 25-28 October 2011

INVERSE DYNAMICS SIMULATION OF HUMAN MULTIBODY DYNAMICS

García-Vallejo, Daniel[*] and Schiehlen, Werner[†]

[*] Departamento de Ingeniería Mecánica y de los Materiales
Escuela Técnica Superior de Ingenieros, Camino de los Descubrimientos s/n, 41092 Sevilla, Spain
e-mail: dgvallejo@us.es,

† Institute of Engineering and Computational Mechanics, University of Stuttgart,
Pfaffenwaldring 9, 70569 Stuttgart, Germany
e-mail: werner.schiehlen@itm.uni-stuttgart.de.

Keywords: Inverse dynamics, overactuation, kinematical loops, parameter optimization, human walking dynamics.

Abstract. *Inverse dynamics simulation is a convenient approach often used in robotics and mechatronic systems for feed-forward control to reproduce a desired output trajectory of a nonlinear multibody system. Usually the engineering systems are completely actuated or underactuated, respectively, for economical reasons. In contrary, the musculoskeletal multi-body systems found in biomechanics are highly overactuated due to the many muscles, and they show switching number of closed kinematical loops. The method of inverse dynamics is extended to overactuated systems by parameter optimization, and simulation results of human walking are presented.*

1 INTRODUCTION

Multibody system dynamics techniques are potentially also very powerful in human walking dynamics and there are many contributions from the multibody dynamics community to this kind of problems [3, 4, 10, 15, 17]. The human body can be assumed to be a multibody system actuated by muscles. The human body actuators, the muscles, have their own dynamics that is formulated similar to proportional-integral force actuators found in engineering. In addition, the alternating contact conditions of the feet on the ground result in a rigid multibody system with a different number of degrees of freedom at each one of the phases of motion.

Parameter optimization techniques have been frequently used for motion synthesis of biped robots [8]. These techniques have been proven to be powerful in two-dimensional human walking simulation as shown by Ackermann [1]. The basics of this approach are the parameterization of the muscle forces and generalized coordinates and the search for their optimal values by minimizing a cost function that includes an energy expenditure estimation and a measure of deviation from normal walking patterns. The method is very much based on inverse dynamics since at each iteration of the optimization algorithm an inverse dynamic problem is solved by using the motion reconstructed from the optimization parameters. The main advantage of this approach is the complete elimination of the forward integrations of the equations of motion, what significantly reduces the computational cost of simulation.

This paper is structured as follows. The second chapter presents the multibody model of the human body to be analyzed, including muscle selection issues and details of the contraction and activation dynamics. Chapter 3 is devoted to the parameter optimization framework used to simulate the three-dimensional motion and muscle forces of the human body model. Finally, some numerical simulation results in Chapter 4.

2 MODEL DESCRIPTION

The human body model used is a three-dimensional rigid multibody system actuated by muscles. The equations of motion of the system are obtained by using the multibody software Neweul-M^2 [12], which generates the equations of motion in symbolic form for efficiently analyzing, simulating and optimizing multibody systems. The skeleton is first considered as an open kinematic chain built from rigid bodies that are connected by holonomic joints and described by a set of n_c generalized coordinates. Thus, starting from the Newton-Euler equations of the rigid bodies in the kinematic chain, the equations of motion are written in terms of the generalized coordinates by virtue of the d'Alembert's principle [18] as

$$\mathbf{M}(\mathbf{q})\,\ddot{\mathbf{q}} + \mathbf{k}(\mathbf{q},\dot{\mathbf{q}}) = \mathbf{q}_r(\mathbf{q},\dot{\mathbf{q}}) + \mathbf{B}\,\mathbf{A}\,\mathbf{f}^m \tag{1}$$

where $\mathbf{M}(\mathbf{q})$ is the $(n_c \times n_c)$- mass matrix of the system, $\mathbf{q}$, $\dot{\mathbf{q}}$ and $\ddot{\mathbf{q}}$ are the $(n_c \times 1)$- position, velocity and acceleration vectors, respectively, $\mathbf{k}(\mathbf{q},\dot{\mathbf{q}})$ is a $(n_c \times 1)$- vector describing the generalized Coriolis forces, $\mathbf{q}_r(\mathbf{q},\dot{\mathbf{q}})$ is a $(n_c \times 1)$- vector including generalized gravitational forces, passive generalized moments at the joints due to tissues interacting with the joints according to the model of Riener and Edrich [16] and generalized viscous damping torques at the knees and hips according to the model of Stein et al. [20] and $\mathbf{B}\,\mathbf{A}\,\mathbf{f}^m$ is a $(n_c \times 1)$- vector that includes the generalized forces exerted by the muscles actuating the model. The $(N_m \times 1)$- vector $\mathbf{f}^m$ summarizes the forces generated by a reduced set of N_m muscles included in the model. Matrix $\mathbf{A}$ is the constant $(n_b \times N_m)$- matrix of moment arms and is used to calculate the torques generated by all muscles at the actuated joints, where n_b is the number of actuated joints, and matrix $\mathbf{B}$ is a $(n_c \times n_b)$- distribution matrix used to obtain the generalized torques due to the torques at the actuated joints.

The three-dimensional model of the human body used in this research is composed of 7 rigid bodies, two thighs, two shanks, two feet, and a body called HAT representing the pelvis, trunk, arms and head, which are connected by holonomic joints, see Figure 1. The thighs are connected at the hips to the HAT by spherical joints, the shanks and thighs are connected by revolute joints representing the knees and the foot and shanks are connected by revolute joints representing the ankles. This is a simplification compared to other three-dimensional models that can be found in Anderson and Pandy [6, 7]. However, this simplification allows the derivation of the symbolical equations of motion of the tree composed by the mentioned 7 bodies without any constraint by software Neweul-M^2 [12]. Such a simple model allows the study of the proposed optimization framework in a three-dimensional simulation, see also Ref. [11].

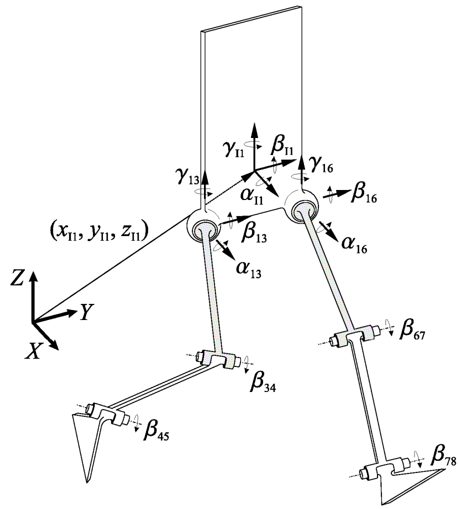

Figure 1: Model of the human body.

The kinematic chain in Figure 1 is described by the following vector of 16 generalized coordinates

$$\mathbf{q} = [x_{I1} \quad y_{I1} \quad z_{I1} \quad \alpha_{I1} \quad \beta_{I1} \quad \gamma_{I1} \quad \alpha_{13} \quad \beta_{13} \quad \gamma_{13} \quad \beta_{34} \quad \beta_{45} \quad \alpha_{16} \quad \beta_{16} \quad \gamma_{16} \quad \beta_{67} \quad \beta_{78}]^T \tag{2}$$

where the subscript I refers to the inertial frame, subscript 1 refers to body HAT, which is in composed of the pelvis and the trunk, subscripts 3 and 6 refer to right and left thighs, respectively, subscripts 4 and 7 refer to right and left shanks, respectively, and subscripts 5 and 8 refer to right and left feet, respectively. When a subscript is written as ij it means a relative motion of body j with respect to body i. It shall be noted here that Neweul-M^2 is programmed based on the most common sequence of rotation 123, while in Biomechanics the sequence 213 is usually considered anatomically meaningful, Zatsiorsky [23] and Allard, Cappozzo et al. [5]. However, while the spatial rotations of the members are the same using the different rotation sequences, for comparison with other authors' results, the 213 sequence has been used.

Once the kinematic chain representing the skeleton is described, the contact of this chain with the ground is added. The contact conditions in the different walking phases are represented by unilateral constraints. However, due to the use of an optimization framework in which it is possible to constrain the normal contact forces to be only positive, the contact with the ground is modelled using simple bilateral constraints associated to the joints attached to the feet. Therefore, the contact forces can be easily added to the model by using a vector of Lagrange multipliers as

$$\mathbf{M}(\mathbf{q})\ddot{\mathbf{q}} + \mathbf{k}(\mathbf{q},\dot{\mathbf{q}}) = \mathbf{q}_r(\mathbf{q},\dot{\mathbf{q}}) + \mathbf{B}\,\mathbf{A}\,\mathbf{f}^m + \mathbf{C}_{ph}^T \boldsymbol{\lambda}_{ph} \quad (ph = 1,2,\ldots 8) \tag{3}$$

where $\boldsymbol{\lambda}_{ph}$ is the vector of Lagrange multipliers at phase *ph* of the motion. Note that the previous equation is used together with constraints equations forcing the normal contact forces to be always positive. Moreover, hard impacts will be avoided.

The contact conditions of different phases of the walking cycle are summarized in Figure 2 in agreement with the model of the foot adopted. Note that A_r and B_r are used to refer to the right heel and right toe, respectively, while A_l and B_l are used to refer to the left heel and left toe, respectively.

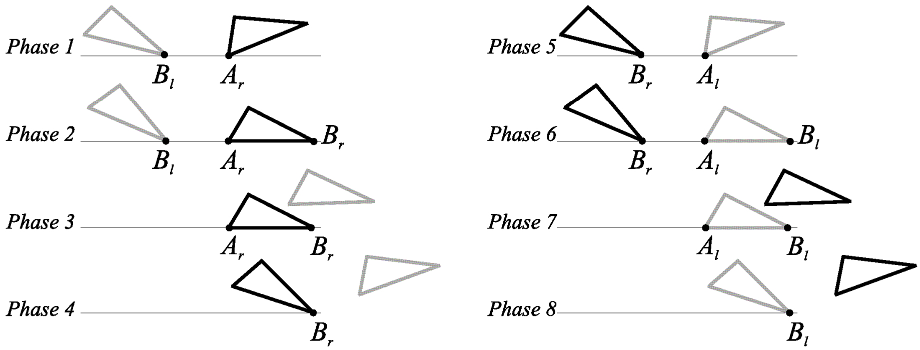

Figure 2: Sketch of the contact conditions.

In the formulation of contact, it is assumed that there is no sliding of the feet during the whole cycle of walking. The contact conditions at the different phases are modelled as follows:

- *Phase 1*: the left toe contact is modelled by constraining the three displacements of point B_l and the rotation of the foot around an axis perpendicular to the flat surface of the ground (pivoting). On another hand, the right heel contact is modelled by constraining the three displacements of point A_r and the rotation of the foot around an axis perpendicular to the flat surface of the ground.
- *Phase 2*: due to the contact of the right toe, a constraint to the vertical displacement of point B_r is added to the constraint set of phase 1.
- *Phase 3*: the contact at the left toe is removed.
- *Phase 4*: the contact at the right heel is also removed. The right toe contact is modelled by constraining the three displacements of point B_r and the pivoting rotation of the foot around an axis perpendicular to the ground.
- *Phase 5*: the left heel gets in contact with the ground and this contact is modelled by constraining the three displacements of point A_l and the pivoting rotation of the foot around an axis perpendicular to the ground.
- *Phase 6*: due to the contact of the left toe, a constraint to the vertical displacement of point B_l is added to the constraint set of phase 5.
- *Phase 7*: the contact at the right toe is removed.

- *Phase 8*: the contact at the left heel is also removed. The left toe contact is modelled by constraining the three displacements of point B_l and the pivoting rotation of the foot around an axis perpendicular to the ground.

2.1 Muscles actuating the multibody model

The muscle groups selected for this research are based on the work of Anderson and Pandy [6]. These authors developed a three-dimensional model for vertical jumping which can also be used for walking analysis even if walking is a less demanding activity. It is also expected that the set of muscles used by these authors could be reduced, since some of them may show only a low enough activation during walking. Such a low activation would results in a small muscle torque at the joints the muscle spans.

There is a need for selecting a criterion which allows one to combine muscles in groups. The first idea to keep in mind is that the muscles to be included in the same group must have the same main function. Then, averaged values of the moment arms will be obtained. This has been done previously by other authors. For instance, Menegaldo et al. [13] suggested to obtain averaged values of certain muscle properties by using as weights the products of the maximum force by the moment arm related to each joint of the different muscles that are to be combined. This criterion gives more importance to the muscles in the group that may produce a larger joint moment during walking. Then, it is required to have the values of the forces exerted by each muscle during a cycle of walking. To that end, the results obtained by Brand et al. [9] are used. These authors obtained the peak force of each one of the musculotendon actuators during a walking cycle of normal gait. With the peak forces, peak joint moments can be obtained and used as a measure of the contribution of each muscle to the motion. This criterion is used in this investigation to average the moment arms for each muscle group from the moment arms calculated by Menegaldo et al. [14].

The previous idea can also be used to neglect certain muscles from the ones used by Anderson and Pandy [6] so that the muscle set can be further reduced for the sake of simplicity. In order to check the contribution to gait of each one of the muscle groups, the product of the averaged moment arm by the maximum force of the muscle obtained by Brand et al. [9] can be used. These products are the maximum values of the moment components corresponding to each muscle group during a walking cycle. Then, comparing the resultant moments one to each other, it is concluded which are the muscles or muscle groups that can be neglected, see Ref. [11].

2.2 Inversion of activation and contraction dynamics

An important part of the optimization process used to simulate a walking cycle is the inversion of the contraction and activation dynamics, see Ackermann [1]. The inversion of the contraction dynamics is needed to obtain the values of the muscle activation, a, since they are required to evaluate the energy expenditure according to the procedure proposed by Umberger et al. [21]. Once the activations are obtained, using their time derivative, $\dot{a}$, it is possible to invert also the activation dynamics so that the neural excitations, u, are also obtained. The neural excitations are required for two reasons: one is that they are also involved in the calculation of the muscle energy expenditure and the other is that they are involved in some of the nonlinear constraints of the optimization procedure since their values must lay in the interval [0, 1].

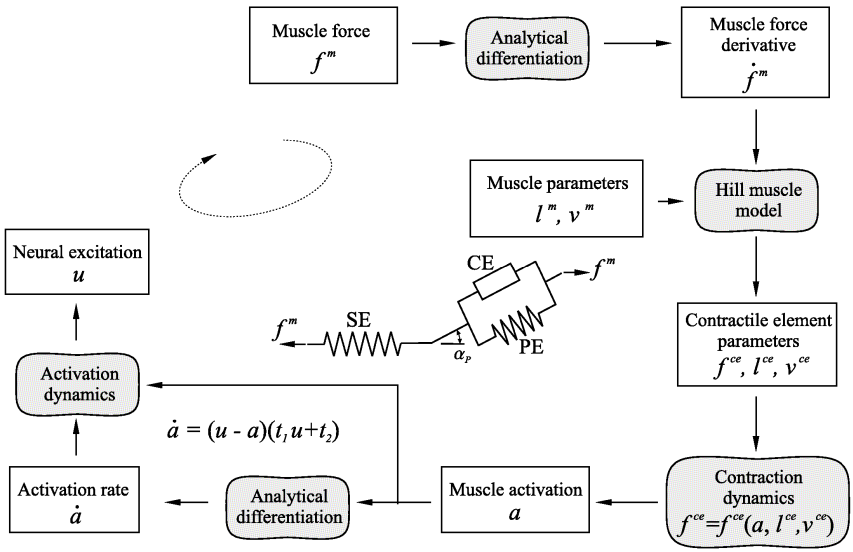

Figure 3: Flow diagram of the inversion of the activation and contraction dynamics.

In the work of Ackermann [1], the muscle forces are parameterized by using cubic splines, which have C^2 continuity. The values of the muscle forces at certain time nodes are included in the set of optimization variables. Then using numerical differentiation, the time derivative of the muscle force at another set of points, the so called control points, is computed by centered finite divided differences and other numerical formulae obtained from truncated Taylor series. Since the control points are not uniformly distributed along the gait cycle, the use of the previously mentioned numerical differentiation formulae leads to a nonuniform distribution of the accuracy of the time derivative along the gait cycle.

The calculation of the time derivative of the muscle force is carried out by implementing the analytical derivative of a higher order spline polynomial in the interpolation subroutine. Furthermore, the time derivative of the activation, what is required when inverting the activation dynamics, can also be obtained after some calculations due to the implementation of the first and second derivatives of the spline polynomials. Figure 3 shows a flow diagram summarizing the inversion process of the contraction and activation dynamics.

3 PARAMETER OPTIMIZATION

The simulation of human walking motion is now treated as a huge parameter optimization problem. The optimization parameters, also called design variables, are used to reconstruct the muscle force histories and the generalized coordinate histories of a walking cycle as well. Such a set of parameters are found by minimizing a cost function which is evaluated based on energetic and aesthetic reasons. Finally, the motion and muscle forces time histories reconstructed from the optimization parameters are asked to fulfill many constraints. The constraints of the constrained optimization problem ensure the fulfillment of the equations of motion of the multibody system, the kinematic constraints as well as other physical and physiological relations, see also Ref. [19].

The complete set of design variables are summarized in vector $\boldsymbol{\chi}$. This vector is itself built from four different vectors as follows:

1. A vector $\mathbf{q}_i$, i = 1, 2, ...n_c, containing all nodal values of the different generalized coordinates.
2. A vector $\mathbf{f}_j^m$, j = 1, 2, ...N_m, containing all nodal values of the different muscle forces. Since each muscle force is parameterized as the generalized coordinates are, a similar number of design variables can arise from muscle forces.
3. A vector with eight components representing the durations of the eight phases of a walking cycle $\mathbf{t}_{ph}$.
4. A vector with geometrical parameters describing the kinematic constraints of the feet on the ground $\mathbf{p}_g$.

According to the previous explanation, the vector of design variables can be written as:

$$\boldsymbol{\chi} = \begin{bmatrix} \mathbf{q}_i^T & \mathbf{f}_j^{mT} & \mathbf{t}_{ph}^T & \mathbf{p}_g^T \end{bmatrix}^T \tag{4}$$

where indices i, j and ph are running from 1 to n_c, N_m and 8, respectively, and g is just a subscript meaning that parameters in $\mathbf{p}_g$ are geometrical. In the three-dimensional model presented before the number of coordinates n_c is equal to 16 while the number of muscles N_m is equal to 28.

3.1 Optimization framework

Minimizing energy expenditure during walking is a reasonable criterion that the central neural system uses when dealing with muscles recruitment, especially when walking long distances. For this reason, it makes sense to obtain muscle forces and generalized coordinates by minimizing the metabolical cost of walking. In this investigation, the energy expenditure model due to Umberger et al. [21] is used as measure of the metabolical cost. This energy measure was also used by Ackermann [1] while other authors have used different cost functions as for example a measure of the muscle fatigue, see Brand et al. [9] and Peasgood et al. [15].

Umberger et al. [21] provided a measure of the metabolical expenditure including thermal and mechanical energy liberation rates during simulated muscle contractions of mammalians at normal body temperature. According to their model, the total energy rate of a single muscle is written as follows:

$$\dot{E} = \dot{E}\left(l^{ce}, v^{ce}, f^{ce}, a, u, \mathbf{p}\right) \tag{5}$$

where l^{ce} is the contractile element length, v^{ce} is the contractile element velocity, f^{ce} is the contractile element force, a is the muscle activation, u is the neural excitation and $\mathbf{p}$ is a vector summarizing all muscle constant parameters required to evaluate the energy rate, see Umberger et al. [21]. The previous expression of the energy rate can be integrated in time in order to obtain the amount of energy spent during walking as

$$E = \int_{t_0}^{t_f} \dot{E}\left(l^{ce}, v^{ce}, f^{ce}, a, u, \mathbf{p}\right) dt \tag{6}$$

A more meaningful measure of energy consumption when considering walking long distances in normal conditions is the energy expended per unit of length what can be obtained by dividing the total energy of one cycle by the distance walked. This is called the total energy of transportation and reads as

$$E^t = \frac{E}{L_R + L_L} \tag{7}$$

where L_R and L_L are the right and the left steps walked in the simulated cycle.

Since the time histories of the muscle forces and of the generalized coordinates are obtained by optimization techniques trying to minimize the energy consumption there is a need to follow a certain motion pattern. Otherwise, in an attempt to reduce the energy expenditure a non-logical solution could be found. For example, standing in equilibrium in vertical position without muscle contraction seems to be a low energy configuration. Therefore, a measured walking motion is used to force the model to follow a certain motion. This fact has some other advantages in the case of designing prosthesis. One of these advantages is that the simulated motion of an individual wearing a prosthesis will be close to normal walking patterns which is desirable for aesthetical reasons. Another advantage is related with the contact forces at the feet. The simulated contact forces will be close to those of a normal walking cycle what would result in no significant modification of the contact forces at the non-damaged foot. This is reasonable in case of non-severe damages since other aspects like pain may be more important than enforcing a symmetric walking motion.

The deviation with respect to normal walking patterns is evaluated as follows:

$$J_{dev} = \int_{t_0}^{t_f} \sum_{i=1}^{n_x} \frac{\left(x_i(t) - x_i^m(t)\right)^2}{\sigma_i^2} dt \tag{8}$$

where x_i is a time dependent variable of the model and x_i^m refers to the experimentally measured value of the same variable. These variables, x_i with $i = 1, 2, ...n_x$, include the generalized coordinates and ground reaction forces. In (8), σ_i is a characteristic measure of the time variability of x_i. Dividing by σ_i the differences between measured and simulated values of all x_i are scaled.

In the work of Ackermann [1], the standard deviation obtained by measuring the walking motion of many subjects and provided by Winter [22] was used as σ_i. Since in this investigation, not a mean walking motion but the walking motion of one particular subject is used, a measured related to the motion used is preferred. Therefore, the mean square deviation with respect to the averaged mean is used as a measure of the time variability as

$$\sigma_i = \frac{1}{T}\sqrt{\int_{t_0}^{t_f} \left(x_i(t) - X_i\right)^2 dt} \tag{9}$$

with

$$X_i = \frac{1}{T}\int_{t_0}^{t_f} x_i(t)\,dt \tag{10}$$

where X_i is the average of $x_i(t)$ in the measured walking cycle. The measured motion used in this research was obtained by Ackermann and Gros [2] by measuring the walking motion of a subject wearing sport shoes and walking at his preferred velocity.

Finally, the value of the cost function is calculated using the metabolical cost of transportation, E^t, and the measure of the deviation from normal walking patterns, J_{dev}, as follows:

$$f = \omega_E E^t / 100 + \omega_J J_{dev} \tag{11}$$

where E^t is divided by the factor 100 to obtain a value with the same order of magnitude of J_{dev} for balancing of the two terms of the cost function (11) to get comparable numbers, and ω_E and ω_J are two weighting factors.

3.2 Parameterization

The procedure suggested by Ackermann [1] and used in this research avoids the forward integration through parameterization of the time histories of the generalized coordinates by using spline polynomials and by searching for their optimum values at certain node positions. Since walking is a periodic motion, other authors have also used Fourier series to parameterize the motion, i.e. Peasgood et al. [15]. Spline functions have many possibilities that can be used to improve the efficiency of the procedure. In fact, it is easy to have access to the derivatives of the parameterized function, avoiding the numerical differentiation used by Ackermann [1]. In addition, the interpolation can be split into two parts: a more computationally expensive one that can be done in a pre-processing stage and the other that is done during the optimization.

It is observed that when periodic boundary conditions are used to obtain the interpolating spline polynomials from a set of points which are not fully periodical in terms of the function values and their derivatives, an oscillating behavior is induced into the spline polynomials. This undesirable oscillating behavior may hamper the convergence of the optimization algorithm. The reasons for this lack of periodicity are twofold. On the one hand, the measured motion which is used as a normal walking pattern and serves as the basis to evaluate the deviation from normal walking patterns is not perfectly periodic. The attempt to minimize such a deviation transfers the mentioned non-periodic behavior to the muscle forces and generalized coordinates.

On another hand, during the iterations of the optimization algorithm any partial result may admit a certain degree of non-periodicity due to numerical reasons. In this research, the above mentioned oscillatory behavior is decreased by forcing the periodicity of the set of points used to calculate the interpolating polynomials. In the case of fifth order periodical splines, the degree of periodicity is defined according to

$$\begin{aligned} &f_1 = f_N \\ &f_1^{'} + O(h^3) = f_N^{'} + O(h^3) \\ &f_1^{''} + O(h^3) = f_N^{''} + O(h^3) \\ &f_1^{'''} + O(h^3) = f_N^{'''} + O(h^3) \end{aligned} \tag{12}$$

where f_1, $f_1^{'}$, $f_1^{''}$ and $f_1^{'''}$ are the values of the function to be interpolated at the first point node and its first, second and third derivatives, respectively, and h is the distance between points. It shall be noted that the order of accuracy used could be selected to be higher. Using Taylor series expansions, it is possible to find the derivatives at the first node by using a backward difference formula and the derivatives at the last node, N, by using a forward difference formula. Then, Equations (12) result in a system of four linear equations from which it is possible to obtain the values of f_1, f_2, f_{N-1} and f_N that improve the periodicity of the data set to be interpolated.

3.3 Constraint formulation

The solution of the optimization algorithm must fulfill a set of constraints as stated above. The set of constraints is summarized as follows:

1. Neural excitations must be bounded in the interval [0, 1]. This kind of constraint ensures that muscle forces are consistent with the activation and contraction dynamics of the muscles.
2. Ground clearance must be positive or equal to zero to ensure no penetration of the feet into the ground.
3. Positive normal contact forces to avoid bilateral constraints between the feet and the ground.
4. Tangent contact forces on the feet must be consistent with Coulomb's friction model to avoid foot sliding.
5. The averaged velocity is fixed.
6. Design variables are bounded. These bounds may be due to some physiological reasons like for example the amplitude of the relative motion allowed by a certain joint.
7. Other physiological constraints that may help to the convergence of the optimization algorithm like for instance constraining the maximal achieved knee flexion during the swing phase or the maximal achieved hip extension during the stance phase, see Ackermann [1].
8. Equations of motion must be fulfilled with a certain tolerance.
9. Kinematic constraints must be fulfilled within a certain tolerance.

Exactly satisfying the equations of motion, although it would be desirable, seems to be extremely difficult. One reason for that is the parameterization of the motion and muscle forces by using splines. Doing so, we are assuming a certain error in the representation of the motion since it does not have to be a combination of splines polynomials. Therefore, we have to accept a small violation of the equations of motion. In order to quantify such an infringement, the constraints are formulated in terms of joint torques since we know approximately the usual range of values from inverse dynamics of normal walking. A detailed discussion can be found in Ref. [11] where it is shown that the optimization problem is well posed.

4 NUMERICAL RESULTS

This Chapter shows some numerical results of the simulations carried out using the optimization framework presented. A two-dimensional symmetrical model will be analyzed to check the performance of the approach and the convergence of the model for different parameterizations.

The two-dimensional symmetrical model can also be found in the work of Ackermann [1] and therefore a comparison of the numerical results and performance is possible. Since many improvements are introduced, the comparison serves also to validate the added modifications. The two-dimensional model used in this section is modelled by using 9 coordinates and 7 bodies. A sketch of the model can be seen in Figure 4. As it is shown, the model is restraint to the sagittal plane reducing the generalized coordinates (2) to

$$\mathbf{q} = [x_{I1} \quad z_{I1} \quad \beta_{I1} \quad \beta_{13} \quad \beta_{34} \quad \beta_{45} \quad \beta_{16} \quad \beta_{67} \quad \beta_{78}]^T \tag{13}$$

The symmetry of the model allows a big simplification in the number of optimization variables. In fact, it is assumed that the left leg experiences in the second half of the walking cycle the same motion as the right leg in the first half. In addition, the motion of the pelvis is assumed to be the same in both halves of the cycle. Muscle forces of the left leg are exactly the same as those of the right one but shifted half a walking cycle. Therefore, the symmetrical model is represented by the generalized coordinates of the pelvis during the first half of the walking cycle and the generalized coordinates and muscle forces of the right leg during the whole walking cycle.

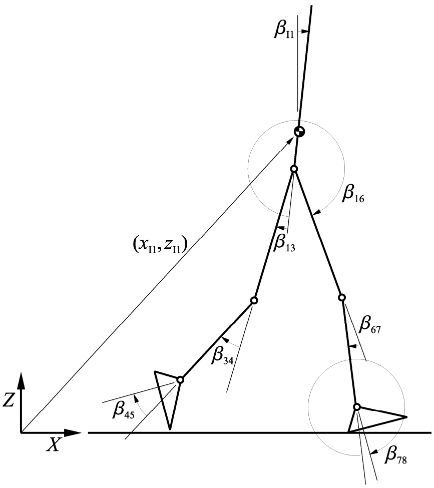

Figure 4: Sketch of the two-dimensional model with its generalized coordinates.

Table 1 shows the results of several models that differ one to another in the number of nodes used to parameterize the generalized coordinates and muscle forces. Every model has an odd number of nodes in order to have a node exactly at the time instant equal to half of the walking period. Thus, the number of nodes ranges from 19 to 35.

NN	*f*	E^t [J/m]	J_{dev}	*CT* [hours]
19	13.33	626.00	7.07	0.55
21	7.54	415.73	3.38	1.85
23	6.52	351.01	3.01	2.87
25	5.50	310.62	2.39	3.25
27	4.99	283.28	2.16	5.65*
29	4.62	254.22	2.08	8.66
31	4.45	246.32	1.99	9.52
33	4.37	238.57	1.98	13.17
35	4.31	236.10	1.95	16.16*

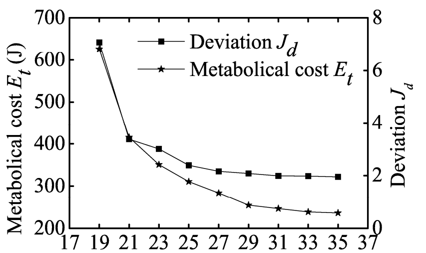

Table 1: Performance of the different models (*NN* stands for number of nodes, *f* is the cost function, E^t is the metabolical cost of transportation, J_{dev} is the measure of deviation from normal walking patterns and *CT* stands for computation time). * Estimated *CT* values.

The convergency of the different models to a unique solution is remarkable. As can be observed in Table 1, increasing the number of nodes always leads to a smaller difference in the value of the cost function *f*. The same behavior is observed in the values of the metabolical cost of transportation, E^t, and the deviation from normal walking pattern, J_{dev}, measured in the lab.

The last column of data in Table 1 shows the computation time required for each model. In the case of the 27 and 35 nodes models, the computation times could not be directly measured due to other processes running on the same computer and their values have been estimated by fitting a polynomial to the rest of values. The tolerances for the fulfilment of the equations of motion and of the kinematical constraints were ε_m = 2 Nm and ε_k = 2 mm as in the work of Ackermann [1]. On another hand, the termination tolerances for the SQP optimization algorithm were fixed to $TolFun = 10^{-4}$, $TolCon = 10^{-4}$ and $TolX = 10^{-6}$, being *TolFun* the termination tolerance for the cost function, *TolCon* the termination tolerance for the constraints violation and *TolX* the termination tolerance for design variables vector. The computation times shown in Table 1 have been obtained using a processor Intel® Xeon® CPU E5530 at 2.40 GHz with 4 cores and 6 GiB RAM. It has been observed that the pre-computation of the matrices involved in the spline interpolation, the elimination of numerical differentiation and the proper formulation of the equations of motion and kinematical constraints have helped to reduce the computation time to achieve a converged solution. Figure 5 shows different positions of a walker during a gait cycle simulated using 29 nodes.

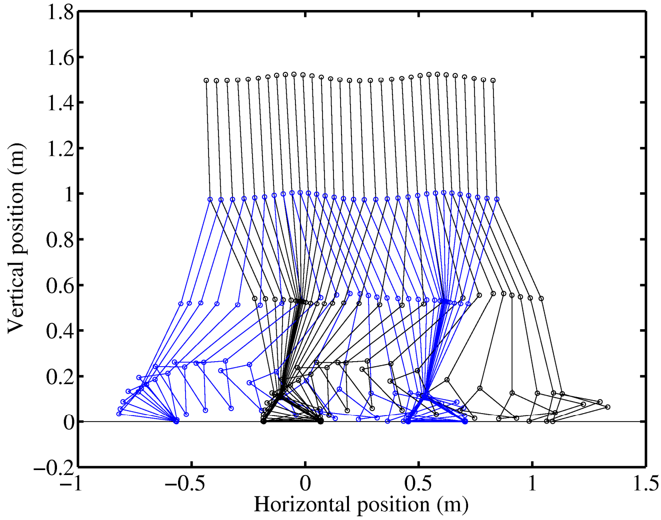

Figure 5: Different positions of the 2D walker during a gait cycle. The left leg is identified by positions -0.5m and 0.5m, the right leg is found at positions -0.1m and 1.0m.

It is worth of mention that the values of the metabolical cost of transportation, E^t, and the deviation from the normal measured motion, J_{dev}, do not coincide with the values reported by Ackermann [1]. These differences are due to the different parameterization used in this research and the different definition of the measure of the deviation from normal walking. Ackermann [1] used the standard deviation to scale the deviation from simulated values and measured ones while the mean square deviation from the mean value has been used in this research. The weighting factors ω_E and ω_J used here are both equal to 1. As shown by Ackermann [1] a difference in the mentioned weighting factors may lead to different values of the optimized magnitudes, i.e., the metabolical cost of transportation, E^t, and the deviation from measured motion, J_{dev}.

5 CONCLUSIONS

Based on the research carried out and on the numerical results obtained, the following conclusions could be drawn. Formulating the equations of motion of the musculoskeletal system by using NewEul-M^2 is very important since it was possible to obtain the equations of the system symbolically with a minimum number of generalized coordinates and joint constraints. However, the symbolical manipulation of the equations was a limiting factor for the complexity of the model finally used.

It was possible to decrease the computational effort of the spline interpolation problem by reducing the size of the problem after some algebraic manipulations and by pre-computing the most expensive part of the information required to evaluate the interpolated function before the optimization algorithm starts.

The errors coming from numerical differentiation and the non-uniform distribution of such errors is avoided by analytical differentiation. The numerical differentiation via finite difference formulae is eliminated by implementing the first and second time derivatives of the interpolating polynomials and by obtaining the analytical derivatives of the contractile element force law. The number of muscles is reduced by grouping muscles with the same mechanical function in muscles groups. This allows a reduction in the number of design variables of the optimization problem without decreasing the possibilities of motion of the model.

The number of iterations of the optimization algorithm is reduced by formulating the constraints associated with the equations of motion and with the kinematic constraints at all control points. Even if the number of constraints of the constrained optimization problem is increasing, the saving in time due to the decrease in the number of iterations justified the implementation of such constraints.

It has been shown that inverse dynamics provides together with parameter optimization an approach which allows to deal with complex multibody systems characterized by overactuation a variable number of degrees of freedom by switching constraints and additional specific design criteria.

REFERENCES

[1] Ackermann, M. *Dynamics and energetics of walking with prostheses*. PhD thesis, Institut für Technische und Numerische Mechanik, Stuttgart, 2007.

[2] Ackermann, M., and Gros, H. *Measurements of human gaits*. Tech. Rep. Zwischenbericht ZB-144, Institut für Technische und Numerische Mechanik, University of Stuttgart, 70550 Stuttgart, 2005.

[3] Ackermann, M., and Schiehlen, W. Dynamic analysis of human gait disorder and metabolical cost estimation. *Arch. Appl. Mech.* **75**, 10-12 (2006), 569–594.

[4] Al Nazer, R., Rantalainen, T., Heinonen, A., Sievänen, H., and Mikkola, A. Flexible multibody simulation approach in the analysis of tibial strain during walking. *Journal of Biomechanics* **41** (2008), 1036–1043.

[5] Allard, P., Cappozzo, A., Lundberg, A., and C.L. Vaughan (Eds.). *Three dimensional analysis of human locomotion*. Wiley, Chichester, 1998.

[6] Anderson, F., and Pandy, M. A dynamic optimization solution for vertical jumping in three dimensions. *Computer Methods in Biomechanics and Biomedical Engineering* **2** (1999), 201–231.

[7] Anderson, F., and Pandy, M. Dynamic optimization of human walking. *Journal of Biomechanical Engineering* **123** (2001), 381–390.

[8] Bessonnet, G., Seguin, P., and Sardain, P. A parametric optimization approach to walking pattern synthesis. *The International Journal of Robotics Research* **24**, 7 (2005), 523–536.

[9] Brand, R., Pedersen, D., and Friederich, J. The sensitivity of muscle force predictions to changes in physiologic cross-sectional area. *Journal of Biomechanics* **19**, 8 (1986), 589–596.

[10] Chenut X, Fisette P, Samin JC. Recursive formalism with a minimal dynamic parametrization for the identification and simulation of multibody system – application to the human body. *Multibody System Dynamics* **8**, 2 (2002), 117-140.

[11] Garcia-Vallejo, D., and Schiehlen, W. 3D-simulation of human walking by parameter optimization. *Arch. Appl. Mech.* (submitted).

[12] Kurz, T., Eberhard, P., Henninger, C., and Schiehlen, W. From Neweul to Neweul-M^2: Symbolical equations of motion for multibody system analysis and synthesis. *Multibody System Dynamics* **24**, 1 (2010), 25–42.

[13] Menegaldo, L., Fleury, A., and Weber, H. Biomechanical modeling and optimal control of human posture. *Journal of Biomechanics* **36** (2003), 1701–1712.

[14] Menegaldo, L., Fleury, A., and Weber, H. Moment arms and musculotendon lengths estimtion for a three-dimensional lower-limb model. *Journal of Biomechanics* **37** (2004), 1447–1453.

[15] Peasgood, M., McPhee, J., and Kubica, E. Stabilization and energy optimization of a dynamic walking gait simulation. In *Proceedings of the ASME 2005 International Design Engineering Technical Conferences & Computers and Information in Engineering* (Long Beach, California, USA, September 24–28, 2005).

[16] Riener, R., and Edrich, T. Identification of passive elastic joint moments in the lower extremities. *Journal of Biomechanics* **32** (1999), 539–544.

[17] Rodrigo, S., Ambrosio, J., Da Silva, M., and Penisi, O. Analysys of human gait based on multibody formulations and optimization tools. *Mechanics Based Design of Structures and Machines* **36**, 4 (2008), 446–477.

[18] Schiehlen, W. Multibody system dynamics: Roots and perspectives. *Multibody System Dynamics* **1** (1997), 149–188.

[19] Schiehlen, W., and Garcia-Vallejo, D. Walking dynamics from mechanism models to parameter optimization. *Procedia IUTAM* (accepted).

[20] Stein, R., Zehr, E., Lebiedowska, M., Popovic, D., Scheiner, A., and Chizeck, H. Estimating mechanical parameters of leg segments in individuals with and without physical disabilities. *IEEE Transactions on Rehabilitation Engineering* **4**, 3 (1996), 201–211.

[21] Umberger, B., Gerritsen, K., and Martin, P. A model of human muscle energy expenditure. *Computer Methods in Biomechanics and Biomedical Engineering* **6**, 2 (2003), 99–111.

[22] Winter, D. *The biomechanics and motor control of human gait: normal, elderly and pathological*. University of Waterloo Press, Waterloo, 1991.

[23] Zatsiorsky, V. *Kinematics of Human Motion.* Human Kinetics, 1998.

Proceedings of MUSME 2011, the International Symposium
on Multibody Systems and Mechatronics
Valencia, Spain, 25-28 October 2011.

DYNAMIC ANALYSIS OF A FIVE-BAR LINKAGE MECHANISM IN TRACTION

Arinola B. Ajayi

Mechanical Engineering Dept.,
Faculty of Engineering, University of Lagos. Nigeria.
e-mail: abajayi@unilag.edu.ng

Keywords: Dynamic analysis, Five – bar linkage mechanism, Pin joint moments, Pin joint reaction, Traction velocity.

Abstract. *In this paper, the dynamic analysis of a five-bar linkage mechanism in traction is presented. The dynamic model of the mechanism is developed with the applied force to the crank arm resolved into two principal plane directions x and y and the resulting reaction forces and moments at the pin joints determined at various traction acceleration of 0, 10, 20, 30 and 40 m/s in the direction of crank rotation as well as in its opposite direction. It was observed that the horizontal reaction forces at the pin joints were decreasing as the traction acceleration increases in the direction of crank rotation while it increases when the acceleration increases in the opposite direction to the crank rotation. It was also observed that the pin joint moments at point A decreases as the traction velocities increases in the crank arm rotation direction while it increases as the acceleration increases in the opposite direction. The converse is the case for pin joint B, while there were no significant differences for pin joint moments at pin joints C and D in all the considered acceleration in both directions. Also, the vertical reaction forces at the pin joints did not change in magnitude as the magnitude and directions of the acceleration were altered. The analysis brings to the fore the importance of the consideration of traction acceleration in the design, development and utilization of five – bar linkage to avoid failure at this critical point.*

INTRODUCTION

Mechanical systems do comprise of linkage mechanisms for the purpose of transfer of forces and motions from one part to another in a desired manner. The literature is saturated with analysis and findings in this area [1 – 6]. These analyses include dynamics and synthesis of such systems. The area of dynamics of five – bar linkage mechanisms in traction has not been fully explored. It is therefore important to take a look at it. This will afford the designers, researchers and developers more insight into the principles and working of these mechanisms. It will also expose point of interest to note at design stage. The objective of this paper is to present a detailed analysis of a five – bar linkage mechanism in traction.

NOMENCLATURE

a_1, a_2, a_3, a_4	distances of CG from the pin end of linkages *AB*, *BC*, *CD*, and *DO* respectively
A_x, B_x, C_x, D_x, O_x	reaction forces at the pin joint *A, B, C, D, and O* respectively in the *x* direction
A_y, B_y, C_y, D_y, O_y	reaction forces at the pin joint *A, B, C, D, and O* respectively in the *y* direction
F_r	applied resultant force to the system
F_x, F_y	resolution of applied force in the horizontal and vertical directions respectively
g	acceleration due to gravity
$I_{ABCG}, I_{BCCG}, I_{CDCG}, I_{DOCG}$	Moments of inertia of linkage *AB, BC, CD* and *DO* respectively
m_1, m_2, m_3, m_4	masses of linkages *AB, BC, CD, and DO* respectively
M_a, M_b, M_c, M_d, M_o	moments about pin joints *A, B, C, D* and *O* respectively
M_{ij*}	moments about pin joint *A, B, C, D* and *O* at different acceleration *0, 10, 20, 30* and *40 m/s*^{2} in the positive and negative crank rotation directions, where $i = a, b, c, d$ *and* o, *j=0,10, 20, 30* and *40 m/s*^{2}, and *= positive or negative crank rotation directions.
r_1, r_2, r_3, r_4	length of linkages *AB*, *BC*, *CD*, and *DO* respectively
r_5	length of the vertical fixed link
r_6	length of horizontal fixed link
$x, \dot{x}, \ddot{x}$	linear displacement, linear velocity and linear acceleration respectively of the mechanism in *x* direction
$\beta_1, \dot{\beta}_1, \ddot{\beta}_1$	linkage *AB* angle, angular velocity and angular acceleration respectively
$\beta_2, \dot{\beta}_2, \ddot{\beta}_2$	linkage *BC* angle, angular velocity and angular acceleration respectively
$\beta_3, \dot{\beta}_3, \ddot{\beta}_3$	linkage *CD* angle, angular velocity and angular acceleration respectively
$\beta_4, \dot{\beta}_4, \ddot{\beta}_4$	linkage *DO* angle, angular velocity and angular acceleration respectively

EQUATION DERIVATIONS AND ANALYSIS

Figure 1, is the translating five-bar linkage mechanism with four active links and the fifth link fixed, a force is applied at point D that makes the crank linkage *DO* rotate clockwise. This mechanism is mounted on a moving platform and they both move together in the same positive *x* direction with velocity, $\dot{x}$ and acceleration $\ddot{x}$. Since the velocity of the platform does not affect the rotation of the mechanism relative to the platform, the mechanism can be treated as a two degree of freedom system. Also, the overall positions of the linkages depend on the input angle of the crank linkage *DO*. The mechanism is assumed to be planar in planar motion. All joints are pins and are revolute.

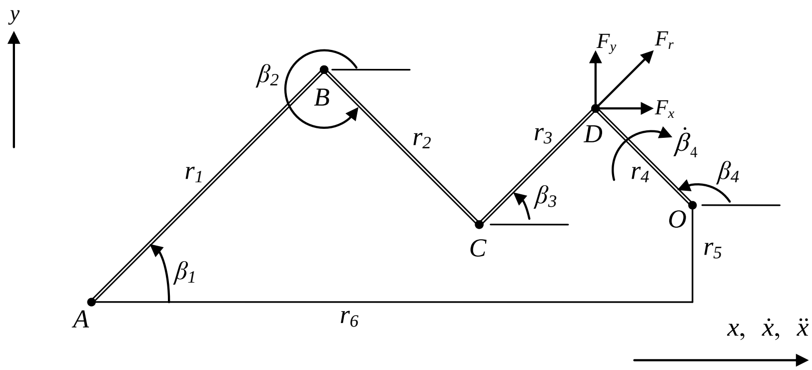

Fig 1: Five – bar linkage mechanism

Position analysis

The position equations in the *x* and *y* directions can be written as:

$$r_1 \cos\beta_1 + r_2 \cos\beta_2 + r_3 \cos\beta_3 + r_4 \cos\beta_4 + r_6 = 0 \tag{1a}$$

$$r_1 \sin\beta_1 - r_2 \sin\beta_2 + r_3 \sin\beta_3 - r_4 \sin\beta_4 + r_5 = 0 \tag{1b}$$

Velocity analysis

Taking the first time-derivatives of Eq. (1a) and Eq. (1b) above and simplify, we obtain

$$r_1[-\sin\beta_1]\dot{\beta}_1 + r_2[-\sin\beta_2]\dot{\beta}_2 = r_3[\sin\beta_3]\dot{\beta}_3 + r_4[\sin\beta_4]\dot{\beta}_4 \tag{2a}$$

$$r_1[\cos\beta_1]\dot{\beta}_1 - r_2[\cos\beta_2]\dot{\beta}_2 = r_3[-\cos\beta_3]\dot{\beta}_3 + r_4[\cos\beta_4]\dot{\beta}_4 \tag{2b}$$

These velocity equations can easily be solved for $\dot{\beta}_1$ *and* $\dot{\beta}_2$,

$$\dot{\beta}_1 = \frac{(r_4\dot{\beta}_4 \sin\beta_4 + r_3\dot{\beta}_3 \sin\beta_3)(-r_2\cos\beta_2) - (r_4\dot{\beta}_4\cos\beta_4 - r_3\dot{\beta}_3\cos\beta_3)(-r_2\sin\beta_2)}{-r_1\sin\beta_1(-r_2\cos\beta_2) - (r_1\cos\beta_1)(-r_2\sin\beta_2)} \tag{3}$$

$$\dot{\beta}_2 = \frac{(-r_4\dot{\beta}_4\cos\beta_4 - r_3\dot{\beta}_3\cos\beta_3)(-r_1\sin\beta_1) - (-r_4\dot{\beta}_4\sin\beta_4 + r_3\dot{\beta}_3\sin\beta_3)(r_1\cos\beta_1)}{-r_1\sin\beta_1(-r_2\cos\beta_2) - (r_1\cos\beta_1)(-r_2\sin\beta_2)} \tag{4}$$

Acceleration analysis

Taking the second time-derivates of position equations Eq. (1a) and Eq. (1b), we have:

$$r_1(-\sin\beta_1)\ddot{\beta}_1 + r_2(-\sin\beta_2)\ddot{\beta}_2 = \left\{\begin{matrix} r_2\dot{\beta}_2^2\cos\beta_2 + r_1(\dot{\beta}_1^2\cos\beta_1) + r_3\ddot{\beta}_3\sin\beta_3 \\ + r_3\dot{\beta}_3^2\cos\beta_3 - r_4\ddot{\beta}_4\sin\beta_4 - r_4\dot{\beta}_4^2\cos\beta_4 \end{matrix}\right\} \tag{5a}$$

$$r_1(\cos\beta_1)\ddot{\beta} - r_2(\cos\beta_2)\ddot{\beta}_2 = \left\{\begin{matrix} r_1\dot{\beta}_1^2\sin\beta_1 - r_2\dot{\beta}_2^2\sin\beta_2 + r_3\dot{\beta}_3^2\sin\beta_3 \\ - r_3\ddot{\beta}_3\cos\beta_3 - l_4\dot{\beta}_4^2\sin\beta_4 + l_4\ddot{\beta}_4\cos\beta_4 \end{matrix}\right\} \tag{5b}$$

The above acceleration equations, Eq. (5a) and Eq. (5b), can easily be solved for $\ddot{\beta}_1$ *and* $\ddot{\beta}_2$,

$$\ddot{\beta}_1 = \frac{\left\{\begin{matrix} \left\{\begin{matrix} r_2\dot{\beta}_2^2\cos\beta_2 + r_1(\dot{\beta}_1^2\cos\beta_1) + r_3\ddot{\beta}_3\sin\beta_3 \\ + r_3\dot{\beta}_3^2\cos\beta_3 - r_4\dot{\beta}_4\sin\beta_4 - l_4\beta_4^2\cos\beta_4 \end{matrix}\right\} r_2(\cos\beta_2) \\ - \left\{\begin{matrix} r_1\dot{\beta}_1^2\sin\beta_1 - r_2\dot{\beta}_2^2\sin\beta_2 + r_3\dot{\beta}_3^2\sin\beta_3 \\ - r_3\ddot{\beta}_3\cos\beta_3 - r_4\dot{\beta}_4^2\sin\beta_4 + l_4\ddot{\beta}_4\cos\beta_4 \end{matrix}\right\} r_2(-\sin\beta_2) \end{matrix}\right\}}{(-r_1\sin\beta_1)(-r_2\cos\beta_2) - r_1(\cos\beta_1)r_2(-\sin\beta_2)} \tag{6}$$

$$\ddot{\beta}_2 = \frac{\left\{\begin{matrix} r_1(-\sin\beta_1)\left\{\begin{matrix} r_1\dot{\beta}_1^2\sin\beta_1 - r_2\dot{\beta}_2^2\sin\beta_2 + r_3\beta_3^2\sin\beta_3 \\ - r_3\ddot{\beta}_3\cos\beta_3 - r_4\dot{\beta}_4^2\sin\beta_4 + r_4\ddot{\beta}_4\cos\beta_4 \end{matrix}\right\} \\ - r_1(\cos\beta)\left\{\begin{matrix} r_2\dot{\beta}_2^2\cos\beta_2 + r_1\dot{\beta}_1^2\cos\beta_1 + r_3\ddot{\beta}_3\sin\beta_3 \\ + r_3\dot{\beta}_3^2\cos\beta_3 - r_4\ddot{\beta}_4\sin\beta_4 - r_4\dot{\beta}_4^2\cos\beta_4 \end{matrix}\right\} \end{matrix}\right\}}{(-r_1\sin\beta_1)(-r_2\cos\beta_2) - r_1(\cos\beta_1)r_2(-\sin\beta_2)} \tag{7}$$

Figure 2 is the free body diagram of the five-bar linkage mechanism which is translating in the positive *x* direction. The motion of the platform will affect the reaction forces in the direction of the movement.

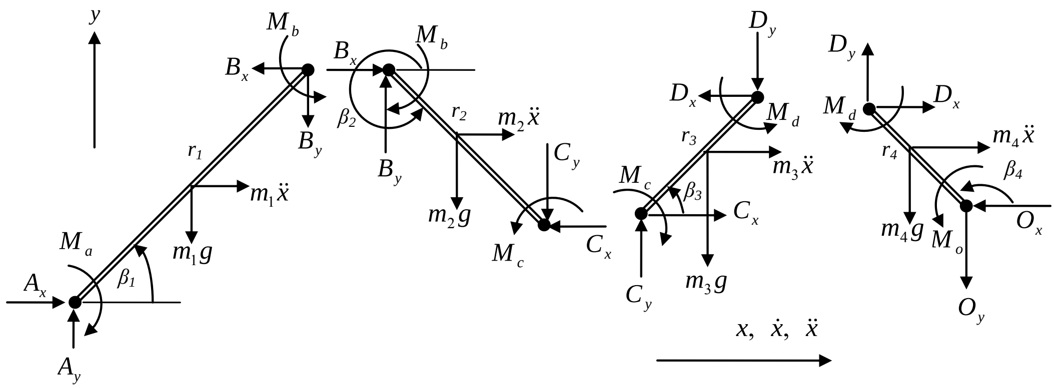

Fig 2: Free body diagram of a five – bar linkage mechanism

Reaction forces at the pins

The joints are assumed to be revolute and frictionless. Therefore, there are no frictional forces developed at the joint. These forces are summed in the *x* and *y* positive directions and simplified to obtain as follows:

$$\sum F_x = 0 : \rightarrow +ve \text{ and } \sum F_y = 0 : \uparrow +ve \tag{8}$$

Linkage *CD*:

$$C_x = D_x - m_3\ddot{x} \text{ and } C_y = D_y + m_3 g \tag{9}$$

Linkage *BC*

$$B_x = C_x - m_2\ddot{x} \text{ and } B_y = C_y + m_2 g \tag{10}$$

Linkage *AB*

$$A_x = B_x - m_1\ddot{x} \text{ and } A_y = B_y + m_1 g \tag{11}$$

Linkage *DO*

$$O_x = D_x + m_4\ddot{x} \text{ and } O_y = D_y - m_4 g \tag{12}$$

Moments developed around the pin joints

The moment equations about the respective pin joints are determined by taking moments about the centre of gravity (CG) of the linkage and simplifying the equations thus:

Link *AB*:

$$M_a = -I_{ABCG}\ddot{\beta}_1 + M_b + a_1[(A_x + B_x)\sin\beta_1 - (A_y + B_y)\cos\beta_1] \tag{13}$$

Link *BC*:

$$M_b = -I_{BCCG}\ddot{\beta}_2 + M_c + a_2[(B_x - C_x)\cos\beta_2 - (B_y + C_y)\sin\beta_2] \tag{14}$$

Link *CD*:

$$M_c = -I_{CDCG}\ddot{\beta}_3 + M_d + a_3[(C_x + D_x)\sin\beta_3 - (C_y + D_y)\cos\beta_3] \tag{15}$$

Link *DO*:

$$M_d = -I_{DOCG}\ddot{\beta}_4 + M_o + a_4[(D_x + O_x)\cos\beta_4 - (D_y + O_y)\sin\beta_4] \tag{16}$$

SIMULATION

The developed dynamic equations can be solved since the values of the parameters are known for design purpose. The values of the parameters to be used for the simulations are given in Table 1 below.

S/N	DESCRIPTION	SYMBOL	VALUES USED
1	Distance of CG from pin end of linkage *AB*	a_1	0.1715m
2	Distance of CG from pin end of linkage *BC*	a_2	0.2165m
3	Distance of CG from pin end of linkage *CD*	a_3	0.1015m
4	Distance of CG from pin end of linkage *DO*	a_4	0.085m
5	Length of linkage *AB*	r_1	0.343m
6	Length of linkage *BC*	r_2	0.433m
7	Length of linkage *CD*	r_3	0.203m
8	Length of linkage *DO*	r_4	0.170m
9	Length of vertical fixed link	r_5	0.212m
10	Length of horizontal fixed link	r_6	0.693m
11	Clockwise angle between the horizontal and the linkage *AB*	β_1	87^0
12	Clockwise angle between the horizontal and the linkage *BC*	β_2	157^0
13	Clockwise angle between the horizontal and the linkage *CD*	β_3	39^0
14	Clockwise angle between the horizontal and the linkage *DO*	β_4	45^0
15	Moments of inertia of linkage *AB* about CG	I_{ABCG}	6.013×10^{-2}
16	Moments of inertia of linkage *BC* about CG	I_{BCCG}	4.469×10^{-2}
17	Moments of inertia of linkage *CD* about CG	I_{CDCG}	5.56×10^{-3}
18	Mass of linkage *AB*	m_1	7.36kg
19	Mass of linkage *BC*	m_2	3.27kg
20	Mass of linkage *CD*	m_3	1.05kg
21	Mass of linkage *DO*	m_4	1.10kg
22	Acceleration due to gravity	g	$9.81m/s^2$
23	Traction/translating acceleration of the mechanism	$\ddot{x}$	$0-40m/s^2$
24	Horizontal reaction force at pin D	D_x	$500N$
25	Vertical reaction force at pin D	D_y	$150N$

Table 1: Values parameters used for simulation

Using the values of parameter given in Table 1 above the horizontal reaction forces developed in Eq. (8 – 12) were determined and are plotted as shown in Fig. (3) and Fig. (4) for traction acceleration of *0, 10, 20, 30* and *40* m/s^2. It is observed in Fig. (3) that the horizontal reaction forces A_x, B_x, and C_x decreases as the traction acceleration increases in the direction of crank rotation while O_x is increasing at a very small rate. In Fig. (4), the horizontal reaction forces A_x, B_x, and C_x increases as the traction acceleration increases in the opposite direction of crank rotation while O_x is decreasing at a very small rate as well.

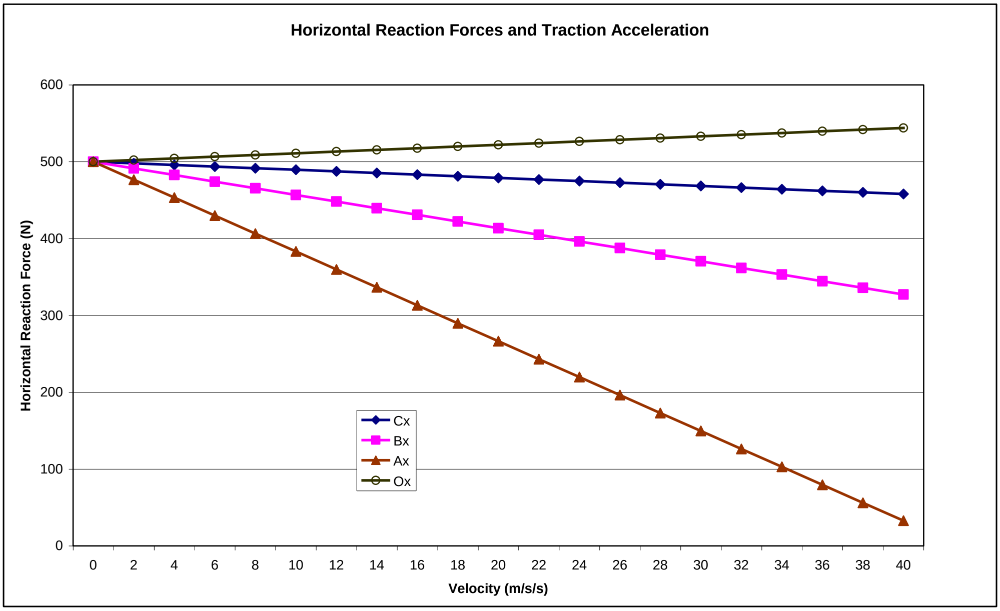

Fig 3: Horizontal reaction forces and traction velocity in positive *x* direction

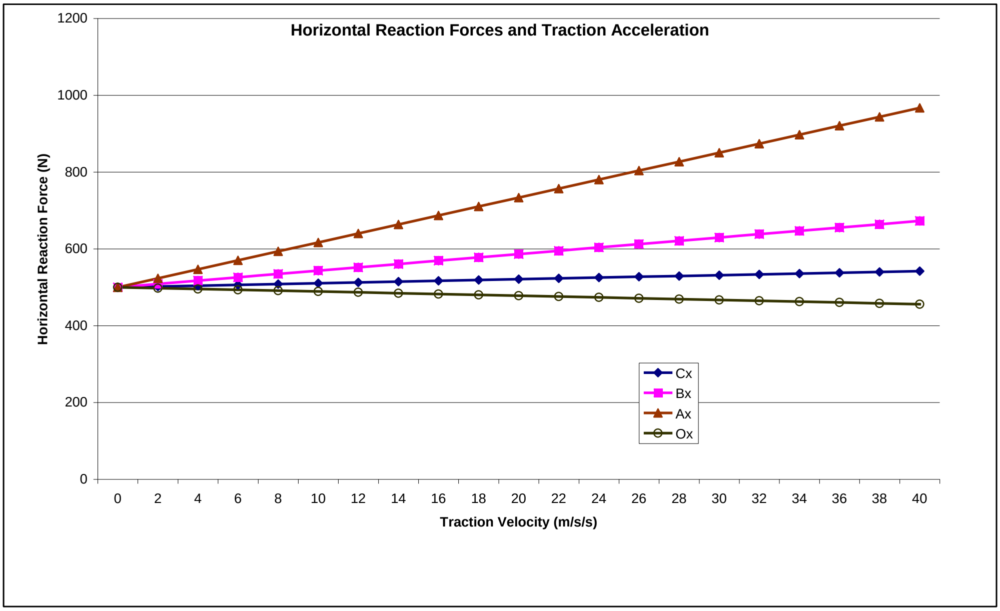

Fig 4: Horizontal reaction forces and traction velocity in negative *x* direction

The parameter values in Table (1) were also used to solve Eq. (13 – 16) to obtain moments M_a, M_b, M_c and M_d at traction acceleration of *0*, *10*, *20*, *30* and *40* m/s^2 both in the direction of crank rotation and the opposite direction as well. It is observed for pin joint moment

M_a, Fig. (5), decreases as the acceleration increases in the direction of crack rotation while it increases as the acceleration increases contrary to crank rotation direction. The pin joint moment M_b, shown Fig (6) on the other hand increases as the acceleration increases in the direction of crank rotation but with lesser magnitude while it decreases in the opposite direction to the crank rotation. The pin joint moments M_c and M_d as shown in Fig. (7) and Fig. (8) does not show any significant variation in magnitude as the acceleration varied along the two directions.

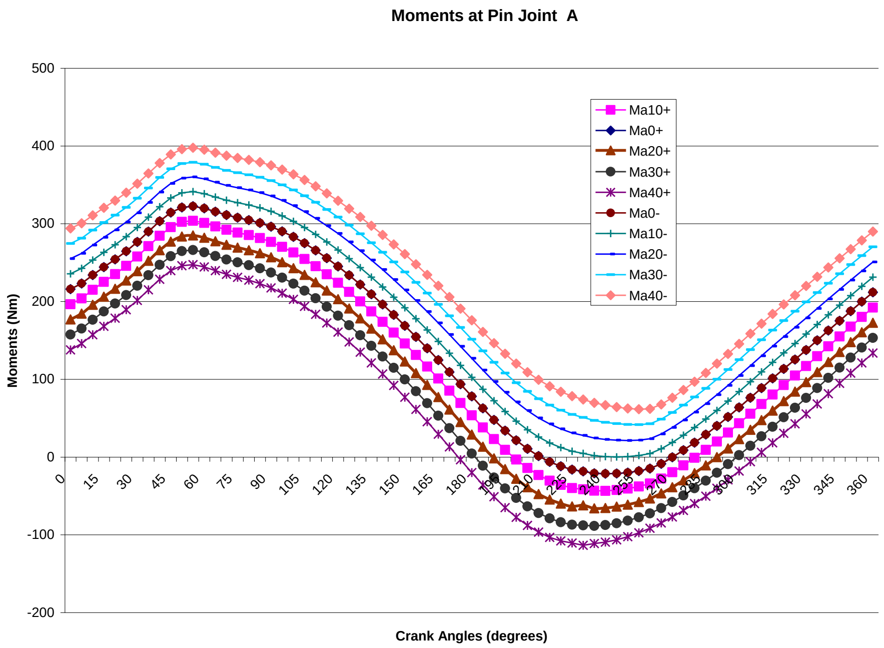

Fig 5: Moments at pin A for traction velocities in the positive and negative *x* direction

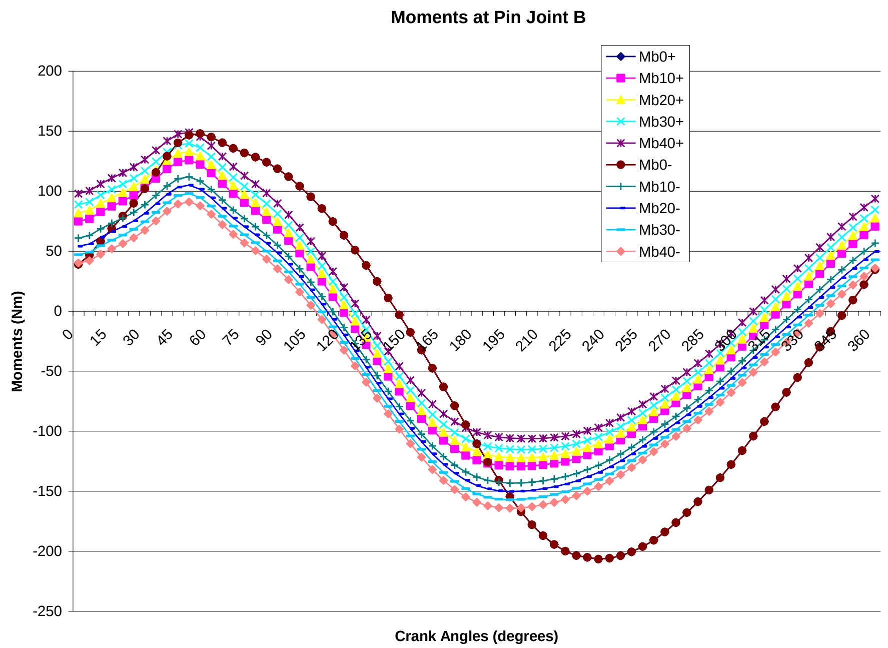

Fig 6: Moments at pin *B* for traction velocities in the positive and negative *x* direction

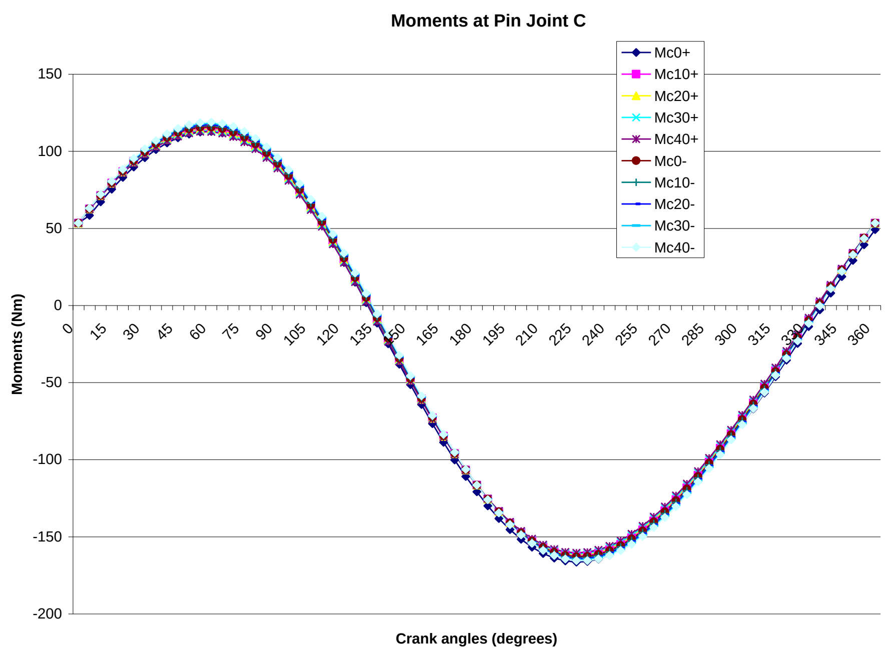

Fig 7: Moments at pin *C* for traction velocities in the positive and negative *x* direction

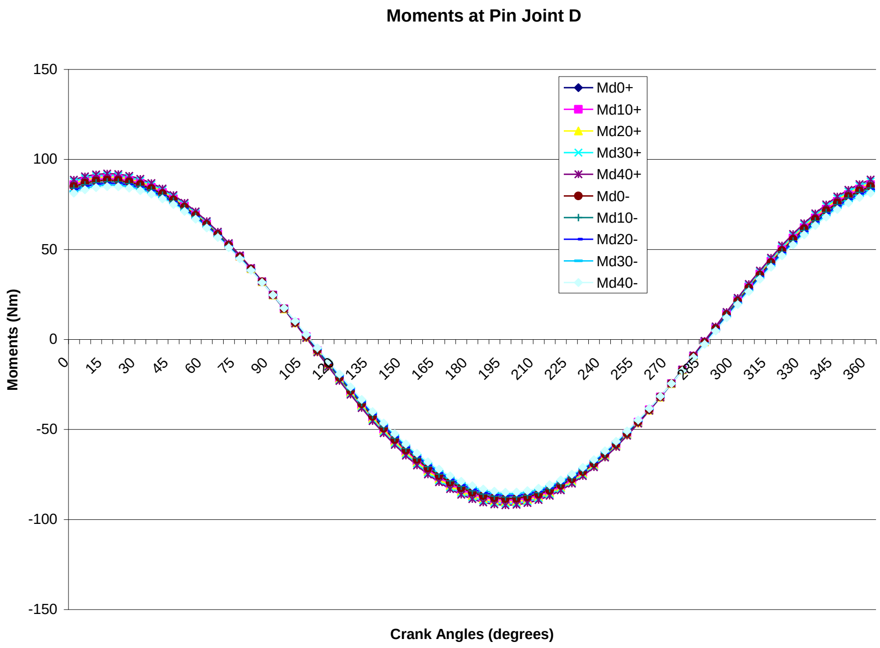

Fig 8: Moments at pin *D* for traction velocities in the positive and negative *x* direction

CONCLUSIONS

The dynamic analysis of a five – bar linkage mechanism in traction has been presented. It was observed that the highest magnitude of reaction occurred at pin joint *A* when the mechanism is moving in the opposite direction the crank arm rotation. The minimum in magnitude is obtained when it is moving in the direction of crank rotation, it eventually reaches zero at about $42.85 m/s^2$ (not shown in Fig (3)). The maximum joint moment, as expected, is developed at pin joint *A* when the acceleration is $40 m/s^2$ in the opposite direction to the crank rotation.

It can be concluded that in design and development of five – bar linkage mechanisms that will be utilized in a traction environment it will be good if the crank rotation and the traction are so arranged to be in the same direction. This will reduce motion induced reactions and moments at the pin joints which can eventually lead to failures. The induced failure could be inform of bearing overload and damage at this point. The mechanism can so be designed to have *zero* reaction at the pin joint *A* which will increase the integrity of the whole mechanism.

REFERENCES

[1] Analytic Approach to Mechanism Design. Online Resource. URL: http://www.colostate.edu/me/program/courses/ME324/notes/PositionAnalysis.ppt (Accessed 2009)
[2] Chang, Z. Nonlinear Dynamics and Analysis of a four-bar linkage with clearance. Proceedings of the 12th IFToMM World Congress, Besancon (France), June 18 – 21, 2007.
[3] Chavdarov, I. Kinematics and Force Analysis of a Five-Link Mechanism by the Four Spaces

Jacoby Matrix.*Problems of Engineering Cybernetics and Robotics,* vol. 55, 53 – 63, 2005.
[4] Rao, A. C. On the Precision Point Synthesis of Linkages. *The International Journal of Mechanical Engineering Education.* Vol.9, n^{o} 3, 213 – 218, July 1981.
[5] Freudenstein, F., Approximate Synthesis of four-Bar Linkage, *Trans ASME,*77, 853 – 861, Aug. 1955
[6] Mclarnan, C. W., Synthesis of Six-Link Plane Mechanism by Numerical Analysis, *Journal of Engineering for Industry, Trans ASME,* Series B, 85, No 1, 5 – 11, 1963.

Proceedings of MUSME 2011, the International Symposium
on Multibody Systems and Mechatronics
Valencia, Spain, 25-28 October 2011

DYNAMICS MODELING OF THE SAAB SEAEYE COUGAR ROV

Alessandro Cammarata*, Mario Musumeci† and Rosario Sinatra*
* Dipartimento di Ingegneria Industriale e Meccanica
Università di Catania, Viale A. Doria 6, 95125 Catania, Italy
e-mail: acamma@dii.unict.it, rsinatra@dii.unict.it,

† Laboratorio Nazionale del SUD- INFN
Viale S. Sofia, 95125 Catania, Italy
e-mail: musumeci@lns.infn.it

Keywords: ROV, dynamics Model, control, numerical simulations.

Abstract. *This paper is focused on the modeling of the Saab Seaeye Cougar ROV. The vehicle has two arms equipped with grippers to link undersea connectors for neutrinos revelators from the base station to the underwater station. Six thrusters move the ROV at a deep of 3500 meters. The dynamics model is developed by means of Matlab/Simulink framework and particular attention is paid to the hydrodynamic wrenches determination and to the control strategies to approach a target.*

1 INTRODUCTION

Remotely Operated Underwater Vehicles (ROVs) are used in underwater tasks for monitoring, maintenance of offshore rigs, assembling of gas and oil pipelines and recovery. An external hull houses a floating to guarantee the buoyancy and the maximum payload to be carried. Sensors and control devices are located at the bottom of the vehicle to increase maneuverability and stability. Electric cables are inside tubes to prevent corrosion.

ROVs are usually tied to the ship by means of an “umbilical” wire carrying either power and data signals. Lamps, cameras, sonar, magnetometers, gyroscopes and other sophisticated devices are the usual equipment.

ROVs are grouped into different categories on the basis of weight, dimensions and power: micro, mini, general, light-, heavy-workclass and trenching.

The Saab Seaeye Cougar (SSC) is a ROV used for the NEMO project (Neutrino Mediterranean Observatory) by the INFN (Istituto Nazionale di Fisica Nucleare). The project is aimed to study neutrinos by means of an huge telescope of two squared kilometers area. The ROV has an external hull fabricated of polypropylene and aluminum alloy that combines strength and corrosion resistance. The floating is split into two parts to easy the instruments housing and increase stability. Manipulators and grippers let the ROV to grasp objects, while a system of sonar, gyroscopes, deep ocean sensors, high resolution cameras and 600 W lamps, makes the vehicle able to move underwater avoiding obstacles and tracking the right trajectory towards targets. SSC can reach more than 3500 meter deep and can carry a payload up to 80 kg. The weight of the whole system is about 344 kg.

In the following sections the dynamics model will be formulated by means of Newton-Euler equations of motion. The dynamics model, along with control strategies, will be implemented by means of Matlab/Simulink.

2 DYNAMICS MODEL FORMULATION

In order to derive the dynamics model of the vehicle different contributes must be considered: weight, buoyancy force, drag and lift forces and torques, main and maneuver thrusts from propellers. SSC is not equipped with rudders or stabilizers, thus the turning and surfacing maneuvers are devoted to the propellers. As can be observed in the CAD model of SSC of Fig. 1 the hull is split into two modules: the upper containing the propellers and one floating; the lower housing control units, the two-arm manipulators and the second floating.

In order to formulate the N-E dynamics equation a global inertial frame and a local body frame are introduced.

The inertial frame is particularly useful to describe trajectories to be accomplished from the vehicle, like so to determine its orientation or velocity with respect to the earth. Otherwise, it is more convenient to express the equations of motion in the body frame. As a matter of fact, the inertia matrix and all the added masses are constant when evaluated in the latter system. Besides, laws of motion are more conveniently expressed into the local system.

.

2.1 Weight, added masses and buoyancy force

Inertial properties of a dipped body moving underwater depend on the mass and inertia of the body as well as on the mass of fluid carried during the movement. This “added mass” measures the additional inertia generated when the water accelerates with the body.

This virtual mass of fluid, moving along with the system, depends on the shape of the body and affect the dynamics of the system. The ROV under exam has a mass of 344 kg and its principal moments of inertia are defined as

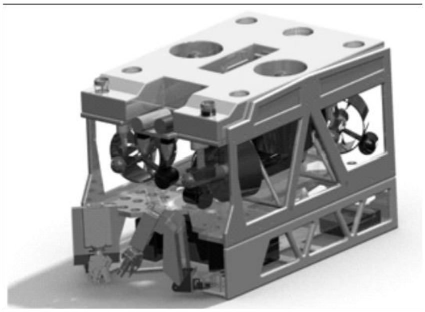

Fig. 1. CAD model of the ROV Saab Seaeye Cougar.

$$I = \begin{pmatrix} 68.9 & 0 & 0 \\ 0 & 92.2 & 0 \\ 0 & 0 & 102.5 \end{pmatrix} \quad (kgm^2) \tag{1}$$

The added masses, not included here for brevity, are calculated referring to the SNAME, the Society of Naval Architects and Marine Engineers and to [1].

Generally, ROVs in normal conditions, thus excluding ascent or descent maneuvers, have neutral behavior: that is, the gravitational force $\mathbf{f}_g$ and the Archimedes buoyant force $\mathbf{f}_b$ have the same magnitude. Then, considering the buoyancy center vector $\mathbf{r}_b=[0.219, 0, 0.289]^T$ (m), when expressed into the body-frame, it is possible to write the wrench array $\mathbf{w}_{gb}$, including both gravitational and buoyant wrenches, i.e.

$$\mathbf{w}_{gb} = \begin{bmatrix} \mathbf{f}_g + \mathbf{f}_b \\ \mathbf{r}_b \times \mathbf{f}_b \end{bmatrix} \equiv \begin{bmatrix} \mathbf{0}_3 \\ \mathbf{r}_b \times \mathbf{f}_b \end{bmatrix} \tag{2}$$

where the wrench is a six-dimensional array including both force and torque vectors. It is clear from Eq.(2) that the different position between center of mass and buoyancy center determines a torque about the local frame y-axis.

2.2 Hydrodynamic wrenches

In order to simplify the treatment, we assume that the velocity component u, along the **x**-axis, i.e. the axis along the longitudinal direction of the vehicle, is much greater than the remaining component v and w. Therefore, we can assume,

$$\tan\alpha \cong \alpha = \frac{w}{u}, \quad \tan\beta \cong \beta = \frac{v}{u} \tag{3}$$

where α and β are the angles of attack, expressed in radiant, in the **x-z** and **x-y** planes, respectively. The hydrodynamic wrenches include the lift and drag forces and torques derived from the interaction system-water.

The lift coefficient C_L is obtained by means of a simplified expression in function of the angle of attack α of the form [2], i.e.,

$$C_L = C_1\alpha + C_2\alpha^2 \equiv d\alpha + e\alpha^2 \tag{4}$$

where C1 and C2 are coefficients functions of the base and front surfaces, respectively equal to (1.49m×1m) and (1m×1m), and parameterized in terms of the aspect ratio of the body and the Reynolds number Re. Considering a maximum velocity of 3.4 knots (1.74 m/s) the

Reynolds number is Re =6388902. Further, the lift coefficient CL will be considered the same in the z- and y-directions.
Similarly, the torque coefficient CT is assumed to be the same both for pitch and yaw rotations, that is

$$C_T = C_3\alpha - C_4\alpha^2 \equiv f\alpha - g\alpha^2 \tag{5}$$

where C_3 and C_4 are coefficients, depending on the base and front surfaces, the volume and the length of the hull; and parameterized in terms of the aspect ratio of the body and the Reynolds number *Re*. In order to find the centre of the resultant hydrodynamic force, the distance from the fore of the vehicle x_{CP} is introduced by the following expression,

$$x_{CP} = \frac{C_T}{C_L} L \tag{6}$$

Where x_{CP} is a fraction of the total length L of the ROV, varying with the angle of attack α. Here, L is equal to 1.49 (m), while the cross section is 1m×1m.

The drag coefficient C_D depends on many factors: the Reynolds number, the rugosity of the surface in contact with the water, the shape of the body and the angle of attack α. The drag coefficient C_D can be expressed as,

$$\begin{aligned} C_D &= C_f + C_{DF} + \Delta C_D \\ &= 1 + C_5\alpha^2 + C_6\alpha^3 \equiv a\alpha^3 + b\alpha^2 + c \end{aligned} \tag{7}$$

where C_f is a term taking into account the friction of the water on the boundary layer, C_{DF} depends on the shape of the body when the angle of attack is null while ΔC_D is the drag induced by the change of the angle of attack α. In similar way, the coefficients C_5 and C_6 are functions of the base and front surfaces, the aspect ratio of the body and the Reynolds number *Re*.

Once C_L, C_D and C_T has been obtained, it is possible to find the lift and drag forces and the pitch and yaw torques acting on the vehicle. Notice that the lift and drag forces are always normal and parallel to the velocity direction, respectively. The pitch and yaw torques come from the reduction of the lift force to the point that is the centre of the resultant hydrodynamic force.

The lift force **L** and the drag force **D** depend on the density of the fluids, the area A_f (1m×1m) of the profile and the relative velocity between system and fluid, i.e.,

$$\|\mathbf{L}\| = \frac{1}{2}\rho C_L A_f V^2, \quad \|\mathbf{D}\| = \frac{1}{2}\rho C_D A_f V^2 \tag{8}$$

in which V is the norm of the linear velocity **v**.

Then, taking into account that either the drag forces acting on the **x-z** plane and those acting on the **x-y** plane can be decomposed into two components, and by substituting C_D from (7), we have

$$\begin{aligned} &D_X = -\frac{1}{2}\rho A_f \left(2cu^2 + bv^2 + c\frac{v^2}{2} + a\frac{v^3}{u} + \right. \\ &\left. bw^2 + c\frac{w^2}{2} + a\frac{w^3}{u} \right), \; D_Y = \frac{1}{2}\rho A_f \left(cuv + b\frac{v^3}{u} + c\frac{v^3}{u} \right), \\ &D_Z = -\frac{1}{2}\rho A_f \left(cuw + b\frac{w^3}{u} + c\frac{w^3}{u} \right) \end{aligned} \tag{9}$$

where the components of **D** are expressed into the body frame. We neglected higher order terms in Eq. (9). Analogously, the expressions for the components of **L** into the **x-z** and **x-y** planes are

$$L_X = 0,\ L_Y = \frac{1}{2}\rho A_f\left[euv + dv^2 + e\frac{v^3}{2u}\right], \qquad L_Z = -\frac{1}{2}\rho A_f\left[euw + dw^2 + e\frac{w^3}{2u}\right] \tag{10}$$

Then, after applying the lift force **L** on the centre of the resultant hydrodynamic force, the pitch torque **T** is readily obtained, namely,

$$\|\mathbf{T}\| = \frac{1}{2}\rho C_T A_f V^2 x_{CP} \tag{11}$$

The components of **T** on the **x-z** plane and on the **x-y** plane are:

$$T_X = 0,\ T_Y = \frac{1}{2}\rho A_f\left[guw + fw^2 + g\frac{w^3}{u}\right]x_{CP}, \qquad T_Z = \frac{1}{2}\rho A_f\left[guv + fv^2 + g\frac{v^3}{u}\right]x_{CP} \tag{12}$$

Finally, the total hydrodynamic wrench $\mathbf{w}_h$, as expressed into the body-frame, is obtained as,

$$\mathbf{w}_h = [D_X,\ \ D_Y + L_Y,\ \ D_Z + L_Z,\ \ 0,\ \ T_Y,\ \ T_Z]^T \tag{13}$$

2.3 External Forces

The ROV is equipped with six thrusters that provide the main and secondary thrusts to move and turn the vehicle. The layout of the axes of the thrusters, along with their distances from the body-frame, is shown in Fig. 2. As can be observed in the same figure four thrusters are positioned in such a way that their axes belong to an horizontal plane and shape into a rhombus. The remaining two thrusters are aligned along the vertical direction and are used for immersion or emersion maneuvers.

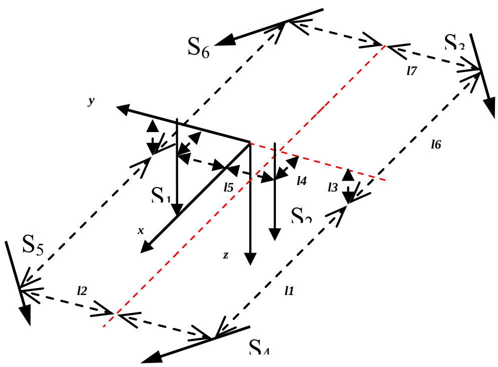

Fig. 2. Layout of the thrusters and geometrical distances.

It is possible to express the wrench $\mathbf{w}_p$, i.e. total force and torque, in terms of the propellers thrusts array **q** by means of a matrix **L** [3], defined as

$$L = \begin{pmatrix} 0 & 0 & \cos\theta & \cos\theta & \cos\theta & \cos\theta \\ 0 & 0 & -\sin\theta & \sin\theta & -\sin\theta & \sin\theta \\ 1 & 1 & 0 & 0 & 0 & 0 \\ l5 & -l5 & -l6 & l6 & -l6 & l6 \\ -l4 & -l4 & -l7 & -l7 & -l7 & -l7 \\ 0 & 0 & l3 & l3 & -l3 & -l3 \end{pmatrix} \tag{14}$$

where θ = 22.37° is the angle between the thruster axes and the x-axis of the body-frame. Thus, we can write the following

$$\mathbf{w}_p = \mathbf{Lq} \tag{15}$$

being **q** a six-dimensional array of thrusts defined as

$$\mathbf{q} = [S_1\ S_2\ S_3\ S_4\ S_5\ S_6] \tag{16}$$

The thrusters are actuated by means of DC brushless motors equipped with speed feedback control, a PID and a gyroscope to assure the best stability underwater. From the datasheet of the ROV, thrusters data are reported in Tab. 1. Following the same table, by applying (15), we obtain:

$$\mathbf{q} = [539\ 539\ 450.4\ 450.4\ 450.4\ 450.4]\ \ [\mathrm{N}] \tag{17}$$

where the generic thrust entry of **q** is considered positive according to the directions plotted in Fig. 2.

Global Thrust	
Direction	Units [N]
Forward	1660
Lateral	1176
Vertical	1078

Table 1: Thrusters Datasheet

S_1	S_2	S_3	S_4	S_5	S_6
Forward					
0	0	450.4	450.4	450.4	450.4
Backward					
0	0	-450.4	-450.4	-450.4	-450.4
Right					
0	0	450.4	450.4	-450.4	-450.4
Left					
0	0	-450.4	-450.4	450.4	450.4
Up					
539	539	0	0	0	0
Down					
-539	-539	0	0	0	0

Table 2: ROV Maneuvers

Upon combining the signs of the thrusts, different maneuvers can be defined, as reported in Table 2. These maneuvers will be used to set the control strategy.

.

3 MODELLING AND NUMERICAL SIMULATIOS

3.1 Modelling of ROV

The dynamics model of the ROV has been implemented by means of Matlab/Simulink. Three blocks are used to reproduce the ROV's dynamics, the fluid interaction between vehicle and the water and the total forces and torques from the propellers, as shown in Fig. 3. A simple on-off control is used to let the ROV reach a target, [4]. Starting from a reference posture, the control checks for the relative position between the vehicle and the target, when this is referred to the body frame. Then, the six maneuvers of Tab. II are activated according to the coordinates of the relative position vector. The on-off control turns on every time the coordinates are larger than a predetermined threshold.

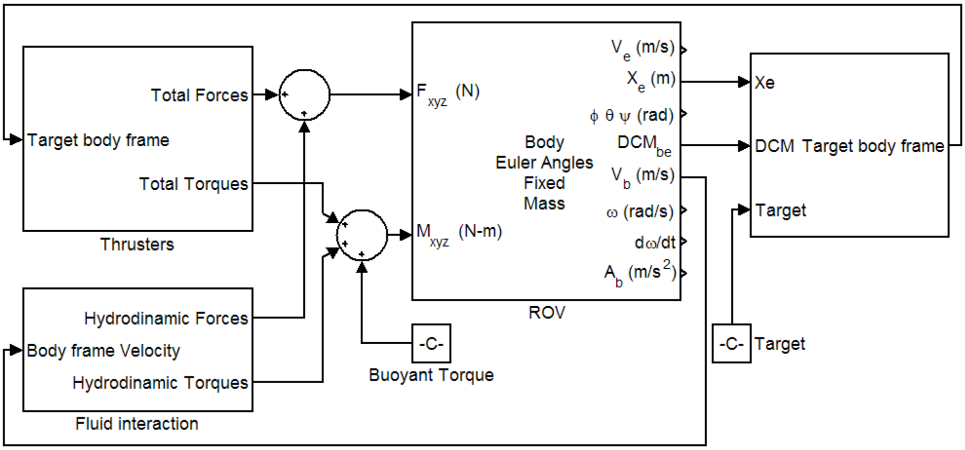

Figure 3: Layout of the dynamics model of the ROV

3.2 Numerical simulation

A simulation is provided in Figs 4-9. Starting from the origin of the inertial frame with an initial velocity of 0.1 (m/s) along the *x*-direction, i.e. the forward direction, the ROV approaches a target located at position $[30, -0.1, 50]^T$ (m) after about 46 s, as shown in Fig. 4. The threshold of the on-off control system is set to 0.1 (m), the latter being in absolute value. Figure 5 reports the components of the distance vector of the ROV from the target, when expressed into the body reference frame. As can be observed in Fig.5, the on-off control activates and turn the ROV towards the target. After few seconds, i.e. about 1.5 s, the *x*-axis of the ROV is aligned with the distance vector, as confirmed by the annulment of the *z*-component of the distance vector.

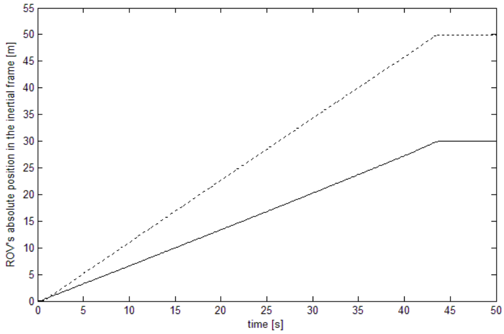

Figure. 4: ROV's absolute position starting from the frame origin:
x-component in solid line; y-component indashed line; z-component in dotted line.

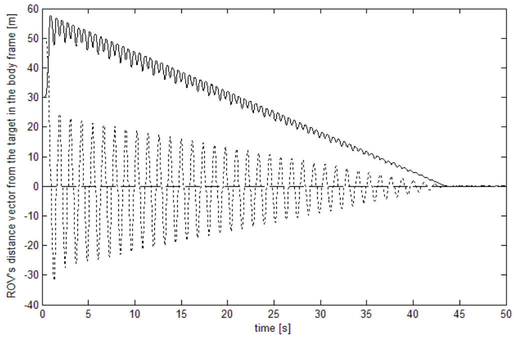

Figure 5: ROV's relative distance vector from the target in body frame:
x-component in solid line; y-component in dashed line; z-component in dotted line.

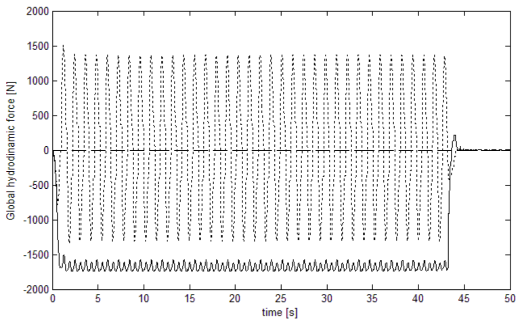

Figure 6: Global hydrodynamic force: x-component in solid line;
y-component in dashed line; z-component in dotted line.

However, the said *z*-component oscillates because of the hydrodynamic forces and torques, reported in Figs. 6-7, thus, the control operates to correct the pitch oscillations, as shown in Figs. 8-9. It can be observed that the *x*-component of the total force from the thrusters is always on because the ROV is aligned with the *x*-body axis pointing straight towards the target.

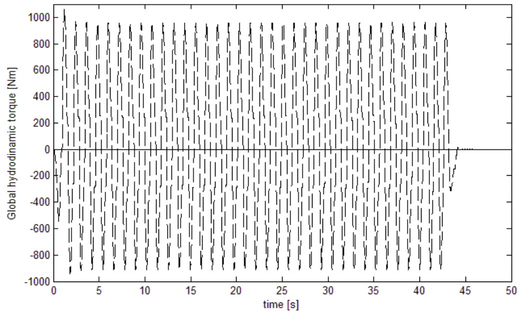

Figure 7: Global hydrodynamic torque: x-component in solid line; y-component in dashed line; z-component in dotted line.

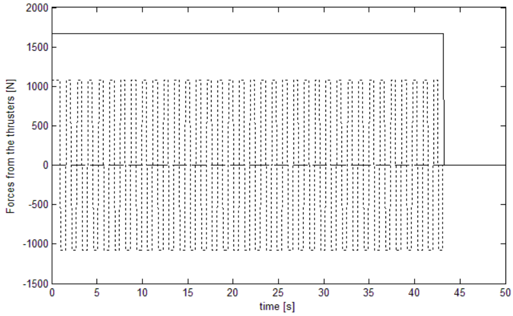

Figure 8: Total force from the thrusters: x-component in solid line; y-component in dashed line; z-component in dotted line.

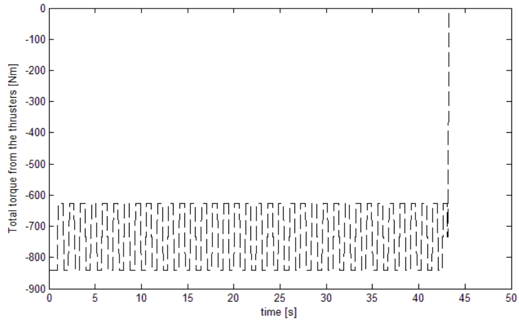

Figure 9: Total torque from the thrusters: x-component in solid line; y-component in dashed line; z-component in dotted line.

The results coming from the numerical simulations reveal good accuracy in positioning and good response, in time domain, from the on-off control system. However, the high frequency of the turning on-off, about 1s, seems to be too high and calls for a deeper analysis of the hydrodynamic coefficients and buoyant center. The said intervention frequency could be reduced relaxing the control threshold.
A virtual reality framework has been implemented by means of VRML (Virtual Reality Modeling Language) to verify the movements of the ROV while approaching its target. Besides, a joystick has been used to move the ROV freely inside the virtual landscape.

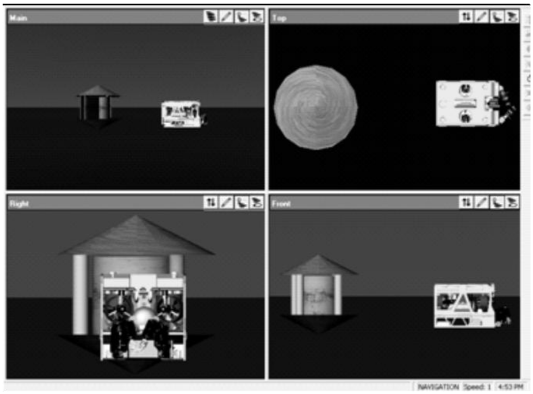

Figure 10: Virtual reality environment: ROV approaching the target.

4 CONCLUSIONS

The dynamics model of the ROV Saab Seaeye Cougar was formulated. Hydrodynamic forces and torques, as well as the thrusts from the six propellers were included into the model. Numerical simulations in Matlab/Simulink were provided to study the behavior of the vehicle. An on-off control was implemented to let the ROV reach a predetermined target. Results showed good response to the external disturbances and precision in positioning from the control system. The high intervention frequency from the control system revealed the need for a more accurate insight of the hydrodynamic parameters.

Finally, a virtual reality environment was developed to verify movements of the ROV inside the virtual landscape.

REFERENCES

[1] A. Korotkin. *Added Masses of Ship Structures*. Springer, 2009.

[2] G. Antonelli, *Underwater Robots - Motion and Force Control of Vehicle-Manipulator Systems*, Springer Tracts in Advance Robotics, 2006.

[3] A. Cammarata, G. La Rosa and R. Leonardi. Dynamic Modelling of a Wet Sub Vehicle. Proceedings of 3rd IC-EpsMsO Int. Conf. on Experiments/Process/System Modeling/Simulation & Optimization, Athens, July 8-11, 2009.

[4] T. Fossen, *Guidance and Control of Ocean Vehicles*, Chichester, U.K. Wiley, 1994.

Proceedings of MUSME 2011, the International Symposium
on Multibody Systems and Mechatronics
Valencia, Spain, 25-28 October 2011

NEWTON-EULER FORMULATION OF A PAN-TILT GIMBAL

José A. Colín-V·[†], Carlos S. López-C[†], Moisés G. Arroyo-C[†], José A. Romero-N[†]

·División de Ingeniería en Mecatrónica, Instituto Tecnológico Superior de Huichapan
Dom. Conocido s/n., El Saucillo, Huichapan, Hidalgo, Mexico.
e-mail: joseangelcr@hotmail,

† Facultad de Ingeniería, Universidad Autónoma de Querétaro
Río Moctezuma 249, Col. San Cayetano, C.P. 76807, San Juan del Río, Qro., México
e-mails: cajun@uaq.mx, arroyoc@uaq.mx, jarn@uaq.mx

Keywords: Multibody dynamics, pan-tilt gimbal, Newton-Euler formulation, recursive equations

Abstract. *The inward and outward recursive equations of motion are derived for a two-axes Pan-Tilt Gimbal (PTG) configuration, using the Newton-Euler (N-E) formulation. For the sake of simplicity, dissipative wrenches were neglected. A pick-and-place operation with the PTG in the shortest possible time was obtained using a 4-5-6-7 interpolating polynomial. The minimum value of the previous maneuver is computed by constant values of rate and acceleration limits supplied by the manufacturer of a commercial PTG.*

1 INTRODUCTION

The PTG under study is shown in Fig. 1. It consists of three mechanical components just as the double-gimbal mechanism (DGM) that according to Osborne, *et, al.* [1] is a multibody mechanical device composed of three rigid bodies, namely, a base, an inner-gimbal and an outer-gimbal. The cylindrical base is coupled to the outer-gimbal by a revolute joint, and the inner-gimbal, which is the disk-shaped payload, is connected to the outer-gimbal also by a revolute joint.

The PTG can be considered as an inertially stabilized platform (ISP) that, according to Hilkert [2], is used to stabilize and point a broad array of sensors, cameras, telescopes, and weapon systems. In general, ISPs are used on land, sea, and air, in both, mobile and fixed installations. Typically, visible and infrared cameras are mounted to hold stable by ISPs on ground vehicles, ships, and aircraft for diverse missions. ISP consists of an electromechanical assembly, bearings, and motors called a gimbal to which a gyroscope, or a set of gyroscopes, is mounted. Therefore, an ISP is a mechanism involving gimbal assemblies, for controlling the inertial orientation of its payload. There are several ISP electromechanical configurations as applications for which they are designed. However, usually an ISP is designed to point and stabilize about two or more axes, and, therefore, most applications require at least two orthogonal axes. In some configurations the sensor or payload to be controlled is mounted directly on the gimbal assembly, while in others, mirrors or other optical sensors are mounted to the gimbal, and the sensor is fixed to the vehicle. Several applications are reported in [3-10]. Although there are several applications for ISPs, all of them have a common goal, to hold or control the line of sight (LOS) of one object with respect to another object or inertial space. However, there are many approaches for stabilizing the LOS of an object so that it does not rotate relative to inertial space, perhaps the most straightforward and most common approach is mass stabilization. The principle of mass stabilization based on the Newton-Euler equations asserts that a body does not accelerate with respect to an inertial frame unless there is an applied torque. Therefore, to prevent that an object rotates with respect to an inertial frame is to guarantee that the applied torque is zero. Despite of good design in the electromechanical assembly, torque disturbances can act on a mechanism causing excessive motion or jitter of the LOS. Inertial rotation of the LOS are caused by numerous primary sources such as the nature of structural dynamics, misalignments between the gyroscopic-sensitive axis, the LOS axis, the axis about which control torques are applied, and the kinematics of multi-axis gimbals that yields to several effects. The abovementioned sources can be due either to a torque disturbance, flexibility in the system, or an erroneous input to the gimbal actuators. Lists of the three categories and many of the individual phenomena commonly encountered in each category are presented in [2].

Torque disturbances are described by Masten [3], including friction within the gimbal axes, spring flexure from electrical cables that cross the gimbal axes, unbalance effects, coupling from other gimbals, and host vehicle motion coupling, as well as internal disturbances within the sensor. Although disturbances arise from several sources, as noted in the previous description, common ISP disturbances are summarized in [11-14].

Moreover, the dynamic equations of motion of a PTG are a set of mathematical equations describing the dynamic behavior of the PTG. These equations are useful for computer simulation of the PTG motion, the design of suitable control equations for a PTG, and the evaluation of the kinematic design and structure of a PTG. The dynamic model of a PTG can be obtained as discussed below. Indeed, two approaches like the Lagrange-Euler (L-E) and Newton-Euler (N-E) formulations could be applied systematically to develop the PTG motion equations. The derivation of the dynamic model of PTG based on the L-E formulation is simple and systematic. However, the N-E equations are very difficult to utilize for real-time control purposes. As an alternative for deriving more efficient equations of motion, algorithms for computing the forces/torques of an open-loop kinematic chain were developed using the N-E equations of motion [15-17].

The N-E formulation results in a set of recursive equations that can be applied to the PTG links sequentially. The most significant aspect of this formulation is that the computation time of the applied torques can be reduced significantly to allow real-time control.

On the order hand, Yoon and Lundberg [18], presented the equations of motion for the two-axes yaw-pitch gimbal configuration derived by the moment equation as well as the Lagrange equations, on the assumption that gimbal has no mass unbalance. Per Skoglar [19], developed a sensor system consisting of infrared and video sensors and integrated navigation system. The sensor system is placed in a camera gimbal and is used on moving platforms, e.g. Unmanned Aerial Vehicles (UAVs), the L-E formulation is used for derivation of the equations of motion for a general robot manipulator and then applied to the gimbal system.

In this article, the dynamic equations of motion of a PTG are developed using the N-E formulation. The result is the derivation of the outward recursion equations that propagate kinematic information such as linear velocities, angular velocities, angular accelerations, and linear accelerations at the mass center of each link from the base coordinate frame to the end-effector coordinate frame and inward recursion equations that propagate the forces and moments exerted on each link from the end-effector of the PTG to the base coordinate frame.

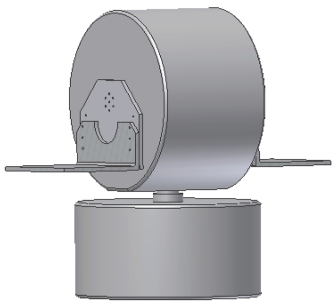

Fig. 1 The pan-tilt gimbal.

2 KINEMATIC MODEL: FORWARD AND INVERSE

A PTG can be considered as a DGM and its mechanical components are shown in Figures 2, 3 and 4 with the same names of the three rigid bodies that conform to a DGM.

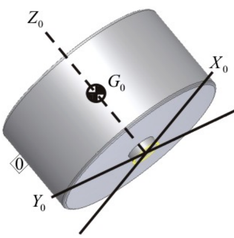

Fig. 2 Base.

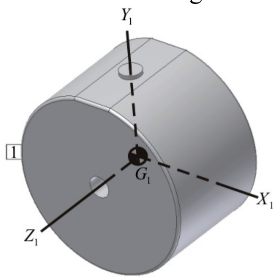

Fig. 3 Outer gimbal.

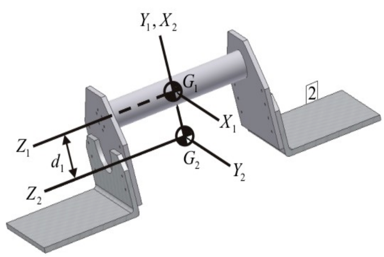

Fig. 4 Inner gimbal.

The PTG can also be considered as a kinematic chain as it is a set of rigid bodies, also called links, coupled by kinematic pairs. A kinematic pair is the coupling of two rigid bodies so as to constrain their relative motion. The most used fashion of describing spatial kinematic chains is via Denavit-Hartenberg (DH) notation. This is introduced to describe the architecture of the PTG, i.e., the relative position and orientation of its neighboring kinematic pair axes. To this end, links and coordinate frames are numbered 0, 1 and 2. Hence, Figures 2, 3 and 4 show the coordinate frames $\{X_0, Y_0, Z_0\}$, $\{X_1, Y_1, Z_1\}$ and $\{X_2, Y_2, Z_2\}$ attached at the base, at the outer-gimbal and at the inner-gimbal, respectively. Two more coordinate frames are attached at the mass center of the corresponding mechanical component. Henceforth, this work will refer to these coordinate frames as F_0, f_1 and f_2 respectively. Moreover, let F_0 be a fixed coordinate frame, whereas f_1 and f_2 be rotational coordinate frames, as shown in Fig. 5. From that figure, f_1 rotates about the axis Z_0 that is the axe of the first kinematic pair q_1 and f_2 rotates about the axis Z_1 that is the axis of the second kinematic pair q_2. Therefore, the outer-gimbal rotates about the axis Z_0 and the inner-gimbal rotates about the axis Z_1. Table 1 shows the DH parameters of the PTG.

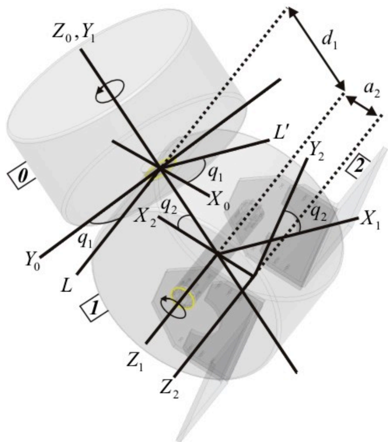

Plane $Z_1Y_1 \rightarrow L \| Z_1$

Plane $X_1Y_1 \rightarrow L' \| X_1$

Plane $Z_2X_2 \rightarrow Z_1 \| Z_2$

$L \perp L'$

Fig. 5: Coordinate frames F_0, f_1 and f_2 with different origins.

Table I. DH parameters of the PTG.

i	α_i (degrees)	d_i (m)	θ_i (degrees)	a_i (m)
1	90	d_1	q_1	0
2	0	0	q_2	a_2

From Figure 5 and Table I, the homogeneous coordinate transformation among the three coordinate frames, namely, F_0, f_1 and f_2 is

$$ {}^{0}\mathbf{T}_2 = {}^{0}\mathbf{T}_1 \, {}^{1}\mathbf{T}_2 \qquad (1) $$

where ${}^{1}\mathbf{T}_2$ and ${}^{0}\mathbf{T}_1$ are given by

$$ {}^{1}\mathbf{T}_2 = \begin{bmatrix} {}^{1}\mathbf{Q}_2 & [\mathbf{a}]_1 \\ \mathbf{0} & 1 \end{bmatrix} \tag{2} $$

$$ {}^{0}\mathbf{T}_1 = \begin{bmatrix} {}^{0}\mathbf{Q}_1 & [\mathbf{d}]_0 \\ \mathbf{0} & 1 \end{bmatrix} \tag{3} $$

Eq. (1) represents the location (position and orientation) of f_2 with respect to F_0. Now, ${}^{1}\mathbf{Q}_2$, ${}^{0}\mathbf{Q}_1$, $[\mathbf{a}]_1$ and $[\mathbf{d}]_0$ are given by

$$ {}^{1}\mathbf{Q}_2 = \begin{bmatrix} -S_2 & C_2 & 0 \\ C_2 & S_2 & 0 \\ 0 & 0 & 1 \end{bmatrix} \tag{4} $$

$$ {}^{0}\mathbf{Q}_1 = \begin{bmatrix} C_1 & 0 & S_1 \\ -S_1 & 0 & C_1 \\ 0 & 1 & 0 \end{bmatrix} \tag{5} $$

$$ [\mathbf{a}]_1 = \begin{bmatrix} a_2 S_2 \\ -a_2 C_2 \\ 0 \end{bmatrix} \tag{6} $$

$$ [\mathbf{d}]_0 = \begin{bmatrix} 0 \\ 0 \\ d_1 \end{bmatrix} \tag{7} $$

where $C_i \equiv \cos q_i$, $S_i \equiv \sin q_i$. Eq. (4) is the rotation carrying f_2 into f_1, Eq. (5) is the rotation carrying f_1 into F_0, vector $[\mathbf{a}]_1$ is the position vector of the origin of f_2 with respect to f_1 whereas vector $[\mathbf{d}]_0$ is position vector of the origin of f_1 with respect to F_0. On the other hand, matrix ${}^{0}\mathbf{T}_2$ can be rewritten as follows

$$ {}^{0}\mathbf{T}_2 = \begin{bmatrix} \mathbf{n} & \mathbf{o} & \mathbf{a} & \mathbf{p} \\ 0 & 0 & 0 & 1 \end{bmatrix} = \begin{bmatrix} n_x & o_x & a_x & p_x \\ n_y & o_y & a_y & p_y \\ n_z & o_z & a_z & p_z \\ 0 & 0 & 0 & 1 \end{bmatrix} \tag{8} $$

where the orthonormal triad $\mathbf{n}, \mathbf{o}, \mathbf{a}$ and the vector $\mathbf{p}$ represent orientation and position of the inner-gimbal, respectively. Thus,

$$ \left({}^{0}\mathbf{T}_1\right)^{-1}\left({}^{0}\mathbf{T}_2\right) = {}^{1}\mathbf{T}_2 \tag{9} $$

Equation (9) yields indeed to twelve relations. However, those that express q_1 and q_2 in terms of constants are of interest. For example, by equating the element (2,4), yields

$$ q_2 = \cos^{-1}\left(\frac{p_z - d_1}{-a_2}\right) \tag{10} $$

Similarly, element (3,4) yields

$$q_1 = \tan^{-1}\left(-\frac{p_y}{p_x}\right) \tag{11}$$

Finally, Eqs. (10) and (11) represent the solution of inverse kinematic of the PTG, and vector $\mathbf{p}$ of Eq.(8) represents the solution of forward kinematic of the PTG, i.e,

$$\mathbf{p} = \begin{bmatrix} a_2\cos(q_1)\sin(q_2) \\ -a_2\sin(q_1)\sin(q_2) \\ d_1 - a_2\cos(q_2) \end{bmatrix} \tag{12}$$

3 KINEMATIC OUTWARD RECURSIONS

From Figure 6 and the abovementioned nomenclature, the equations written below are readily derived:

$$\boldsymbol{\omega}_i = \boldsymbol{\omega}_{i-1} + \boldsymbol{\omega}_i^* \tag{13}$$

$$\mathbf{v}_i = \boldsymbol{\omega}_i \times \mathbf{p}_i^* + \mathbf{v}_{i-1} \tag{14}$$

$$\dot{\boldsymbol{\omega}}_i = \dot{\boldsymbol{\omega}}_{i-1} + \dot{\boldsymbol{\omega}}_i^* \tag{15}$$

$$\dot{\mathbf{v}}_i = \dot{\boldsymbol{\omega}}_i \times \mathbf{p}_i^* + \boldsymbol{\omega}_i \times (\boldsymbol{\omega}_i \times \mathbf{p}_i^*) + \dot{\mathbf{v}}_{i-1} \tag{16}$$

where $\dot{\boldsymbol{\omega}}_i^*$ is given by

$$\dot{\boldsymbol{\omega}}_i^* = \frac{d^*\boldsymbol{\omega}_i^*}{dt} + \boldsymbol{\omega}_{i-1} \times \boldsymbol{\omega}_i^* \tag{17}$$

and $\boldsymbol{\omega}_i^*$ is given by

$$\boldsymbol{\omega}_i^* = \mathbf{k}_{i-1}\dot{q}_i \tag{18}$$

being $\dot{q}_i$ the magnitude of the angular velocity of f_i with respect to f_{i-1}. Similarly,

$$\frac{d^*\boldsymbol{\omega}_i^*}{dt} = \mathbf{k}_{i-1}\ddot{q}_i \tag{19}$$

Eqs. (13-19) contain kinematic information from F_0 to f_i of the ith link. These equations are called outward recursion equations. One obvious disadvantage of the previous equations is that all vector and matrix quantifies are referenced to F_0. The consequence of this disadvantage is that the calculation time is longer. In order to reduce the numerical complexity of the outward recursions, all vector and matrix quantifies of the ith link will be expressed with respect to its own coordinate frame. Luh *et al*. [17] improved motion equations by referring all velocities, accelerations, inertial matrices, location of centers of mass of each link and forces/moments in their own coordinate frame; as a consequence, the computation is shorter. Hence, angular velocities and accelerations can be computed recursively, as indicated below,

$${}^i\mathbf{Q}_0\boldsymbol{\omega}_i = {}^i\mathbf{Q}_{i-1}({}^{i-1}\mathbf{Q}_0\boldsymbol{\omega}_{i-1} + \mathbf{z}_{i-1}\dot{q}_i) \tag{20}$$

$$\begin{aligned} {}^i\mathbf{Q}_0\dot{\boldsymbol{\omega}}_i = {}^i\mathbf{Q}_{i-1}\Big[& {}^{i-1}\mathbf{Q}_0\dot{\boldsymbol{\omega}}_{i-1} + \mathbf{z}_{i-1}\ddot{q}_i + \\ & ({}^{i-1}\mathbf{Q}_0\boldsymbol{\omega}_{i-1} \times \mathbf{z}_{i-1}\dot{q}_i)\Big] \end{aligned} \tag{21}$$

where $z_{i-1} = [0,0,1]^T$. The linear acceleration is given by

$$\begin{aligned} {}^i\mathbf{Q}_0\dot{\mathbf{v}}_i = {}^i\mathbf{Q}_{i-1}[& ({}^{i-1}\mathbf{Q}_0\dot{\boldsymbol{\omega}}_i \times \mathbf{p}_i^*) + \\ & ({}^{i-1}\mathbf{Q}_0\boldsymbol{\omega}_i) \times ({}^{i-1}\mathbf{Q}_0\boldsymbol{\omega}_i \times \mathbf{p}_i^*)] + {}^i\mathbf{Q}_{i-1}({}^{i-1}\mathbf{Q}_0\dot{\mathbf{v}}_{i-1}) \end{aligned} \tag{22}$$

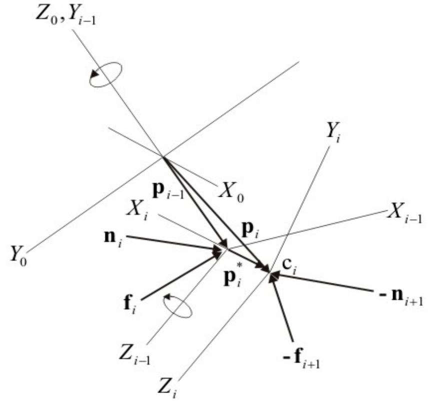

Fig. 6: Relationship between coordinate frames f_i and f_{i-1}

As ${}^{i-1}\mathbf{Q}_i$ is an *orthogonal matrix,* then

$$\left({}^{i-1}\mathbf{Q}_i\right)^{-1} = {}^{i}\mathbf{Q}_{i-1} = \left({}^{i-1}\mathbf{Q}_i\right)^T \tag{23}$$

Hence, using Eq. (20), angular velocities of the PTG are computed recursively for i = 1, 2. As the base link is a fixed inertial frame, then

$$\boldsymbol{\omega}_0 = 0, \quad \dot{\boldsymbol{\omega}}_0 = 0, \quad \mathbf{v}_0 = 0, \quad \dot{\mathbf{v}}_0 = 0$$

For $i = 1$

$${}^{1}\mathbf{Q}_0\boldsymbol{\omega}_1 = \begin{bmatrix} 0 \\ \dot{q}_1 \\ 0 \end{bmatrix}$$

For $i = 2$

$${}^{2}\mathbf{Q}_0\boldsymbol{\omega}_2 = \begin{bmatrix} C_2\dot{q}_1 \\ S_2\dot{q}_1 \\ \dot{q}_2 \end{bmatrix}$$

Now, using eq. (21), angular accelerations are computed recursively for $i = 1,2$.
For $i = 1$

$${}^{1}\mathbf{Q}_0\dot{\boldsymbol{\omega}}_1 = \begin{bmatrix} 0 \\ \ddot{q}_1 \\ 0 \end{bmatrix}$$

For $i = 2$

$${}^{2}\mathbf{Q}_0\dot{\boldsymbol{\omega}}_2 = \begin{bmatrix} -S_2\dot{q}_1\dot{q}_2 + C_2\ddot{q}_1 \\ C_2\dot{q}_1\dot{q}_2 + S_2\ddot{q}_1 \\ \ddot{q}_2 \end{bmatrix}$$

Now, using eq. (22), linear accelerations are computed recursively for i = 1,2. In turn, $\mathbf{p}_2^*$ and $\mathbf{p}_1^*$ are given by

For $i = 1$

$$^1\mathbf{Q}_0\dot{\mathbf{v}}_1 = \begin{bmatrix} 0 \\ 0 \\ 0 \end{bmatrix}$$

For $i = 2$

$$^2\mathbf{Q}_0\dot{\mathbf{v}}_2 = \begin{bmatrix} a_2\dot{q}_2^2 + a_2 S_2^2 \dot{q}_1^2 \\ a_2\ddot{q}_2 - C_2 a_2 S_2 \dot{q}_1^2 \\ - S_2 a_2 \ddot{q}_1 - 2C_2 a_2 \dot{q}_1 \dot{q}_2 \end{bmatrix}$$

4 LINKS DYNAMICS: INWARD RECURSION

A free-body diagram of the end-effector is shown in Figure 7. From this figure, the Newton-Euler equations are

$$\mathbf{f}_n = m_n \ddot{\mathbf{c}}_n - \mathbf{f} \quad (24)$$

$$\mathbf{n} = \mathbf{r} \times \mathbf{f} \quad (25)$$

$$\mathbf{n}_n = \mathbf{I}_n \dot{\omega}_n + \omega_n \times \mathbf{I}_n \omega_n - \mathbf{n} + \mathbf{p}_n^* \times \mathbf{f}_n \quad (26)$$

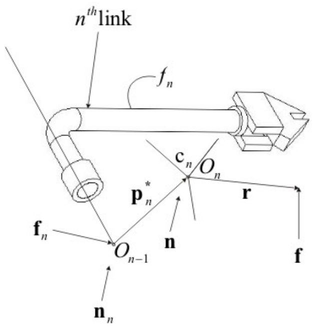

Fig.7: Free-body diagram of the end-effector.

where $\ddot{\mathbf{c}}_n$ is the linear acceleration of the mass center of the nth link with respect to F_0, $\mathbf{n}$ is the external moment exerted on the end-effector that is added by moving the external force $\mathbf{f}$ of its application point to the mass center of the end-effector, $\mathbf{r}$ is the vector of position of application point from the origin of f_n that is attached to the mass center of the end-effector and $\mathbf{I}_n$ is the *centroidal inertia matrix* of the nth link with respect to the orientation of F_0. The Newton-Euler equations for the remaining links are derived of Figure 6, namely,

$$\mathbf{f}_i = m_i \ddot{\mathbf{c}}_i + \mathbf{f}_{i+1} \quad (27)$$

$$\mathbf{n}_i = \mathbf{I}_i \dot{\boldsymbol{\omega}}_i + \boldsymbol{\omega}_i \times \mathbf{I}_i \boldsymbol{\omega}_i + \mathbf{n}_{i+1} + \mathbf{p}_i^* \times \mathbf{f}_i \quad (28)$$

The force $\mathbf{f}_{i+1}$ of eq. (27) and $\mathbf{n}_{i+1}$ of Eq. (28) propagate the forces exerted and the moments on each link from the end-effector to the ith link. Once vector $\mathbf{n}_i$ is available, the actuator torques denoted by $\boldsymbol{\tau}_i$ on the ith kinematic pair is the sum of projections of $\mathbf{n}_i$ on axis z_{i-1} and the viscous friction force. Since the ith kinematic pair is a revolute, then

$$\boldsymbol{\tau}_i = (\mathbf{n}_i^T)(^0\mathbf{Q}_{i-1}\mathbf{z}_{i-1}) + b_i \dot{q}_i \quad (29)$$

where b_i is the viscous damping coefficient for joint i in the above equations. Analogously, in order to reduce the numerical complexity of the inward recursions, all vector and matrix quantities of the ith link will be expressed with respect to its own coordinate frame. Hence, the Newton-Euler equations for the end-effector are below

$$ {}^{n}\mathbf{Q}_0\mathbf{f}_n = m_n\,{}^{n}\mathbf{Q}_0\ddot{\mathbf{c}}_n + {}^{n}\mathbf{Q}_0\mathbf{f} \tag{30} $$

$$ \begin{aligned} {}^{n}\mathbf{Q}_0\mathbf{n}_n &= ({}^{n}\mathbf{Q}_0\mathbf{I}_n{}^{0}\mathbf{Q}_n)({}^{n}\mathbf{Q}_0\dot{\boldsymbol{\omega}}_n) + \\ &({}^{n}\mathbf{Q}_0\boldsymbol{\omega}_n)\times[({}^{n}\mathbf{Q}_0\mathbf{I}_n{}^{0}\mathbf{Q}_n)({}^{n}\mathbf{Q}_0\boldsymbol{\omega}_n)] - \mathbf{n} + \\ &({}^{n}\mathbf{Q}_0\mathbf{p}_n^{*})\times({}^{n}\mathbf{Q}_0\mathbf{f}_n) \end{aligned} \tag{31} $$

Now, the Newton-Euler equations for the remaining links are given below

$$ {}^{i}\mathbf{Q}_0\mathbf{f}_i = m_i\,{}^{i}\mathbf{Q}_0\ddot{\mathbf{c}}_i + {}^{i}\mathbf{Q}_{i+1}({}^{i+1}\mathbf{Q}_0\mathbf{f}_{i+1}) \tag{32} $$

$$ \begin{aligned} {}^{i}\mathbf{Q}_0\mathbf{n}_i &= ({}^{i}\mathbf{Q}_0\mathbf{I}_i{}^{0}\mathbf{Q}_i)({}^{i}\mathbf{Q}_0\dot{\boldsymbol{\omega}}_i) + \\ &({}^{i}\mathbf{Q}_0\boldsymbol{\omega}_i)\times[({}^{i}\mathbf{Q}_0\mathbf{I}_i{}^{0}\mathbf{Q}_i)({}^{i}\mathbf{Q}_0\boldsymbol{\omega}_i)] + \\ &{}^{i}\mathbf{Q}_{i+1}({}^{i+1}\mathbf{Q}_0\mathbf{n}_{i+1}) + ({}^{i}\mathbf{Q}_0\mathbf{p}_i^{*})\times({}^{i}\mathbf{Q}_0\mathbf{f}_i) \end{aligned} \tag{33} $$

$$ {}^{i}\mathbf{Q}_0\boldsymbol{\tau}_i = ({}^{i}\mathbf{Q}_0\mathbf{n}_i)^T({}^{i}\mathbf{Q}_0{}^{0}\mathbf{Q}_{i-1}\mathbf{z}_{i-1}) + b_i\dot{q}_i \tag{34} $$

Finally, the inward recursion equations (24-34) propagate the forces and torques exerted on each link from the end-effector to the base. Hence, inward recursion equations for the third PTG are computed recursively, assuming that there are not load conditions, i.e.,

$$ \mathbf{f} = \mathbf{n} = \mathbf{0} $$

for $i = 2$

$$ {}^{2}\mathbf{Q}_0\mathbf{f}_2 = m_2\begin{bmatrix} a_2\dot{q}_2^2 + a_2S_2^2\dot{q}_1^2 \\ a_2\ddot{q}_2 - C_2a_2S_2\dot{q}_1^2 \\ -S_2a_2\ddot{q}_1 - 2C_2a_2\dot{q}_1\dot{q}_2 \end{bmatrix} $$

$$ \begin{aligned} {}^{2}\mathbf{Q}_0\mathbf{n}_2 &= ({}^{2}\mathbf{Q}_0\mathbf{I}_2{}^{0}\mathbf{Q}_2)({}^{2}\mathbf{Q}_0\dot{\boldsymbol{\omega}}_2) + \\ &({}^{2}\mathbf{Q}_0\boldsymbol{\omega}_2)\times[({}^{2}\mathbf{Q}_0\mathbf{I}_2{}^{0}\mathbf{Q}_2)({}^{2}\mathbf{Q}_0\boldsymbol{\omega}_2)] + \\ &({}^{2}\mathbf{Q}_0\mathbf{p}_2^{*})\times({}^{2}\mathbf{Q}_0\mathbf{f}_2) \end{aligned} $$

where ${}^{2}\mathbf{Q}_0\mathbf{I}_2{}^{0}\mathbf{Q}_2$ is the centroidal inertia matrix of the inner-gimbal relative to the centroidal coordinate frame f_2. Remember that $\mathbf{p}_2^{*}$ is given by eq.(6), hence, it must be carried from f_2 into F_0. For $i = 1$

$$ \begin{aligned} {}^{1}\mathbf{Q}_0\mathbf{f}_1 &= m_1\,{}^{1}\mathbf{Q}_0\dot{\mathbf{v}}_1 + {}^{1}\mathbf{Q}_2({}^{2}\mathbf{Q}_0\mathbf{f}_2) \\ {}^{1}\mathbf{Q}_0\mathbf{n}_1 &= ({}^{1}\mathbf{Q}_0\mathbf{I}_1{}^{0}\mathbf{Q}_1)({}^{1}\mathbf{Q}_0\dot{\omega}_1) + \\ &({}^{1}\mathbf{Q}_0\omega_1)\times[({}^{1}\mathbf{Q}_0\mathbf{I}_1{}^{0}\mathbf{Q}_1)({}^{1}\mathbf{Q}_0\omega_1)] + {}^{1}\mathbf{Q}_2({}^{2}\mathbf{Q}_0\mathbf{n}_2) + \\ &({}^{1}\mathbf{Q}_0\mathbf{p}_1^{*})\times({}^{1}\mathbf{Q}_0\mathbf{f}_1) \end{aligned} $$

where ${}^{1}\mathbf{Q}_0\mathbf{I}_1{}^{0}\mathbf{Q}_1$ is the centroidal inertia matrix of the outer-gimbal relative to the centroidal coordinate frame f_1. Recalling that $\mathbf{p}_1^{*}$ is given by Eq. (7).
Finally, torques at the kinematic pairs axes are given by

$$ {}^{2}\mathbf{Q}_0\boldsymbol{\tau}_2 = ({}^{2}\mathbf{Q}_0\mathbf{n}_2)^T({}^{2}\mathbf{Q}_0{}^{0}\mathbf{Q}_1\mathbf{z}_1) + b_2\dot{q}_2 $$

$$ {}^{1}\mathbf{Q}_0\boldsymbol{\tau}_1 = ({}^{1}\mathbf{Q}_0\mathbf{n}_1)^T({}^{1}\mathbf{Q}_0\mathbf{z}_0) + b_1\dot{q}_1 $$

For the sake of simplicity, the dissipative forces and moments were not included here, therefore, $b_i = 0$ for $i = 1, 2$.

5 TRAJECTORY PLANNING

For illustration purposes, in this work a 4-5-6-7 interpolating polynomial [20] was used for trajectory planning, that is,

$$s(\tau) = -20\tau^7 + 70\tau^6 - 84\tau^5 + 35\tau^4 \qquad (35)$$

where $0 \le s \le 1$, $0 \le \tau \le 1$, and $\tau = t/T$, T being the time for the complete operation. Clearly, the polynomial satisfies eight conditions related to the s and the vanishing of its three first derivatives at 0 and 1. Let $\boldsymbol{\theta}_I$ and $\boldsymbol{\theta}_F$ be the vectors of the kinematic pairs at the initial and final robot configurations, respectively, and $\boldsymbol{\theta}(t)$ the vector of joint coordinates . Thus, the range of motion can be written in the form

$$\boldsymbol{\theta}(t) = \boldsymbol{\theta}_I + (\boldsymbol{\theta}_F - \boldsymbol{\theta}_I)s(\tau) \qquad (36)$$

and

$$\dot{\boldsymbol{\theta}}(t) = (\boldsymbol{\theta}_F - \boldsymbol{\theta}_I)\frac{1}{T}s'(\tau)$$

$$\ddot{\boldsymbol{\theta}}(t) = (\boldsymbol{\theta}_F - \boldsymbol{\theta}_I)\frac{1}{T^2}s''(\tau)$$

$$\dddot{\boldsymbol{\theta}}(t) = (\boldsymbol{\theta}_F - \boldsymbol{\theta}_I)\frac{1}{T^3}s'''(\tau)$$

The maximum value of $s'(\tau)$ and the ith kinematic pair rate are found as

$$s'_{\max} = \left(\frac{1}{2}\right) = \frac{35}{16} \qquad (37)$$

$$(\dot{\boldsymbol{\theta}}_i)_{\mathbf{max}} = \frac{35(\boldsymbol{\theta}_i^F - \boldsymbol{\theta}_i^I)}{16T} \qquad (38)$$

and the maximum value of $s''(\tau)$ and the acceleration were computed as

$$s''_{\max} = s''\left(\frac{1}{2} - \frac{\sqrt{5}}{10}\right) = \frac{84\sqrt{5}}{25} \qquad (39)$$

$$(\ddot{\boldsymbol{\theta}}_i)_{\mathbf{max}} = \frac{(\boldsymbol{\theta}_i^F - \boldsymbol{\theta}_i^I)}{T^2}\frac{84\sqrt{5}}{25} \qquad (40)$$

The foregoing relations were used to determine the minimum time T during which it is possible to perform a given PPO while considering the physical limitations of the motors.

6 RESULTS AND DISCUSSION

A PPO is to be performed with the PTG in the shortest possible time considering the physical limitations of one commercial. Hence, the maneuver is defined so that the 2-dimensional vector of kinematic pairs is given by a common shape function $s(\tau)$ defined above in Eq. (35). Thus, considering the physical limitations of commercial one, $(\boldsymbol{\theta}_F - \boldsymbol{\theta}_I)$ of Eq. (36) is given by

$$\boldsymbol{\theta}_F - \boldsymbol{\theta}_I = \begin{bmatrix} q_1^F \\ q_2^F \end{bmatrix} - \begin{bmatrix} q_1^I \\ q_2^I \end{bmatrix} = \begin{bmatrix} 180 \\ 140 \end{bmatrix} - \begin{bmatrix} 0 \\ 0 \end{bmatrix} = \begin{bmatrix} 180 \\ 140 \end{bmatrix}$$

and rate and acceleration limits are configurable from 0.15 °/s to 150 °/s for the rate and 10 °/s^2 o 150 °/s^2 for acceleration of two kinematic pairs. So that,

For q_1

$$T_{rate\,\mathbf{max}} = 2\frac{5}{8}seg \qquad T_{acceleration\ \mathbf{max}} \approx 3\,seg$$

and for q_2

$$T_{rate\,\mathbf{max}} = 2\frac{1}{24}seg \qquad T_{acceleration\ \mathbf{max}} \approx 2.65\,seg$$

Thus, Eqs. (38) and (39) allow to determine T for each kinematic pair so that the rates and accelerations lie within the allowed limits. For motors of different physical limitations, the minimum values of T , allowed by the kinematic pairs, will be the largest one. Obviously, the minimum value sought, $T_{\min}$, is nothing but the maximum of the foregoing values, i.e,

$$T_{\mathbf{min}} = \mathbf{max}\{T_i\}_1^n = 3seg \tag{41}$$

With T defined in eq. (41) as the time taken by the maneuver. The values of masses for links are given below

$$m_1 = 2.233\,\text{kg} \qquad m_2 = 0.946\,\text{kg}$$

And the values of the centroidal inertia matrix $({}^n\mathbf{Q}_0\mathbf{I}_n{}^0\mathbf{Q}_n)$ are given for each link in $\text{kg}-\text{m}^2$ by

$$({}^2\mathbf{Q}_0\mathbf{I}_2{}^0\mathbf{Q}_2) = \begin{bmatrix} 0.010 & 0 & 0 \\ 0 & 0.010 & 0 \\ 0 & 0 & 0.010 \end{bmatrix} \textit{for link } 2$$

$$({}^1\mathbf{Q}_0\mathbf{I}_1{}^0\mathbf{Q}_1) = \begin{bmatrix} 0.010 & 0 & 0 \\ 0 & 0.013 & 0 \\ 0 & 0 & 0.010 \end{bmatrix} \textit{for link } 1$$

The values of masses and of the centroidal inertia matrix were estimated with the help of sketches of one commercial PTG and a software of computer aided design. Eqs. (20-22) and (30-34) were plotted for each link, and are displayed in Figs 8-18, about its own coordinate frame assuming that there were not load conditions. Finally, assuming that there are load conditions balanced on mass center of link 2 of 9 kg and, that the dissipative forces and moments were neglected, then,

$$\mathbf{f} = (9.81)(9)\mathbf{z_0}[N]$$

$$\mathbf{r} = \mathbf{0}$$

$$\mathbf{n} = \mathbf{r}\times\mathbf{f} = \mathbf{0}$$

$$b_i = 0 \text{ for } i=1,2.$$

Eq. (34) is plotted for each link of the PTG, as shown in Figs. 19 and 20.

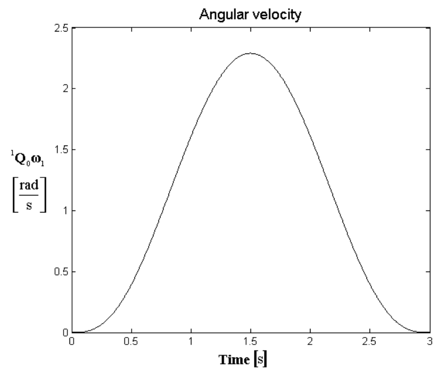

Fig. 8: Angular velocity of link 1.

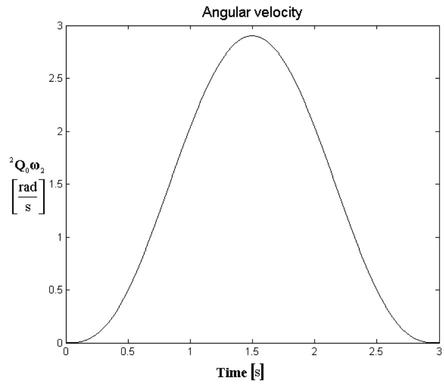

Fig. 9: Angular velocity of link 2.

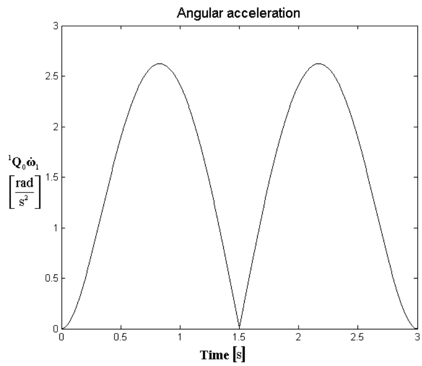

Fig. 10: Angular acceleration of link 1.

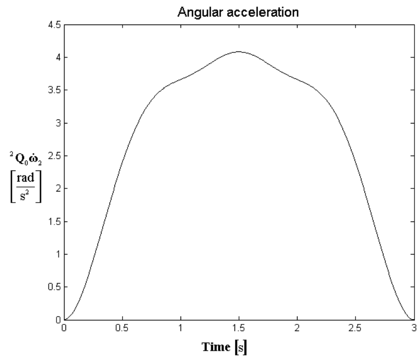

Fig. 11: Angular acceleration of link 2.

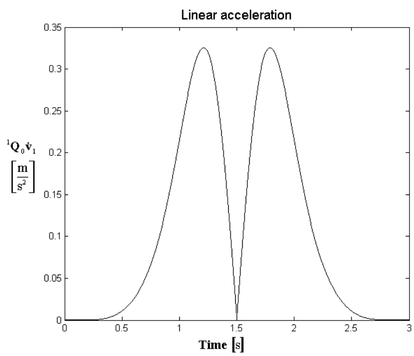

Fig. 12: Acceleration of mass center of link 1.

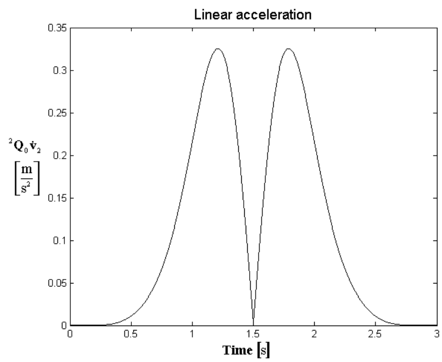

Fig. 13: Acceleration of mass center of link 2.

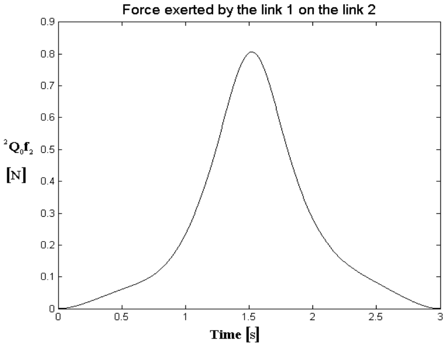

Fig. 13: Force exerted by link 1 on link 2.

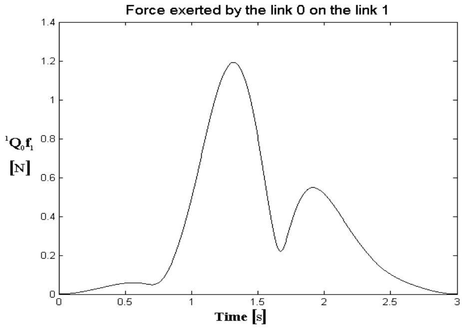

Fig. 14: Force exerted by the link 0 on the link 1.

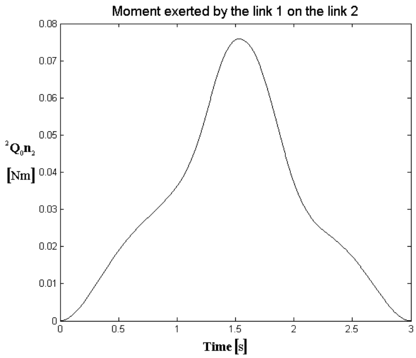

Fig. 15: Moment exerted by link 1 on link 2.

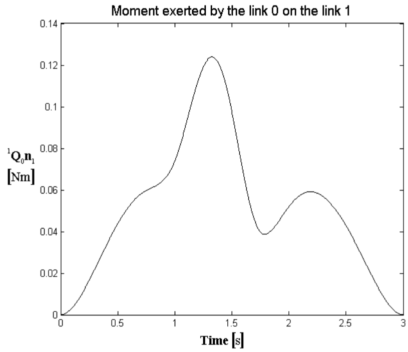

Fig. 16: Moment exerted by link 0 on link 1.

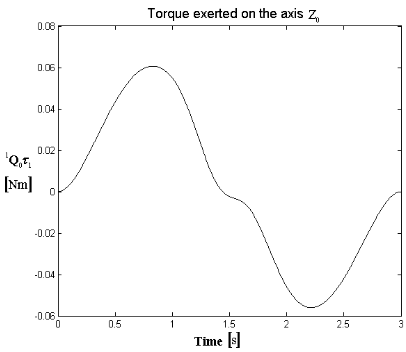

Fig. 17: Torque exerted on the axis Z_0.

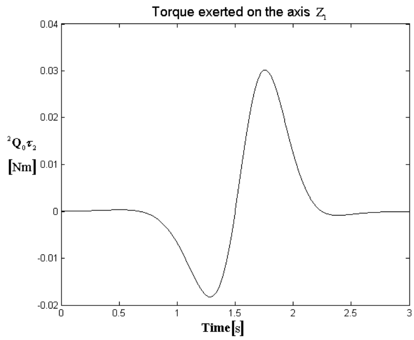

Fig. 18: Torque exerted on the axis Z_1.

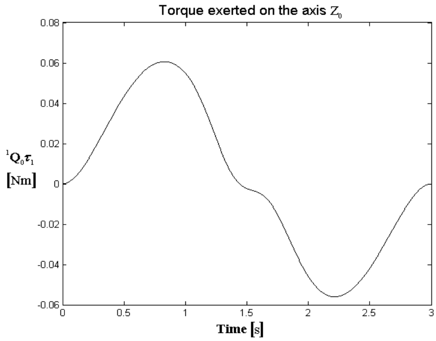

Fig. 19: Torque exerted on the axis Z_0 for a given load.

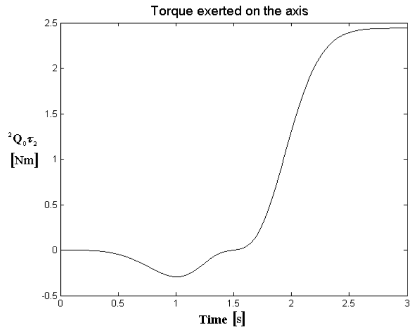

Fig. 20: Torque exerted on the axis Z_1 with load.

Finally, it is important that the load conditions were balanced on the rotation axis Z_1 instead of mass center of link 2, since it is not located on the origin of f_1. Although the load was balanced about mass center of link 2, a torque arose exerted on the axis Z_1 when the link 2 reached the final position of 140º from the relaxed position (matching position of the frames f_1 and f_2), this torque can be looked at as a disturbance that control system of the PTG needs to overcome for keeping the load in the final position as shown in Fig. 20. On the other hand, the disturbance, shown in Fig. 18, almost vanished.

7. CONCLUSIONS

The analysis presented here allows computing recursively the torques required by a particular maneuver while the driver of the PTG allows it. On the other hand, load conditions were balanced on the rotation axis to avoid the generation of torques added to disturbances arising from the design of the electromechanical assembly or from any other sources. This principle of mass stabilization is best achieved when the amount of disturbances is reduced.

REFERENCES

[1] J. Osborne, G. Hicks, and R. Fuentes, Global analysis of the double-gimbal mechanism, *IEEE Contr Syst Mag*, 28, 44-64, 2008.

[2] J. M. Hilkert, Inertially stabilized platform technology, Concepts and principles. *IEEE Contr Syst Mag*, 28: 26-46, 2008.

[3] M. K. Masten, Inertially stabilized platforms for optical imaging systems. *IEEE Contr Syst Mag*, 28: 47-64, 2008.

[4] J. de Bruin, Control systems for mobile Satcom antennas, *IEEE Contr Syst Mag*, 28: 87-101, 2008.

[5] M. Algrain and R. Powers, Line-of-sight pointing accuracy-stability analysis and computer simulation for small spacecraft, *Proc. 10th Conference on Acquisition, Tracking, and Pointing*, Orlando, FL, USA, 1996.

[6] J. Ortega, Gunfire performance of stabilized electro-optical sights, *Proc.13th Conference on Acquisition, Tracking, and Pointing*, Orlando, FL, USA, 1999.

[7] M. Guelman, A. Kogan, A. Kazarian, A. Livine, M. Orenstien, H. Michalik, and S. Arnon, Acquisition and pointing control for inter-satellite laser communications. *IEEE Transaction on Aerospace and Electrononic Systems*, 40: 1239-1249, 2004.

[8] H. G. Wang and T. C. Williams, Strategic inertial navigation systems-high-accuracy inertially stabilized platforms for hostile environments. *IEEE Contr Syst Mag*, 28: 65-85, 2008.

[9] A. Lawrence, *Modern Inertial Technology*, 2nd Ed., Springer-Verlag, 1998.

[10] J. C. DeBreuin, Derivation of line-of-sight stabilization equations for gimbaled-mirror optical systems. *Proc. Conference on Active and Adaptive Optical Components*, San Diego, CA, USA, 1992.

[11] M. Algrain M. and D. Ehlers, Suppression of gyroscope noise effects in pointing and tracking systems. *Proc. 8th Conference on Acquisition, Tracking, and Pointing*, Orlando, FL, USA, 1994.

[12] P. Dahl, Solid Friction Damping of Mechanical Vibrations, *Proc. Conference on AIAA Guidance and Control*, Boston, Mass, 1976.

[13] D. Kimbrell and D. Greenwald, Deterministic errors in pointing and tracking systems II-Identification and correlation of dynamic errors. *Proc. Conference on Acquisition, Tracking, and Pointing*, Orlando, FL, USA, 1991.

[14] M. Todd and K. Johnson, *Int J Mech Sci*, 29: 339-354, 1987.

[15] W. M. Armstrong, Recursive solution to the equations of motion of an N-link manipulator. *Proc. Int. Conf. on Theory of Machines. Mechanisms*, 1343-1346, 2007.

[16] D. E. Orin, R. B. McGhee, M. Vukobratovic, and G. Hartoch, Kinematic and kinetic analysis of open-chain linkages utilizing Newton-Euler methods. *J. Math. Biosci*, Vol. 43, 107-130.

[17] L. Y. S. Luh, M. W. Walker, and R. P. Paul, On line computational Scheme for Mechanical Manipulators. *ASME Transactions on Dynamic systems, measurements and control*, 120, 69-76, 2006.

[18] S. Yoon and J. B. Lundberg, *IEEE Trans Aerosp Electron Syst*, 37, 1083-1091, 2001.

[19] P. Skoglar. Modelling and control of IR/EO-gimbal for UAV surveillance applications. *Ph D Thesis*, Linkoping. 2002.

[20] J. Angeles, *Fundamentals of Robotic Mechanical Systems: Theory, Methods, and Algorithms*, 2nd Ed., Springer-Verlag, 2003.

Proceedings of MUSME 2011, the International Symposium
on Multibody Systems and Mechatronics
Valencia, Spain, 25-28 October 2011

ANALYSIS OF WEAR IN GUIDE BEARINGS FOR PNEUMATIC ACTUATORS AND NEW SOLUTIONS FOR LONGER SERVICE LIFE

Guido Belforte[1], Andrea Manuello Bertetto[2],
Luigi Mazza[1] and Pier Francesco Orrù[2]

[1] Department of Mechanics-Politecnico di Torino
Corso Duca degli Abruzzi, 24.
10129 Torino, Italy
e-mail: guido.belforte@polito.it;luigi.mazza@polito.it

[2] Department of Mechanical Engineering-University of Cagliari
Piazza d'Armi.
09123 Cagliari, Italy
e-mail: manuello@dimeca.unica.it;pforru@unica.it

Keywords: Pneumatics, pneumatic actuators, rod guide bearings, sealing systems

Abstract. *Pneumatic actuation by high efficiency cylinders is one of the most commonly used ways of moving grippers and arms in robotics. The paper describes a general methodology for establishing the life of linear pneumatic actuators through a detailed analysis of behaviour as wear progresses. To optimize cylinder life vs. lost energy, the study focuses on the rod-bushing interaction, investigating pressure distribution on the sliding interface. Finite Element models of the rod guide system in different working conditions were developed in order to analyze contact pressure distribution at the rod/guide interface. In addition, new solutions consisting of two different front rod guide bearing mounting designs were proposed in order to redistribute pressure at the rod/guide interface, thus improving performance and cylinder service life.*

1 INTRODUCTION

Pneumatic actuation by means of linear actuators (cylinders) is one of the most commonly used ways of moving grippers and arms in robotics. To an increasing extent, wear resistant, highly reliable and highly efficient pneumatic components are required in all industrial applications, in particular for automatic systems and robotics. There is a specific need to define the performance of pneumatic cylinders in terms of service life, determined mainly by the behaviour of sliding parts: seals, guide bearing and piston slide ring. Several standards cover life analysis for pneumatic cylinders, with ISO 10099, CNOMO E06.22.115.N, and ISO 19973 being the references in this field. To overcome the limitations of these standards, the major manufacturers and several research centres have investigated various methods for defining and measuring linear actuator life, as studies and research in this area can contribute to improving the performance and durability of components and systems featuring sliding seals and guides. Such components include pneumatic cylinders used extensively in industrial applications, where they are nominally subjected to axial loads but, typically, can also be subject to a radial load. This load component puts significant stress on seals and guide systems, thus penalizing actuator performance in terms of durability and service life. To be able to schedule system maintenance correctly and prevent damage and machine downtime, it is important that the durability of pneumatic cylinders and actuators can be assessed in advance as a function of the main operating parameters.

A general method for evaluating pneumatic actuator service life and performance, with particular reference to sliding parts, was developed in [1, 2]. A radial load was applied to the rod in order to ensure that wear test conditions are similar to the actual service and operating conditions for a pneumatic cylinder. As the applied load is higher than that contemplated by standards, accelerated life tests were carried out. An extensive failure analysis and classification of damage modes made it possible to establish preventative maintenance procedures. In [3, 4] a self-diagnostic approach using the change in velocity as a parameter for monitoring was identified; a strategy for detecting faults was defined order to aid the identification of a specific failure. The importance of surface treatment on bearing efficiency and micromechanical aspects were investigated in [5-7]. In particular, a model was developed to predict the normal load increase due to the entrapment of wear particles at the sliding counterface. A criterion for determining pneumatic actuator life was defined in [8] by means of an analytical model aimed at predicting rod/guide bearing wear. In [9-10], attention focused on the evaluation of sealing system performance and efficiency; in particular, the contact pressure distribution at the sealing surface was found to be of fundamental importance to good system operation.

This paper analyses pneumatic linear actuator behaviour when significant radial loads are acting on the cylinder rod. In particular, the rod guide/bearing interaction is considered as regards actions at the sliding interface. The investigation was carried out both experimentally and numerically by means of finite element analyses. A finite element model for analysing the contact mechanism between the front head guiding system and the sliding rod in a linear pneumatic actuator under radial loads was developed in order to investigate contact pressure along the contact surface. The most important parameters influencing rod/guide coupling wear resistance were identified. The commercial configuration was used as starting point in designing two different front guide bearing mounting solutions in order to redistribute contact pressure, reduce peak pressure and thus ensure more advantageous operating conditions in terms of wear and durability. Numerical and experimental results were analysed and compared in order to define the most advantageous assembly configuration for the existing guide bearing.

2 MATERIALS AND TEST METHOD

The cylinders employed in the tests are double acting pneumatic cylinders as shown schematically in Figure 1. The rod (1), to which the external load is applied, is connected to the piston (2); the piston seals (3) prevent compressed air leakage between the chambers. The cylinder bore (4) is secured between the cylinder front (5) and rear head (6). The rod seal (7) on the rod front head (5) is used to prevent compressed air leakage to the outside environment. Piston rod linear motion is guided by means of the piston slide ring (8) and the guide bearing (9). Lubricated-for-life polyurethane lip seals are used.

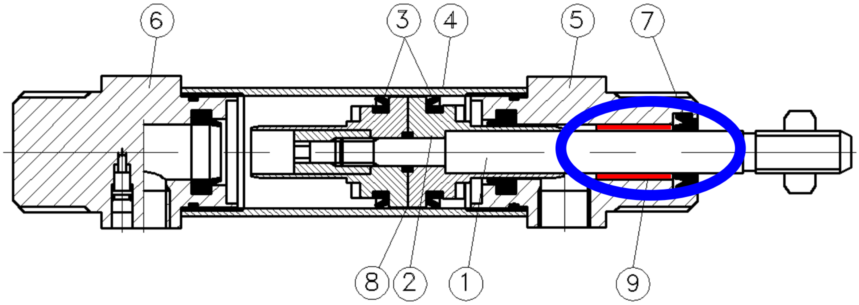

Figure 1: Cylinder schematics.

CNOMO and ISO standards establish test methods for performing wear cycles on commercial cylinders subjected to radial loads applied to the rod, specifying cylinder supply pressure, compressed air supply, filtration conditions, rod velocity and the load applied to the rod. In the investigation presented herein, tests were carried out on cylinders subjected to radial load, taking into account the conditions established by standards (ISO 10099, 1999; CNOMO E06.22.115.N, 1992; ISO/DIS19973, 2005), but considering a more severe loading condition with higher radial load.

A test rig, shown in Figure 2a, was designed and manufactured to perform wear and life tests. The cylinders are rigidly retained to a fixed frame which keeps the axis horizontal, while a weight is applied to the cylinder rods to impose a radial load. Tests consist of performing complete rod extension and retraction cycles, controlled by an electro-pneumatic circuit, until seals can no longer prevent leakage. The basic conditions for these tests included compressed dry air, filtration (40 µm), supply pressure 6.3 bar, and mean velocity of about 0.3 m/s. Tests were carried out on groups of five-seven cylinders with 50 mm bore and 250 mm stroke. Cylinder groups were subjected to a radial load of 100 N.

Several test parameters were measured in order to evaluate cylinder life and define cylinder failure under the radial loads, checking for seal leakage and rod axis misalignment in particular. As cylinder failure is often caused by seal collapse, a leakage test was carried out to highlight this phenomenon. Cylinder operation was periodically interrupted and the front chamber or the rear chamber were pressurised separately to an initial pressure of 10 bar as illustrated in Figure 2b. A circuit (1) was supplied with filtered compressed air (2) having a regulated pressure (3). A valve (4) isolates the chamber under test (3) and the pressure drop Δp is measured after one hour by means of manometer (4). The cylinder is considered to be completely unserviceable upon reaching a relative pressure drop of 10 bar, corresponding to complete chamber emptying.

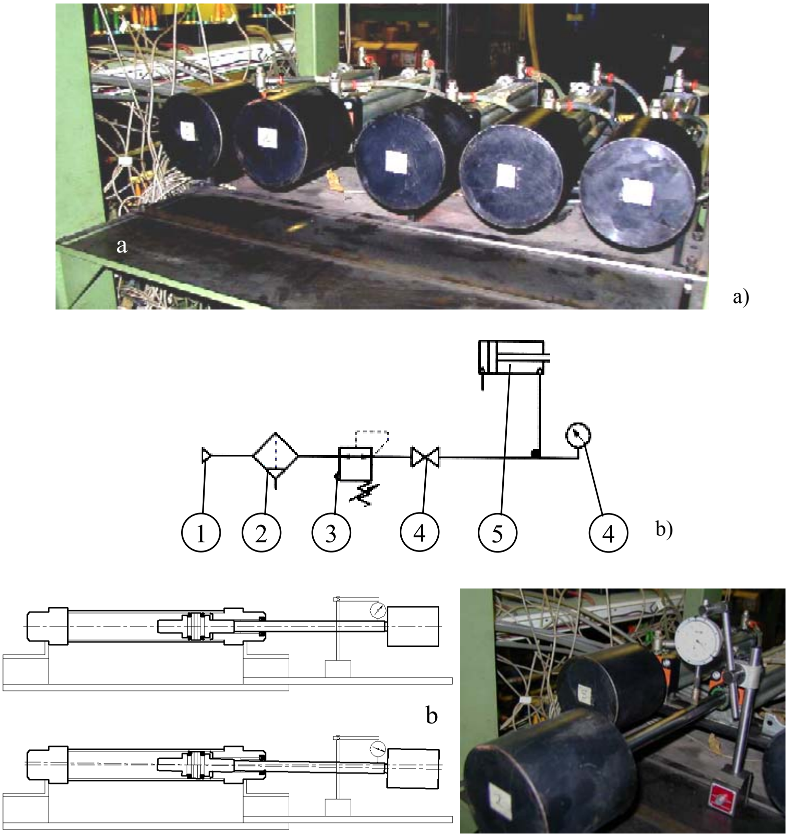

Figure 2: Cylinder life test rig (a), leakage circuit (b), wear measurement schematics (c)

Cylinder rod front bearing wear is a fundamental parameter influencing cylinder operating conditions and service life. As the cylinder can no longer move when the rod front bearing reaches a certain level of wear, it is important to evaluate how wear progresses during the cylinder's operating life. Guide bearing wear was evaluated by measuring the progress of rod misalignment arising from increases in the clearance between rod and front guide. Test rig schematics for this measurement are shown in Figure 2c. The cylinder is secured to the fixed frame and the rod extended until the piston touches the cylinder front head; a linear displacement gauge (comparator) is placed in a precisely defined point. Bearing clearance and wear consumption can be calculated by means of this measurement.

As the free body diagram in Figure 3 shows, reaction force Rb during cylinder reciprocating motion with the rod under radial load is higher than reaction force Rp in order to guarantee equilibrium; Rp is the slide ring reaction acting on the piston and Q is the radial load applied at the free end of the rod. The free body diagram refers to static conditions (no inertial load) without friction. Unfortunately, as will be shown later, this reaction force is distributed on a small contact area along the contact surface between the rod and the guide bearing.

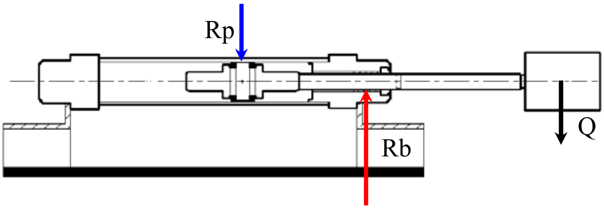

Figure 3: Rod - piston free body diagram.

To obtain better contact pressure distribution at the rod/guide bearing interface, two different guide bearing installations in the front head are proposed. Figure 4 shows a comparison of the original front head (Figure 4a) and the modified unit (Figure 4b). The original solution consists of a guide bearing (2) press-fit in the front head body (1); the modified versions are provided with a low stiffness mating support between the head body and the external surface of the guide bearing. This support is tapered, with the thicker side assembled on the internal part of the head so that the bearing can change orientation slightly to accommodate for rod deformation under load, which should occur while maintaining an acceptable rod angular misalignment. The first modified solution consists of a tapered support consisting of a homogeneous polymeric material having a Young's modulus of 450 MPa (E1) and a Poisson's ratio of 0.45. To make it possible to install the support, it was necessary to insert a spacer (4) beside the tapered support.

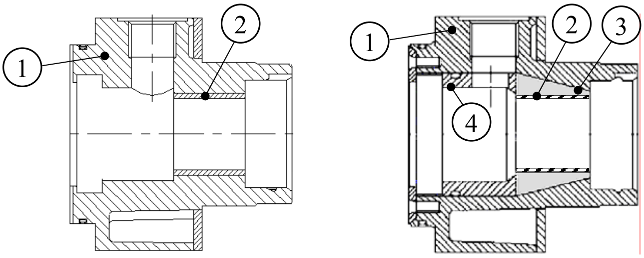

Figure 4: Original and modified front head.

The second solution features a tapered support consisting of two polymeric materials (bi-material version); in this case, the thinner conical part is made of polyurethane (Adiprene®, Young's modulus 200 MPa- E2). Figure 5 shows the three different analysed solutions: the commercial rod/guide bearing assembly (5a), the first modified solution provided with a single tapered support (5b), and the second modified solution provided with a double tapered support (5c). The ratio of the axial length of the polyurethane portion (L_2) to total bearing length (L) is 40%.

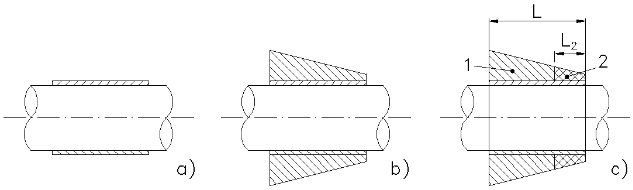

Figure 5: The analysed rod-bearing assembly.

The assembly sequence of the two modified configurations is shown in Figure 6, which depicts the head body (1), the tapered support (3) coupled to the guide bearing, the spacer (4) and the flange (5).

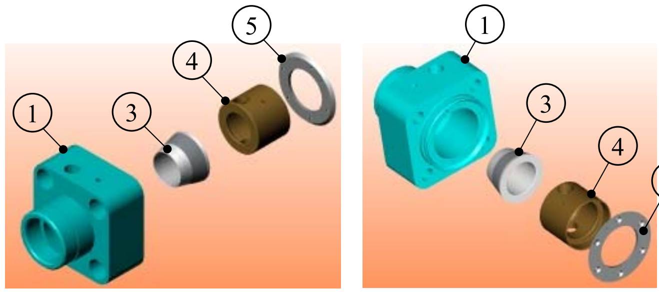

Figure 6: Assembly sequence for the modified configuration.

3 THE NUMERICAL MODEL

The distribution of contact forces at the sliding interface gives rise to wear phenomena that lead to actuator collapse as a result of the deterioration in rod seal and guide system operating conditions. The interface forces are clear from such consequences on the actuator as rod misalignment. Guide bearing wear measurements yield information about the performance of the actuator as a whole, but nothing about the local distribution of the forces exchanged at the interface. An analysis of this distribution could provide the foundation for optimising contact pressure patterns and thus increasing actuator life.

The guide bearing/rod system's structural behaviour was investigated through a numerical finite element analysis implemented using a commercial code (ANSYS Rel.11.0). The model represents the moving member of the actuator, coupled to the rod guide bearing housed in the cylinder front head.

A radial load of 100 N was applied to the free end of the rod, assembled horizontally. At the opposite end, a system of constraints was applied on the horizontal diameter so that the only degree of freedom is a rotation around a horizontal axis perpendicular to the rod axis, as can be seen in Figure 7. These constraints were produced by preventing the three independent translation movements. This reproduces the actual constraint on the cylinder's moving member (piston and rod) that results from assembling it in the cylinder bore. The constraint between piston and the cylinder bore, in fact, is a running fit produced by the piston slide ring which, with small angular displacements as the rod flexes, is low in stiffness.

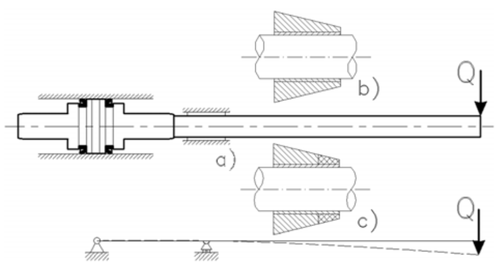

Figure 7: Load and constraint modelled by finite element method.

In turn, the rod is inserted in a guide bearing with a running fit that entails contact friction. As regards the constraints in the rod guide bearing, which is press-fit in the cylinder front head, all movements have been prevented at the seat-bearing interface, or in other words on the outer surface of the bearing.

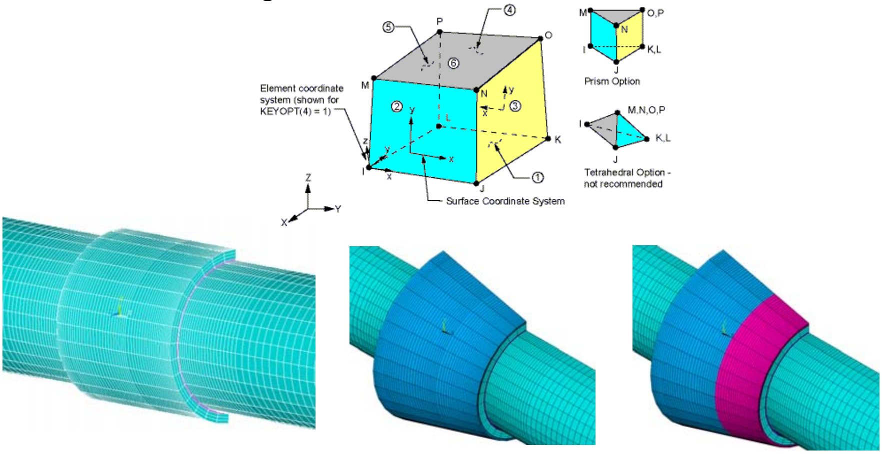

Figure 8: Detail of the bearing mesh.

Figure 8 shows details of the models of the bearing and rod assembly, which take advantage of the conditions of symmetry for the case in question. An increased mesh density is used at contact. The model was defined using SOLID 45 8-node hexahedral elements. Average element size is approximately 1.30 mm per side, while mesh density is increased in the area where the stress gradient is believed to be higher by using approximately 0.25 mm elements; a sensitivity analysis was conducted by using an increasingly fine discretization until the results were no longer sensitive to further increases in mesh density.

Contact between bearing and rod was modelled using surface-surface CONTACT 170 and TARGET 174 elements. As constraints and loads are geometrically symmetrical with respect to the vertical plane, only one half of the structure was modelled and constraints were applied to enforce the symmetry.

The bearing was modelled with a radial thickness of 0.25 mm of material consisting of a bronze alloy and PTFE, with a steel outer race having a radial thickness of 1.25mm. The presence of the PTFE film (whose thickness is in the order of a few µm) between the rod and bearing was taken into account through the contact elements' friction coefficient. Operation was modelled for the fully extended position.

Clearance is completely taken up at the bottom contact because of the downward-acting load applied at the end of the rod, while rod deflection along the length of the bearing does not take up the clearance at the top. This phenomenon was modelled by eliminating the contact elements at the upper interface.

4 FEM RESULTS

The analysis compared contact pressures along the lower generating line of the rod at the interface with the bearing. Contact pressure is plotted in the graph in Figure 9. The three curves refer to the three different solutions under study: the commercial unit and the two configurations provided with a tapered polymeric support around the front guide bearing. Analyses were carried out considering the cylinder rod completely extended in the outstroke position.

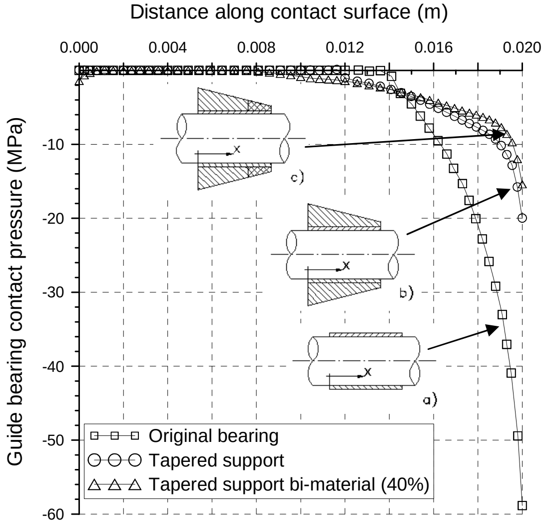

Figure 9: Contact pressure along the contact surface.

As can be seen, the contact pressure in the commercial solution a) is concentrated in a small portion of the contact surface near the outer extreme section of the guide bearing, where the contact pressure reaches its maximum. Most of the axial length of the bearing is not used to distribute contact pressure. A pattern of this kind is clear from such consequences on the actuator as bearing damage, rod misalignment and premature breakdown.

Configuration b), with a tapered support consisting of a single polymeric material, shows a different pattern, as peak contact pressure is lower than in the commercial case a). The contact pressure distribution is smoother and entails a better redistribution over the axial length.

Configuration c) refers to a tapered support consisting of two polymeric materials (bi-material); the contact pressure distribution pattern is similar to the previous case b). The pressure peak is lower than in the other cases, and a better redistribution over a longer axial length is achieved. As configurations b) and c) reduce peak pressure and redistribute contact pressure over a longer bearing axial length, they should provide more advantageous conditions in terms of wear and durability.

5 TEST RESULTS

Results are given below for tests carried out to evaluate front head bearing wear and rod travel distance to failure. Wear at the guide bearing versus displacement is shown in Figure 10 for the commercial cylinder, configuration a) and the modified solution with the tapered support, configuration b). Configuration b) shows a higher travel distance to failure than the commercial case a), while cylinders with the tapered polymeric support benefit from the more advantageous contact pressure with reduced peak pressure and better redistribution over the contact length on the front guide bearing.

As can be seen, maximum clearance at failure is very close to 1.0 - 1.2 mm. This limit is due to the fact that, in most cases, cylinders fail as a result of front head seal collapse: guide bearing wear leads to rod misalignment, whereupon operating fluid pressure and friction forces unseat and extrude the seal. For this reason, changes in sealing efficiency (leakage test) are sufficiently significant for purposes of cylinder life pred iction. Among the other param e-ters that might be taken into consideration in predicting failure, an important role seems to be played by measured bearing wear. In most cases, in fact, after the initial running-in phase and an intermediate phase with a low wear rate, w ear behaviour rises sharply to a m aximum level prior to reaching the travel distance to failure. This information could help in predicting cyl-inder service life.

Though meaningful for laboratory tests, the seali ng efficiency analysis is not feasible for systematic checks in service given the need for special equipment and long testing periods.

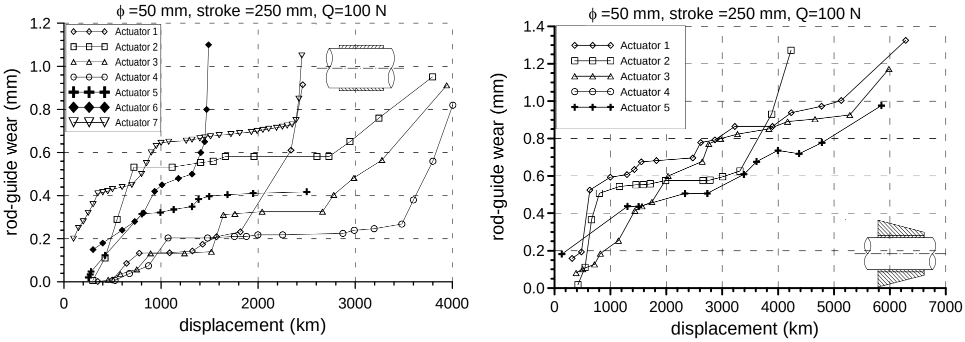

a) b)

Figure 10: Clearance at guide bearing versus displacement (configuration a) and b)).

Figure 11 shows wear at guide bearing versus increasi ng displacement for the new con-figuration c) provided w ith a tapered support m ade of two polym eric materials. Despite the low wear values, which would seem to indicate good performance, travel distance to failure is lower than that of the o riginal solution a). Consequently, this design shows the worst per-formance of the three configurations under study.

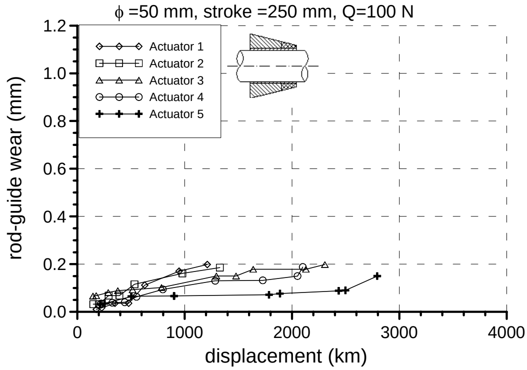

Figure 11: Clearance at guide bearing versus displacement (configuration c)).

Figure (12) shows rod travel distance to failure for the th ree cylinder groups under test; groups of at least 5 cylinders were considere d. Differences in perform ance from the stand-point of cylinder service life can be readily observed. To su mmarize the results obtained, av-erage service life values are shown in Figure 13. Cylinders in configuration b), whose front head is provided with a tapered support consisting of a single material, show the best performance. Solution b), in fact, shows significant improvement in terms of service life, which is nearly double that of the original configuration a).

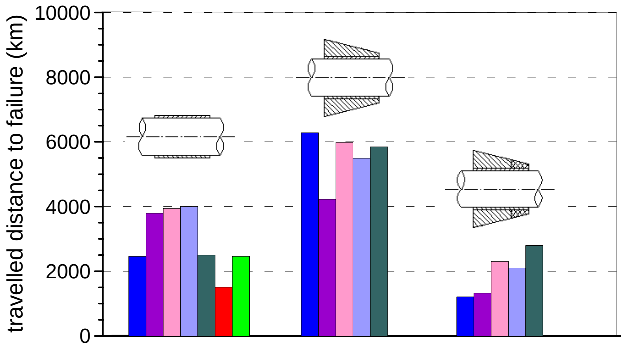

Figure 12: Travel distance to failure.

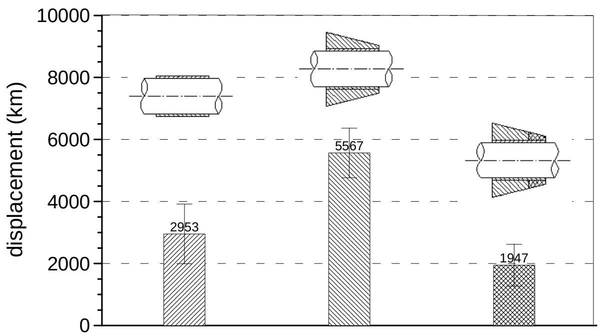

Figure 13: Travel distance to failure.

6 CONCLUSIONS

The paper investigated pneumatic linear actuator service life when significant radial loads are acting on the cylinder rod. In particular, the rod/guide bearing interaction was found to be fundamental in defining performance and actuator travel distance to failure. For this purpose, contact pressure distribution at the sliding interface was analysed starting from the commercial configuration since, in this configuration, most of the axial length of the bearing is not used to distribute contact pressure: the contact pressure is concentrated in a small portion of the contact surface near the outer extreme section of the guide bearing. To improve cylinder performance, new solutions consisting of different front rod guide bearing mounting designs were proposed in order to redistribute pressure at the rod/guide interface, thus improving performance and cylinder service life. New cylinders with the front head provided with a tapered support consisting of a single material show the best performance. This new configuration provided significant improvement in terms of service life, with durability values about twice those of the commercial configuration.

ACKNOWLEDGEMENTS

This work was funded by MIUR, the Italian Ministry of Education, Universities and Research.

REFERENCES

[1] G. Belforte, T. Raparelli, L. Mazza. Analysis of Typical Component Failure Situations for Pneumatic Cylinders Under Load, Lubrication Engineering STLE, vol. 48 nº 11, 840-845, 1992.

[2] G. Belforte, A. Manuello Bertetto, S. Liu, L. Mazza. Wear and Failure Analysis in Pneumatic Cylinders Under Radial Load. Proceedings of the 11th Int. Sealing Conference, Dresden, Germany, May 3-4, 1999.

[3] D.S. Evans. Condition Monitoring of Industrial Fluid Power Systems using Programmable Controllers. Proceedings of the Int. Conf. On Recent Advances in Mechatronics, ICRAM'95, Istanbul, Turkey, August, 1995.

[4] D.S. Evans. Inference Mechanism Applied to On-line Electro-Pneumatic Fault Detection and Diagnosis. Dissertation, Mechatronics 98, 1998.

[5] N.P. Barykin, F.A. Sadykov, I.R. Aslanian. Wear and failure of babbit bushes in steam turbine sliding bearings, *Journal of Materials Engineering and Performance*, vol. 1 n° 1, 110-115, 2000.

[6] V.K. Nikolaev, V.A. Domoratsky,. Bronze-Teflon bearing of glide for exploitation in conditions of a see environment. *Friction and Wear (Trenie i Iznos) International Scientific Journal*, vol. 22, n° 2, 180-185, 2001.

[7] M. Mosleh, N. Sakab, N.P. Suhb. A mechanism of high friction in dry sliding bearings, *Wear*, vol. 252, n°1-2, 1-8, 2002.

[8] G. Belforte, A. Manuello, L. Mazza. Life prediction of guide bearings for linear pneumatic actuators. Proceedings of the 2nd European Conf. on Tribology ECOTRIB 2009, Pisa, Italy, June 7-10, 2009.

[9] A. Manuello, L. Mazza, Contact analysis and wear in two pneumatic reciprocating seals, *Int. Journal of Mech. and Control*, vol. 1, n° 1, 43-49, 2000.

[10] G. Belforte, A. Manuello, M. Conte, L. Mazza, C. Visconte, Experimental and numerical evaluation of contact pressure in pneumatic seals, *Tribology International*, vol. 42, 169-175, 2009.

Proceedings of MUSME 2011, the International Symposium
on Multibody Systems and Mechatronics
Valencia, Spain, 25-28 October 2011

CONTROL SYSTEM AND DATA ACQUISITION FOR A RECIPROCATING COMPRESSORS FRICTION TEST STAND

Luigi Mazza, Andrea Trivella, Roberto Grassi

Department of Mechanics-Politecnico di Torino
Corso Duca degli Abruzzi, 24.
10129 Torino, Italy
roberto.grassi@polito.it

Keywords: Friction, linear motor, life test, data acquisition, compressor.

Abstract. *The paper presents an innovative test bench conceived for friction measurements in piston sealing and guide rings for reciprocating compressors. After a short introduction concerning the problematic the test bench is designed for, we will focus on the mechatronic aspects of the design in order to achieve a safe operational mode even during long lasting unmanned tests. The working principles and the construction techniques will be described with particular attention to the guidance system of the moving elements and to the friction force measurement system. Preliminary test results on a sample of guide ring will also be shown.*

INTRODUCTION

Mechanical design is now more involved in the aspects of eco sustainability in order to minimize the emission of pollutants and to reduce energetic consumption. Reciprocating compressors are an interesting application where eco-sustainable design can lead to encouraging results. By using innovative low friction materials it is possible to develop new families of compressor able to reach high energetic efficiency even without using lubricants. To achieve the goal it is vital to accurately design the sliding elements, develop testing rigs to evaluate the performance of the new components and/or the new materials.

The state of the art concerning the study about contact characteristics, friction and wear in the cylinders between sealing, guide rings and barrel is full of applications. In some of the cases the study was carried out using specific case samples, in other cases specific testing machines were designed to investigate and measure the real component.

In [1] the behaviour of guide ring – barrel contact is investigated with respect to the advantages obtained by the use of Laser Surface Texturing on the external surface of the ring. The test was conducted using samples which consist in a section of the ring (40° arc). An electric driven crank system provides reciprocating motion. The results showed a reduction of the friction about 25% with respect to an identical ring without texturing.

In [2] is shown a test rig to evaluate wear phenomena between the piston ring and its housing on a piston from an hydraulic motor. Wear has been estimated from the mass reduction of the ring itself, from contact surface shape variations and from the roughness. Moreover the effects on the wear behaviour of some characteristic dimensions of the housing has been taken into account.

In [3] the effects of lubrication on friction wear in the contact between piston and barrel of a diesel engine cylinder were studied. Annular guide rings and a flat testing surface to simulate the barrel were used. Tests were conducted with a standard test bench according to the ASTM normatives. It allowed to measure the friction force and the wear under several pressure and temperature conditions and with different kinds of lubricants.

In [4] the wear of guide rings and sealings for reciprocating compressors was studied. The rings were manufactured in PTFE with different additives: carbon, molybdenum disulphide, bronze and ceramic. Samples were tested in controlled environment (O2 atmosphere, air and noble gas) and without lubrication. The test rig is a reciprocating compressor on which sensors and instruments were applied for the purpose.

In [5] are represented the studies conducted to evaluate the friction coefficient and the wear on sealing rings from refrigerator gas compressors. Test were conducted without lubrication by using a "pin–on-disk" standard test bench. The "pin", manufactured in steel, represent the ring while the DLC (Diamond-Like Carbon) coated steel disk represents the barrel. Tests were conducted in controlled atmosphere and the results are shown in function of the type of cooling gas which was used for the test.

In [6] a study for measuring the friction force in automotive engine guide rings. The test rig was obtained by modifying one of the four cylinders of a commercial engine and setting instrumentation on it. The barrel was modified to float axially then was connected to the frame with load cells. Said cells act as a support for the barrel and measure the friction force exchanged with the piston.During operation the cylinder is never pressurized. Tests can also be

conducted at different temperatures by heating the barrel with an electric resistance. Friction is studied in function of the lubrication for different position of the piston in the barrel.
This paper presents an innovative test bench conceived for friction measurements in piston sealing and guide rings for reciprocating compressors. The stand is designed in order to simulate the typical operating conditions for a compressor in order to evaluate the behaviour of the rings in terms of friction force and wear. The bench is powered with a modern technology consisting in a couple of linear motors, propelling units able to reach excellent acceleration and speed performance. Such an extreme performance is needed to reach the operating values typical of a reciprocating piston compressor; the choice over that kind of motion was also due to the necessity of variating the parameters of the motion profile in order to perform life endurance tests. The working principles and the construction techniques will be described with particular attention to the guidance system of the moving elements and to the friction force measurement system. First test results on a sample of guide ring will be presented.

1 DESCRIPTION OF THE TEST BENCH

The test rig visible in figure 1 whose sketch design is in figure 2 consists in a linear motor (1) which carries a custom designed piston (2) which can house samples obtained from guide sealing rings (3) shaped as a circumference arc. The motor drives the piston across a barrel (4) from a commercial compressor.

The barrel is supported by a rigid plate (5) suspended on an air bearing system (6) with negligible friction. The air bearing system guides the barrel-plate group across the direction of the friction force which is obviously the axis of the barrel itself. The mentioned force is then measured with a load cell (7) which connect the barrel-plate group to the frame (8).

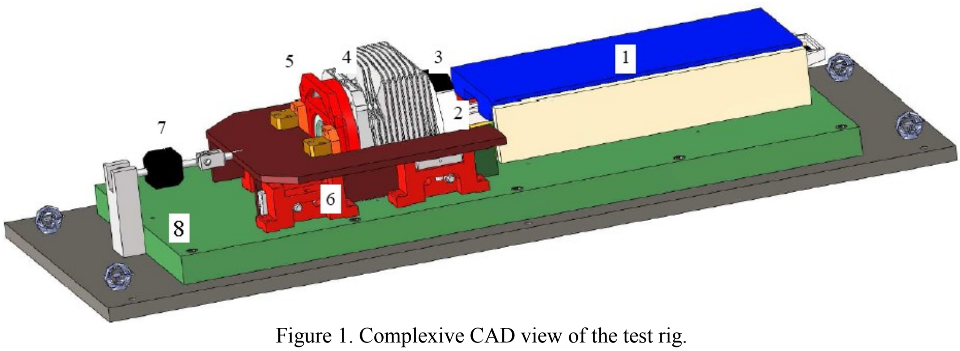

Figure 1. Complexive CAD view of the test rig.

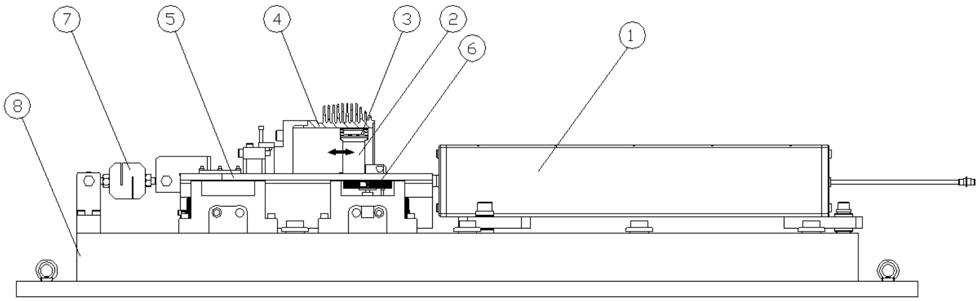

Figure 2 : Schematic view of the test rig.

The friction force generated in the contact between ring samples and barrel is transmitted to the load cell and therefore measured. The piston was designed to press radially the sample against the barrel internal surface to simulate the load applied on the sealing rings and reproduce the contact pressure between ring and barrel.

The bench is powered with a modern technology consisting in a couple of linear motors which are the core of the actuator (1). It is designed to reach the operating speed of a reciprocating piston compressor which ranges up to 5 m/s and implies accelerations higher than 25 times the gravity. .Figure 3a shows the test rig while a close view of the barrel under test is in figure 3b.

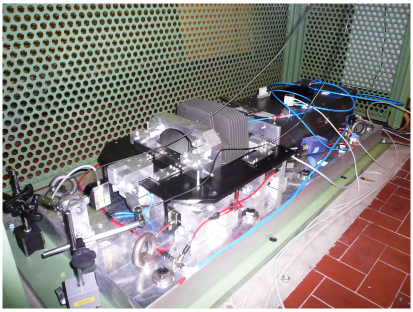

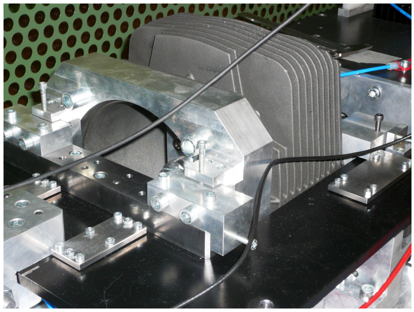

Figure 3a : The test rig Figure 3b : Particular of the barrel

The test rig is designed to perform tribological measurements during which the friction characteristics are evaluated referring to specific ring samples. The test bench in its actual configuration is designed for operating with compressor piston rings but the implements can easily be changed to reconfigure the apparatus for other sealing systems or friction testing purposes.

2 ACTUATION AND POWER TRANSFER

The linear actuator used in the application is able to exert a peak force of 1.370 N and a continuative thrust of 490N, supported by a series of pneumatic bearings with a tolerance under 20 micrometers, can reach a peak speed value of 5 m/s in a stroke of 100 mm with accelerations ranging up to 250 m/s^2.

Such extreme performance and the small cycle time require a particular driver consisting in two DSPs running at 800 MHz which automates the whole functionalities. Programmed in a subset of the ANSI C language it drives a set of IGBT switching modules which provide the necessary 3 phase currents to the motor coils drawing power from a 600 V DC bus. The DC bus can output a maximum of 40 A in sustained mode with peaks ranging to 80A by discharging the regenerative capacitors which will recover the kinetic energy during deceleration. Regenerative DC bus is vital to contain energy consumption when the motion profile implies cyclic acceleration/deceleration. The driver itself provides open loop protection against coil overheating by recording the integrative value of the motor current taken into account the thermal characteristics of the mounting. This feature, with appropriate control, closes the loop into the main program cycle by introducing time delays between the runs in order to let the motor cool down before a new starts. It then performs a real time adaptation which allows to minimize the pauses between the cycles and increase productivity during life tests.

3 PERFORMANCE ASSESSMENT

Figure 4 shows a typical trapezoidal profile obtained during a test. One motor was powered during this experiment and the piston accelerated at 150 m/s^2 and reached a target speed of 3,5 m/s (red line), the motion was completed in 100 mm while the motor reached its maximum peak current of 20 A (yellow line).

The motion profile must reproduce the characteristics encountered in modern reciprocating compressors which range up to 5 m/s. To achieve such speed in the same stroke lengths of a compressor it is necessary to accelerate at more than 20 g.

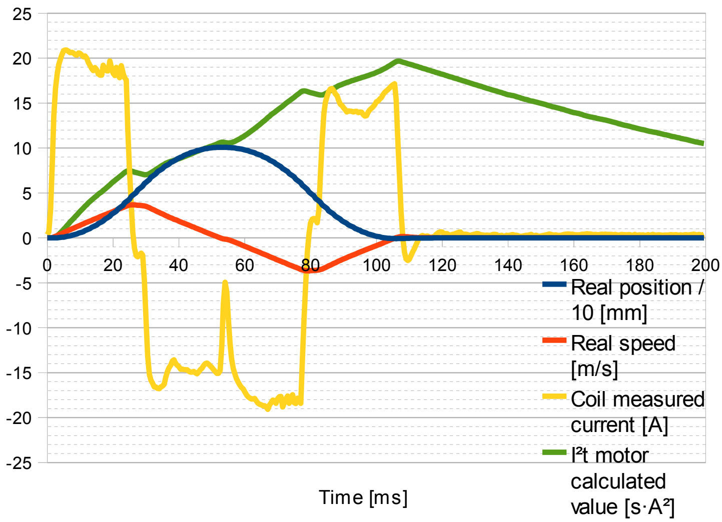

Figure 4 : Motion profile acquired during a test.

By using a trapezoidal velocity profile it is possible to reach and hold the target speed for a stroke of 10 .. 15 mm to allow the correct friction force measurement during one stroke. The system allows to accelerate at 250 m/s2 in its definitive configuration with both the motors coupled. The driver allows also to perform tests with only one motor for refining the control parameters and when the tuning is complete both motors are put together and controlled in a gantry strategy with software limitations of the interaction force between the two.

4 SAFETY ISSUES

The linear actuation relies on pneumatic bearing which is the only technology able to reach such speed with low energy consumption by avoiding friction. The pneumatic bearing system requires uninterruptable filtered air supply which is ensured by a pneumatic accumulator and strictly monitored from the actuator program.

An UPS ensure the same level of protection on the electric side by keeping the 24V control power line free from electrical power down. Every aspect is monitored by the control software which performs different behaviours on reaction to the possible power failures. Figure 4 shows the structure of the safety and control hardware where M1 and M2 represent the couple of motors to be controlled.

The power line (400 VAC) enters the electronic rack through an RF filter to suppress high frequency disturbances which arises from the driver and is interrupted by the main safety relay which is directly driven by the electronics.

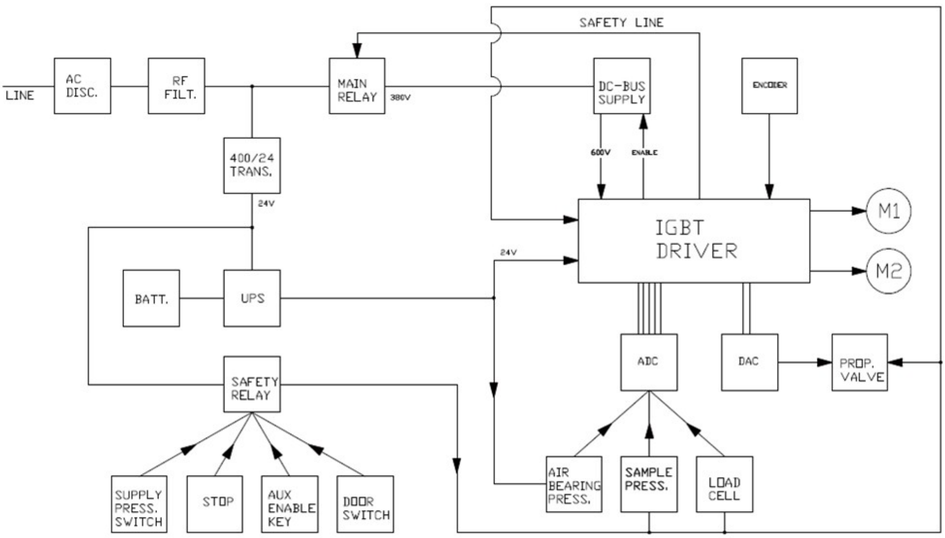

Figure 5 : Functional blocks of the control hardware.

The safety relay enables the main AC to be sent to the HVDC converter which provides the 600 V DC bus to supply the power section of the driver. A 24 V transformer provide low voltage to the safety lines and the auxiliaries such as signal conditioners then the 24 V current is sent through the UPS to power the logic of the IGBT driver. This solution ensures automatic back up of the supply to the electronics which will be able to activate the braking also in defect of the main power.

The auxiliary supply line is controlled by user key switch and hardware safeties prevent unauthorized start-up when the air pressure from the pneumatic circuit is too low.

In the meanwhile a secondary pressure sensor is directly connected to the driver logic in order to ensure a faster intervention in the case of a pneumatic failure which would lead to a loss in the supply pressure of the air bearings. High performance pressure sensors with a dynamic of 5000 Hz are used for this purpose in order to be able to detect a pressure fall before it goes under a safe value even during a cycle (intervention time of some ms).

Unmanned 24/7 operation is the target which will soon be achieved for testing the operational life of compressor components.

5 FORCE MEASUREMENTS

The measurement of the friction force is demanded to the load cell which is subjected to the only force coming from the piston, the test rig is aligned and the plane containing the pneumatic bearings is kept perfectly horizontal with a tolerance of 1/1000 slope.

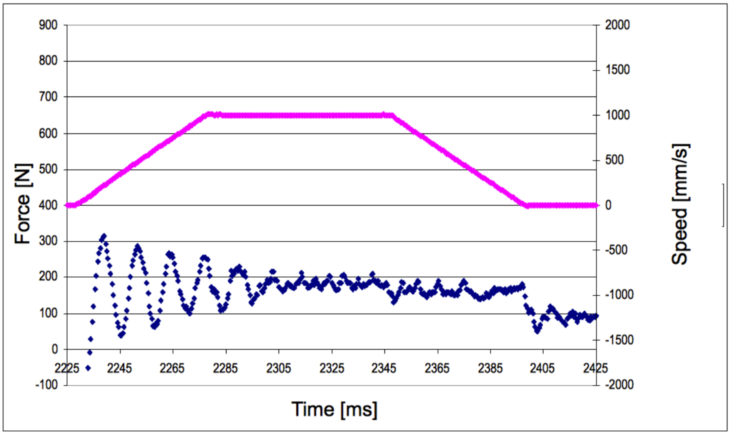

Figure 6 : Acquired friction force

Figure 6 shows a typical results of force and velocity signals acquired during the motion with the use of the conventional load cell.

The typical spring-mass behaviour of the measure chain is noticeable and shows the exact representation of the influence of the measure chain on the measurement itself. The force signal oscillates around an average value with a sinusoidal behaviour at a frequency of approximately 80 Hz. It is due to the oscillation of the barrel (ca 25 kg mass) supported by a frictionless bearing and connected to the frame with an inadequately stiff load cell. The measurement

is in this case feasible because the frictional decay leads the sinusoidal component to vanish some milliseconds after the target speed has been reached. Two solutions have been adopted, proved the acceptance of a ballistic measurement during the data processing the force signal has been averaged considering the data when the speed was in range. A second solution is to identify the sequence of at least four minimum and maximum of oscillation and extract the estimated friction coefficient from the decay. The first method is the one actually in use for processing the data coming from the preliminary tests.
Different setups of the force measurement chain have been designed in order to gain the best performance. Originally the system was designed to operate with a conventional strain gauge load cell for performing friction force measurements while the cell would have been substituted with an iron bar for performing wear analysis and life tests. This choice is due to the fact that using a conventional load cell for life measurements is useless because the huge amount of data gathered would never be processed and on the other side a fatigue load cell would have proved to be not accurate enough for a friction force measurement.
The conventional load cell is installed on the machine at the moment. The iron bar will then be equipped with a simple set of strain gauges in order to have a cheap recording of an average force value even during longlasting tests for monitoring purposes.
The results of a first session performed on a polymeric sample with the speed not exceeding 4 m/s is then shown in figure 7. The values have been averaged and a final value of the friction force could be obtained. The tests were conducted at different pressure levels under the membrane and it is all resumed in the figure. The validity of the acquired data has been then verified by evaluating a conventional friction coefficient. The acquired friction force has been compared with the product of the pressure under the membrane and the ideal measure of the contact surface. The values obtained confirm that the friction coefficient value is coherent with the characteristic data of these polymers. As visible in figure 8 the friction coefficient varies with the speed with a tendency which approximates the Stribeck law and remains stable with the pressure.

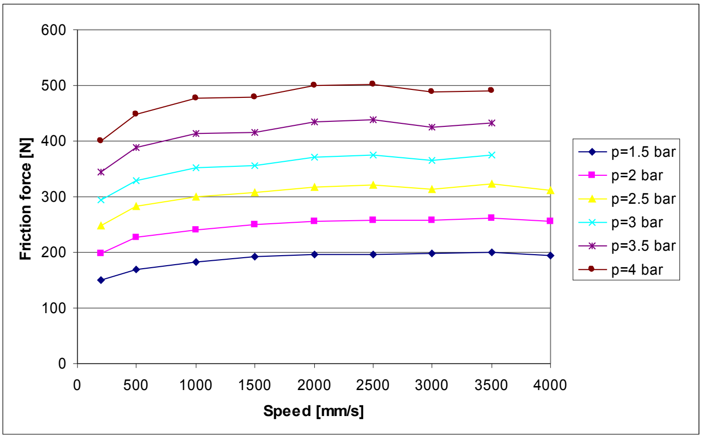

Figure 7 : Acquired friction force.

During the construction a third measurement system was taken in consideration, based on a piezoelectric load cell and a charge amplifier. This product allows to reach an extremely higher stiffness with respect to a strain gauge system with the same accuracy and appears to be a valid alternative which will improve the dynamic of the whole measure chain.

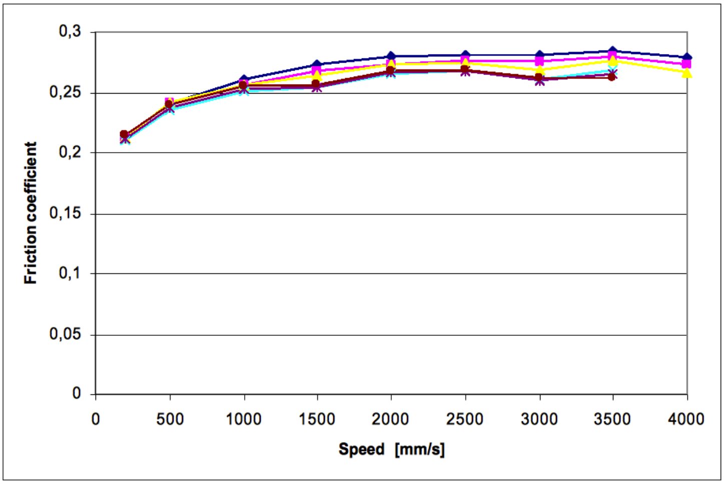

Figure 8 : Evaluated friction coefficient.

6 CONCLUSIONS

The test rig which has been presented in the paper is the response to the need of performing tribological measurements during which the friction characteristics are evaluated referring to specific ring samples. The test bench operates with compressor piston rings but the implements can easily be changed to reconfigure the apparatus for other testing purposes. The stand described in this paper can simulate the typical operating conditions for a compressor and is used to evaluate the behaviour of the rings in terms of friction force and wear. The effectiveness of using electric linear motors has been proved and it will lead to an innovative class of friction force measurements at high speed which tends to be more close to the industrial needs.

The set up campaign of the control hardware led to the assessment of the most of the initial specifications. The control is proved to be able to run the motor at 4 m/s with a tolerance in speed generation less than 5 % taken into account the overshoot while any ripple and/or inaccuracy in the motion profile stays adequately below this value after the transitory has ended. The effective acceleration obtained during the tests is above the specification: 260 m/s^2 have been proved to be reachable but for safety reasons the motor will not run exceeding the initial specifications.

Particular care was given to measuring sensors and security aspects, the unit can perform unmanned 24/7 operation and can react to events like electrical power failures by automatically restarting the testing cycle after the restoration. The dynamic issues in force measurement have proved to be noticeable and their effect will be minimized with the installation of an higher class piezoelectric load cell which will increase the natural frequency of the measuring side of more than an order of magnitude.

The first assessment campaign proved the reliability of the whole system even if affected by dynamic problems. The repeatablity of the measure has been verified for speeds not exceeding 4 m/s by testing a statistically accepted number of samples and verifying that the dispersion of the measurement data is acceptable. The data analysis was performed by averaging the force value after the transitory.

Next steps will lead to the assessment of the measure chain for target speed by introducing the ballistic measurement and conditioning the data taking into account the dynamic of the measure chain itself. Accuracy calculations and error spreading evaluation will therefore be necessary because the influence of new parameters such as mass and stiffness will have to be taken into account.

The expected result will be a testing machine able to perform pure linear friction measurements directly on a portion of a piston ring in operative conditions at speeds only reachable with Pin on Disc and similar technologies with high repeatability.

It will also be equipped with a standard holder for high speed friction and wear testing on flat samples on an interchangeable counterpart.

ACKNOWLEDGEMENTS

This paper refers to a comprehensive research project named ISECOMP funded by Regione Piemonte aimed to evaluate the environmental issues concerned with the use of low friction materials in air compression.

REFERENCES

[1] G. Ryk, I. Etsion. Testing piston rings with partial laser surface texturing for friction reduction. Wear 261 (2006) 792–796.

[2] U.I. Sjodin, U.L.-O. Olofsson. Experimental study of wear interaction between piston ring and piston groove in a radial piston hydraulic motor. Wear 257 (2004) 1281–1287.

[3] J.J. Truhan, J.Qu, P.Blau. A test rig to measure friction and wear of heavy duty diesel engine piston rings and cylinder liners using realistic lubricants. Tribology International 38 (2005), 211-218.

[4] By Dr Chris Radcliffe – Hoerbiger Rings & Packings Ltd. Sealing material developments for reciprocating gas compressors. Sealing Technology November 2005, 7-11.

[5] J.D.B. De Mello, R. Binder, N.G. Demas, A.A. Polycarpou. Effect of the actual environment present in hermetic compressors on the tribological behaviour of a Si-rich multifunctional DLC coating. Wear 267 (2009) 907–915.

[6] Sung-Woo Cho, Sang-Min Choi, Choong-Sik Bae. Frictional modes of barrel shaped piston rings under flooded lubrication. Tribology International 33 (2000) 545–551.

Proceedings of MUSME 2011, the International Symposium
on Multibody Systems and Mechatronics
Valencia, Spain, 25-28 October 2011

A HYDRAULIC SHAKE TABLE FOR VIBRATION TESTING: MODEL PARAMETERS ESTIMATION AND VALIDATION

Giandomenico Di Massa, Stefano Pagano, Salvatore Strano, Francesco Timpone

Department of Mechanics and Energetics – University of Naples "Federico II", Italy
e-mails: gdimassa@unina.it, pagano@unina.it, salvatore.strano@unina.it, francesco.timpone@unina.it

Keywords: electro-hydraulic actuator model, parameters identification, shake table.

Abstract. *This paper presents the study of a test rig, with electro-hydraulic actuation, adopted to characterize vibration isolators (vibration absorbers for machineries, seismic isolators, etc.). The machine was designed primarily to characterize elastomeric seismic isolators in order to find their hysteretic response under periodic deformations and to give its mathematical expression by means of the Bouc-Wen model. The test rig can also be used as a vibrating table in order to simulate horizontal ground motions and to characterize the dynamic behavior of small isolated systems, sensitive to accelerations. An application could be the study of electric cabinets or statues subject to seismic accelerations. In the first application the motion of the shake table of the rig is contrasted by the insulators restoring force; in the second case the actions derive from the relative motion between the shake table itself and the suspended body; in both cases the control system must guarantee the desired motion of the shake table or the desired force acting on it. The goal of the paper is to present a mathematical model of the electro-hydraulic actuation necessary to develop an accurate control system. The model parameters have been obtained using an iterative optimization technique starting from experimental data. The proposed method can be also used in many systems hydraulically actuated, whereby the identification of several parameters, is required to study the system dynamics.*

1 INTRODUCTION

Passive isolators are used to reduce the horizontal acceleration transmissibility. They consist of elements that dissipate energy and prevent system from the dangerous conditions of resonance. These insulators are characterized by means of experimental tests during which they are periodically deformed in the horizontal direction while a constant vertical load is applied. Through these tests it is possible to deduce the force-displacement cycle, and subsequently derive the parameters of the Bouc-Wen hysteretic model that allows to describe the cycle analytically. Due to the relatively low frequency required for seismic testing, servohydraulic (electro-hydraulic) shakers are generally used with a control system to guarantee the shake table to follow the desired displacement law; for this purpose it is necessary to develop an accurate dynamic model of the actuation system. Moreover the knowledge of this model is important for other purposes, like, for example, the preliminary simulation testing or the simulations performed to modify the machine components, etc.

The electro-hydraulic actuation system moving the shake table is characterized by an high power/mass ratio and a fast response [1] but, as well-known, it exhibits a significant nonlinear behavior due to the flow/pressure characteristics, variations in the trapped fluid volume due to piston motion and fluid compressibility. Moreover, other factors, such as flow forces and their effects on the spool position and friction could contribute to the nonlinear behavior of the system [4]; these nonlinearities make the mathematical model more complex.

In the following, a mathematical model of the actuation system is described; then the procedure adopted to identify the system parameters and the correspondent results are reported; finally, starting from the estimated parameters, the model validation is performed.

2 TEST RIG DESCRIPTION

The main parts of the test rig are reported in Fig. (1) and Fig. (2); it consists of a fixed base, a hydraulic actuator moving a shake table (plant size of 1800x1590 mm) on linear guides with recirculating ball-bearing. On the shake table, the bottom side of the DUT (device under test) is fixed, while the upper end of the device is connected to the vertical slide that can (vertically) translate with respect to the contrasting structure.

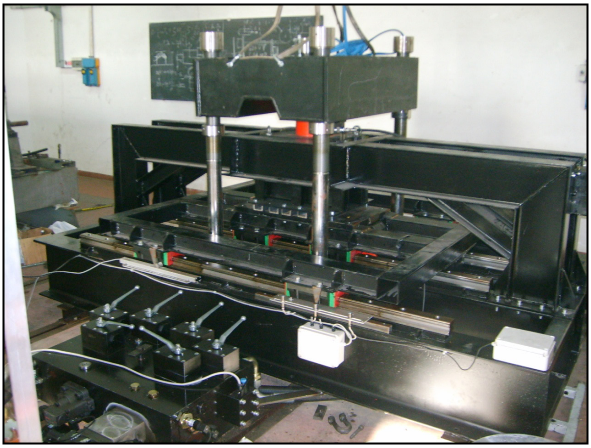

Figure 1 – Test rig

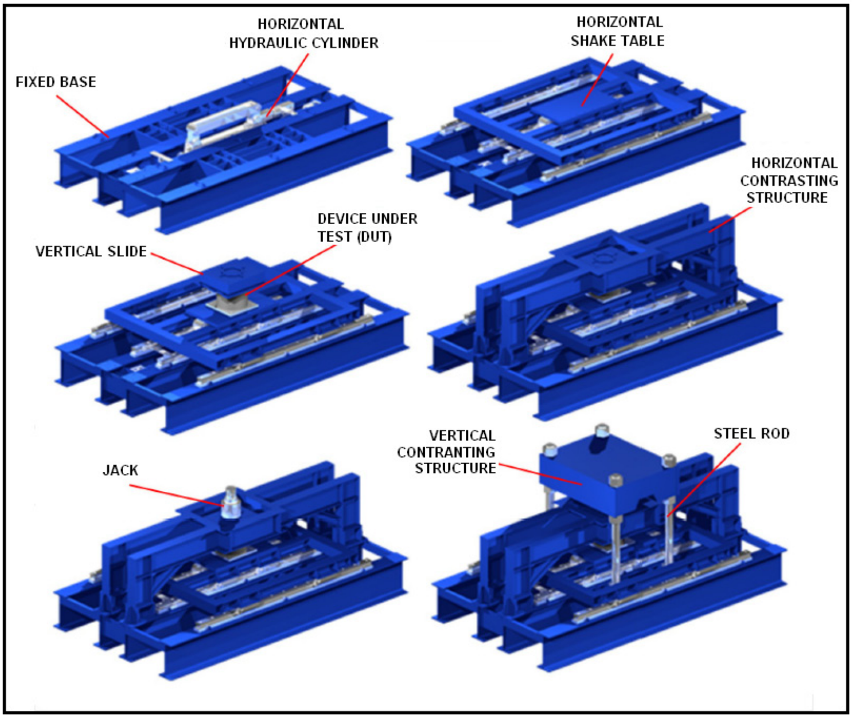

Figure 2 – Test rig components

The vertical hydraulic jack exerts a force (max 850 kN) on the vertical slide, which in turn exerts a compression effort to the DUT. The contrasting structure absorbs the jack force and transmits it to the base trough four steel rods.

The main parts of the hydraulic power unit depicted in Fig. (3) consists of an axial volumetric piston pump powered by a 57 kW electric motor. The pump is characterized by a variable displacement in the range 70-140 cm^3, a maximum pressure of 210 bar and the maximum flowrate equal to 313 l/min. Downstream of the pump there is a pressure relief valve.

The other three main parts of the hydraulic circuit are the four way-three positions proportional valve, the flow distribution system (that will be described in detail below) and the hydraulic cylinder.

The horizontal hydraulic cylinder is constituted by a cylindrical barrel divided into two equal parts by a diaphragm; inside each part there is a piston whose rod is connected to the fixed base; so, the actuator has a mobile barrel and fixed pistons. In Fig. (4) are also highlighted the four feeding chambers (1A, 2A, 1B, 2B) that are supplied through holes drilled along the axis of the rods.

The flow distribution system allows to have a large operation field. In fact, through a system of six three-way valves and two servo-valves it is possible to have different power configurations . The horizontal force can vary in the range of 50-190kN and the maximum speed in the range of 0.5-2.2m/s; the maximum stroke is 400mm (± 200mm) and it's possible to assign a harmonic motion with maximum frequency of 10Hz.

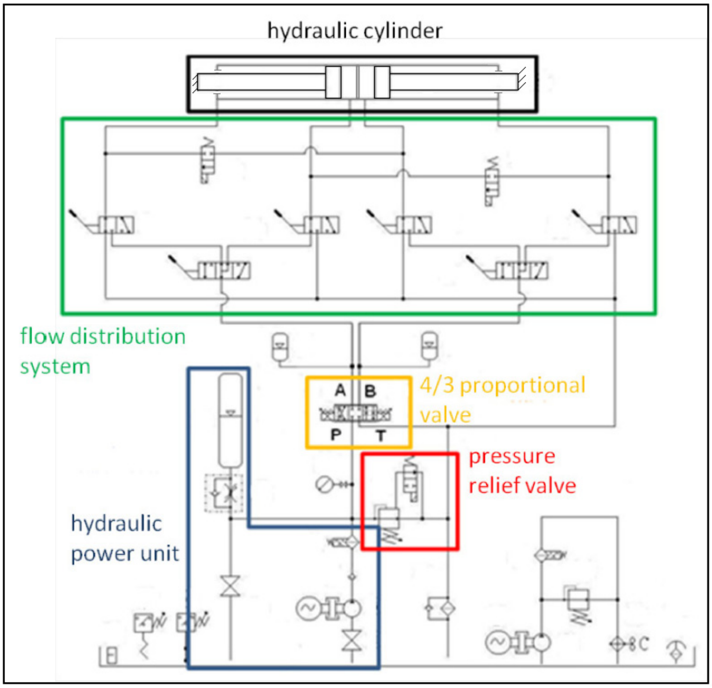

Figure 3 – Hydraulic circuit

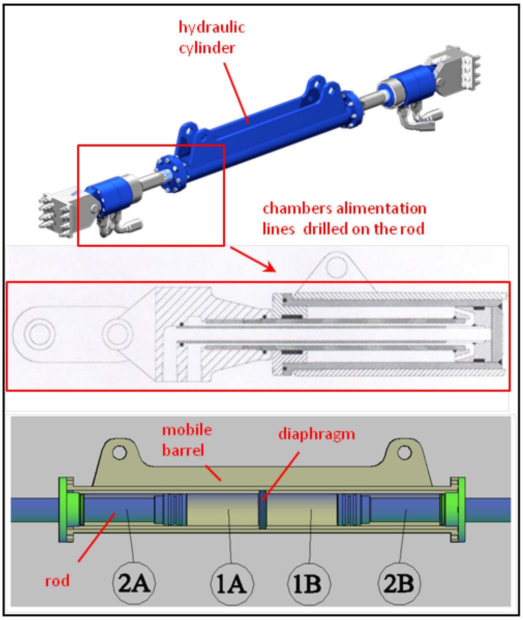

Figure 4 – Hydraulic cylinder details

With reference to the sketch of Fig. (4), it is possible to choose one of the following power configurations:

a) 1A + 2B (or 1B +2 A): condition of maximum load and minimum speed;
b) 2A + 1A (or 1B +2 B): condition of minimum load and maximum speed;
c) 1A (or 1B): intermediate state;
d) 2A (or 2B): intermediate state.

The position of the horizontal shake table and the force exerted by the actuator on it are detected by a position sensor and a load cell respectively, placed between the shake table and the actuator, according to the sketch in Fig. (5). In the same figure it is shown that the force couple ($F \cdot h$) acting on the whole system (hydraulic cylinder + shake table), caused by the action of the cylinder and the reaction of the DUT, is balanced by the vertical reactions of the linear guides ($R \cdot d$).

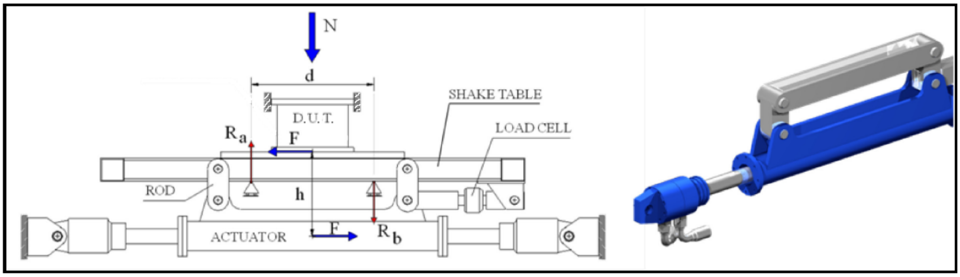

Figure 5 – Reaction forces of the linear guides

As depicted in Fig. (6), disassembling the two contrasting structures, including the four steel rods and the hydraulic jack, the machine can also be used as a vibrating mono-axial shake table, in order to simulate horizontal ground motions and to allow the experimental study of small isolated systems, sensitive to accelerations.

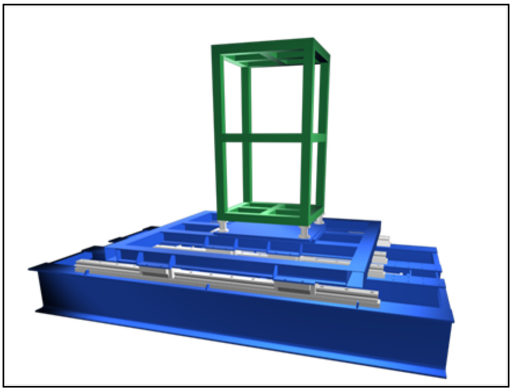

Figure 6 – A light suspended structure on the shake table

3 THE MATHEMATICAL MODEL

The mathematical model of the actuation system is referred to the power configuration 1A+2B (or, equivalently, 1B+2A) as indicated in Fig. (7).

Moreover the model regards only the shake table movements without the force exerted by the DUT or the actions due to a suspended mass (Fig. (8)).

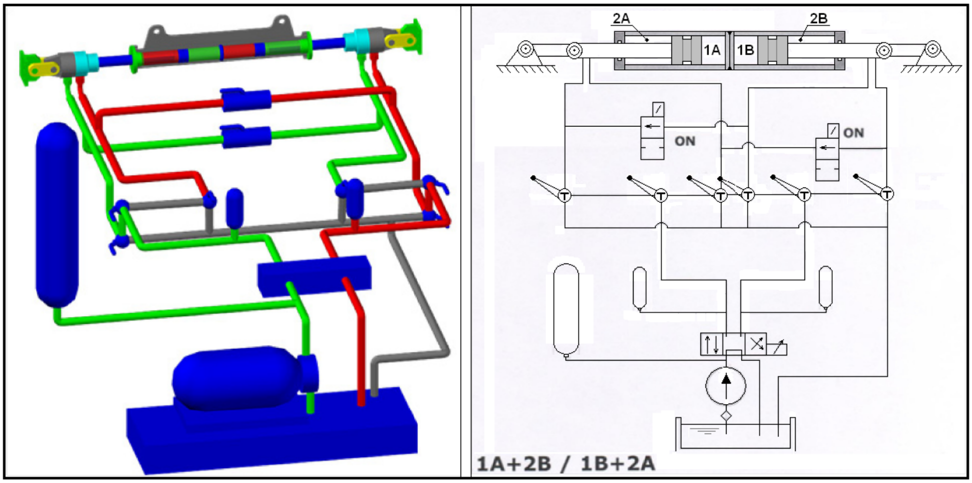

Figure 7 – Selected power configuration,
in the right figure green and red colors indicate parts of the circuit
connected with the pump and the tank respectively

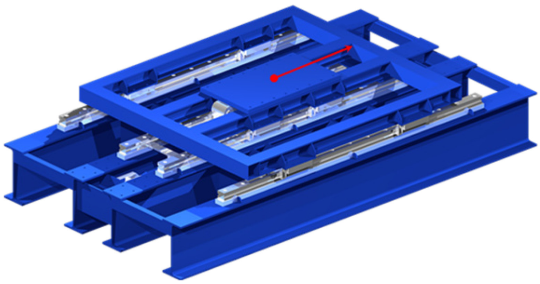

Figure 8 – Shake table without external force

In order to write the mathematical model of the hydraulic circuit, the following hypothesis have been done: a) fluid properties not depending on the temperature; b) equal piston areas for each sides; c) equal oil volume for each side; d) the presence of the accumulators is neglected.

Furthermore the shake table is modeled as a one DOF system on which act the actuation force and the friction forces. In particular the actuator can be modeled as a double-ended hydraulic cylinder driven by a four-way spool valve. As reported in Fig. (9) the actual cylinder was replaced with a cylinder with fixed barrel and mobile piston with load area equal to the equivalent area obtained with the actual flow distribution system depicted in Fig. (7).

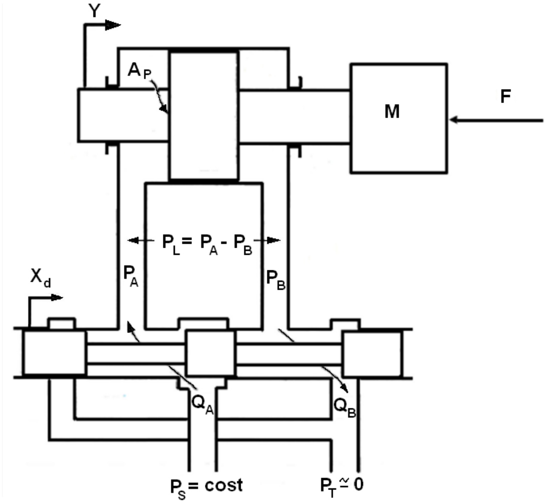

Figure 9 – Schematic of hydraulic actuator adopted for the mathematical model

The differential equations governing the hydraulic actuation system dynamics are given in [1]. The control pressure dynamics is given by:

$$\frac{V_0}{2\beta}\dot{P}_L = -A_p\dot{y} + Q_L, \tag{1}$$

where:
- $P_L = P_A - P_B$ is the load pressure;
- $V_0 = V_A = V_B$ is the oil volume contained between the piston and the valve in each side for the particular case of the centered piston position;
- A_p is the equivalent piston area;
- $Q_L = (Q_A + Q_B)/2$, commonly called *load flow*, represents the average flows in the two lines;
- β is the effective Bulk modulus;
- y is the piston displacement.

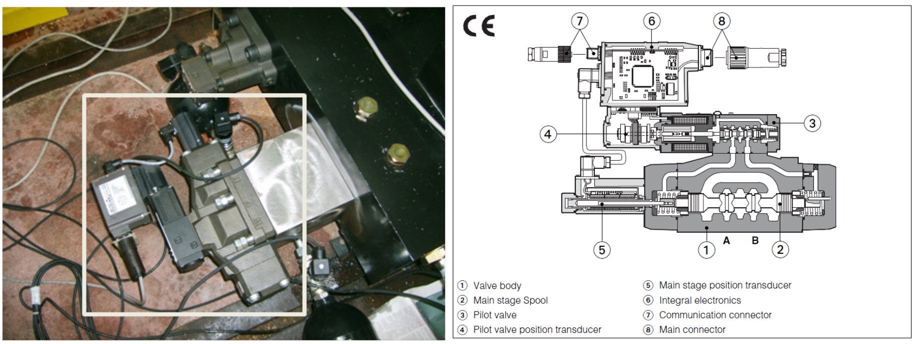

Figure 10 – Four-way valve

Analyzing the datasheet of the valve (ATOS, mod. DPZ0-LE-370-L540 - Fig. (10)) and using the results of the study of the actuator dynamics reported in [1] it's possible to write the load flow as follows:

$$Q_L = \frac{f(v_e)}{\sqrt{2\Delta P_{rif}}}\sqrt{P_s - sign(v_e)P_L}\ , \tag{2}$$

where P_s is the supply pressure that we assume constant and regulated by the pressure relief valve, ΔP_{rif} is the valve reference pressure drop, v_e is the spool position signal from the main stage of the valve that is proportional to the spool position x_d, reported in Fig. (9); finally $f(v_e)$ is the maximum flow that passes through the valve at the reference pressure drop and has the follow expression:

$$f(v_e) = k_q v_e\ , \tag{3}$$

where k_q is the slope of the linear function reported in Fig. (11).

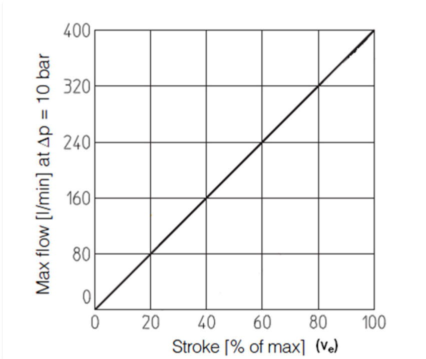

Figure 11 – flow-tension characteristic at the reference pressure drop

The following two relationships must be considered in order to relate v_e with the valve input tension u_c:

- the first one is the relationship between u_c and v_c that is the effective valve command tension regulating by the integral electronic driver of the valve:

$$v_c = \begin{cases} k_{ep}u_c + v_{e0} & if \quad u_c \geq 0 \\ k_{en}u_c + v_{e0} & if \quad u_c < 0 \end{cases}, \tag{4}$$

  where v_{e0}, k_{ep} and k_{en} are parameters that allow to model the bias, positive scale, negative scale regulation respectively as indicated in Fig. (12).

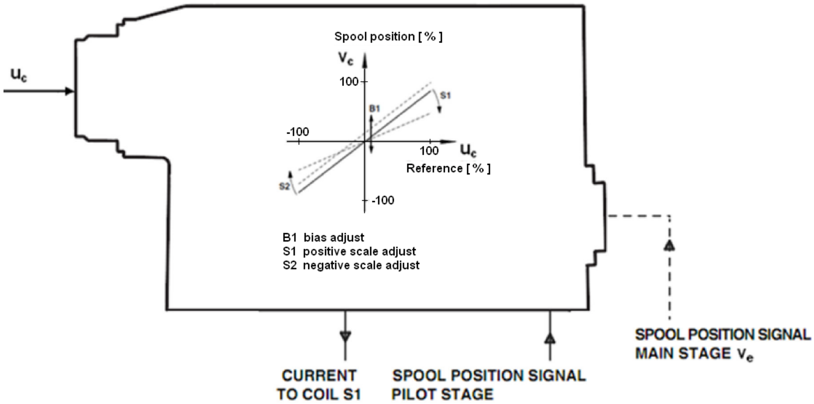

Figure 12 – Analog electronic driver integrated to the valve

- the second relationships describes the dynamics of the valve (Fig. (13)):

$$\frac{\ddot{v}_e}{\omega_{nv}^2} + \frac{2\xi_v}{\omega_{nv}}\dot{v}_e + v_e = v_c\,, \tag{5}$$

where parameters ω_{nv} and ξ_v are the natural frequency and damping ratio of the servo-valve, respectively.

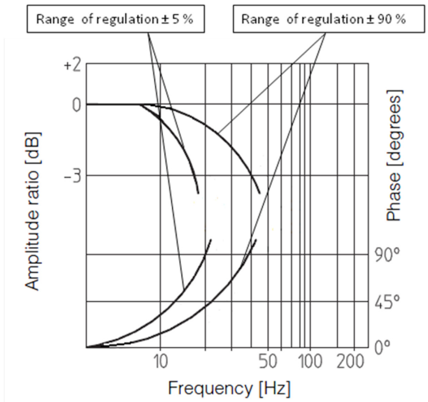

Figure 13 – Bode diagrams of the valve

Differently from the diagrams reported in Fig. (13), the parameters ω_{nv} and ξ_v have been considered not depending on the regulation value.

The preliminary experimental tests executed with the same u_c law at different supply pressure (Fig. (14)) have shown that the real expression of $f(v_e)$ isn't linear as indicated in the datasheet, but it is described by a non symmetric law with respect to v_e and it presents a dead zone.

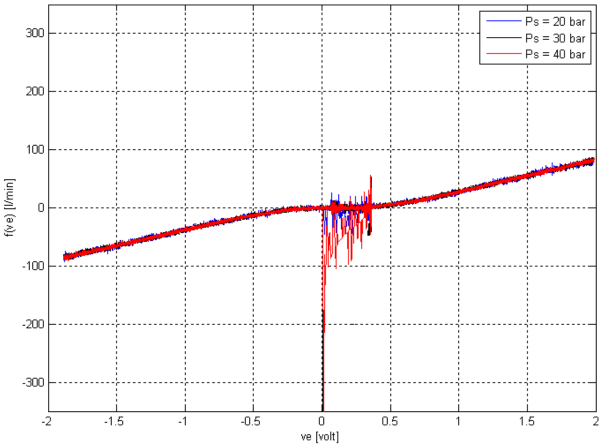

Figure 14 – Experimental flow-tension characteristic at the reference pressure drop

For this reason Eq. (3) was substituted by the following relationship:

$$f(v_e) = \begin{cases} k_{qn}(v_e - v_{en}) & if \quad v_e < v_{en} \\ 0 & if \quad v_{en} \le v_e \le v_{ep} \\ k_{qp}(v_e - v_{ep}) & if \quad v_e > v_{ep} \end{cases}, \tag{6}$$

where v_{en} and v_{ep} are the limits of the dead zone, and k_{qn} and k_{qp} are the adopted gains if v_e is negative or positive respectively.

The equation of motion of the shake table is:

$$m_{tot}\ddot{y} + \mu mg\,\mathrm{sgn}(\dot{y}) + F_{hyd} = A_p P_L, \tag{7}$$

being m_{tot} the total mass including the mass of the shake table, the hydraulic cylinder, the oil and the mechanical connections between actuator and moving table, while mg is the weight acting on the guides. The second term of the Eq. (7) represent the friction force due to linear guides, so μ is the friction coefficient, while F_{hyd} is the total force resistance in the hydraulic circuit.

In the literature friction in hydraulic actuators is often described using nonlinear velocity dependent models; for example, in [3] the friction is described by an exponential Stribeck friction model, in [4] the friction model includes Karnopp stick-slip model and the Stribeck effect. The friction model adopted in this paper is constituted by a viscous term, proportional to the velocity, and a coulombian term, that has the following form:

$$F_{hyd} = \sigma\dot{y} + F_c\,\mathrm{sgn}(\dot{y}) \tag{8}$$

where σ is the viscous coefficient and F_c is the coulombian term.

Finally the equations governing the dynamics of the whole system (shake table + electro-hydraulic actuator) are:

$$\begin{cases} m_{tot}\ddot{y} + (\mu mg + F_c)\operatorname{sgn}(\dot{y}) + \sigma\dot{y} = A_p P_L \\ \dfrac{V_0}{2\beta}\dot{P}_L = -A_p\dot{y} + Q_L \\ Q_L = \dfrac{f(v_e)}{\sqrt{2\Delta P_{rif}}}\sqrt{P_s - sign(v_e)P_L} \\ \ddot{v}_e = -\omega_{nv}^2 v_e - 2\xi_v\omega_{nv}\dot{v}_e + \omega_{nv}^2 v_c \end{cases} \quad . \tag{9}$$

Eq. (9) completely describe the classical fifth order nonlinear dynamics of electro-hydraulic system.

In order to check if this model captures the key components of the system dynamics, a detailed Matlab/Simulink model was developed; the same model was used for the parameter estimation using experimental data as it will be shown in the next section.

4 PARAMETERS ESTIMATION

Experimental tests have been carried out in order to identify the model parameters.

As indicated in Fig. (15) in our system it's possible to acquire the follow signals: pressure in *A, B, P* and *T* (Fig. (3)), valve spool position v_e, the displacement of the shake table y and the force that the hydraulic cylinder transmits to the table (Fig. (5)).

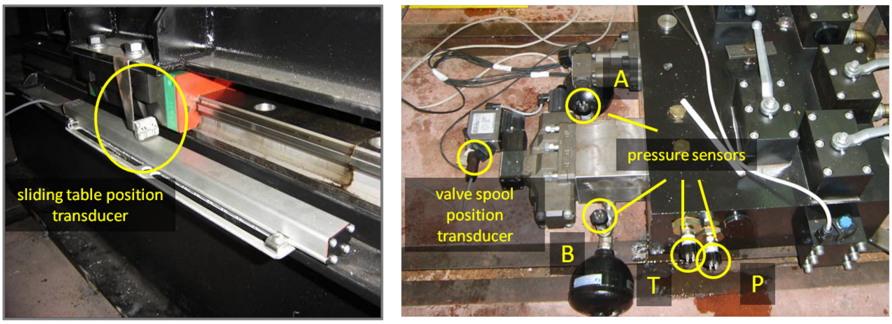

Figure 15 – Test rig sensors

The identification procedure is based on the minimization of the least square error between experimental data and the simulated ones. In particular the minimization has been done with respect to three types of experimental data referred to different state space variables of the model: v_e, y and P_L.

For the identification algorithm we have chosen as input data the tension imposed to the valve u_c that is the variable that the operator can assign to the system together with the reference pressure value of the pressure relief valve P_s. Concerning the experimental output data, we have chosen v_e in order to identify the dynamics of the flow control valve, y for the identification of all the parameters governing the displacements of the shake table and, finally, P_L is used in order to estimate the global force resistance law due to the hydraulic circuit and other friction resistance in the linear guides.

In order to estimate the dynamics of the system with a reference continuously variable input, a triangular type signal for the valve tension input u_c was chosen; moreover the tests was conducted for different value of P_s. Fig. (16) shows a typical set of experimental input and output data.

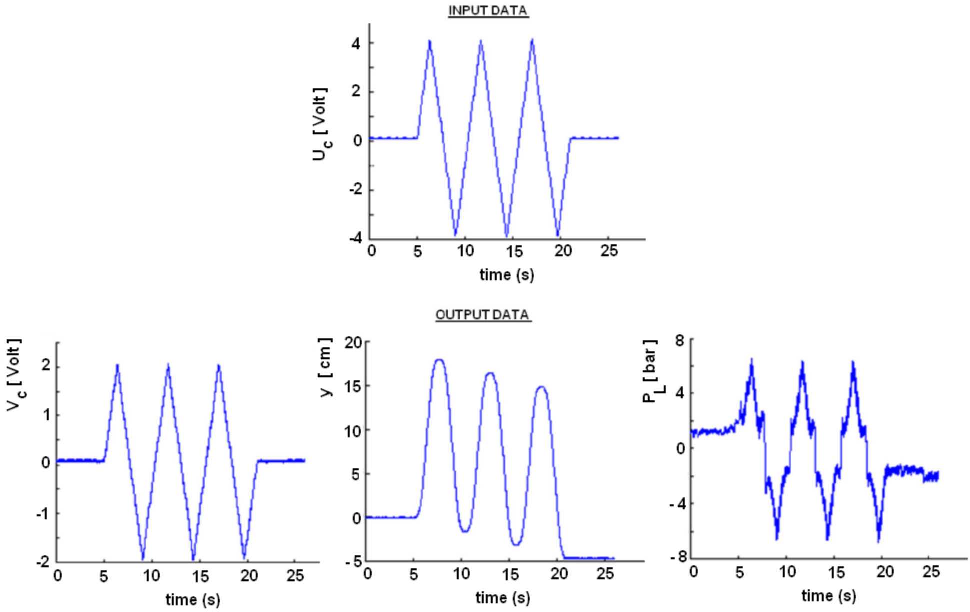

Figure 16 – Input and output experimental data used in the identification procedure

In Fig. (17), a sketch of the parameters estimation procedure, is reported.

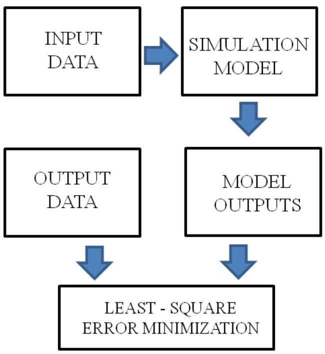

Figure 17 – Identification procedure

Referring to Fig. (17), the procedure consists in giving the input data to the model and to perform a minimization of the least share error between the measured time histories of the quantities v_e, y and P_L and the simulation ones.

The algorithm was implemented in Matlab/Simulink environment and the comparison between experimental and simulated data (gray and blue lines respectively), for different inputs, are reported in Fig. (18).

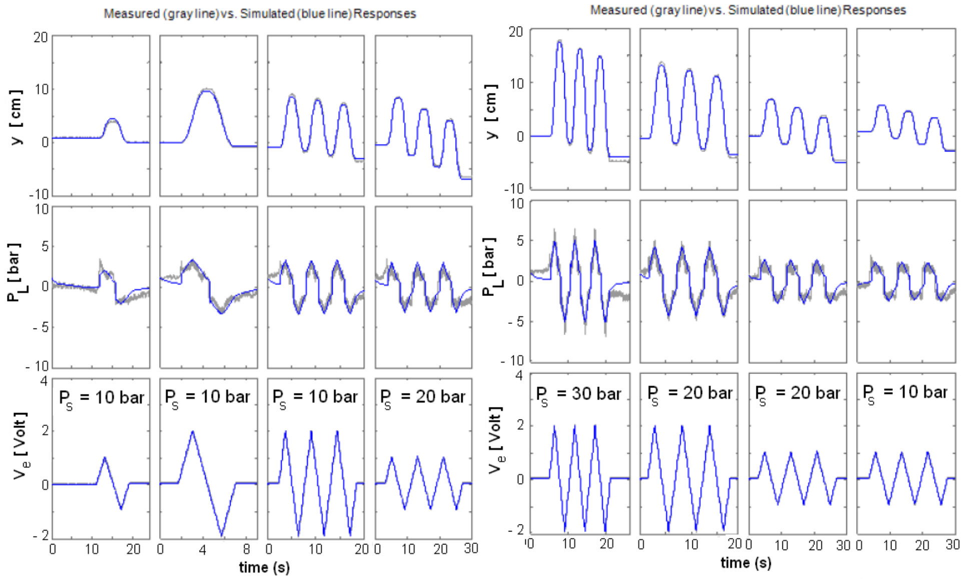

Figure 18 – Identification results

The experimental and simulated responses are very close each other; only if v_e assumes small values it's possible to note some discordances, in particular for P_L signals. These differences are due to the simplified model of the flow control valve: in fact when the tension input is close to zero there are leakages that determines a little variation of the load pressure P_L not previewed in the model. Moreover the differences between simulation and experimental results are due to other unmodeled effects such as the variation of oil properties with temperature, losses in the numerous elbows and fittings in the oil passages. In table 1 the values of the estimated parameters are reported.

Estimated parameter	A_p	μ	v_{e0}	F_c	$k_{en}=k_{ep}$ $=k_e$	V_0	β	ξ_v	k_{qn}	k_{qp}	m	m_{tot}	σ	v_{en}	v_{ep}	ω_{nv}
Value	0.01	0.11	0.01	971.76	0.49	0.004	9.96E+07	0.92	49.71	52.05	402.01	441.32	23555	-0.21	0.43	152.30
Unit	m^2	-	V	N	-	m^3	Pa	-	$l\ min^{-1}\ V^{-1}$	$l\ min^{-1}\ V^{-1}$	kg	kg	$N\ s\ m^{-1}$	V	V	$rad\ s^{-1}$

Table 1 – Estimated parameters

5 MODEL VALIDATION

Adopting the estimated parameters same simulations were performed for different sets of input data; the results were compared with the experimental ones obtained with the same input data. In particular for the model validation the tests were performed for a fixed value of P_s (40 bar) and u_c time histories of square and sinusoidal shape. Some results are reported in Fig. (19).

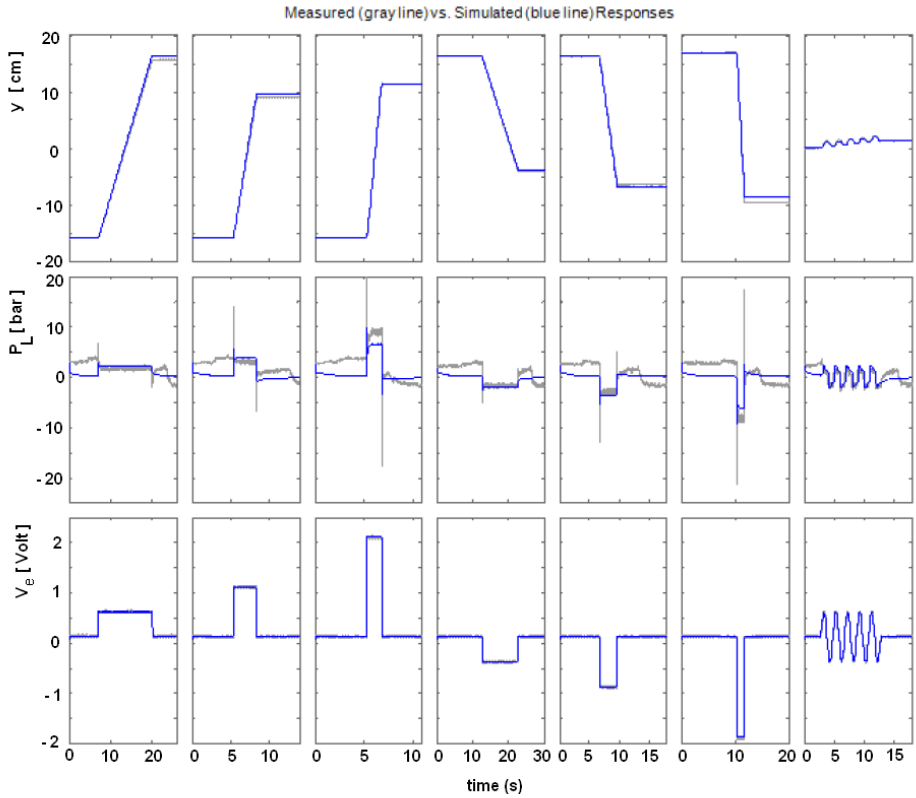

Figure 19 – Validation results

Even these further tests show a good accordance between experimental data and the simulated ones except for small values of v_e. From both Fig. (18) and Fig. (19) it's possible to note an asymmetric behavior of the shake table for symmetric tension input; to identify this asymmetric behavior a non linear valve flow-tension law was adopted (Eq. (6)). The model allows to predict the actual motion of the shake table and so it can be used in order to develop an open loop displacement control or a feedforward action for a closed loop controller.

6 CONCLUSIONS

A procedure that permits to identify the main parameters of a hydraulically actuated system model, starting from some measurements, has been presented. The above procedure gives results in good accordance with the experimental ones in terms of shake table position and force resistance estimation. Furthermore, the model is able to characterize the servovalve behavior well even without the direct measure of the valve flows.

The results can be used for controller design. In particular it is possible to develop a force feedback control or a position feedback control based on specific application. This model could be used to test different control strategies in simulation environment and moreover to predict the system response in the case of mechanical, hydraulic or electrical components modification.

REFERENCES

[1] Merritt, H. E. (1967). *Hydraulic control systems*. New York: Wiley.

[2] D. Maneetham, N. Afzulpurkar. Modeling, Simulation and control of high speed nonlinear hydraulic servo system. *World Journal of Modelling and Simulation*, vol. 6, nº 1, pp. 27-39, 2010.

[3] L. Márton, S. Fodor, N. Sepehri. A practical method for friction identification in hydraulic actuators, *Mechatronics,* vol. 21, pp. 350-356, 2011

[4] A. Alleyne and R. Liu. A simplified approach to force control for electro-hydraulic systems. *Control Eng. Pract.*, vol. 8, p.1347 , 2000.

Proceedings of MUSME 2011, the International Symposium
on Multibody Systems and Mechatronics
Valencia, Spain, 25-28 October 2011

AN EXPERIMENTAL VALIDATION OF COLLISION FREE TRAJECTORIES FOR PARALLEL MANIPULATORS

G. Carbone [1], F. Gómez-Bravo [2], O. Selvi [3]

[1]LARM: Laboratory of Robotics and Mechantronics, University of Cassino,
e-mail: carbone@unicas.it,
web page: http://webuser.unicas.it/weblarm/larmindex.htm

[2]Escuela Politécnica Superior, Universidad de Huelva,
e-mail: fernando.gomez@diesia.uhu.es

[3]Izmir Institute of Technology
e-mail: ozgunselvi@iyte.edu.tr

Keywords: Collision free trajectories, Trajectory validation, Parallel Manipulators Motion Planning.

Abstract. *This paper addresses the generation of collision free trajectories in presence of obstacles for parallel manipulators having less than six d.o.f.s (degrees of freedom). In particular, a systematic approach is proposed for validating the trajectories generated by a motion planning method in presence of obstacles. The proposed planning algorithm is based on combining a quick random search algorithm together with an optimization method that aims to obtain shorter paths that are as far as possible from obstacles. The proposed systematic validation approach is based on a probabilistic method that includes Kalman filtering of experimental data. Experimental tests have been carried out by operating a CaPaMan (Cassino Parallel Manipulator) prototype at LARM in Cassino. Results are reported and discussed to show the feasibility and effectiveness of the proposed approach to generate and validate suitable collision free trajectories for parallel manipulators.*

1 INTRODUCTION

Autonomous precise manipulation among obstacles is a great challenge and represents a valuable tool for numerous tasks. For instance, surgical robot applications will benefit from the development of manipulators capable of avoiding collision with different elements involved in surgery, [1]. Considerable research activity has been carried out in order to obtain optimal paths with serial robots and the corresponding literature is very rich, as shown for example in [2-13]. For example, in [2] Lin at al. have proposed a procedure to determine a cubic polynomial joint trajectory through an algorithm for minimizing the travelling time subject to physical constraints on joint velocities, accelerations and jerks. In [3] Shin and Mckay have presented a solution to the problem of minimizing the power consumption of moving a serial robotic manipulator along a specified end-effector path subject to input torque/force constraints, by taking into account the dynamics of the manipulator. Similarly, attempts have been made to address the path planning of robots having parallel architecture, [14-18]. Nevertheless, it is still missing a systematic approach to generate optimal collision free trajectories for parallel manipulators with less than 6 d.o.f.s. In fact, these types of manipulators have a very narrow workspace. Additionally, there might be singularities within the workspaces that are not reachable or must be carefully avoided due to control problems, [19, 20].

This paper proposes a systematic approach for validating the trajectories generated by a motion planning method that provides collision free optimal trajectories for parallel robots having less than 6 d.o.f.s in presence of obstacles. The proposed planning algorithm is based on combining a quick random search algorithm together with an optimisation method that aims to obtain shortest paths that are as far as possible from obstacles as preliminary reported in [21]. Then, in this paper a systematic validation approach is proposed as based on a probabilistic method. In fact, usually values of the most outstanding variables are not directly available and it is necessary to estimate them from the data provided by the sensors. But, sensors and/or the input signal are affected by a significant uncertainty so that deterministic techniques do not provide enough tools to estimate the system state [22]. Therefore, it is necessary to use probabilistic approaches. Several probabilistic methods have been developed to cope with these problems as described for example in [23-30]. The most known techniques are the Kalman Filter (KF) [23], [24], [25] and the Extended Kalman Filter (EKF) [26]. The KF provides an optimal estimation of the system state, but only when linear systems and Gaussian noises are involved [23]. For non-linear systems, the EKF can be used, which approximates the system by its first order linearization [26].

In this paper, a general collision free motion planning is described as reported in section 2. Section 3 reports a case of study of the proposed path planning procedure to obtain collision free optimal trajectories for the parallel manipulator CaPaMan (Cassino Parallel Manipulator) that has been designed and built at LARM: Laboratory of Robotics and Mechatronics in Cassino as described for example in [31-34]. Then, the computed collision free optimal trajectories for CaPaMan need to be experimentally validated. For this purpose, section 4 describes a systematic approach for validating the computed trajectories as based on a suitable Kalman filtering. Section 5 describes the experimental set-up and tests that have been carried out by operating CaPaMan parallel manipulator. Experimental data have been processed by means of the proposed systematic approach. Finally, theoretical and experimental data are compared. Results are reported and discussed to show the feasibility and effectiveness of the proposed approach to generate and validate suitable collision free trajectories for parallel manipulators.

2 COLLISION FREE MOTION PLANNING

A systematic approach for computing collision free optimal trajectories for parallel robots needs to take into account different aspects such as presence, size and shape of obstacles; number of degrees of freedom that can be controlled at same time; movable ranges, maximum reachable velocities, acceleration, jerks; control speed (clock rate); safety issues. This approach focus attention on obtaining collision free trajectories, attending to optimise the length and the distance to the obstacles accomplishing the constraints imposed by the mechanical characteristics of the manipulator.

The solution addressed in this paper is based on the assumption that the manipulator will evolve in a known scenario. The task of the robot will be specified as a set of configurations (the task configurations T.C.s) that the tool carried by the manipulator has to reach (one should define position and orientation of a target). Additionally, the scenario will be described as a set of obstacles distributed along the Cartesian work space of the robot. Then, the proposed approach is based on searching for collision free trajectories in the Joint Space Ω. The dimension of Ω will be equal to the manipulator d.o.f.s. For this purpose, the collision free sub-space ($\Omega_f \in < \Omega$), i.e. the set of configurations in which no collision exist, has to be determined. Thus, the planning method has to provide a sequence of joint configurations (a joint path) Ξ, accomplishing $\Xi \in \Omega_f$.

This procedure can be suitable, for instance, for surgery applications where the scenario (the patient and the surgical instrument positions) can be defined before to the operation. Then, no changes in the obstacles distribution are expected and optimal motion is desired. If that is the case, the task configurations would represent different points over the patient that the tool, carried by the manipulator, would have to reach in order to perform any surgical task. Then, considering the inverse kinematics model, the T.C.s are turned to a set of Task-Points (T.P.s) in the joint space that the manipulator has to reach. After that, a controller will make the manipulator joints follow the joint path so that the robot accomplishes the predefined task. The flow-chart in Fig.1 illustrates the above-mentioned general procedure.

The first step of the proposed technique involves generating the joint matrix Θ that contains information about the regions of the joint space that will not present collision with the obstacles of the scenario (i.e. Ω_f). Then, the information on collisions is transferred from the Cartesian to the joint space. At first, the proposed algorithm uses a mechanism for collision detection based on a discrete description of the Cartesian space and manipulator geometry. The manipulator is described by means of a set of prisms defined by surfaces and edges. At a later time, points regularly spaced will represent those edges and surfaces (the *cluster points* C_p). In this way, the manipulator will get defined by a spotted set of C_p each of whom will have three Cartesian coordinates. At same time, a grid matrix for the Cartesian space (the *Cartesian matrix* Ψ) is defined. Each element of this matrix represents a portion of the space, whose value is defined according to

$$\Psi_{ijk} = \Psi([x, y, z]) = \begin{cases} 1 \;\; if \;\; [x, y, z] \text{ is occupied by an obstacle} \\ 0 \;\; \text{otherwise} \end{cases} \tag{1}$$

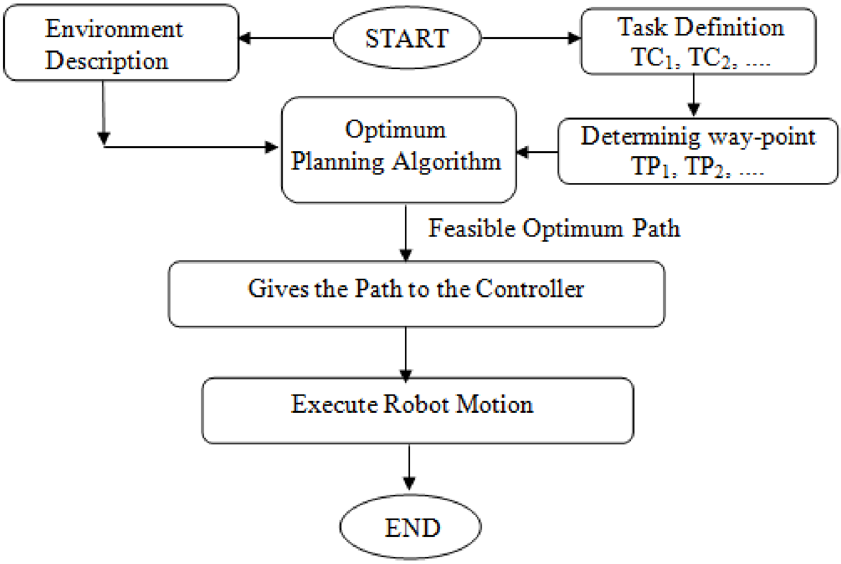

Fig. 1. Flow chart of the general planning /control approach.

Given a manipulator's configuration, Ξ_h, the collisions detection can be performed by applying the equations of the direct kinematics to each one of the C_p. Using these equations, it is possible to know the Cartesian clusters's positions at the joint configuration Ξ_h (${}^hC_p[x,y,z]$). Then, the following free collision configuration condition can be derived:

Collision free configuration condition. - Let a manipulator be geometrically defined by k cluster points C_p, let Ξ_h be a point of a ε-grid representation of the manipulator's joint space Ω, and Ψ the Cartesian matrix of the manipulator's environment. Then, Ξ_h accomplishes $\Xi_h \in \Omega_f$ if and only if

$$\sum_{l=1}^{k} \Psi\left({}^hC_p[x,y,z]_l\right) = 0 \qquad (2)$$

The collision detection can be implemented by checking the cells of the Cartesian matrix associated to each of the robot cluster position. From (2), if only one ${}^hC_p$ is located in an occupied area, it means that this configuration present a collision. Thus, it is possible to use Ψ to determine Θ. An iterative algorithm has been implemented, testing each configuration against collision. The flow-chart in Fig.2 illustrates the above-mentioned steps.

Once the joint matrix Θ has been obtained, and considering the via-points, the optimum planning algorithm will provide an optimum feasible path, Fig.2. The planning algorithm [21] is based on generating optimal joint paths by means of a random generation's algorithm, represented by the "Rapidly Exploring Random Trees" (RRT), along with an optimization method provided by Genetics Algorithms (G.A.). This procedure takes advantage of both methods: a fast trajectory path generation, due to RRT; and a optimization technique implemented by G.A. In section 4 the above-mentioned general procedure is implemented with a specific case of study by referring to the parallel manipulator CaPaMan.

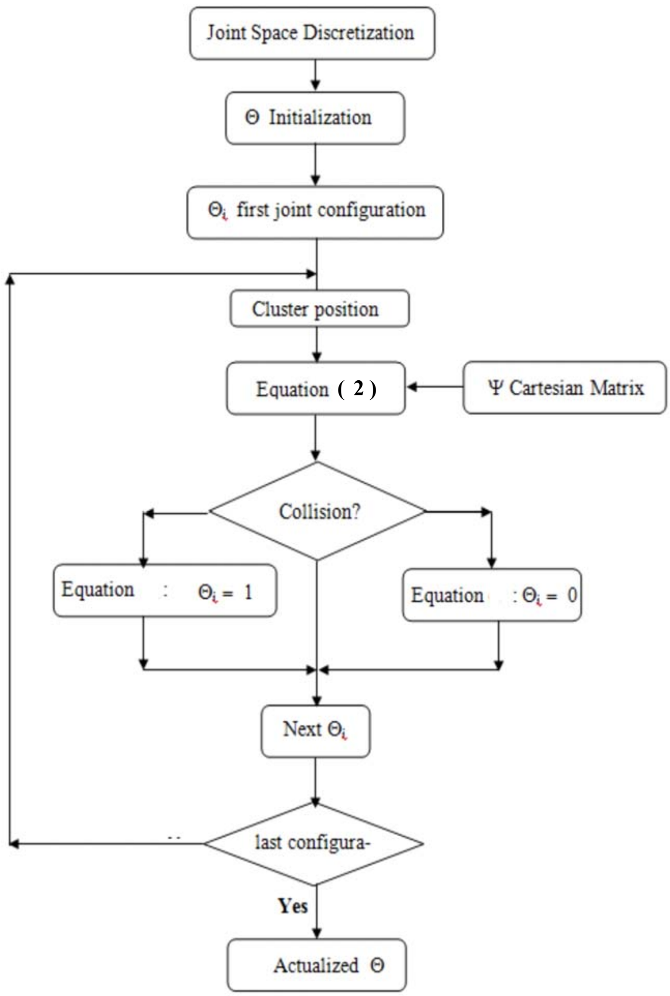

Fig. 2. Flow chart describing the Joint Matrix generation procedure.

3 PROBABILISTIC TECHNIQUES FOR EXPERIMENTAL VALIDATION

3.1 Probabilistic Approach

The state estimation problem using probabilistic techniques can be formulated as follow [26]. If (3) is the model of a non-linear and time-variant system,

$$\begin{aligned} X_{k+1} &= f(X_k, u_k, w_k) \\ Z_k &= h(X_k, v_k) \end{aligned} \tag{3}$$

where

- k denotes the time instant
- X is the state vector.
- *f(...)* defines the system dynamics.
- u is the inputs vector.
- w is the vector that models the system error sources.
- Z is the sensor measurements vector.
- *h(...)* defines the sensor model.
- v is the vector that models the sensor measurement error sources.

The problem consists in obtaining the best estimation of X_k that minimizes the error for some given criteria.

From the Bayesian point of view, the system propagates the probability density function (PDF) of the state vector, conditioned on the sensor measurement data. That is, a function that defines the probability of a specific state vector being the real state of the system given the data provided by the sensor. More formally, the PDF can be specified by

$$P(X_k \mid Z_1 \dots Z_k, u_0 \dots u_{k-1}) \tag{4}$$

This expression defines the likelihood of being X the real state at the time instant t=k, knowing the sensor measurement until t=k and the system inputs until t=k-1. Given this PDF, the state estimation is calculated by minimizing some criteria, as the mean, the mode or the median [26]. Usually [1], linear relations have been used for modeling the evolution of the measurement provided by a sensor. In this case, a traditional Linear Time Invariant (LTI) representation is considered as

$$\begin{aligned} X_{k+1} &= AX_k + Bu_k + Gw_k \\ Z_{k+1} &= CX_k + v_{k+1} \end{aligned} \tag{5}$$

Where w_k is a matrix representing the uncertainty of the model and v_k is a matrix modeling de natural noise of the sensor. Both will be modeled as zero mean Gaussians variables, with covariance matrices R and Q respectively.

These equations are a particular case of Eq.(3), when linear relation are involved. This model will be completely observable due to the sensor measurements (Z).

3.2 Kalman Filtering

The Kalman Filter (KF) [24] is a set of mathematical equations that supply a computationally efficient way to estimate the state of a linear system exposed to Gaussian noise and uncertainties. This estimation minimizes the mean quadratic error using the state system model and the sensor measurements.

Under the assumptions of Gaussian distributions and linear system, the KF provides an optimal state estimation [24]-[26]. The filter algorithm is divided in two phases: prediction and correction. In the first one, the evolution of system state is predicted at time instant k+1 using the data (state, input and covariance matrices) available at instant k. In the second one, this prediction is corrected with the sensor measurement at time instant k+1.

The following equations denote the prediction phase

$$\begin{aligned}\hat{X}^{*}_{k+1} &= A\hat{X}_{k} + BU_{k}\\ \hat{P}^{*}_{k+1} &= A\hat{P}_{k}A^{T} + GQG^{T}\end{aligned} \tag{6}$$

where $\hat{X}^{*}{}_{k+1}$ is the predicted value of the estate at the time instant k+1, $\hat{P}_k$ is the covariance matrix of the estate components estimated at the time instant k, and $\hat{P}^{*}{}_{k+1}$ is the predicted covariance matrix at the time instant k+1.

The following equations represent the correction phase

$$\begin{aligned}K_{k+1} &= \hat{P}^{*}_{k+1}C^{T}\left(C\hat{P}^{*}_{k+1}C^{T} + R\right)^{-1}\\ \hat{X}_{k+1} &= \hat{X}^{*}_{k+1} + K_{k+1}\left(Z_{k+1} - C\hat{X}^{*}_{k+1}\right)\\ \hat{P}_{k+1} &= \left(I - K_{k+1} * C\right)\hat{P}^{*}_{k+1}\end{aligned} \tag{7}$$

where K_{k+1} is known as the optimal Kalman gain, that allow obtaining the estimated value $\hat{X}_{k+1}$. Likely $\hat{P}_{k+1}$, the final estimated covariance matrix, is also calculated from K_{k+1}.

As mentioned above, the KF is only optimal when the equations in (3) are linear. For non-linear systems the EKF can be used, but it is necessary to linearize the system [23] and the estimate is not optimal [26].

The planning method provides not only the temporal evolution of the joint variables but also the theoretical values of the acceleration an angular velocity of the manipulator platform. They demonstrate that the resulting movements are smooth and suitable for precise manipulation [21]. The aim of the present paper is to illustrate that the real values are very close to the ones theoretically calculated. However, in this paper these real values are not directly measured. Instead, they are estimated from the data recorded from four accelerometers. In fact, as shown for example in the studies [35, 36] the minimum numbers of accelerometers need to directly calculate the angular velocity for a 3D motion of a rigid body is twelve. In this research four of four axis accelerometers are placed in the corners to keep symmetry and using the mathematical calculations in [37] this configuration of 4 sensors is used to keep the replacement errors of sensor minimum. The value provided by the accelerometers present uncertainty due to the noise. Therefore, a Kalman Filter has been applied so that a robust estimation of the real values is obtained. In the next section the basis of this technique is introduced.

4 A CASE OF STUDY OF COLLISION FREE MOTION

In the following a case of study is presented by applying the procedures in Figs.1 and 2 to CaPaMan parallel manipulator. The proposed path planning is shown in Fig.3a). It illustrates CaPaMan and the tool moving through the task configurations TC1, TC2 , TC3 and again TC1. The Task Configurations have been selected so that the tool has to move around a cylindrical obstacle. Obviously, direct motion between the configurations will cause collisions. In Fig.-3 b) the trajectory followed by the end of the tool in the Cartesian space is represented with a continuous black line. It is to note how this trajectory avoids colliding with the obstacle.

The trajectory keeps within a circle which radius is 6 cm long far from the obstacle. This proposed path planning illustrates the capability of the proposed method for providing free collision paths even if the selected T.C. lay very close to the obstacles. Figure3 (c) illustrates the joint space and the joint path provided by the A.G. Fig. 3 d) presents the evolution of the parallel manipulator joints variables. The red dashed lines shows the moments in which the correspondent T. P. is reached. The time required by the planning algorithm to obtain this trajectory was an average of 12 s. with a 2.93 GHz Intel Core i3.

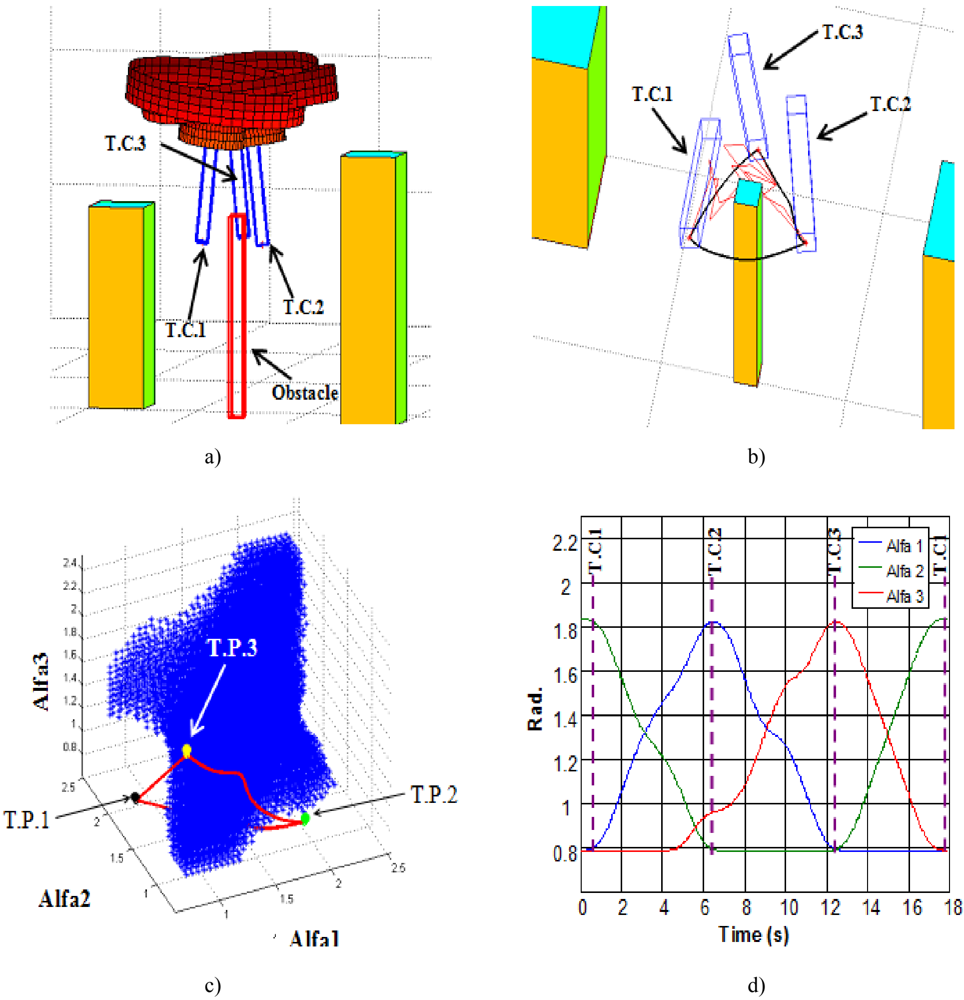

Fig.3. Results of collision free motion planning for CaPaMan: a) Task Configurations; b) Cartesian trajectory of the tool; c) CaPaMan joint space and the joint path; d) Joint variables evolution.

5 EXPERIMENTAL VALIDATION OF THE PLANNED TRAJECTORY

A laboratory test-bed has been settled up for validating both the proposed collision free motion planning and the proposed validation procedure. The test-bed consists of CaPaMan prototype together with suitable accelerometers that have been located beneath the movable plate. In particular, four 3-axial accelerometers have been properly installed at points P1 (P1x, P1y, P1z), P2 (P2y, P2z), P3 (P3x, P3y, P3z), P4 (P4x, P4y, P4z) as shown in Fig 4.

The above-mentioned sensors are connected to a 5 Volts power supply and to a National Instruments acquisition board, as described in the scheme of Fig.5.

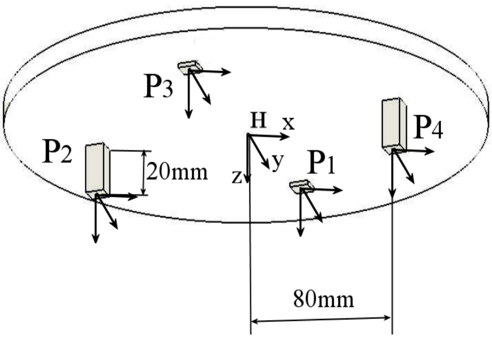

a)

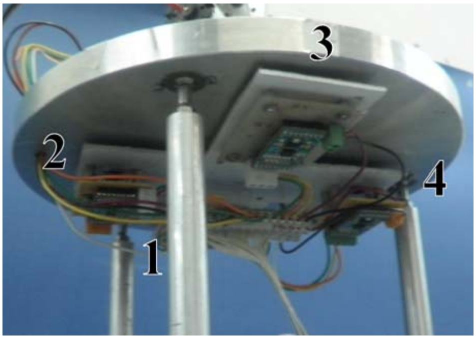

b)

Fig.4 Location and orientation of accelerometers: a) a scheme; b) a photo of the sensors installed on CaPaMan.

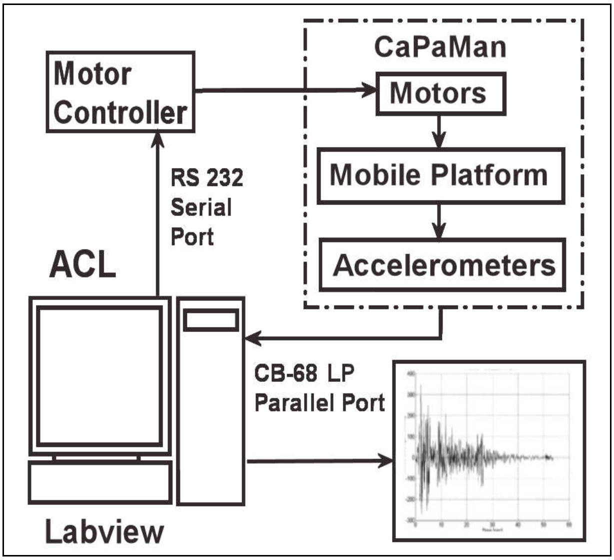

Fig.5 A scheme of the proposed test-bed.

The controller of CaPaMan has been synchronized with the acquisition board to obtain a synchronized measurement during the operation of CaPaMan. The control of CaPaMan has been achieved by writing a suitable routine in ACL programming language that is the dedicated programming language of the controller.

A suitable Virtual Instrument has been developed in LabView environment to manage the signals coming from the sensors. Then, the measured acceleration data from the accelerometers have been used to estimate the accelerations of the point H at the centre of the movable plate and the plate angular velocity.

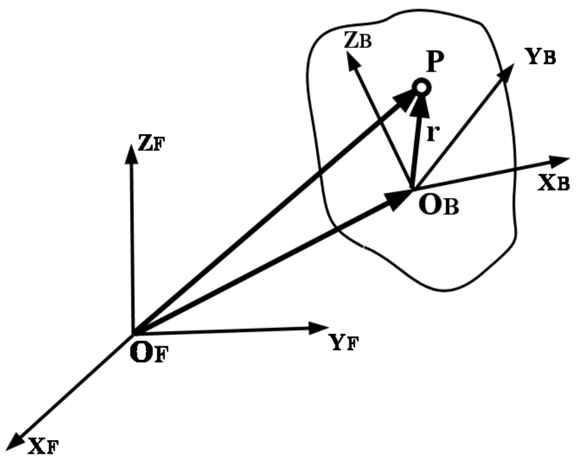

Fig.6 Point P in Frames O_B and O_F

The acceleration of a point P fixed on a rigid body with a position $\mathbf{r}$ can be expressed by equation [37].

$$\mathbf{a}_P = \mathbf{a}_B + \boldsymbol{\alpha}_B \times \mathbf{r} + \boldsymbol{\omega}_B \times (\boldsymbol{\omega}_B \times \mathbf{r}) \qquad (8)$$

Where acceleration $\mathbf{a}_B$, the angular velocity $\boldsymbol{\omega}_B$ and the angular acceleration $\boldsymbol{\alpha}_B$ are described for the relative movement of the rigid body O_B with respect to the fixed frame O_F . The terms of the equation $\boldsymbol{\alpha}_B$ x $\mathbf{r}$ can be described as tangential acceleration and $\boldsymbol{\omega}_B$ x($\boldsymbol{\omega}_B$ x $\mathbf{r}$) as centripetal acceleration.

In order to calculate the acceleration as measured by a sensor that is attached at position $\mathbf{r}$ within a body the sensitivity axis $\mathbf{s}$ and the sensor's metrological signal offset $\mathbf{a}_0$ must be added in above equation

$$\mathbf{a}_S = \mathbf{s}^T \left(\mathbf{a}_B + \boldsymbol{\alpha}_B \times \mathbf{r} + \boldsymbol{\omega}_B \times (\boldsymbol{\omega}_B \times \mathbf{r})\right) + \mathbf{a}_0 \qquad (9)$$

This can be written in vector form as

$$\mathbf{a}_S = \mathbf{c}\,\mathbf{z} + \mathbf{a}_0 \tag{10}$$

where

$$\mathbf{c} = \begin{bmatrix} s_x \\ s_y \\ s_z \\ s_z r_y - s_y r_z \\ s_x r_z - s_z r_x \\ s_y r_x - s_x r_y \\ -(s_y r_y + s_z r_z) \\ -(s_x r_x + s_z r_z) \\ -(s_x r_x + s_y r_y) \\ s_x r_y + s_y r_x \\ s_x r_z + s_z r_x \\ s_y r_z + s_z r_y \end{bmatrix} \text{ and } \mathbf{z} = \begin{bmatrix} a_{B,x} \\ a_{B,y} \\ a_{B,z} \\ \boldsymbol{\alpha}_{B,x} \\ \boldsymbol{\alpha}_{B,y} \\ \boldsymbol{\alpha}_{B,z} \\ \boldsymbol{\omega}_{B,x}^2 \\ \boldsymbol{\omega}_{B,y}^2 \\ \boldsymbol{\omega}_{B,z}^2 \\ \boldsymbol{\omega}_{B,x}\boldsymbol{\omega}_{B,y} \\ \boldsymbol{\omega}_{B,x}\boldsymbol{\omega}_{B,z} \\ \boldsymbol{\omega}_{B,y}\boldsymbol{\omega}_{B,z} \end{bmatrix} \tag{11}$$

by using four sensors with totally twelve axis it is possible to directly compute the quadratic terms of $\boldsymbol{\alpha}_B$ as well as $\mathbf{a}_B$ and $\boldsymbol{\omega}_B$. So the system becomes linear and can be written in matrix vector form as

$$\mathbf{y} = \mathrm{A}\,\mathbf{z} + \mathbf{a}_{0,S} \tag{12}$$

where

$$\mathbf{y} = \begin{bmatrix} \mathbf{a}_{S1} \\ \mathbf{a}_{S2} \\ \vdots \\ \mathbf{a}_{S12} \end{bmatrix}, \quad \mathrm{A} = \begin{bmatrix} \mathbf{c}_{S1} \\ \mathbf{c}_{S2} \\ \vdots \\ \mathbf{c}_{S12} \end{bmatrix} \text{ and } \mathbf{a}_{0,S} = \begin{bmatrix} \mathbf{a}_{0,S1} \\ \mathbf{a}_{0,S2} \\ \vdots \\ \mathbf{a}_{0,S12} \end{bmatrix} \tag{13}$$

By inverting A it is possible to calculate the relative body movement held by vector z for a given measurement vector y applying

$$\mathbf{z} = \mathrm{A}^{-1}\left(\mathbf{y} - \mathbf{a}_{0,S}\right) \tag{14}$$

The values obtained form the sensors are filtered by applying a Kalman Filter, so that a robust estimation of the acceleration and velocity components are obtained.

For this purpose, the filter has been conveniently configured in order to be applied to each accelerometer. Thus, the vector state of the accelerometer *i*, is composed by the values measured along each axe and the corresponding rate of change, i.e. X_{1i}= Pix, X_{2i}= ΔPix /Δt… and so on. Accordingly each state vector has 6 component. The model for predicting the future values is build with the matrices:

$$A = \begin{bmatrix} 1 & \Delta t & 0 & 0 & 0 & 0 \\ 0 & 1 & 0 & 0 & 0 & 0 \\ 0 & 0 & 1 & \Delta t & 0 & 0 \\ 0 & 0 & 0 & 1 & 0 & 0 \\ 0 & 0 & 0 & 0 & 1 & \Delta t \\ 0 & 0 & 0 & 0 & 0 & 1 \end{bmatrix} ; \quad B = 0 \tag{15}$$

As was mentioned before, the uncertainty associated to the prediction is modelled by a zero mean gaussian distribution, by defining the covariance matrix *Q* and the matrix *G*:

$$Q = \begin{bmatrix} \mu_{m1}^2 & \mu_{m1} \cdot \mu_{m2} & 0 & 0 & 0 & 0 \\ \mu_{m1} \cdot \mu_{m2} & \mu_{m2}^2 & 0 & 0 & 0 & 0 \\ 0 & 0 & \mu_{m1}^2 & \mu_{m1} \cdot \mu_{m2} & 0 & 0 \\ 0 & 0 & \mu_{m1} \cdot \mu_{m2} & \mu_{m2}^2 & 0 & 0 \\ 0 & 0 & 0 & 0 & \mu_{m1}^2 & \mu_{m1} \cdot \mu_{m2} \\ 0 & 0 & 0 & 0 & \mu_{m1} \cdot \mu_{m2} & \mu_{m2}^2 \end{bmatrix} ; G = I \tag{16}$$

where *I* is the identity matrix and, μ_{m1} and μ_{m2} are the standard deviations associated to the prediction uncertainty.

The uncertainty of the virtual sensor has been modelled using a zero mean gaussian distribution function with the covariance matrix *R*. Thus, the observation model is achieved by defining *C* and *R*:

$$C = \begin{bmatrix} 1 & 0 & 0 \\ 0 & 1 & 0 \\ 0 & 0 & 1 \end{bmatrix} ; R = \begin{bmatrix} \sigma_{px}^2 & 0 & 0 \\ 0 & \sigma_{py}^2 & 0 \\ 0 & 0 & \sigma_{pz}^2 \end{bmatrix} \tag{17}$$

where σ_{px}, σ_{py}, σ_{pz} are de standard deviations associated to the noise of each of the accelerator axes.

The characterization of the probabilistic model of the uncertainty gave the values in Table 1.

Table 1: Standard deviations

μ_{m1} (m/s^2)	μ_{m2} (m/s^3)	σ_{px} (m/s^2)	σ_{py} (m/s^2)	σ_{pz} (m/s^2)
0.01	0.05	0.5	0.5	0.5

According to this, from each accelerometer i, a set of estimated values (a_{ix}, a_{iy}, a_{iz}) are obtained. The value of the acceleration of the point H, and the angular velocity of the rigid body is calculated by using the equations:

$$\begin{bmatrix} \dfrac{-a_{1x}-a_{2x}}{2} \\ \dfrac{-a_{1y}-a_{2y}}{2} \\ \dfrac{-a_{1z}-a_{2z}}{2} \end{bmatrix} = \begin{bmatrix} a_{Hx} \\ a_{Hy} \\ a_{Hz} \end{bmatrix}; \quad \begin{aligned} \omega_X &= \pm\sqrt{\tfrac{1}{2}\left(\frac{a_{HY}-a_{P2Y}+a_{HX}-a_{P1X}}{r}+\frac{a_{P3Z}-a_{HZ}}{L}\right)} \\ \omega_Y &= \pm\sqrt{\tfrac{1}{2}\left(\frac{a_{P1X}-a_{HX}-a_{HY}-a_{P2Y}}{r}+\frac{a_{P3Z}-a_{HZ}}{L}\right)} \\ \omega_Z &= \pm\sqrt{\tfrac{1}{2}\left(\frac{a_{HY}-a_{P2Y}-a_{HX}-a_{P1X}}{r}-\frac{a_{P3Z}-a_{HZ}}{L}\right)} \end{aligned} \tag{18}$$

The above-mentioned equations have been derived from the theorem of accelerations of a rigid body and described in equations (10) –(14)

Several experiments have been made in order to test the trajectories provided by the proposed approach. In the experiments an obstacle is placed under the CaPaMan and motor position data needed for the trajectory avoidance is sent to motors with motor controller (Scorbot-ER V) by using the ACL programming language. Experiments have been made in different speeds. 21 points on the trajectory are used for the motion. Time differences between the points are experimented as 0.09 seconds, 0.45 seconds and 0.9 seconds to see the motion in different speeds. The motors move the mobile platform and by the help of accelerometers the acceleration information of the mobile platform through the National instruments Usb-6020 data acqusition card is processed and exported as excel file with the LabView software.

Particularly, this article shows the results of testing the manipulation motion described in section 2. Along these movements the tool describes a closed path around an obstacle, without presenting collision. Videos of the operation of CaPaMan have been made and verified at slow speed to validate the operation of CaPaMan moving the tool along the closed path while avoiding collision with the obstacle. In particular, Fig. 5 shows a photo sequence of CaPaMan during this operation. Fig. 6 and 7 show the data recorded during these experiments. Fig. 6 presents the components of the acceleration of the centre of the movable plate when the path was performed in 18 s. In Fig. 6 a), c), and e), the non filtered values of the acceleration components, calculated from (9) are represented. In Fig. 6 b), d), and f) the values estimated with the K.F. versus the theoretical values are illustrated. In Fig. 7 a), c), and e), the non filtered values of the angular velocity components, calculated from (9) are represented. In Fig. 7 b), d), and f) the values estimated with the K.F. versus the theoretical values are illustrated.

Both figures illustrates that the theoretical predicted values of the components are very close to the values estimated from the virtual sensor.

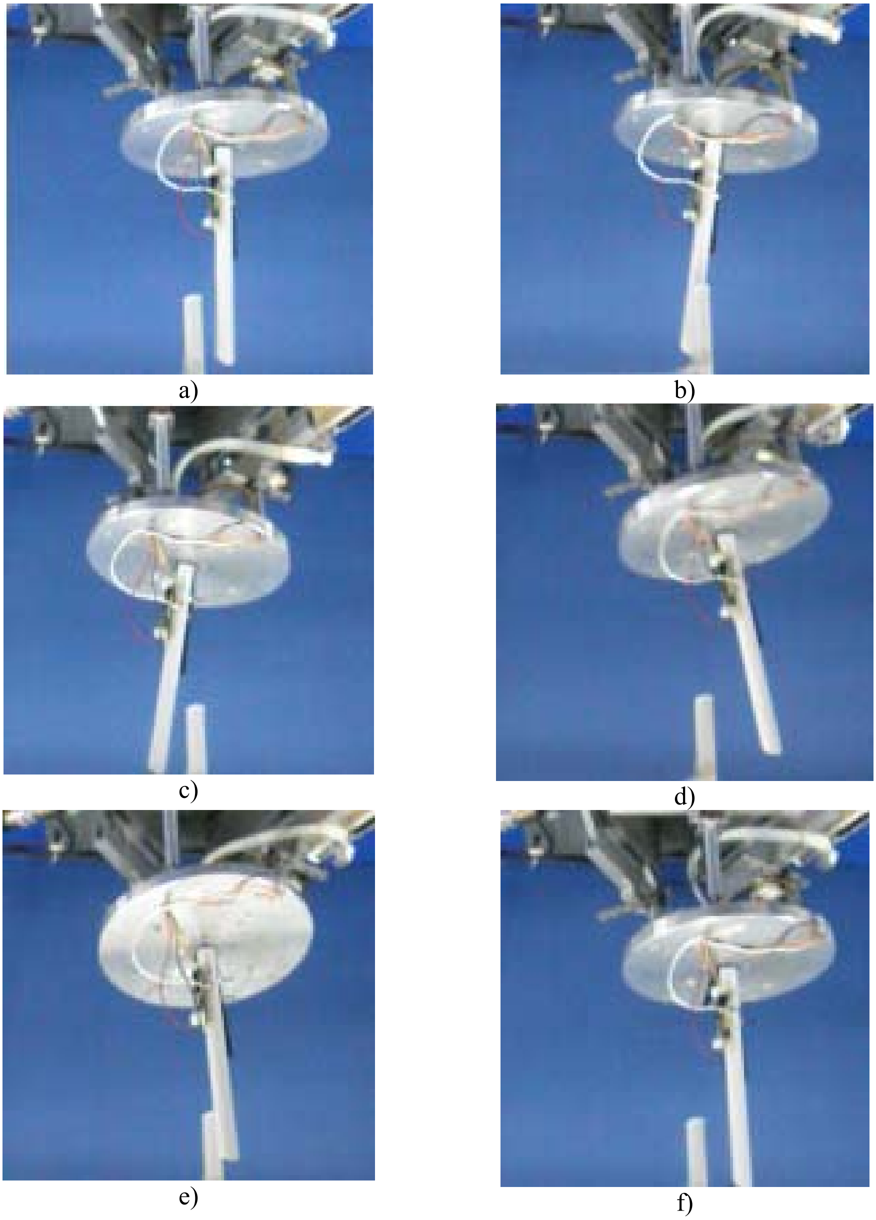

Fig.7 Snapshots of CaPaMan operation during a path to avoid a cylindrical obstacle: a) fist configuration; b) second configuration; c) third configuration; d) fourth configuration; e) fifth configuration; f) sixth configuration.

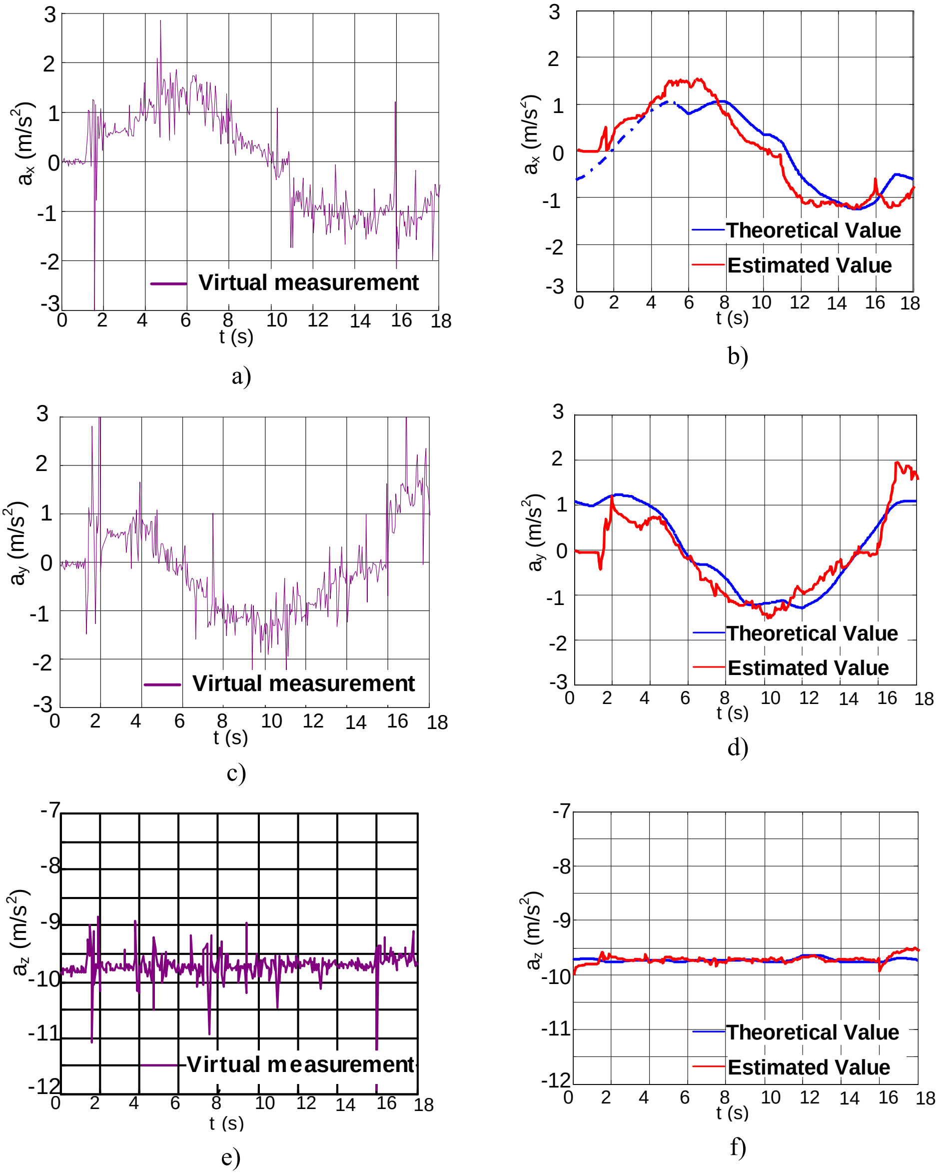

Fig.8 Acceleration components versus time for performing the planned path in 18 s: a) measured acceleration along x-axis data before applying KF; b) comparison of theoretical and measured acceleration along x-axis data after applying KF; c) measured acceleration along yaxis data before applying KF; b) comparison of theoretical and measured acceleration along y-axis data after applying KF; a) measured acceleration along z-axis data before applying KF; b) comparison of theoretical and measured acceleration along z-axis data after applying KF.

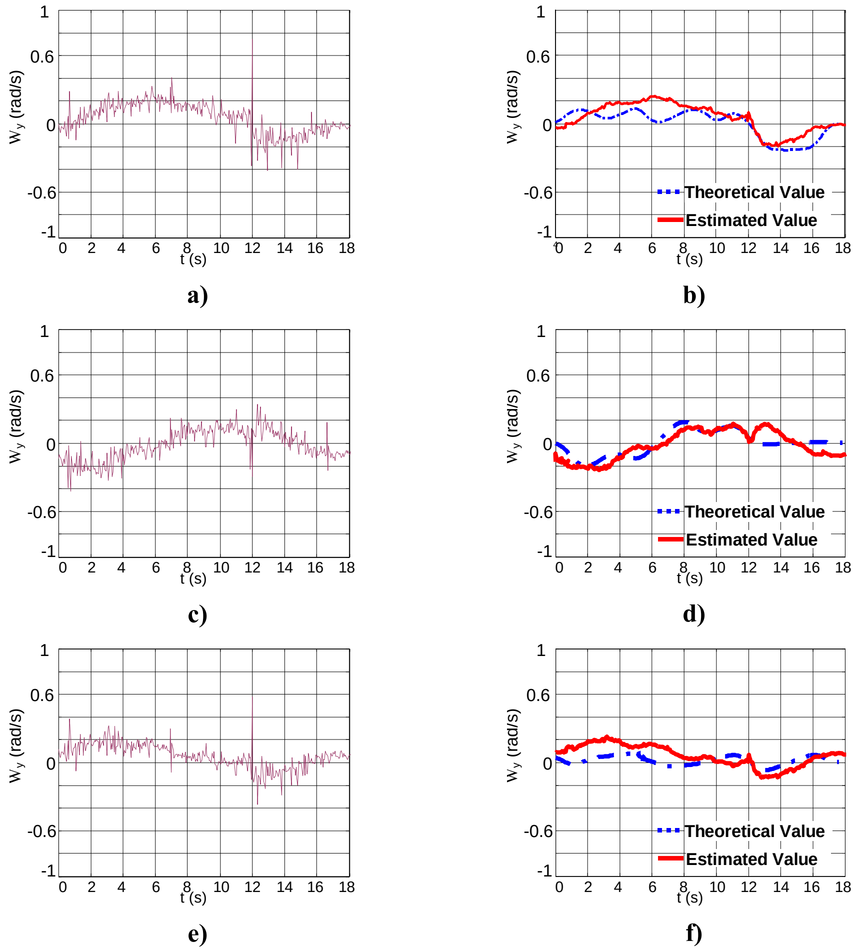

Fig.9 Angular velocities components versus time for performing the planned path in 18 s: a) measured angular velocity along x-axis data before applying KF; b) comparison of theoretical and measured angular velocity along x-axis data after applying KF; c) measured angular velocity along y-axis data before applying KF; b) comparison of theoretical and measured angular velocity along y-axis data after applying KF; a) measured angular velocity along z-axis data before applying KF; b) comparison of theoretical and measured angular velocity along z-axis data after applying KF.

6 CONCLUSIONS

A planning algorithm has been implemented to compute optimal collision free trajectories for the parallel manipulator CaPaMan. A suitable systematic validation approach has been proposed as based on a suitable test-bed and proper processing of experimental data. Experimental tests have been carried out by operating CaPaMan (Cassino Parallel Manipulator) at LARM in Cassino. Experimental results have been processed as based on the proposed validation procedure. Results show that suitable collision free trajectories have been generated for CaPaMan. The experimentally measured trajectories very well match the trajectories that have been theoretically computed at path planning stage in terms of positions, velocities, and accelerations. Additionally the proposed validation approach has been found suitable for systematically validating the operation of CaPaMan parallel manipulator. Results can be conveniently extended to any parallel manipulators provided that suitable experimental data can be made available by means of a proper sensor set-up.

ACKNOWLEDGEMENTS

Third author wishes to thank Izmir Institute of Technology and Prof. Dr.Tech.Sc. Rasim Alizade for supporting a six months stay at LARM in 2010 within Erasmus-Socrates Program.

REFERENCES

[1] T. Lueth, J. Bier, "Robot Assisted Intervention in Surgery", J.M. Gilsbach and H.S. Stiel (Editors), Neuronavigation-Neurosurgical and Computer Scientific Aspects, Springer-Verlag, Wien, 1999.
[2] Lin C.S., Chang P.R., Luh J.Y.S., "Formulation and Optimization of Cubic Polynomial Joint Trajectories for Industrial Robots", IEEE Trans. Automat. Contr., Vol. 28, pp. 1066-1073, 1983.
[3] Shin K.G., Mckay N.D., "A Dynamic Programming Approach to Trajectory Planning of Robotic Manipulators", IEEE Trans. Automat. Contr., Vol. AC-31, No. 6, pp. 491-500, 1986.
[4] Saramago S.F.P., Valder S.J., "Trajectory Modeling of Robots Manipulators in the Presence of Obstacles", Journal of Optimization Theory and Applications, Kluwer Academic, Vol. 110, No. 1, pp. 17-34, 2001.
[5] Saramago S.F.P., Ceccarelli M., "Effect of Some Numerical Parameters on a Path Planning of Robots Taking Into Account Actuating Energy", Mechanism and Machine Theory, Vol. 39, No.3, pp.247-270, 2004.
[6] Siméon, T., Laumond, J.-P. and Nissoux, C., Visibility-based probalistic roadmaps for motion planning. Advanced Robotics Journal. 0169-1864. v14 i6. 477-494.
[7] R. Bohlin, L. Kavraki, Path-planning using lazy prm, in: Proceedings of IEEE International Conference on Robotics and Automation, San Francisco, CA, April 2000, pp. 521-528
[8] O Khatib, Real-time obstacle avoidance for manipulators and mobile robots, International Journal of Robotics Research, v.5 n.1, p.90-98, 1986
[9] Lahouar, S., Zeghloul, S. and Romdhane, L., Real-time path-planning for multi-DoF robot manipulators in dynamic environment. International Journal of Advanced Robotic Systems. 1729-8806. v3 i2. 125-132.
[10] Ceccarelli, M., Valero, F., Mata, F. and Cuadrado, I. ,Generation of adjacent configurations for a collision-free path-planning of manipulators. International Journal of Robotica. v14. 391-396, 1996
[11] Jérîme Barraquand , Jean-Claude Latombe, Robot motion planning: a distributed representation approach, International Journal of Robotics Research, v.10 n.6, p.628-649, Dec. 1991
[12] Gu Fang , M. W. M. G. Dissanayake, A neural network-based method for time-optimal trajectory planning, Robotica, v.16 n.2, p.143-158, 1998
[13] Ong, C. J. and Gilbert, E. G. 1998. Robot path planning with penetration growth distance. J. of Robotic Systems, 15(2): 57-74.
[14] Merlet, J.-P., A generic trajectory verifier for the motion planning of parallel robots. ASME Journal of Mechanical Design. v123 i4. 510-515.
[15] Dasgupta, B. and Mruthyunjaya, S., Singularity-free path-planning for the Stewart platform manipulator. Mechanism and Machine Theory. v33 i6. 711-725.
[16] Sen, S., Dasgupta, B. and Mallik, K., Variational approach for singularity-free path-planning of parallel manipulators. Mechanism and Machine Theory. v38. 1165-1183.
[17] Dash, A.K., I-Meng, C., Yeo, H. and Yang, G., Workspace generation and planning singularity-free path for parallel manipulators. Mechanism and Machine Theory. v40. 776-805.
[18] Carbone G., Ceccarelli M., Oliveira P.J., Saramago S.F.P., Carvalho J.C.M., "An Optimum Path Planning of CaPaMan (Cassino Parallel Manipulator) by Using Inverse Dynamics", Robotica: An International Journal, Vol.26, N.2, 2008, pp.229-239, 2008.
[19] Jean-Pierre P. Merlet, Parallel Robots, Kluwer Academic Publishers, 2000.
[20] Ceccarelli M., Fundamentals of Mechanics of Robotic Manipulation, Kluwer Academic Publishers, 2004.
[21] F. Gomez-Bravo, G. Carbone, D. Lopez, J. C. Fortes, "Planificación de Trayectorias Libres de Colisión en Manipuladores Híbridos", IX Congreso Iberoamericano de Ingeniería Mecánica. Las Palmas de Gran Canaria.. 2009. pp. 10-65-10-72.
[22] Maybeck, Peter S. (1979). "Stochastic Models, Estimation, and Control", Volumen 1, Academic Press, Inc.
[23] Grewal, M. S., and Andrews, A. P. (1993). "Kalman Filtering Theory and Practice". Upper Saddle River, NJ USA, Prentice Hall.
[24] Kalman, R. E.. (1960) "A new approach to linear filtering and prediction problems". Trans. ASME, Journal of Basic Engineering, 82:35–45.
[25] Welch, G. and Bishop, G. (2001) "An introduction to the kalman filter". en Siggraph 2001 course material., available in http://www.cs.unc.edu/~welch/media/pdf/kalman_intro.pdf
[26] Ribeiro, M. I.. (2004) "Kalman and Extended Kalman Filters: Concept, Derivation and Properties", available in http://users.isr.ist.utl.pt/~mir/pub/kalman.pdf
[27] Schiele, B. and Crowley, J. L., (1994) "A comparison of position estimation techniques using occupancy grids" en Proceedings of IEEE Conference on Robotics and Automation (ICRA), vol. 2, pp. 628–1634.
[28] Gomez Bravo, F., Vale A. and Ribeiro, M. I. (2006) "Particle-filter approach and motion strategy for cooperative localization", in Internacional Conference on Informatics in Control, Automation and Robotics 2006 (ICINCO - 2006)

[29] Gordon, N. J., Salmond, D. J., and Smith, A. F. M., (1993) “Novel Approach to Nonlinear/Non-Gaussian Bayesian State Estimation”, IEE Proceedings-F, Vol. 140, No. 2, 1993, pp. 107-113

[30] Liu, J. S., Chen, R. and Logvinenko, T. (2001) “A theoretical framework for sequential importance sampling and resampling”. In A. Doucet, N. de Freitas and N.J. Gordon editors, Sequential Monte Carlo in Practice. Springer-Verlag, January.

[31] Ceccarelli Marco, Parallel Manipulator Architectures from CAPAMAN Design, Proceedings of the RAAD 2010, 19th International Workshop on Robotics in Alpe-Adria-Danube Region RAAD 2010, June 22-25, 2010, Budapest, paper 55. DOI 10.1109/RAAD.2010.5524588

[32] Ceccarelli M., "A New 3 D.O.F. Parallel Spatial Mechanism", IFToMM Journal Mechanism and Machine Theory, 1997, Vol.32, n.8, pp.895-902.

[33] E. E. Hernandez-Martinez, L. Conghui, G. Carbone, M. Ceccarelli, C. S. Lopez-Cajun, Experimental and Numerical Characterization of CaPaMan 2bis Operation, Journal of Applied Research and Technology, Vol.8 No.1 April 2010, pp-101-119. ISSN 1665-6423

[34] Liang C., Hernández-Martínez E.E., Carbone G., Ceccarelli M., “A Comparison of Simulations and Experimental Tests on Operation Performance of CapaMan2 bis”, IEEE International Conference on Mechatronics and Automation ICMA 2009, Changchun, paper no.640, 2009.

[35] B. Zappa, G. Legnana, A.J. van der Bogert, R Adamini, On the number and placement of accelerometers for angular velocity and acceleration determination, ASME J.Dyn.Syst.Meas.Contr.123(3) (2001) 552-554

[36] C. Peters, A. Buhmann, D. Maurath, Y. Manoli, A novel full accelerometer based inertial navigation system, in: Proc. Mikrosystemtechnik Kongress, 2005, pp.233-236

[37] P. Schopp, L Klingbeil, C. Peters, A. Buhmann, Y. Manoli, Sensor fusion algorithm and calibration for a gyroscope free IMU, Proc. Chem. (2009), Proc. Eurosensors XXIII Conference, 1323-1326

Proceedings of MUSME 2011, the International Symposium
on Multibody Systems and Mechatronics
Valencia, Spain, 25-28 October 2011

COMPUTER SIMULATIONS OF THE COAL WAGON LABORATORY EXCITATION AND INFLUENCE OF THE SWEEP LOAD TEST PARAMETER

Pavel Polach* and Michal Hajžman*

* Section of Materials and Mechanical Engineering Research
Výzkumný a zkušební ústav Plzeň s.r.o., Tylova 1581/46, 301 00 Plzeň, Czech Republic
e-mails: polach@vzuplzen.cz, hajzman@vzuplzen.cz
web page: http://www.vzuplzen.cz/

Keywords: Coal Wagon, Computer Simulations, Laboratory Tests, Kinematic Excitation, Sweep Load, Rate of Frequency Change.

Abstract. *This paper is focused on computer simulations of experimental investigations in the field of rail vehicle dynamics. The aim of laboratory tests and computer simulations is the investigation of dynamic properties of leaf springs of two types used in a freight wagon and the verification of the developed approach to the wagon multibody modelling. In future, verified wagon models can be used for studying the dynamics of complex vehicles in different driving situations or for various laboratory excitations. In order to understand the wagon behaviour in more detail the influence of the sweep load test parameter (rate of frequency change) on wagon dynamic response to the kinematic excitation of wheels on the test stand is examined.*

1 INTRODUCTION

Computer simulations intended for investigation of properties of mechanical systems should be performed hand in hand with experimental measurements on real subjects. In this way were investigated the properties of the MGR Coal Hopper HAA two-axle open coal wagon (Fig. (1)) too.

The aim of laboratory tests and computer simulations is the investigation of dynamic properties of leaf springs of two types used in the MGR Coal Hopper HAA wagon. A standard type of the utilized leaf springs is a parabolic steel one (see Fig. (2)). This spring has some undesirable properties such as corrosion of leaves and silting of an inter-leaf space. Therefore it can be efficient to replace them with the composite glass-reinforced plastic (GRP) leaf springs (see Fig. (2)) of better properties. The original goal of the computer simulations of the experimental tests is the verification of the developed approach to the wagon multibody modelling and the basic comparison of the steel parabolic leaf spring and the composite GRP leaf spring qualities. The verified multibody models can be used for studying the wagon dynamic behaviour in different driving situations or for various laboratory excitations in future.

Figure 1: The partly loaded MGR Coal Hopper HAA wagon on the test stand.

Multibody models of the MGR Coal Hopper HAA wagon were created using the **alaska** (Ref. [1]) and the SIMPACK (Ref. [2]) simulation tools. A special approach was used for the modelling of leaf springs on the basis of measured vertical characteristics (Ref. [3]). The finite segment method (Ref. [4]) in combination with nonlinear torque and friction elements was utilized. The chosen approach is a compromise between a complex massless force model (Ref. [5], Ref. [6]) and a full flexible body model (Ref. [7]). A usual problem in the course of modelling real vehicles is the consistency of real parameters and ideal parameters, which can be obtained from drawings or the CAD models. Therefore the sensitivity analysis of a dynamic response to the change of the chosen multibody models parameters was performed (Ref. [3]) and the influence of the possible asymmetry of a wagon load was investigated (Ref. [8]).

In order to understand the wagon behaviour in more detail the influence of the sweep load test parameter *k* (see Eq. (3)) at the wagon laboratory excitation on the wagon dynamic response is investigated.

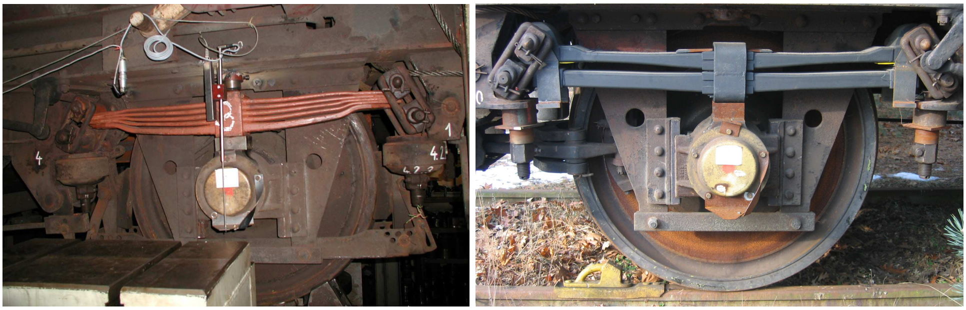

Figure 2: The five-leaf parabolic steel spring and the two-leaf composite spring.

2 EXPERIMENTAL LABORATORY TESTS

The MGR Coal Hopper HAA wagon was tested empty and partly loaded (three load variants) on a test stand in the Dynamic Testing Laboratory of Výzkumný a zkušební ústav Plzeň s.r.o. (former ŠKODA VÝZKUM s.r.o.). The loading was realized by means of concrete panels (see Fig. (1)). The empty wagon total mass was 13 967 kg, the first load variant wagon mass was 22 846 kg, the second load variant wagon mass was 31 562 kg and the third load variant wagon mass was 39 839 kg. A wagon dimensional drawing (third load variant) is in Fig. (3).

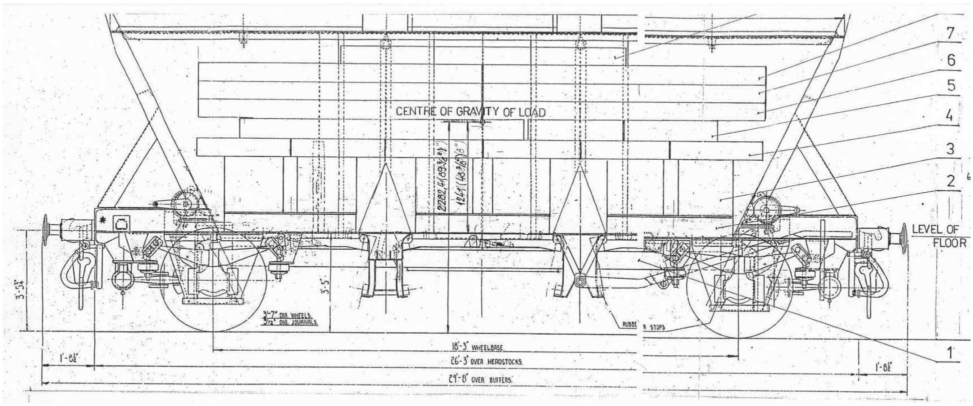

Figure 3: Dimensional drawing of the loaded wagon (taken from Ref. [9]).

Five-leaf parabolic steel springs and two-leaf composite springs (see Fig. (2)) were used in the wagon suspension. The wagon wheels were mounted on the hydraulic servo valves of the test stand, which can experimentally simulate a vertical kinematic excitation of the wagon.

The wagon was subjected to several loading modes on the test stand. One of the loading modes was the kinematic excitation of the wheels by a wideband sweep signal (wideband sweep signal is especially appropriate to the nonlinearity study) in a vertical direction. The front wheels were excited by loading servo valves in phase (“bump test”) or out of phase (“roll test”). The list of the parameters of the loading modes of this type is given in Table 1.

Time history of vertical displacements $y(t)$ of the wagon wheels kinematically excited by a wideband sweep signal on the test stand can be described using relation

$$y(t) = A \cdot \sin[\omega(t) \cdot t] , \tag{1}$$

where A is the amplitude of vertical displacements, t is time and $\omega(t)$ is the angular frequency.

For time depending linearly variable angular frequency $\omega(t)$ it holds

$$\omega(t) = 2 \cdot \pi \cdot f(t) , \tag{2}$$

where $f(t)$ is frequency.

Time depending linearly variable frequency $f(t)$ can be formulated by relation $f(t) = k \cdot t$ (k is the constant rate of frequency change). Then the time history of vertical displacements of kinematically excited wheels can be determined using relation

$$y(t) = A \cdot \sin\left(2 \cdot \pi \cdot k \cdot t^2\right) . \tag{3}$$

<table>
<tr><th colspan="3">Kinematic excitation of wagon wheels on the test stand</th></tr>
<tr><td>Loading mode</td><td colspan="2">Parameters of wideband sweep signal</td></tr>
<tr><td rowspan="2">“bump test”</td><td rowspan="2">A = 1 mm, range of excitation frequencies $f(t)$ from 0 Hz to 30 Hz, excitation of the front wheelset wheels in phase</td><td>$k = 0.2\ \mathrm{Hz \cdot s^{-1}}$</td></tr>
<tr><td>$k = 0.03\ \mathrm{Hz \cdot s^{-1}}$</td></tr>
<tr><td rowspan="2">“bump test”</td><td rowspan="2">A = 0.5 mm, range of excitation frequencies $f(t)$ from 0 Hz to 30 Hz, excitation of the front wheelset wheels in phase</td><td>$k = 0.2\ \mathrm{Hz \cdot s^{-1}}$</td></tr>
<tr><td>$k = 0.03\ \mathrm{Hz \cdot s^{-1}}$</td></tr>
<tr><td rowspan="2">“roll test”</td><td rowspan="2">A = 0.5 mm, range of excitation frequencies $f(t)$ from 0 Hz to 30 Hz, excitation of the front wheelset wheels out of phase</td><td>$k = 0.2\ \mathrm{Hz \cdot s^{-1}}$</td></tr>
<tr><td>$k = 0.03\ \mathrm{Hz \cdot s^{-1}}$</td></tr>
</table>

Table 1: List of the selected loading modes on the test stand.

The value of the rate of frequency change k at the experimental measurements was chosen according to experience and possibilities of the test stand. It had to be high enough to avoid long-term resonant states of the wagon, which could be dangerous for both the test stand and the wagon itself and low enough not to “skip” the resonant frequency. In addition the rate of loading was limited by the feasibility of loading servo valves. Computationally the influence of the rate of frequency change k is examined in this paper. Of course, at computer simulations the change of the frequency change rate k can be arbitrarily changed.

The measured (and documented) dynamic quantities, which are usable for the multibody models verification, were relative displacements between the wheels and the wagon body (see Fig. (4) and Fig. (5) for the illustration of experimental results). In Fig. (4) envelopes of the experimentally measured relative displacements between the wheels and the wagon body of the empty wagon (with the five-leaf parabolic steel springs of the front suspension and the two-leaf composite springs of the rear suspension) at the “bump test”, at the vertical displacements amplitudes on the front wheels of A = 0.5 mm and at rate $k = 0.2\ \mathrm{Hz \cdot s^{-1}}$ are given (DS1 – left front wheel, DS2 – right front wheel, DS3 – left rear wheel, DS4 – right rear wheel). In Fig. (5) envelopes of the experimentally measured relative displacements between the wheels and the wagon body of the empty wagon (with the five-leaf parabolic steel springs of the front suspension and the two-leaf composite springs of the rear suspension) at the “roll test”, at the vertical displacements amplitudes on the front wheels of A = 0.5 mm and at rate

$k = 0.2$ Hz·s^{-1} are given. The cause of the asymmetry of displacements in Fig. (5) is in a partial release of wagon wheels from short steel beams, in which the wagon wheels flanges were laid, and a subsequent small shift of wagon wheels on the test stand (the wagon was empty without concrete panels). At the loaded wagon the asymmetry of displacements can be caused by a possible shift of concrete panels (wagon load – see Ref. [8]).

In this paper the results of simulations with the wagon with the same leaf springs as at one of the experimental measurements, the results of which are in Fig. (4) and Fig. (5), are given (i.e. with the five-leaf parabolic steel springs in the front suspension and the two-leaf composite springs in the rear suspension).

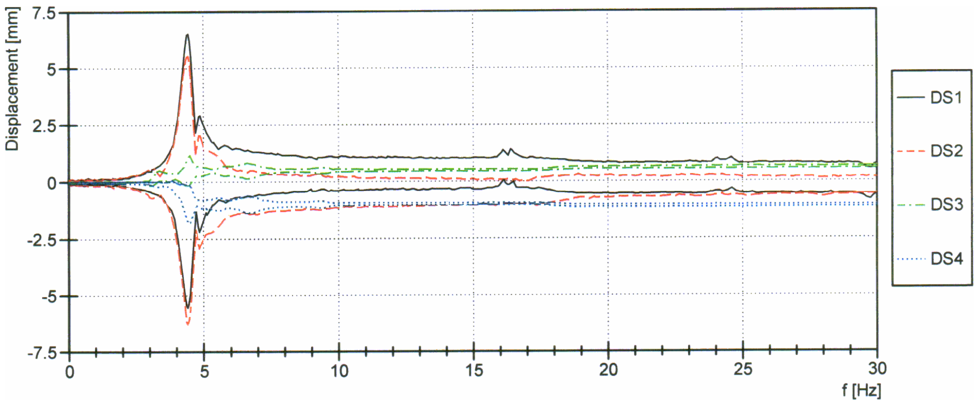

Figure 4: Envelopes of the experimentally measured relative displacements between the wheels and the wagon body of the empty wagon at the "bump test".

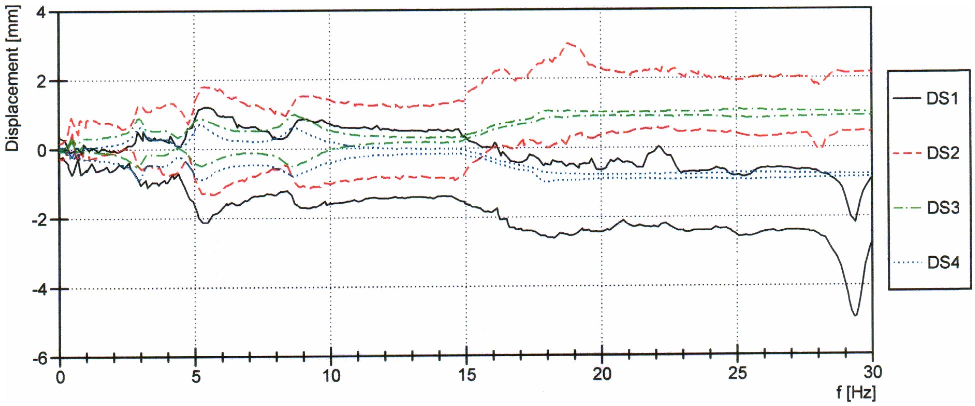

Figure 5: Envelopes of the experimentally measured relative displacements between the wheels and the wagon body of the empty wagon at the "roll test".

3 MULTIBODY MODELS OF THE WAGON

Multibody models of the empty wagon and three variants of the partly loaded one, which correspond to the wagon loading with concrete panels during testing on the test stand in the Accredited Dynamic Testing Laboratory of Výzkumný a zkušební ústav Plzeň s.r.o., were created. It is possible to simulate the laboratory kinematic excitation of the wagon wheels by a wideband sweep signal in vertical direction with multibody models. Time histories or frequency domain responses of kinematic and dynamic quantities reflecting the wagon examined properties are the output of the computer simulations and the experimental measurements (Ref. [3], Ref. [8], Ref. [10], Ref. [11], Ref. [12] and Ref. [13]).

Multibody models of the MGR Coal Hopper HAA wagon were created mainly on the basis of Ref. [9] and Ref. [14].

Module multibody models of the MGR Coal Hopper HAA goods wagon, intended for simulating laboratory tests, were created in the **alaska** (Ref. [1]) and the SIMPACK (Ref. [2]) simulation tools. Multibody models of an empty wagon and three variants of a partly loaded wagon, which correspond with the wagon loading at laboratory tests (Ref. [9]), were created.

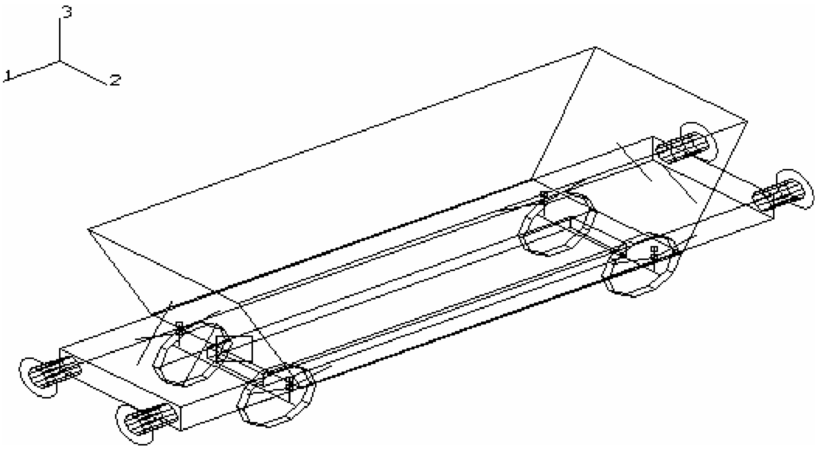

Figure 6: Visualization of the empty MGR Coal Hopper HAA wagon multibody model in the **alaska 2.3** simulation tool.

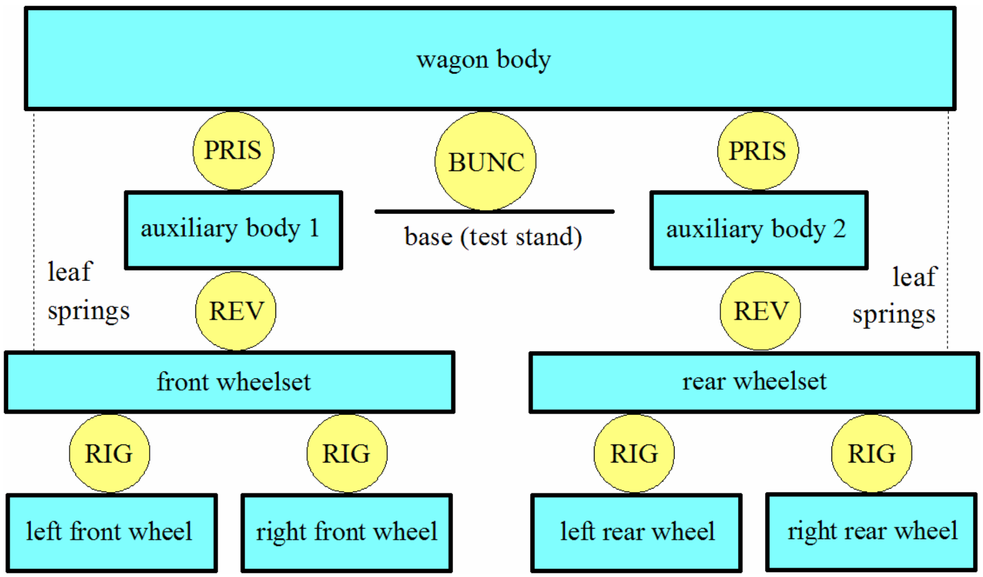

Figure 7: Kinematic scheme of the MGR Coal Hopper HAA wagon multibody model in the **alaska 2.3** simulation tool.

Simple multibody models of the MGR Coal Hopper HAA goods wagon (see Fig. (6)) in the **alaska 2.3** simulation tool are formed by nine rigid bodies mutually coupled by nine kinematic joints. The number of degrees of freedom (DOF) of the multibody models in kinematic joints is ten. In multibody models the five-leaf parabolic steel and the GRP leaf springs can be considered in the wagon suspension.

A kinematic scheme of wagon multibody model is in Fig. (7). Rectangles designate the rigid bodies, circles designate the kinematic joints (BUNC – unconstrained, BSPH – spherical, PRIS – prismatic in vertical axis, REV – revolute around longitudinal axis, RIG – rigid, i.e. without DOF).

In the wagon multibody models leaf springs are modelled by connecting appropriate points by the force spring damper elements. Nonlinear deformation characteristics of the five-leaf parabolic steel and the GRP leaf springs were assessed on the basis of the laboratory measured static characteristics stated in Ref. [15] (see Fig. (8)); for the reason that **alaska 2.3** simulation tool does not enable the spring damper element characteristics to be hysteresis curves the characteristics were averaged. Linear coefficients of the vertical damping of steel and composite springs were taken from Ref. [9].

The wheels and the loading servo valves contact are modelled by a contact force with defined stiffness and damping. Sources for the assessment of the linear vertical stiffness and the linear coefficient of vertical damping in the wheel-test stand contact are given in Ref. [16].

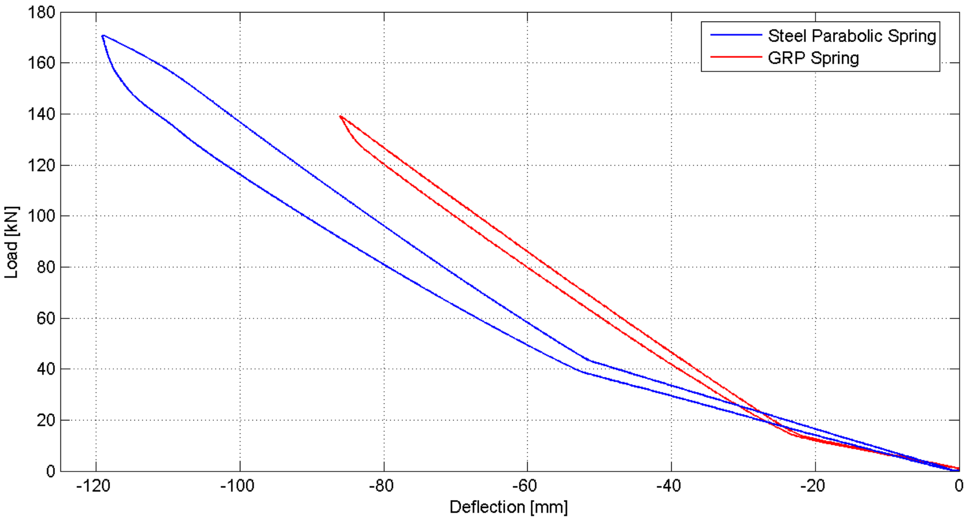

Figure 8: Vertical static characteristics of both parabolic steel five-leaf and two-leaf composite springs (taken from Ref. [15]).

The multibody model created in the SIMPACK simulation tool consists of twenty four bodies (including frame = laboratory stand, without “dummy bodies”) connected by kinematic joints and constraints (see Fig. (9) and Fig. (10)). Considering the aim of the modelling, the wagon body can be represented by one rigid body, which has six DOF with respect to the frame. The laboratory stand is considered to be a rigid reference frame. The front and the rear wheelsets are connected with the frame using a special user defined joint, which allows rotating around x-axis and translation along z-axis (see Fig. (9)). The wagon body and the wheelsets are mutually connected by four leaf springs.

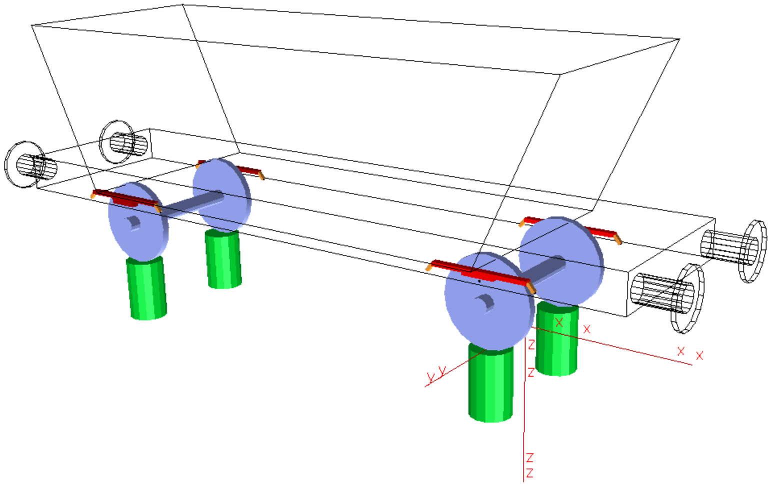

Figure 9: Visualization of the empty MGR Coal Hopper HAA wagon multibody model on the test stand in the SIMPACK simulation tool.

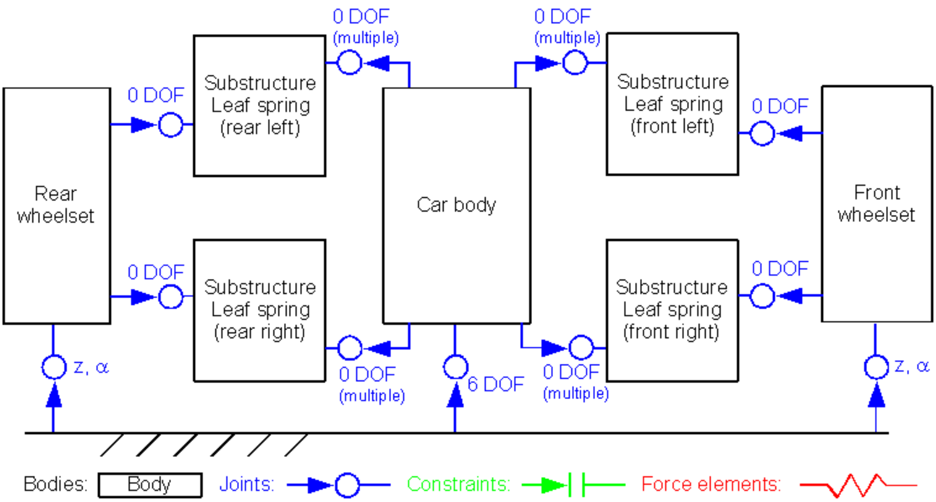

Figure 10: Kinematic scheme of the MGR Coal Hopper HAA wagon multibody model in the SIMPACK simulation tool (taken from Ref. [12]).

The SIMPACK simulation tool allows using substructures that can represent some parts of the multibody model. The overall structure of the model in Fig. (10) shows the topology of the multibody model based on the modelling of leaf springs as separated substructures (their kinematic scheme is Ref. [3] or Ref. [8]). More information of the leaf spring modelling is given in Ref. [3], Ref. [13] and Ref. [17]. The joints denoted as 0 DOF in Fig. (10) are used in the course of the multibody model pre-processing in the SIMPACK simulation tool, but finally two bodies connected by 0 DOF joint merged during the automatic generation of equations of motion (one body is usually called a “dummy body”). Kinematic scheme in Fig. (10)

represents a direct method of the multibody model preparation in the SIMPACK simulation tool. Angle α denotes the rotations around x axle (see Fig. (9)).

4 RESULTS OF SIMULATIONS

The influence of the frequency change rate of the sweep load on the dynamic response of the MGR Coal Hopper HAA wagon was investigated by means of the simulations of the "bump test" and the "roll test" at the vertical displacements amplitudes on the front wheels of A = 0.5 mm, at excitation frequencies $f(t)$ range from 0 Hz to 30 Hz (see Fig. (11) to Fig. (20)). The compared quantities were the computed resonant frequencies and relative displacements between the wheels and the wagon body (empty and all three load variants) with the five-leaf parabolic steel springs in the front suspension and the two-leaf composite springs in the rear suspension (the same as in Ref. [3] and Ref. [8] and the same as in Fig. (4) and Fig. (5)).

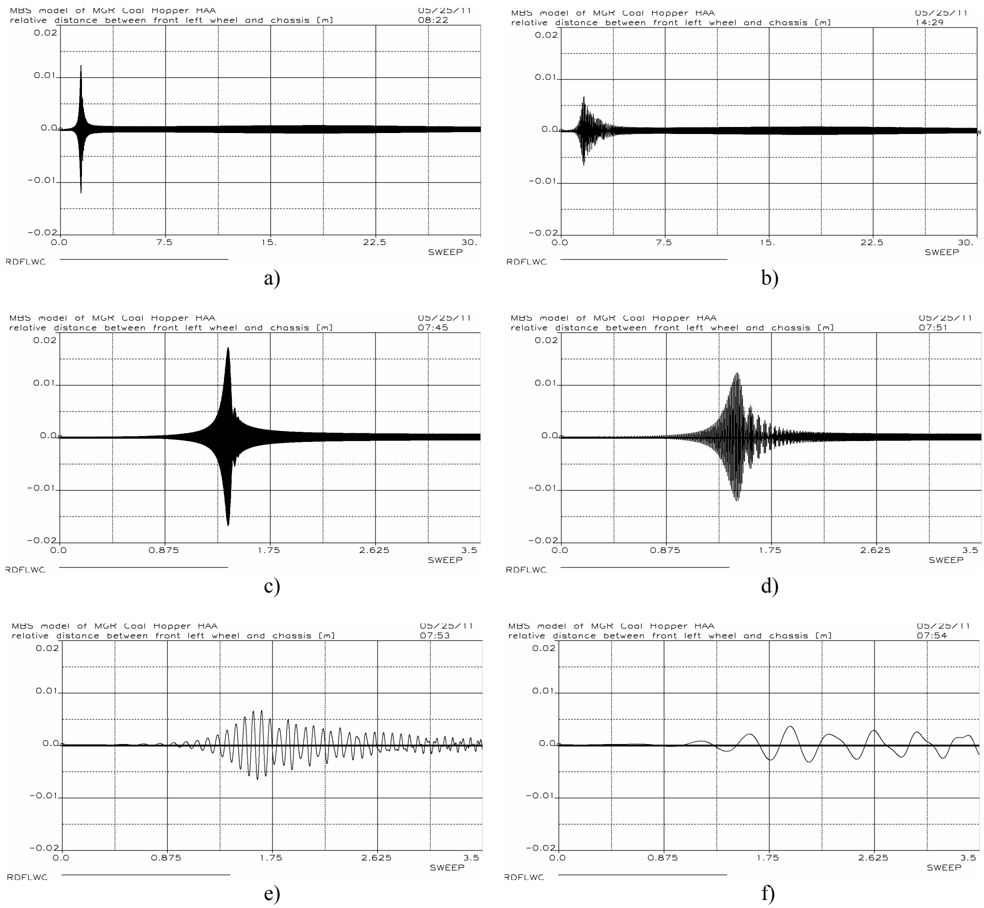

Figure 11: The computed relative displacements between the left front wheel and the wagon body of the empty wagon at the "bump test" – a) rate of frequency change k = 0.03 Hz·s^{-1} (up to 30 Hz), b) rate of frequency change k = 0.2 Hz·s^{-1} (up to 30 Hz), c) rate of frequency change k = 0.005 Hz·s^{-1} (up to 3.5 Hz), d) rate of frequency change k = 0.03 Hz·s^{-1} (up to 3.5 Hz), e) rate of frequency change k = 0.2 Hz·s^{-1} (up to 3.5 Hz), f) rate of frequency change k = 1 Hz·s^{-1} (up to 3.5 Hz).

In Fig. (11) and Fig. (12) the frequency dependencies of the relative displacements between the wheels and the wagon body are given for the empty wagon (the dependencies the second and the third load wagon variant are of the same character). The dependencies of the relative displacements between the wheels and the wagon body are slightly different in the case of the “bump test” with the first load wagon variant (at simulating the “bump test” two resonant peaks are very significant in these frequency dependencies of the relative displacements – in more detail see Conclusions chapter). The dependencies in Fig. (11) to Fig. (14) are given (except Figs. a) and Figs. b)) at excitation frequencies range from 0 Hz to 3.5 Hz because this range is sufficient enough for the results evaluation (e.g. Ref. [8]).

In Fig. (11) to Fig. (14) there are results and outputs from the **alaska 2.3** simulation tool.

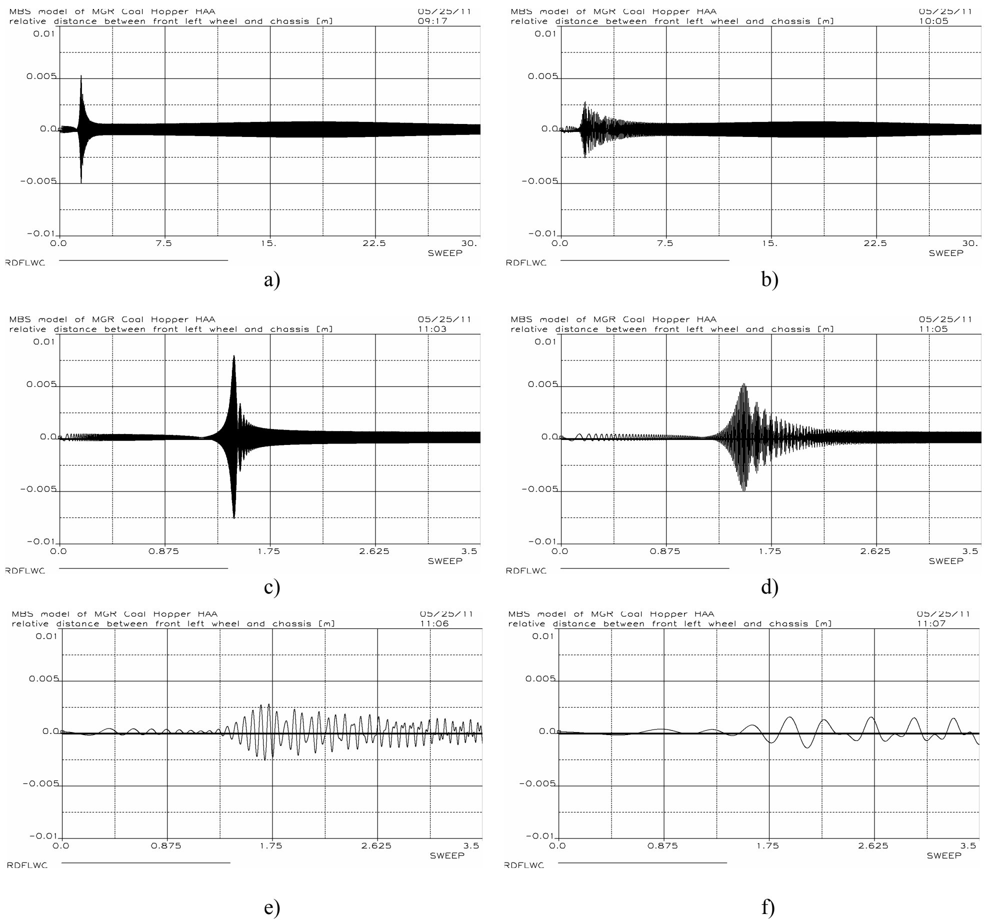

Figure 12: The computed relative displacements between the left front wheel and the wagon body of the empty wagon at the “roll test” – a) rate of frequency change $k = 0.03\ \mathrm{Hz{\cdot}s^{-1}}$ (up to 30 Hz), b) rate of frequency change $k = 0.2\ \mathrm{Hz{\cdot}s^{-1}}$ (up to 30 Hz), c) rate of frequency change $k = 0.005\ \mathrm{Hz{\cdot}s^{-1}}$ (up to 3.5 Hz), d) rate of frequency change $k = 0.03\ \mathrm{Hz{\cdot}s^{-1}}$ (up to 3.5 Hz), e) rate of frequency change $k = 0.2\ \mathrm{Hz{\cdot}s^{-1}}$ (up to 3.5 Hz), f) rate of frequency change $k = 1\ \mathrm{Hz{\cdot}s^{-1}}$ (up to 3.5 Hz).

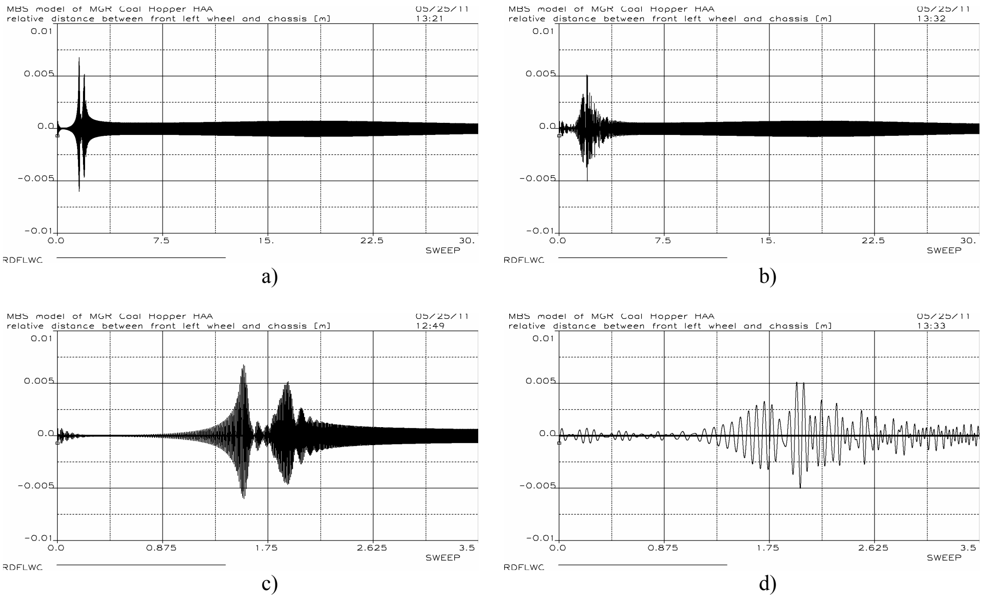

Figure 13: The computed relative displacements between the left front wheel and the wagon body of the first load wagon variant at the "bump test" – a) rate of frequency change $k = 0.03$ Hz·s^{-1} (up to 30 Hz), b) rate of frequency change $k = 0.2$ Hz·s^{-1} (up to 30 Hz), c) rate of frequency change $k = 0.03$ Hz·s^{-1} (up to 3.5 Hz), d) rate of frequency change $k = 0.2$ Hz·s^{-1} (up to 3.5 Hz).

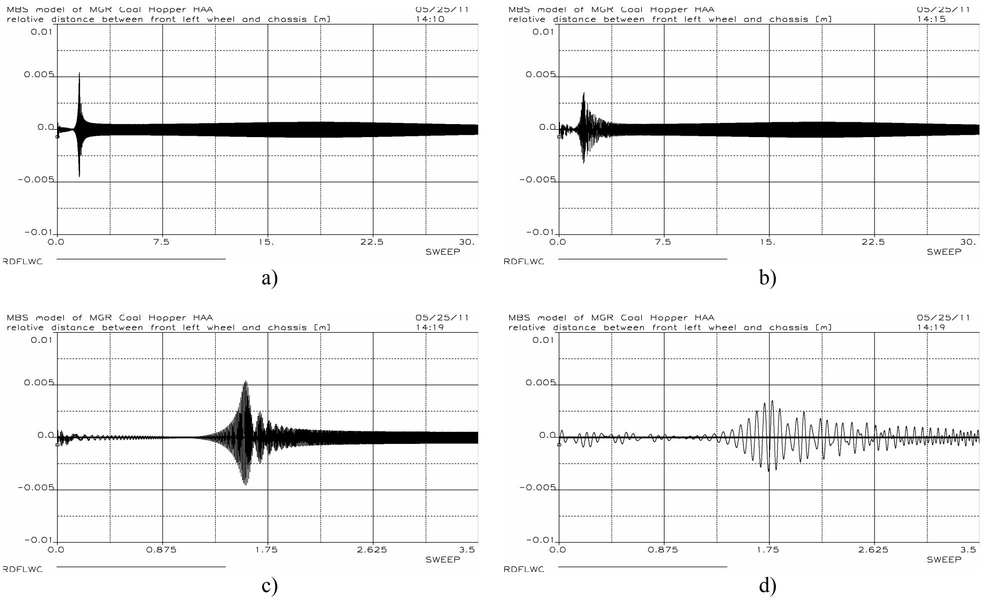

Figure 14: The computed relative displacements between the left front wheel and the wagon body of the first load wagon variant at the "roll test" – a) rate of frequency change $k = 0.03$ Hz·s^{-1} (up to 30 Hz), b) rate of frequency change $k = 0.2$ Hz·s^{-1} (up to 30 Hz), c) rate of frequency change $k = 0.03$ Hz·s^{-1} (up to 3.5 Hz), d) rate of frequency change $k = 0.2$ Hz·s^{-1} (up to 3.5 Hz).

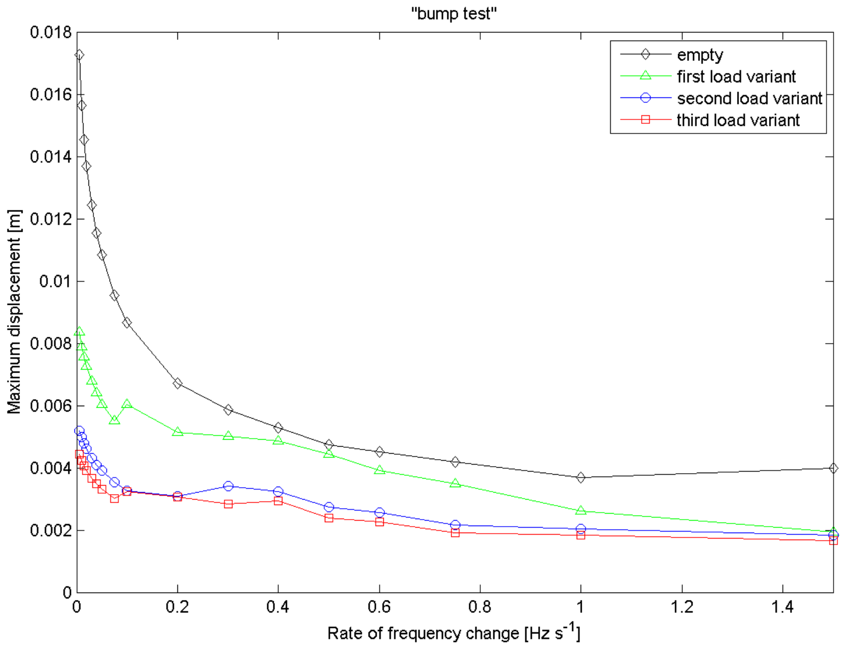

Figure 15: The maximum relative displacement between the left front wheel and the wagon body at resonant frequencies at the “bump test”.

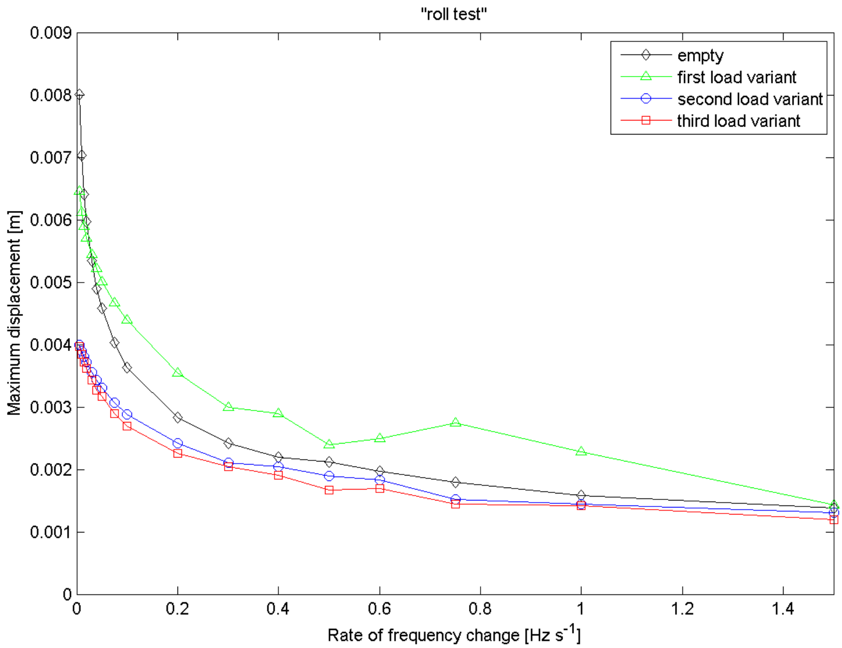

Figure 16: The maximum relative displacement between the left front wheel and the wagon body at resonant frequencies at the “roll test”.

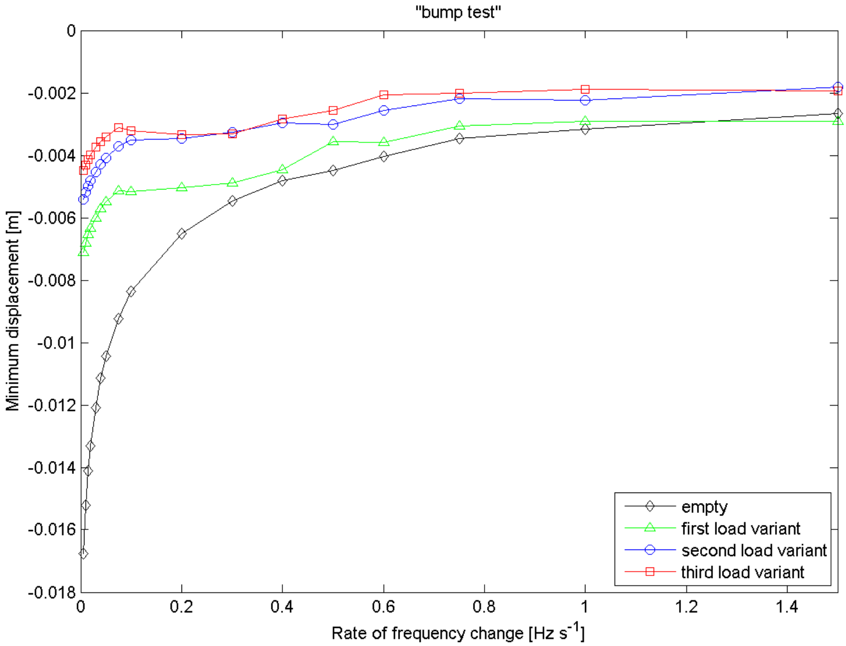

Figure 17: The minimum relative displacement between the left front wheel and the wagon body at resonant frequencies at the “bump test”.

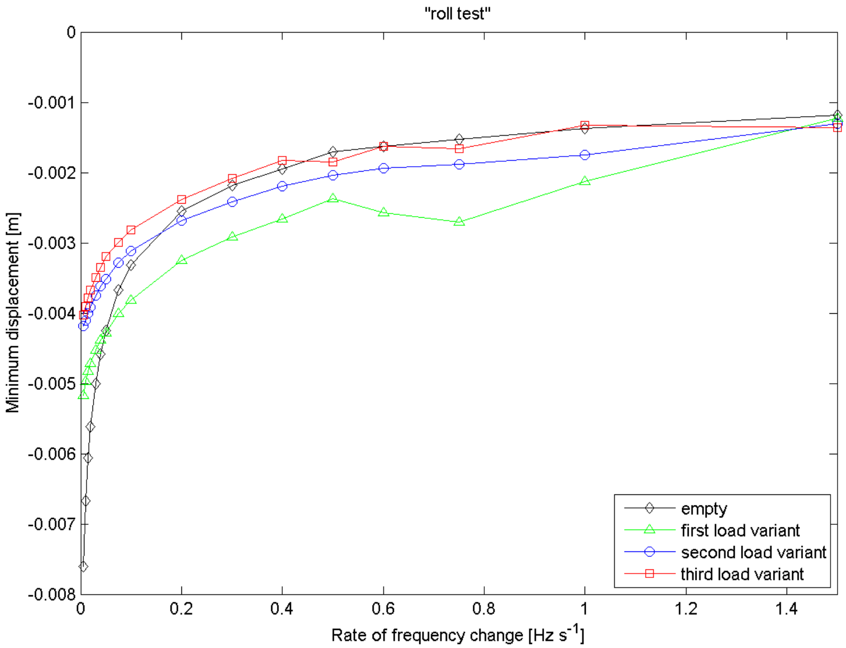

Figure 18: The minimum relative displacement between the left front wheel and the wagon body at resonant frequencies at the “roll test”.

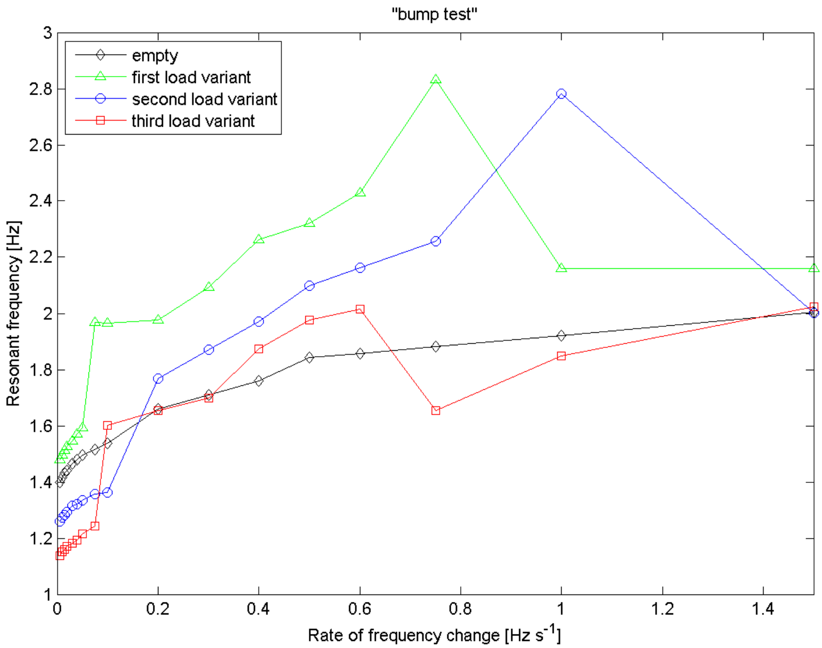

Figure 19: The resonant frequencies of the wagon at the “bump test”.

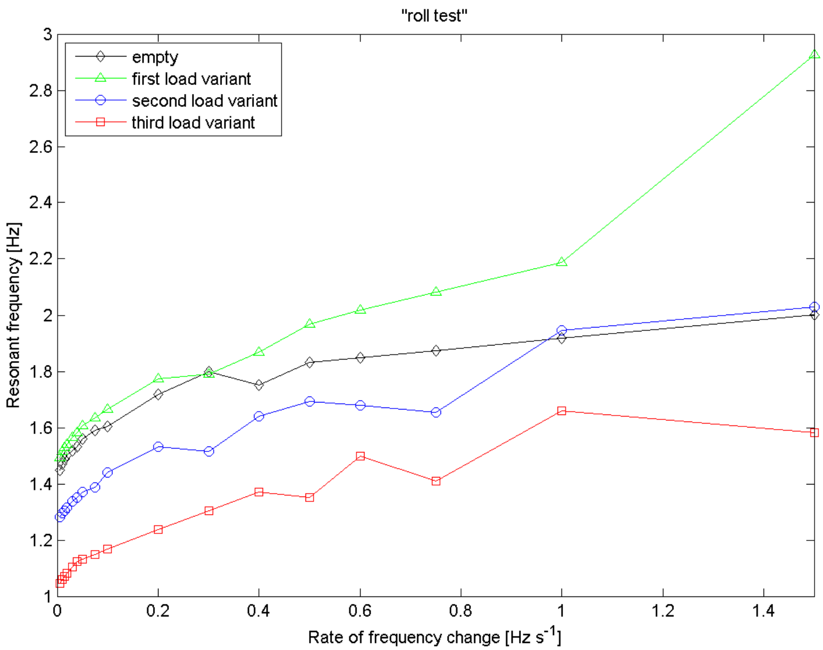

Figure 20: The resonant frequencies of the wagon at the “roll test”.

5 CONCLUSIONS

The influence of the frequency change rate *k* of the sweep load of the wheels on the dynamic response of the MGR Coal Hopper HAA wagon was examined. From the results of the computer simulations it is evident that the influence of the sweep load parameter *k* significantly influences results of the laboratory tests. Even a small change of parameter *k* causes a deviation of the relative displacements between the wheels and the wagon body.

Maximum relative displacement between the wheels and the wagon body at resonant frequency decreases directly proportionally to the increasing of the frequency change rate *k* at simulating both the “bump test” and the “roll test” (see Fig. (15) to Fig. (18)). The more loaded wagon, the smaller maximum relative displacements (see Fig. (15) to Fig. (20)). At resonant vibration in the course of the “roll test” the absolute values of both the maximum and the minimum relative displacements are lower (see Fig. (15) to Fig. (18)) than in the course of the “bump test”. Values of resonant frequencies of more loaded wagon are (at the same value of parameter *k*) lower than values at less loaded wagon (see Fig. (19) and Fig. (20)). The empty wagon at which the lower resonant frequencies are caused by the lower stiffness of the leaf springs, is the exception. (see Fig. (8)).

It is evident (from the graphs in Fig. (19) and Fig. (20)) that the information capacity of the sweep tests (both the “bump test” and the “roll test”) is sufficient (in the case of the MGR Coal Hopper HAA wagon) up to the rate of frequency change $k = 0.05\ \mathrm{Hz \cdot s^{-1}}$. As it was already mentioned, at the lower value of parameter *k* it is necessary to pay a great attention to the possible danger of the wagon rolling at the wagon laboratory tests. At higher values of the rate of frequency change *k* the resonant frequency values (especially above $k = 0.6\ \mathrm{Hz \cdot s^{-1}}$) are already considerably biased. At simulating “bump test” two resonant peaks (at the lower values of the rate of frequency change *k* – see Fig. (11) and especially Fig. (13)) appear in frequency dependencies of the relative displacements between the wheels and the wagon body. This fact is caused by a different stiffness of the five-leaf parabolic steel springs in the front suspension and the two-leaf composite springs in the rear suspension. At the “roll test” and at higher values of parameter *k* during the “bump test” only one resonant peak occurs because the conditions of sufficient intensity or the character of excitation for exciting the resonant peaks caused by the stiffness of the springs in the rear suspension are not fulfilled – see Fig. (11) to Fig. (14)).

Different values of the resonant frequencies identified at the experimental measurements (see Fig. (4)) and at the simulations with the wagon multibody models are caused by the used imperfect leaf springs model (it is mentioned e.g. in Ref. [11] and Ref. [12]). That is why the following work will continue the work started e.g. in Ref. [3], Ref. [13] and Ref. [17] devoted to the improvement in the approach to the leaf spring model more thoroughly (e.g. Ref. [4]).

ACKNOWLEDGEMENTS

The paper has originated in the framework of solving the project of the Ministry of Education, Youth and Sports of the Czech Republic 1M0519 “Research Centre of Rail Vehicles”.

REFERENCES

[1] *alaska 6.0, Modeling and Simulation of mechatronical Systems*. Institut für Mechatronik e.V., Chemnitz, 2010.

[2] *SIMPACK 8.902, User Manual*. SIMPACK AG, Gilching, 2009.

[3] P. Polach, M. Hajžman. Computer simulations of the freight wagon laboratory excitation. *Mechanics Based Design of Structures and Machines: An International Journal*, vol. 39, nº 2, 194-209, 2011.

[4] A.A. Shabana. Flexible Multibody Dynamics: Review of Past and Recent Developments. *Multibody System Dynamics*, vol. 1, nº 2, 189-222, 1997.

[5] D.E. Petersen, M. Hoffmann. *Dry friction and impact dynamics in railway vehicles*. M.Sc.Eng. Thesis, Informatics and Mathematical Modelling, Technical University of Denmark, Lyngby, 2003.

[6] M. Hoffmann. *Dynamics of European two-axle freight wagons*. Ph.D. Thesis. Denmark, Technical University of Denmark, Lyngby, 2006.

[7] H. Sugiyama, A.A. Shabana, M.A. Omar, W.-Y. Loh. Development of nonlinear elastic leaf spring model for multibody vehicle systems. *Computer Methods in Applied Mechanics and Engineering*, vol. 195, nº 50-51, 6925-6941, 2006.

[8] P. Polach, M. Hajžman. Computer Simulations of the Coal Wagon Laboratory Excitation and Influence of the Wagon Asymmetry. Proceedings of ECCOMAS Thematic Conference Multibody Dynamics 2011, Brussels, Belgium, July 4-7, 2011.

[9] J. Václavík, J. Chvojan, M. Kotas. *Interaction between coal wagon and rail at shaker rig at different performance conditions using UIC parabolic five leave steel suspensions*. Technical Report ŠKODA VÝZKUM s.r.o., VYZ 54/02/2003, Plzeň, 2003.

[10] P. Polach, M. Hajžman, J. Václavík, J. Chvojan. Computer simulations of coal wagon excitations on a test stand and comparison with experimental results. *Acta Mechanica Slovaca*, vol. 10, nº 1/2006, 405-412, 2006. (in Czech)

[11] P. Polach, M. Hajžman, J. Václavík, J. Chvojan. Computer Simulations of the Coal Wagon Laboratory Kinematic Excitation. Proceedings of the 45th International Conference Experimental Stress Analysis 2007, Hotel Výhledy, Czech Republic, June 4-7, 2007.

[12] P. Polach, M. Hajžman. Modified Approach to Computer Simulations of the Coal Wagon Laboratory Kinematic Excitation. Proceedings of the 46th International Scientific Conference Experimental Stress Analysis 2008, Horní Bečva, Czech Republic, June 2-5, 2008.

[13] M. Hajžman, P. Polach. Parameter identification of a leaf spring dynamic model. Proceedings of the National Conference with International Participation Engineering Mechanics 2009, Svratka, Czech Republic, May 11-14, 2009.

[14] J. Chvojan, J.Y. Cherruault, M. Kotas, R. Mayer, N.M. Gil Marcos, J. Václavík. Dynamic investigation on freight wagon suspensions. Proceedings of the 12th International Conference on Experimental Mechanics, Bari, Italy, August 29 – September 2, 2004.

[15] I. Černý. *Static and dynamic fatigue tests of the glass-reinforced plastic leaf springs used in the freight wagons*. Technical Report SVÚM a.s., No. 40E148/1, 2005. (in Czech)

[16] P. Polach. *Multibody models of MGR Coal Hopper HAA goods wagon in* ***alaska*** *software intended for laboratory tests simulations*. Research Report ŠKODA VÝZKUM s.r.o., VYZ 0773/2005, 2005. (in Czech)

[17] M. Hajžman, P. Polach. Modelling of leaf springs in the framework of multibody models. Proceedings of the 9th International Scientific Conference Applied Mechanics 2007, Malenovice, Czech Republic, April 16-19, 2007.

Proceedings of MUSME 2011, the International Symposium
on Multibody Systems and Mechatronics
Valencia, Spain, 25-28 October 2011

TRAJECTORY GENERATION THROUGH THE EVOLUTION OF THE OPTIMAL PATH

Francisco Rubio, Francisco Valero and Josep Ll. Suñer

Centre for Research in Vehicle Technology
Polytechnic University of Valencia, Camino de Vera 0, 46022 Valencia, Spain
e-mail: frubio@mcm.upv.es,
web page: http://www.upv.es/citv/Comun/inicio.htm

Keywords: Optimal trajectory, Dynamics of Robots, Obstacle Avoidance, Off-line Programming.

Abstract. *An efficient algorithm is presented to obtain trajectories of industrial robots working in static environments. The procedure starts with the obtention of an optimal path without the presence of obstacles, to find its evolution until a collision-free trajectory is generated. This is a direct algorithm that works in a discrete space of trajectories, where the global solution is approximated as the discretization is refined. The solutions obtained are efficient trajectories close to the minimum time that meet the physical limitations of the robot, collision avoidance, and where you can restrict the energy consumed.*

1 INTRODUCTION

Trajectory planning of robots is a very important issue for those industrial activities which have been automated. The introduction of robots in industry seeks to upgrade not only the standard quality but also productivity while the working times are increased and the useless times reduced. Trajectory planning has an important role to play in order to achieve these objectives (the motion of robot arms will have an influence on the work done).

Formaly, the trajectory planning problem pursue to find the force inputs (control) $u(t)$ to move the actuators so that the robot follows a trajectory $q(t)$ that enables it to go from the initial configuration to the final one while avoiding obstacles (the trajectory planning problem is also known as the complete motion planning).

Therefore, an important part to obtain an efficient trajectory plan lays on the robot actuators. Ultimately they will generate the robot motion. And it is very important to get a smooth behavior of robot to be able to work, for example, with enough precision. Therefore, the trajectory planning algorithms should take into account the characteristics of the actuators. As well as a smooth motion of the robot, it is also necessary to monitor some working parameters to verify the efficiency of the process, just in case we seek to optimize some objective function. Among the most important working parameters and variables are the time required to get the trajectory done, the input torques, the energy consumed and the power transmitted. Also the kinematic properties of the robot´s links are important as for example the velocities, accelerations and jerks.

The trajectory algorithm should also not forget the presence of possible obstacles in the workspace. Therefore it is very important to model efficiently both the workspace and the obstacles. The quality of the collision avoidance procedure will depend on this modelization.

As it was said before, it is desirable to optimize some of the working parameters mentioned earlier or some of the objective functions. The optimization criteria most widely used can be classified as follows:

(1) Minimum time required which is bounded to productivity.

(2) Minimum jerk which is bounded to the quality of work, accuracy and equipment maintenance.

(3) Minimum energy consumed or minimum actuator effort both link to savings.

(4) Hybrid criteria, e.g. minimum time and energy.

2 OBTENTION OF THE COLLISION-FREE TRAJECTORY

The problem of obtaining a feasible and efficient trajectory for a robot in an environment with static obstacles while allowing the motion between two given configurations (c^i and c^f) is posed. It is necessary to understand an efficient trajectory as that one which is near to the minimum time trajectory having a reduced computational cost and subject to the limitations of the robot dynamics as well as the jerk and consumed energy constraints. Of course, the feasibility of the trajectory means that there are no collisions with obstacles.

The proposed process for resolving the problem involves the following steps:

a) Obtention of minimum time trajectory (s_{min}).

Using the procedure described in [1] and [2], power constraints on the actuators have been added and the trajectory s_{min} is obtained corresponding to the sequence of configurations $C = \{c_i, c_f\}$. This procedure minimizes the time needed to perform the motion considering constraints on power and torque actuators, and constraints on maximum jerk and energy consumption in the trajectory, but initially the algorithm does not consider collisions, therefore you can obtain an optimal time trajectory which can cause collisions.

b) Search collisions.
The first configuration c_c from s_{min} which has collision is identified and then the previous configuration c_a is searched whose distance exceeds a set value so that the smallest obstacle can never be between c_c and c_a configurations.

c) Obtaining adjacent configurations.
Six adjacent configurations to c_a are achieved as defined ($c_a{}^j$ j=1,…,6).

d) Obtaining offspring trajectories.
For each one of the adjacent configurations l obtained in the previous section and which do not collide, a offspring trajectory s_k is obtained which came from from s_{min}. The passing points for each trajectory s_k, is $C^k = C \cup c_a^k$ (k = 1, ..., l)

e) Trajectory selection.
A set of trajectories ordered by time is generated, $T_t = \{s_1 \ldots s_l\}$, taking the minimum time trajectories s_1 and checking collisions as it was done in section b. If s_1 has no collision then the algorithm goes to the next section f, otherwise it returns to c and the process is repeated.

f) Reduction of passing points.
In the event that the collision-free trajectory s_1 is not a first generation one (direct offspring from s_{min} with a sequence of three configurations), we have:

s_1 such that $C^1 = \{c_i, c_2, c_3, \ldots, c_{m-1}, c_f\}$ (m being the number of configurations that define the trajectory).

By eliminating intermediate configurations from s_1 (except for the initial and final configurations), new trajectories are obtained, and those minimum time trajectories are called s_r without collisions obtained by reducing the passing points from s_1. There may be no trajectory s_r. If there is s_r , it is the solution of the problem, if not, s_1 is taken as a solution.

3 RESULTS

The example in Figure 1 starts from a trajectory with collisions between the two following configurations:

c^i = (-96.0 °, -11.0 °, 111.0 °, 0.0 °, -8.0 °, 0.0 °)

c^f = (77.5 °, -14.7 °, 134.3 °, 0.0 °, -30.0 °, 0.0 °)

The results are shown in the next table.

Trayectory	Nº of Passing Configurations	Time (seg)	Energy consumed (Jul)
s_{min}	0	1.5682	79
s_1	11	4.2595	376
s_r	2	2.2786	267

Table 1: Results from example 1.

21493.08 seconds of execution time on a computer with Intel ® Xeon ™ processors with 3 GHz CPU

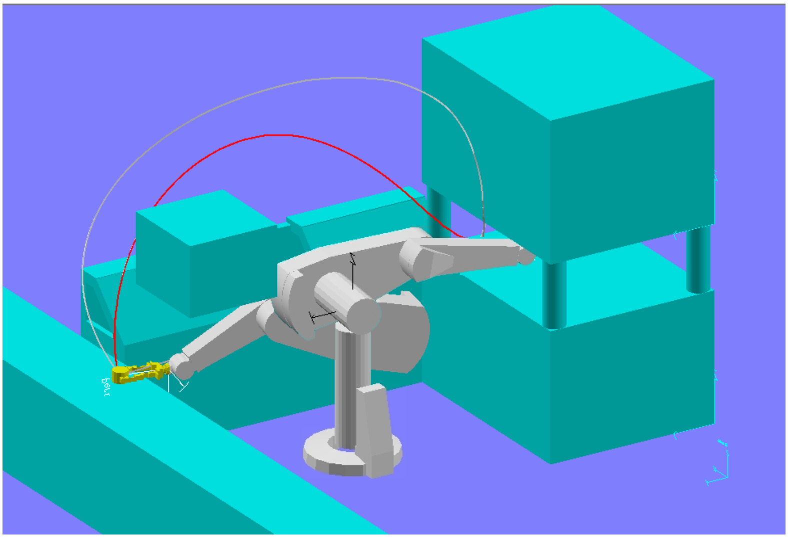

Figure 1. Trajectory

4 CONCLUSIONS

An efficient procedure for obtaining trajectories in industrial robots has been presented. An example is shown in Fig. 1.

The time required to run the trajectory are close to optimal one, as it is demonstrated in the examples. Example in Fig 1 requires 1.4563 seconds to run the trajectory avoiding obstacles, while optimal time without obstacles is 1.1360 seconds. Comparing the results it can be observed how the execution times are about 1/100 of those presented in [4]. These results confirm the above statements.

The computational time needed to obtain a solution is very dependent on the complexity of the work environment, so the example in Fig. 1 requires great amount of time, while the other examples requires a computational time of the order of 1 / 10000 compared to those of [4].

In the simplest examples the computational time is less than the execution time

REFERENCES

[1] F. Valero, J. Ll. Suñer, V. Mata, F. Rubio. Optimal time trajectory for robots with torque jerk and energy constraints. *Multibody Dynamics 2009. ECCOMAS THEMATIC CONFERENCE*. (ISBN 978-83-7207-813-1). 2009.

[2] F. Valero, V. Mata, and A. Besa. Trajectory planning in workspaces with obstacles taking into account the dynamic robot behavior. *Mechanism and Machine Theory* (ISSN 0094-114X) V 41 pp 525–536 (2006).

[3] J.L. Suñer, F. Valero, J.J. Ródenas, and A. Besa. Comparación entre procedimientos de solución de la interpolación por funciones splines para la planificación de trayectorias de robots industriales. *8º Congreso Iberoamericano de Ingeniería Mecánica.* ISBN: 978-9972-2885-31, 2007.

[4] F. Rubio, F. Valero, J.L Sunyer and A. Garrido, The simultaneous algorithm and the best interpolation function for trajectory planning. *Industrial Robot,* ISSN: 0143-991X, vol. 37, nº 5, 441-451, 2010.

Proceedings of MUSME 2011, the International Symposium
on Multibody Systems and Mechatronics
Valencia, Spain, 25-28 October 2011

EFFECT OF COOPERATIVE WORK IN OBJECT TRANSPORTATION BY MULTY-AGENT SYSTEMS IN KNOWN ENVIRONMENTS

Renato Miyagusuku, Jorge Paredes, Santiago Cortijo and José Oliden

Mechatronic Engineering School
Universidad Nacional de Ingeniería, Lima, Perú
e-mail: rmiyagusuku@giscia.com

Keywords: optimization, multi-agent systems, evolutionary algorithms, path planning, Computer vision

Abstract. *Multi-agent optimization of object transport in known environments is addressed, in order to picture the main advantages regarding cooperative work in nontrivial problems like the one mentioned. Computational simulations are used to compare the effectiveness of non cooperative, partial cooperative and totally cooperative work; the total time needed to complete the tasks is used as the cost function. Stochastic trajectory planners are used to solve navigations issues that arise when obstacles are present at the environment; and a computer vision system is used to obtain feedback of the agents and their environment. Both aspects needed for practical feasibility.*

1 INTRODUCTION

The increasing interest in real life complex problem solutions has encouraged the development of multi-agent systems. Multi-agent systems date from the 80's with [1-3] and works like [4-6] can give us a good look of these systems state of the art. According to Sahin [7], some of the most attractive characteristics these systems posses are its inherent robustness, flexibility and scalability. Keeping these in mind, this paper analyses a particular study case; object transport within known environments, and measures the effectiveness of algorithms that give the system the ability to cooperate and how communication within the system helps to improve their performance.

Given a know environment with obstacles; it is desired to transport N boxes, using a team of K agents. The main multi-agent system's goal is to deliver all boxes optimizing the time needed to successfully complete this task. An evolutionary algorithm is used to decide the order in which agents should transport the boxes so time is reduced. In addition a path planner and a computer vision system are designed so obstacles can be avoided.

In order to measure the advantages of non cooperative behavior (when agents do not share goals and just try to optimize their own work), cooperative behavior and how communication may affect it, four scenarios are simulated. First scenario works as control sample; it is commanded to only one agent to transport all boxes; the time needed to complete this task is measured. Second scenario tests the non cooperative behavior; all agents are commanded to move the boxes not considering their peers' actions. Third and fourth scenarios test the cooperative behavior. On the one hand, in the third scenario agents communicate their current status, but not their intentions. On the other hand, in the last scenario agents do communicate their intent. The boxes initial and desired positions are randomly selected. Moreover, some physical tests are also held, using a system of 3 mobile robots.

2 ALGORITHMS DESIGN

In this section we present the design of the evolutionary algorithm, the path planner and the computer vision system.

2.1 Evolutionary algorithm

Well known approaches to nonlinear optimization are evolutionary algorithms [10]. In our case, the variable to optimize is the time required to complete the task. Time can be considered proportional to:

$$t_t = \sum_{i=1}^{n} d_{i-1}^{i} + w_i \ , \tag{1}$$

where the distance d_{i-1}^{i} resents the distance between the previous box's desired position and the current box's initial position; the distance w_i, represents the distance between current box's initial and desired position, plus the time needed by the agent to grab and release the box. Furthermore, considering agents move at a constant speed; and that the environment, all boxes' initial and desired positions are known, matrix D can be easily calculated:

$$\boldsymbol{D} = \begin{bmatrix} d_{11}+w_1 & d_{12}+w_1 & \dots & d_{1n}+w_1 \\ d_{21}+w_2 & d_{22}+w_2 & \dots & d_{2n}+w_2 \\ \vdots & \vdots & \ddots & \vdots \\ d_{n1}+w_n & d_{n2}+w_n & \dots & d_{nn}+w_n \end{bmatrix}, \tag{2}$$

this way the cost function for the algorithm is calculated much faster, as it becomes:

$$J = \sum_{z(i=1)}^{z(n)} D_{(z-1,z)}, \tag{3}$$

where z is a vector that contains the order in which boxes must be delivered. If there is more than one agent, then the cost function is considered as

$$J = \max(J_1, J_2 \ldots J_K) \tag{3}$$

as it most accurately shows the total time needed to finish the task (the task shall not be considered finished as all agents finish their share of work)

Evolutionary algorithm considers 0.7 probability of crossover, 0.2 probability of mutation, and 0.1 probability of self reproduction.

2.2 Path planner

An RRT (Rapidly Exploring Random Trees) [11-12] is proposed for path planning and obstacle avoidance. This is a stochastic algorithm that randomly explores the environments empty spaces. It avoids local minima (unlike other algorithms as Potential Fields, as explained by professor Latombe [3]), but it is computationally more expensive. In order to find a path between two points, an exploring tree is generated from each of those. Once those trees intercept, the path is computed. Some variations like RRT-Ext and RRT-Basic [14] have appeared in order to reduce computing time. In this work is also proposed using of searching algorithms as NNS (Nearest Neighbor Search) [15] that can also improve computing efficiency.

2.3 Computer vision system

State feedback is required to verify the agents' behavior. In this work we use an 640x480 pixels web camera fixed above the workspace and 3 Moway[9] robots. The camera has a free look of the entire workspace surface as seen in figure 1.

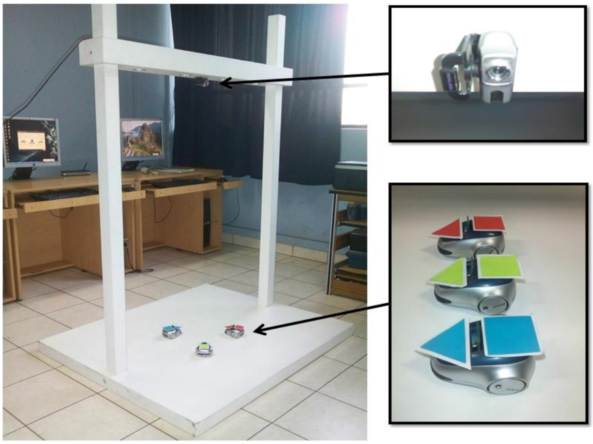

Figure 1: Moway robots and computer vision system

Discretization and resizing of the map are necessary issues, as real time implementation is required. Computer vision algorithm uses colors to identify the agents; for this purpose, colored papers were glued over the agents. Color filtering was done using HSV color scale because of its easy-suppression of brightness feature, from which binary-images are obtained (as shown in Figure 8). Those binary-images are noise-filtered by using erotion and dilation procedures. That way stable state feedback is achieved. Implementation was coded using Emgu[8] libraries in a C# environment. Communication between agents and the computer vision was achieved thanks to Moways' communications dlls, provided by the manufacturer.

3 SIMULATIONS

Several simulations were held for each scenario previously mentioned. These simulations were performed using Matlab. Figure 2 shows one of these simulations, square boxes represent the boxes' initial positions, and circles theirs desired positions. Every initial and desired position for each box has a different color and is surrounded by an ellipsoid, while lines show the order of delivery. Table shows the boxes and the agent positions, as well as the cost function J and the delivery order vector **z**.

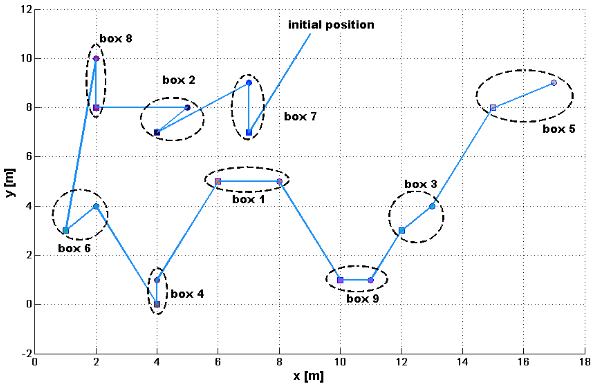

	Initial position	Desired position
Box 1	(06,05)	(08,05)
Box 2	(04,07)	(05,08)
Box 3	(12,03)	(13,04)
Box 4	(04,00)	(04,01)
Box 5	(15,08)	(17,09)
Box 6	(01,03)	(02,04)
Box 7	(07,07)	(07,09)
Box 8	(02,08)	(02,10)
Box 9	(10,01)	(11,01)

Initial position = (09,11)
J = 52.7521 aut[1]
z = [7 2 8 6 4 1 9 3 5]

Figure 2: Optimized order for 9 boxes transport with 1 agent.

Figure 3 shows the second scenario, considering 3 agents and the same distribution of boxes as figure 2. Each agent's movements are followed with different colored lines. In many cases we can observe that an agent reaches a box, but it has already been delivered, this is due to the lack of communication between agents.

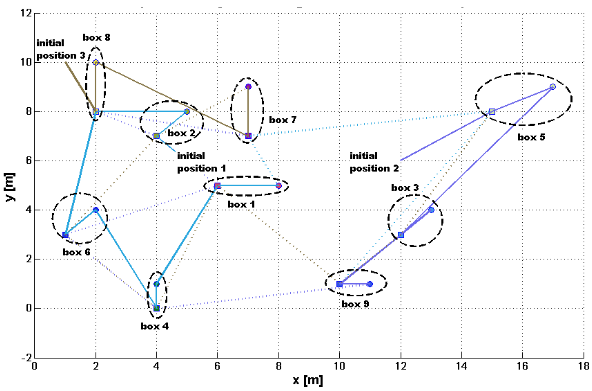

Dotted lines and underlined z numbers show unproductive work done by agents

Agent	z
1	[**2** $\underline{8}$ **6 4 1** $\underline{7}$ $\underline{5}$ $\underline{9}$ $\underline{3}$]
2	[**5 3 9** $\underline{4}$ $\underline{6}$ $\underline{1}$ $\underline{2}$ $\underline{8}$ $\underline{7}$]
3	[**8 7** $\underline{2}$ $\underline{6}$ $\underline{4}$ $\underline{1}$ $\underline{9}$ $\underline{3}$ $\underline{5}$]

Agent	$P_{initial}$	J_i
1	(05,06)	46.0150
2	(12,06)	47.1711
3	(01,10)	44.6166

J = max(Ji) = 47.1711 uat

Figure 3: Optimized order for 9 boxes transport with 3 agents (non cooperative).

[1] aut: arbitrary unit of time

Figure 4 shows the same simulation in the third scenario, in which boxes' current status is communicated between agents. It can be seen that agents no longer try to transport already delivered boxes, saving time and energy.

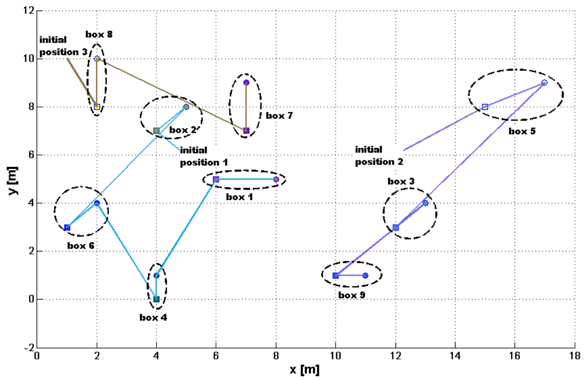

Agent	z
1	[2 6 4 1]
2	[5 3 9]
3	[8 7]

Agent	$P_{initial}$	J_i
1	(05,06)	22.5900
2	(12,06)	20.3087
3	(01,10)	12.0670

J = max(Ji) = 22.5900 aut

Figure 4: Optimized order for 9 boxes transport with 3 agents (cooperative with partial communications)

Figure 5 shows simulation in the fourth scenario, in this case agents also communicate which box they shall deliver next, as well as which box they are currently delivering.

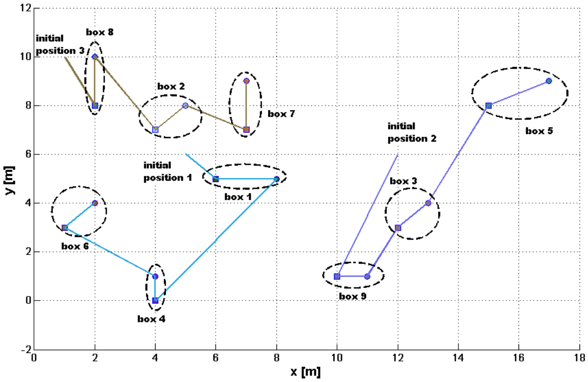

Agent	z
1	[1 4 6]
2	[9 3 5]
3	[8 2 7]

Agent	$P_{initial}$	J_i
1	(05,06)	15.8371
2	(12,06)	16.7437
3	(01,10)	13.4920

J = max(Ji) = 16.7437 aut

Figure 5: Optimized order for 9 boxes transport with 3 agents (cooperative with total communications)

Regarding the path planner, simulations were performed in order to compare different RRT's variations. One of these simulations is shown in figure 6; in which the path is computed by RRT Ext with knn-search[15] (a kind of NNS algorithm) from an initial position at (-0.75, -0.7 5) to a desired one (0.75, 0.75).

Figure 6a shows exploring trees branches while figure 6b shows path found and its post-processing simplification.

Figure 7 shows a simulation using cooperative algorithms with full communication between agents (same as figure 5), and several obstacles avoidance.

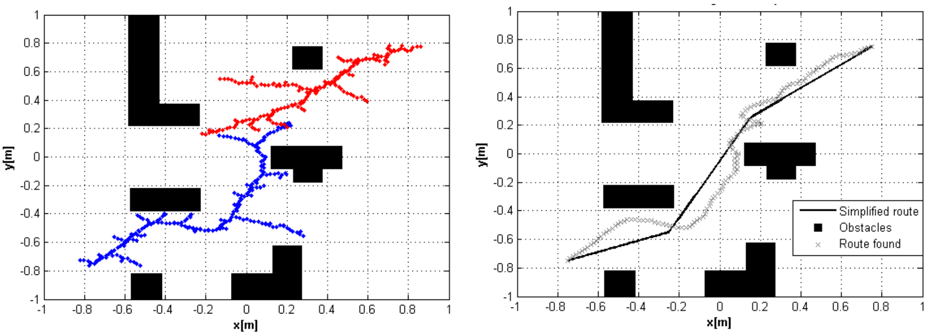

Figure 6: (a) Exploring tree branches. (b) Path found by exploring branches and simplified route computed after post processing.

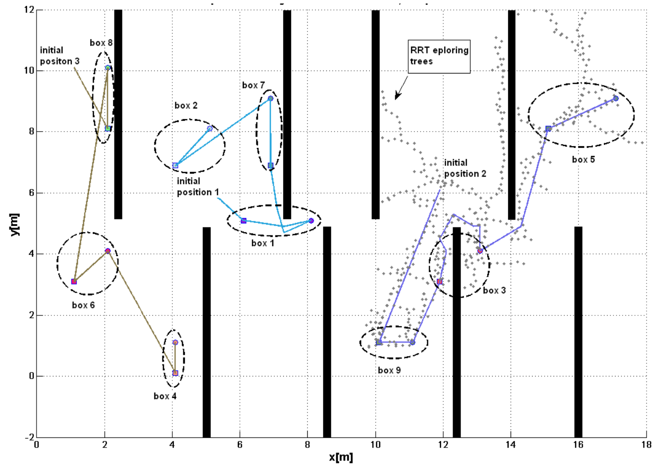

Agent	z
1	[1 7 2]
2	[9 3 5]
3	[8 6 4]

Agent	$P_{inicial}$	J_i
1	(05,06)	17.6342
2	(12,06)	19.5256
3	(01,10)	18.1935

J = max(Ji) = 19.5256 aut

Figure 7. Box transport in an environment with obstacles

Regarding physical implementation, figure 8 shows a computer vision interface written in visual C#, which also handles the communications with agents and previously discussed algorithms (evolutionary and RRT,). That interface shows camera's capture (top-left square), robot's tracking (top-right square) and obstacles (bottom-right square).

4 DISCUSSION OF RESULTS AND CONCLUSIONS

Regarding the non cooperative and cooperative algorithms, figure 9 shows the results obtained from the four different scenarios; considering 100% as needed time for 1 agent to deliver the 9 boxes. The table in figure 9 shows that on average, non cooperative behavior just saves up to 33.5% of the time, while cooperative behavior with partial communications saves 58.4% of time and full communications saves 64.7% of time. This shows how important cooperative algorithms can be, as they can boost the systems efficiently greatly.

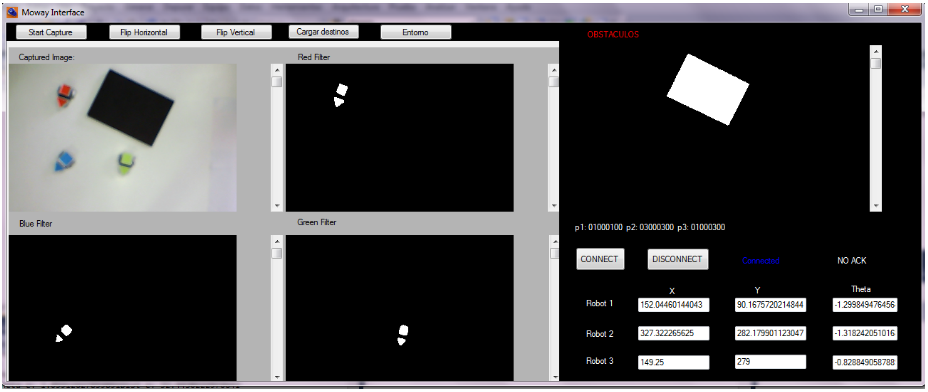

Figure 8. System Interface (C#)

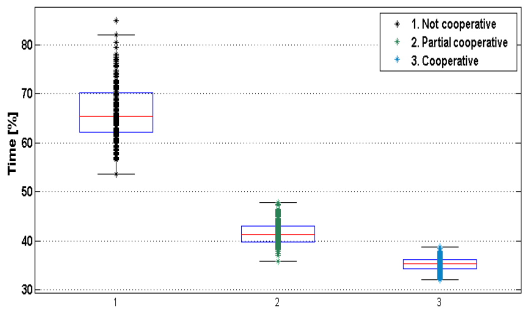

Case	Mean	Standard deviation
Non cooperative (1)	66.5	5.8
Cooperative with partial communica-tions (2)	41.6	2.2
Cooperative with full communications (3)	35.3	1.4

Figure 9: Time comparison of transporting 9 boxes.

Another interesting result obtained was the analysis of RRT's variations (RRT Ext, RRT Basic) and their improvement with knn-search. Figure 10 shows that RRT Basic, in average, needs around 0.905 seconds to find paths and RRT Ext just needs 0.187, being this, a great improvement in time. In the other hand their optimized versions with knn-search algorithm show even better performances, needing only 0.281 and 0.078 seconds respectively.

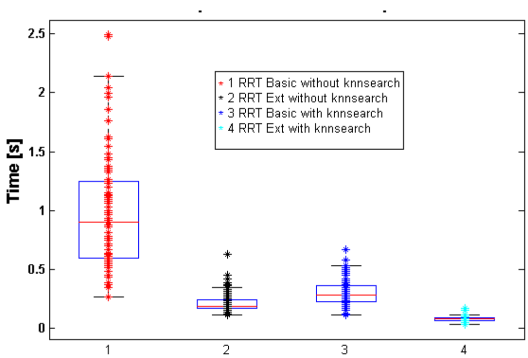

	Mean	Standard deviation
(1) RRT Basic without knnsearch	0.905	0.48
(2) RRT Ext wit-hout knnsearch	0.187	0.079
(3) RRT Basic with knnsearch	0.281	0.104
(4) RRT Ext with knnsearch	0.078	0.023

Figure 10: Time Comparison of RRT computation.

5 CONCLUSIONS

Regarding cooperative and non cooperative behavior, cooperative behavior proves to be significantly more efficient. Furthermore, communication between agents are also important as it can increase its efficiently. However, a more complete analysis is needed in order to get generalize those conclusions. About RRT's variations analized, RRT Ext is recommended over RRT Basic, and using knn-search is strongly recommended, as it notably decreases computation time required for both RRT's variations. Finally, implementation feasibility of those algorithms is proved by successful physical implementations done using the computer vision system and three Moway-robots. However, it is still required to improve color filtering used or switching to more sophisticated feedback sensors, taking advantage of distributed sensing; specially for those cases where having a plan view of the entire workspace with a camera is not feasible or practical. Nonetheless, for this particular implementation such configuration was plausible and adequate.

REFERENCES

[1] T. Fukuda and S. Nakagawa, "A dynamically reconfigurable robotic system (concept of a system and optimal configurations)," in International Conference on Industrial Electronics, Control, and Instrumentation, pp. 588–597, 1987.

[2] G. Beni, "The concept of cellular robotic system," in Intelligent Control, pp. 57–62, 1988.

[3] G. Beni, From Swarm Intelligence to Swarm Robotics. Lecture Notes in Computer Science, Springer Berlin / Heidelberg, 2006.

[4] L. Panait and S. Luke, "Cooperative multi-agent learning: The state of the art," Autonomous Agents and Multi-Agent Systems, vol. 11, pp. 387–434, November 2005.

[5] D. A. V. Veldhuizen and G. B. Lamont, "Multiobjective evolutionary algorithms: Analyzing the state-of-the-art," Evolutionary Computation, vol. 8, pp. 125–147, 2000.

[6] L. Parker, "Current state of the art in distributed autonomous mobile robotics," Distributed Autonomous Robotic Systems, 2000.

[7] E. Sahin, "Swarm robotics: From sources of inspiration to domains of application" Middle East Technical University, 2005.

[8] Documentación de la web: http://www.emgu.com

[9] Robot Moway: http://www.moway-robot.com

[10] Holland, John H (1975), Adaptation in Natural and Artificial Systems, University of Michigan Press, Ann Arbor

[11] Steven M. La Valle (1998), Rapidly-Exploring Random Trees: A New Tool for Path Planning, Iowa State University (Department of Computer Science.)

[12] Steven La Valle and James Kuffner(1999), Rapidly-Exploring Random Trees, Iowa State University and Stanford University.

[13] Lydia E. Kavraki, Petr Svestka, Jean-Claude Latombe and Mark H. Overmars, Probabilistic Roadmaps for Path Planning in High-Dimensional Configurations Spaces. IEEE Trans. On Robotics and Automation, 12(4), pp 566-580, 1996.

[14] Steven La Valle and James Kuffner(1999), Randomized Kynodinamic Planning, Iowa State University and Stanford University.

[15] Abdelmalik Moujahid, Iñaki Inza y Pedro Larrañaga ,Clasificadores K-NN.
Departamento de Ciencias de la Computacion e Inteligencia Artificial Universidad del País Vasco-Euskal Herriko Unibertsitatea

Proceedings of MUSME 2011, the International Symposium
on Multibody Systems and Mechatronics
Valencia, Spain, 25-28 October 2011

HUMAN COMPUTER INTERFACE BASED ON HAND TRACKING

Pedro Achanccaray[*], Cristian Muñoz[*], Luis Rojas[*] and Ricardo Rodriguez[†]

[*] Faculty of Mechanical Engineering
National University of Engineering, Tupac Amaru 210, Lima 25, Peru
e-mails: pachanccaray@giscia.com, cmunoz@giscia.com, lrojas@giscia.com
web page: http://www.uni.edu.pe

† Control System and Artificial Intelligence Research Group
National University of Engineering, Tupac Amaru 210, Lima 25, Peru
e-mail: robust@uni.edu.pe

Keywords: Hand Tracking, Condensation, Computer Vision, Particles Filter.

Abstract. *The idea of making interaction between human and computers easier and more natural is very attractive. In order to achieve this, it is necessary to reduce the equipment required. Vision-based Human Computer Interaction (HCI) has the potential of making this possible. This project develops a condensation based algorithm to control different devices with the gestures performed by the hand. These kinds of HCI are not very common because of its complexity. For that reason, the implementation of a background subtraction filter was necessary before hand tracking. Also, the Catmull-Rom's curves were used to model the hand. Results of hand filtering, detecting and tracking are illustrated in the paper. Finally, a possible application is given by controlling basic movements of a helicopter in a virtual world.*

1 INTRODUCTION

A way to improve the interaction between human and computers have become an important topic for developing interfaces which could make it easier and natural for people to use. Touch Panels are a good example of these kinds of interfaces. They are easy to control by the users and do not require additional equipment. However, these devices require hardware and are expensive.

For that reason, attempts to develop vision-based interactive interfaces have increased. Some of them focus on developing an interface to control robots [3] or create surfaces such as touch panels, but only with cameras as sensors [5] for different purposes. In each case, it is necessary to create a specific and robust algorithm.

This paper proposes a virtual interactive interface in order to make the system more natural for users, without complicated equipment. The user could send different instructions to the system by hand movements.

Our approach is based on 2D model of the human hand, which helps us to reduce the complexity of the involved computations and still obtain good results as will be shown later.

Section 2 describes the method used and focuses on the measurement model and improvements of it to reduce computational cost. Results are presented in section 3, which includes tracking efficiency graphics and applications of the purposed system.

2 VISUAL TRACKING METHOD

2.1 Overview

Improving the way that humans interact with computers by using an interface based on visual tracking, is a very valuable goal but, unfortunately, there is a crucial problem. The fact is that an object can generate different images depending on i ts pose or illumination. Silhouette-based approaches simplify the problem by reducing the variability of the object representations.

In this case the silhouette contour of the hand is modeled by a Catmull Rom´s curve [6] whose state is estimated using a particle filter. This model is shown in Fig. (1). The choice of a particle filter (or condensation algorithm) as the track engine comes from its capability to work in the presence of nonlinearities and non-Gaussian noise models. The details of this filter and its associated formalism can be found in [1, 2, and 7]

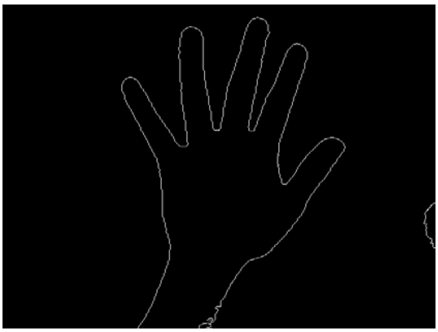

Figure 1. Contour template for hand

2.2 Dynamic Model

The dynamic model is represented by the Eq. (1):

$$X_K = A[\alpha * X_{k-1} + (1-\alpha) * X_{K-2}] + W_K \quad (1)$$

Where W_K is the gaussian noise, X_K is a characteristic measure of the object to track in each image, α is the smoothing parameter, its value varies from 0 to 1 depending on the former image and A is an experimental constant. So, the non-lineal dynamic of the object is based on evaluating the neighborhood of the previous object and predict the next position, taking as reference the Gaussian likelihood of the object position.

2.3 Particles Filter

In the visual contour tracking, the main task is to find the template configuration of object that will continue through the **T** frames in the video sequence. The configuration around the template, for the frame object is denoted by x_t, with t=1…T. To find the target object, a number of measurements are made in each frame, calculating the probability on the hypothetical boundary. Measurements in the frame t are denoted by Z_t, and measurements taken up to frame **t** are denoted by Z_t.

$$\boldsymbol{Z}_t = \{z_1 z_2 z_3 \ldots z_M\} \quad (2)$$

$$\mathrm{Z_t} = \{\mathrm{Z_1 Z_2 Z_3} \ldots \mathrm{Z_t}\} \quad (3)$$

The functional form of measurement point likelihood as formulated by Blake and Isard has the form $\mathbf{p(z|x)}$, where **z** is the set of features found along the measurement line, and **x** is the position of the hypothesized contour on the measurement line [4]. The Eq. (5) explains how to obtain it.

$$\mathrm{x_t} = \{\mathrm{x_1 x_2 x_3} \ldots \mathrm{x_M}\} \quad (4)$$

$$\mathrm{p(z_m|x_m)} = \mathrm{A} * \mathrm{e}^{-\left(\frac{(\mathrm{z_m}-\mathrm{x})^2}{2\mathrm{c}^2}\right)} \quad (5)$$

Where **c** is the standard deviation of the Gaussian, $\mathbf{v_m} = \mathbf{z_m} - \mathbf{x}$ is the distance between the **m** feature found on the measurement line, and the position of the hypothesized contour on the measurement line is **x**. Generally, x is at the midpoint of the measurement line. Fig. (2) shows how an analysis is performed for a set point along the entire hypothetic boundary; the weight of the set point is given by Eq. (5), which is evaluated along each adjustment point over the measurement line [4].

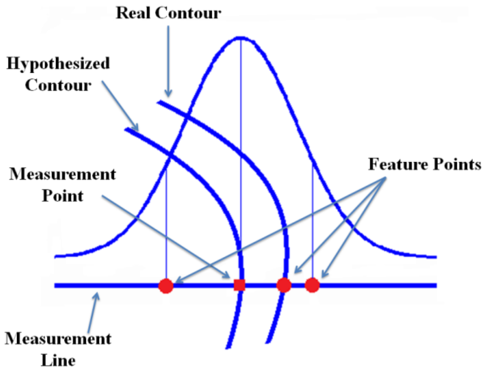

Figure 2. Measurement line normal to a hypothesized contour.

Then, the likelihood of the entire contour at time **t** is the product of each of the likelihoods of each of the **M** measurement points.

$$p(Z_t|x_t) = \prod_{m=1}^{M} p(z_m|x_m) \tag{6}$$

The weighted particle set, approximately, a probability density. In the Fig. (3), the particles are the green ellipses and their weights are proportional to their area. Picking one of the particles is approximately, the same as drawing randomly from the continuous probability function. One of the strengths of this weighted particle set representation is that, it allows the representation of multimodal distributions.

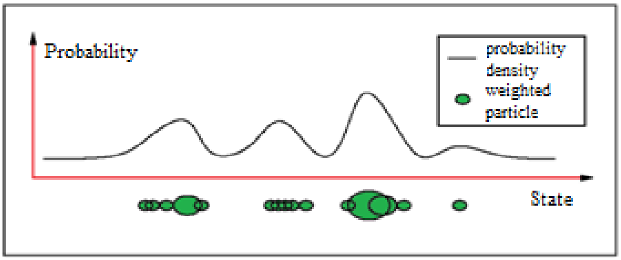

Figure 3. Weighted particles set approximation of a probability density, taken from [5].

The information of interest, for the location of the target object, is expressed as a conditional probability, $\mathbf{p_t(x_t|Z_t)}$, this is the probability of a hypothesized contour given the history of measurements. However, in general, it is difficult to calculate $\mathbf{p_t(x_t|Z_t)}$ directly. For that reason, the Bayes theorem is applied to each time-step, obtaining a posterior $\mathbf{p_t(x_t|Z_t)}$ based on all available information.

$$p(x_t|Z_t) = \frac{p_t(Z_t|x_t)p_{t-1}(x_t|Z_{t-1})}{p_t(Z_t)} \tag{7}$$

Fig. (4) shows an outline of various particles, which have different weights (denoted by the size of its circumference). According to Bayes theorem, after obtaining these values, is performed Monte Carlo analysis to obtain such particles.

All particles have the same weight, but there will be more concentrated where there had been a particle with a higher weight. Then, it compares the real shape with the outline hypothetical, getting the new weights for the particles.

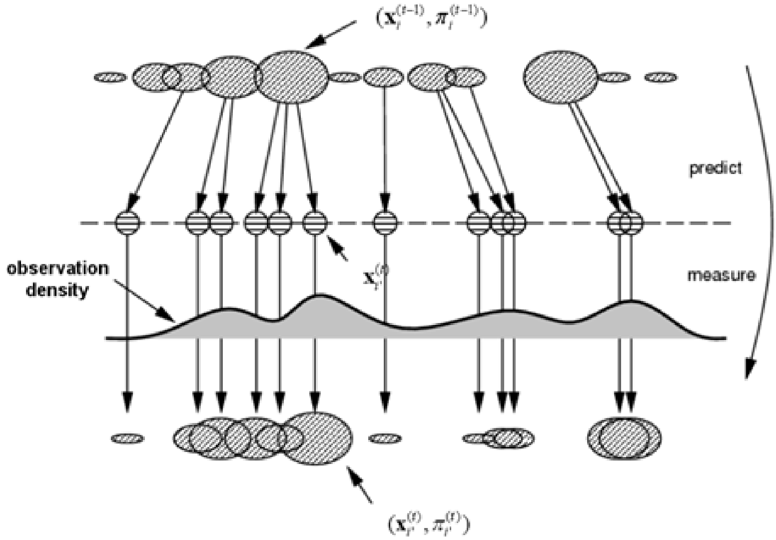

Figure 4. Condensation algorithm step by step, taken from [5]

In the Fig. (4), $\mathbf{x}^{(t)}$ is the environment configuration, $\boldsymbol{\pi}^{(t-1)}$ and $\boldsymbol{\pi}^{(t)}$ are the weights of the particles present in the frame.

2.4 Background Subtraction

In order to reduce the computational cost and make the system more robust, it was necessary to make a process of background subtraction to extract the hand silhouette. It was done in two steps. First, a skin color classifier was developed and then, morphological operations were applied to reduce the noise.

2.4.1. Skin color classifier

A skin color classifier was implemented in the YCrCb space color [8]. This space color was chosen because; it allows us to control the variation of brightness, which is a huge problem in this kind of interfaces. Fig. (5) shows the result of the classifier.

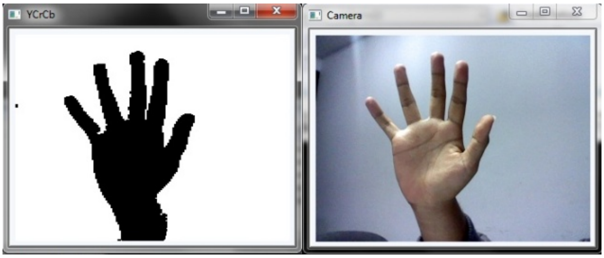

Figure 5. Skin Color classifier.

2.4.2. Noise reduction and Edge Detection

In the Fig. (5), the hand silhouette is not perfect. For that reason, it was necessary to reduce the noise using morphological operations such as Erosion and Dilatation. Then, for edge detection the Canny filter was applied. Fig. (6) shows the morphological operations and the Canny filter.

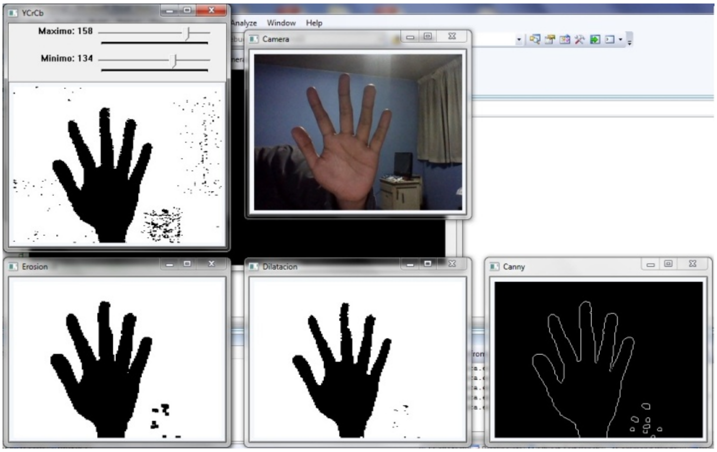

Figure 6. Result of the Skin color classifier [top left], Erosion [bottom left], Dilatation [bottom centre] and Canny Filter [bottom right].

2.5 Hand contour model

In this part, it will be explained all the hand parameters. These parameters were taken from a hand model, which is an articulated curve template built by Catmull Rom's curves from 50 control points. Fig. (7) shows the 14 parameters which were considered to have a better control of the hand silhouette. With this parameters, it can be defined a function which will represent the hand silhouette.

$$F(x, y, \propto, \lambda, \theta_0, l_0, \theta_{!}, l_1, \theta_2, l_2, \theta_3, l_3, \theta_4, \theta_5) \quad (8)$$

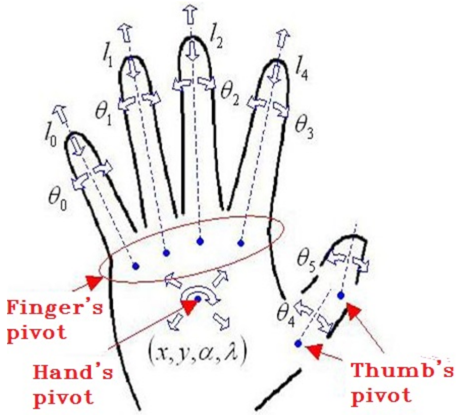

Figure 7. Parameters of the hand silhouette, taken from [5].

Where:

X and **Y** are the coordinates of the hand centroid.

α is the rotation angle of the whole hand,

λ is the hand scale,

$\boldsymbol{\theta_0}, \boldsymbol{\theta_1}, \boldsymbol{\theta_2}, \boldsymbol{\theta_3}$ are the angles formed by the fingers, pinky, ring, middle and index finger with the hand palm respectively,

$\mathbf{l_0}, \mathbf{l_1}, \mathbf{l_2}, \mathbf{l_3}$ are the lengths of fingers: pinky, ring, middle and index respectively received from the camera point of view,

$\boldsymbol{\theta_4}$ is the angle between the first segment of the thumb with respect to the palm,

$\boldsymbol{\theta_5}$ is the angle of the second segment of the thumb on the first segment.

3 RESULTS

3.1 Tracking results

The presented method has been implemented on a Dual Core 2.20 GHz laptop running Windows 7. To manage the images taken from the camera, the OpenCV (Open Computer Vision) libraries developed by Intel were used [9]. These libraries were useful to develop the skin color classifier and implement the condensation algorithm. Fig. (8) shows some tracking examples.

Figure 8. Hand Tracking

In order to measure the tracking results, efficiency curves were used. These curves are based on the mean square error, which is the sum of every little error between each point of the contour of the hand and its respective theoretical point. Eq. (9) explains how the efficiency was calculated.

$$Efficiency = \sum \frac{\left| XY_{hypothetic\,particle} - XY_{real\,particle} \right|}{error_{max}} * (Number\ of\ Particles) \tag{9}$$

Where:

$error_{max}$ is the maximum difference of pixels between the hypothetic and real contour (see Fig. (2)), $XY_{hypothetic\,particle}$ are the coordinates of the hypothetic particle and $XY_{real\,particle}$ are the coordinates of the real particle, which comes from the camera.

Fig. (9) and (10) show the efficiencies of the algorithm during movements of translation and rotation. In both cases, the efficiency starts with a low value (63%), because the tracking is beginning and the hand is not necessarily in the same position of the template, then it increases (83%) when the tracking is more stable.

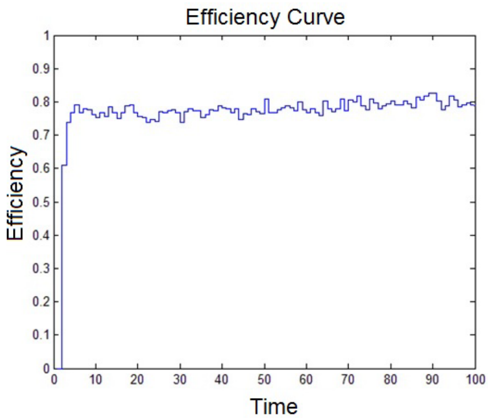

Figure 9. Efficiency Curve for hand tracking in translation state.

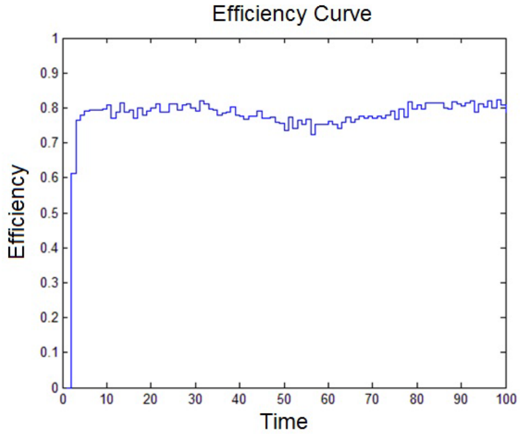

Figure 10. Efficiency Curve for hand tracking in rotation state.

3.2 Applications

3.2.1. Interface for Videogames

To manage the virtual interface, it has been considered the realization of buttons that indicate which actions were taken. These will be hidden later not to be relevant. Fig (11) and Fig. (12) show that, it was possible to identify the actions taken by the hand either upward or diagonally.

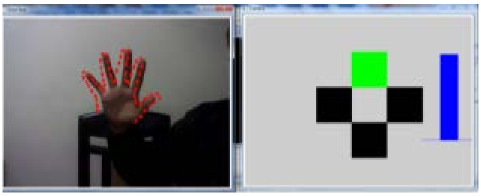

Figure 11. Identification of motion of the hand upward.

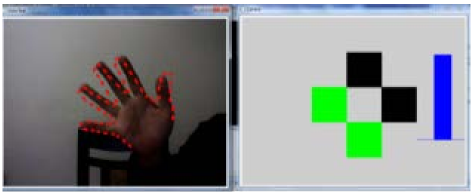

Figure 12. Identification of hand movement on the diagonal.

The screen was divided into 3 sections, top, middle and bottom, which gave the above signals, lower average in the boxes on the right side of the above figure. Once signal senses are confirmed, they interact with the virtual world developed in OpenGL (Open Graphic

Library) to manipulate an example model (in this case was a helicopter) with good results as Fig (13) shows.

Figure 13. Virtual World developed in OpenGL (left) and Control of an object by Virtual Interface (right).

The helicopter is moved in the direction of the hand rotation digitally, and taking into account the approach of the hand defines the orientation of the head tilting or ascending helicopter.

4 CONCLUSIONS

The YCrCb color space was useful and helpful for the application that was required, as can be seen in Fig. (5), because this provides proper hand isolation and a better control of brightness than in other color spaces.

The tracking efficiency is around 81% for the various movements that made the silhouette of the user's hand and a minimum of 65%, this indicates that tracking is fast and efficient for various applications such as simulation in virtual environments and control by communication protocols. The minimum value is given at the beginning, which has not yet detected the hand.

The proposed interface is suitable for different kind of applications, as demonstrated with the sample object (a helicopter). That's why; the program developed could be changed depending of the required application.

As a future work and to increase the degrees of freedom (DOF) of the system, it will be implemented a tracking for each finger, so it will allow users to simulate to touch a surface.

REFERENCES

[1] A. Doucet, Nando de Freitas, and N. Gordon. *Sequential Monte Carlo Methods in Practice, chapter An Introduction to Sequential Monte Carlo Methods*. Springer, USA, 2001.

[2] A. Blake, M. Isard, and J. MarcCormick. *Sequential Monte Carlo Methods in Practice, chapter Statistical Models of Visual Shape and Motion*. Springer, USA, 2001.

[3] P. Menezes, L. Brethes, F. Lerasle, P. Danes, and J. Dias. Visual Tracking of Silhouettes for Humand-Robot Interaction Proceedings of the International Conference on Advanced Robotics (ICAR01), vol. 2, Coimbra, 2003.

[4] A. Blake and M. Isard. *Active Contours*. Springer, 1998.

[5] M. Tosas. Visual Articulated hand tracking for Interactive Surfaces. PhD. Thesis, University of Nothingham, 2006.

[6] E. Catmull and J. Clark. A class of local interpolating splines. *Computer Aided Geometric Design*, 317-322, Academic Press, New York.

[7] M. Isard and A. Blake. Condensation, conditional density propagation for v isual tracking Proceedings of the European Conference on Computer Vision, 1996.

[8] J. Christophe and T. Shigeru. Comparative performance of different chrominance spaces for color segmentation and detection of human faces in complex scene images Proceedings of the 12th Conference on Vision Interface, 1999.

[9] G. Bradski and A. Kaehler. *Learning OpenCV*. O'Reilly, 2008.

Proceedings of MUSME 2011, the International Symposium
on Multibody Systems and Mechatronics
Valencia, Spain, 25-28 October 2011

ON THE BIOMECHANICAL DESIGN OF STANCE CONTROL KNEE ANKLE FOOT ORTHOSIS (SCKAFO)

Pedro Moreira[*], Pedro Ramôa[†], Luís F. Silva[*] and Paulo Flores[*]

[*] CT2M/DSM Department of Mechanical Engineering
University of Minho, Campus de Azurém, 4800-058 Guimarães, Portugal
e-mails: {pfsmoreira,lffsilva,pflores}@ dem.uminho.pt

[†] Department of Industrial Electronics
University of Minho, Campus de Azurém, 4800-058 Guimarães, Portugal
e-mail: pg18413@alunos.uminho.pt

Keywords: Biomechanics Project, Human Gait, Knee Flexion, SCKAFO, Electromechanical Knee Joint

Abstract. *The main purpose of this research work is to design a dynamic Stance Control Knee-Ankle-Foot-Orthosis (SCKAFO) to support patients with gait disorders, namely for patients with muscular weakness and dystrophy in quadriceps femoris muscle group. Patients with quadriceps muscular weakness are regularly prescribed a Knee-Ankle-Foot-Orthosis (KAFO).This orthotic device locks the knee in the full extension during stance phase and remains locked during the swing phase. Due to the absence of knee flexion, the KAFO users must adopt abnormal gait patterns. These abnormal gait patterns lead to compensatory movements in order to overcome the weak muscular control. A new type of orthosis, referred as Stance-Control-Knee-Ankle-Foot-Orthosis (SCKAFO), has recently emerged to allow knee flexion during the swing phase while providing controlled knee flexion in stance phase In this work several commercial SCKAFO designs are presented and their limitations are discussed. A SCKAFO electromechanical knee locking system is proposed and its requirements can be established of the intended function the knee and ankle orthotic joints should feature in order to approach a normal gait.The new dynamic SCKAFO proposed in this work should have a superior performance when compared to those currently available in the market, and aspects such as weight, cost, type of actuation and metabolic cost will play a crucial role. The new orthotic device will allow a more natural gait pattern and consequently reducing metabolic cost. An improvement in this issue will be a huge effort in reducing the high rejection rate for these orthotic devices users.*

1 INTRODUCTION

Normal walking in humans may be defined as a method of locomotion involving the use of two legs alternately to provide both support and propulsion. Walking is a periodic process and gait describes the manner or style of walking. The gait cycle is the period of time between any two identical events in the walking cycle nevertheless initial contact has been selected as the starting and completing event. The gait cycle is divided into two periods for each foot, Stance and Swing. Stance is the time when the foot is on the ground, constituting nearly 58 to 61% of the gait cycle. Swing corresponds to the tim e when the foot is in the air, constituting the remaining 39 to 42% of the gait cycle time. Double support is the period of time in which both feet are in contact with the ground. The two pe riods of double-limb support (occurring at beginning and end of stance) represent about 16 to 22 % of gait cycle [1, 2].

The gait cycle can be described in the phasic terms of initial contact, loading response, midstance, terminal stance, preswing, initial swing, midswing and terminal swing. Stance period consists of the first five phases, the re maining three ones correspond to swing period, as it is illustrated in Fig. (1).

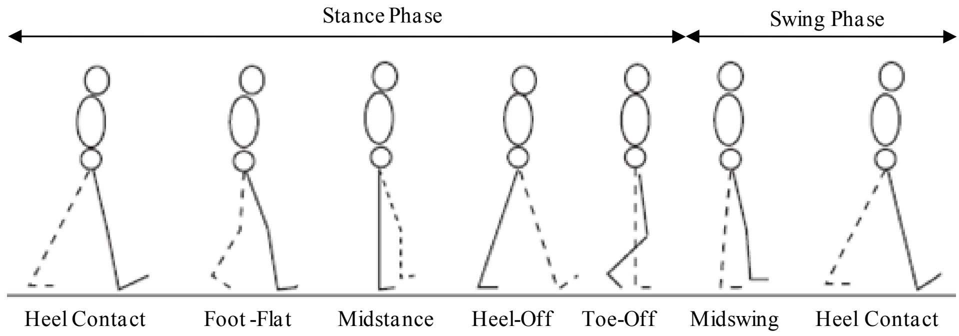

Figure 1: A typical normal gait cycle illustrating the events of gait {adapted from [2]}

The knee and ankle articulation are utm ost significance in the management of the hum an giat. The knee plays a crucial role in the m anagement of the flexion/extension m otion during the human gait. The human knee is no doubt one of the most complex articulations. In simple manner, it can be said that during a norm al gait cycle, the knee exhibits two flexion and two extension peaks [3], as it is illustrated in Figure 2.

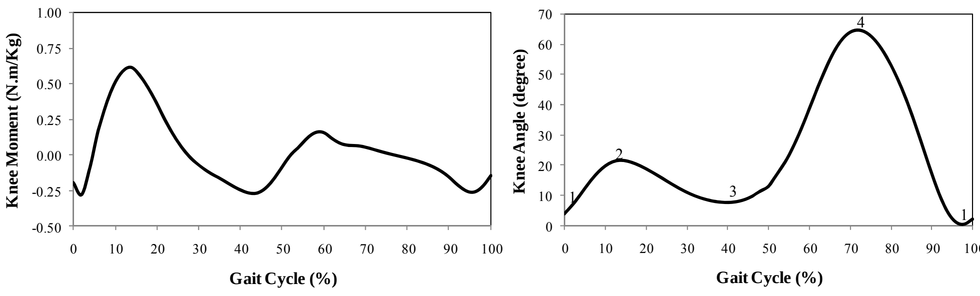

(a) (b)

Figure 2: (a) Knee angle during a normal gait cycle (b) Knee moment during a normal gait cycle { adapted from[4]}

The knee is fully extended before heel cont act, flexes during the lo ading response and the early part of mid-stance. This first flexion phase is called the stance phase knee flexion (point 2 in Figure 2). The knee extends again (point 3 in Figure 2) during the late part of the m id-stance, then starts flexing, reaching a peak during heel contact. This flexion phase is called the swing phase knee flexion (point 4 in Figure 2). The knee extends again prior to the next heel contact (point 1 in Figure 2) [1-3]. This phenomenon can be observed in Figure 2, w hich represents a complete gait cycle.

In the plot of Figure 2 b, the evolution of the knee moment during the gait cycle can be observed. The knee moment corresponds to the moment of force caused by the muscular action that will counteract the foot ground reaction force. In the beginning of the gait cycle, there is a flexor moment caused by the m uscular action that counterattacks the extension m oment produced by the heel contact. Between 5% and 27 % of gait cycle, the f oot ground reaction force causes a flexor m oment of the knee and the m uscular action counterattacks this moment inducing extension in the knee. The patient s with muscular weakness and dystrophy of *quadriceps femoris* muscular group do not have this type of muscular action. The actuation system of the new orthosis should act and prevent kne e flexion [3]. Between 27% and 50% of gait cycle the foot ground reaction force causes an extension moment and the muscular action regulates the knee full extension. At the end of th e gait cycle, a flexor moment caused by the muscles is used to control the knee extensi on and to prepare the heel impact in the ground. The knee moment during a normal gait cycle (Figure 2) reaches its maximum value during the stance phase (0.62 Nm/kg) [1].

The ankle is usually within a few degrees of the neutral position for dorsiflexion/plantarflexion at the time of initial contact. After initial contact, the ankle plantarflexes, bringing the forefoot down onto the ground. During mid-stance, the tibia moves forward over the foot, and the ankle joint becom es dorsiflexed. Before opposite initial contact, the ankle angle again changes, a m ajor plantarflexion taking place until just after toe off. During the swing phase, the ankle moves back into dorsiflex ion until the forefoot has cleared the ground (around feet adjacent), after which so mething close to the neutral position is m aintained until the next initial con tact. The ankle moment during a norm al gait cycle (Figure 3) reaches its maximum value during the stance phase (1.6 Nm/kg) [1-3].

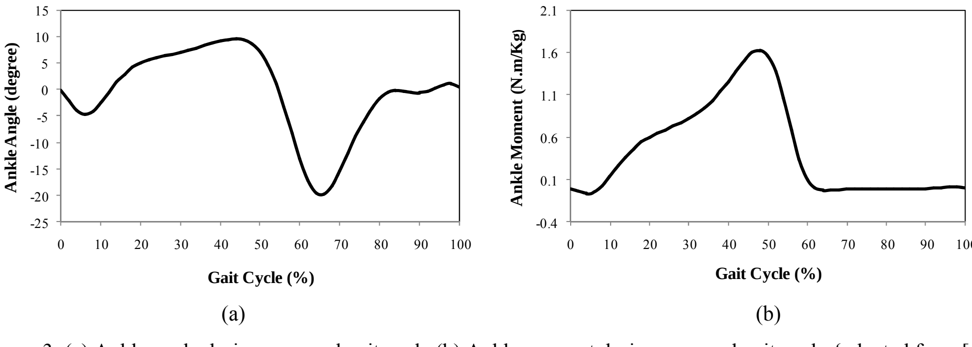

Figure 3: (a) Ankle angle during a normal gait cycle (b) Ankle moment during a normal gait cycle {adapted from [4]}

This paper is organized in five sections , namely introduction, knee-ankle-foot-orthosis (kafo) and stance phase nee-ankle-foot-orthosis (sckafo) solutions for gait disorders caused by muscular weakness/distrophy of *quadriceps femoris* muscle group, orthotic knee locking systems for kafo and sckafo orthotic devices, de sign guidelines and control of a electromechanical knee locking system and concluding remarks.

The main motivation for this research work comes from a specific need from patients with *quadriceps femoris* muscular weakness. The *quadriceps femoris* muscle group is com posed by a total of eight m uscles responsible for the knee flexion-extension m otion, namely: *Biceps Femoris Short Head*, *Vastus Medialis, Vastus Lateralis, Vastus Intermedius, Rectus Femoris, Biceps Femoris Long Head, Semitendinosus* and *Semimembranosus* (Figure 4a)[1, 5]. This set of muscles plays a crucial role in the human gait because the abnormal flexion/extension motion of the knee can induce irregular and unsafe gait patterns This particular type of muscular weakness of lower limb can be the result of different diseases, such as peripheral neurological diseases (poliomyelitis and post-po lio syndrome, spina b ifida, poly ne uropathy), muscular diseases (Duchenne m uscular dystrophy, Becke r's muscular dystrophy, m yasthenia gravis) and central neurological diseases (multiple sclerosis, cerebral palsy, Parkinson disease, brain injury, stroke and spinal cord injury [6, 7]. The result of the reduced m uscle-strength or muscle-control in these diseases is the cause for a common pathological gait. When a patient with muscular weakness touches the ground with his foot (heel contact), they does not have enough muscle strength to oppose the reaction force fro m the ground that m akes him flex the knee instead of extend.

Figure 4b depicts description of the six grades of manual muscle tests, in order to c haracterize the patient muscles control. Manual muscle testing is a procedure for the evaluation of the function and strength of individual m uscles and muscle groups based on effective performance of limb movement in relation to the forces of gravity and manual resistance. Maximum muscular strength is the m aximum amount of tension or force that a m uscle or muscle group can voluntarily exert in one maximal effort, when the type of muscle contraction, limb velocity, and joint angle are specified. Grade 0 repr esents a non-active muscle and a grade 5 represents a normal muscle [1, 3, 8].

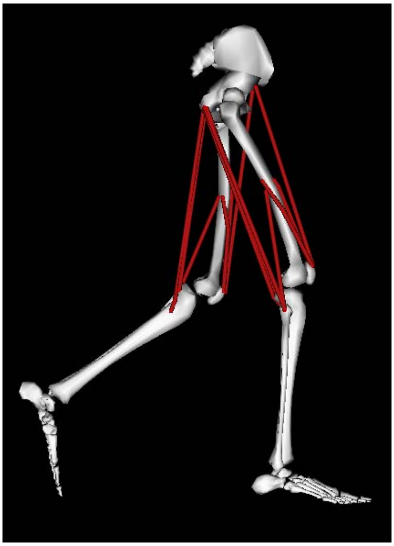

(a)

Grade 5 – Patient can hold a position against maximum resistance and through complete range of motion

Grade 4 –Patient can hold a position against strong to moderate resistance, has full range of motion

Grade 3 – Patient can tolerate no resistance but can perform m ovement through the full range of motion

Grade 2 – Patient has all or partial range of motion in the gravity-free position

Grade 1 – Muscle(s) can be palpated while patient is performing the action in the gravity-free position

Grade 0 – No contractile activity can be felt in the gravity eliminated position

(b)

Figure 4: (a) Configuration of a generic biomechanical model with *quadriceps femoris* muscle actuators [9] (b) Grades and descriptions of manual muscle tests

2 DESCRIPTION OF KNEE-ANKLE-FOOT-ORTHOSIS (KAFO) AND STANCE CONTROL KNEE-ANKLE-FOOT-ORTHOSIS (SCKAFO) SYSTEMS

Since last century, the Knee-Ankle-Foot Orthosis (KAFO) has been used for decades to overcome weakness and instability of the leg. Knee-Ankle-Foot -Orthosis (KAFO) is an orthotic device that locks the knee in the full extension during stance phase and remains locked during the swing phase. Due to the absence of knee flexion, the KAFO users must adopt abnormal gait patterns (Figure 5a). A new type of orthosis, referred as Stance-Control-Knee-Ankle-Foot-Orthosis (SCKAFO), has recently emerged to allow knee flexion during the swing phase while providing controlled knee flexion in stance phase for patients with *quadriceps femoris* muscle weakness with muscle grade at least 3, as described by Johnson et al. [10]

There are some disadvantages when the patients make use of these orthotic devices. The ankle and knee internal moments will increase because the patients have an extra weight in their leg. Most of the orthotic devices nowadays avaiable are heavy, bulky, noisy, expensive, unattractive and offers a limited locking position. It should be highlighted that some compensatory movements will take place such as hip elevation during phase (hip hiking), ankle plantarflexion of the contralateral foot (vaulting), increased upper-body lateral sway and leg circumduction [11]. On the other hand, the prescription of these devices allow the patients to obtain a more symmetric gait, improved mobility, improved gait kinematics, reduced compensatory movements and energy consumption.

Overall, the SCKAFO orthosis promotes a more natural gait kinematics for orthosis users, compared to the conventional KAFO users, as Figure 5b shows [11, 12].

The first materials used in the KAFO conception were heavy metallic alloys, wood, leather and textile. The typical configuration of a KAFO consists of leather or thermoplastic thigh and calf bands attached to metal uprights joined by a footplate, as can be observe in Figure 5a. For that reason the first orthoses were considered heavy and und unattractive. During the last years, great improvements have been made in the cosmetic finish of the KAFO. New materials such as carbon fibers, thermoplastics and polymers are responsible not only for the weight reduction but also to turn the orthotic device more attractive [13]. More recently a new type of KAFO has emerged, namely the SCKAFO dynamic orthosis. Figure 5 depicts the evolution of different types of knee orthosis.

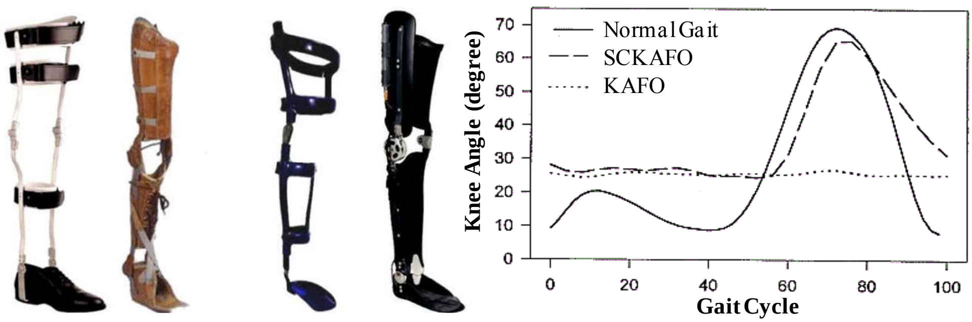

(a) (b)

Figure 5: (a) Historic evolution of knee orthotic devices from KAFO (left devices) to SCKAFO (right devices) (b) Knee angle during human gait: (1) without orthosis, (2) with SCKAFO and (3) with KAFO {adapted from [11]}

3 ORTHOTIC KNEE LOCKING SYSTEMS

Over the last few years the development of knee locking systems for orthotic devices has been an active research topic and still is an open engineering problem. The knee structural mechanism must support the high flexion moments that occurs during human gait. The knee joint components that are mechanical efficient and sufficiently safe are not light and small [12]. There are three types of KAFO orthotic knee joints available.

The bail lock (Figure 6a) is easy to unlock when moving from standing to sitting. It is useful when an individual is using bilateral KAFOs or has decreased hand function. One disadvantage is the cosmetic quality caused by the posterior volume.

The drop or ring lock (Figure 6b-c) is a second method for maintaining the knee locked in extension. It has cosmetic qualities, but requires good hand function to operate.

The offset knee joint (6a) is used to provide increased knee stability by moving the mechanical knee axis posterior to the anatomic knee joint, thus enabling the individual to easily position their center of mass anterior to the knee joint axis. Unilateral weakness of the quadriceps can be addressed with a KAFO with an offset free knee joint used in conjunction with a dorsiflexion stop at the ankle, and approximately 10 degrees of plantarflexion range of motion at loading response. The advantages for using this design include decreased energy consumption, caused by a more normal center of mass pathway during swing phase, ease in moving from sitting to standing, and an improved gait appearance. Disadvantages include instability when going down an incline or negotiating uneven terrain [12].

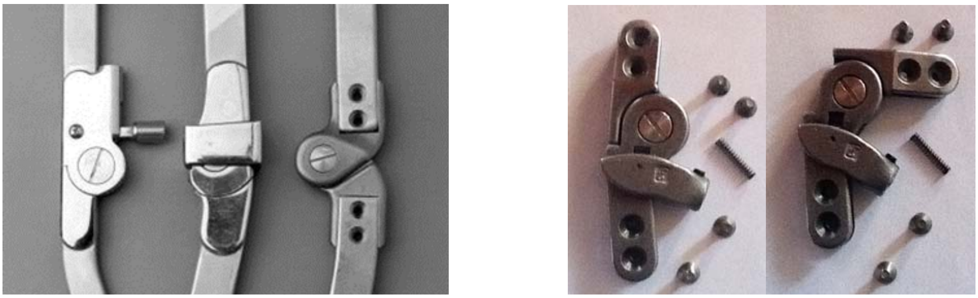

(a) (b) (c)

Figure 6: (a) Bail, ring/drop and offset lock respectively (b) Ring/drop lock in locking position (c) Ring/drop lock in unlocking position

There are different type of actuation systems that allow free motion in the swing phase and provide knee flexion at any knee angle in the stance phase, such as mechanical [11, 14, 15], electromechanical [6, 16-19], pneumatic[20], hydraulic and hybrid [21, 22]. The hybrid actuation combines the Functional Electrical Stimulation (FES) with a mechanical or electromechanical system. The electric stimulation is applied to muscles of the leg to improve its trajectory during swing phase, and an orthosis is responsible to provide the necessary torque during the stance by means of mechanical systems [22, 23]. However the use of Functional Electrical Stimulation presents important limitations such as rapid muscle fatigue, high complexity of work and difficult motion control. Depending on the type of pathology presented by the patient, an appropriate actuation system and commercial SCAKO is recommended for the specific case [8, 13, 24-26].

In the following sections, a brief description of the most relevant SCKAFO orthotic devices and respective locking systems, is offered, namely Otto Bock Free Walk and Becker UTX, Horton Stance Control Orthosis, Fillauer Swing Phase Lock and Becker Orthopedic 9001 E-Knee. There are other SCAKO orthotic devices that are developed but still remains in patent process and are not commercial available, such as Controlled Electromechanical Free-Knee Brace and Ottawalk Belt-Clamping Knee Joint [27]. It is important to highlight that are an interest of the academic researchers in the study of the performance of this devices.

3.1 Otto Bock Free Walk and Becker UTX

These orthoses are produced by two different companies, namely Otto Bock HealtCare and Becker Orthopedic, respectively. These orthotic devices shared the same ratchet/pawl locking system illustrated in Figure 7. A spring-loaded pawl locks the knee automatically when the knee fully extends to heel contact (Figure 7 a). When the ankle is 10 º dorsiflexed allows the control cable to the pawl to pull down and disengage the lock (Figure 7 b).

These orthosis only can be prescribed to patients without limitations in *tibialis anterior* muscle. This muscle is responsible for the ankle dorsiflexion/plantarflexion. The knee full extension is required to engage the knee locking system and the simultaneous extension and 10º of ankle dorsiflexion is required to eliminate the flexion moments, about the knee and free the pawl from friction to disengagement [17].

The knee will be unsupported if flexed during the mid-stance and this situation is common when users walk on stairs and during stumbling. It has been reported that the orthotic devices are the lightest and most cosmetically attractive of all commercial SCKAFO. However, the users of these orthotic devices feel insecure because these devices have a delicate tubular steel structure [27].

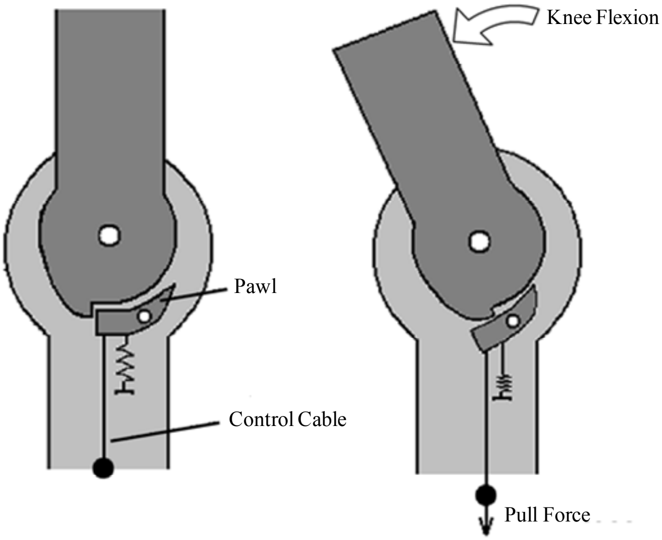

Figure 7: (a) Spring-loaded pawl locks knee when full knee extension (b) Dorsiflexion of foot at end of stance phase pulls on control cable connected to disengage lock system {adapted from [27]}

3.2 Horton Stance Control Orthosis

The Horton Stance Control Orthosis is produced by Horton Technology and presents a locking system with a unidirectional clutch design and involves jamming an eccentric cam into a friction ring that is attached to the upper-knee joint (Figure 8). A thermoplastic stirrup is positioned just below the thermoplastic ankle-foot-orthosis (AFO) shell and goes along the length of the orthosis being attached to a pushrod that is attached to the eccentric cam [15].

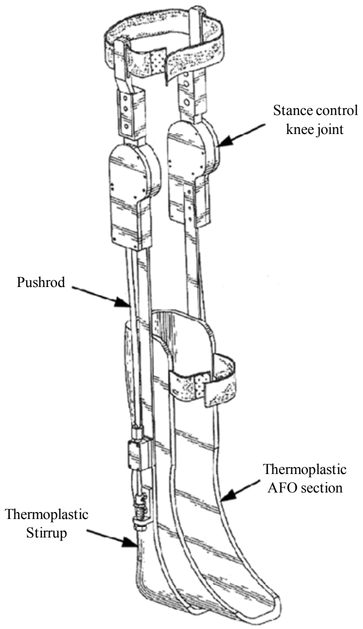

(a)

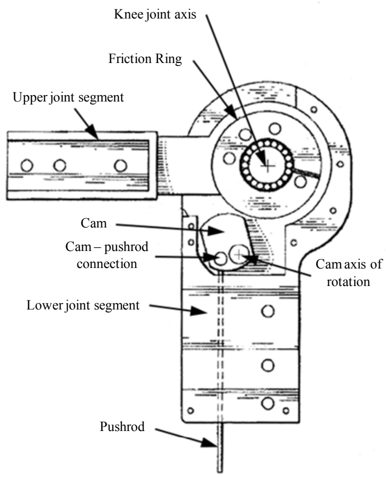

(b)

Figure 8: (a) Horton Stance Control Orthosis (b) Locking mechanism (unlocked) {adapted from [27]}

When heel contact occurs, the stirrup is pushed upward to engage the pushrod and drive the cam into the friction ring. The surface of hardened steel cam and friction ring is textured with microgrooves that eliminate slip between the cam and friction ring. When the cam is engaged, knee flexion causes the friction ring to load the cam, thereby locking the system. Knee extension pushes the cam away from the friction ring, allowing free motion. When the foot plantar flexes, the cam will push upward to engage the lock. In this orthosis there is a switch on the side of each joint that allows three different modes: automatic stance/swing, constant free knee motion and constant locked knee extension. These different modes add versatility to the orthosis. Constant locked knee extension can be useful for orthosis users walking in unsure surroundings, and free knee motion mode facilitates daily activities, such as driving a car.

The Horton Stance Control Orthosis is bulky and joints are relatively large by KAFO standards. This design allows locking the knee at any angle but some users may not tolerate the bulk of this orthotic device. The sensitive locking mechanism may restrict users to walk with a consistent step length and speed to achieve reliable engagement [15, 27].

3.3 Fillauer Swing Phase Lock

The SCKAFO orthotic device developed by Fillauer, presented a novel gravity-actuated knee-joint locking mechanism. The locking system consists of a weighted pawl falls in and out position, depending on user's thigh angle, as it is depicted in Figure 9.

When the hip is flexed with the thigh anterior to the body, as in terminal swing, the weighted pawl falls into locked position to prevent knee flexion (Figure 9a). The knee must be fully extended to fall into the locking position. When the hip swings behind the body prior to the swing phase, the pawl disengages and the knee flexes freely (Figure 9b). An extension knee moment is required to disengage the locking system. The hip angle required to engage and disengage the pawl is manually set on the joint by an orthotist. There are three modes remaining to the locking system of this orthotic device: manual lock, free swing and automatic lock/unlock. Since the locking mechanism depends on limb-segment orientation, this SCKAFO is not appropriate for users to securely climb stairs or walk on uneven ground [27].

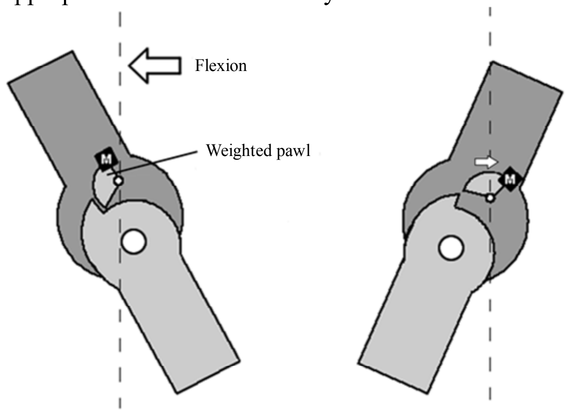

(a) (b)

Figure 9: (a) Weighted pawl falls in locked position (b) Weight pawl falls out of engagement {adapted from [27]}

3.4 Becker Orthopedic 9001 E-Knee

The Becker Orthopedic 9001 E-Knee uses a magnetically activated one-way dog clutch (Figure 10). The joint incorporates two circular ratchet plates coupled with a tension spring. When foot pressure sensors below the foot detect foot contact, the electromagnetic coil is energized and the ratchet plates are forced together. When the locking system is engaged, the ratchet plates allow angular motion in only one direction. During the stance phase, knee flexion is resisted, while knee extension is still allowed.

The ratchet plates experience two disadvantages. The first disadvantage is that orthotic device generates a clicking sound when rotated under engagement (when patients extend their knee in stance).The aesthetics are an important issue to take into account by the user. If an orthosis generates two much noise, probably it will be rejected by the user. The second disadvantage consists in the lack of confidence by the users because the locking mechanism cannot engage rapidly. The 9001 E-Knee is bulky, heavy and the cost is relatively high compared with other SCKAFO [27].

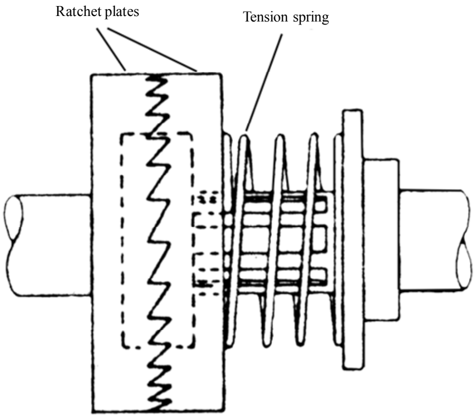

Figure 10: Locking mechanism of Becker Orthopedic 9001 E-Knee {adapted from [27]}

3.5 Dynamic Knee Brace System

Kaufman et al. [11, 14] introduced a new SCKAFO technology by introducing a electromechanical knee-joint control. The system is composed of mechanical hardware and an electronic control system. The mechanical locking system consists of a wrap-spring clutch and uses a close-wound helical spring to transmit torque across a pair of mating concentric hubs (Figure 11). When the knee flexion occurs, the spring tightens over both concentric hubs, thus preventing knee flexion by stopping the relative motion between the two hubs. Knee extension causes the spring to unwind and allow relative motion of the two hubs. To disengage the clutch selectively in swing, the spring is loosened by pulling back on one end of the spring via a solenoid. The wrap-spring clutch has the unique ability to switch from stance to swing mode while loaded in flexion. This kind of joint mechanism demands less mental and physical effort from the user to control the orthosis than SCKAFO that require a knee extension to switch from stance to swing mode. When installed in a SCKAFO, this locking mechanism founds to be heavy and unattractive [27].

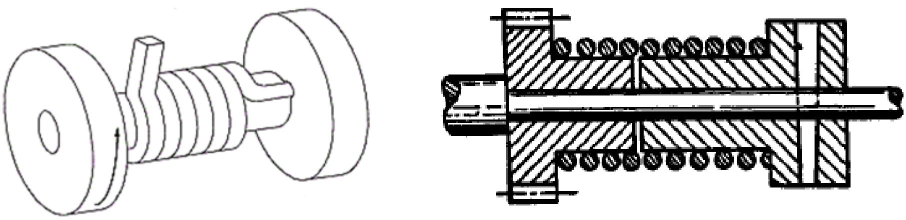

Figure 11: Wrap-spring clutch mechanism {adapted from [27, 28]}

3.6 Ottawalk Belt-Clamping Knee Joint

Yakimovich et al. [17, 18, 27] developed a friction-based belt-clamping mechanism to provide free motion during swing in a SCKAFO knee joint. During the stance phase, the joint resists knee flexion and allows the knee to extend freely at any angle. When the knee moves into flexion (Figure 12), the belt tension will increase. A knee extension moment at any time during stance phase reduces belt tension, thereby releasing the clamp to allow the belt to travel freely for knee extension. For free knee flexion and extension in swing, a plate is displaced into the path of the clamp lever to prevent belt-clamping. A pushrod activated by foot pressure or ankle angle is used for displacing the switch plate between stance and swing phase. The elasticity in the belt allows some knee flexion in early stance rather than abrupt mechanical locking. This helps absorb shock at heel contact.

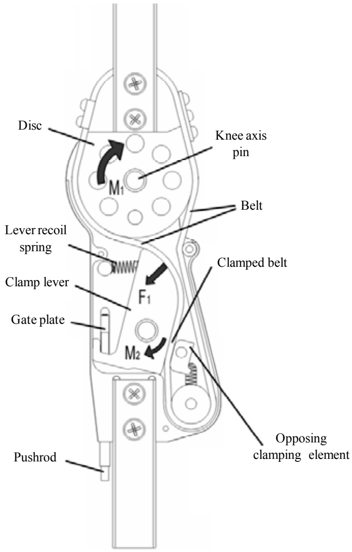

Figure 12: Friction-based Ottawalk belt-clamping knee joint in stance model {adapted from [27]}

3.7 Dual Stiffness Knee Joint

The Moreno et al. [6] have developed a SCKAFO that expands on earlier use of springs at knee joint by offering two levels of torsional elasticity at the knee. To detect stance and swing phases for the braced limb, gyroscopes and dual-axis accelerometers are positioned on the foot and shank, and an angular position sensor is located at the knee. The joint uses two stainless steel compression springs of stiffness K_1 and K_2, where $K_1 >> K_2$, to achieve two levels of torsional stiffness. During stance, the device uses stiffness K_1 in the knee joint for shock absorption during initial mid stance and for energy return during knee extension. During swing, the device switches to stiffness K_2 to store and recover spring energy that assists knee extension in terminal swing. The SCKAFO is bulky and, because of the solenoid power requirements, has an approximately 2.5 hours battery life. However, the orthosis can be modified for mechanical control by pulling on a cable during ankle dorsiflexion. This dual-spring knee joint is not yet commercially available.

4 DESIGN GUIDELINES OF A ELECTROMECHANICAL KNEE LOCKING SYSTEM

The requirements for a new electro mechanical knee locking system can be established of the intended function the knee and ankle orthotic joints should feature in order to approach a normal gait, as can be observed in section 1. If an external actuation system is going to be designed, it must be inspired in the functional actions of the musculo-skeletal system during the gait cycle. The main purpose is to do a reliable replication of the musculo-skeletal apparatus.

A design that exactly duplicates the dynamic behavior of the knee during the normal gait cycle is out of chance. First of all, during the stance phase the knee angle variation is quite small (Figure 2a). In order to simplify the biomechanical design, a fixed angle during the stance phase is proposed. This characteristic simplifies the task of the electromechanical locking system that will still locked during this stage [28, 29].

Patients with muscular weakness in the *quadriceps femoris* muscle group do not have muscle control and the main objective is to assist extension. The maximum knee moment occurs in this phase and will be the main parameter taking into account in the actuation system.

In order to synchronize the locking and unlocking functions and actuation in the knee and ankle articulations, it will be necessary obtain biomechanical parameters that allow us to identify in which phase of gait the patient wearing the orthosis remains. This is the first step to control the actuation and locking system [29]. These biomechanical parameters will be obtained using sensors. There are three types of sensors that can be used in this application: three axis accelerometers (Figure 13a), force resistors (Figure 13b) and rotational encoders (Figure 13c).

(a) (b) (c)

Figure 13: Different type of sensors (a) three-axis accelerometer (b) force resistor (c) rotational encoder {adapted from [29]}

During the gait cycle it is necessary to distinguish the stance and swing phases with foot resistors placed in the plantar surface of the foot. With these sensors the contact between the foot and the ground will be known at each time step of the gait cycle (Figure 14b). A total of three force sensing resistor will be proposed to check which part of the foot is in contact with the ground. The first sensor will be placed in the heel, the second in the 5th metatarsal head and the third in the big toe (Figure 14a).

A force sensing resistor (Figure 13b) will vary its resistance depending on how much pressure is being applied to the sensing area. The harder the force applied, lower is the resistance. These sensors are simple to set up and great for sensing pressure and are indicated for applications where the measure the amount of force being applied over an area is necessary [29].

Location of the force sensing resistor				
Heel	5th metatarsal	Big toe	Actuation	Gait Cycle
On	On	Off	Locked	Heel Contact
O	On	Off	Locked	Midstance
On	Off	Off	Locked	Midstance
On	On	On	Locked	Midstance
On	Off	On	Locked	Midstance
Off	On	On	Locked	Heel Off
Off	Off	On	Locked	Pre-swing
Off	Off	Off	Unlocked	Toe off

(a) (b)

Figure 14: (a) Location of the force sensing resistors (b) Control of the locking system taking into account the signal from the force sensing resistors

The accelerometers (Figure 13a) or rotational encoders (Figure 13c) will be used to measure the knee and ankle articulations angles. The analysis of these biomechanical parameters will be a useful tool to check the kinematic of the referred articulations during the gait cycle. A microcontroller (Figure 15a) will processes and interprets the signal from the force resisting sensors and accelerometers or encoders and will send a signal to a RC servo motor (Figure 15b) in order to lock or unlock the knee electromechanical joint of the orthotic device. The microcontroller is an open-source physical computing platform based on a simple I/O board and a development environment that implements the Processing/Wiring language [29].

(a) (b)

Figure 15: (a) Microcontroller (b) RC servo motor {adapted from [29] }

An actuator will be coupled to the RC servo motor in order to lock or unlock the knee electromechanical joint. The selection of the appropriate actuator for this application is still in study. This actuator could be mechanical (pawl, cam follower, pinion, pin), pneumatic or hydraulic. First of all, a typical Knee-Ankle-Foot-Orthosis (KAFO) with a ring/drop locking system will be instrumented with the sensorial apparatus (Figure 16). In the KAFO depicted in Figure 16 only the thigh and calf components are presented. The RC servo motor will be coupled to a steel cable that will allow locking or releasing the ring of the knee locking system. This methodology will be used in order to validate the sensorial apparatus, the signal processing of the microcontroller and the action of the RC servo motor. After this instrumentation, the foot part will be added to the orthosis and the ankle will be instrumented.

Figure 16: A typical KAFO (Knee-Ankle-Foot-Orthosis) without the foot component

Summarizing, the main functions of this orthotic device are *i)* when the foot reach the ground the knee joint blocks and remains blocked in the stance phase; *ii)* free flexion in swing phase. All of the commercial SCAFO presented before satisfy at least of those requirements. Although, in this research work the following requirements will taken into account:

- Locking the knee or resisting knee or ankl e flexion, instead of full knee extension (climb and descend stairs, stand with a flexed knee and stabilize after stumbling);
- Maximum knee flexion angle of 120º;
- Unlocking the knee at any angle (allowing to sit and climb/descend stairs);
- Smoothly switching between stance and swing modes;
- Switching stance-swing mode without requiring knee full extension to unload the joint;
- Decrease total orthosis weight, with special consideration to locking mechanism;
- Sizing the orthotic components in order to support a considerable patient weight;
- Ergonomic and cosmetic design (maximum reduction of contact area between the orthotic device and leg);
- Reduce switching noise between swing and stance phase;

5 CONCLUDING REMARKS

The main purpose of this research work is to design a dynamic Stance Control Knee-Ankle-Foot-Orthosis (SCKAFO) to support patients with gait disorders, namely for patients with muscular weakness and dystrophy in *quadriceps femoris* muscle group. Special attention will be given to the behavior of the knee and ankle articulations during the gait cycle. The requirements for a new electromechanical knee locking system can be established of the intended function the knee and ankle orthotic joints should feature in order to approach a normal gait. The most relevant knee locking systems for orthotic devices (KAFO and SCKAFO) has been presented and discussed. In order to synchronize the locking and unlocking functions and actuation in the knee and ankle articulations, it will be necessary obtain biomechanical parameters that allow us to identify in which phase of gait the patient wearing the orthosis remains. These biomechanical parameters will be obtained using sensors (accelerometer, force resistor and encoder). A microcontroller will processes and interprets the signal from the force resisting sensors and accelerometers or encoders and will send a signal to a RC servo motor in order to lock or unlock the knee electromechanical joint of the orthotic device.

For future work, a typical Knee-Ankle-Foot-Orthosis (KAFO) with a ring/drop locking system will be instrumented with the sensorial apparatus. This methodology will be used in order to validate the sensorial apparatus, the signal processing of the microcontroller and the action of the RC servo motor. The selection and application of the mechanical actuator for the orthotic device will be also performed.

ACKNOWLEDGMENTS

The first authors would like to thank the Portuguese Foundation for Science and Technology (FCT) for the PhD Grant SFRH/BD/64477/2009.

REFERENCES

[1] M. W. Whittle. *Gait Analysis: An Introduction*, 4th ed. Philadelph ia: Butterworth Heinemann Elsevier, USA, 2007.

[2] H. Lakany. Extracting a gait analysis signature. *Pattern Recognition*. 41, 1627-1637, 2008.

[3] D. A. Winter. *Biomechanics and Motor Control of Human Movement*, 3rd ed. Toronto: John Wiley & Sons, Canada 1990.

[4] D. A. Winter. The Biomechanics and Motor Control of Human Gait: Normal, Elderly and Pathological, 2nd Edition University of Waterloo Press, Canada, 1991.

[5] M. Ackermann and W .Schiehlen. Dynamic analysis of human gait disorder and metabolical cost estimation, *Archive of Applied Mechanics* 75, 569-594, 2006.

[6] A. Cullel, J.C. Moreno, E. Rocon, A. Forner-Cordero and J. L. Pons. Biologically based Design of an Actuator System for a Knee-Ankle-Foot orthosis, *Mechanism and Machin Theory* 44, 860-872, 2009.

[7] S. Fatone. A Review of the Literature Pe rtaining to KAFOs and HKAF Os for Ambulation, *Journal of Prosthetics and Orthotics* 18 (3S), 137, 2006.

[8] S. Hwang, S. Kang, K. Cho and Y. Ki m. Biomechanical effect of electrom echanical knee-ankle-foot-orthosis on knee joint control in patients with poliomyelitis, *Medical & Biological Engineering & Computing* 46, 541-549, 2008.

[9] L. Delp, F. C. Anderson, A. S. Arnold, P. Loan, A. Habi b, C. T. John, E. Guendelm an and D. G. Thelen. Open-source software to create and analyze dynam ic simulations of movement. *IEEE Transactions on Biomedical Engineering BME*, 54, 11, 1940-1950, 2007.

[10] G. R. Johnson, M. Ferrarin, M. Harrinton, H. Hermens, I. Jonkers, P. Mak and J. Stallard. Performance Specification for Lower Limb Orthotic Devices, *Clinical Biomechanics* 19, 711-718, 2004.

[11] K. R. Kaufman, S. E. Irby, J. W. Matheswson, R. W. Wirta and D. H. Sutherland. Energy-Efficient Knee-Ankle Foot Orthosis: a Case Study, *Journal of Prosthetics and Orthotics* 8 (3), 79, 1996.

[12] J. D. Hsu, J. W. Michael, *AAOS Atlas of Orthoses and Assistive Devices*, Mosby Elsevier, Philadelphia, USA, 2008.

[13] M.A. Brehm, A. Beelen, C. A. M. Doorenbosc h, J. Harlaar and F. Nollet. Effect of carbon-composite knee-ankle-foot orthoses on walk ing efficiency and gait in for mer polio patients, *Journal of Rehabilitation Medicine* 39, 651-657, 2007.

[14] S. E. Irby, K. R. Kaufm an, R. W. Wirta and D. H. Suth erland. Optimization and Application of a W rap-Spring Clutch to a Dynamic Knee-Ankle-Foot Orthosis, *IEEE Transactions on Rehabilitation Engineering* 7 (2), 130-134, 1999.

[15] A. G. Mc Millan, K. Kendrick, J. W. Mich ael, J. Aronson. And G. W . Horton. Preliminary Evidence for Effectiveness of a Stance Control Ortho sis, *Journal of Prosthetics and Orthotics* 16 (1), 6, 2004.

[16] M. Ackermann and F. G. Cozman. Automatic Knee Flexion in Lower Limb Orthoses, *Journal of the Brazilian Society of Mechanics and Sciences Engineering*, 31 (4), 305, 2009.

[17] T. Yakimovich, J. Kofman and E. D. Lemaire. Design and Evaluation of a Stance-Control Knee-Ankle-Foot-Orthosis Knee Joint, *IEEE Transactions on Neural Systems and Rehabilitation Engineering* 14 (3), 361-369, 2006.

[18] T. Yakimovich, E. D. Lemaire and J. Kofman. Preliminary Kinematic Evaluation of a New Stance-Control Knee-Ankle-Foot Orthosis, *Clinical Biomechanics* 21, 1081-1089, 2006.

[19] A. Zissimopoulos, S. Fatone and S. A. Gard. Biomechanical and energetic effects of a stance-control orthotic knee joint, *Journal of Rehabilitation Research and Development* 44 (4), 503-514, 2007.

[20] G. S. Sawicki and D. P. Ferris. A pneumatically powered knee-ankle-foot-orthosis (KAFO) with myoelectric activation and inhibition, *Journal of NeuroEngineering and Rehabilitation* 6 (23), 2009.

[21] P. J. Greene and M. H. Granat. A knee and ankle flexing hybrid orthosis for paraplegic ambulation, *Medical Engineering & Physics* 25, 539-545, 2003.

[22] G. M. Lyons, T. Sinkjaer, J, H. Burridge, J.H. and D. J. Wilcox, D.J. A Review of Portable FES-Based Neural Orthoses for the correction of Drop Foot, *IEEE Transactions on Neural Systems and Rehabilitation Engineering* 10 (4), 260-279, 2002.

[23] H. Kagaya, Y. Shimada, K. Sato, M. Sato, K. Iizuka G. Obinata. An Electrical Knee Lock System for Functional Electrical Stimulation, *Archives of Physical and Medical Rehabilitation* 77, 870-873, 1996.

[24] J. P. J. Bakker, H. Beckerman, B. A. Jong and G. J. Lankhorst. The effects of knee-ankle-foot orthoses in the treatment of Duchnenne muscular dystrophy: review of literature, *Clinical Rehabilitation* 14, 343-359, 2000.

[25] M. E. Garralda, F. Muntoni, A. Curniff and A. D. Caneja. Knee-Ankle-Foot Orthosis in Children with Duchene Muscular Dystrophy: User Views and Adjustment, *European Journal of Paediatric Neurology* 10, 186-191, 2006.

[26] J.S. Hebert and A. B. Liggins. Gait Evaluation of an Automatic Stance-Control Knee Orthosis in a Patient with Postpoliomyelitis, *Archives of Physical and Medical Rehabilitation* 86, 1676-1680, 2005.

[27] T. Yakimovich and E. D. Lemaire and J. Kofman. Engineering design review of stance-control knee-ankle-foot orthoses, *Journal of Rehabilitation Research and Development* 46 (2), 257-268, 2009.

[28] J.E. Shigley and C. R. Mischke. *Mechanical Engineering Design*, McGraw-Hill International Editions, 5th edition, 1989.

[29] W. Bolton. *Mechatronics: A Multidisciplinary Approach*, Prentice Hall, 4th edition, USA, 2008.

Proceedings of MUSME 2011, the International Symposium
on Multibody Systems and Mechatronics
Valencia, Spain, 25-28 October 2011

DEVELOPMENT OF A CONTROL SYSTEM FOR MODELLING A 5MW WIND TURBINE AND CORRELATION BETWEEN DIFFERENT EXISTING CODES

José Manuel Yepes Rodriguez* and Dr. Omar Aït-Salem Duque†

* MSC Software S.A.
Avenida Manoteras, 32,Edificio A 1ª Planta, 28050, Madrid, Spain
e-mail: josemanuel.yepesrodriguez@mscsoftware.com,
web page: *www.**mscsoftware**.com/*

†MSC Software S.A.
Avenida Manoteras, 32,Edificio A 1ª Planta, 28050, Madrid, Spain
e-mail: omar.ait-salemduque@mscsoftware.com

Keywords: Wind turbine Modeling, Controller, Multibody Systems, Flexible bodies, Vibration Modes, Adwimo.

Abstract. *A wind turbine is a complex mechanical system of blades, shafts, bearings, gears, generator, tower, controls and so on. The high coupling of all components makes a system-oriented approach inevitable. The present paper gives an insight on the modeling details of Wind turbines, mixing both rigid bodies and flexible ones. A specific controller has been developed to simulate the real behavior of a 5 MW Wind Turbine, under realistic conditions of a certain type of wind. The results are then compared between two different codes.*

1 INTRODUCTION

1.1 Motivation

Wind energy industry is a growth industry that has become more and more important because political and economic reasons. Large amounts of money are invested in research of renewable energy sources that could replace traditional ones.

High performance is a prerequisite for the large number of simulations, which are needed for the design and the certification of a wind turbine. High accuracy is the complementary prerequisite for cost-effective design; design risks have to be identified in the earliest possible design stage and to be removed before building prototypes. The last statement is really important for this industry, as the dimensions of a wind turbine are huge and as one has to assure, that the prototype is successful. Design optimization is becoming a key factor for meeting requirements of customers with respect to maintenance cost and product life time and to assure competitive product pricing.

In order to decrease wind turbine testing costs, multibody simulations have been used recently. CAD simulations also let design engineers testing new prototypes and hence shortening the developing cycles for wind turbines. There a number of codes to cope with this type of problems, the one used in this paper is ADWIMO (ADvanced WIndturbine MOdeling) developed by MSC Software[1], this code is designed to provide the environment for efficient modeling and analysis of wind turbines as plug-in for Adams.

In this platform a controller has been designed in order to perform certain simulations under realistic conditions, in order to validate the solution the results are then compared with FAST [2]which is a free public software certified by NREL.

1.2 Objectives

The main objective of this paper is to build a wind turbine multibody model in ADWIMO including a control system to analyze simulation results to evaluate code features and load calculations in the wind turbine system.

Along with the main objective, there are some secondary goals for this work as analyzing the data flow, preprocessor and postprocessor features and user interface to establish the strengths and weaknesses of the present simulation codes.

1.3 Method

First step in this paper is building (in terms of simulation) the wind turbine model. As technical wind turbine data is confidential, a public model developed by NREL was used for the job. Once the data has been collected, the model is built according to those specifications.

As in most of the codes of multibody most of bodies are modeled as rigid parts, but in this case, and for the seek of accuracy, flexible bodies are used by definition for the blade and the tower. Multiple flexible bodies provide an efficient approximation for geometric non-linearity present in long blades. The used code is prepared to support flexible bodies for hub, main

[1] MSC Software is software developer company

[2] FAST is a NTWC Design Code available at http://wind.nrel.gov/designcodes/simulators/fast/.

shaft and engine frame. These flexible parts are generated using an FE code to generate the necessary files for the assembly. Once the model is up and running, some tests are performed to check logical responses to deterministic inputs as constant speed winds or start-up winds.

At this point, values in ADWIMO should be compared either with real data or a different code results. As test results are no available, comparison to a certificated code should be established. Between all codes, reasons to choose FAST, also developed by NREL, are baseline NREL wind turbine is already developed and its capabilities are considered to be minimum required features for a wind turbine load calculation software.

Comparison between both codes is carried out in two steps. At the first step, constant wind speed results are discussed to ensure ADWIMO values are correct in steady state and to quantify differences in the model because wind turbine modeling. PI controller is removed for running these analyses so blade pitch angle is set according to model documentation. Special interest is required for deformation in flexible bodies and blade pitch influence in rotor angular velocity as sources of the general wind turbine response.

The Second part of this study analyses the results for both codes in real wind conditions (random input). In this case, PI controller is developed and used in simulations to compare kinematic and dynamic wind turbine behavior. Special attention is paid on transient effects and maximum and minimum loads in the wind turbine structure. To perform these analyses, random real wind data input is generated by TurbSim based on some meteorological parameters but some wind turbine data is also necessary as input.

2 SIMULATION MODEL

The baseline model used in this study is the 5MW Reference Wind-Turbine Baseline Model [3]developed by the National Renewable Energy Laboratory (NREL) of EE UU.

The 5MW Reference Wind Turbine Baseline Model was developed in order to provide wind energy industry a baseline model so fast comparisons and correlations could be carried out between different projects on a homogeneous and reliable basis. Therefore, NREL model is a three blade horizontal axis wind turbine (HAWT) oriented upwind with a variable speed, collective blade pitch control system based on the biggest wind turbine prototypes in the world. Main properties for this baseline model are included in Tab. (1).

Rating	5 MW
Rotor Orientation, Configuration	Upwind, 3 Blades
Control	Variable Speed, Collective Pitch
Drivetrain	High Speed, Multiple-Stage Gearbox
Gearbox Ratio	97:1
Rotor	126 m
Blade Length	61.5 m
Hub Diameter	3m
Hub Height	90 m
Tower Height	87.6 m
Cut-In, Rated, Cut-Out Wind Speed	3 m/s, 11.4m/s, 25m/s
Cut-In, Rated Rotor Speed	6.9 rpm, 12.1rpm

[3] 5MW Reference Wind-Turbine Baseline Model users guide can be found in the Ref. [10]

Rated Generator Speed	1173.7 rpm
Rated Tip Speed	80 m/s
Blade Mass	17,740 kg
Rotor Mass	110,000 kg
Hub Mass	56,780 kg
Nacelle Mass	240,000 kg
Tower Mass	347,460 kg
Overhang, Shaft Tilt, Precone	5 m, 5º, 2.5º
Coordinate Location of Overall CM	(-0.2m, 0.0m, 64.0m)

Table 1: Gross Properties for the NREL 5MW Baseline Wind Turbine. Table created by NREL

Below rated rotor speed, blade pitch angle is supposed to be zero. Above this speed, control system calculates blade pitch angle by using a PID to keep a constant rotor angular velocity. To simplify the model, an arbitrary zero gain is set for derivative loop. Also a low pass filter with is exponential smoothing is used to mitigate high frequency excitation of the control system.

Although a cut out wind speed is introduced in the model, FAST control system doesn't use this characteristic so it will not be included in ADWIMO model.

Further 5MW Reference Wind-Turbine Baseline Model information can be found in the references.

3 ADWIMO MODEL

The 5MW wind turbine model setup process in ADWIMO is described in this section.

3.1 Blade

Blades are modeled as flexible bodies so both aerodynamic and structural properties for the blade are required for the 5MW model.

Structural properties in the blade are used to calculate loads and displacements. These properties are defined by section along the blade axis using the blade root as reference for the local coordinate system. Required structural properties are x coordinate, lineal density, stiffness, inertia and center of mass of each section which are included in a text file as an input for FE code. Running the FE software, a mnf file is created which contains structural properties and natural modes of vibration for the blade. As an option, blade can be split in several flexible bodies for advanced modeling.

Aerodynamic properties are used to calculate lift and drag forces on the blade. Calculating these wind loads involves using AeroDyn[4] and a sheet with aerodynamic coefficients for each section. Taking into account rotational speed of the rotor, AeroDyn uses the coefficients in the sheets to calculate wind forces in each section. As the structural properties, aerodynamics properties are defined by section but it is not necessary to define the same number of sections for them.

[4] AeroDyn is a code developed by NREL for calculating loads on the blade based on wind speed. For further information consult Ref [15]. AeroDyn ia available at http://wind.nrel.gov/designcodes/simulators/aerodyn/.

3.2 Tower

A flexible body is used for the tower in the 5 MW wind turbine model. To do this a text file is required with structural properties for the tower as z coordinate, lineal density stiffness, inertia and thickness of the wall. The reference coordinate system is in the base of the tower. As for blades, these properties are included in a text file which should be run in an FE code to obtain the modal neutral file that is required for the system. This modal neutral file contains structural properties listed above and natural modes of vibration for the tower.

3.3 Hub and Main shaft

Hub and main shaft are modeled as rigid bodies in this paper. Basic characteristics are defined for the hub as for example, the number of blades, mass, inertia and location. All information is in a text file which contains all the properties for both parts. If required both the hub and main shaft could be modeled as flexible bodies, like it was done for the tower, but due to limitations of the FAST code, in order to make plausible the comparison it was decided to keep them as rigid.

3.4 Mainframe and Generator frame

Mainframe and generator frame are also modeled as rigid bodies. It has taken into account the mass and dimensions for nacelle and the generator is also built up in a same manner. If desired both parts could modeled with an FE code, creating a neutral file which could contain this information.

3.5 Gearbox

A very complex model for the gearbox can be used in ADWIMO. However, the simplest model was used for this project. By selecting on the gearbox option, the basic gearbox model with mass and inertia characteristics, and placing it in the model between the main shaft and the generator. For more advanced gearbox modeling, the basic model can be replaced using the same attaching points for the new one.

3.6 Control System

Control system is modeled as two loops with rotor angular velocity as main control variable. The first loop is a conventional variable speed controller for the rotor speed. The second loop is a PI controller for collective blade pitch. Both loops are connected by using blade pitch to determine the area of the torque curve the wind turbine is working in.

Control system is setup using internal variables in ADAMS environment. Using an external library as control system is also possible although all used variables cannot be plotted in real time so first option was chosen to improve the control system development.

Blade pitch and rotor angular velocity are inputs for the speed controller. Blade pitch determines the part of the curve the generator is working at and rotor angular velocity is used to calculate rotor torque according to torque curve of the generator. This curve is included in the model as a tabulated data by using the spline in Fig. (1). To implement this loop in the model, just variables that store the rotor angular velocity and blade pitch and torque curve spline are needed.

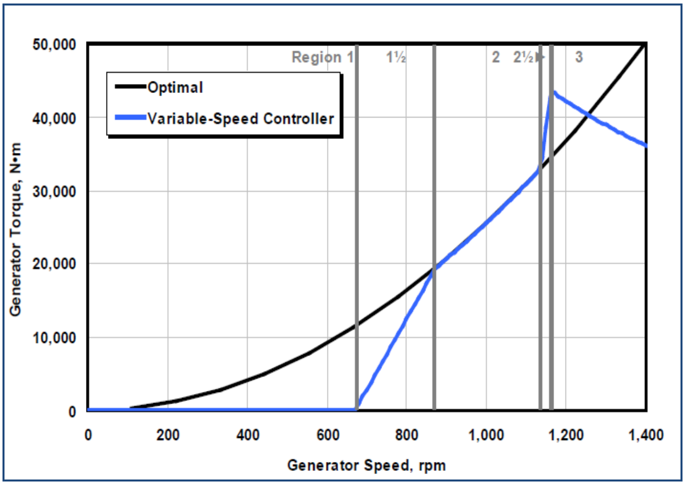

Figure 1: Torque vs Speed response of the variable speed controller. Figure by NREL

In order to simplify the system, a PI controller is used for the collective blade pitch. The input variable for the blade pitch controller is the rotor angular velocity error. The gains for PI controller are included in the references but it is important to notice these values are not constants due to the sensitivity to aerodynamic to rotor collective blade pitch so a feedback is needed in this loop.

To model this loop, some states variables were created as nominal rotor speed, zero blade pitch gains and minimum and maximum blade pitch angles. It was also defined a function to measure the generator velocity error and to modify PI gains according to pitch angle to calculate the blade pitch angle for the next step. Fig. (2) shows PI gains versus blade pitch.

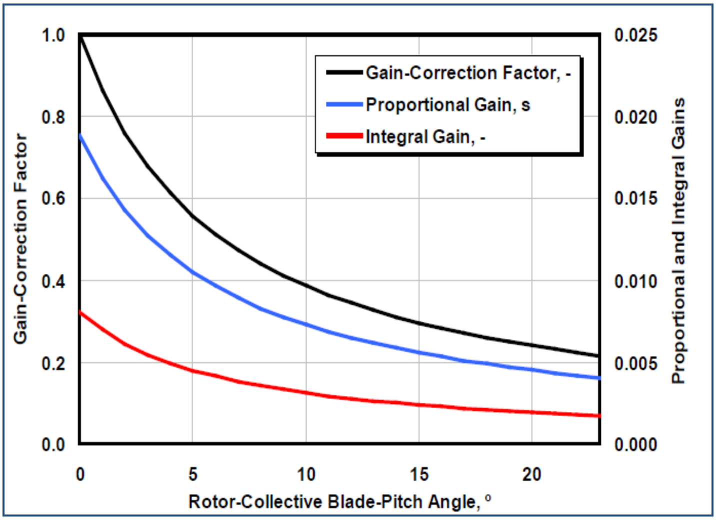

Figure 2: Baseline blade pitch control system gains. Figure by NREL

4 MODEL SETUP

Differences between the ADWIMO model and the FAST one that might affect the results and the hence the conclusions, so a discussion on this issue is presented in this section to establish the basis the work in order to have a common framework. So the models should be tuned so they have the same characteristics.

The first thing to take into account is the mass of the model. Tab. (2) lists mass of each component in the model. Main differences are for the gearbox and generator. In total, ADWIMO model has 99.376 kg more than FAST model.

Component		ADWIMO	FAST
Tower		347.293 kg	347.460 kg
Blade		17.755 kg	17.740 kg
Hub		56.780 kg	56.780 kg
Drive Train	Gearbox	43.721 kg	-
	HSS	1.215 kg	-
	LSS	1.215 kg	-
Nacelle		240.000 kg	240.000 kg
Generator	Rotor	30.148 kg	-
	Stator	23.199 kg	-
Total Wind Turbine Mass		796.836 kg	697.460 kg

Table 2: Mass differences in ADWIMO and FAST 5MW windturbine model. Own elaboration.

Some adjustments are also required for flexible bodies. According to the maximum number of natural modes in FAST, three natural vibration modes are used for each blade and four for the tower. Natural modes of vibration are defined in the modal neutral file in ADWIMO model while FAST uses the polynomial coefficients stored in the .txt file for the blades.

The first three vibration modes of the blade, correspond to flapwise modes (1st and 3rd) and edgewise mode (2nd). First and second flapwise modes are tip displacement and rotation out of xz plane and first edgewise mode is the tip displacement in the xz plane.

Due to wind turbine characteristics, natural frequencies for the blade can be calculated as an isolated body, with restrained displacements and rotations in its root, as wind turbine mass is about twenty times blade mass.

Mode	FAST	ADWIMO	Error
1st flapwise mode	0,6675 Hz	0,6695 Hz	0,30 %
1st edgewise mode	1,0793 Hz	1,0694 Hz	0,92 %
2nd flapwise mode	1,9233 Hz	1,9299 Hz	0,02 %

Table 3: Natural frequencies and error for the first three blade natural modes of vibration. Own elaboration.

Natural frequencies for blade are quite similar in FAST and ADWIMO as shown in Tab. (3). The error is below 1 % in all three modes. Blade modeling is accepted to be good enough to go into the next stage.

For the tower, four natural modes of vibration are included in the model. These four modes are displacement and rotation along x axis and y axis of the tower. Displacement and rotation along x axis are first and second fore-aft modes while displacement and rotation along y axis are first and second side-to-side modes.

Mode	FAST	ADWIMO	Error
1st fore-aft mode	0,3240 Hz	0,2916 Hz	10,00 %
1st side-to-side mode	0,3120 Hz	0,2928 Hz	6,15 %
2nd fore-aft mode	2,9003 Hz	2,4425 Hz	15,78 %
2nd side-to-side mode	2,9361 Hz	2,3115 Hz	21,27%

Table 4: Natural frequencies and error for the first four tower natural modes of vibration. Own elaboration.

Results in Tab. (4) contain natural frequencies and error values. Differences in natural frequencies are larger than 20% in some cases. The main explanation for these differences is the mass in the model. ADWIMO model has higher mass (as take into account the power-train) so natural frequencies decreases accordingly. Removing the mass of these parts was considered as an option but the influence in further results recommended to work along with these differences although the high error in natural frequencies for the tower.

5 CONSTANT BLADE PITCH ANALYSIS

The objective of constant blade pitch analysis is to study the behavior of the 5MW wind turbine model in steady states without taking into account transient effects.

5.1 Simulation Setup

Studying the steady states for the model involves removing the PI blade pitch controller. By removing this controller, one degree of freedom is added to the model. In order to remove this additional degree of freedom, either blade pitch or rotor angular velocity must be fixed with regards to wind speed. As wind speed is the independent variable and we are working with a variable speed generator, the fixed variable should be the blade pitch.

In order to take into account all the possibilities, steady states for the model are studied in all wind conditions. To eliminate transient wind effects, constant wind simulations are performed from 3m/s to 25m/s wind speed increasing wind speed by 1m/s for each simulation. According to NREL documentation, blade pitch is fixed depending on wind speed to obtain maximum wind power.

5.2 Results

The results of this section focus on the most important parameters as tip speed ratio (TRS) and displacement flapwise and edgewise.

Tip speed ratio provides information about the general wind turbine performance as the relationship between tip speed and wind velocity as indicated in Eq. (1).

$$\lambda = \frac{\omega R}{u_1} \tag{1}$$

ADWIMO results match FAST ones for every steady state in this section except for 12 m/s constant wind speed as showed in Fig. (3). This difference disappear when using the PI controller for this constant wind speed by modifying slightly blade pitch angle.

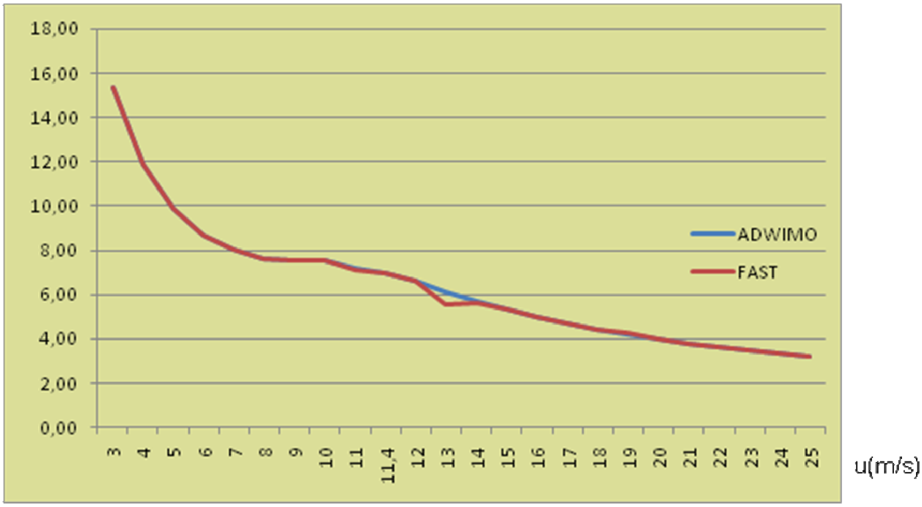

Figure 3: TSR vs wind speed response for ADWIMO and FAST 5MW model.

Flapwise displacement, measures the tip deflection out of the blade xz plane. Large tip displacements increment the loads in the blade and in the wind turbine structure. Results of Fig. (4), correspond to flapwise tip displacement, this curve is divided in two areas by rated speed with values slightly higher in FAST simulations with wind speed below the rated one. Main difference is a 20% flapwise displacement at rated speed.

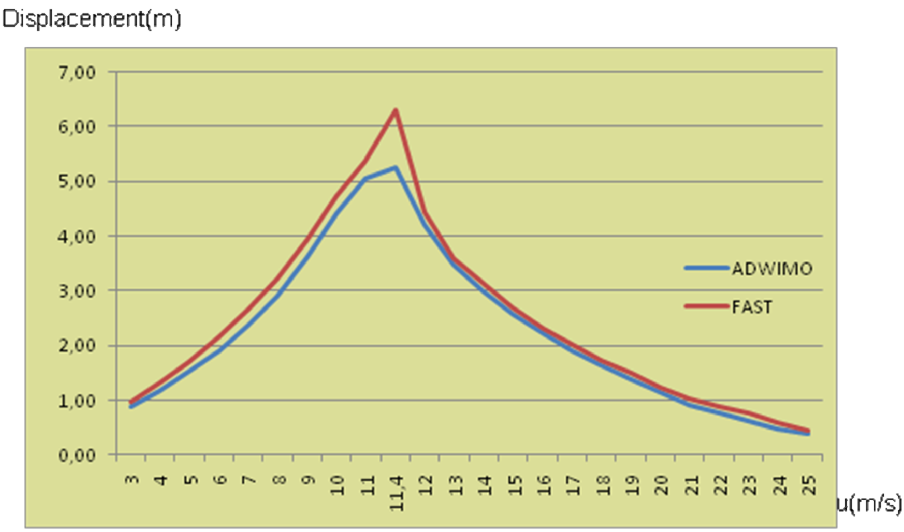

Figure 4: Flapwise tip displacement response for ADWIMO and FAST 5MW model.

As the main difference is located at a certain wind speed, results can be considered acceptable to continue with next stage as these constant wind conditions will not appear in real wind conditions.

Tip deflection in the blade xz plane is called edgewise displacement. There are large differences between ADWIMO and FAST although a similar trend can be observed for wind speed over the rated speed as seen in Fig. (5).

Having analyzed the results, the main reasons for the observed differences are due to the way of modeling a wind turbine. ADWIMO model includes a torsion degree of freedom and an inertia perpendicular to the blade axis which are not included in FAST. Removing this DOF and inertia from ADWIMO model was tried without success and FAST capabilities would not include them so working along with these differences was decided.

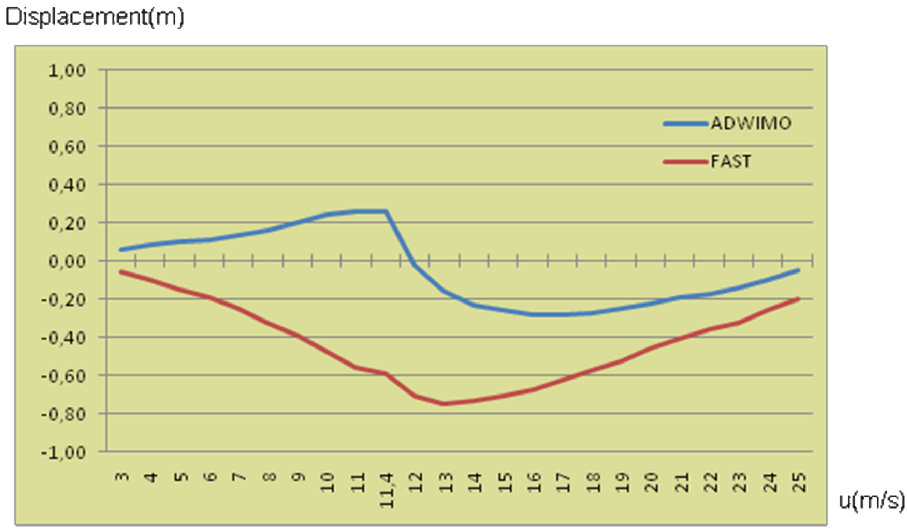

Figure 5: Edgewise tip displacement response for ADWIMO and FAST 5MW model.

6 REAL WIND CONDITION ANALYSIS

The objective of real wind condition analysis is to compare the results for both codes in realistic wind conditions with PI controller studying transient effects

6.1 Simulation setup

Winds in real life are not constant so simulations in real conditions should be done to compare results in a more realistic situation using PI controller.

Wind speed data is generated with TurbSim[5] which creates a random wind speed record based on some meteorological variables and statistical parameters like average wind speed, hub height temperature. This input is stored as a txt file.

Transient effects in the wind turbine start up are not considered in this study as this maneuver requires a detailed study. For this reason, initial rotor angular velocity is set slightly under rated speed to focus on wind speed transient effects. However, initial blade pitch is set to zero to start PI controller.

6.2 Results

Though we have many results to analyze, the present section will focus on the ones based on a 18m/s average speed TurbSim wind, as an example with a duration of 600 seconds. Wind profile is showed in the Fig. (6).

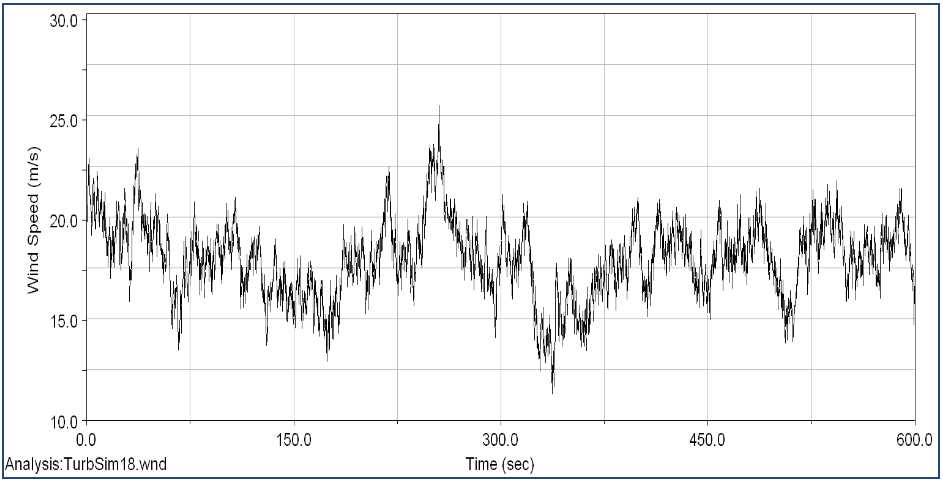

Figure 6: Random TurbSim wind input profile with 18m/s average wind speed.

The results in this section are focused in the wind turbine kinematic and dynamic behavior by analyzing blade pitch angle, rotor angular velocity and loads in the blade

Rated speed is the optimum for variable speed wind turbine. Wind speed and direction changes in the wind modify lift and drag forces on the blade. To obtain a constant angular velocity, blade pitch is adjusted by PI controller to provide the rotor the necessary motion torque to keep the constant rated speed for the wind turbine.

Studying Fig. (7), it can be concluded ADWIMO and FAST results are similar. The trend in both codes is identical; however values aren't exactly the same. ADWIMO results are more stable with fewer oscillations than FAST. The reasons of these differences are a more sensitive controller in FAST and higher mass in ADWIMO model which increases its inertia.

[5] Turbim is a code developed by NREL for creating random wind profile. For further information consult Ref [9]. It can be download at http://wind.nrel.gov/designcodes/preprocessors/turbsim/.

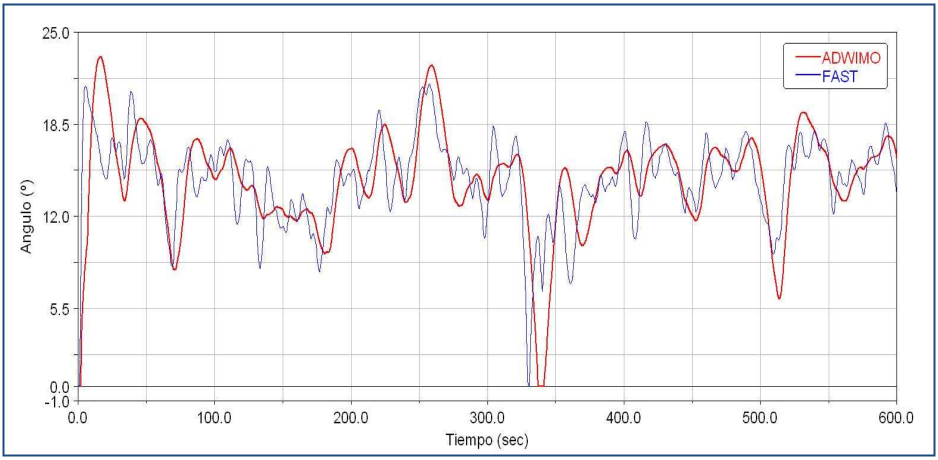

Figure 7: Blade pitch angle response for 18m/s average speed wind in ADWIMO and FAST.

The main goal for the control systems is obtain a constant speed wind turbine speed to improve power quality. When the wind turbine speeds up, PI controller increases blade pitch to reduce lift. On the other hand, PI controller decreases blade pitch to accelerate wind turbine up to the rated speed.

Results for rotor angular velocity in Fig. (8) show important differences between ADWIMO and FAST although both codes present results around the rated speed. Differences in blade pitch also affect this values but the most important difference remain in the step size in the simulation along with blade pitch differences. Step size for ADWIMO is smaller than FAST one so a smooth curve is obtained in ADWIMO as a result of a higher number of points. This higher number of step makes ADWIMO results slightly retarded respect to FAST ones for most of the force and displacement values.

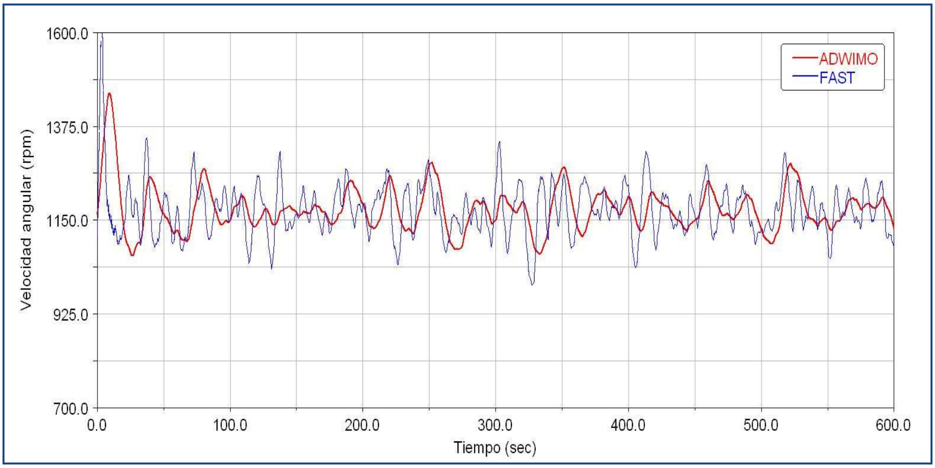

Figure 8: Rotor angular velocity response for 18m/s average speed wind in ADWIMO and FAST.

Once kinematic study has been done, dynamic analysis should be done. Among all forces and deformations included in the model, force in the root of the blade along local x axis is presented in this report as representative on the blade dynamics. This force is directly related to flapwise displacement and provides the torque on the hub.

Results in ADWIMO and FAST in Fig.(9)present a similar trend for the whole simulation but ADWIMO values are retarded respect to those in FAST as for blade pitch and rotor angular velocity results. Maximum and minimum values are similar in both codes so ADWIMO results are considered acceptable.

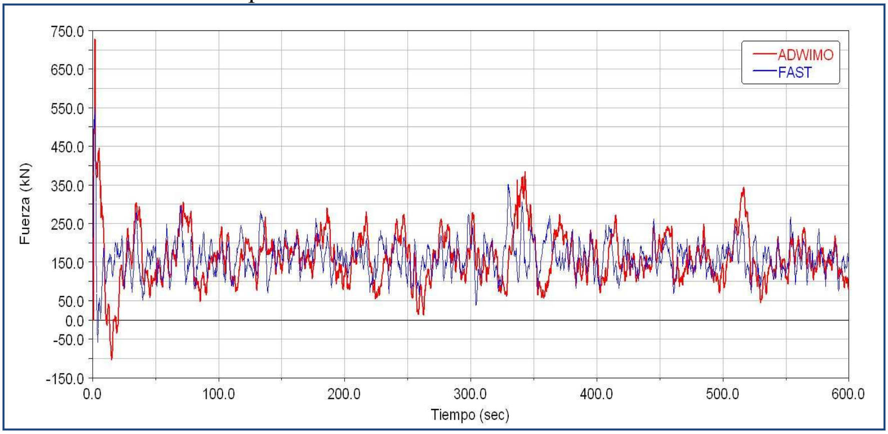

Figure 9: Blade root forces along x axis response for 18m/s average speed wind in ADWIMO and FAST.

For the rest of results, main differences appear for edgewise displacement. These differences were noticed in the constant blade pitch analysis. In real wind conditions, differences remain in the analysis although frequency is the same for both codes so x axis inertia is the cause of these differences.

7 DISCUSSION

In this section, previous results are discussed and both codes features are compared along the simulation process.

7.1 ADWIMO Capabilities

Based on results, ADWIMO has a higher computational capacity than FAST as a more complex model can be developed in ADWIMO. Model complexity in ADWIMO can be increased by using more natural modes of vibration and more degrees of freedom based on the interaction with FE codes.

Using modal neutral files as an input for the wind turbine parts, means that the accuracy of the analysis, depends on the number of natural frequencies extracted from the FE code. However just a reasonable number of them should be included as computational time would increase. Next ADWIMO studies should compare this capability with more advanced codes.

Increasing degrees of freedom should improve results accuracy. As multibody software, ADWIMO degrees of freedom are included in the model when adding parts. If these parts are rigid bodies, six degrees will added but when using flexible bodies, degrees of freedom depend on FE model. For example, as explained in Sec. 5.2, torsional degree of freedom is included in ADWIMO but not in FAST. These differences affect some requests but overall results look pretty similar in both codes.

As a combination of these features, critical components as blades could be introduced in the model by creating several parts. The blade could be split in a certain number of attached sections, so a mnf would be necessary for each section. By using this method, degrees of freedom and natural modes are increased in the model improving model accuracy.

Step size in both codes is different. While FAST uses a constant step size, variable step size is available in ADWIMO. When adjusting setting simulation in ADWIMO, a maximum step size is defined. Step size is modified according to simulation to improve results between those values. The consequence of variable step size is a smaller step size in ADWIMO which affects the results as explained in Sec. 6.2.

Computational time is higher in ADWIMO than in FAST. To compare these computational times, a dimensionless parameters is defined in Eq. (2). Simulated time is the real time. CPU time is the time used by the computational for each simulation. Same computer was used to time CPU time.

$$SimulationRatio = \frac{SimulatedTime}{CPUTime} \tag{2}$$

By using the Simulation Ration, all simulations can be compared at the same time. The average value is 10.8 for FAST and 3.4 for ADWIMO. This result means ADWIMO is about three times slower than FAST as for one CPU second, 3.4 real seconds are simulated in ADWIMO and 10.8 in FAST. The main reason for this difference is the step size. As rule of thumb, the smallest step size is, the higher computational is. A higher number of requests and generating graphics file also slow down ADWIMO computational capacity. Anyway, real time simulation can be run in both codes.

As an FE code is necessary to create flexible bodies in ADWIMO model, it is also possible to generate an output file to study load calculation and fatigue life more in deep including a safety coefficient.

7.2 ADWIMO User Interface

To discuss about ADWIMO feature work flow will be divide in two stages: preprocessing, and postprocessing.

In the preprocessing, although editable text files are used in both codes as input files, ADWIMMO interface provides users a step by step method to build up a model just by filling all the sheets in the main menu. By working in ADWIMO environment, user is allowed to pick up any files without bringing txt files up so no modifications are saved.

Once the model is assembled, a graphic representation is available in ADWIMO as seen in Fig. (10). Looking at this wind turbine representation provides users a better understanding and an easier approach to the model. For further concerns, graphical topology of the model is also available.

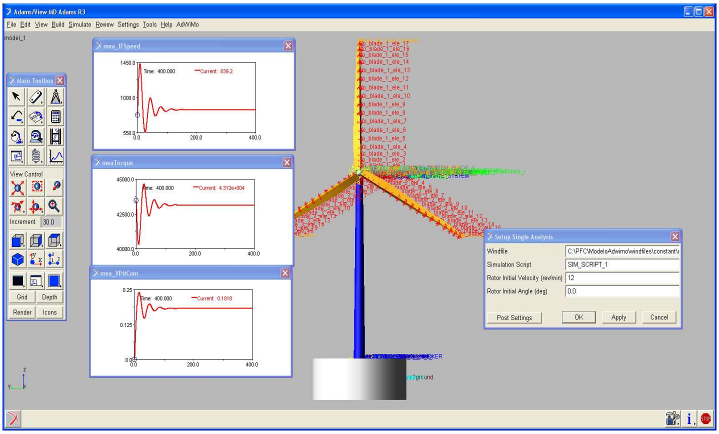

Figure 10: Preprocessor user interface in ADWIMO

Natural modes of vibration for all parts can also be modified on the displayed model by using right click without opening files. These modifications consist on activating/deactivating natural modes of vibration, modifying damping or scaling deformations to be more noticeable. In the event of using a new component for the wind turbine, just replacing the input file for this part is necessary as information on natural modes of vibration is stored in the modal neutral file.

Based on ADAMS features, new functions, design variables and state variables can be defined in ADWIMO to personalize the model. By creating these variables or modifying the default ones, users can include in the model requests for a deeper study of specific issues.

FAST output is just a text file which contains the results of the simulations. For ADWIMO there are several output files: a summary of the simulation, a txt file with the results and a file with the graphics of the simulation. In the summary, user can find useful information about settings and commands in the simulation scrip but also look for error messages if the simulation crashed. Graphics file give users the chance to play animations about the simulations to observe the kinematic of the wind turbine, the deformations in the flexible bodies and the aerodynamic forces on the blades.

Differences between ADWIMO and FAST are larger for postprocessing as there are no available tools for FAST output file. On the other hand ADWIMO generates ASCII output files and also postprocessing tools to work the different curves and plotss. Postprocessor user interface is shown in Fig. (11). These features decreases the postprocessing time as no further actions are required when looking into the standard results or the user defined requests.

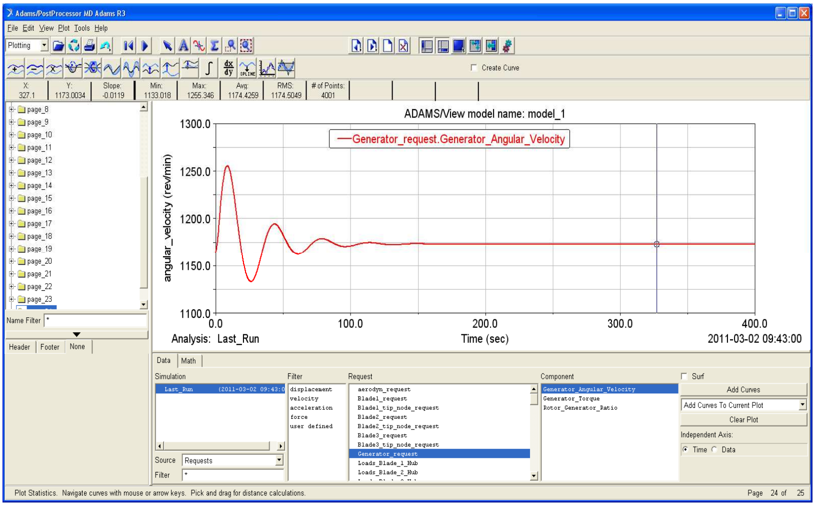

Figure 11: Postprocessor user interface in ADWIMO

ADWIMO also has a feature to export the post-processed results. All the plots can be exported as pictures with jpg extension. Animations can be exported in video format compatible with most video players.

8 CONCLUSIONS

- A complex wind turbine model with flexible bodies has been developed in this work, with acceptable response under realistic conditions.
- Simulation results in ADWIMO are acceptable compared to other codes such as FAST both steady state and transient regimen. Maximum values for loads and trends are similar to those obtained by using certificated codes for wind turbine load calculation.
- The developed control system enables simulations of the response of the wind turbine to non-deterministic loadings such as the real wind conditions.
- The presented features provided in this paper show the current state of the art of the tools used in the simulation of wind turbines, providing a better understanding of the real behavior by means of the post-processing tools such as plots and videos.
- As future work the presented tools should be tested under other conditions such as emergency stops.
- The next steps for the present work will be:
  - The discretization of the blades into more flexible bodies.
  - The inclusion of more modes which have not been taken into account.

REFERENCES

[1] Bossanyi, E. A., GH Bladed Version 3.6 User Manual, 282/BR/010, Garad Hassan and Partners Limited, Bristol, UK, December 2003.

[2] Buhl, M. A Simple Mode-Shape Generator for Towers and Rotating Blades, NWTC Design Codes. USA. July 2005.

[3] Garcia de Jalón, J and Bayo, E. *Kinematic and Dynamic Simulation of Multibody Systems: The Real-Time challenge*. Springer-Verlag, New-York, 1994

[4] Goezinne, F., Terms of reference DOWEC. DOWEC Dutch Offshore Wind Energy Converter 1997–2003, September 2001.

[5] Gonzalez Palacios, A. *Principios de Conversión de la Energía Eólica: Cargas sobre el rotor de una aeroturbina*. CIEMAT. Madrid, 1995.

[6] Hansen, M. H., Hansen, A., Larsen, T. J., Sørensen, and Fuglsang, P., Control Design for a Pitch-Regulated, Variable-Speed Wind Turbine, Roskilde, Denmark: Risø National Laboratory, January 2005.

[7] Hau E, *Wind Turbines: Fundamentals, Technologies, Application and Economics*, Springer 2000

[8] Jonkman, J. M. and Buhl Jr., M. L. FAST User's Guide, NREL/EL-500-38230, Golden, CO: National Renewable Energy Laboratory, August 2005.

[9] Jonkman, J. TurbSim User's Guide, Version 1,50. National Renewable Energy Laboratory, August 2009.

[10] Jonkman, J, Butterfield, S, Musial W, Scott, G. Definition of a 5-MW Reference Wind Turbine for Offshore System Development. NREL, USA, February 2009.

[11] Lecuona Neumann, Antonio. *Energía eólica. Principios básicos y tecnología*. Universidad Carlos III de Madrid. Madrid, 2005.

[12] Kooijman, H. J. T., Lindenburg, C., Winkelaar, D., and van der Hooft, E. L., "DOWEC 6 MW Pre-Design: Aero-elastic modeling of the DOWEC 6 MW pre-design in PHATAS," DOWEC Dutch Offshore Wind Energy Converter 1997–2003, Petten, the Netherlands: Energy Research Center of the Netherlands, September 2003.

[13] Laino, D. J. and Hansen, A. C., User's Guide to the Wind Turbine Dynamics Aerodynamics Computer Software AeroDyn, Salt Lake City, USA, December 2002.

[14] Malcolm, D. J. and Hansen, A. C., WindPACT Turbine Rotor Design Study, NREL/SR-500-32495, Golden, CO: National Renewable Energy Laboratory, August 2002.

[15] Moriarty, P. J. and Hansen, A. C., AeroDyn Theory Manual, NREL/EL-500-36881, Golden, CO: National Renewable Energy Laboratory, December 2005.

[16] Stol, K.A.; Geometry and Structural Properties for the Controls Advanced Research Turbine (CART) from Model Tuningt. NREL, November 2003.

Proceedings of MUSME 2011, the International Symposium
On Multibody Systems and Mechatronics
Valencia, Spain, 25-28 October 2011

MECHATRONIC DEVELOPMENT AND DYNAMIC CONTROL OF A 3 DOF PARALLEL MANIPULATOR

Marina Vallés[*], Miguel Díaz-Rodríguez[**], Ángel Valera[*] , Vicente Mata[†], Álvaro Page[‡]

[*]Instituto de Automática e Informática Industrial
Universitat Politècnica de València, Camino de Vera s/n, 46022 Valencia, Spain
e-mail: {mvalles, giuprog}@isa.upv.es

[**]Departamento de Tecnología y Diseño, Facultad de Ingeniería
Universidad de los Andes, La Hechicera, 5101 Mérida, Venezuela
e-mails: dmiguel@ula.ve

[†]Centro de Investigación en Tecnología de Vehículos
Universitat Politècnica de València, Camino de Vera s/n, 46022 Valencia, Spain
e-mails: vmata@mcm.upv.es

[‡]Dpto. Física Aplicada
Universitat Politècnica de València, Camino de Vera s/n, 46022 Valencia, Spain
e-mails: alvaro.page@ibv.upv.es

Keywords: Parallel Manipulator, Robot Control, Mechatronics, Kinematics

Abstract. *The aim of this paper is to develop, from the mechatronic point-of-view, a low-cost parallel manipulator (PM) with 3-DOF. The robot has to be able to generate and control one translational motion and two rotary motions (rolling and pitching). Applications for this kind of parallel manipulator can be found at least in driving-motion simulation and in the biomechanical field. An open control architecture has been developed for this robot, which allows the implementation and testing of different dynamic control schemes for a PM with 3-DOF. Thus, the robot developed can be used as a test bench where control schemes can be tested. In this paper, several control schemes are proposed and the tracking control responses are compared. The schemes considered are based on passivity-based control and inverse dynamic control. The control algorithm considers point-to-point control or tracking control. When the controller considers the system dynamics, an identified model has been used. The control schemes have been tested on a virtual robot and on the actual prototype.*

1 INTRODUCTION

A Parallel Manipulator (PM) consists of a mobile platform connected to a fixed base by means of several kinematic chains. These manipulators have an end-effector attached to the mobile platform. PMs have advantages over its counterpart serial robots, essentially that load is shared by several links connecting the mobile platform to the base, thus, PMs have high stiffness, load-carrying capacity, high speed, and high accuracy. However, PMs have small workspaces and singularity problems. In addition, the forward kinematic solution, the system dynamics, and the control of PMs are difficult to develop compared to a serial robot.

Due to their advantages, PMs have several applications. These manipulators have been implemented as: motion simulators, tire-testing machines, fly simulators, and medical applications. Several PMs mechanical architectures and applications can be found in [1]-[4]. Research on PMs was first focused on 6 Degrees of Freedom (DOF) platforms. However, 6-DOF are not always required for many applications. Hence, the number of research works on PMs with less than 6-DOF is increasing. The reason is that a PM with limited DOFs maintain the inherent advantages of parallel mechanisms but presents additional benefits such as the reduction of total costs in manufacturing and operations. For instance, the well-known Delta Robot has 3 translational DOF (3T) [4]. This PM is well suited to pick-and-place tasks [5]. The translational 3T PM has not only been implemented in pick-and-place tasks, but also in medical applications such as cardiopulmonary resuscitation equipment [6], and as machine tools [7]. When combined translational and rotary motions are required, 3-PRS [8] and 3-RPS [9] architectures have been proposed. Here the notation R, P and S stands for the revolute, prismatic and spherical joint, respectively.

The purpose of this paper is twofold. The first one is to develop, starting from scratch, the completed mechatronic design of a low-cost robot with 3-DOF. These manipulators have to be able to generate and control one translational motion (1T) and two rotary motions (2R) (rolling and pitching). With this type of motion (2T1R), driving-motion can be simulated. The roll angle reproduces cornering while the pitch angle creates the illusion of acceleration and braking. The up and down motion can be reproduced by controlling the heave. Another possible application is for ankle injury treatment in which the mobile platform simulates the foot trajectory during physiotherapy exercises [10].

The second objective of the paper is to develop an open control architecture, which allows the implementation and testing of dynamic control schemes for PM with 3-DOF. The reason for building an open architecture is that the control is a field where there is still great potential for study in order to improve their accuracy [11]. Thus, the robot developed can be used as a control scheme bench. In this paper, several control schemes are proposed and the tracking of control responses is compared. The schemes considered are based on passivity-based control [13] and 2) inverse dynamic control [14]. The control algorithm considers point-to-point control or tracking control. When the controller considers the system dynamics, an identified model [15] has been used. The control schemes have been tested over a virtual robot and an actual prototype.

The remainder of this paper is organized as follows. Section 2 concerns the kinematics of the 3-DOF parallel robot. Section 3 is devoted to the mechatronic design of the robot. Section 4 deals with the control schemes implemented. Section 5 presents the results while Section 6 summarizes the main conclusions.

2 PARALLEL ROBOT DESIGN

The choice of parallel robot architecture and movement is guided by the need for developing a low-cost robot able to generate angular rotation in two axes (roll and pitch) and heave as a linear motion. Two alternative design architectures were considered: 3-RPS and 3-PRS. The 3-PRS architecture was selected after comparing the advantages and disadvantages of each one of the alternatives. For instance, one of the advantages of PRS architecture is that the actuators are located at the fixed base. In the case of 3-RPS architecture, the actuators move around the revolution joints.

2.1 Presentation of the 3-DOF Parallel Robot

Fig. (1) shows the CAD model of the robot designed. The manipulator can be seen as three legs connecting the moving platform to the base. Each leg consists of: 1) a motor, which drives a ball screw, 2) a slider and 3) a connecting rod. The lower part of the ball screws are perpendicularly attached to the base platform. The positions of the ball screws at the base are in equilateral triangle configuration. The ball screw transforms the rotational movement of the motor into linear motion. The prismatic joint (P) is assumed to be between the sliders and the corresponding ball screw. The connecting rod is joined to the upper part of the ball screw by means of a revolution joint (R). The moving platform is joined to the connecting rod through spherical joints (S). In this way, each leg has PRS joints.

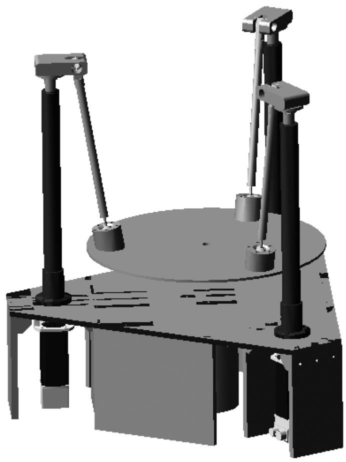

Figure 1: CAD model of the 3-PRS robot

2.2 Direct Kinematics

The direct kinematics of a PM consists of given the actuators linear motions finding the roll (γ) and pitch (β) angles and the heave (z).Denavit-Hartenbert (D-H) notation can be used to establish the generalized coordinates of the kinematic model. Table 1 shows the D-H parameters for the robot considered. From the table it can be seen that with 9 generalized coordinates, robot kinematics can be defined. The location of the coordinate systems for modeling the kinematics is shown in Fig (2).

i	1	2	3	4	5	6	7	8	9
d_i	q_1	0	0	0	0	q_6	0	q_8	0
a_i	0	0	l_a	0	0	0	0	0	0
θ_i	π/6	q_2	q_3	q_4	q_5	5π/2	q_7	-π/2	q_9
α_i	0	π/2	0	π/2	π/2	0	π/2	0	π/2

Table 1: D-H Parameters for the 3-DOF PM.

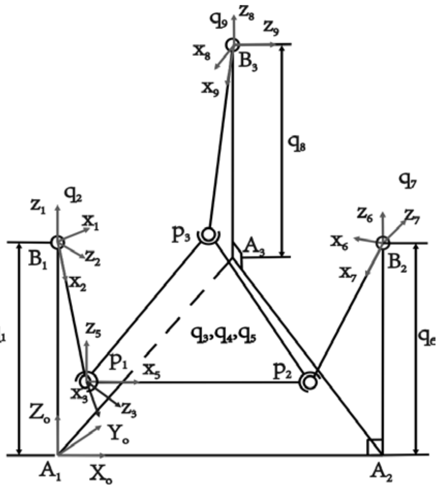

Figure 2: Location of the coordinate systems.

The robot has 3-DOF, and applying the geometric approach it can be seen that the length between $p_i a p_j$ is constant and equal to l_m. Thus,

$$f_1(q_1,q_2,q_6,q_7) = \left\| \left(\vec{r}_{A_1B_1} + \vec{r}_{B_1p_1}\right) - \left(\vec{r}_{A_1A_2} + \vec{r}_{A_2B_2} + \vec{r}_{B_2p_2}\right) \right\| - l_m = 0 \tag{1}$$

$$f_2(q_1,q_2,q_8,q_9) = \left\| \left(\vec{r}_{A_1B_1} + \vec{r}_{B_1p_1}\right) - \left(\vec{r}_{A_1A_3} + \vec{r}_{A_3B_3} + \vec{r}_{B_3p_3}\right) \right\| - l_m = 0 \tag{2}$$

$$f_3(q_6,q_7,q_8,q_9) = \left\| \left(\vec{r}_{A_1A_3} + \vec{r}_{A_3B_3} + \vec{r}_{B_3p_3}\right) - \left(\vec{r}_{A_1A_2} + \vec{r}_{A_2B_2} + \vec{r}_{B_2p_2}\right) \right\| - l_m = 0 \tag{3}$$

In the forward kinematics the position of the actuators is known, thus the system of equations (1)-(3) can be seen as a nonlinear system with $q_{2,}$ q_7 and q_9 as unknown. Newton's numerical method is chosen to solve the nonlinear system. The method is iterative and can be written as,

$$\begin{bmatrix} q_2 \\ q_7 \\ q_9 \end{bmatrix}^{i+1} = \begin{bmatrix} q_2 \\ q_7 \\ q_9 \end{bmatrix}^{i} - \mathbf{J}_i^{-1} \begin{bmatrix} f_1(q_2,q_7) \\ f_2(q_2,q_9) \\ f_3(q_7,q_9) \end{bmatrix}^{i} \tag{4}$$

In the equation, *i* means that the variables and functions are evaluated at the iteration *i*. The matrix $\mathbf{J}$ is the Jacobian matrix of f_i with respect to the variables $[q_2, q_7, q_9]$. The iterative process ends when,

$$\sqrt{\left(f_1(q_2, q_7)^i\right)^2 + \left(f_1(q_2, q_9)^i\right)^2 + \left(f_1(q_7, q_9)^i\right)^2} < \varepsilon \tag{4}$$

The parameter ε is a small positive quantity established by the user.

The Newton method requires an initial approximation as close as possible to the solution value. In this case this is not a problem since the initial pose of the link connecting the platform to the actuator is around 2π/5. The subsequent initial approximation considers the values of the previous pose of the robot.

The location of the mobile platform is defined using a local coordinate system attached to it. Having found the generalized coordinates for the robot's legs, the position of points p_i can be found. These three points share the plane of the platform. Based on these points, the rotational matrix of the platform with respect to the base can be built. A local axis X_p is defined as a unit vector $\vec{u}$ with the direction given by $p_1 p_2$ The axis Z_p is defined by the vector $\vec{v}$ and is an axis perpendicular to the plane defined by points p_1, p_2 and p_3. Finally, the axis Y_p is defined by the direction of the axis $\vec{w}$, which is determined by the vector product between the $\vec{u}$ and $\vec{v}$ axes. The rotation matrix of the moving platform is given by,

$$^{O}R_p = \begin{bmatrix} \vec{u}^T & \vec{v}^T & \vec{z}^T \end{bmatrix} \tag{5}$$

The remaining generalized coordinates q_3, q_4, q_5 can be found from the rotation matrix.

2.3 Inverse Kinematics

The inverse kinematics consist of given the roll (γ) and pitch (β) angle and the heave (z), finding the actuators linear motion. Using an X-Y-Z fixed-angle system; the rotational matrix can be defined as,

$$^{O}R_p = \begin{bmatrix} c_\alpha c_\beta & c_\alpha s_\beta s_\gamma - s_\alpha c_\gamma & c_\alpha s_\beta c_\gamma - s_\alpha s_\gamma \\ s_\alpha c_\beta & s_\alpha s_\beta s_\gamma - c_\alpha c_\gamma & s_\alpha s_\beta c_\gamma - c_\alpha s_\gamma \\ -s_\beta & c_\beta s_\gamma & c_\beta c_\gamma \end{bmatrix} \tag{5}$$

In the above equation, c_* and s_* stand for $\cos(*)$ and $\sin(*)$, respectively. Given γ and β the yaw angle (α) can be found as follows,

$$\alpha = \mathbf{atan}2\left(s_\beta s_\gamma, \left(c_\gamma + c_\beta\right)\right) \tag{9}$$

Having found the angle α, the remaining terms of the rotational matrix can be found. The actuator positions can be found by the following expressions [3],

$$q_1 = p_x{}^2 + p_y{}^2 + p_z{}^2 + 2h\left(p_x u_x + p_y u_y + p_z u_z\right) - 2g\,p_x - 2g h u_x + g^2 + h^2 \tag{6}$$

$$q_2 = p_x{}^2 + p_y{}^2 + p_z{}^2 - h\left(p_x u_x + p_y u_y + p_z u_z\right) + \sqrt{3}h\left(p_x v_x + p_y v_y + p_z v_z\right) \\ + g\left(p_x - \sqrt{3}p_y\right) + gh\left(u_x - \sqrt{3}u_y\right)/2 + gh\left(v_x - \sqrt{3}v_y\right)/2 + g^2 + h^2 \quad (7)$$

$$q_3 = p_x{}^2 + p_y{}^2 + p_z{}^2 - h\left(p_x u_x + p_y u_y + p_z u_z\right) - \sqrt{3}h\left(p_x v_x + p_y v_y + p_z v_z\right) \\ + g\left(p_x - \sqrt{3}p_y\right) - gh\left(u_x - \sqrt{3}u_y\right)/2 + gh\left(v_x - \sqrt{3}v_y\right)/2 + g^2 + h^2 \quad (8)$$

In the equation, $h = l_m / \sqrt{3}$, $g = l_b / \sqrt{3}$, $p_x = -hu_y$, $p_y = -h\left(u_x - v_y\right)$, $p_z = z$ and l_b are the lengths between $A_i A_j$.

3 MECHATRONIC ROBOT DEVELOPMENT

For the parallel robot implementation, three CC servomotors equipped with power amplifiers have been used. The actuators are AEROTECH BMS465 AH brushless servomotors, and the power amplifiers are AEROTECH BA10.

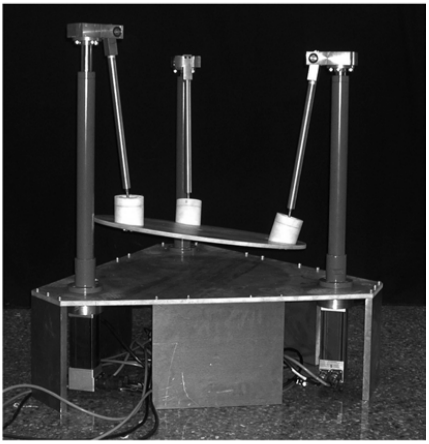

Figure 3: 3-PRS parallel robot implemented.

Featuring rare-earth neodymium iron boron magnets and a high pole-count robot, the AEROTECH BMS465 brushless, slotless servomotor provides a very high torque, acceleration and smoothness in a small package. These motors can be equipped with a variety of encoder resolution options for any application. In addition to the standard RS-422 line driver output, an optional amplified sine-wave encoder can be used to provide ultra-high resolution. They offer encoder multipliers as an option, as well as external multiplier boxes (resolutions as high as 1,000,000 counts per revolution are achievable). The performance specifications of BMS465 motors are 2.86N-m stall torque (continuous), 11.43N-m peak torque and 2,000 rpm.

The AEROTECH BA10 amplifier is Aerotech's stand-alone drive for brushless or single-phase DC brush motors. This amplifier can run in velocity mode or torque mode using a self-commutating, low ripple, modified six-step algorithm. It accepts a standard ±10VDC as a velocity or torque (current) command from any motion controller. The continuous output current is 5A, with 10A of peak output current. The BA10 amplifier is based on a 20 kHz IGBT for reliable operation in a compact package. It is completely self contained, requiring only AC line power, and the amplifier is fully protected. The DC-isolated power stage minimizes loop noise. The amplifier accepts a quadrature encoder or tachometer input for velocity feedback. The encoder signal is converted to a voltage representing speed.

In order to implement the control architecture for the parallel robot, an industrial PC has been used. It is based on a high performance 4U Rackmount industrial system with 7 PCI slots and 7 ISA slots. It has a 3,06GHz Intel® Pentium® 4 processor and two GB DDR 400 SDRAM. The industrial PC is equipped with 2 Advantech™ data acquisition cards: a PCI-1720 and a PCL-833.

The PCI-1720 card has been used for supplying the control actions for each parallel robot actuator. It provides four 12-bit isolated digital-to-analog outputs for the Universal PCI 2.2 bus. It has multiple output ranges (0~5V, 0~10V, ±5V, ±10V), programmable software and an isolation protection of 2500 VDC between the outputs and the PCI bus. The PCL-833 card is a 4-axis quadrature encoder and counter add-on card for a ISA bus. The card includes four 32-bit quadruple AB phase encoder counters, an onboard 8-bit timer with a wide range time-based selector and it is optically isolated up to 2500V.

Fig. (4) shows the control architecture based on an industrial PC developed for this study.

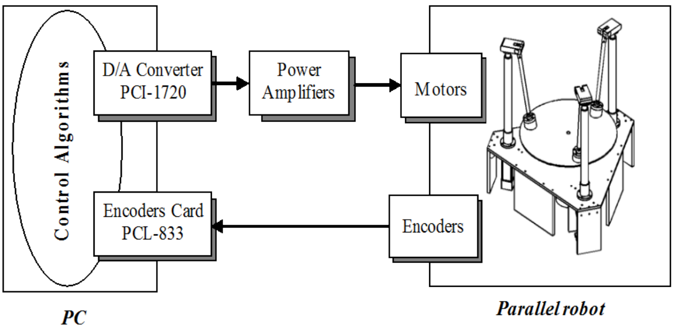

Figure 4: Robot control architecture.

4 DYNAMIC-BASED CONTROL SCHEMES

4.1 Passivity-based Control

In recent years, the passivity-based approach to robot control has gained a lot of attention. This approach solves the robot control problem by exploiting the robot system's physical structure, and specifically its passivity property. The design philosophy of these controllers is to reshape the system's natural energy in such a way that the tracking control objective is achieved [13].

In the point-to-point problem (regulation), the controllers based on passivity could be viewed as particular cases of the next general control law:

$$\tau_e = -K_p e - K_d v - u \qquad (1)$$

Where $e = q - q_d$ and u and v vary according to the kind of controller:

Controller (point-to-point problem)	***u***	***v***
PD+G	$-G(q)$	$\dot{q}$
PD+G0	$-G(q_d)$	$\dot{q}$
PID	$K_i\int_0^t e\,\mathrm{dt}$	$\dot{q}$

Table 2: Passivity-based point-to-point controllers.

The first controller implemented was the PD with gravity term compensation. This controller is composed of two parts: the first part is a lineal feedback of the state and the second part is the gravity forces compensation.

The second control strategy was also proposed by the same authors. It is a variation on the first controller where gravity compensation is done in the desired final position.

These controllers are very simple but they have two main drawbacks: the first one is the computational complexity of the gravity term. Depending on the robot and/or its dynamic modelling, it can be so high that it is impossible to calculate it in real-time. On the other hand, the dead-zone phenomenon or any error in the gravity term estimation can cause a variation in the equilibrium point and therefore a stationary position error. A practical solution to attempt to solve these problems is to insert an integral action in the control law. These laws are basically the same as the PD, but the gravity compensation has been changed by the error integral.

For the tracking problem, the kinetic and potential energy must be modified as required in passivity-based controllers. The general expression of the controllers that can be found in the literature is as follows:

$$\tau_e = M(q)a + C(q,\dot{q})v_1 + G(q) - K_p e - K_d v_2 \tag{2}$$

Where a, v_1, v_2 and e varies according to the kind of controller (see Table 3). In all these controllers the control law has two parts, robot dynamics compensation and a proportional and differential controller.

Controller (tracking problem)	***a***	***v₁***	***a***	***v***
Paden, Panja	$\ddot{q}_d$	$\dot{q}_d$	$q-q_d$	$\dot{e}$
Slotine, Li	$\ddot{q}_r$	$\dot{q}_r$	0	$\dot{e}+A_1e$
Sadegh, Horowitz	$\ddot{q}_r$	$\dot{q}_r$	$q-q_d$	$\dot{e}+A_1e$

Table 3: Passivity-based tracking controllers.

The first controller is a variation of the PD with gravity compensation. The second one is a tracking controller based on the sliding mode theory. In the last one, some modifications are introduced in the control law and in the energy function. It allows for probing the system's asymptotic stability using the Lyapunov theory.

4.2 Inverse Dynamic Control

Some controllers have been implemented with the control architecture depicted previously. The first class of controllers is based on the inverse dynamic method. This control approach makes a regular static state feedback that transforms the nonlinear system into a linear one (this is known as the inverse dynamic or feedback linearization problem). Assuming the dynamic model as:

$$x^{(n)} = f(x) + b(x)u \tag{3}$$

Where $f(x)$ is a nonlinear state function and u is the control input. If you use the expression:

$$u = \frac{1}{b}\left[v - f\right] \tag{4}$$

the nonlinearities will be cancelling, and the simple input-output relationship will be obtained:

$$x^{(n)}=v \tag{5}$$

Where v is a new lineal input vector to be defined below.

In the robot case, the controllers based on the inverse dynamics could be viewed such as particular cases of the following general control law [14]:

$$\tau_c = M(q)v + C(q,\dot{q})\dot{q} + G(q) \tag{6}$$

Inverse dynamic control (6) shows how the nonlinearities such as Coriolis terms as well as gravity terms can be simply compensated for by adding these forces to the control input. Depending on the expression v, different controllers can be obtained:

Control algorithm	$\boldsymbol{v}$
Point-to-point control	$-K_d\dot{q} - K_p e$
Tracking control	$\ddot{q}_d - K_d\dot{q} - K_p e$
Tracking control with integral action	$\ddot{q}_d - K_d\dot{q} - K_p e - K_i\int_0^t e(u)du$

Table 4: Inverse dynamic controllers.

The first controller implemented was the point-to-point controller. In this case, proportional and derivative terms compose the linear auxiliary control input v, and the robot system is exponentially stable by a suitable choice of the matrices K_d and K_p.

The second controller is very similar to the first, but in this case the robot must follow a given time-varying trajectory $q_d(t)$ and its successive derivatives $\dot{q}_d$ and $\ddot{q}_d$, which respectively describe the desired velocity and acceleration. This tracking control is very simple but it has several drawbacks: any error in the estimation robot dynamics can cause a variation in the equilibrium point and therefore a position error. The second problem that can occur is related to the dead-zone phenomenon: in this case the static friction at the motor shafts can also provoke a position error. A practical solution to attempt to solve these problems is to insert an integral action into the control law. This is the case of the last controller, where the integral of the error has been added.

4.3 Real-Time Control Implementation

The control unit developed for this study is based on an industrial PC. It is a totally open system and it gives a powerful platform for programming high level tasks. Thus any controller and/or control technique can be programmed and implemented, such as automatic trajectory generation, control based on external sensing using force sensor or artificial vision, etc. In this study, the PC runs on the Windows XP operating system and two development environments have been used: Matlab and Microsoft Visual C++.

For the rapid development of the parallel robot controllers, Simulink schemes have been used in this application. Therefore, the Matlab Real-Time Workshop (RTW) and Real-Time Windows Target (RTWin) toolboxes have been used, which produce codes directly from Simulink models and automatically generate programs that can be run in environments like Linux, VxWorks, DOS and Windows. These toolboxes feature a rapid and direct path from system design to hardware implementations, seamless integration with Matlab and Simulink, a simple and easy interface, an open and extensible architecture, a fully configurable code generator etc.

Fig. (5) shows a Simulink/RTW scheme used for the parallel robot control. Measurements for the three angular positions of the joints of the robot are obtained by means of the Advantech encoder card. It must be taken into account that, because they are incremental encoders, it is necessary to program the initial values when the system starts.

With the real robot position and motion references, the PC computes the necessary control actions for the robot joints. These control actions are sent to the power amplifiers of the control unit by means of digital/analog converters.

In this system, the Embedded Matlab Functions have been used to implement the control algorithm: the Paden passivity-based tracking control. This controller calculates the action controls by means of the robot dynamic equation (gravity, Coriolis and Inertial terms) and a PD controller. Four additional blocks are needed. The first one implements a routine for solving the forward position problem of the 3 DOF PM with a PRS configuration (cine3DOF embedded function). It obtains the 9 generalized coordinates that define the robot kinematics by means of the concepts in [3], [15], and the nonlinear position problem is solved by using a Newton-Rhapson algorithm.

The second one implements a routine for solving the Velocity Problem of a 3 DOF parallel robot (vel3DOF embedded function). The procedure used in this routine is based on the concepts in [15], and uses the Denavit-Hartenbert notation.

Because this scheme establishes the robot control in the joint space, another embedded function is necessary. The third one (*Inverse Kinematics*) implements the inverse kinematic problem of the parallel robot. This block uses the roll-pitch and heave references desired for the robot, providing the references for the three actuators of the robot joints (q_1, q_2 and q_3 positions, velocities and accelerations). Finally, in order to compare the references and the real robot variables in the task space, the fourth embedded function block calculates the direct kinematic problem. With it, the roll, pitch and heave of the parallel robot is calculated.

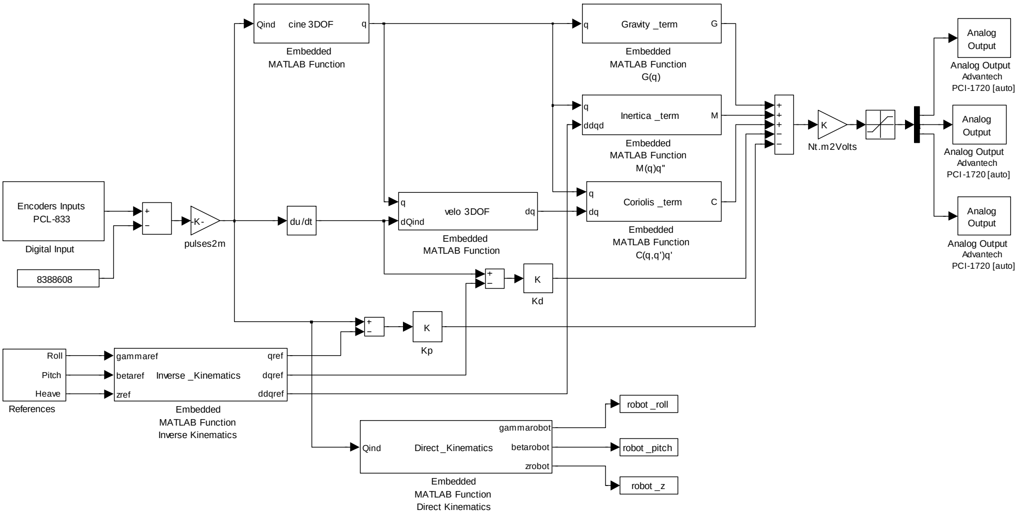

Figure 5: Paden passivity-based Robot controller.

Once the good functionality of the controller has been analyzed and the parameters of the controllers (gain matrices and constants, for example) have been tuned with Matlab, the development of the final control application can be performed. In order to do this, in this study Microsoft Visual C++ (MSVC) has been used, which is a very well-known development environment. MSCV is a commercial, integrated development environment (IDE) product from Microsoft for the C, C++, and C++/CLI programming languages. It has tools for developing and debugging the C++ code, a code especially written for the Microsoft Windows API, the DirectX API, and the Microsoft .NET Framework. For access to the data acquisition cards, the Advantech *PC-LabCard Software Driver* has been used, which provides the required drivers for the Advantech cards (A/D and D/A conversions, encoders, digital input/output, counters/timers, etc.) and allows control of the card's functions using high-level languages. In addition, these drivers make programming easier because each function pulls its parameters from a common parameter table.

The C++ application implemented establishes robot control using the passivity-based and inverse dynamic control algorithms presented in Section 4.1 and 4.2. In order to program these algorithms, the NAG Numerical Library has been used.

The sampling period used to establish control of the parallel robot is 10ms. Tests developed have proved that this period is large enough, as the mean controller execution time obtained (which includes encoder readings, controller calculations and digital/analog conversions) is less than 4ms.

5 RESULTS

Using the parallel robot and its open control systems, different control algorithms have been developed and tested. The control strategies solved the point-to-point and tracking problems. Fig. (6) shows the reference and the real parallel robot values of heave, roll and pitch. As can be seen, the robot response follows the references with a very small error.

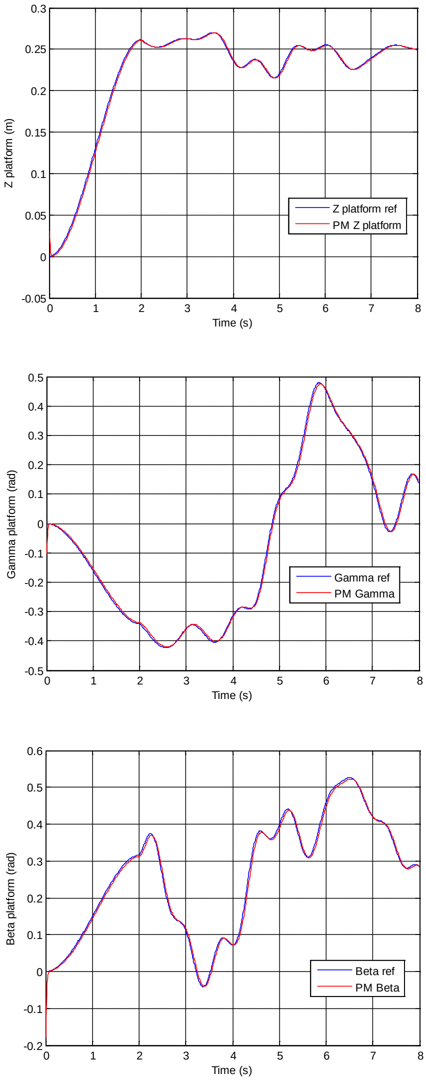

Figure 6: Heave, roll and pitch parallel robot response.

Figs. (7) and (8) show the joint space robot response. Fig. (7) shows the robot position (q1, q2 and q3, in meters) and the action control (in volts) for the point-to-point control problem. The curves plotted in green are the robot references. The curves plotted in blue belong to the inverse dynamic controller. The black curves belong to the PID controller, and the red curves belong to the PD with a gravity compensation controller.

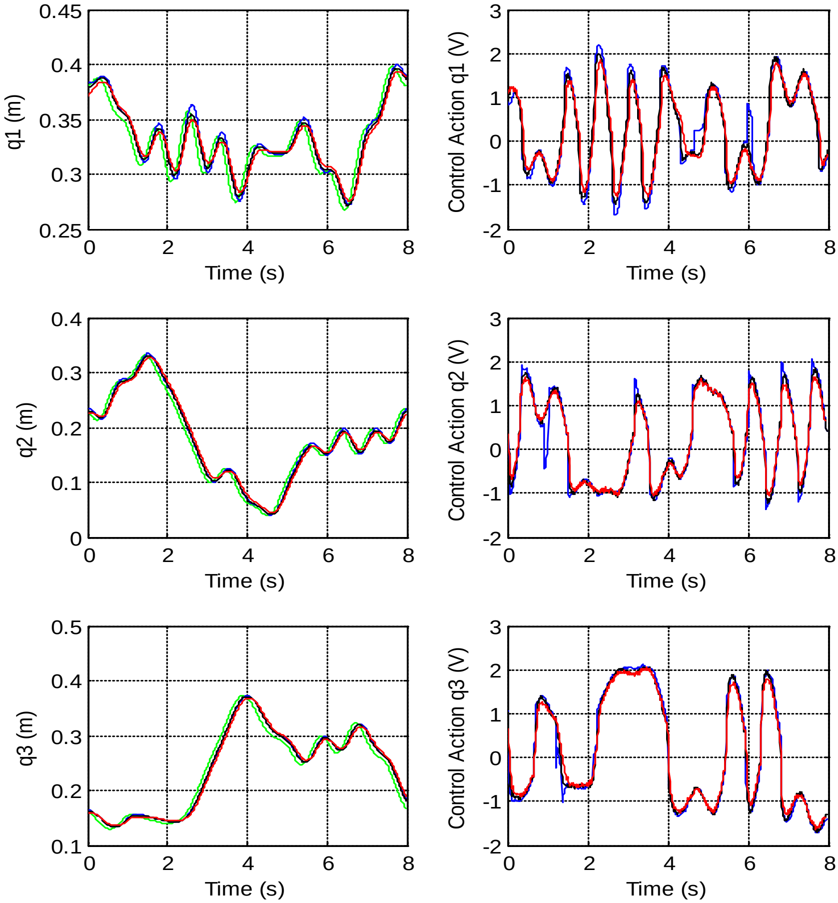

Fig. (8) shows the robot response for the tracking control problem. As in the last case, the references are plotted in green. The curves in blue belong to the inverse dynamic controller, and the red curves belong to the Paden passivity-based controller.

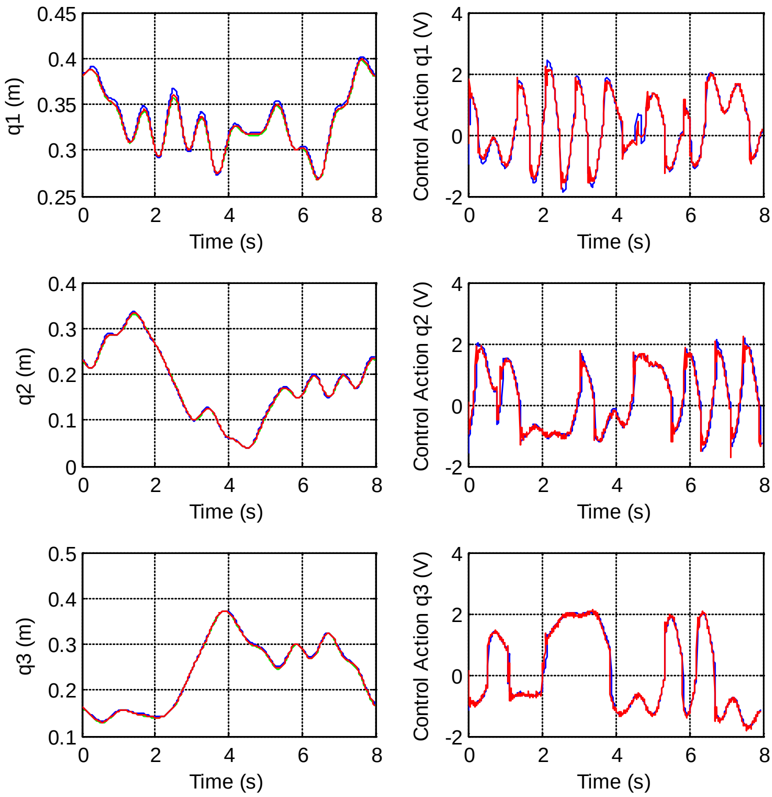

Table 5 shows the mean error and the quadratic mean error between the references and the real position of the three links of the parallel robot for the point-to-point problem.

Controller	$\frac{\sum_i e_i}{n}$			$\sqrt{\frac{\sum_i e_i^2}{n}}$		
	1	***2***	***3***	***1***	***2***	***3***
PD+G	-0.00111	-0.00117	-0.00108	0.01126	0.01325	0.01364
PID	-0.00124	-0.00046	-0.00124	0.00856	0.00949	0.00965
Inv. Dynamics	-0.00233	-0.00142	-0.00177	0.01016	0.00925	0.01030

Table 5: Link robot position errors (mean and RMS) for point-to-point control.

Table 6 shows the error for the tracking problem.

Controller	$\frac{\sum_i e_i}{n}$			$\sqrt{\frac{\sum_i e_i^2}{n}}$		
	1	***2***	***3***	***1***	***2***	***3***
Inv. Dynamics	-0.00239	-0.00145	-0.00186	0.00343	0.00300	0.00234
Passivity-based	-0.00061	-0.00057	-0.00059	0.00080	0.00099	0.00075

Table 6:Link robot position errors (mean and RMS) for tracking control.

6 CONCLUSIONS

In this paper the mechatronic design, mechanical structure, electric actuators and control system of a low-cost 3-DOFPRS parallel manipulator has been fully developed. Open control architecture has been developed for this robot, and, two control schemes have been proposed: Passivity-based control and Inverse dynamic control. The control algorithm considers point-to-point control or tracking control. Both direct and inverse kinematic equations for the PM have been obtained for application to the control system. When the controller considers the system dynamics, dynamic parameters obtained through an identification process have been used. The control schemes have been tested over a virtual robot and over the actual prototype. Different results showing the tracking accuracy of proposed controllers are included.

ACKNOWLEDGEMENTS

The authors wish to express their gratitude to the Plan Nacional de I+D, Comisión Interministerial de Ciencia y Tecnología(FEDER-CICYT) for the partial financing of this study under the projects DPI2009-13830-C02-01 and DPI2010-20814-C02-(01, 02).

REFERENCES

[1] D. A. Steward. A platform with 6 degree of freedom. *Proceedings of the Institution of mechanical engineers*. Part 1 vol. 15, 371-386, 1965.

[2] V.E. Gough, S.G. Whitehall. Universal *tire test machine. Proceedings of 9th International Technical Congress FISITA, 117-135, 1962.*

[3] J.-P Merlet.*Parallel Robots*. Kluwer, London, U.K., 2000.

[4] L. W. Tsai.*Robot Analysis: The Mechanics of Serial and Parallel Manipulator*. Wiley Interscience, Canada, 1999.

[5] R. Clavel. DELTA, a fast robot with parallel geometry. Proceedings of 18th International Symposium on Industrial Robot, Lausanne, April, 91-100, 1988.

[6] F. Pierrot, V. Nabat, O. Company, S. Krut, P. Poignet, Optimal design of a 4-dof parallel manipulator : From academia to industry, *IEEE Transactions on Robotics*, vol. 25, nº 2,213-224, 2009.

[7] Y Li, Q. Xu. Design and Development of a Medical Parallel Robot for Cardiopulmonary Resuscitation. *IEEE/ASME Transaction on Mechatronics*, vol. 12, nº 3, 265–273, 2007.

[8] D. Chablat, P. Wenger. Architecture optimization of a 3-DOF translational parallel mechanism fro machining applications, the Orthoglide. *IEEE Transactions on Robotics and Automation*, vol. 19, nº 3, 403-410, 2003.

[9] K.M. Lee, S. Arjunan. A three-degrees-of-freedom micromotion in-parallel actuated manipulator. *IEEE Transactions on Robotics and Automation*, vol. 7 nº 5, 634–641, 1991.

[10] Y. Li, Q. Xu. Kinematics and stiffness analysis for a general 3-PRS spatial parallel mechanism. Proceeding of 15th CISM/IFToMM Symposium in Robot Design, Dynamics and Control, Montreal, Canada, 2004.

[11] C. E., Syrseloudis and I. Z. Emiris.A parallel robot for ankle rehabilitation-evaluation and its design specifications. Proceeding of 8th IEEE International Conference on-BioInformatics and BioEngineering, 2008. Athens, 1-6, October, 2008

[12] F. Piccot, N. Andreff, P. Martinet. A review on the dynamic control of parallel kinematic machines: Theory and Experiments.*The international Journal of Robotics Research,* vol. 28, nº 3, 395-416, 2009.

[13] R. Ortega, M. Spong. Adaptive Motion Control of Rigid Robots: a Tutorial, *Automatica*, vol. 25, pp. 877-888, 1989.

[14] N. Rosillo, A. Valera, F. Benimeli, V. Mata, V, F. Valero, Real-time solving of Dynamic Problem in Industrial Robots, Industrial Robot, vol. 38, n. 2, pp. 119-129, 2011

[15] N. Farhat, Identificación de Parámetros Dinámicos en Sistemas de Cadena Cerrada. Aplicación a Robot Paralelos. Phd, Universidad Politécnica de Valencia, 2006.

Proceedings of MUSME 2011, the International Symposium
on Multibody Systems and Mechatronics
Valencia, Spain, 25-28 October 2011

FLEXIBLE PNEUMATIC ACTUATION FOR BLOOD PRESSURE RECOVERY

Andrea Manuello Bertetto, Silvia Meili

Dipartimento di Ingegneria Meccanica
Università degli Studi di Cagliari, piazza d'Armi. 09123 Cagliari, Italy
e-mail: manuello@dimeca.unica.it,meili@dimeca.unica.it

Alberto Concu, Antonio Crisafulli

Dipartimento di Scienze della Vita e dell'Ambiente
Università degli Studi di Cagliari, via Porcell, 4. 09124 Cagliari, Italy
e-mail: concu@unica.it,crisafulli@tiscali.it

Keywords: Biomechanics, Flexible Actuators, Multi-body
Abstract. *Improving poor blood circulation is an issue of concern for people undergoing lower extremities motion impairment. Paraplegic patients encounter different level disorders due to inadequate oxygen pump power caused by reduction in volume and wall thickness of the heart chambers, so that an artificial system would be needed to speed up blood flow in order to strengthen the cardiac muscle. In this paper a calf-plantar sequential pneumatic compression innovative device, consisting of three sensorized and PLC-controlled chambers that inflate to a physiological value of pressure is designed and realised. The device performs a massage on the calf surface and on the foot sole and, in addition, carries out the ankle passive movement. To design this innovative device, preliminary tests were performed on patients, using a commercial device normally devoted to lymphatic drainage massage. The new device was then tested and the pressure trends in the actuator chambers are reported in the paper. The massage is performed by the new device at a given controlled pressure level and frequency, which is approximately the human pace. The ankle flexible actuator drives the joint between the two calf and foot segments. The mechatronic apparatus was tested under real working conditions. Air pressure transducers, one for each actuator, were used to feedback control the actuation system.*

1 INTRODUCTION

In paraplegic subjects the spinal cord is cut and, due to absence of leg muscle contraction, venous return to the heart is reduced and this may induce a reduction of cardiac output as well. Cardiovascular control during physical exercise has been widely studied. Normally physical exertion induces cardiovascular adjustments which consist in an increase of heart rate (HR), stroke volume (SV), cardiac output (CO) and a fall in peripheral vascular resistance (PVR) (1). Many medical and biomechanical researchers evaluate the possibility of replacing striate muscle pump on limb veins with the application to legs of mechanical actuators, thus restoring end diastolic filling pressure of ventricles. In this occurrence, a cardiac output compensation would occur and aerobic capacity would be restored in these patients.

Pneumatic actuators are widely used within electromechanical systems in biomechanics. The typical pneumatic actuator is light and robust and for this reason it encounters more and more interest in biomechanical area. In particular, a specific kind of pneumatic actuator, commonly flexible pneumatic actuator (FPA), can produce a large displacement together with a large force by means of the deformation of a flexible structure under the action of a pressurized fluid. Conventional actuators do not always meet the needs of the applications in advanced robotics. This is true for biomedical, aerospace, mobile robots. In these applications a high force to weight ratio and a flexible structure, which can adapt the actuator geometry during assembly, are important features to meet the requirements. The flexible pneumatic actuators (FPA) are provided with interesting characteristics as the absence of any relative sliding motion of mechanical parts, the absence of lubricants and dynamic seals, and compliance.

For these characteristics the FPA muscles were extensively studied and used in numerous non-conventional applications, [1-3]. A great effort was made for proposing and fabricating novel types of flexible pneumatic actuator (FPA) as well, in order to improve the pull capabilities of the muscle [4]. A few works were presented on the modeling of pneumatic muscles [5-9]. Many researchers studied a particular type of flexible actuator powered by pressurized fluid, namely flexible Pneumatic Balloon Actuators (PBA's) introduced by Schwörer et al. [10], Konishi et al. [11] and others [12, 13]. For a more thorough state of the art of flexible fluid actuators, we refer to two recently published review papers [14, 15]. The operation of these actuators is based on the same mechanism as the joints of certain insects like spiders [16-18]. Essentially, these actuators comprise two flexible layers with different bending stiffness, that are bonded together at the edges to form a balloon. Because of this asymmetrical stiffness, the actuator bends when pressurized, which generates the actuation motion. The asymmetric bending stiffness can be achieved using for instance different layer thicknesses or different Young's moduli [19]. A promising research activity in the robotics community is the development of devices attempting to imitate biological forms which are based on flexible structures and often fluid powered. Numerous examples may be found out either as manipulators, actuators, grippers and hands, or mobile robots. For each of mentioned robotics areas, several relevant advantages may be stressed when using flexible structures over traditional robots. Manipulators as well as grippers or flexible hands can operate with delicate objects without causing any damage because of their own compliance. Furthermore, the robot hands can approximate the manipulation skills and grip force of the human hand when using fluidic actuators [20], [21]. These types of structures have significant potential for improved performance over traditional manipulators in the areas of obstacle avoidance and manipulation [22]. Moreover these manipulators have the inherent ability to conform to environmental constraints on contact. Flexible manipulators may boast a drastic simplification in design over traditional devices still being hyper-redundant in number of degrees of freedom [23]. No heavy motors and transmission boxes are required as well as only static sealing, with no relative motion, are used. Thus these devices seem to be well suited for operating in clean room, food and agriculture industries as well since they do not need lubricants and wear particles are not released. A common inspiration from biology guides the researchers in developing fluidic muscles or actuators as well. Very numerous applications, from the human inspired muscle through angular or revolute actuators can be found in the recent bibliography [24-26]. The striking characteristic of these motors is the high ratio between the actuation force and weight. However the robotic area where probably the fluidic flexible structure devices are more spread is the mobile robots. There are several prototypes fabricated to be able to work in unstructured or even hostile environment based on a flexible structure driven by fluid. By exploiting the absence of electrical power, these robots may operate with radioactivity or in presence of electromagnetic fields. Some flexible robots were built for navigating through pipes [27], swimming [28], climbing [29]. Despite of the several advantages mentioned, a strong shortcoming in using these devices is their control strategy. Fluidic flexible robots require sophisticated controls in order to reach accurate and repeatable positioning. Further their dynamics modeling has to fight with the deformable structure and with not-conventional actuations. An extended bibliography can be found about the flexible robots modeling issue [30, 31]. However the experimental applications are often limited to simple cases. Many approximate models, i.e. finite elements, Myklestad’s method, Ding-Holzer method, screw theory have been proposed in order to overcome the difficulty in applying the distributed parameter approach. However, models of robots with continuum structure were rarely dealt with [32]. In any case a large interest was demonstrated in this kind of actuators, in particular for recovering fundamentals functions of paraplegic subjects.

The biomechanical research community recently evaluated the possibility of replacing striate muscle pump on limb veins with the application to legs of mechanical actuators, thus restoring end diastolic filling pressure of ventricles. In this occurrence, a cardiac output compensation would occur and aerobic capacity would be restored in these patients.

In spinal cord injured (SCI) individuals there is a partial loss of nervous control over circulation, and this fact may explain some of the altered circulatory responses to effort occurring in SCI persons [33-35]. The absent peripheral vasoconstriction below the level of the spinal lesion and the lower stroke volume (SV) increment compared to able-bodied subjects are well known phenomena during physical activity in SCI patients [36].

The inability of SCI patients to increase venous return during exercise has been reported several times and has been associated with a disturbed redistribution of blood during exercise due to the lack of sympathetic-mediated vasoconstriction below the level of the spinal cord lesion [34, 35, 37]. This fact impairs venous return and cardiac filling and in part explains the low SV during exercise shown by these patients [36].

Some studies employing antigravity suit found that this kind of device could increase peak oxygen uptake and decrease heart rate in relation to workload during arm crank exercise. Moreover, subjects with SCI demonstrated significantly higher SV with the application of a pneumatic device capable of inducing lower body positive pressure, while able body individuals’ performance was unaffected by this kind of intervention. These studies suggest that for individuals with SCI, the use of devices that increase venous return to the heart could augment exercise capacity by preventing the redistribution of blood to the lower extremities [38, 39].

In this paper a calf-plantar sequential pneumatic compression innovative device and ankle actuator, consisting of three sensorized and PLC-controlled chambers that inflate to a physiological value of pressure, is designed and realised. To design this innovative device, preliminary tests were performed on patients, using a commercial device, normally devoted to lymphatic drainage massage. Main purpose of these preliminary tests was to verify the effectiveness of the compression on patient legs to restore circulation efficiency. After these preliminary tests the new device was designed and realised. The new device was then tested and the pressure trends in the actuator chambers are reported in the paper. Massage is performed at a given frequency which is approximately the human pace. The ankle flexible actuator drives the joint between the two calf and foot segments. The mechatronic apparatus was then tested under real working conditions. Air pressure transducers, one for each actuator, were used to feedback control the actuation system.

2 PRELIMINARY TESTS ON PATIENTS UNDER INCREMENTAL EFFORT

A preliminary study, to verify the effectiveness of the compression on patient legs to restore circulation efficiency and to identify the minimum threshold of pressure values to be applied to the lower limbs and the sizes of the muscle areas to be involved in the actuators action, was performed. After this study the forces and pulses trends as a function of time to be applied on different areas of the limbs, where the actuators will be assembled, will be identified.

To this purpose a commercial device, normally devoted to lymphatic drainage massage, was used. This device, shown in Fig. (1), consists of a sheath/boot with four sleeve sectors assembled in sequence from foot to thigh, each independently supplied by compressed air, to perform a sequential inflation. The sectors are indicated in Fig (1) as Ch#.

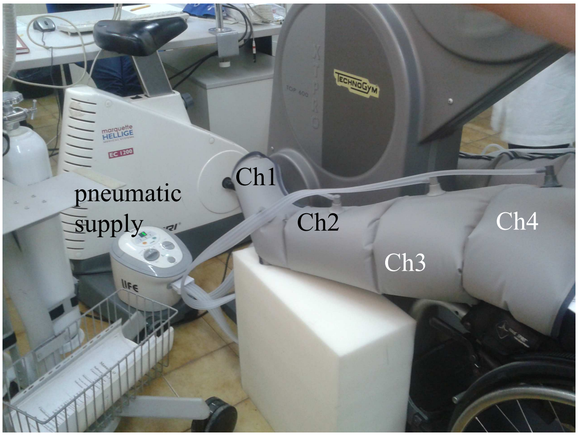

Figure 1: The peristaltic device on a leg of a paraplegic patient.

By this way a peristaltic compression, having a rostral-caudate trend corresponding to a pressure wave from foot to thigh, is implemented. The pressure level is about 50 mm Hg; this level is higher than the venous pressure in the lower limbs, which typically varies in a range from 10 to 20 mm Hg, as the air pressure inside the pressurized chambers can be significantly higher than that transmitted to the veins, here not detected. The time period of pressure increment in each chamber is about 15-20 s, so the peristaltic cycle has a period of about 1 min.

The preliminary tests were performed on eleven patients.

The volume variation of the cardiac chambers was detected by the bi-dimensional echocardiography shown in Fig. (3). Similarly, the volume oscillation of the cardiac chambers was detected in the same patient, without the peristaltic device, comparing the test results in the two different conditions.

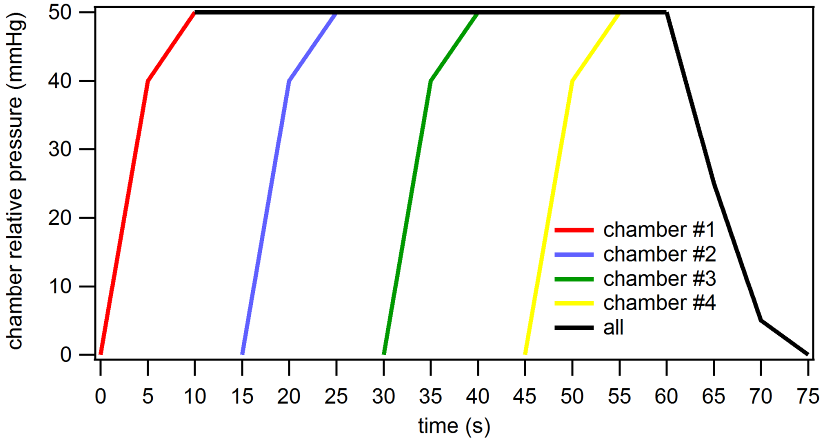

Figure 2: The pressure trend in time air-supplying the four chambers of the boot.

The volume oscillations of cardiac chambers are higher when the peristaltic device is applied to the legs of the patient during the incremental effort test compared to incremental effort testing without it.

Each boot consists of four chambers; they are air-supplied in a peristaltic way, as represented in the graph in Fig. (2). The chambers, from the lower one around the foot to the upper one on the thigh, are inflated in turn after 15 s each. The chambers are then deflated altogether and after 3 s the cycle starts again. So, the device is cycle powered approximately every 75 s. The maximum pressure value in the chambers is 50 mmHg.

A paraplegic patient is then given an incremental effort test by means of an arm-ergometer, as shown in Fig. (3).

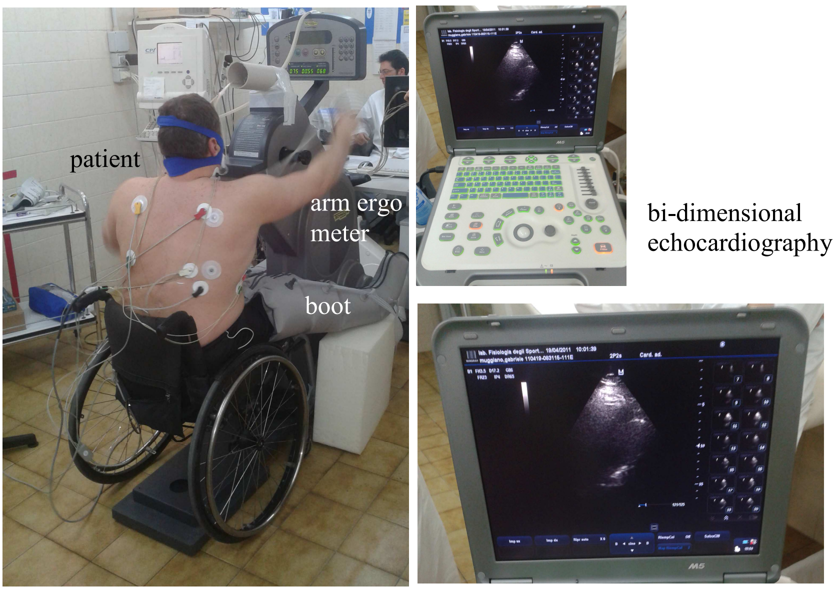

Figure 3: A patient having a bi-dimensional echocardiogram during an incremental effort test he is using an arm ergometer and is wearing a peristaltic device

During this test peristaltic devices were applied onto the patient legs. The arm ergometer load, applied by an electromagnetic brake, is imposed at 30% of the maximal effort, which was detected for each patient from a previous test: so, the ergometer load changes for each patient as a function (30%) of their respective maximum tolerable load. The hemodynamic parameters are shown in table 1, where the mean values for the eleven patients are reported. In particular, the effectiveness of applying pressure on the legs to recovery circulation efficiency is shown by the increment of the end diastolic volume and the cardiac output (grayed fields in table 1). This confirms that the pressure action on the legs is capable to support the heart action.

In Table 1 the measured parameters are reported, both with the ergometer load and without it; and combining the results obtained using the boot or not.

	without the ergo meter load		*imposing the ergo meter load*	
Hemodynamic Parameter	**without pressure on the legs**	**with pressure on the legs**	**without pressure on the legs**	**with pressure on the legs**
HR(bpm) heart rate	88,3	85,8	114,2	110,3
SV(ml) stroke volume	65,1	63,7	72,1	85,7
CO (ml/min) cardiac output	5752,3	5478,6	8284,6	9457,8
EDV(ml) end diastolic volume	141,5	157,9	180,4	226,5

Table 1: Four hemodynamic parameters showing (highlighted values in particular) how patients cardiac function improves when having pressure applied on their legs.

3 THE BLOOD PRESSURE RECOVERY DEVICE

The development and use of robotic systems for rehabilitation is a widely investigated topic and a many such devices are commercially available in order to answer to the needs of different therapies.

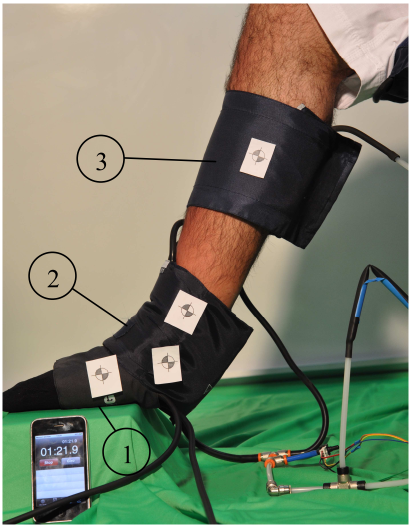

Figure 4: The blood pressure recovery device.

The purpose of this research is a device that will combine two different functions: it will produce a distributed pressure action and it will passively move limbs in a controlled way. The use of external aid devices (static, manually operated or motorized) exerting the pressure action with the aim of improving the return of blood and lymph from circulatory periphery to central systems is been adopted since a long time.

In Fig. (4) the device put on by a patient is represented. Three balloon actuators can be seen: the first one acts (1) on the foot sole, to recover the pressure coming from the soil during the gait; the second one (2) performs the ankle rotation in a sagittal plane; the third one (3) radially compresses the calf and simulates a pumping action from the gastrocnemius muscle on the leg veins, as whilst walking.

In Fig. (5) the scheme of one of the circuits-supplying each of the three balloon actuators is shown. On the right hand side a photograph of the circuit is shown.

The compressed air comes from the supply (1) and is processed within the FRL (Filter, Pressure Reducer, Lubricator) group. The compressed air flow is then controlled by the electrovalve (3) and drives the balloon actuator (4), here represented as a single effect cylinder. The regulator valves (5) allow the speed control of the balloon actuation. The pressure switch (6) gives a signal for the commutation of the electrovalve (3), avoiding to reach too high a pressure level in the actuator (4) with danger for the patient. To have an easier actuator exhausting phase during the actuation cycle, the environment is depressurized downstream the valve by the vacuum generator ejector (7), supplied through the flow regulator (8). In the photograph the preliminary circuit used for driving one balloon actuator can be seen. The system is closed-loop controlled by a PLC.

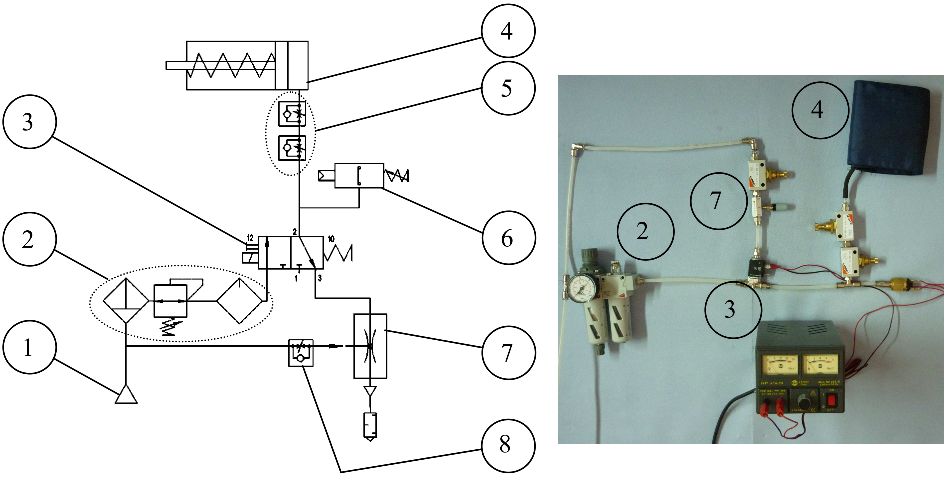

Figure 5: One of the three circuits supplying the balloon actuators of the blood pressure recovery device.

A NI cDAQ-9172 CompactDAQ chassis, equipped with a NI9219 4-Channel, 24-Bit, analog input module, was used to read pressure data coming from three Honeywell 24PC Series transducers.

The pressure trend of the three balloon actuators, each detected by a pressure transducer assembled on the supply circuit, near the actuator supply port, is referred to in Fig. (6).

The curve (1) is the pressure trend vs. time in the actuator acting on the foot sole; the curves (2) and (3) represent, in turn, the pressure in the actuator performing the ankle rotation and in the actuator acting a radial compression of the calf. The pressure trend of the actuator

(1) has a maximum level of 0.2 bar; the actuators (2) and (3) reach a level of 0.1 bar. Frequency is 0.2 Hz, as the one of a slow walking healthy person.

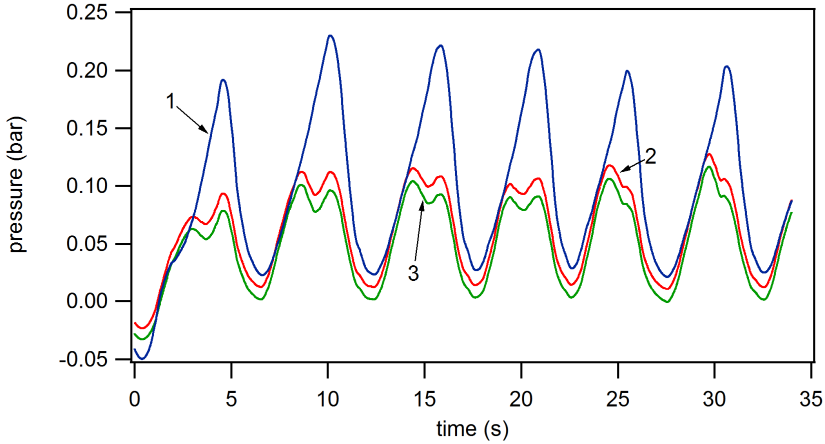

Figure 6: The pressure trend of the three balloon actuators.

4 CONCLUSIONS

Effectiveness of the mechanical action on leg muscles of paraplegic patients in restoring end diastolic filling pressure of ventricles was assessed using a commercial device: a cardiac output compensation and aerobic capacity improvement has been ecocardiogradiography-monitored on these patients during incremental effort tests.

To this purpose an innovative device has been set up which applies to the patient leg a pulsing pressure reaching levels and having a trend suitable for restoring circulation efficiency. The new device was then tested and the pressure trends in the actuator chambers are reported in the paper. Massage is performed at a given frequency which is approximately the human pace. In future works the innovative device will be tested on patients following given authorised formal clinical trials.

ACKNOWLEDGEMENTS

This research was founded by the Italian Ministry of Research (MIUR).

REFERENCES

[1] H. F. Schulte Jr., 1961. The characteristics of the McKibben artificial muscle. Application of external power in prosthetics and orthotics, *Nat. Acad. Sci.-Nat. Res. Council* Washington DC, 1961.

[2] C. P. Chou, B. Hannaford. Static and dynamic characteristics of McKibben pneumatic artificial muscles. IEEE International Conference on Robotics and Automation, San Diego, CA, May 8–13, 1994.

[3] R. T. Pack, J. L. Christopher Jr., K. Kawamura. A rubbertuator-based structure-climbing inspection robot. IEEE 1997 International Conference on Robotics and Automation, Albuquerque, New Mexico, April 20–25, 1997.

[4] C. Ferraresi, W. Franco, A. Manuello. Straight fibers pneumatic muscle: an actuator with high traction force. Sixth Scandinavian International Conference on Fluid Power, Tampere, May 26–28, 1999.

[5] S. Hirai, P. Cusin, H. Tanigawa, T. Masui, S. Konishi, S. Kawamura, 2000. Qualitative synthesis of deformable cylindrical actuators trough constraint topology. Proceedings of the IEEE/RSJ Int. Conference on Intelligent Robots and Systems, 2000.

[6] C. P. Chou, B. Hannaford. Measurement and modeling of McKibben pneumatic artificial muscles. *IEEE Transactions on Robotics and Automation*, vol. 12, n° 1, 90–102, 1996.

[7] T. Raparelli, F. Durante, P. Beomonte Zobel. Numerical modelling and experimental validation of a pneumatic muscle actuator. Fourth JHPS, International Symposium on Fluid Power Tokyo _99, Novembre Tokyo, 1999.

[8] B. Gorissen, M. De Volder, A. De Greef, D. Reynaerts. Theoretical and experimental analysis of pneumatic balloon microactuators, *Sensors and Actuators* A 168, 58–65, 2011.

[9] A. Manuello Bertetto, M. Ruggiu. Characterization and modeling of air muscles, *Mechanics Research Communications*, vol. 31, 185–194, 2004.

[10] M. Schwörer, M. Kohl, W. Menz, Fluidic microjoints based on spider legs, Proc. Actuator 98, 103–106, (1998).

[11] S. Konishi, F. Kawai, P. Cusin. Thin flexible end-effector using pneumatic balloon actuator, *Sens. Actuators* A vol. 89, 28–35, 2001.

[12] R. Abe, K. Takemura, K. Edamura, S. Yokota. Concept of a micro finger using electro-conjugate fluid and fabrication of a large model prototype, *Sens. Actuators* A 136, (2007), 629–637, 2007.

[13] Y.-W. Lu, C.J. Kim. Microhand for biological applications, *Appl. Phys. Lett.*, vol. 89, 164101–164103, 2009.

[14] M. De Volder, D. Reynaerts. Pneumatic and hydraulic microactuators: a review, *J. Micromech. Microeng.*, vol. 20, 2010.

[15] A. De Greef, P. Lambert, A. Delchambre. Towards flexible medical instruments: review of flexible fluidic actuators, *Precision Eng.*, vol. 33, 311–321, 2009.

[16] M. Schwörer, M. Kohl, W. Menz. Fluidic microjoints based on spider legs, Proc. Actuator 98, 103–106, 1998.

[17] D. Parry, R. Brown, The hydraulic mechanism of the spider leg, *J. Exp. Biol.*, vol. 36, 423–433, 1959.

[18] L. Zentner, S. Petkun, R. Blickhan. From the spider leg to a hydraulic device, *Technische Mechanik*, vol. 20, 21–29, 2000.

[19] O.C. Jeong, S. Konishi, All PDMS pneumatic microfinger with bidirectional motion and its application, *J. Microelectromech. Syst.*, vol. 15, n°4, 896–903, 2006.

[20] S. Schultz, C. Pylatiuk, G. Bretthauer. A new ultra light anthropomorphic hand, Proc. of the 2001 IEEE International Conference on Robotics & Automation, Seoul, Korea, May 21-26, 2001.

[21] S. Dohta, Y. Ban, H. Matsushita. Application of a flexible strain sensor to a pneumatic rubber hand, Proc. of the Sixth Triennal International Symposium on Fluid Control, Measurement and Visualization, Sherbrooke (Qc) Canada, August 13-17, 2000.

[22] M. W. Hannan, I. D. Walzer. Analysis and experiments with an Elephant's Trunk Tobot, *The International journal of the Robotics society of Japan*, vol. 15, n° 8, 847-858, 2001.

[23] C. Ferraresi, A. Manuello Bertetto, L. Mazza. Design and realisation of a flexible pneumatic actuator for robotic, Proc. of 5th Scandinavian International Conference on Fluid Power, SICFP 97, Linkoping, Sweden, May 28-30, 1997.

[24] F. Daerden, D. Lefeber, B. Verrelst, R. Van Ham. Plated pneumatic artificial muscles: actuators fpr automation and robotics. 2001 IEEE – ASME Int. Conf. On Advanced Intelligent Mechatronics, Como, Italy, July 8-12, 2001.

[25] S. Hirai, P. Cusin, H. Tanigawa, T. Masui, S. Konishi, S. Kawamura. Qualitative Synthesis of Deformable Cylindrical Actuators trough Constraint Topology. Proc. of the 2000 IEEE/RSJ int. Conference on intelligent Robots and Systems, Kagawa, Japan, October 31–November 5, 2000.

[26] T. Noritsugu, M. Kubota, S. Yoshimatsu. Development of pneumatic rotaty soft actuator made of silicone rubber. Proc. of the Sixth Triennal International Symposium on Fluid Control, Measurement and Visualization, Sherbrooke (Qc) Canada, August 13-17, 2000.

[27] A. B. Slatkin, J. Burdick. Development of a robotic endoscope. Proceedings of the International Conference on Intelligent Robots and Systems, Pittsburgh, Pennsylvania, USA, August 05-09, 1995.

[28] M. Sfakiotakis, D. M. Lane, B. C. Davies. An experimental undulating-fin device using the parallel bellows actuators. Proc. of the 2001 IEEE International conference on Robotics & Automation, Seoul, Korea, May 21-26, 2001.

[29] A. Manuello Bertetto, M. Ruggiu. Pole Climbing Pneumatic Robot., Proc. of the Fifth JFPS International Symposium on Fluid Power, Nara, Japan, November 12-15, 2002.

[30] T. Yoshikama, K. Hosoda. Modeling of flexible manipulators using virtual rigid links and passive joints. *International Journal of Robotics Research*, vol. 15, n° 3, 290-299, 1996.

[31] X. Ding, J. M. Selig. Dynamic modeling of a compliant arm with 6-dimensional tip forces using screw theory. *Robotica*, vol. 21, pp. 193-197, 2003.

[32] D. J. O'Brien, D. M. Lane. 3D force control system design for a hydraulic parallel bellows continuum actuator. Proc. of the 2001 IEEE International conference on Robotics & Automation, Seoul, Korea, May 21-26, 2001.

[33] F. Dela, T. Mohr, C. M. R. Jensen, H. L. Haahr, N. H. Secher, F. Biering-Sørensen, M. Kjær. Cardiovascular control during exercise. Insights from spinal cord-injured humans. *Circulation*, vol. 107, 2127-2133, 2003.

[34] M. T. E. Hopman. Circulatory responses during arm exercise in individuals with paraplegia. *Int J Sports Med*, vol. 15, 126-131, 1994.

[35] P. L. Jacobs, E. T. Mahoney, A. Robbins, M. Nash. Hypokinetic circulation in persons with paraplegia. *Med Sci Sports Exerc*, vol. 34, 1401-1407, 2002.

[36] A. Crisafulli, R. Milia, S. Vitelli, M. Caddeo, F. Tocco, F. Melis, A. Concu. Hemodynamic Responses To Metaboreflex Activation: Insights From Spinal Cord-Injured humans. *Eur J Appl Physiol*. Vol. 106, 525-533, 2009.

[37] G. M Davis, G. J. Servedio, R. M. Glaser, S. C. Gupta, A. G. Suryaprasad. Cardiovascular responses to arm cranking and FNS-induced leg exercise in paraplegics. *J. Appl Physiol*, vol. 69, 671-677, 1990.

[38] C. Bazzi-Grossin, P. Bonnin, O. Bailliart, H. Bazzi, A. W. Kedra, J. P. Martineaud. Maximal exercise in spinal cord injured subjects: effects of an antigravity suit. *Sci Sports*, vol. 11, n° 3, 173-179, 1996.

[39] K. H. Pitetti, P. J. Barrett, K. D. Campbell, D. E. Malzahn. The effect of lower body positive pressure on the exercise capacity of individuals with spinal cord injury. *Med Sci Sports Exerc*, vol. 26, n° 4, 463-468, 1994.

Proceedings of MUSME 2011, the International Symposium
on Multibody Systems and Mechatronics
Valencia, Spain, 25-28 October 2011

OBJECT ORIENTED MODELING FOR WALKING MACHINES

Mauricio Alba, Juan Carlos García Prada and Cristina Castejon

Department of Mechanical Engineering
Universidad Carlos III de Madrid, Avenida de la Universidad 30, 28911 Madrid, Spain
e-mail: dalba@ing.uc3m.es,
web page: http://maqlab.uc3m.es/

Keywords: Simulation, walking robots, multibody systems, object oriented modeling, modelica.

Abstract. *In this paper the advantages of object oriented modeling applied to walking robots is exposed. The selected tool is the Modelica® language using Dymola® implementation. First, a procedural model is implemented using the equations of motion of Raibert's hopping monopod. After that, more complex walkers (a passive dynamics system and an actuated robot) using standard libraries are modeled and simulated. Instead of procedural modeling the Modelica® multibody library is used in order to develop some examples of object oriented modeling. Because this library does not support contact or mechanical looks, those objects are added, and their mathematical description is explained. With both techniques exposed a short comparison is performed to address advantages and disadvantages.*

1 INTRODUCTION

Simulators of complex systems are very useful tools in order to test algorithms before they can be implemented. In this way, prototypes are protected from bugs normally introduced in early stages of development. If a careful mathematical description of the original system is performed, the simulator can be as accurate as required. The problem is how to determine the degree of accuracy required in early stages of development.

Originally simulators have been made using the paradigm of procedural programming; the idea is to develop discreet reusable code blocks that could stand on their own, in other words functions that accept variables and give an output. The topology is intrinsically defined by the differential equations of the system and therefore embedded in the code. Modifications or upgrading of the model implies deep changes in the structure.

Bond graph theory opened a new way to see dynamical systems. Power ports are the mean to define such models. With these concepts the paradigm of object oriented modeling is introduced in the design of simulators. In this way a simulator is considered to be composed of objects that interact with each other. With this approach the upgrade and modification of the model is restricted to each object, therefore it is not necessary a complete refurbishment of the program, but only a modification of the objects of interest in the process.

2 OBJECTIVES

Design of a simulator for a specific system is often seen as a challenge, and only developed if the application really demands it. The complexity found in walking robots discourages the development of such systems. Or even, if a simulator is ever developed, the information obtained from it is not taken as reliable.

In this paper the results of simulation of walking robots in the object oriented modeling language Modelica® using Dymola® implementation are exposed. The objective is to show the advantages of object oriented modeling over procedural techniques. Although there are countless of similar software providing similar solutions, as for example MATLAB Simulink®, Yobotics®, 20Sims®, etc. the selection of this software was based on code transparency offered by Dymola®, required to achieve the objective.

Changes in the topology has been seen as very problematic in procedural modeling, in this paper those changes are also explained and they are shown as trivial tasks when seeing from the model oriented point of view. It is not the objective of this paper to compare different object oriented modeling techniques or software, because normally this is left to the taste of the researcher.

3 MOTIVATION

In robotics projects with high budgets, it is common to find very impressive simulators with a very detailed description of the original systems. The availability of tools to develop powerful simulators and the potential savings of time, by testing in a virtual world, is a very attractive motivation to deep into this field. An example is shown in Fig. (1) and exposed in Ref. [1], where a virtual environment was developed to the HRP-2 robots.

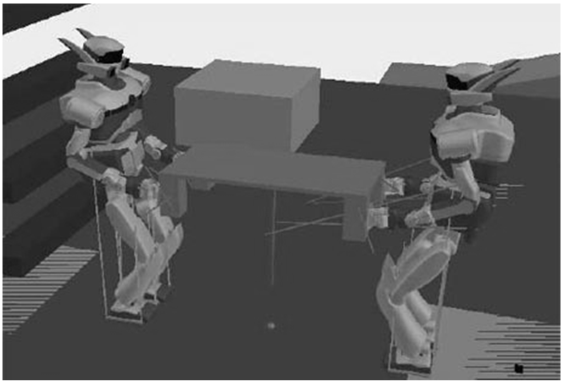

Figure 1: Simulator of the HRP-2

The available tools and computational power available in any laboratory is more than enough to obtain impressive results, the only barrier remaining is the lack of information about how the simulator is done, and it is often the principal cause to stop a serious simulation line inside a project with a lower budget. Therefore, an informative document showing practical examples of the simulation of walking systems has been identified to be of interest of other researchers in the field.

4 SIMULATING IN MODELICA

Modelica® is a non-proprietary, object oriented language, focused on modeling complex physical systems containing multi-physics phenomena. The language is equation oriented in order to provide self-descriptive qualities. For example a bouncing ball is written as follows:

```
Vy=der(y);
ay=der(Vy);
m*ay=-m*g;
when y<=0 then
reinit(Vy,-cr*pre(Vy));
end when;
```

Where `y`, `Vy` and `ay` are the position, velocity and acceleration of the ball respectively, `cr` is the coefficient of restitution, and `g` is the acceleration of gravity. Operator `der` is used to express the derivative of a variable, while `reinit` operator is used to change the value of a variable by the value defined in the second argument of the function. In this case when `y` reaches a value minor or equal to zero triggers the `reinit` operator and the direction of the velocity is changed and reduced by a factor of `cr`, simulating the bouncing.

The example just developed shows that equations are introduced directly into the code. If the equations are well structured, they can be simulated without requiring further steps. But the language also includes classes that allow defining connectors and other structures in order to create objects instead of only procedures. Although the modeling in Modelica® is acausal the programming can be designed as a bong graph structure Ref. [2], thanks to the classes provided in the language specification Ref. [3].

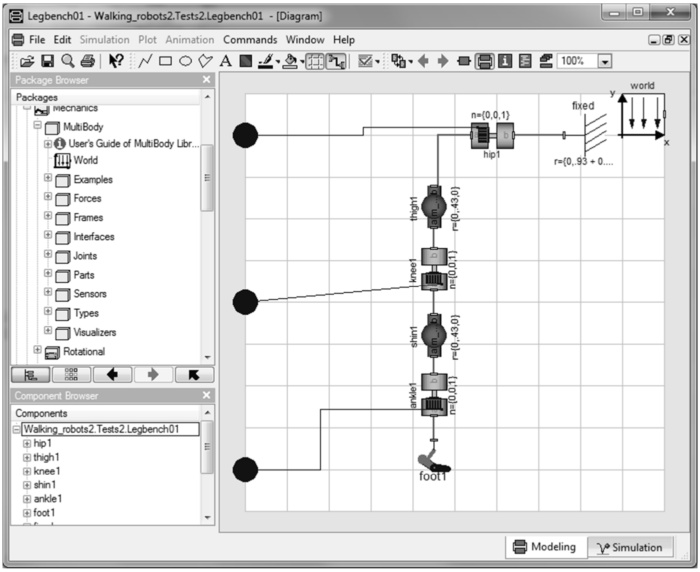
Figure 2: Simulation of a robotic leg. The figure shows the modeling environment.

The standard library provides a complete set of components in different engineering domains, but the most relevant when simulating walking robots is the Multiboby library. The library is composed by a set of joints, bodies, sensors, forces, etc. that provides the basis to develop a kinematic chain without effort. In Fig. (2) a robotic leg was developed using the objects provided by the standard library included in Dymola®.

In this section a quick overview of how Modelica® works has been exposed. To understand the real potential of the language authors encourage to read the bibliography provided in this paper, especially Ref. [2], Ref. [3] and Ref. [4]. Unfortunately a deeper exposition of the software used in this paper is out of the scope.

5 SIMULATION OF A HOPPING ROBOT

In this section the simulation of a hopping robot will be performed, this case is an example of procedural modeling. This means that the equations of the system will be derived and then introduced into the program. Any change in the system would be required to rewrite all the mathematics. The selected system is shown in Fig. (3), taken from Ref. [5]. It is composed by a leg actuated by compressing a spring and body. The equations of motion are obtained using free body diagrams and D'Alembert principle:

$$\begin{gathered}(J_l - m_l R l_1)\ddot{\theta}\cos\theta - m_l R\ddot{x}_0 = \cos\theta(l_1 F_z \sin\theta - l_1 F_x \cos\theta - \tau) \\ -R(F_z - F_{leg}\sin\theta + m_l l_1 \dot{\theta}^2 \sin\theta)\end{gathered} \tag{1}$$

$$\begin{gathered}(J_l - m_l R l_1)\ddot{\theta}\sin\theta + m_l R\ddot{z}_0 = \sin\theta(l_1 F_z \sin\theta - l_1 F_x \cos\theta - \tau) \\ +R(F_z - F_{leg}\cos\theta + m_l l_1 \dot{\theta}^2 \cos\theta - m_l g)\end{gathered} \tag{2}$$

$$\begin{aligned}(J_l + mRr)\ddot{\theta}\cos\theta + m_l R\ddot{x}_0 + mR\ddot{r}\sin\theta + mRl_2\ddot{\phi}\cos\phi = \cos\theta(l_1 F_z \sin\theta \\ -l_1 F_x \cos\theta - \tau) + RF_{leg}\sin\theta + mR(r\dot{\theta}^2\sin\theta + l_2\dot{\phi}^2\sin\theta - 2\dot{r}\dot{\theta}\cos\theta)\end{aligned} \tag{3}$$

$$\begin{aligned}(J_l + mRr)\ddot{\theta}\sin\theta - m_l R\ddot{z}_0 - mR\ddot{r}\cos\theta + mRl_2\ddot{\phi}\sin\phi = \sin\theta(l_1 F_z \sin\theta \\ -l_1 F_x \cos\theta - \tau) - R(F_{leg}\cos\theta - mg) - mR(r\dot{\theta}^2\cos\theta + l_2\dot{\phi}^2\cos\theta + 2\dot{r}\dot{\theta}\sin\theta)\end{aligned} \tag{4}$$

$$\begin{aligned}(J_l l_2\ddot{\theta}\cos(\theta-\phi) - JR\ddot{\phi} = l_2\cos(\theta-\phi)(l_1 F_z\sin\theta - l_1 F_x\cos\theta - \tau) \\ -R(l_2 F_{leg}\sin(\phi-\theta) + \tau)\end{aligned} \tag{5}$$

The meaning of the variables is shown in Fig. (3). The robot is composed by two main parts, the body and the leg. These two elements are connected between them by a rotary joint. This joint is actuated by a torque motor and becomes the first control input. This input is responsible for the equilibrium and velocity of the robot. The leg has a built-in spring excited by an actuator that works as the second input. In that way the energy lost by each collision during the jumping cycle is restored. The actuator also regulates the height of jumping. The floor was modeled as one point contact, therefore the values of F_x and F_z are:

$$F_x = \begin{cases} -k_g(x_0 - x_{td}) - b\dot{x}_0 & z \le 0 \\ 0 & z > 0 \end{cases} \tag{6}$$

$$F_z = \begin{cases} -k_g z_0 - b\dot{z}_0 & z \le 0 \\ 0 & z > 0 \end{cases} \tag{7}$$

Where x_{td} is the point in which x the robot makes the first contact with the floor, k_g is the stiffness constant of the floor, and b is the damping coefficient. The leg actuator, composed by a spring, a mechanical lock and the actuator itself, is modeled as:

$$F_{leg} = \begin{cases} -k_{stop} r_{s\Delta} - b_{stop}\dot{r} & r_{s\Delta} > 0 \\ -k_{leg} r_{s\Delta} & r_{s\Delta} \le 0 \end{cases} \tag{8}$$

Where k_{stop} is the force constant of the mechanical lock and b_{stop} is the damping constant of the mechanical lock, k_{leg} is the spring constant of the leg and $r_{s\Delta}$ is the deformation of the spring and is equal to:

$$r_{s\Delta} = r - w_l + r_{s0} \tag{9}$$

where r_{s0} is the equilibrium length of the spring.

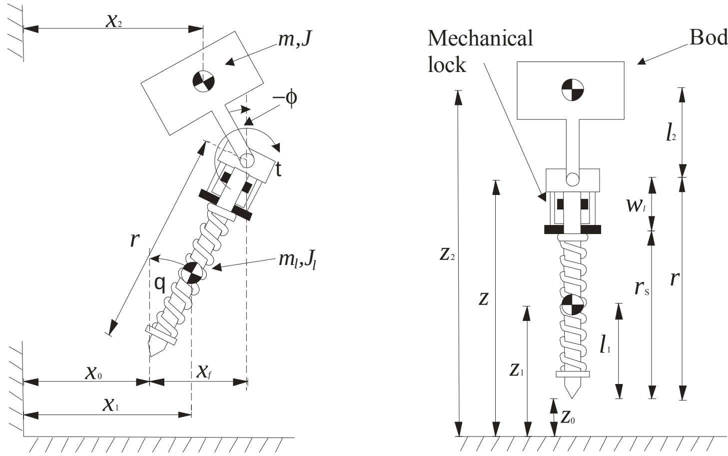

Figure 3: Schematic of the hopping robot.

5.1 Results

The original control system was replaced with a modified version of the original controller developed in Ref. [5]. The modified version was proposed to avoid the steady state error in the original controller. Therefore the control law is stated as follows:

$$\theta_d = -\arcsin\left(\frac{\dot{x}T_s}{2r} - \frac{k_p(\dot{x}_d - x) + k_i\int(\dot{x}_d - \dot{x})dt + k_p d(\dot{x}_d - \dot{x})/dt}{r}\right) \tag{10}$$

A stroboscopic animation of the system and the plot of the error can be seen in Fig. (4) and Fig. (5) respectively.

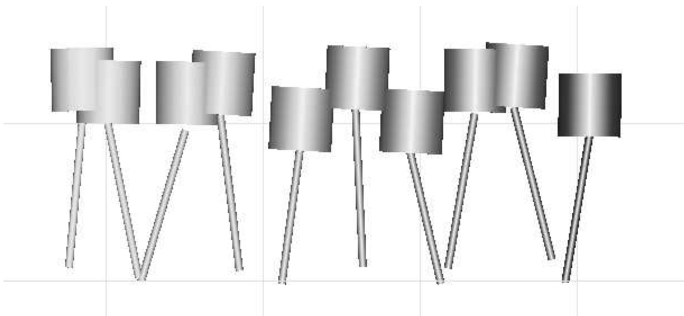

Figure 4: Stroboscopic picture of the hopping robots.

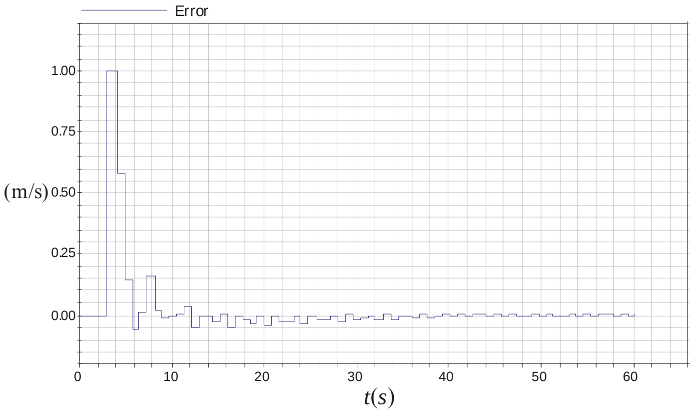

Figure 5: Plot of the simulated error speed of the robot.

6 SIMULATION OF A PASSIVE DYNAMICS SYSTEM

The delicate stability and the simplicity of construction of a passive walker, was the chosen system to being simulated. Although, not a robotic system, the ability to generate a natural gait using limit cycles, makes it the perfect candidate to prove Modelica® for the task proposed in this paper.

The walker itself is modeled with the multibody library of Modelica® (Ref. [6]). The interaction between the floor and the feet was modeled as point contacts similar to the one described by Eq. (6). The difference is the introduction of a cloud of points to describe the curvy surface of the feet present in passive walkers. The modified contact model is written as:

$$F_{y_i} = \begin{cases} kx_i - b\dot{x}_i & \text{IF } y_i \le 0 \\ 0 & \text{ELSE} \end{cases} \tag{11}$$

In order to calculate the tangent reaction of the floor, a similar approach than the one found in [7] was used. The total reaction force F_t, calculated from the sum of F_{yi}, is used to calculate the tangential force F_x:

$$F_{y_i} = \mu F_t \cdot \begin{cases} 1 & \text{IF } |v_t| \le v_{\min} \\ |v_t| / v_{\min} & \text{ELSE} \end{cases} \tag{12}$$

where μ is a parameter describing viscous friction and $v_{\min}$ is the reference velocity. Although this model allows slippage, the simulations demonstrated the usefulness of this model for the proposed application.

In Ref. [7] is stated that using a spring-mass model for contact is not a good approach due to the problem that the spring constant remains without changes, even though when the penetration between the bodies is increased. Because in the model proposed in this paper the contact of every point is calculated individually. Raising the deep of penetration will add more springs in parallel, and therefore, giving the effect of increasing resistance when there is a deeper penetration.

6.1 Knee lock

The joint models included in the multibody library do allow infinite displacements in their degrees of freedom. A modified rotational joint was created in order to model the knee lock present in these machines. The lock was modeled as a conditional torque as follows:

$$\tau_{knee} = \begin{cases} k\theta - b\dot{\theta} & \text{IF}\,\theta \le \theta_c \\ 0 & \text{ELSE} \end{cases} \tag{13}$$

Where τ_{knee} is the reaction moment, k and b are the stiffness and damping coefficient, and θ_c is the angle where the mechanical lock is located. The implementation in Modelica® is done by extending the rotational joint in the multibody library and replacing the value of the variable τ_{knee} with the one in the eq. (13).

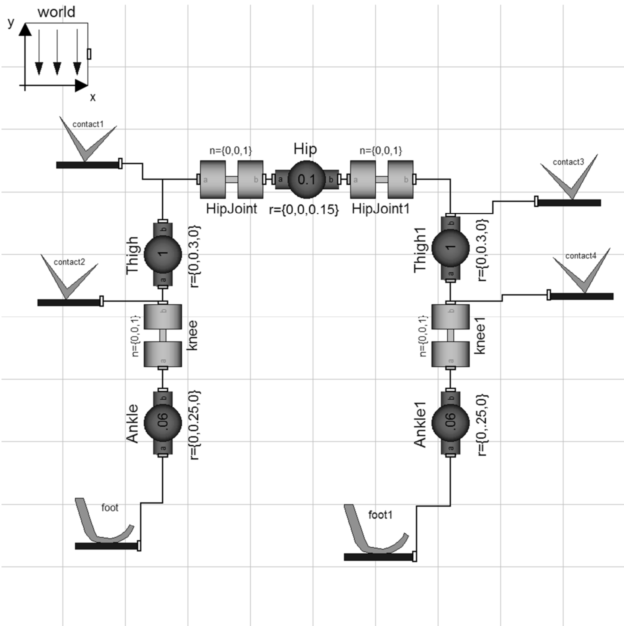

Figure 6: Schematic of the passive walker in Dymola®.

6.2 Passive walker model

The graphic environment of Dymola® is very similar to other tools like Simulink or 20Sims. The elements are dragged and dropped into the workspace and then connected, each component has its independent parameters to introduce the mass properties and other mechanical characteristics. The implementation can be seen in Fig. (6).

Because passive walkers need a source of energy provided by an inclined plane, the last was simulated by changing the gravity vector in the world component in the model. Once the model was settled the initial values an different parameters were estimated by trial and error, taking into account the recommendations in Ref. [8] Maybe the most challenging part when simulating this system was the initial conditions. It is well know that a passive walker needs "trained hands" in order to provide a working gait. The results of the simulation can be seen in Fig. (7). The limit cycles showed complete convergence generating a stable gait.

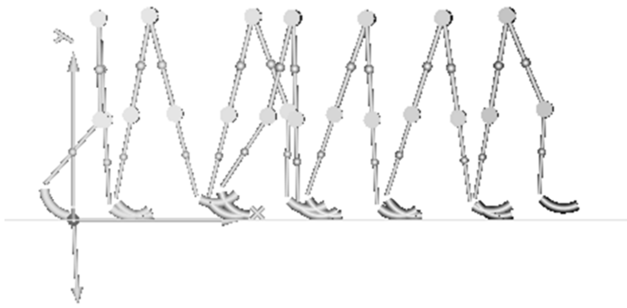

(a)

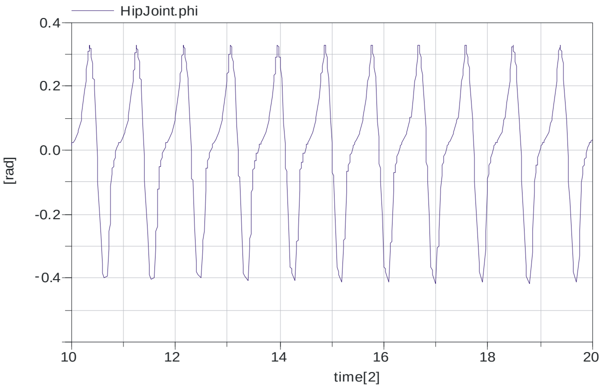

(b)

Figure 7: Simulation of a passive walker. (a) stroboscopic animation of the biped. (b) limit cycle generated by the hip.

7 SIIMULATION OF A BIPED WITH A FLYWHEEL

In section 5 the simulation of a hopping robot was performed. It was done by using the differential equations of the system directly. This approach leads to a simulator with low flexibility. In the next section the object oriented modeling paradigm was used in order to create a passive walker. The results were quite satisfactory, but the problem was that no control system was encountered in the system, as happens normally in this kind of machines.

In this section a fully actuated robot is developed, adding a control system object that is independent of the model of the robot. Only the model and the basis of its control system will be exposed in this section, details are exposed in Ref. [9].

7.1 The robot

The robot is composed by a flywheel connected by a bisected hip with actuators to each leg, the knees are also actuated. Despite the robot having point feet, the acceleration of the flywheel allows to apply torque to the floor by means of the dynamic equivalence Ref. [10] shown in Fig. (8). The left pendulum of the figure is composed by a point mass and is actuated at its base. By the other hand, the pendulum in the right side is composed by an actuated flywheel, and it has a free joint at the base.

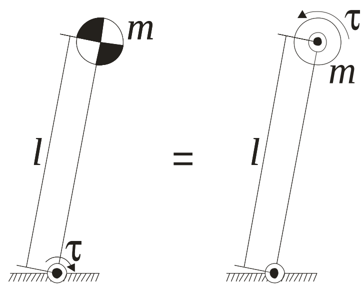

Figure 8: Dynamically equivalent pendulums.

Once the dynamic equivalence is considered, the robot as described in the previous paragraph and shown in Fig (9) is considered a fully controllable system. This conclusion is done because the robot is considered that can actuate over all its degrees of freedom.

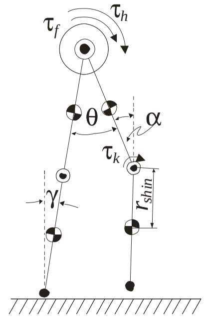

Figure 9: Schematic of the biped robot

7.2 The control law of the robot

The control of the robot is done by linearizing the system using the center of percussion. The idea is to consider the system as an inverted pendulum with a point mass; therefore the body attitude can be controlled with a PD scheme as follows:

$$\tau_h = k_{po}(\gamma - \theta_s/2) + k_{do}\dot{\gamma} - m\left|\vec{r} \times \vec{g}\right| - \tau_f - \tau_k \tag{14}$$

where τ_h is the torque at the hip coming from the stance leg, τ_f is the torque of the swinging leg, τ_k is the torque at the knee, m is the mass of the robot, r is the position of the center of mass of the robot and k_{po} and k_{do} are the controller constants. The swinging leg has a similar control law:

$$\tau_f = k_p(\theta - \theta_s) + k_d\dot{\theta} - m_{leg}\left|\vec{r}_{leg} \times \vec{g}\right| - \tau_k \tag{15}$$

here k_p and k_d are the controller constants, θ_s is the desired position of the leg, and m_{leg} is the mass of the leg. The selection of the constants of both controllers must be selected according to Ref. [9] in order to obtain stable gait. It must be noticed that the legs alternate its function as stance and swinging leg according to the phase of the gait, therefore state machine was also implemented. The double stance phase of the gait is not modeled, and the transition of steps is assumed to happen instantly.

7.3 Simulation results

The design of the system has been made attempting to follow the natural dynamics of a system, in which control is carried out around the torque of each joint. This produces a very natural and smooth gait, with a highly anthropomorphic appearance. Fig. (10) is a stroboscopic picture of the animation. Another observation is that there are jerks at the beginning of each step. These jerks were observed in videos of the simulations. This can be explained by the fact that the double stance phase is almost a singularity so that the inverted pendulum changes its center of rotation (i.e zero moment point) almost instantaneously. For a better appreciation of the foregoing a video can be found in:
http://maqlab.uc3m.es/proyectos/pasibot/flywheelbiped.avi.

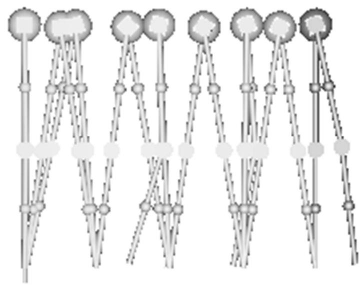

(a)

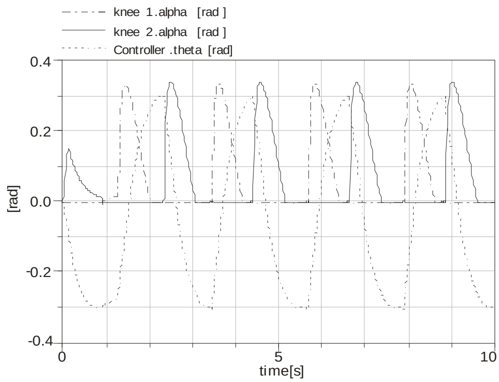

(b)

Figure 10: Simulation of the flywheel biped. (a) stroboscopic animation of the robot, (b) plot of the limit cycles.

8 CONCLUSIONS

In this paper the authors try to expose the advantages of object oriented simulation applied to walking machines of different types. In the first part of the paper one of the Raibert hopping machines is implemented, the model was programmed by introducing the equations of motion directly into the software. The result was a fixed model that cannot accept changes in its topology. Upgrading thereof is not possible in a simple way, because the equations of motion define the system itself, any change in any component will required the reformulation of the equations.

In the second part the modeling of a passive walker was developed. In this case the model used objects belonging to the Modelica® standard library, because the library is not ready to simulate walking machines the required additional parts were created and a model combining the standard parts of the multibody library was done. The simulations demonstrated great stability and a natural behavior. Besides the object oriented quality of Modelica® was exploded to make the model of the machine exposed. The fact that the objects of the classes were easily modified illustrates the ability of the object oriented modeling technique to upgrade existing models or to create models from the scratch.

Finally the simulations were completed by introducing an actuated walking machine. The principal addition when comparing with the previous simulation is that a control system block was created. The addition proves the possibility of the model to accept inputs. The parameterization of the model is automatically done inside the objects composing the model, showing the advantages of object oriented modeling over procedural methods, in the last ones the control system is embedded into the equations of motion.

ACKNOWLEDGEMENTS

This project has been financed by the Spanish Interministry Commission for Science and Technology (MICYT) under project number DPI 2006-15443-C02-02. The authors would like to express their gratitude to Alfonso Urquia and Sebastian Dormido for their advice about Dymola® and Modelica®, which proved fundamental in performing successful simulations.

REFERENCES

[1] N. Kanehira, T.U. Kawasaki, S. Ohta, T. Ismumi, T. Kawada, F. Kanehiro, S. Kajita, and K. Kaneko, “Design and experiments of advanced leg module (HRP-2L) for humanoid robot (HRP-2) development,” *IEEE/RSJ International Conference on Intelligent Robots and System*, 2455-2460. 2002.

[2] W. Borutzky, *Bond Graph Metodoloy: Development and Analysis of Multidisciplinary Dynamic System Models*, London: Springer, 2010.

[3] Modelica Association, *Modelica Language Specification V3.2*, 2010.

[4] W. Borutzky, “Bond graph modeling from an object oriented modeling point of view,” *Simulation Practice and Theory*, vol. 7, nº1, 439-461. 1999.

[5] M. Raibert, *Legged Robots that Balance*, Cambridge: 1986.

[6] M. Otter, H. Helmqvist, and F. Cellier, “Modeling of Multibody Systems with the Object-Oriented Modeling Language Dymola,” *Proc. NATO/ASI, Computer-Aided Analysis of Rigid and Flexible Mechanical Systems*, Troia, 27-46. 1993.

[7] M. Otter, H. Elmqvist, and J. Diaz, “Collision Handling for the Modelica Multibody Library,” *Proc. of the International Modelica conference*, Hamburg. 45-53. 2010

[8] T. McGeer, “Passive Dynamic Walking,” *The International Journal of Robotics Research*, vol. 9, 62-82. 2010.

[9] M. Alba, J.C.G. Prada, J. Meneses, and H. Rubio, “Center of percussion and gait design of biped robots,” *Mechanism and Machine Theory*, vol. 45, nº 11, 1681-1693. 2010

[10] J. Pratt, “Exploiting inherent robustness and natural dynamics in the control of bipedal walking robots” Massachusetts Institute of Technology, 2000.

Proceedings of MUSME 2011, the International Symposium
on Multibody Systems and Mechatronics
Valencia, Spain, 25-28 October 2011

COMPARISON OF DIFFERENTS METHODS TO CALCULATE COMPLIANT DISPLACEMENTS OF MULTIBODY SYSTEMS

Rogério Sales Gonçalves* **and João Carlos Mendes Carvalho***
* School of Mechanical Engineering, Federal University of Uberlândia, Campus Santa Mônica, CEP 38400-902, Uberlândia – MG – Brazil
e-mail: rsgoncalves@mecanica.ufu.br, jcmendes@mecanica.ufu.br

Keywords: Stiffness Analysis, Compliant Displacements, MSA, FEA, Jacobian Matrix.

Abstract. *This paper addresses the problem of a multibody systems stiffness evaluation. Multibody systems consist on a kinematic chain composed of links that can be rigid or flexible, interconnected by joints. One of the outstanding problems in the multibody system study is to obtain a standard procedure, easily applied and computational, to determine the compliant displacements in workspace multibody system. In order to analyze and compare the methodologies proposed in literature, i.e.: the methods based on Jacobian matrix, finite element analysis and the matrix structural analysis, this paper presents a modeling applied to a two degree of freedom serial structure. For that the compliant displacements are obtained by methodologies presented by Komatsu and Yoon; Tsai; Matrix Structural Analysis (MSA) and Finite Element Analysis (FEA). Finally results considering the flexibility of links and joints are discussed and compared.*

1 INTRODUCTION

Multibody systems consist on a kinematic chain composed of links that can be rigid or flexible, interconnected by joints. One of the outstanding problems in the multibody system study is to obtain a standard procedure, easily applied and computational, to determine the compliant displacements in its workspace.

Stiffness can be defined as the capacity of a mechanical system to sustain loads without excessive changes of its geometry [1]. These produced changes on geometry, due to the applied forces, are known as deformations or compliant displacements.

Compliant displacements in a robotic system produces negative effects on static and fatigue strength, wear resistance, efficiency (friction losses), accuracy, and dynamic stability (vibration). The growing importance of high accuracy and dynamic performance for parallel robotic systems has increased the use of high strength materials and lightweight designs improving significant reduction of cross-sections and weight. Nevertheless, these solutions also increase structural deformations and may result in intense resonance and self-excited vibrations at high speed [1]. Therefore, the study of the stiffness becomes of primary importance to the design of multibody robotic systems in order to properly choose materials, component geometry, shape and size, and interaction of each component with others. Some examples of design procedures based on stiffness analysis can be found in [2-4].

The overall stiffness of a manipulator depends on several factors including the size and material used for links, the mechanical transmission mechanisms, actuators and the controller [5]. In general, to realize a high stiffness mechanism, many parts should be large and heavy. However, to achieve high speed motion, these should be small and light. Moreover, one should point out that the stiffness is greatly affected by both the position and the values of the mechanical parameters of the structure parts [6].

There are three main methods have been used to derive the stiffness model of manipulators [7]. These methods are based on the calculation of the *Jacobian matrix* [8-10]; the *Finite Element Analysis* (FEA) [11-12] and the *Matrix Structural Analysis* (MSA) [7; 13-14].

In order to evaluate the main methodologies for obtaining the compliant displacement of a multibody system, simulations had been carried out for a two degree of freedom (dof) serial robotic structure. The analyzed methods are those presented by Komatsu [15-17] and Yoon et al. [18-19]; Tsai [5]; Matrix Structural Analysis (MSA) [20-22] and Finite Element Analysis (FEA). Finally the results are discussed and compared.

2 METHODS FOR OBTAINING COMPLIANT DISPLACEMENTS

As stiffness can be defined as the ability of a mechanical system to support loads without excessive changes in its geometry [1], the multibody system stiffness study is equivalent to obtain the stiffness matrix, K, of the analyzed structure, which represents the measure of the ability of the structure to resist deformations due to the action of external loads.

The main sources of robot compliant are the joints, including the actuators, and links (segments). Thus, according to the main structure compliant sources, several methods for modeling have been proposed whose usual methods are presented in section 2.1 to 2.3.

2.1 Methods Based on Jacobian Matrix

The Jacobian matrix methods have been studied by several authors such as [5; 8-10; 15-19].

First, the model calculations using the Jacobian matrix considered only the joint compliant. Subsequently, the segments compliant were also considered like a spring, giving rise the models called lumped stiffness model [8].

For a structure with n generalized coordinates and m operational coordinates the efforts, τ_i, transmitted through the *i-th* joint can be related to the corresponding joint deflections Δq_i, for small deflections, by a linear approximation given by [5]:

$$\boldsymbol{\tau}_i = k_i \ \Delta \boldsymbol{q}_i \tag{1}$$

where k_i is called the joint stiffness constant (or lumped stiffness parameter). Equation (1) can be written in matrix form for the n generalized coordinates as:

$$\boldsymbol{\tau} = \chi \ \Delta \boldsymbol{q} \tag{2}$$

where $\boldsymbol{\tau} = [\tau_1, \tau_2, ..., \tau_n]^T$, $\Delta \boldsymbol{q} = [\Delta q_1, \Delta q_2, ..., \Delta q_n]^T$ and $\chi = diag[k_1, k_2, ..., k_n]$ a n x n diagonal matrix.

The joint compliant displacements $\Delta \boldsymbol{q}$ are related to the end-effector compliant displacements $\Delta \boldsymbol{x} = [\delta_x \ \delta_y \ \delta_z \ \phi_x \ \phi_y \ \phi_z]$, by the Jacobian matrix of a robotic serial structure, J, given by Eq. (3), as

$$\Delta \boldsymbol{x} = J \ \Delta \boldsymbol{q} \tag{3}$$

Where δ_x; δ_y and δ_z are the linear compliant displacements in the directions of the Cartesian axes and ϕ_x; ϕ_y e ϕ_z are the angular compliant displacements around the Cartesian axes

The efforts applied at the end-effector, $F = [F_x \ F_y \ F_z \ M_x \ M_y \ M_z]^T$, where F_x; F_y and F_z are the forces applied in the direction of Cartesian axes, and M_x; M_y and M_z are the torques applied around the Cartesian axes, are related to joint efforts by the transposed Jacobian matrix of robotic serial structure, Eq. (4), as

$$\tau = J^T F \tag{4}$$

From Equations (1) to (4) it can be obtained:

$$\Delta x = C \ F \tag{5}$$

where $C = J \ \chi \ J^T$ is the compliant matrix of the structure.

The stiffness matrix for serial robot, K_s, considering only the joint compliant, is obtained by:

$$K_s = C^{-1} = J^{-T} \ \chi \ J^{-1} \tag{6}$$

The compliant displacements due to links are described on section 2.1.1.

Figure (1) shows the schematic of a 2 dof serial robotic manipulator, which is used to compare the main techniques presented in this paper for the compliant displacements calculation. For modeling of the 2 dof serial manipulator, were set an inertial frame $O_0 x_0 y_0$, and the auxiliary reference $A_1 x_1 y_1$, fixed on the movable body length L_1 and $Bx_2 y_2$, fixed on the movable body length L_2. The angles θ_1 and θ_2 are the generalized coordinates (joints) and the O_0A and O_1B have lengths L_1 and L_2 respectively.

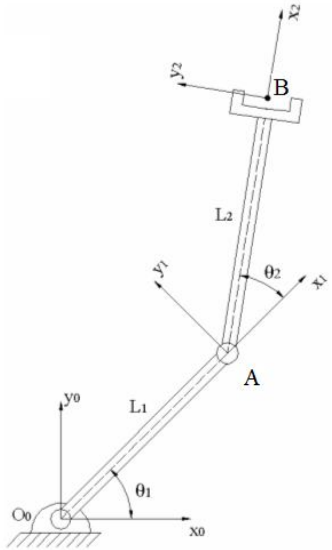

Figure 1: 2 dof serial manipulator.

2.1.1 Calculus of Compliant Displacements Using the method of Yoon et al. [18-19] and Komatsu [15-17]

The flexibility calculus for serial structure, according to Yoon et al. [18-19] and Komatsu et al. [15-17] is based on the Jacobian matrix and can be performed by considering the structure composed of several deformable joints and segments like shown in Fig. (2), which segments C_{li} are modeled as deformable segments; the joints flexibility are represented by C_{joint} and the generalized coordinates are the angles θ_i ($i = 1,..., n$).

Yoon et al. [18-19] generalized the proposed method by Komatsu et al. [15-17] considering also parallel robot structures.

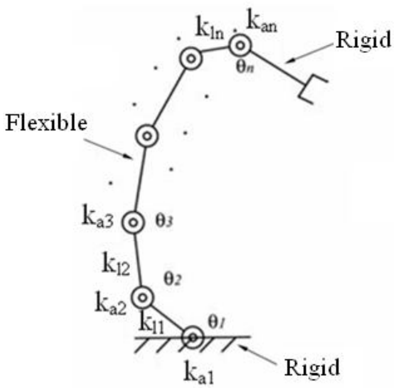

Figure 2: Model proposed by Yoon et al. [18-19].

From their proposed method the segments and joints compliant displacements can obtained by

$$\begin{aligned} C_T &= J_e(\theta,\, e)\, C_e\;\, J_e^T(\theta,\, e) \\ C_e &= diag\big(C_{e1}\;\, C_{e2}\;\, \ldots\, C_{en}\big) \end{aligned} \tag{7}$$

Where C_T is the compliant matrix of the end-effector, θ the angle of the joint, $J_e(\theta,e)$ are the Jacobian matrices for each joint and each elastic deformation, C_e is the compliant matrix which is defined by the structural characteristics of all elements, C_{ej} ($j = 1,\ldots, n$) is the compliant matrix of each element.

For comparison purposes will be considered separately the effect of compliant segments, Eq. (8) and the effect of compliant joints, Eq. (9).

The amount due to compliant segments is calculated by Eq. (8).

$$\begin{aligned} C_l &= J_l\, k_l^{-1}\, J_l^T \\ k_l &= diag(k_1, k_2, \ldots, k_n) \end{aligned} \tag{8}$$

Where J_l is the Jacobian Matrix obtained in relation to compliant segments, Eq. (18), and k_i ($i = 1, \ldots, n$) are the segments lumped stiffness parameters, Eq. (17).

The amount due to compliant joint is calculated by Eq. (9).

$$\begin{aligned} C_{art} &= J_{art}\, {k_{art}}^{-1}\, {J_{art}}^T \\ k_{art} &= diag(k_{a1}, k_{a2}, \ldots, k_{an}) \end{aligned} \tag{9}$$

Where J_{art} is the Jacobian Matrix of serial robotic structure and k_{ai} ($i = 1, \ldots, n$) are the joint lumped stiffness parameters.

The compliant matrix, Eq. (7), considering the compliance of segments and joints can be rewrite by Eq. (10)

$$C_T = C_l + C_{art} \tag{10}$$

Considering the compliant displacements is possible to write the kinematics model, Fig. (3). Thus, the coordinates of points A and B can be obtained by:

$$\begin{aligned} x_A &= L_1 \cos(\theta_1) - V_1\, sen(\theta_1) \\ y_A &= L_1\, sen(\theta_1) + V_1 \cos(\theta_1) \\ x_B &= x_A + L_2 \cos(\theta_1 + \eta_1 + \theta_2) - V_2\, sen(\theta_1 + \eta_1 + \theta_2) \\ y_B &= y_A + L_2\, sen(\theta_1 + \eta_1 + \theta_2) - V_2 \cos(\theta_1 + \eta_1 + \theta_2) \end{aligned} \tag{11}$$

From Figure 3(a) the forces F_x and F_y applied at point B can be decomposed in the normal direction of the segments, Fig. (3b), resulting in the efforts:

$$\begin{aligned} F_1 &= F_x\;\, sen(\theta_2) \;+\; F_y\;\, \cos(\theta_2) \\ F_2 &= F_y \\ M_1 &= L_2\;\, F_y \\ M_2 &= 0 \end{aligned} \tag{12}$$

Where F_1 and F_2 are the forces obtained from F_x and F_y applied at A and B, perpendicular to segments 1 and 2, respectively. M_1 and M_2 are the moments applied at A and B, respectively, due to the force F_y.

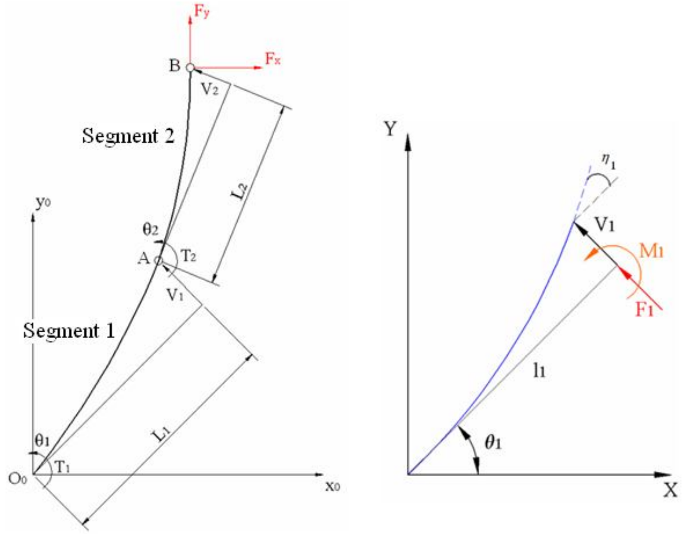

(a) (b)

Figure 3: (a) Model for application of the methodology of Komatsu et al. [15-17]; (b) Linear compliant displacement (V_1) and angular compliant displacement (η_1).

Applying the elastic differential line equation [23] for a cantilever, the linear compliant displacements, V_1 and V_2, and angular compliant displacements η_1, η_2, due to the efforts F_1, F_2, M_1 and M_2, are calculated by:

$$
\begin{aligned}
V_1 &= \frac{L_1^3}{3E_1 I_1} F_1 + \frac{L_1^2}{2E_1 I_1} M_1 \\
V_2 &= \frac{L_2^3}{3E_2 I_2} F_2 + \frac{L_2^2}{2E_2 I_2} M_2 \\
\eta_1 &= \frac{L_1^2}{2E_1 I_1} F_1 + \frac{L_1}{E_1 I_1} M_1 \\
\eta_2 &= \frac{L_2^2}{2E_2 I_2} F_2 + \frac{L_2}{E_2 I_2} M_2
\end{aligned}
\tag{13}
$$

Substituting Eq. (12) in (13), and after mathematical manipulations, one can write the angular compliant displacement as [15-17]:

$$
\begin{aligned}
\eta_1 &= \frac{3}{2L_1} V_1 + \frac{3E_2 I_2 L_1 L_2}{2E_1 I_1 (2L_2^3 + 3L_2^2)} V_2 \\
\eta_2 &= \frac{3(L_2^2 + 2L_2)}{2L_2^3 + 3L_2^2} V_2
\end{aligned}
\tag{14}
$$

From Figures (1) and (3), the configuration of end-effector, point B, considering the kinematics model and compliant displacements is given by $\boldsymbol{f_T}$:

$$\boldsymbol{f_T} = \begin{Bmatrix} x_B \\ y_B \\ \theta_T \end{Bmatrix} \tag{15}$$

Where:

$$\theta_T = \theta_1 + \eta_1 + \theta_2 + \eta_2 \tag{16}$$

The calculus of the segments deformation is performed by Eq. (8) applied to two dof serial manipulator:

$$\begin{aligned} C_l &= J_l\, k_l^{-1}\, J_l^T \\ k_l &= diag(k_1, k_2) \end{aligned} \tag{17}$$

As J_l is the Jacobian matrix it can be obtained by differentiating the Eq. (15) respect to deformations $\boldsymbol{x_l}$ as:

$$J_l = \frac{\partial \boldsymbol{f_T}}{\partial \boldsymbol{x_l}} \quad ; \qquad \boldsymbol{x_l} = \begin{Bmatrix} V_1 \\ V_2 \end{Bmatrix} \tag{18}$$

Then the Jacobian matrix can be done by:

$$J_l = \begin{bmatrix} Jl_{11} & Jl_{12} \\ Jl_{21} & J_{22} \\ Jl_{31} & Jl_{32} \end{bmatrix} \tag{19}$$

Where

$$Jl_{11} = -sen\theta_1 - \frac{3L_2 sen(\theta_{aux})}{2L_1} - \frac{3V_2\cos(\theta_{aux})}{2L_1} \tag{20}$$

$$Jl_{12} = -\frac{3\,sen(\theta_{aux})\,E_2\,I_2\,L_1}{4L_2E_1I_1} - sen(\theta_{aux}) - \frac{3V_2\cos(\theta_{aux})\,E_2\,I_2\,L}{4L_2^2\,E_1\,I_1} \tag{21}$$

$$Jl_{21} = \cos\theta_1 + \frac{3\,L_2\cos(\theta_{aux})}{2\,L_1} - \frac{3\,V_2 sen(\theta_{aux})}{2\,L_1} \tag{22}$$

$$Jl_{22} = \frac{3\cos(\theta_{aux})\,E_2I_2L_1}{4L_2\,E_1\,I_1} + \cos(\theta_{aux}) - \frac{3V_2 sen(\theta_{aux})\,E_2I_2L_1}{4\,L_2^2\,E_1\,I_1} \tag{23}$$

$$Jl_{31} = \frac{3}{2\,L_1} \tag{24}$$

$$Jl_{32} = \frac{3\,E_2\,I_2\,L_1}{4\,L_2^2\,E_1\,I_1} + \frac{3}{2\,L_2} \tag{25}$$

and,

$$\theta_{aux} = \theta_1 + \frac{3V_1}{2L_1} + \frac{3E_2 I_2 L_1 V_2}{4L_2^2 E_1 I_1} + \theta_2 \tag{26}$$

Furthermore, to calculate the segments compliant matrix, Eq. (17), it is necessary to determine the coefficients k_1, k_{12} and k_2, which are lumped stiffness coefficients of the first segment, the coupling between the segments and the second segment, respectively. The calculation of these coefficients is accomplished by using the equation of strain energy for bending [23], Eq. (28), and the strain energy of the system related to V_1 and V_2, Eq. (27) [15-17]:

$$U = \frac{\left(k_1 V_1^2 + k_{12} V_1 V_2 + k_2 V_2^2\right)}{2} \tag{27}$$

$$U = \frac{1}{2E_1 I_1}\int_0^{l_1}\left(F_1 x_1 + M_1\right)^2 dx_1 + \frac{1}{2E_2 I_2}\int_0^{l_2}\left(F_2 x_2 + M_2\right)^2 dx_2 \tag{28}$$

Solving Eqs. (27) and (28), and after mathematical simplifications, it can be obtained:

$$k_1 = \frac{3E_1 I_1}{L_1^3} \tag{29}$$

$$k_{12} = 0 \tag{30}$$

$$k_2 = \frac{9 L_1 L_2 E_2^2 I_2^2 (4L_1 - 4L_1 \cos\theta_2 + L_2) + 12 E_1 I_1 E_2 I_2 L_2^3}{4E_1 I_1 L_2^6} \tag{31}$$

$$U = \frac{\left(k_1 V_1^2 + k_{12} V_1 V_2 + k_2 V_2^2\right)}{2} \tag{32}$$

Thus, replacing Eqs. (29) to (32) and (13) in Eq. (19) one can obtain C_l.

The calculus of the compliant matrix due joint is obtained by applying Equation (9) to the model of Fig. (1).

$$\begin{aligned} C_{art} &= J_{art}\, k_{art}^{-1}\, J_{art}^{T} \\ k_{art} &= diag(k_{a1}, k_{a2}) \end{aligned} \tag{33}$$

The calculus of the Jacobian matrix due to joints, J_{art}, is given by differentiating Eq. (9) related to $\boldsymbol{x}_{art}$ as:

$$J_{art} = \frac{\partial \boldsymbol{f_T}}{\partial \boldsymbol{x_{art}}} \quad ; \qquad \boldsymbol{x_{art}} = \begin{Bmatrix} \theta_1 \\ \theta_2 \end{Bmatrix} \tag{34}$$

$$J_{art} = \begin{bmatrix} -L_1 sen\theta_1 - V_1\cos\theta_1 - L_2 sen(\theta_{aux}) - V_2\cos(\theta_{aux}) & -L_2 sen(\theta_{aux}) - V_2\cos(\theta_{aux}) \\ L_1\cos\theta_1 - V_1 sen\theta_1 + L_2\cos(\theta_{aux}) - V_2 sen(\theta_{aux}) & L_2\cos(\theta_{aux}) - V_2 sen(\theta_{aux}) \\ 1 & 1 \end{bmatrix} \tag{35}$$

where θ_{aux} is given by Eq. (26).

The calculus of the stiffness constants k_{a1} and k_{a2} can be determined by experimental data or from catalogs.

Thus, it is possible, from Eqs. (33) and (35), to obtain the compliant matrix due to the joints.

Finally, the compliant matrix of a two dof serial robotic manipulator is given by:

$$C_T = C_l + C_{art} \tag{36}$$

2.1.2 Model Presented by Tsai

The model proposed by Tsai [5] becomes equivalent to the model proposed by Komatsu et al. [15-17] when the segments are rigid and taking into account only the compliant joints. Thus, the calculus of compliant matrix can be obtained from:

$$\begin{aligned} C &= J\chi^{-1}J^T \\ \chi &= diag(k_1, k_2, ..., k_n) \end{aligned} \tag{37}$$

Where $J = J_{art}$ and $\chi = k_{art}$ are given by Eq. (35) and (33) respectively.

2.1.3 Model Component Matrix Formulation

Ceccarelli [24] proposed a methodology to obtain the stiffness matrix considering the compliant of segments and joints.

Using the lumped stiffness model [24-25], the stiffness matrix can be obtained numerically by defining an appropriate manipulator model, which takes into account the lumped stiffness model of the segments and active joints. This methodology is called “Component Matrix Formulation” [24].

By the proposed method, the stiffness matrix K is given as

$$K = C_F \; K_P \; C_K \tag{38}$$

Where C_F is a matrix for the force and torque transmission from the manipulator extremity to the joints, K_P is a matrix including the lumped spring parameters and C_K is a matrix describing the compliant displacement of the manipulator extremity in function of the deformations of manipulator components [24].

It should be noted that the methodology proposed by [24] obtain the stiffness matrix by the Jacobian matrix expanded to consider the segments.

Thus, the proposed model in Eq. (32) can be calculated as:

$$K = J^{-t} \, K_P \, J^{-1} \tag{39}$$

Where

$$C_F = J^{-t} \quad \text{and} \quad C_K = J^{-1} \tag{40}$$

J is the Jacobian matrix of serial robot structure and K_p is calculated as a diagonal matrix containing the lumped spring parameters of the robot’s actuator, similar to the χ matrix proposed by [5].

2.2 Matrix Structural Analysis – MSA method

In this section, the stiffness matrix is obtained using the *Matrix Structural Analysis* (*MSA*), also known as the *displacement method* or *direct stiffness method* (*DSM*). The methods of structural analysis is based on the idea of breaking up a complicated system into component parts obtaining discrete structural elements, with simple elastic and dynamic properties that can be readily expressed in a matrix form. The discrete structure is composed by elements which are joined by connecting nodes. When the structure is loaded each node suffers translations and/or rotations, which depend on the configuration of the structure and the boundary conditions. For example, in a fixed linkage no displacement occurs. The nodal displacement can be found from a complete analysis of the structure. The matrices representing the beam and the joint are considered as building blocks which, when fitted together in accordance with a set of rules derived from the theory of elasticity, provide the static and dynamic properties of the whole structure [13].

The stiffness matrix k_j of a *j-th* three-dimensional straight bar with uniform cross-sectional area is

$$k_j = \begin{bmatrix} k_{bj} & -k_{bj} \\ -k_{bj} & k_{bj} \end{bmatrix} \tag{41}$$

where k_{bj} is given by:

$$k_{bj} = \begin{bmatrix} \frac{A_j E_j}{L_j} & 0 & 0 & 0 & 0 & 0 \\ 0 & \frac{12 E_j I_{zj}}{L_j^3} & 0 & 0 & 0 & \frac{6 E_j I_{zj}}{L_j^2} \\ 0 & 0 & \frac{12 E_j I_{yj}}{L_j^3} & 0 & -\frac{6 E_j I_{yj}}{L_j^2} & 0 \\ 0 & 0 & 0 & \frac{G_j J_j}{L_j} & 0 & 0 \\ 0 & 0 & -\frac{6 E_j I_{yj}}{L_j^2} & 0 & \frac{4 E_j I_{yj}}{L_j} & 0 \\ 0 & \frac{6 E_j I_{zj}}{L_j^2} & 0 & 0 & 0 & \frac{4 E_j I_{zj}}{L_j} \end{bmatrix} \tag{42}$$

On Equation (42) E_j and G_j are, respectively, the modulus of elasticity and the shear modulus of element *j;* I_{yj}, I_{yz} are the moment of areas about the *Y* and *Z* axes, respectively. J_j is the Saint-Venant torsion constant and A_j is the cross-sectional area.

The stiffness of a joint is given by [21, 22]:

$$k_{jo\,\mathrm{int}} = \begin{bmatrix} k_C & -k_C \\ -k_C & k_C \end{bmatrix} \tag{43}$$

Where $k_c = diag(k_{tx}, k_{ty}, k_{tz}, k_{rx}, k_{ry}, k_{rz})$; k_{tx}, k_{ty}, k_{tz} are the translation stiffness and k_{rx}, k_{ry}, k_{rz} the rotational stiffness along the axes X, Y and Z, respectively.

Application of *MSA* needs to write the stiffness matrices of all elements in the same reference frame. This transformation, element by element, must be held before the assembly of the stiffness matrix of the structure. This transformation matrix, T_j, can be obtained from the linear algebra.

Thus, the stiffness matrix of the elements in a common reference frame (elementary stiffness matrix), for segments, k_j^e, and for joints, $k_{jo\,\mathrm{int}}^e$, can be written as:

$$[k_j^e] = [T_j][k_j][T_j]^T \tag{44}$$

$$[k^{e}_{joint}] = [T_j][k_{joint}][T_j]^T \tag{45}$$

After obtaining the stiffness matrix of each segment and joint in a common reference frame, the stiffness matrix of whole structure can be obtained using the *MSA*. Based on how the structure elements are connected, from their nodes, it is possible to define a connectivity matrix. As each segment and joint stiffness are known, the global stiffness matrix is obtained by a superposition procedure. This global stiffness matrix is singular because the system is free. After application of the boundary conditions, for example, where the displacements are known, the new matrix is invertible and the compliant displacements can be done by:

$$\{\boldsymbol{U}\} = K^{-1}\,\{\boldsymbol{W}\} \tag{46}$$

Where $\boldsymbol{U}$ is the vector of compliant displacements and $\boldsymbol{W}$ the vector with external applied wrenches. This procedure is described in detail in [21].

Figure (4) illustrates the model developed for application of the MSA methodology.

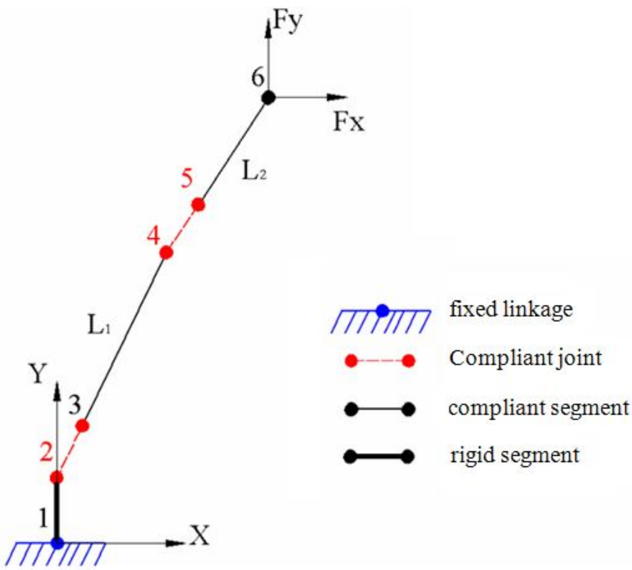

Figure 4: Model MSA 2 dof serial manipulator.

In Figure (4), points 1 to 6 are the nodes, the segment defined by the nodes 1-2 is considered a rigid base and the segments defined by the nodes 3-4 and 5-6 are flexible. The rotational joints are represented by nodes 2-3 and 4-5. It should be emphasized that the nodes which define the rotational joint have the same position. The inertial frame has its origin at node 1.

Firstly the stiffness matrices of each element are obtained both for the three segments and two joints.

To obtain the stiffness matrix relative to the segments, they are considered as beam elements with circular cross section, neglecting the effects of shear forces and calculated by Eq. (42).

The joint stiffness matrix is given by Eq. (43).To calculate the joint compliant matrix are required the linear stiffness parameters k_{lx}, k_{ly}, k_{lz} and angular stiffness parameters k_{ax}, k_{ay}, k_{az}.

These parameters can be obtained according to the manufacturers' catalog or by experimental tests.

Before performing the assembly of the stiffness matrix of the manipulator as a whole the matrices of each element relative to the inertial frame O_{XYZ} must be written. This is done using the transformation matrix $[T_j]$, Eqs. (44) and (45). The nodes coordinates 1 to 6 are obtained by the kinematics model of the robot.

The segment defined by nodes 1 and 2, corresponding to the base of the robot, can be considered flexible or not. In this example it is considered as rigid segment. For this, in this element stiffness matrix is considered its modulus of elasticity as 10 times larger than the other segments. This value was obtained by computer simulations so that the displacements of the base do not influence the calculation of the system flexibility.

From the segments and joints stiffness matrix in relation to the inertial frame can be done the assembly of the stiffness matrix of the whole structure. Since each node has 6 dof, the size of this square matrix is 6.n = 36. The assembly of this matrix must conform to the numbering of the nodes shown in Fig. (4). Thus it is possible to establish a connectivity matrix between elements, which indicates, for example, nodes 2 and 3 (forming the rotational joint) have the same linear displacement and angular displacement, except the rotation around the joint axis. Thus, according to Fig. (4) and Table (1), can be written for each node, the quantification of degrees of freedom which represents the number of possible movements.

	Nodes					
Compliant Displacement	**1**	**2**	**3**	**4**	**5**	**6**
Linear compliant displacement in x direction (δ_x)	1	7	13	19	25	31
Linear compliant displacement in y direction (δ_y)	2	8	14	20	26	32
Linear compliant displacement in z direction (δ_z)	3	9	15	21	27	33
Angular compliant displacement around x (ϕ_x)	4	10	16	22	28	34
Angular compliant displacement around y (ϕ_y)	5	11	17	23	29	35
Angular compliant displacement around z (ϕ_z)	6	12	18	24	30	36

Table 1: Degrees of freedom related to Fig. (4).

The connectivity matrix can be mounted as:

$$\begin{array}{c} \begin{bmatrix} 1 & 2 & 3 & 4 & 5 & 6 & 7 & 8 & 9 & 10 & 11 & 12 \\ 7 & 8 & 9 & 10 & 11 & 12 & 13 & 14 & 15 & 16 & 17 & 18 \\ 13 & 14 & 15 & 16 & 17 & 18 & 19 & 20 & 21 & 22 & 23 & 24 \\ 19 & 20 & 21 & 22 & 23 & 24 & 25 & 26 & 27 & 28 & 29 & 30 \\ 25 & 26 & 27 & 28 & 29 & 30 & 31 & 32 & 33 & 34 & 35 & 36 \end{bmatrix} \end{array} \begin{array}{l} \rightarrow \text{segment } 1-2 \\ \rightarrow \text{joint } 2-3 \\ \rightarrow \text{segment } 3-4 \\ \rightarrow \text{joint } 4-5 \\ \rightarrow \text{sement } 5-6 \end{array} \tag{47}$$

The connectivity matrix allows the stiffness matrix assembly of the whole structure. This provides the element position inside the structure stiffness matrix.

The obtained matrix is singular because the structure has no restrictions. So, must be applied the boundary condition that, in this case corresponds to a fixed node 1. As in the fixed node all displacements are zero one can eliminate these degrees of freedom of the system (1-6), corresponding to node 1. Thus, the new square matrix is a 30x30 dimensional and is invertible.

In Figure 4 efforts can be applied in all nodes. In this example, efforts are applied only at node 6, for comparison with other methodologies.

Thus, the compliant displacements can be calculated by Eq. (40). Where K is a 30x30 matrix and the vector $\{\boldsymbol{W}\}$, applied in the nodes 2-6 is a 30x1 vector. Thus, the flexible displacement vector $\{\boldsymbol{U}\}$ is a 30x1 vector.

2.3 FEA Model - Finite Element Analysis

It was also performed simulation with a finite element model using the commercial software Ansys®. In this model was considered only the compliant segments, which were modeled as beam elements, type BEAM4. Figure (5) presents the model of 2-dof robotic manipulator to a specified position ($\theta_1 = 90°$ e $\theta_2 = -90°$) which elements discretization are divided into 10 parts, and the compliant displacements when it was applied a unit force in the direction of axis X.

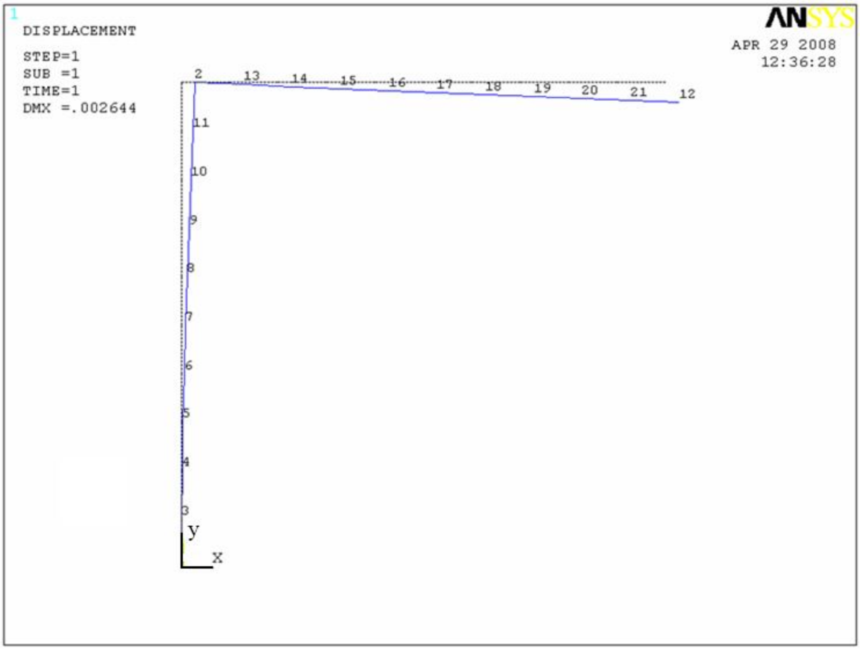

Figure 5: *FEA* model compliant displacements (blue line).

3 COMPARISON AND DISCUSSION BETWEEN THE RESULTS

Tables (2), (3) and (4) show the results for comparison using the methodologies presented by Komatsu and Yoon, Tsai, *MSA* and *FEA* for displacements at point *B*.

For these calculations was considered the 2 dof robotic manipulator configuration, Fig. (1), as: $\theta_1 = 90°$ and $\theta_2 = -90°$. Unit force was applied toward the X inertial axis, $F_x = 1\ N$ and $F_y = 0$. For all models, the segments, constructed into steel with elastic modulus $E = 2e^{11}\ N/m^2$, were modeled having a length of $0.3\ m$ and circular cross section with a diameter of $0.005\ m$.

The joints lumped parameters for the models of Komatsu, Yoon and Tsai were adopted for numerical simulations, as:

$$k_{a1} = k_{a2} = 1000\ N\ m/rad \tag{48}$$

For the joint compliant simulation, using the *MSA*, were adopted the following values for numerical simulation:

$$k_{lx} = k_{ly} = k_{lz} = 2e^{11}\ N/m \text{ e } k_{ax} = k_{ay} = 2e^{11}\ N\ m/rad \quad (49)$$

$$k_{az} = 1000\ N\ m/rad \quad (50)$$

The values of Eq. (49) were used, for comparison with other theories, to not influence the results. It is considered only a rotation around *z* axes. So it has $k_{az} = k_{a1} = k_{a2}$.

Table (2) presents the comparative results when using only the joints compliant, and segments are rigid. Table (3) shows the results when considering only the segments flexibility and neglecting the joints flexibility. Finally, Table (4) presents the results considering both the flexibility of joints and segments. The dash (–) on Tables indicates that the methodology was not applied to the example, due to the model does not consider it.

	Methodologies			
Compliant Displacements	Komatsu e Yoon	Tsai	MSA	FEA
δ_x [mm]	0,3729	0,3729	0,2518	–
δ_y [mm]	-0,1658	-0,1659	-0,3249	–
δ_z [mm]	0	0	0	–
ϕ_x [rad]	0	0	0	–
ϕ_y [rad]	0	0	0	–
ϕ_z [rad]	0	0	-0,0011	–

Table 2: Calculation of compliant displacements only considering the joints flexibility.

	Methodologies			
Compliant Displacements	Komatsu e Yoon	Tsai	MSA	FEA
δ_x [mm]	1,4347	–	1,4668	1,4668
δ_y [mm]	-2,1676	–	-2,2001	-2,2002
δ_z [mm]	0	–	0	0
ϕ_x [rad]	0	–	0	0
ϕ_y [rad]	0	–	0	0
ϕ_z [rad]	-0,0073	–	-0,0073	-0,0073

Table 3: Calculation of compliant displacements only considering the segments flexibility.

	Methodologies			
Compliant Displacements	Komatsu e Yoon	Tsai	MSA	FEA
δ_x [mm]	1,5234	–	1,5720	–
δ_y [mm]	-2,2567	–	-2,3050	–
δ_z [mm]	0	–	0	–
ϕ_x [rad]	0	–	0	–
ϕ_y [rad]	0	–	0	–
ϕ_z [rad]	-0,0073	–	-0,0076	–

Table 4: Calculation of compliant displacements considering the joints and segments flexibilities.

When considering only the joints flexibility, Table (2), the results using the method of Komatsu and Yoon, compared with the model used by Tsai, provide the same results. As presented, this was expected because both use the calculation of Jacobian matrix. In the modeling using the *MSA* results are different due to the no knowledge of values corresponding to k_{lx}, k_{ly}, k_{lz}, k_{ax} and k_{ay}, and these values were adopted for the purpose of numerical calculation. For a more accurate result would require experimental testing to determine these parameters, obtaining an appropriate match with the data used by Komatsu and Yoon.

Considering the model with only the segments flexibility, Table (3), the results are coincident to the *MSA* model and *FEA*. With the methodology of Komatsu and Yoon results are quite similar.

By considering both joints and segments flexibilities, Table (4), the results for the model of Komatsu and Yoon and *MSA* are close.

Considering only the flexibility of joints, Table (2), the model proposed by Tsai is more convenient due to the fact that this is derived from the calculation of the Jacobian of the robotic structure. Even so, the calculation of this Jacobian can become complicated depending on the number of structure dof and type of structure considered. For example, for a parallel robotic structure obtaining the Jacobian matrix is not simple.

When considering only the segments flexibility, Table (3), using the *MSA* method is more favorable because unlike the methodology used by Komatsu and Yoon, it is not necessary to calculate differential equations, as is the case of calculating the Jacobian considering the segments flexibility. As shown by Eqs. (1) to (30) this calculation is complicated and susceptible to calculation errors. In this example was considered the modeling of a 2 dof serial robotic manipulator. If the number of dof was larger, it implicated in more calculations of differential equations. Furthermore, when applying the methodology of Komatsu and Yoon is also necessary to calculate the value of the efforts acting on each segment, a task can be complicated depending on the number of segments and forces and/or moments in the model.

The same comments are valid for the model considering simultaneously the segments and joints flexibilities, Table (4).

Although the *FEA* and *MSA* have the same basic equations, Eqs. (41-42), (44) and (46), one can point out some advantages of the *MSA* method: a) A robotic structure is composed by segments and joints. Then, each segment and each joint can be modeled by only two nodes for the *MSA* analysis. Otherwise on the *FEA* each beam is divided in several nodes and the joints stiffness, in general, are not considered. b) Using a commercial *FEA* software (the usual procedure) one do not have the control of the solver. The *MSA* method one can follow step-by-step the stiffness matrix assembling. c) In the FEA method at each variation of the structural configuration a remeshed must be made, increasing the computational cost. In the *MSA* method is only necessary improve the inverse kinematic model to obtain the stiffness mapping for all structure configuration.

Thus, in order to standardize the calculation for different types of structures and the ease of computational implementation, the best method of calculation is the *MSA*. Could be considered a disadvantage of the method the fact that the *MSA* does not know the parameters of the joints. But both the *MSA* method as for the other, the parameters of the joints must be obtained through catalogs or by experimental tests.

4 CONCLUSIONS

In this paper was performed the comparison between the main existing methods for calculating the multibody systems compliant displacements.

The methodologies developed by Komatsu and Yoon, Tsai, *MSA* and *FEA* have been detailed and applied in the case of a two dof serial robotic manipulator.

For application of the presented methodology the kinematic model of the structure and the stiffness matrices of its elements (segments, joints/actuators) must be known.

The great advantage of the matrix structural analysis, *MSA*, method to obtain the stiffness matrix of a whole structure is not to require calculating the Jacobian of the structure, like the methods of Komatsu/Yoon and Tsai, therefore, does not need to work with differential equations. Another advantage is that the method *MSA* enables to perform the mapping of compliant displacements for nodes related to different configurations of the structure.

The use of *FEA* method produces satisfactory results, but its major drawback is the need to develop a model for each position to be examined and getting your mesh, and then apply for a (solver) finite elements software. Thus, for example, to map the stiffness of the structure, using the *FEA* method is inconvenient.

Future research includes the application and comparison of these methodologies in a parallel robotic structure.

ACKNOWLEDGEMENTS

The authors are thankful to CNPq, CAPES and FAPEMIG for the partial financing support of this research work.

REFERENCES

[1] E.I. Rivin. *Stiffness and Damping in Mechanical Design*. Marcel Dekker Inc., New York, 1999.

[2] X.-J. Liu, Z.-L. Jin, F. Gao. Optimum Design of 3-Dof Spherical Parallel Manipulators with Respect to the Conditioning and Stiffness Indices. *Mechanism and Machine Theory*, vol. 35, nº 9, 1257-1267, 2000.

[3] N. Simaan, M. Shoham. Stiffness Synthesis of a Variable Geometry Planar Robot. 8th International Symposium on Advances in Robot Kinematics ARK 2002, Lenarcic J. and Thomas F. (Editors), Kluwer Academic Publishers, Caldes de Malavella, 463-472, 2002.

[4] G. Carbone, H.O. Lim, A. Takanishi, M. Ceccarelli. Optimum Design of a New Humanoid Leg by Using Stiffness Analysis. 12th International Workshop on Robotics in Alpe-Andria-Danube Region RAAD 2003, Cassino, paper 045RAAD03, 2003.

[5] L.W. Tsai. *Robot Analysis: The Mechanics of Serial and Parallel Manipulators*. John Wiley & Sons, New York, 1999.

[6] W. K. Yoon, T. Suehiro, Y. Tsumaki, M. Uchiyama. Stiffness Analysis and Design of a Compact Modified Delta Parallel Mechanism, *Robotica*, vol. 22, 463-475, 2004.

[7] D. Deblaise, X. Hernot, P. Maurine. A Systematic Analytical Method for PKM Stiffness Matrix Calculation, 2006.

[8] D. Zhang, F. Xi, C. M. Mechefske, S. Y. T. Lang. Analysis of parallel kinematic machine with kinetostatic modeling method. *Robotics and Computer-Integrated Manufacturing*, vol. 20(2), 151-165, 2004.

[9] F. Majou, C. M. Gosselin, P. Wenger, D. Chablat. Parametric stiffness analysis of the orthoglide. Proc. of the 35th International Symposium on Robotics, Paris, France, 2004.

[10] O. Company, F. Pierrot, J. C. Fauroux. A method for modeling analytical stiffness of a lower mobility parallel manipulator. Proc. of IEEE ICRA: Int. Conf. on Robotic and Automation, Barcelona, Spain, 2005.

[11] B. C. Bouzgarrou, J. C. Fauroux, G. Gogu, Y. Heerah. Rigidity analysis of T3R1 parallel robot with uncoupled kinematic. Proc. of the 35th International Symposium on Robotics, Paris, France, 2004.

[12] C. Corradini, J. C. Fauroux, S. Krut, O. Company. Evaluation of a 4 degree of freedom parallel manipulator stiffness. Proc. Of the 11th Word Cong. In Mechanism & Machine Science, IFTOMM'2004, Tianjin, China, 2004.

[13] J. S. Przemieniecki. *Theory of Matrix Structural Analysis*. Dover Publications, Inc, New York, 1985.

[14] W. Dong, Z. Du, L. Sun. Stiffness influence atlases of a novel flexure hinge-based parallel mechanism with large workspace. Proc. of IEEE ICRA: Int. Conf. On Robotic and Automation, Barcelona, Spain, 2005.

[15] T. Komatsu, M. Uenohara, S. Iikura, H. Miura, I. Shimoyama. Compliance Control for a Two-Link Flexibel Manipulator. The Japan Society of Mechanical Engineers (in Japanese), 1990.

[16] T. Komatsu, M. Uenohara, S. Iikura, H. Miura, I. Shimoyama. Dynamic Control for Two-Link Flexible Manipulator. The Japan Society of Mechanical Engineers (in Japanese), 1989.

[17] T. Komatsu, M. Uenohara, S. Iikura, H. Miura, I. Shimoyama. Vibration Control for Two-Link Flexible Manipulator using a Wrist Force Sensor. The Japan Society of Mechanical Engineers (in Japanese), 1990.

[18] W. K. Yoon, T. Suehiro, Y. Tsumaki, M. Uchiyama. Stiffness Analysis and Design of a Compact Modified Delta Parallel Mechanism. *Robotica*, vol. 22, 463-475, 2004.

[19] W. K. Yoon, T. Suehiro, Y. Tsumaki, M. Uchiyama. A Method for Analyzing Parallel Mechanism Stiffness Including Elastic Deformations in the Structure. Proceedings of the IEEE/RSJ International Conference on Intelligent Robots and Systems IROS'02, Lausanne, 2875-2880, 2002.

[20] R. S. Gonçalves, J. C. M. Carvalho. Singularities of Parallel Robots Using Matrix Structural Analysis. Proceedings of the XIII International Symposium on Dynamic Problems of Mechanics – DINAME, Angra dos Reis, RJ, Brazil, 2009.

[21] R. S. Gonçalves. Estudo de Rigidez de Cadeias Cinemáticas Fechadas. Universidade Federal de Uberlândia. Thesis (in Portuguese), 2009.

[22] R. S. Gonçalves, J. C. M. Carvalho. Stiffness analysis of parallel manipulator using matrix structural analysis. EUCOMES 2008, 2-nd European Conference on Mechanism Science, Cassino, Italy, 2008.

[23] C. A. G. M. Branco. *Mecânica dos Materiais*. Fundação Calouste Gulbenkian, Lisboa – Portugal, 1998.

[24] M. Ceccarelli, *Fundamentals of Mechanics of Robotic Manipulation*, Kluwer, Dordrecht, 2004.

[25] M. Ceccarelli, G. Carbone. A Stiffness Analysis for CaPaMan (Cassino Parallel Manipulator), *Mechanism and Machine Theory*, vol.37, n.5, 427-439, 2002.

Proceedings of MUSME 2011, the International Symposium
on Multibody Systems and Mechatronics
Valencia, Spain, 25-28 October 2011

NUMBER SYNTHESIS OF METAMORPHIC MECHANISMS USING SUBGRAPH CONSTRAINTS

Martín Pucheta*, Agostino Butti†, Valerio Tamellini†, Alberto Cardona* and Luca Ghezzi†

* Centro Internacional de Métodos Computacionales en Ingeniería CIMEC
INTEC (UNL/CONICET), Güemes 3450, S3000GLN Santa Fe, Argentina
e-mails: {mpucheta,acardona}@intec.unl.edu.ar

† Low Voltage Products Division, ABB S.p.A.
Viale dell'Industria 18, 20010 Vittuone (Milan), Italy
e-mails: {agostino.butti,valerio.tamellini,luca.ghezzi}@it.abb.com

Keywords: Topological Synthesis, Metamorphic Mechanisms, Graph Theory, Finite-State Machine, Low-Voltage Circuit Breakers.

Abstract. *A metamorphic mechanism has the capacity of changing its topology and configuration under different operation conditions. This paper presents a systematic method for the topological synthesis of mechanisms taking into account metamorphic transformations of links and changes in the degrees-of-freedom (DOF). The method is based on Graph Theory concepts and can be applied to the design and re-design of mechanisms satisfying complex metamorphic requirements. The topological design space is represented by an atlas of graphs of simple-jointed mechanisms. The parts to move, with input and output motion defined, are also represented by a graph and this graph is searched inside an atlas. For the first time, the topological requirements involving link transformations are expressed in terms of subgraphs or submechanisms with a given DOF containing prescribed input and output parts. The algorithm executes two subgraph searches inside atlases of mechanisms with different DOFs. An application to the design of a family of low-voltage circuit-breaker mechanisms is shown.*

1 INTRODUCTION

A metamorphic mechanism (MM) [1] –also called reconfigurable mechanism or mechanism with variable topology [2]– has the capacity of changing its topology and configuration under different operation conditions. The transformations of links and/or joints produce changes over the mobility of one or more members preserving or changing the degrees of freedom of the mechanism. The transformations of links can consist in changes of connectivity by collapsing or releasing bodies subject to contact (e.g., binary to ternary link) or changes of function (e.g., input to passive, movable to fixed), among other possibilities. The transformations of joints can consist of changes in type (e.g., cam to revolute) or changes in a property, for instance, the axis orientation of a joint can change from planar to outer-planar (e.g., prismatic to slider).

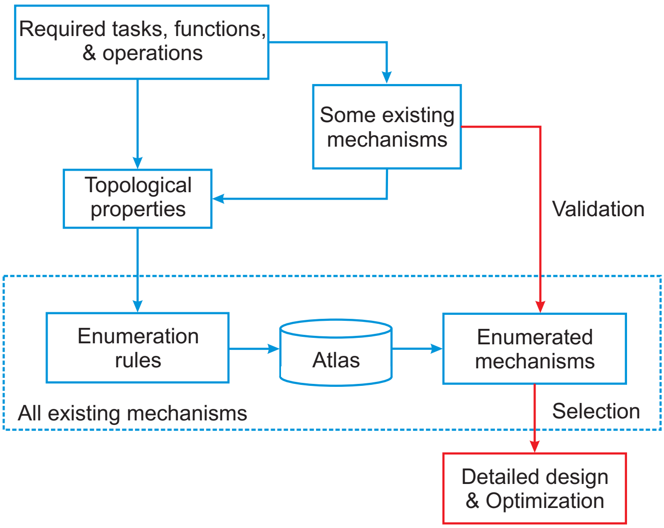

Figure 1: Automated conceptual design of mechanisms.

In the last 20 years, the mathematical modelling and computer-aided synthesis of metamorphic mechanisms [1] have attracted new attention of the multi-body community including packaging [3, 4], machine, mechanism [5, 2], and robot designers [6]. However, the redesign of metamorphic mechanisms is relatively new. From the topological point of view, several advances have been made on the representation of metamorphic mechanisms [3, 5, 7, 8]; however, few of them are focused on the enumeration [9, 6]. The size of the enumeration impacts on the number of required multi-body simulations and optimizations at the detailed design stage (see Fig. 1). For this reason, the rules for topological enumeration must contain all information related to desired kineto-static and dynamic behaviors.

This work has the objective of finding a practical methodology for cataloguing and enumerating the existent and eventually new low-voltage circuit breaker (LVCB) mechanisms from the point of view of mechanism topology. The final goal is to formalize the current design knowledge and improve designs. These electro-mechanical devices are used to protect human lives in electrical circuits. The mechanisms under study form a family among a wide variety of circuit breakers with different features and requirements. Existing LVCB mechanisms of this family have complex requirements involving multiple stable states, multiple operations and several functions. Some of the most important operational requirements are: fast interruption of the electric circuit (to be performed in some milliseconds), low energy of actuation (of manual, electrical, thermal, or magnetic origin), and reduced variability of forces and moments required by the mechanical parts. Their performance is constantly improved in current designs using well-known experimental and numerical optimization procedures. However, these procedures do not allow to establish whether a design with a different topology would provide a better performance.

The conceptual design of metamorphic mechanisms is a difficult combinatorial problem: the number of solutions grows exponentially with the number of operations to be satisfied and with the number of changes allowed to be performed by the different links and joints. This paper presents a systematic method for the topological synthesis of mechanisms [10], taking into account metamorphic transformations of links and degrees-of-freedom required for the main operations. The method is based on Graph Theory concepts and can be applied to the design and re-design of mechanisms satisfying complex metamorphic requirements. An application to the design of circuit breaker mechanisms is shown.

2 PROBLEM DESCRIPTION

A LVCB mechanism has two kinds of inputs: a manual handle, denoted as I_1 in Fig. 2, and one or more internal inputs (actuated by a bimetal, magnetic plunger, relay, etc.) which actuate over a delatching lever (DL), see I_2 and I_3 in Fig. 2. The main output O_1 of the mechanism is the contact carrier, it contains and also isolates the metallic contacts which close the electric circuit. The contact carrier is closed only by closing the handle (manually or automatically through accessories that move the handle remotely). Under electrical failure conditions, the internal inputs must open the contacts *even when the handle is intentionally locked*; the configuration of the remaining parts of the mechanism may also be considered as an output O_2. The problem to solve consists in enumerating the mechanisms that contain these input and output parts, and fulfill a given set of operations or transitions as described below. Springs and members able to store energy are ignored at this initial stage.

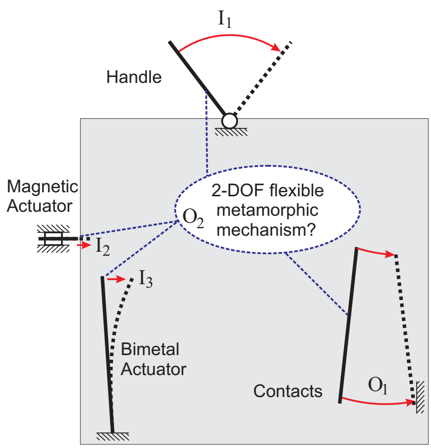

Figure 2: Required input and output parts to move.

2.1 Stable states, energy requirements, and transitions

The operations of the mechanisms can be represented by a finite-state machine (FSM) [5, 2, 11], either in tabular or graphic form, see the digraph of a LVCB mechanism in Fig. 3. A finite state machine is an algebraic structure, denoted as $M = (\boldsymbol{S}, \boldsymbol{I}, f, s_0, \boldsymbol{O})$, and consists of a finite set of states $\boldsymbol{S}$, a finite input alphabet $\boldsymbol{I}$, a transition function f that assigns a next state to every pair of state and input ($f : \boldsymbol{S} \times \boldsymbol{I} \rightarrow \boldsymbol{S}$), an initial state s_0, and a subset $\boldsymbol{O}$ of $\boldsymbol{S}$ consisting of final or output states. In the metamorphic mechanisms context, each state corresponds to configurations with different mobility, including partial structures and over-constrained mechanisms.

This useful discrete representation is not enough to describe the continuous transitions between states, which can be further composed of more discrete sub-states with topological changes between them.

In this work, the FSM representation is used to identify the number of stable states of the LVCB mechanisms (and thus the n-stability requirements) and is also useful for analyzing the requirements of the transitions. It is worth to mention that mechanisms designed for other applications can have the same FSM representation (motion homomorphic [2]), thus the number of existing designs can be increased. The basic maneuvers common to all circuit breakers can be represented by one FSM, see Fig. 3 and its tabular representation in Appendix A.

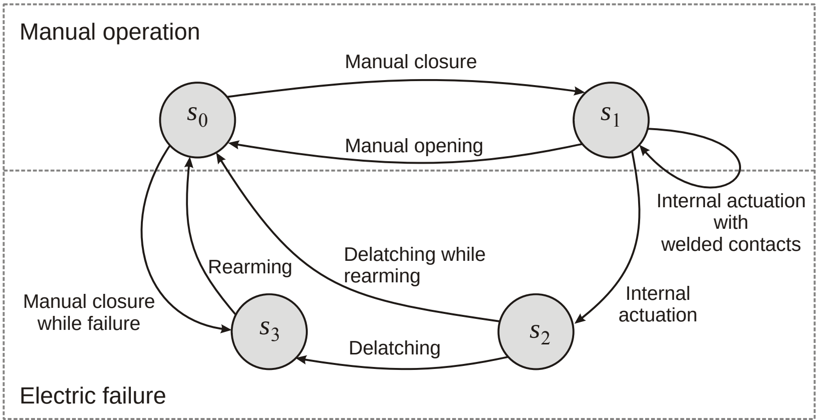

Figure 3: Required operations and stable states: s_0: open (armed), s_1: closed, s_2: open contacts after delatching, s_3: safe delatched position.

The meaning of the states in Fig. 3 is the following:

- s_0: Contacts in off status, armed mechanism.
- s_1: Contacts in on status, armed mechanism.
- s_2: Contacts still in on status, disarmed mechanism produced by motion of the magnetic or bi-metal actuator (electric failure).
- s_3: Contacts in off status, disarmed mechanism in safe configuration.

The operations consist of a set of the following transitions:

1. Manual Closure s_0 to s_1 with delatching sub-mechanism armed.
2. Manual Opening s_1 to s_0 with delatching sub-mechanism armed.
3. Electro-mechanical Disarming s_1 to s_2 by means of internal actuation.
4. Mechanical Delatching and Rearming s_2 to s_0 by means of delatching process with unloaded handle.
5. Mechanical Delatching s_2 to s_3 by means of delatching process with locked handle.
6. Automatic mechanical Rearming s_3 to s_0 by means of handle spring.
7. Manual Closure s_0 to s_3 with disarmed delatching sub-mechanism (some internal input is activated).

8. Failure with welded contacts; this undesired situation corresponds to a failure of the mechanism due to several reasons, e.g., a failure in the internal actuators.

Manual operation consists of opening and closing, between two stable states. While the handle is in one of these two states or in a transition, a sub-mechanism independent of the handle position, hereafter called delatching sub-mechanism, must be able to open the contacts under electric failure. Therefore, the mechanism topology must have at least 2 degrees-of freedom (DOF). Since this opening under failure must be performed in a prescribed short time, necessarily, a considerable amount of energy must be stored when the mechanism is closed. This energy is stored in the main springs often connected directly to the contact carrier and depends on human hand force, length of the handle, and de-multiplication of the mechanism.

In terms of energy requirements, s_0, s_1 and s_3 are constrained stable states whereas s_2 is a highly-unstable state; see for instance the state G in Fig. 4. The mechanism has a bi- or tri-stable behavior depending on whether the handle position is free or locked, respectively.

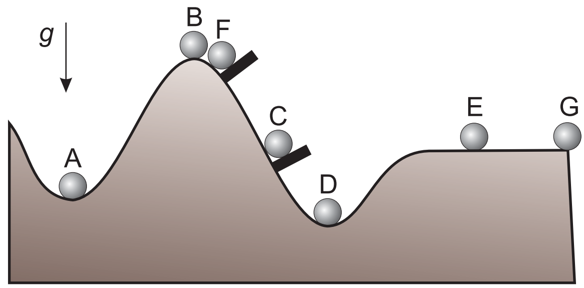

Figure 4: Possible energy states. (A) and (D) are stable; (B) is unstable; (C,F) are externally constrained stable; (E) is neutrally stable; (G) is in neutrally state but near to a highly-unstable transition.

3 GRAPH REPRESENTATIONS OF MECHANISMS WITH VARIABLE TOPOLOGY

Graph representations are adequate for modeling the initial topology and for imposing desired topological constraints [12]. This technique is well defined for mechanisms with simple joints; bodies are represented by vertices and joints by edges connecting a pair of vertices [13].

Mechanisms with multiple joints (i.e., joints with more than two incident members) can be represented by larger mechanisms with simple joints; however, the conversion is not unique and several binary joints mechanisms equivalent to a mechanism with multiple joints can be found [14, pp. 107-108].

A mechanism with higher pairs has its own graph representation but also admits –using several conversion rules– a graph representation in terms of lower pairs (allowing one-dof per joint) called *associated linkage* [13] or *generalized linkage* [14]. These simplified linkage mechanisms with only lower pairs permit the representation of any more complex planar mechanism and also allow the systematic enumeration of new mechanisms. Yan [14, 99-106] described the lower pair representations of most joints and links and called them generalized joint and members, respectively.

Figure 5 illustrates some joints commonly used in LVCB mechanisms and also shows their graph representation. The edges or lines connecting bodies will hereafter drawn as “dotted”, “dashed”, “solid”, and “double”, in line with the reduction of 0, 1, 2, and 3 DOFs, respectively. Using this representation, several existing mechanisms of the market were analyzed and described by hand and converted into a lower-pair representation useful to express requirements and to validate the results.

The design resources used in metamorphic mechanisms can be represented as follows:

- Variable topology: The representation is the conventional kinematic chain with additional indicators of links and joints. Changes can be expressed as a sequence of graphs (one graph for each state or configuration) or, as a unique graph with a sequence of joints labels (e.g., see the unified graph in Ref. [5]).
- Metamorphic bodies or links: Bodies joined together are represented by a main body followed by another one attached to it, parenthesized; for instance, 0(1,2) means that bodies B_1 and B_2 are considered as attached to the ground, denoted by default as B_0.
- Metamorphic joints: A metamorphic joint can basically change its:
    - Type: Type changes can be produced inside the same order or between different orders, that is, from a lower kinematic pair to a higher kinematic pair and vice versa. A joint can also loose or gain mobility, for example, a 3-DOF spherical joint can be converted into a 1-DOF hinge by locking two of its axes.
    - Characteristics: change of joint characteristics, for instance, the change of orientation of the joint axis, denoted as x, y, z, or as ν if its direction is made arbitrary; a change of motion orientation for a prismatic joint is illustrated in Ref. [9].

It should be noted that changes are produced either by different kineto-static conditions while the motion takes place or by external actuation; magnitude and direction of the reaction forces in singular configurations are the key for obtaining the desired energy characteristics and behavior in dynamic transitions.

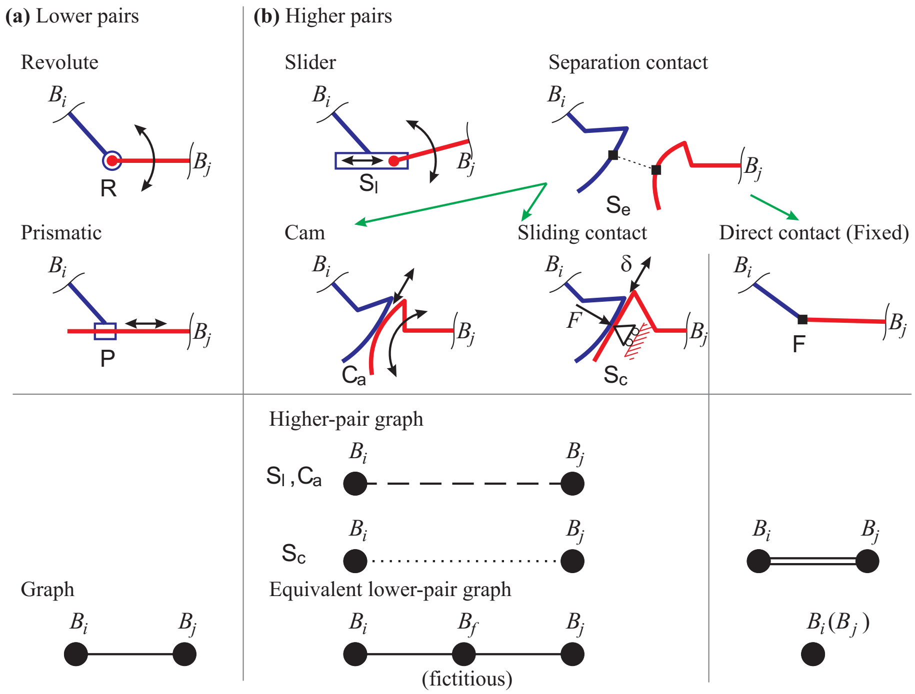

Figure 5: Types of joints and their lower-pair graph representation.

3.1 Example of graph representation

The mechanism shown in Fig. 6 is used as an example of the identification of the topology; see also the names of the bodies in Tab. 1. This mechanism has a metamorphic joint between the rod (R), the contact carrier (CC), and the delatching lever (DL); it is composed by two sliders formed by DL and CC. The rod is trapped by three points, two from DL and one from CC, and they form a revolute joint denoted as [R]. This metamorphic joint works as a revolute joint in normal operation, and it is converted into a slider in the delatching operation (the rod slides over the contact carrier). While rearming, the rod slides in the opposite sense over CC and pushes DL until forming the revolute joint again.

Body	ID	Code	Body	ID	Code
Handle	1	H	Rod	2	R
Delatching Lever	3	DL	Contact-Carrier	4	CC
Mobile Contact	5	C	Magnetic Actuator	6	M_A
Latching Spring	7	K_L	Contact Spring	8	K_C
Opening Spring	9	K_O	Handle Spring	10	K_H

Table 1: Names given to parts of a circuit breaker mechanism

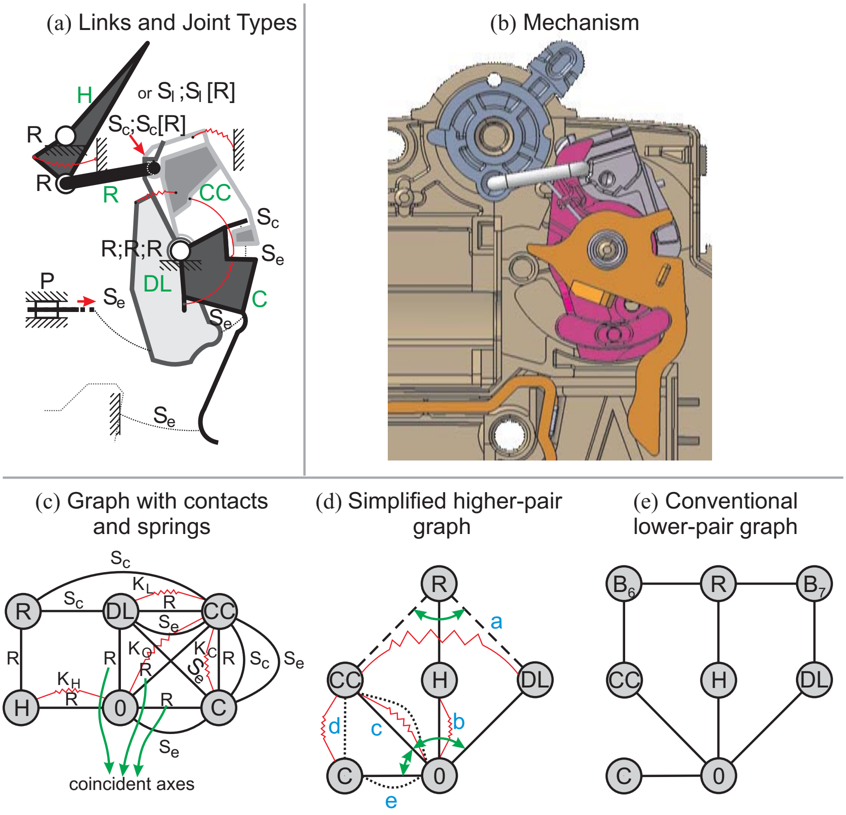

Figure 6: Example of graph representation of a circuit breaker mechanism

In Fig.6-c, the graph considers the contacts (separated and effectively in contact) and springs. All states can be catalogued using that representation and also represented in a more compact form called unified graph like the one shown in Fig. 7; however, we found it cumbersome and unfriendly to be used by the designer.

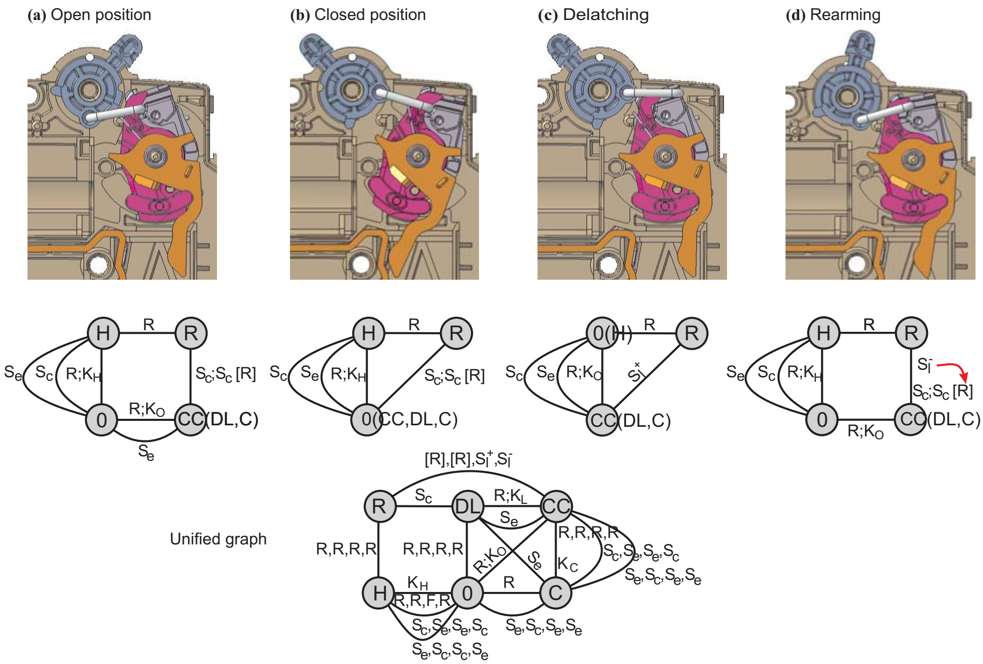

Figure 7: Example of graph representation including contacts.

The representation can be further simplified by the graph shown in Fig. 6-d where each pair of open and closed contacts is represented by a unique edge. Finally, Fig. 6-e shows the lower pair representation. The two latter representations can be combined with a Phase/Joint table to express the metamorphic changes as shown Figs. 8 and 9. Using this representation, 26 existing designs were catalogued and stored for validation.

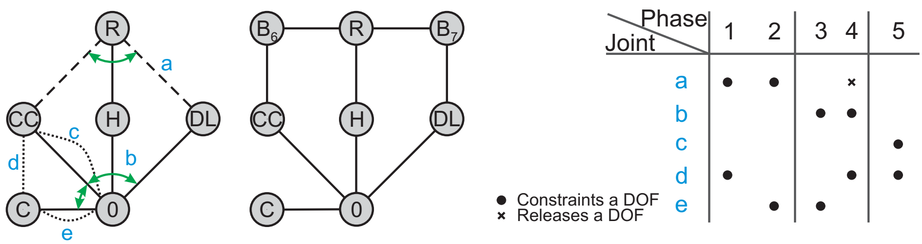

Figure 8: Chosen graph representation and phase/joint table.

The Phase/Joint table considers the joint changes for each state, see Fig. 9. A black bullet means that the joint restrains a DOF, and a cross represents the DOF released when delatching takes place. For instance, in the 2+1 DOF topology shown in open position in Fig.9(1), the contacts C are maintained in contact with CC by joint b, and another DOF is reduced by joint a (that avoids that the rod could slide through CC) thus reducing the DOFs to one.

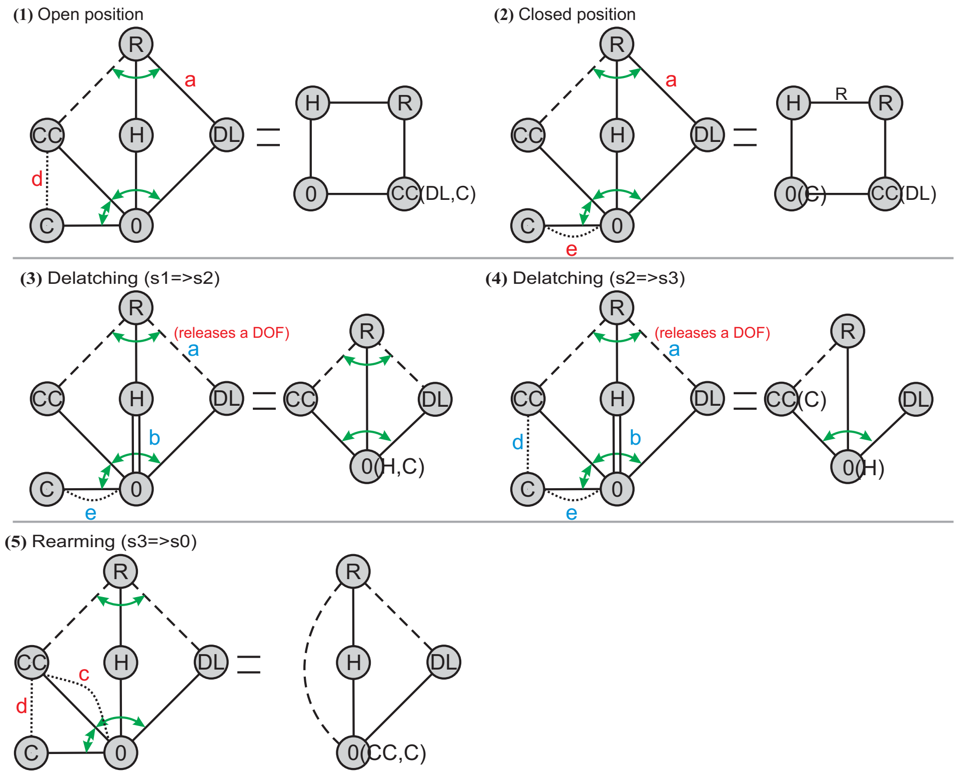

Figure 9: Graphs states in correspondence with the graph and the Phase/Joint table.

4 METHODOLOGY FOR ENUMERATION

The lower-pair representation of linkages is used in this work: both, the description of the parts to move and the atlas data base are given in this form. An enumeration synthesis solver [10] was modified to take into account new design constraints related to metamorphic changes. This solver was used to search the parts to move inside every mechanism taken from an atlas without repetitions and satisfying topological constraints.

The atlas data base determines the search design space. A set of 39 graphs of 2-DOF kinematic chains were included in the atlas [13, app. D, tabs. D7 to D14]: 39 kinematic chains with 5 links - 5 joints (1), 7 links - 8 joints (3), and, 9 links - 11 joints (35) were codified. Assignment of the fixed link or ground derives in 232 different mechanism topologies.

By representing existing mechanisms in terms of graphs, several common topological properties were identified for the different operational conditions and then used in the enumeration. The enumeration also serves to establish a topological classification of existing mechanisms.

4.1 Initial graph and topological constraints.

The parts to move were firstly represented in a graph as shown in Fig. 10.

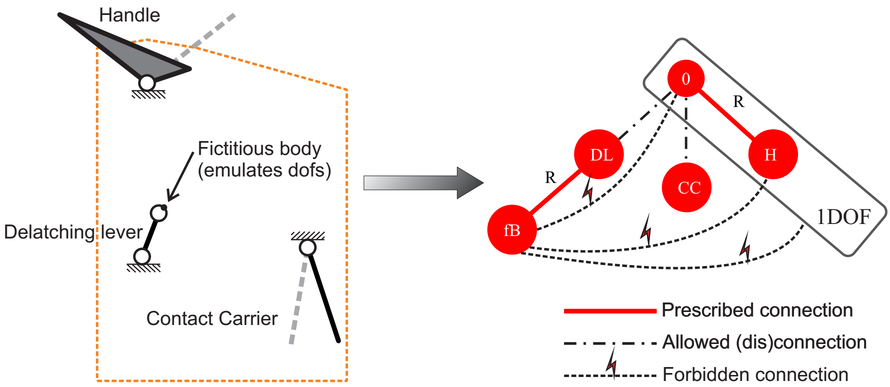

Figure 10: Topological configuration imposed on the initial parts.

Labels were assigned to each part. A series of constraints were defined, based on the functioning requirements, for the search of feasible mechanism topologies.

- Required bodies:

  [B1] There must exist at least five bodies: 0 (ground), H (handle), CC (contacts carrier), DL (delatching lever), and fB (fictitious body emulating the DOF of the contact).

- Connectivity constraints imposed on the initial graph:

  [C1] H is connected to 0.
  [C2] DL is connected to a fictitious body fB.
  [C3] fB is never hinged to 0;
  [C4] fB is never hinged to H;
  [C5] fB is never hinged directly to a 1 DOF sub-graph containing both 0 and H.
  [C6] DL can either be connected to 0 or be a floating link (hereafter, "floating" means not connected to ground);
  [C7] CC can either be connected to 0 or be a floating link.
  [C8] If CC is a floating link, it cannot be connected to H.

- Degree constraint (number of bodies connected) imposed on bodies of the desired solution:

  [D1] H: binary;
  [D2] DL: binary;
  [D3] fB: binary.

- Metamorphic constraints related to prohibited or allowed changes:

  [T1] There is not a 1DOF subgraph containing: 0, H, CC;
  [T2] There is not a 1DOF subgraph containing: 0, DL, fB, H;
  [T3] There is not a 1DOF subgraph containing: 0, DL, fB, CC.

The metamorphic constraints are expressed in terms of subgraphs constraints. For instance, if the handle and the contact carrier belong to a 1DOF submechanism, locking of the handle will also lock the contacts; topologies with these undesired configurations are rejected by constraint T1. The constraints T2 and T3 ensure that the mechanism is able to delatch even when the handle is fixed. Note also that no degree constraint is imposed on the contact carrier and on the rod.

To compute constraints C5, T1, T2, and T3, the method involves the simultaneous use of two atlases: a 2-DOF atlas as design space and a 1-DOF atlas to compute the constraints. Candidate solutions are taken from the design space, and all those that contain any sub-mechanism of those defined in the 1-DOF constraints atlas, are rejected.

In order to satisfy constraints like C6 and C7, the problem was split into four cases, which are mutually exclusive. They are denoted as Ia, Ib, IIa, and IIb; see Fig. 11. In this way, the complexity is reduced and the information is easier to be handled.

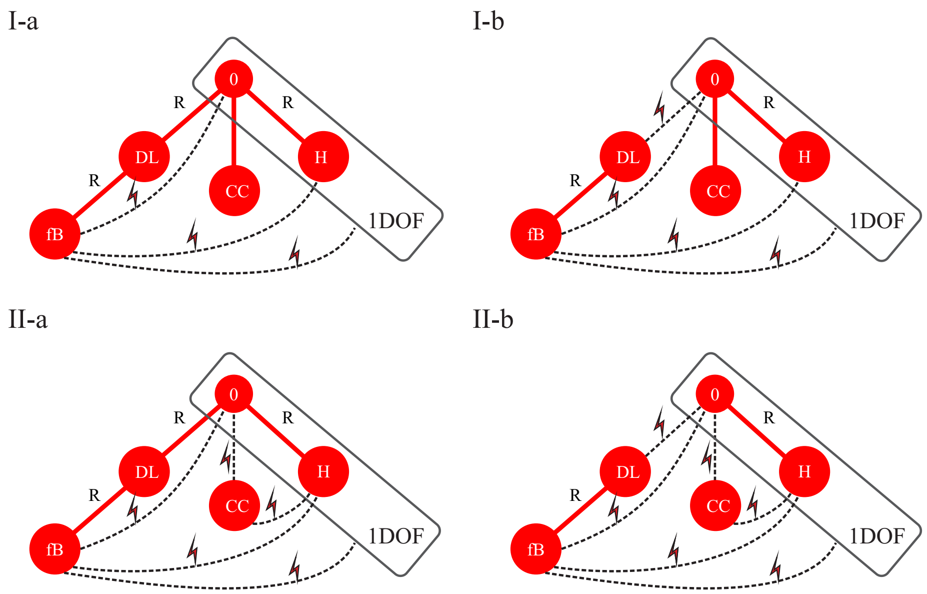

Figure 11: Subdivision of the problem into four mutually-exclusive cases: (Ia) grounded DL and CC; (Ib) floating DL and grounded CC; (IIa) grounded DL and floating CC; (IIb) floating DL and CC.

5 RESULTS

The searches in an atlas of 2-DOF mechanisms, with up to 9 links-11 joints, resulted in a set of 617 topologically different mechanisms, which were classified in complexity order.

Most existing mechanisms for breakers appeared within this set (for example, the existing mechanism in Fig. 9 can be found as Mech_Ia 1 in Fig. 12), resulting in a topological classification of designs; several potential candidates for new mechanisms were also established.

Results were represented by automatic sketching to help designers understand the proposals. The first results of problem Ia are shown in Fig. 12.

5.1 Post-processing of the results and further research

All topological simplifications assumed in the enumerated topologies must be evaluated as possible forms of adding parts: e.g., to consider a contact mounted over the contact carrier, the use of a slider for achieving a contact pressure DOF, and the use of 0-DOF chains for amplifying the mechanical advantage of the delatching lever.

The presented enumeration can be used as a source of new designs. Firstly, the designs can be developed with lower pairs until functionality is ensured. Then, using manual assignment, the designers can try the inverse transformation from lower pairs to multiple joints and higher pairs (such us contact pairs, sliders, and others), possibilities of making axes of joints coincident, addition of springs, separation contacts (stops), etc. All of these design considerations will increase the combinatorial explosion from each of the enumerated alternatives. The automation procedures of the mentioned transformation will be addressed in future research.

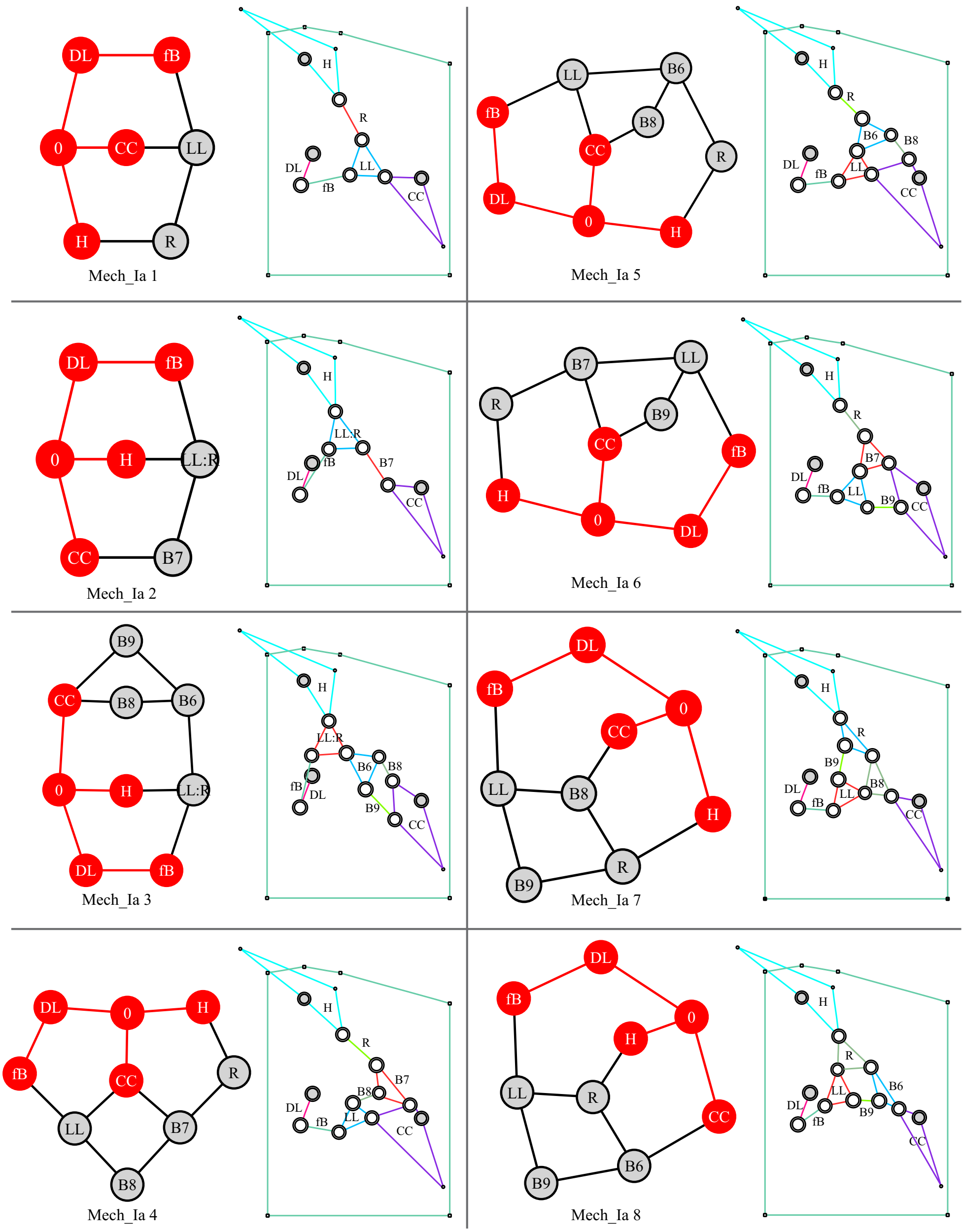

Figure 12: Mechanisms satisfying the initial graph and constraints Ia.

6 CONCLUSIONS

Mechanisms for fulfilling complex operations involving metamorphic changes were enumerated using Graph Theory concepts and combinatorial algorithms. The presented problem is difficult because one sub-mechanism of the mechanism must have a mobility independent from other sub-mechanism which can or cannot be locked.

The main contribution of this work is to give a way to express topological constraints for metamorphic changes in the form of sub-graph constraints.

The many feasible concepts were represented in the form of physical sketches. They were used as a source of potential new designs of mechanisms for circuit breakers.

ACKNOWLEDGEMENTS

This work received financial support from ABB Switzerland Ltd., Corporate Research, contract 2009-447-01 (SAT UNL 537362), and from the Argentinean institutions Universidad Nacional del Litoral (CAI+D 2009 PI65-330), Agencia Nacional de Promoción Científica y Tecnológica (ANPCyT PICT-2010-1240), and Consejo Nacional de Investigaciones Científicas y Técnicas (CONICET).

REFERENCES

[1] L.-P. Zhang and J. S. Dai. An overview of the development on reconfiguration of metamorphic mechanisms. In *Proceedings of ASME/IFToMM REMAR 2009 Conference*, pages 1–11, London, United Kingdom, June 2009.

[2] H.-S. Yan and C.-H. Kuo. Representations and identifications of structural and motion state characteristics of mechanisms with variable topologies. *Transactions of the Canadian Society for Mechanical Engineering*, **30**(1):19–40, 2006.

[3] J. S. Dai and J. R. Jones. Matrix representation of topological changes in metamorphic mechanisms. *Journal of Mechanical Design*, **127**(4):837–840, 2005.

[4] D. Li, Z. Zhang, and J.M. McCarthy. A constraint graph representation of metamorphic linkages. *Mechanism and Machine Theory*, **46**(2):228–238, 2011.

[5] C.-H. Kuo. *Structural characteristics of mechanisms with variable topologies taking into account the configuration singularity*. Master's thesis, National Chen Kung University, Tainan, Taiwan, Republic of China, 2004.

[6] D. Martins and R. Simoni. Enumeration of planar metamorphic robots configurations. In *Proceedings of ASME/IFToMM REMAR 2009 Conference*, pages 580–588, London, United Kingdom, June 2009.

[7] Z. Lan and R. Du. Representation of topological changes in metamorphic mechanisms with matrices of the same dimension. *Journal of Mechanical Design*, **130**(7):074501–1 – 074501–4, 2008.

[8] B. Slaboch and P. A. Voglewede. Development of planar mechanism state matrices for reconfigurable mechanisms. In *Proceedings of ASME IDETC/CIE 2010 Conference*, Montreal, Quebec, Canada, August 2010. Paper DETC2010-28108.

[9] H.-S. Yan and C.-H. Kang. Configuration synthesis of mechanisms with variable topologies. *Mechanism and Machine Theory*, **44**(5):896–911, May 2009.

[10] M.A. Pucheta and A. Cardona. An automated method for type synthesis of planar linkages based on a constrained subgraph isomorphism detection. *Multibody System Dynamics*, **18**(2):233–258, 2007.

[11] K. H. Rosen. *Discrete Mathematics and Its Applications*. McGraw-Hill, 6th edition, 2007.

[12] M.A. Pucheta. *Computational methods for design and synthesis of planar mechanisms*. PhD thesis, Universidad Nacional del Litoral, Santa Fe, Argentina, 2008.

[13] L.-W. Tsai. *Mechanism Design: Enumeration of Kinematic Structures According to Function*. CRC Press, Boca Raton, 2001.

[14] H.-S. Yan. *Creative Design of Mechanical Devices*. Springer-Verlag, Singapore, 1998.

APPENDIX

A. Transition and output functions of the LVCB mechanism

The transition function *f* is a mapping from state space to the state space for the feasible combinations of the inputs. It can be tabulated as shown in Table 2, which is also known as the “next state” table [2,11].

$f(\mathbf{S},\mathbf{I})\rightarrow\mathbf{S}$	Input			
	I_1=on I_2 and I_3=off	I_1=off I_2 and I_3=off	I_1=on I_2 or I_3=on	I_1= free I_2 and I_3=off
State	Next State			
s_0	s_1	-	s_3	-
s_1	-	s_0	s_2	-
s_2	s_3	-	-	s_0
s_3	-	-	-	s_0

Table 2: Transition function of the circuit-breaker mechanism (normal operation in grey).

For a given present state and the same set of input values of the previous table, the “outputs” table (Table 3) shows the values of the outputs for the associated “next state”.

$g(\mathbf{S},\mathbf{I})\rightarrow\mathbf{O}$	Input			
	I_1=on I_2 and I_3=off	I_1=off I_2 and I_3=off	I_1=on I_2 or I_3=on	I_1= free I_2 and I_3=off
State	Ouputs			
s_0	O_1=on; O_2=armed	-	O_1=off; O_2=disarmed	-
s_1	-	O_1=off; O_2=armed	O_1=on; O_2=disarmed	-
s_2	O_1=off; O_2=disarmed	-	-	O_1=off; O_2=armed
s_3	-	-	-	O_1=off; O_2=armed

Table 3: Output function of the circuit-breaker mechanism (normal operation in grey).

In these tables, the cells with grey background in the first two columns of data correspond to the normal or manual operation. The other cells correspond to the electric failure.

Proceedings of MUSME 2011, the International Symposium
on Multibody Systems and Mechatronics
Valencia, Spain, 25-28 October 2011

DYNAMICS OF SENSITIVE EQUIPMENTS ON WRS ISOLATORS

Giandomenico Di Massa, Stefano Pagano, Ernesto Rocca and Salvatore Strano

Dipartimento di Meccanica ed Energetica
Università di Napoli Federico II, Naples, Italy
e-mail: gdimassa@unina.it; pagano@unina.it; erocca@unina.it; salvatore.strano@unina.it

Keywords: vibration isolator, Bouc-Wen model, wire rope springs, ball transfer unit (BTU).

Abstract. *Wire rope springs (WRS) are widely used to protect sensitive equipment from shock or vibrations but they do not have the characteristics of a seismic isolator that must have an high vertical stiffness to support the vertical load with an acceptable vertical deflection and, at the same time, a low horizontal stiffness to isolate low frequency ground horizontal acceleration of an earthquake.*

To take advantage of their peculiar characteristics due to the dry friction that arises among the wires, they can be adopted in parallel with a Ball Transfer Unit (BTU), able to support vertically the sensitive equipment's weight and to allow the equipment itself to move in any horizontal direction with low friction. The WRS-BTU isolator can be considered rigid in the vertical direction and the horizontal stiffness can be properly chosen to give the isolated system a low natural frequency and a suitable re-centering force.

In order to evaluate the feasibility of adopting an isolator based on WRS and BTU, a prototype was developed and tested. In this paper, the description of the seismic isolator prototype and some experimental results are presented; it is also presented a procedure to identify the restoring force by means of the Bouc-Wen model. Finally, adopting this analytical description of the restoring force, the non-linear behavior of sensitive equipment suspended on these isolators, for different operational conditions, is simulated.

1 INTRODUCTION

A very attractive way of improving the seismic performance of a structure is given by the possibility of an increase of both the period of vibration and the energy dissipation capacity of the system. This can be obtained by making use of specific elements designed to isolate part of the structure from the full intensity of the seismic motion (reduction of the seismic energy transfer into the structure) and/or to dissipate a large amount of energy.

For example, isolation devices have the main aim to increase the period of vibration of the structure towards a lower amplification range of the response spectrum for the design ground motion, thus reducing the input energy into the structure; it is also necessary to provide supplemental damping thus reducing the structure displacement.

The functions of an isolating/dissipating system are generally: (i) supporting gravity loads and providing for (ii) lateral flexibility (period shift), (iii) restoring force and (iv) energy dissipation (either of hysteretic, in the case of displacement activated dampers, or viscous nature, in the case of velocity activated dampers);

For light structures, the use of the common elastomeric steel-reinforced isolation systems, is neither economical nor, for most cases, technically suited. This is because the design of the bearings is compromised by the need to meet two functions: to provide a low horizontal natural frequency, demanding a very low stiffness for light structures, and to safely support the structure under large horizontal deflections induced by the earthquake, demanding a large plan area [6].

A seismic isolation system, suitable for light structures, has been developed; the system consists of a wire rope spring and a BTU (Ball Transfer Unit). The WRS springs have hysteretic non-linear behavior depending on the diameter, length and wire rope configuration. The restoring force is difficult to model since it cannot be described by an analytical expression depending on instantaneous displacement and velocity; it mainly depends on both instantaneous and past historical rope deformation [1].

In the literature there are no analytical models or design criteria to foresee the stiffness and damping isolator characteristics; to evaluate the feasibility to adopt an isolator based on WRS and BTU, an isolator prototype was developed and tested on a bi-axial press to detect the horizontal force-displacement cycle. These first experimental tests were performed to analyze the influence of the WRS cables' length on the isolator's static and dynamic characteristics. Starting from the experimental results, an analytical description of the restoring force, based on the Bouc-Wen model, was identified and the dynamics of a sensitive equipment, suspended on the isolators, was studied. An analytical formulation of the dissipation energy is also presented.

Due to their low cost this type of isolator can be adopted when elastomeric steel-reinforced isolators are not commercially available as, for example, for low weight equipment or for works of art. A further economic benefit can be achieved by adopting commercial wire rope spring, not necessarily integrated into a unique support with the BTU.

2 PROTOTYPE DESCRIPTION

The isolator prototype comprises (Fig.1):

- two steel plates (UP and LP) with plant size of 160x160 mm;
- wire rope cables that, with the two plates, realize the WRS; the experimental tests were performed adopting 8 cables with a diameter of 5mm;
- a BTU, able to sustain a vertical load up to 1400 N, that allows the upper plate to move in any horizontal direction, in a 50 mm radius circular area, with low friction. The

BTU's are generally adopted for the transportation of bulk materials or for box packages and are constituted of a main ball that sits atop smaller recirculating balls contained in a hemispherical cup. In this application, it is mounted in a "ball-up configuration" so that the main ball is in contact with the intrados of the upper plate to avoid that dust or debris settling on the rolling surface and affecting the regular rolling of the main ball; this configuration could lead different stresses distribution in the equipment structure, due to the change of the BTU reaction position;

- a deformable elastomeric pad placed between the BTU and the lower plate that allows all the BTU's supporting the equipment to share the vertical load that is necessary if the isolation system consists of more than three isolators (statically indeterminate system).

The isolator can be considered as an extension of the mono-directional one introduced by Demetriades et al. [2], made of a wire rope spring and a locked caster.

A care must be posed when designing the complete isolator system as the device is an unilateral constraint and it is so necessary to prevent the lifting of the upper plate from the BTU, in any operating condition. For this reason it can be used only with a favorable centre of mass height and BTU wheelbase ratio.

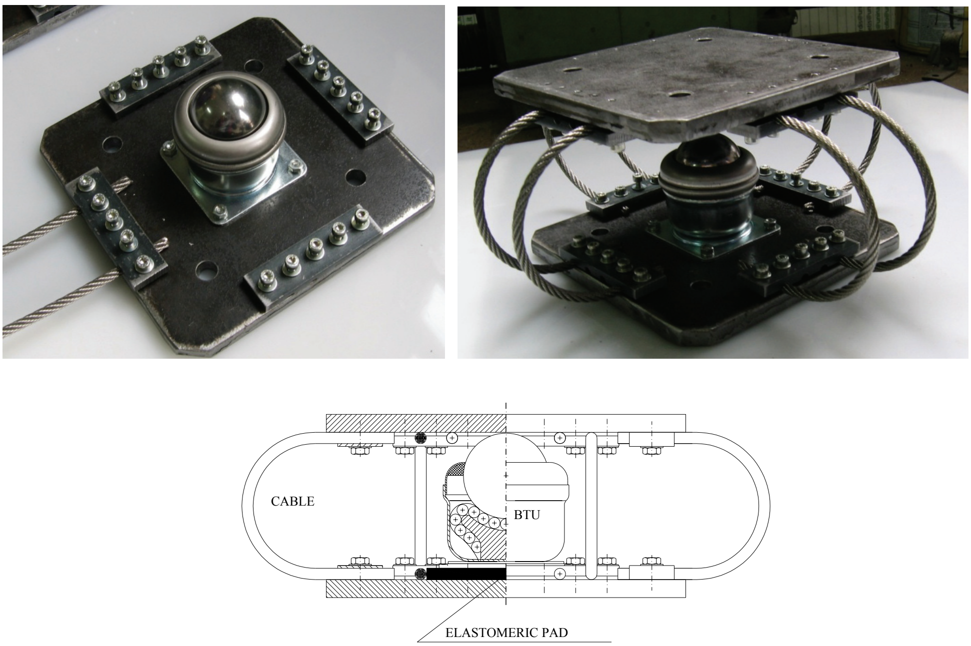

Figure 1 – Isolator prototype

3 THE EXPERIMENTAL TESTS

To test the prototype a bi-axial press was adopted (Fig. 3) tuned to impose at the isolator lower plate an horizontal harmonic displacement with a frequency of 0.05 Hz and an amplitude of 20 mm (stroke = 40 mm); the tests were repeated for several values of the vertical load.

The first tests were conducted without cables in order to characterize the BTU friction forces; figure 2 shows a force-displacement diagram and the trend of the friction coefficient versus the vertical load deduced from upper and lower branch of the hysteretic cycle.

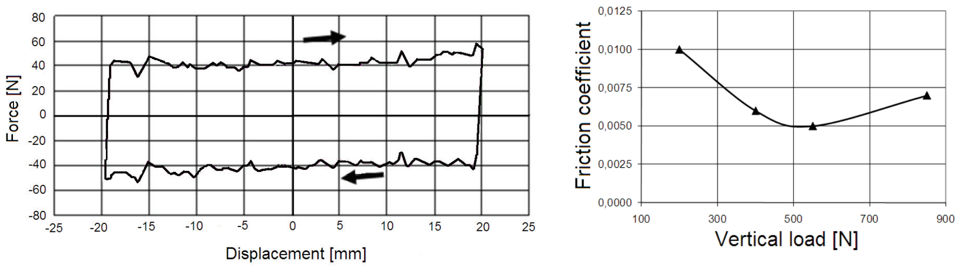

Figure 2 – BTU friction coefficient

Further tests were performed mounting the cables and avoiding the contact between the BTU and the rolling surface; in figure 4, the horizontal force-displacement diagrams, obtained for three different cables' length, are reported; even in these cases an harmonic relative motion was imposed, between the two plates, with a frequency of 0.05 Hz and an amplitude of 20 mm.

The three hysteretic cycles have, approximately, the same cycle areas; the equivalent viscous damping, $\sigma_{eq}=A/(\pi\omega X^2)$, proportional to the hysteretic cycle area A and depending on the motion amplitude X and circular frequency ω, is approximately equal to 3.5 Ns/mm.

The cycles mainly differ for the slopes of the branches. With short cables the horizontal stiffness has a progressive trend (Fig.4a). By increasing the cable length the isolator could have a not sufficient re-centering force (Fig. 4b); in this case the cycle branches exhibit a very small (positive) slope. A further increase of the cable length leads to static instability with a negative restoring force (Fig. 4c).

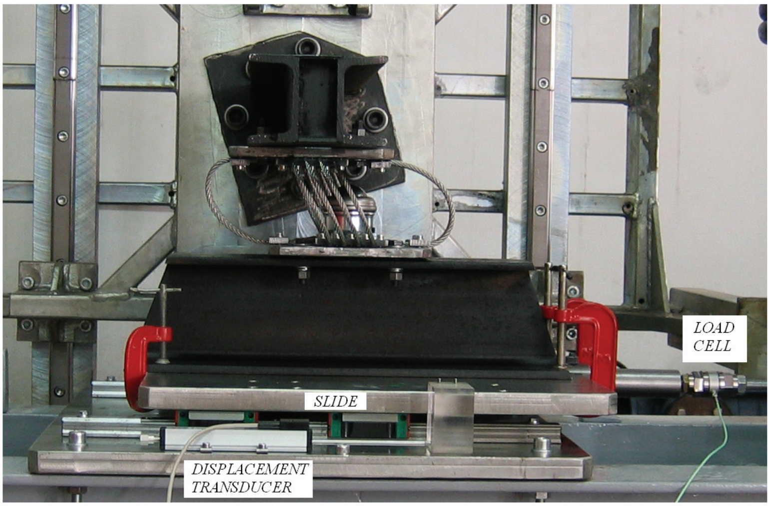

Figure 3 - Isolator on the bi-axial press

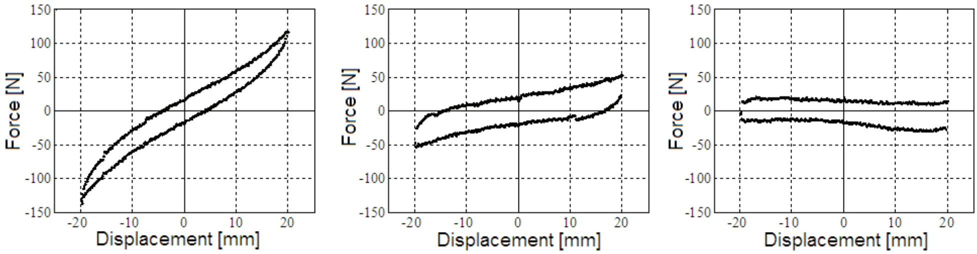

Figure 4 – Hysteretic cycle for 85 mm, 105 mm, 125 mm cables' length

4 THE ISOLATOR REACTION

The isolator reaction has been modeled as the sum of a component, F_c , exerted by the wire ropes action and a friction force, F_r , due to the rolling resistance of the BTU. In the following the analytical expressions of the above components are reported in order to obtain a model that can be used to describe the isolator dynamic behavior.

4.1 The wire rope spring reaction force

The WRS component of the isolator restoring force is modeled as the sum of three independent components:

$$F_c(t) = F_{el}(t) + F_h(t) + F_{nl}(t) \tag{1}$$

where: F_{el}, is the elastic component, proportional to the displacement; F_h is the hysteretic component and F_{nl} is a non-linear component proportional to the cube of the displacement .

The hysteresis supplies restoring forces and dissipates energy. The restoring force depends not only on the instantaneous deformation, but also on the history of the deformation; one of the most utilized way to express this force is the Bouc-Wen model, that essentially consists of a first-order non-linear differential equation that relates the input displacement $x(t)$ to the output restoring force $z(t)$, as follows:

$$\dot{z}(t) = D^{-1}(A\dot{x}(t) - \beta|\dot{x}(t)||z(t)|^{n-1} z(t) - \gamma\dot{x}(t)|z(t)|^{n}) \tag{2}$$

By appropriately choosing the set of parameters (A, D, β, γ), it is possible to accommodate the response of the model to the real hysteresis loops; the use of system identification techniques is a practical way to perform this task.

In [5], the physical and mathematical properties of the Bouc-Wen model are deeply discussed and it was found that if the system parameters respect the following constraints:

$$n \geq 1; \quad D > 0; \quad A > 0; \quad \beta + \gamma > 0; \quad \beta - \gamma \geq 0 \tag{3}$$

the model is valid independently on the exciting input. When conditions (3) are satisfied, Eq. (2) can be expressed in the "normalized" form. Defining the following parameters:

$$z_0 = \sqrt[n]{\frac{A}{\beta+\gamma}}; \qquad w(t) = \frac{z(t)}{z_0}; \qquad \rho = \frac{A}{Dz_0} > 0; \qquad \sigma = \frac{\beta}{\beta+\gamma} \geq \frac{1}{2} \tag{4}$$

it follows:

$$\dot{w}(t) = \rho\dot{x}(t)\left\{1 + |w(t)|^n \sigma\left[1 - \text{sgn}(\dot{x}(t)w(t)) - \frac{1}{\sigma}\right]\right\} \tag{5}$$

Finally, in [3] it is demonstrated that *w(t)* is bounded in the range [-1; 1] .

The terms of the above-defined restoring force model (1) and $\dot{z}(t)$ can be expressed as follows:

$$\begin{aligned} &F_{el}(t) = \alpha k x(t) \\ &F_h(t) = (1-\alpha)Dkz(t) \\ &F_{nl}(t) = k_3 x^3(t) \\ &\dot{z}(t) = D^{-1}(A\dot{x}(t) - \beta|\dot{x}(t)||z(t)|^{n-1} z(t) - \gamma\dot{x}(t)|z(t)|^n) \end{aligned} \tag{6}$$

With α comprised in the interval (0 ; 1) [5].

In the normalized form, the restoring force has the following form:

$$F_c(t) \;=\; F_{el}(t) + F_h(t) + F_{nl}(t) \;=\; k_x x(t) + k_w w(t) + k_3 x^3(t)\,, \tag{7}$$

with:

$$\dot{w}(t) = \rho\dot{x}(t)\left\{1 + |w(t)|^n \sigma\left[1 - \text{sgn}(\dot{x}(t)w(t)) - \frac{1}{\sigma}\right]\right\},$$

being:

$$k_x = \alpha k > 0; \quad k_w = (1-\alpha)Dkz_0 > 0; \quad k_3 > 0\,. \tag{8}$$

Coefficient k_3 is always greater than zero if the restoring force has an hardening behavior. As reported above, the experimental force-displacement cycle, adopted to characterize the restoring force exerted by the cables, was obtained avoiding the contact between the BTU and the rolling surface, in order to eliminate the contribution of correspondent rolling friction force. The data were detected with a two-channel control monitor (*Kistler, CoMo View Type 5863A21*) that samples at equal displacement intervals (but not at constant time interval).

In figure 5, the displacement and the force data vectors (*Xdata* and *Fdata*) are plotted versus the detected samples.

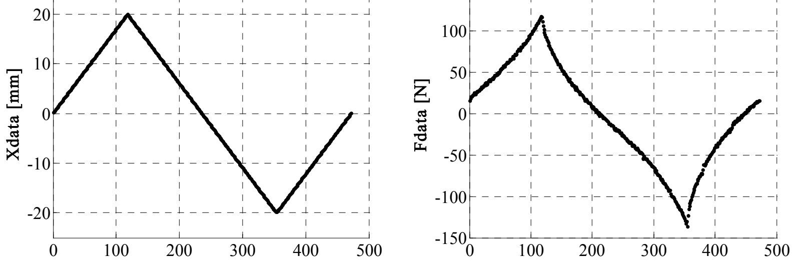

Figure 5 - Displacement and the force data vectors

To identify the Bouc-Wen parameters it was necessary to reconstruct the cycle to relate, for any time, the values of force, displacement and velocity.

The harmonic displacement law is characterized by a circular frequency ω and by an amplitude X corresponding to the maximum amplitude of the *Xdata* vector; it can be expressed by the following expression: $x(t) = X\sin(\omega t)$.

The analytical expression of the force can be expressed interpolating the *Fdata* vector with the Fourier series:

$$F(t) = a_0 + \sum_{n=1}^{8}[a_n \cos(n\omega t) + b_n \sin(n\omega t)] \tag{9}$$

In figure 6 the trend of the reconstructed X and F signals are reported in function of time and, in figure 7, the acquired cycle and the reconstructed one are compared.

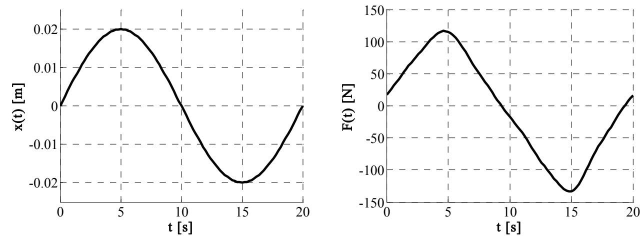

Figure 6 – Reconstructed X and F signals

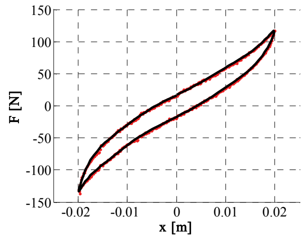

Figure 7 – Cycles' comparison

The optimization algorithm adopted to identify the parameters of the hysteretic model is based on a sequential quadratic programming (SQP). In particular a *Matlab* implemented algorithm (*fgoalattain*) was adopted to evaluate the constrained minimum of a non linear vectorial function starting from assigned initial conditions.

As the experimental test was performed at a very low frequency (0.05Hz), the inertial force contribution can be considered negligible; if the BTU-ball is not in contact with the rolling surface, the measured force can be attributed only to the cables restoring forces.

To identify the model parameters, a certain number of reference points of the reconstructed cycle were chosen with a constant time step, as shown in figure 8.

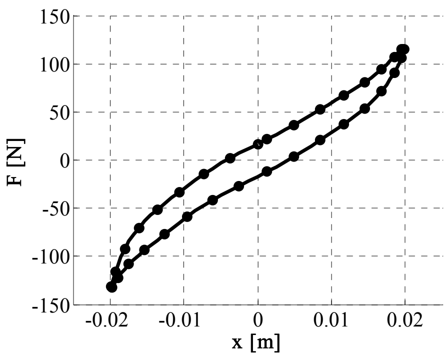

Figure 8 – Reference points on the reconstructed hysteretic cycle

Indicating with t_i the generic time value, corresponding to a reference point, the goal function to be minimized is:

$$Q(\bar{y}) = \left[F_c(\bar{y}, t_i) - F(t_i)\right]^2 \tag{10}$$

where $\bar{y}$ is a 6-parameter vector that must be identified by the least mean squared method: $\bar{y} = \{\rho, \sigma, n, k_x, k_3, k_w\}$.

The optimization algorithm allows to define several constraints on the parameters; the ones adopted in the present case are:

$$\rho > 0; \quad \sigma \geq \frac{1}{2}; \quad n \geq 1; \quad k_x > 0; \quad k_w > 0; \quad k_3 > 0 \ . \tag{11}$$

The identified parameters values are reported in table 1.

Parameter	*ρ [1/m]*	*σ [-]*	*n [-]*	*k_x [N/m]*	*k_w [N]*	*k_3 [N/m³]*
Value	333.33	2.5	2	4200	16.065	2700000

Table 1 - Identified parameters' values

In figure 9, the reconstructed cycle (dotted line) and the identified one (continuous line) are reported for $k_3 = 0$ (fig. 9 a) and $k_3 = 2700000$ *N/m³* (Fig. 9b), respectively. In figure 9b the two cycles are almost coincident and the maximum error is equal to 5.2 N (about the 4% of the maximum measured force).

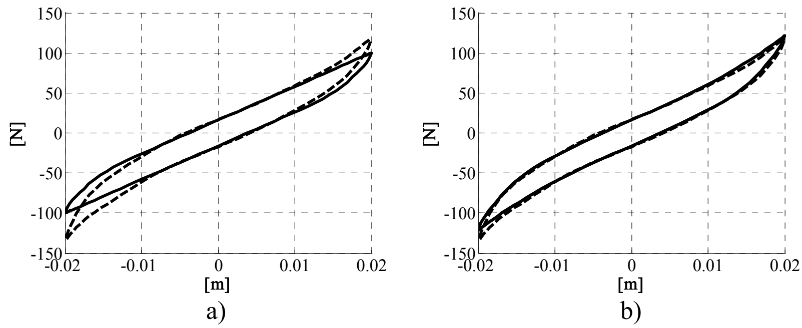

Figure 9 – Influence of k_3 on the cycle shape

The knowledge of these parameters allows to define the prototype horizontal restoring force and to evaluate its dynamic behavior for different excitations.

In figure 10, some hysteretic cycles are reported for different values of the displacement amplitude.

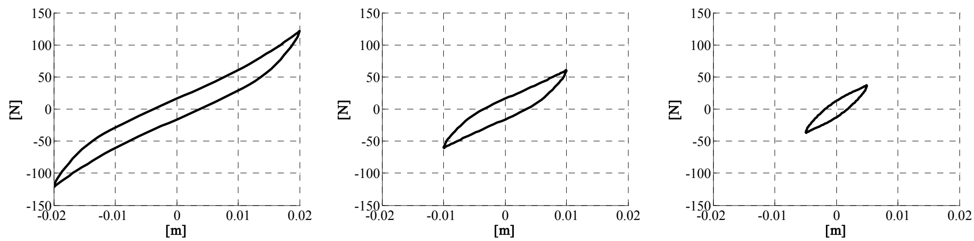

Figure 10 – Hysteretic cycles for different displacement values

4.2 The friction force

The BTU rolling friction force can be expressed through a Coulomb model:

$$F_r = C_a N \cdot \mathrm{sgn}[\dot{x}(t)] \tag{12}$$

The values of the friction coefficient C_a, versus the vertical load N, were experimentally identified and are reported in figure 3.

4.3 The resulting isolator reaction

The resulting isolator reaction, $F=F_c+F_r$, is hence:

$$F(t) = k_x x(t) + k_w w(t) + k_3 x(t)^3 + C_a N \cdot \mathrm{sgn}[\dot{x}(t)] \tag{13}$$

In figure 11, the comparison between a cycle obtained without (dotted line) and with (continuous line) friction force contribution (in the case of N = 800N, C_a = 0.006) and for a fixed amplitude of the displacement, is shown.

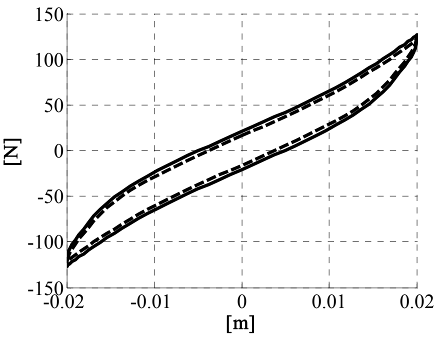

Figure 11 - Cycle comparison

5 CABINET DYNAMIC BEHAVIOUR

To evaluate the efficiency of the isolator prototype, a “laboratory cabinet” was realized (Fig.12); its dimensions (600x700x1200mm) and its inertial characteristics are nearly equal to that of sensitive equipment (for examples, a unit power supply) that must not be affected by high accelerations. It is constituted by a steel structure at which are connected several masses whose positions may be changed to simulate different inertial conditions. Four isolators sustain the cabinet and it will be tested on a vibrating shake-table able to reproduce the operating conditions similar to those of an earthquake.

The numerical simulations were performed adopting the mass configuration represented in figure 13 (cabinet with 12 masses of 5 kg); the cabinet inertial properties are reported in table 2. Hence, the results of the numerical simulations, conducted taking into account the above-defined restoring force model, are reported.

The system can be considered as a rigid mass on four isolators; if the cabinet center of mass is vertically aligned with respect to the centre of the isolators stiffness, it can be modeled as a one degree of freedom vibrating system.

Figure 12 – Laboratory cabinet on WRS-BTU isolators

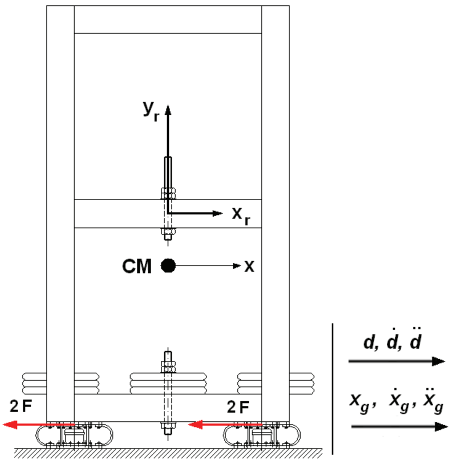

Figure 13 – Cabinet sketch

Mass	$m = 140$ kg
Dimensions	$L_X = 0{,}70$ m $L_Y = 1{,}20$ m $L_Z = 0{,}60$ m
Center of mass position	$X_r = 0{,}000$ m $Y_r = -0{,}244$ m $Z_r = 0{,}000$ m
Mass moment of inertia with respect to a reference system with the origin in the center of the mass	$I_{xx} = 31{,}52$ kg m^2 $I_{yy} = 14{,}78$ kg m^2 $I_{zz} = 29{,}28$ kg m^2 $I_{xy} = I_{yz} = I_{xz} = 0$ kg m^2

Table 2 - Cabinet geometric-inertial characteristics

By indicating with *x(t)* the cabinet displacement and with F the restoring force exerted by each isolator, the cabinet motion equation is:

$$m\ddot{x} + 4F = 0 \tag{14}$$

The relative displacement between cabinet and ground is:

$$d(t) = x\ (t) - x_g(t) \tag{15}$$

The first simulations regard the cabinet dynamic behavior forced to vibrate by a harmonic ground acceleration:

$$\ddot{x}_g(t) = a_g \sin(\omega t) \tag{16}$$

where a_g is the ground horizontal acceleration amplitude. The corresponding ground displacement has the following form:

$$x_g(t) = -\frac{a_g}{\omega^2}\sin(\omega t) \tag{17}$$

The cabinet equation in term of relative motion is:

$$m\ddot{d} + 4F = -m\ddot{x}_g \tag{18}$$

Indicating with $a_{\max}$ and $a_{g,\max}$ the maximum amplitude of the cabinet acceleration and of the ground acceleration, respectively, in figure 14, the trend of the ratio $T_a = a_{\max}/a_{g,\max}$, versus the period T of the forcing ground acceleration, is reported. The diagram, obtained for a very small value of the ground acceleration ($a_g = g/10000$ m/s^2), reaches the maximum value for $T = 0.38$ s.

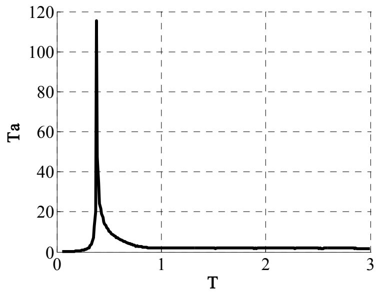

Figure 14 - T_a trend *for* $a_g = g/10000$ m/s^2

In figure 15, it can be seen the same diagram obtained for $a_g = g/10$ m/s^2 without (Fig.15a) and with (Fig.15b) the term proportional to the cube of the displacement. In the first case the maximum value of the ratio occurs for $T = 0.57$ s while, with the cube term, the maximum occurs for $T = 0.21$s and the curve is characterized by a non-linear behavior with a jump; it means that this value (point *c*) is reached only decreasing the forcing period. Increasing the forcing period the maximum T_a occurs for T= 0.45s (point b).

In the points *a* and *b* two fold bifurcations occur yielding a pair of symmetric limit cycles (one stable and the other one unstable). Two cyclic-fold bifurcations lead to jumps according to the circumstance that the responses for an increasing or decreasing frequency are different. In figure 15b the solid line represents the stable solutions and the dashed line represents the unstable ones. When the period increases the response jumps from *a* to *b*; similarly, the response jumps from *c* to *d* for a decreasing of forcing period.

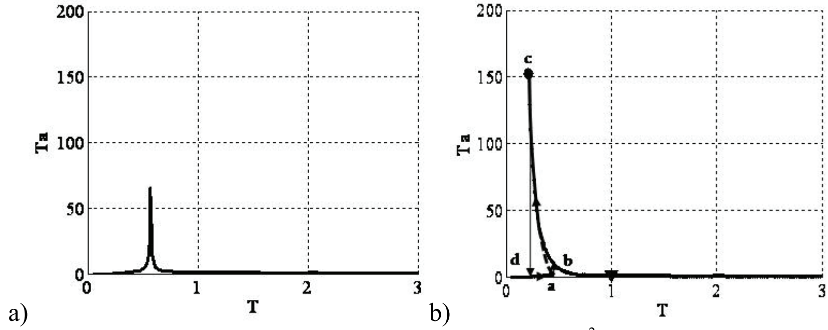

Figure 15 - T_a trend *for* $a_g = g/10$ m/s^2

In figure 16, the cycle obtained for the two above mentioned values of a_g are reported.

An approximate medium value of the isolators horizontal stiffness, k_h , was evaluated from the slopes of the two branches of the force-displacement cycle, in correspondence of the centered cabinet position.

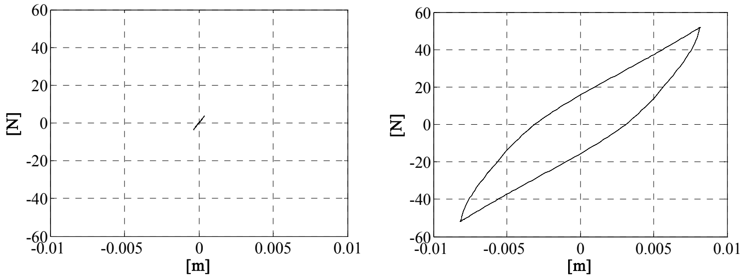

Figure 16 – Hysteretic cycle obtained for *b* and *c* conditions indicated in Fig .15b

In figure 17 are respectively reported two steady-state responses of the system for $T = 0.40$ s, obtained for different initial conditions; in particular, figure 17a is the time history while in figure 17b the correspondent stable limit cycles are reported in the phase space.

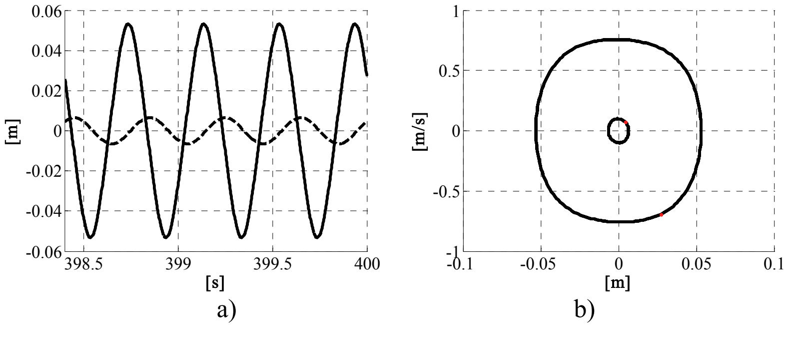

Figure 17 - Time history and limit cycles for T=0.40s and for two different initial conditions

Another typical consequence of the hardening behavior is that the natural system period decreases when the motion amplitude increases (Fig. 15b).

Other simulations were performed varying the ground acceleration amplitude for a fixed value of the forcing period to evaluate the influence of the stiffness increasing with the displacement.

For T = 0.45 s (Fig. 18) the T_a diagram is characterized by a “discontinuity”; for $a_{g,\max}$≈0.558m/s^2, T_a suddenly increases and then slowly decreases. In figure 19 two cycles respectively, for $a_{g,\max}$ = 0.55 m/s^2 and $a_{g,\max}$ = 0.57 m/s^2, are reported to highlight that in the neighborhood of this particular value, a small variation of $a_{g,\max}$ can produce a significant variation of the hysteresis cycles.

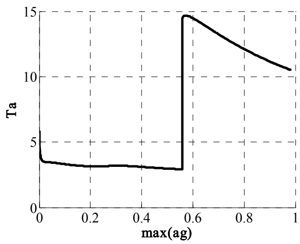

Figure 18

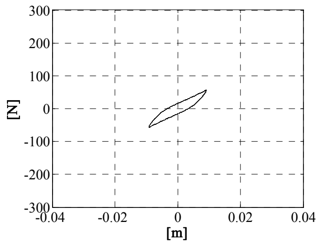

Figure 19a

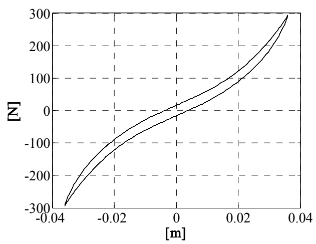

Figure 19b

In the figure 20, the cabinet free vibrations are reported for three different values of the rolling BTU friction coefficients (C_a = 0, C_a = 0.007 and C_a = 0.1). In all the cases the free motion is due to an initial condition on the position (x_0 = 0.02 m). In the last case, due to the high value of the friction coefficient the final cabinet position is different from the static equilibrium position. The intermediate C_a value is approximately equal to those ones experimentally relieved (v. Fig. 3).

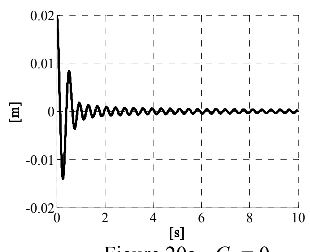

Figure 20a - C_a = 0

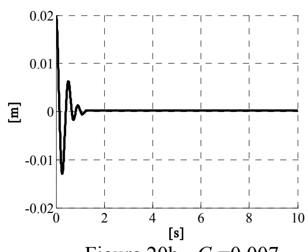

Figure 20b - C_a=0.007

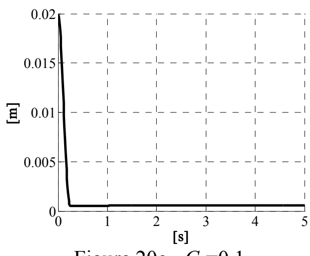

Figure 20c - C_a=0.1

The diagram of the dissipated energy E_d of the isolator, for different values of the ground displacement in the range [0 ; 0.02 m], is reported (Fig. 21). The expression of E_d was obtained in an analytical form with the procedure reported in the appendix. The proposed calculus of E_d is valid in the case of $n = 2$ (the value estimated for the isolator; see table 1).

It is interesting to note that for small oscillations around the static equilibrium position the dissipated energy is very small; then E_d increases linearly in function of the amplitude of the displacement.

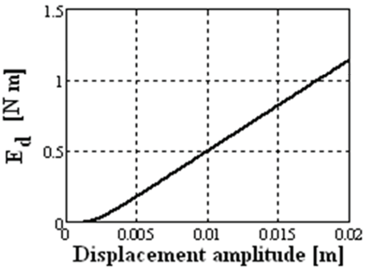

Figure 21 – Energy dissipation

Finally, an approximate medium value of the isolators horizontal stiffness, k_h , was evaluated from the slopes of the two branches of the force-displacement cycle (Fig. 16), in correspondence of the centered cabinet position .

For smaller values of a_g (Fig. 14), it results: $k_{hA} \approx 10000$ N/m, while for $a_g = g/10$ m/s^2 (Fig. 15a) $k_{hB} \approx 4200$ N/m; for a cabinet mass of 140 kg , the approximate values of the linearized natural periods are:

$$T_{hA} = 2\pi\sqrt{\frac{m}{4k_{hA}}} = 0.3717 \text{ s} \qquad ; \qquad T_{hB} = 2\pi\sqrt{\frac{m}{4k_{hB}}} = 0.5736 \text{ s}$$

These values are approximately equal to those corresponding to the maximum values of T_a for the two cases reported above. The maximum value of T_a , in the case of smaller values of a_g , is greater than the one obtained for $a_g = g/10$ m/s^2. This is due to the damping how it can be seen from the correspondent hysteretic cycles (Fig. 16).

6 CONCLUSIONS

- A seismic isolator prototype constituted of WRS and a BTU was realized and the first experimental tests were performed.
- In the paper, the analytical instruments have been developed to conduct a theoretical study of the isolator and to evaluate its isolating capacity. A Bouc-Wen model has been employed to describe the isolator wire rope restoring force; this model has been adopted in the motion equation of a cabinet suspended on this kind of isolator, to describe the dynamic behavior under different operational conditions.
- The results of the Bouc-Wen identification and the numerical simulations of an isolated cabinet are reported and discussed.

APPENDIX – Evaluation of the dissipated energy

The fourth equation of (6) can be divided, according to the sign of $\dot{x}(t)$ e $w(t)$, in the following equations:

$$\begin{array}{ll} w(t)\geq 0; \dot{x}(t)\geq 0 & \dot{w}(t)=\rho\dot{x}(t)\left[1-w(t)^n\right] \\ w(t)\leq 0; \dot{x}(t)\geq 0 & \dot{w}(t)=\rho\dot{x}(t)\left[1+(2\sigma-1)(-w(t))^n\right] \\ w(t)\geq 0; \dot{x}(t)\leq 0 & \dot{w}(t)=\rho\dot{x}(t)\left[1+(2\sigma-1)w(t)^n\right] \\ w(t)\leq 0; \dot{x}(t)\leq 0 & \dot{w}(t)=\rho\dot{x}(t)\left[1-(-w(t))^n\right] \end{array} \qquad \text{(I)}$$

Excluding the values for which the function $\dot{x}(t)$ assumes zero value, from (I) it is possible to obtain the derivative of the function $w(t)$ with respect to displacement, for the different traits of the cycle:

$$\begin{array}{ll} w(t)\geq 0; \dot{x}(t)> 0 & \dfrac{dw}{dx}=\rho\left[1-w(t)^n\right] \\ w(t)\leq 0; \dot{x}(t)> 0 & \dfrac{dw}{dx}=\rho\left[1+(2\sigma-1)(-w(t))^n\right] \\ w(t)\geq 0; \dot{x}(t)< 0 & \dfrac{dw}{dx}=\rho\left[1+(2\sigma-1)w(t)^n\right] \\ w(t)\leq 0; \dot{x}(t)< 0 & \dfrac{dw}{dx}=\rho\left[1-(-w(t))^n\right] \end{array} \qquad \text{(II)}$$

Eqs. (II) show that the derivatives are always positive and that, when the function $w(t)$ becomes zero they have the same value equal to ρ. By setting n = 2 it is possible to solve analytically the differential equations (II) by the method of separation of variables:

$$\begin{array}{ll} w(t)\geq 0; \dot{x}(t)\geq 0 & w_+^l(t)=\tanh\left[\rho(x(t)+c_+^l)\right] \\ w(t)\leq 0; \dot{x}(t)\geq 0 & w_-^l(t)=\dfrac{1}{\sqrt{2\sigma-1}}\tan\left[\rho\sqrt{2\sigma-1}(x(t)+c_-^l)\right] \\ w(t)\geq 0; \dot{x}(t)\leq 0 & w_+^u(t)=\dfrac{1}{\sqrt{2\sigma-1}}\tan\left[\rho\sqrt{2\sigma-1}(x(t)+c_+^u)\right] \\ w(t)\leq 0; \dot{x}(t)\leq 0 & w_-^u(t)=\tanh\left[\rho(x(t)+c_-^u)\right] \end{array} \qquad \text{(III)}$$

where the notations l and u are referred to the loading and unloading phases respectively (i.e. they are referred to the sign of the function $\dot{x}(t)$ and the notations + and - are referred to the sign of the function $w(t)$).

When $w(t)$ becomes zero, the functions corresponding to the loading and unloading phases have the same value, therefore:

$$c_+^l=c_-^l=c^l$$
$$c_+^u=c_-^u=c^u$$

If the time series of the displacement is a *wave T-periodic function* (i.e. continuous in the interval [0, +∞[and periodic with a period $T > 0$), the following equations are valid:

$$\max(w(t)) = \max(w_+^l(t)) = \tanh\left[\rho(X_{\max} + c^l)\right] = \max(w_+^u(t)) = \frac{1}{\sqrt{2\sigma - 1}} \tan\left[\rho\sqrt{2\sigma - 1}(X_{\max} + c^u)\right]$$

$$\min(w(t)) = \min(w_-^l(t)) = \frac{1}{\sqrt{2\sigma - 1}} \tan\left[\rho\sqrt{2\sigma - 1}(X_{\min} + c^l)\right] = \min(w_-^u(t)) = \tanh\left[\rho(X_{\min} + c^u)\right]$$

and:

$$\begin{cases} \tanh\left[\rho(X_{\max} + c^l)\right] - \dfrac{1}{\sqrt{2\sigma - 1}} \tan\left[\rho\sqrt{2\sigma - 1}(X_{\max} + c^u)\right] = 0 \\ \dfrac{1}{\sqrt{2\sigma - 1}} \tan\left[\rho\sqrt{2\sigma - 1}(X_{\min} + c^l)\right] - \tanh\left[\rho(X_{\min} + c^u)\right] = 0 \end{cases} \tag{IV}$$

where X_{max} and X_{min} are the maximum and minimum values of the displacement.

The (IV) is a system of two equations with two variables; hence, it is possible to numerically find the following functions:

$$c^u = f_u(X_{\max}, X_{\min}, \rho, \sigma)$$
$$c^l = f_l(X_{\max}, X_{\min}, \rho, \sigma)$$

The dissipated energy is expressed by the area enclosed by hysteretic loops, besides in the Bouc –Wen model only the response of the hysteretic term dissipates energy [4], hence the dissipated energy E_d is given by the cyclic integral of $w(t)$ particularized along the different intervals:

$$E_d = k_w \left[\int_{-c^l}^{X_{\max}} w_+^l(x)dx - \int_{-c^u}^{X_{\max}} w_+^u(x)dx - \int_{X_{\min}}^{-c^u} w_-^u(x)dx + \int_{X_{\min}}^{-c^l} w_-^l(x)dx \right].$$

Solving the integrals, we obtain:

$$E_d = k_w \left\{ \left[x - \frac{\log(\tanh(\rho(x + c^l)) + 1)}{\rho} \right]_{-c^l}^{X_{\max}} - \left[\frac{\log(\tan^2(\rho\sqrt{2\sigma - 1}(x + c^u)) + 1)}{2\rho(2\sigma - 1)} \right]_{-c^u}^{X_{\max}} + \right.$$
$$\left. - \left[x - \frac{\log(\tanh(\rho(x + c^u)) + 1)}{\rho} \right]_{X_{\min}}^{-c_u} + \left[\frac{\log(\tan^2(\rho\sqrt{2\sigma - 1}(x + c^l)) + 1)}{2\rho(2\sigma - 1)} \right]_{X_{\min}}^{-c^l} \right\}$$

or also:

$$E_d = k_w \left\{ \left[X_{\max} + c^l - \frac{\log(\tanh(\rho(X_{\max} + c^l)) + 1)}{\rho} \right] - \left[\frac{\log(\tan^2(\rho\sqrt{2\sigma - 1}(X_{\max} + c^u)) + 1)}{2\rho(2\sigma - 1)} \right] + \right.$$
$$\left. - \left[-c^u - X_{\min} + \frac{\log(\tanh(\rho(X_{\min} + c^u)) + 1)}{\rho} \right] + \left[- \frac{\log(\tan^2(\rho\sqrt{2\sigma - 1}(X_{\min} + c^l)) + 1)}{2\rho(2\sigma - 1)} \right] \right\} \tag{V}$$

The (V) expresses the dissipated energy as a function of the parameters that characterize the hysteresis cycle:

$$E_d = g(X_{\max}, X_{\min}, \rho, \sigma) \tag{VI}$$

Thus, the preliminary design of hysteretic systems is considerably facilitated.

REFERENCES

[1] Y.Q. Ni, J. M. Ko, C. W. Wong - Identification of non-linear hysteretic isolators from periodic vibration tests - *Journal of Sound and Vibration* - 1998 Vol. 217(4), 737-756.

[2] G.F. Demetriades, M.C. Constantinou, A.M. Reinhorn – Study for wire rope systems for seismic protection of equipment in buildings – Eng. Struct.– 1993 Vol.15, n.5.

[3] F. Ikhouane, J. Rodellar – On the hysteretic Bouc-Wen model, part I – *Nonlinear Dynamics*, 2005.

[4] A.E. Charalampakis, V.K. Koumousis - On the response and dissipated energy of Bouc–Wen hysteretic model - *Journal of Sound and Vibration* 309 (2008) 887–895.

[5] M. Ismail, F. Ikhouane, J. Rodellar - The Hysteresis Bouc-Wen Model, a Survey – *Arch. Comput. Methods Eng* (2009) 16: 161–188.

Proceedings of MUSME 2011, the International Symposium
on Multibody Systems and Mechatronics
Valencia, Spain, 25-28 October 2011

OPTIMAL DIMENSIONAL SYNTHESIS OF LINKAGES USING EXACT JACOBIAN DETERMINATION IN SQP ALGORITHM

Ramon Sancibrian*, Ana de Juan*, Angel Sedano†, Pablo Garcia*, Miguel Iglesias*, Fernando Viadero*, Alfonso Fernandez*

* ETSIIT
University of Cantabria, Avda. De los Castros s/n, 39005 Santander, Spain
e-mail: `sancibrr@unican.es`,
`web page: http://grupos.unican.es/ingmec/`

† MTOI
C/ Maria Viscarret 1, Ártica (Berrioplano), 31013 Navarra, España

Keywords: Kinematic Synthesis, Dimensional Synthesis, Mechanism Design, Computational Kinematics.

Abstract. *This paper presents a general method for the dimensional synthesis of mechanisms. This method is based on the well-known Sequential Quadratic-Programming algorithm (SQP). However, several modifications have been introduced in order to improve the robustness and efficiency of the method. One of these modifications in the improved SQP approach is the use of the exact Jacobian instead finite differences (FD) methods. The paper explains how to obtain the Jacobian for any structural kinematic chain. Furthermore, the method introduces several steps in order to prepare the mechanism to be optimized. These steps consist in the translation, rotation and scaling of the mechanism to be designed. Furthermore, the formulation implemented in the algorithm avoids singular configurations providing greater robustness than the conventional approach. In the paper several examples are provided to demonstrate the main characteristics of the method.*

1 INTRODUCTION

Dimensional synthesis of mechanisms involves obtaining the geometry parameters of a chosen kinematic chain to allow the mechanism to perform a given task. Different tasks can be established leading to the three different problems defined in the literature [1-3]. These are: function generation, path generation and rigid-body guidance. This does not mean that there are no other problems besides those established in the basic literatures [4-6], but these are the most frequently studied by the engineers in this field. In all of them the definitions of the prescribed points or poses, through which the tracking point must pass, are necessary. The parameters defining the prescribed positions or poses are called the objective or the desired ones, because the quality of the solution is measured by how close the generated motion is to the desired one. The generated parameters are given by the generated linkage, obtained during the successive iterations searching for the optimal solution.

Several publications in mechanism optimization can be found in the literature [7-15]. These methods are based on both deterministic and stochastic procedures. In all these works different approaches have been considered to minimize an objective function which is established as the difference between the desired and generated parameters. Some of these approaches use classical optimization algorithms to obtain the solution [7-11]. Other methods consider the necessary deformation of the mechanism to achieve the prescribed points [12-13]. Thus, they minimize the linkage deformation energy to obtain the solution.

An important issue always present in synthesis problems is how to compare the desired and generated function. Different techniques have been developed to solve this problem in the literature. For instance, Fourier descriptors have been used in closed path problems [14]. Other authors try to establish the global properties of the curves in order to avoid the influence of the translation and rotation [15].

The effect of singular configurations during the optimization process is another problem that should be solved. There are a few papers dealing with this point in the literature. For instance, [16] tries to avoid singularities introducing angular stiffness based on the deformation approach, or in [5] the authors use the control of the norm to solve this problem.

The study of the aforementioned problems is crucial in obtaining a good rate of convergence. The efficiency of the method can be reduced if all these points are not tackled in a suitable way. In this paper the SQP method is used to search for the optimum. This method is well suited to general nonlinear constrained optimization problems and was first studied during the sixties by Wilson [17], and a great deal of research has been devoted to this class of methods since that time. For instance, one important contribution to the SQP method is provided by Schittkowski [18]. One of the main drawbacks of the SQP method appears when it is not possible to obtain a differentiable objective function. In this case the algorithm loses efficiency and robustness.

In the method proposed here, the kinematic synthesis is formulated to solve the aforementioned problems. Mixed coordinates are used to ensure that the method is general (relative coordinates for closed-loop chains and absolute coordinates for reference points). The synthesis problem is treated as a standard equality constrained optimization where inequality constraints are added to solve some particular characteristics of the mechanism to be synthesized. The comparison between the generated and desired function is done by three previous steps which are called translation, rotation and scaling. Singular configurations are avoided during the optimization process by including a special formulation based on the value of the determinant of the Jacobian. In the following section we present a discussion of the new formulation applied to the kinematic synthesis as well as the differentiation procedure to obtain the exact Jacobian.

2 PROBLEM FORMULATION

The proposed method belongs to the category of dimensional synthesis and its goal is to develop a linkage fulfilling a set of desired parameters which are established by the analyst. Since the methodology is approximate (the solution will not be exact) some of these requirements will be fulfilled with more accuracy than others. In the proposed formulation, design requirements are introduced as constraints. By constraints we mean a set of equations whose violation is forbidden during the optimization process. This is done in order to fulfill some geometrical conditions governing the kinematic behavior of the mechanism to be designed. Thus, we can express the constraints as follows,

$$\mathbf{\Phi}\left[\mathbf{q}_i(\mathbf{w}),\mathbf{w}\right]=0 \tag{1}$$

where vector $\mathbf{q}_i$ represents the dependent coordinates, vector **w,** the dimensions of the linkage or the so-called design variables and *i* indicates the linkage position. That is,

$$\begin{aligned}\mathbf{w}^T &= \left[L_1\ L_2 \ldots\right] \\ \mathbf{q}_i^T &= \left[\theta_1\ \theta_2 \ldots x_1\ y_1 \ldots\right]_i\end{aligned} \tag{2}$$

Different types of coordinates can be used in Eq.(2) i.e. natural, relative, mixed, etc. If the whole motion of the linkage is considered Eq.(1) can be reformulated as follows,

$$\mathbf{\Phi}\left[\mathbf{q}(\mathbf{w}),\mathbf{w}\right]=0 \tag{3}$$

where,

$$\mathbf{q}^T = \left[\mathbf{q}_1^T\ \mathbf{q}_2^T \ldots \mathbf{q}_p^T\right] \tag{4}$$

In Eq.(4) the subscript *p* stands for the number of prescribed poses. Due to the dependence of coordinates on the design parameters, the constraints can be expressed as,

$$\mathbf{\Phi}(\mathbf{w})=0 \tag{5}$$

However, the analyst should never forget the dependence that Eq.(5) has on the dependent coordinates.

The constraint equations have different forms depending on the particular problem to be solved. Furthermore, in the same problem different kinds of constraint can be found. For instance, kinematic constraints are those governing the kinematics of the mechanism whereas synthesis constraints give the synthesis conditions that must be fulfilled during the optimization process. Furthermore, there could be some additional constraints giving some special condition in the mechanism including limitations in weight, size, etc. This type of constraint is normally defined by means of inequalities. However, they can be transformed into equality constraints by using the so-called slack variables [19]. In the proposed method all these constraints can be formulated as the vector given by Eq.(5).

The synthesis error must assess how far the desired parameters are from the generated ones. It can be formulated as follows,

$$\mathbf{\Pi}(\mathbf{w})=\boldsymbol{\delta}_g-\boldsymbol{\delta}_d=0 \tag{6}$$

where $\boldsymbol{\delta}_g$ represents the generated parameters and $\boldsymbol{\delta}_d$ the desired ones. The norm of the error is the objective function and it should be minimized to solve the synthesis problem as follows,

$$minimization \quad F=\frac{1}{2}\left\|\mathbf{\Pi}(\mathbf{w})\right\| \tag{7}$$

The stationary condition for Eq.(7) is,

$$\mathbf{\Pi}_w^T \mathbf{\Pi} = 0 \tag{8}$$

where,

$$\mathbf{\Pi}_w = \frac{\partial \mathbf{\Pi}}{\partial \mathbf{w}} \tag{9}$$

Quadratic Programming (QP) is the heart of the SQP algorithm. The QP subproblem employed in the SQP algorithm is based on expanding the objective function quadratically about the current design point. In contrast, the constraints are expanding linearly. Thus the subproblem can be formulated as follows,

$$\begin{aligned} &\textit{Minimize} \quad \tilde{F}(\Delta\mathbf{w}) = F(\mathbf{w}_j) + \nabla\mathbf{F}(\mathbf{w}_i)^T \Delta\mathbf{w}_i + \frac{1}{2}\Delta\mathbf{w}_j{}^T \nabla^2 \mathbf{F}(w_j)\Delta\mathbf{w}_j \\ &\textit{Subject to} \quad \tilde{\mathbf{\Phi}}(\Delta\mathbf{w}) = \mathbf{\Phi}(\mathbf{w}_j) + \nabla\mathbf{\Phi}(\mathbf{w}_i)\Delta\mathbf{w}_i = 0 \end{aligned} \tag{10}$$

where j stands for the iteration step. In Eq.(10), the term $\nabla\mathbf{F}(\mathbf{w})$ is the Jacobian and $\nabla^2\mathbf{F}(\mathbf{w}_j)$ is the Hessian matrix. In an actual implementation the real Hessian is not used. Instead a metric **H** is used that is updated in each iteration. Several researchers [19, 20] have shown that the BFGS update for the Hessian provides an efficient implementation of the SQP method. The accuracy in determining the Jacobian is of the utmost importance because errors in its estimation could lead to an important loss in efficiency and robustness. Numerical approaches such as Finite differences can be used; however, exact differentiation provides better results. If the numerical approach is used, the errors involved in computation could lead to a less accurate search direction, using more computational time to achieve the optimal solution. On the other hand, methods based on exact differentiation require differentiable expressions within the range of interest. The use of exact differentiation has enormous advantages in the algorithm accuracy and improves the efficiency. In dimensional synthesis the number of prescribed conditions is limited when a large number of variables are involved because more computations are necessary to obtain derivatives. When a large number of design variables or precision poses are involved the optimization process can be too slow, or even stop without achieving the optimal solution. In this paper exact differentiation is used to obtain the Jacobian. To do that the following formulation is proposed,

$$\nabla\mathbf{F}(\mathbf{w}) = \frac{\partial F}{\partial \mathbf{w}} = \mathbf{\Pi}_q \frac{\partial \mathbf{q}}{\partial \mathbf{w}} = \mathbf{\Pi}_q \mathbf{q}_w \tag{11}$$

where $\mathbf{q}_w$ can be obtained from the constraints. That is,

$$\mathbf{q}_w = -\frac{\partial \mathbf{\Phi}}{\partial \mathbf{q}}^{-1} \frac{\partial \mathbf{\Phi}}{\partial \mathbf{w}} = \mathbf{\Phi}_q^{-1}\mathbf{\Phi}_w \tag{12}$$

where $\mathbf{\Phi}_q$ is the matrix of partial derivatives of the constraint equations with respect to the dependent coordinates, and $\mathbf{\Phi}_w$ is the matrix of partial derivatives of the same equation with respect to the design variables. Vector $\mathbf{q}_w$ contains the elements of the Jacobian. Thus, to obtain the Jacobian matrix it is necessary to compute the derivatives of the constraints. The formulation proposed allows the computations of matrixes $\mathbf{\Phi}_q$ and $\mathbf{\Phi}_w$ in an exact form, and therefore, the calculation of $\mathbf{q}_\mathbf{w}$ is done directly from these matrixes. Once the Jacobian is determined, the SQP algorithm provides the descent direction and the step size. Thus, the increment in the vector of the design variables $\Delta\mathbf{w}$ is obtained for the j iteration. However, an optimization strategy should be included in the algorithm in order to succeed.

3 OPTIMIZATION STRATEGY

The optimization includes a strategy to improve the efficiency and robustness of the method by means of: 1) reducing the error between the desired and generated values at the beginning of the iterations, 2) avoiding the singular positions of the mechanism during the optimization process and 3) verifying the assembly when the design parameters are modified.

In order to reduce the error between the desired and generated values three steps are included before starting the dimensional synthesis process. They are: translation, rotation and scaling. To do so, some design variables are added to form a new vector. That is,

$$\mathbf{w}^T = \left[\mathbf{w}_t^{\ T}\ \mathbf{w}_r^{\ T}\ \mathbf{w}_s^{\ T}\ \mathbf{w}^T \right] \tag{13}$$

where subscripts t, r and s stand for translation, rotation and scaling, respectively. The translation and rotation variables do not affect the dimensions of the links. These parameters only change the position of the mechanism in order to find the best relative position with respect to the desired parameters. The scaling variable is a scale factor multiplying all the dimensions of the linkage. Thus, the form of the output function is not modified, only scaled. With these new design variables the optimization process is used sequentially step by step.

The determinant of the constraint equation Jacobian is used to avoid the singular positions of the mechanisms. Singular positions appear when the following condition is fulfilled,

$$det(\mathbf{\Phi}_q) = 0 \tag{14}$$

This condition occurs when $\mathbf{\Phi}_{\mathrm{q}}$ is rank deficient. That means that the mechanism is in a bifurcation point and the mechanism can take any of the two branches. For this reason this situation must be avoided. To do so, Eq.(14) is introduced as an inequality constraint,

$$det(\mathbf{\Phi}_q) < \varepsilon_s \tag{15}$$

where ε_{s} is a small number.

Finally, once the new dimensions are obtained during the optimization process the analysis of the mechanism must be done. For any specified position i, Eq.(1) represents a nonlinear system of equations in $\mathbf{q}_i$. The analysis of the mechanisms consists in solving this system to ensure that it is always equal to zero. The synthesis process ensures the fulfillment of the constraints given by Eq.(5). However, if the step size is too long, the synthesis process could lead to situations where Eq.(1) is not fulfilled. This means that the dimensions of the mechanisms are such that it cannot be assembled for that position. To ensure that the new dimensions produce a linkage that can be assembled, the following inequality constraint is defined,

$$\left\| \Phi(\mathbf{q}_i \mathbf{w}) \right\| < \varepsilon_c \tag{16}$$

where ε_c is a tolerance. If Eq.(16) is not fulfilled, the step size should be reduced until the adequate assembly of the linkage occurs.

4 NUMERICAL RESULTS

In the following paragraphs the definitions of two mechanisms are described based on the aforementioned formulation. Closed-loop constraints are used because this formulation provides both a low number of dependent coordinates and small size in the Jacobian matrix.

4.1 Example 1

In example 1, a function generation problem for one-input/one-output is considered. The mechanism here is the Stephenson III as shown in Figure 1. The input link is number two and the output link is number six. Kinematic constraints are formulated for each prescribed pose in the following way,

$$\Phi_i = \begin{Bmatrix} L_1 \cos\theta_1 + L_2 \cos(\theta_{20} + \theta_{2i}) - L_3 \cos\theta_{3i} - L_4 \cos\theta_{4i}; \\ L_1 \sin\theta_1 + L_2 \sin(\theta_{20} + \theta_{2i}) - L_3 \sin\theta_{3i} - L_4 \sin\theta_{4i}; \\ -L_4 \cos\theta_{4i} + L_5 \cos\theta_5 + L_6 \cos\theta_{6i} + L_7 \cos\theta_{7i} - L_8 \cos(\theta_{3i} - \beta_1); \\ -L_4 \sin\theta_{4i} + L_5 \sin\theta_5 + L_6 \sin\theta_{6i} + L_7 \sin\theta_{7i} - L_8 \sin(\theta_{3i} - \beta_1); \end{Bmatrix} = \mathbf{0}; \quad i = 1,2,...p \tag{17}$$

The desired output function is defined as,

$$\boldsymbol{\delta}_d = \begin{cases} \frac{\pi}{15}[1 - \cos(2\theta_2)]; & 0 \geq \theta_2 \geq \frac{2\pi}{4} \\ \frac{\pi}{15}; & \frac{2\pi}{4} > \theta_2 \geq \frac{3\pi}{4} \\ \frac{\pi}{15}[1 - \cos(2\theta_2)]; & \frac{3\pi}{4} > \theta_2 \geq 2\pi \end{cases} \tag{18}$$

This function can be divided into three parts: rise, dwell and return. The number of prescribed poses defining the I/O function is 30. The vector of design variables is,

$$\mathbf{w}^T = [L_1\ L_2\ L_3\ L_4\ L_5\ L_6\ L_7\ L_8\ \beta_1\ \theta_1\ \theta_5\ \theta_{20}]; \tag{19}$$

and the dependent coordinates,

$$\mathbf{q}_i^T = [\theta_{3i}\ \theta_{4i}\ \theta_{6i}\ \theta_{7i}] \tag{20}$$

In this function generation, the problem's translation is not necessary so only rotation and scaling is used as previous steps.

The first column of Table 1 shows the initial guess values for the design parameters. The second and third columns give the values of the design parameters at the convergence for the conventional SQP and the improved approach, respectively.

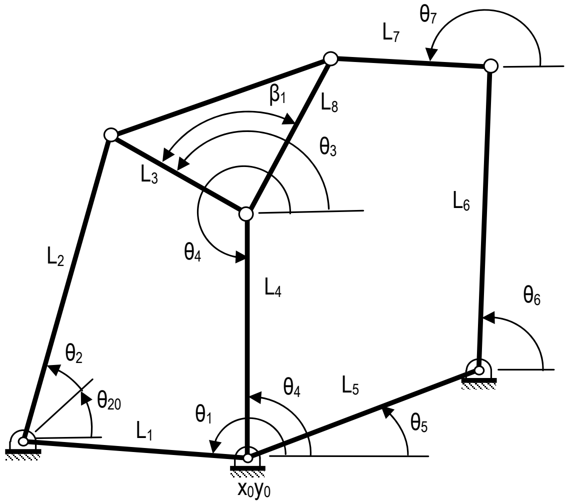

Figure 1: Stephenson III linkage

	Initial guess	Conventional SQP (Convergence)	Improved SQP (Convergence)
L1 (mm)	101.98	77.30	104.12
L2 (mm)	30.00	29.00	13.54
L3 (mm)	100.49	155.94	128.91
L4 (mm)	60.00	107.45	46.09
L5 (mm)	126.49	144.31	133.02
L6 (mm)	160.00	151.46	92.99
L7 (mm)	136.01	129.05	193.12
L8 (mm)	50.00	29.17	74.04
β (mm)	-210.85	-218.32	-58.67
θ_1 (deg)	29.44	103.70	288.77
θ_5 (deg)	18.33	-154.80	133.02
θ_{20} (deg)	90.00	65.04	125.48

Table 1: Design variables for the initial guess mechanism and final linkages.

Figure 2a shows the structural error for the initial guess mechanism and the solutions. In this figure, it is easy to see how the improved SQP achieves an accurate solution. On the other hand, the conventional SQP presents an inaccurate result. This is because the mechanism reached a singular configuration during the optimization process. Thus, the linkage could not evolve beyond this point. Figure 2b shows the objective function together with the solutions. Table 2 gives the values for the optimization process. The number of iterations is lower for the conventional approach. This is because the optimization process stops when the singular configuration is reached. Table 2 also shows the number of evaluations of the objective function and its value at convergence.

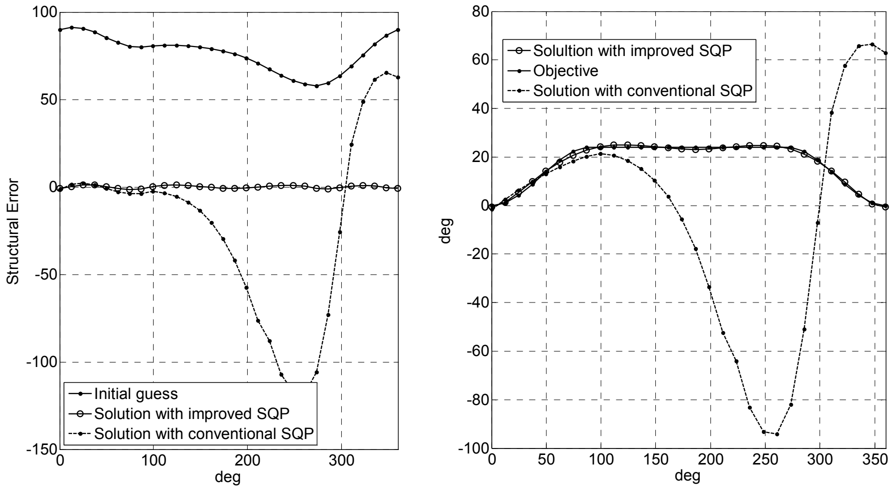

a) b)

Figure 2: a) Structural Error for initial guess and the solutions and b) objective and generated functions.

	Conventional SQP	Improved SQP
Iterations	882	983
F-value	91698	0.00214353
F-evaluations	327342	131844

Table 2: Comparative values of the two approaches in Example 1

4.2 Example 2

In this example a path generation problem is considered. Figure 3 shows the scheme of the four-bar mechanism used in this example. The coupler point 4, indicated by its Cartesian coordinates (x_4, y_4) in the Figure, is used to generate the path. The kinematic constraints are the following,

$$\mathbf{\Phi} = \begin{Bmatrix} L_1 \cos\theta_1 - L_2 \cos(\theta_1 + \theta_{20} + \theta_2) + L_3 \cos\theta_3 + L_3 \cos\theta_3 \\ L_1 \sin\theta_1 - L_2 \sin(\theta_1 + \theta_{20} + \theta_2) + L_3 \sin\theta_3 + L_3 \sin\theta_3 \\ x_4 - x_0 - L_1 \cos\theta_1 + L_2 \cos(\theta_1 + \theta_{20} + \theta_2) - L_5 \cos(\theta_5 + \beta) \\ y_4 - y_0 - L_1 \sin\theta_1 + L_2 \sin(\theta_1 + \theta_{20} + \theta_2) - L_5 \sin(\theta_5 + \beta) \end{Bmatrix} = \mathbf{0} \tag{21}$$

The vectors of design variables and dependent coordinates are,

$$\begin{aligned} \mathbf{w}^T &= [x_0 \; y_0 \; \theta_1 \; \theta_{20} \; L_1 \; L_2 \; L_3 \; L_4 \; L_5 \; \beta] \\ \mathbf{q}_i^T &= [\theta_{3i} \; \theta_{4i} \; x_{4i} \; y_{4i}] \end{aligned} \tag{22}$$

The desired path is an elipse which is given by,

$$\boldsymbol{\delta}_d = \begin{Bmatrix} x_{4d} = 10 + 60\cos(\theta_d) \\ y_{4d} = 140 + 30\sin(\theta_d) \end{Bmatrix} \quad 0 \le \theta_d \le 2\pi \tag{23}$$

The Grashof condition is imposed in order to obtain full rotation in the input link. Table 3 shows the values of the design parameters at the convergence for the initial guess, conventional SQP and improved approach. Table 4 shows the comparative values at the convergence. Due to the use of the exact Jacobian, the improved SQP approach achieves convergence with a lower number of iterations and function evaluations. Furthermore, the accuracy achieved is greater than that obtained with the conventional method.

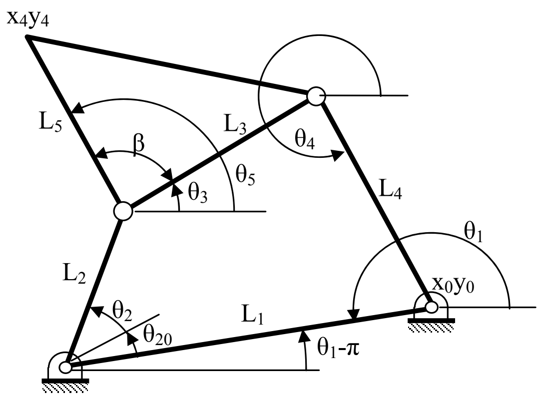

Figure 3: Four-bar linkage

	Initial guess	Conventional SQP (Convergence)	Improved SQP (Convergence)
x_0 (mm)	0	-441.31	111.4866
y_0 (mm)	0	-1225.40	2587.20
θ_1 (deg)	180	23.69	24.323
θ_{20} (deg)	0	90.02	69.422
L1 (mm)	100	452.963	2.39E+07
L2 (mm)	40	2.37E+07	597.793
L3 (mm)	92.19	150.253	2.29E+07
L4 (mm)	60.82	23690000	3.14E+07
L5 (mm)	72.80	150.253	8685349
β (deg)	93.41	291.30	-49.19

Table 3: Design variables for the initial guess mechanism and final solutions.

	Conventional SQP	Improved SQP
Iterations	2753	1575
F-value	3.81	1.81E-03
F-evaluations	254860	148170

Table 4: Comparative values of the two approaches in Example 2

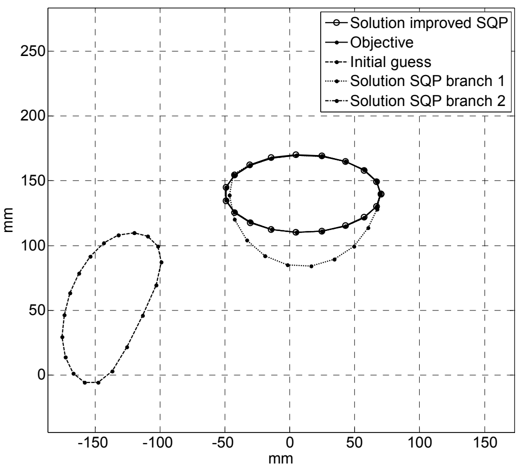

Figure 4: Generated, desired and obtained paths

Figure 4 shows the results obtained with the conventional and improved approaches. The improved SQP approach provides the best solution (see the F-value in second column of Table 4) and is coincident with the desired path. The linkage obtained with the conventional approach has a singular position and for this reason two branches can be obtained. One of the branches has good accuracy (see the F-value in the first column of Table 4) and is almost coincident with the desired path. The other branch provides a greater error and therefore can not be considered adequate. In any case, a mechanism with a singular configuration providing two branches cannot be considered because it is not possible to control which branch is followed by the linkage during the motion. When the improved SQP approach is used the solution is always free of singularities due to the formulation implemented.

4.3 Example 3

In this case, the same four-bar linkage as in the previous example has been used. Thus, the constraints, the design variables and dependent coordinates are the same. However, the objective path is a square angle which is a difficult curve to generate. Figure 5 shows the objective path together with the initial guess and the solution provided by the improved SQP approach. The conventional SQP algorithm falied to find out the optima and for this reason did not achieve convergence. Thus, the results for the conventional approach are not shown in the paper. The third column of Table 5 shows the values of the design parameters at the convergence. Table 6 gives the number of iterations, the value of the objective function and the number of the evaluation when the algorithm achieves convergence.

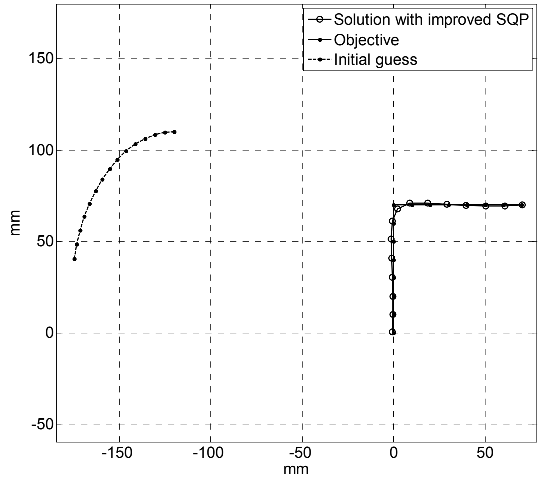

Figure 5: Generated, initial guess and objective paths.

	Initial guess	Improved SQP (Convergence)
x_0 (mm)	0	-298.00
y_0 (mm)	0	380.69
θ_1 (deg)	180	348.43
θ_{20} (deg)	0	135.57
L1 (mm)	100	433.14
L2 (mm)	40	72.20
L3 (mm)	92.19	229.52
L4 (mm)	60.82	277.10
L5 (mm)	72.80	287.29
β (deg)	93.41	54.40

Table 5: Design variables for the initial guess mechanism and the improved approach.

	Improved SQP
Iterations	2743
F-value	1.35E-08
F-evaluations	200887

Table 6: Numerical values obtained in Example 3

5 CONCLUSIONS

In this paper an improved SQP algorithm has been presented. The improved approach provides greater efficiency and robustnes than the conventional one. This is mainly because the Jacobian is obtained using exact differentiation. However, some other strategies are included in the algorithm, to reduce the error prior to the optimization process namely, translation, rotation and scaling of the mechanism. Furthermore, an inequality constraint is included in order to avoid singular configurations during the optimization. The examples show that the method achieves convergence with a lower number of iterations and function evaluations. In all cases the solution has a good accuracy and the generated function fits very well with the desired one. In the three examples the improved SQP achieves the convergence free of singularities, whereas the conventional method fails when the objective function requires a large number of iterations.

ACKNOWLEDGEMENT

This paper has been developed in the framework of the Project DPI2010-18316 funded by the Spanish Ministry of Education and Science.

REFERENCES

[1] A.G. Erdman,; G.N. Sandor, 1997: Mechanism design: analysis and synthesis. Upper Saddle River, New Jersey: Prentice-Hall

[2] C.H. Suh, C.W. Radcliffe, Kinematics and mechanisms design, Willey, New York, 1978.

[3] J.J. Uicker, G.R. Pennock, S.E. Shigley, Theory of Machines and Mechanisms, Oxford University Press, 2011.

[4] J. Angeles, A. Alivizatoss and R. Akhras, An unconstrained nonlinear least-square method of optimization of RRRR planar path generators, Mechanism and Machine Theory 23 (5), 343-353, 1988.

[5] J.F. Collard, Geometrical and Kinematics optimization of closed-loop multibody systems, Ph.D. Thesis, Catholic University of Louvain, 2007.

[6] A. Perez and J. M. McCarthy, Clifford Algebra Exponentials and Planar Linkage Synthesis Equations, J. Mech. Des. 127(5), 931-940, 2005.

[7] J. M. Jimenez, G. Alvarez, J. Cardenal, and J. Cuadrado. A simple and general method for kinematic synthesis of spatial mechanisms. Mechanism and Machine Theory 32(3), 323–341, 1997.

[8] E.C. Kinzel, J. P. Schmiedeler, and G. R. Pennock, Kinematic Synthesis for Finitely Separated Positions Using Geometric Constraint Programming, J. Mech. Des. 128(5), 1070-1079, 2006.

[9] X. Du, P.K. Venigella, D. Liu, Robust mechanism synthesis with random and interval variables, Mechanism and Machine Theory, Volume 44, Issue 7, July 2009, Pages 1321-1337

[10] D. Mundo, G. Gatti, D.B. Dooner, Optimized Five-bar linkages with non-circular gear for exact path generation, Mechanism and Machine Theory, 44(4) 751-760, 2009.

[11] N. Diab, A. Smaili, Optimum exact/approximate point synthesis of planar mechanism, Mechanism and Machine Theory 43(12) 1610-1624, 2008.

[12] R. Avilés, J. Vallejo, I. Fernández de Bustos, J. Aguirrebeitia, G. Ajuria, Optimum synthesis of planar linkages using a strain-energy error function under geometric constraints, Mechanism and Machine Theory, Volume 45, Issue 1, January 2010, Pages 65-79.

[13] R. Avilés, A. Hernández, E. Amezua, O. Altuzarra, Kinematic analysis of linkages based in finite elements and geometric stiffness matrix, Mechanism and Machine Theory, Volume 43, Issue 8, August 2008, Pages 964-983

[14] I. Ullah, S. Kota, Optimal synthesis of mechanisms for path generation using Fourier Descriptors and global search methods, Journal of Mechanical Design 119(4) 504-519, 1997.

[15] A. Smaili, N. Diab, Optimum synthesis of hybrid-task mechanisms using ant-gradient search method, Mechanism and Machine Theory 42(1) 115-130, 2007.

[16] F. C. Park, J. W. Kim, Singularity analysis of closed kinematic chains, Journal of Mechanical Design, 121, 32-38, 1999.

[17] R. B. Wilson, A simplical algorithm for concave programming. Doctoral Thesis, Graduate School of Business Administration. Harvard University, Boston, 1963.

[18] K. Schittkowski, www.ai7.uni-bayreuth.de/refercs.htm

[19] P.E. Gill, W. Murray, M.H. Wright, 1981: Practical optimization. New York: Academic Press

[20] M.C. Biggs, Constrained minimization using recursive quadratic programming: some alternate subproblem formulation, towards global optimization, 341-349, 1975.

Proceedings of MUSME 2011, the International Symposium
on Multibody Systems and Mechatronics
Valencia, Spain, 25-28 October 2011

ASSEMBLY MODE CHANGE OF SPHERICAL 3-R$\underline{P}$R PARALLEL MANIPULATOR

Mónica Urízar[*] and Manfred L. Husty[†]

[*] Faculty of Engineering in Bilbao
University of the Basque Country, Department of Mechanical Engineering, Alameda de Urquijo s/n, 48013 Bilbao, Spain
e-mail: `monica.urizar@ehu.es`,
`web page: http://www.ehu.es/compmech`

† Institute of Basic Sciences in Engineering
University Innsbruck, Unit Geometry and CAD, Technikerstrasse 13, 6020 Innsbruck, Austria
e-mail: `manfred.husty@uibk.ac.at`,
`web page: http://geometrie.uibk.ac.at`

Keywords: spherical parallel manipulator, Direct Kinematic Problem, kinematic image space, non-singular transition.

Abstract. *In this paper, the authors will investigate the spherical 3-R$\underline{P}$R parallel manipulator, focusing on the feasibility of performing non-singular transitions between different Direct Kinematic Problem solutions. Making use of the kinematic mapping approach, a geometric interpretation of the constraint equations that define the motion of the robot will be given. Several different designs of the manipulator will be studied, obtaining and analyzing the direct singularity surface of each case in the kinematic image space. It will be shown that a general design of this robot allows assembly mode change, meaning that the operational workspace can be enlarged. On the other hand, two specific architectures in which, contrary to the general case, performing non-singular transitions is not possible will be also analyzed.*

1 INTRODUCTION

The workspace of parallel manipulators is usually complex and internally divided by the Direct Kinematic Problem (DKP) singularity locus. Besides, the singularities produced by the Inverse Kinematic Problem (IKP) establish the boundary of the workspace. In general, parallel manipulators have multiple DKP and IKP solutions, called assembly modes and working modes respectively. Since in [1] the authors showed that it is feasible to perform transitions between different DKP solutions without crossing any singularity, that is, guaranteeing the control of the robot all along the trajectory, many other researchers have focused on analyzing several ways of joining different DKP solutions via paths totally free of singularities [2-6]. The purpose is to take advantage of the ability of some architectures that allow assembly mode changing in order to enlarge the manipulator's range of motion.

There are many different mathematical methods in dealing with mechanism analysis and synthesis. Matrix and vector methods are most common to derive equations that describe the mechanisms [7]. Generally these methods have the disadvantage that one has to deal with sines and cosines, which are eliminated using half tangent substitutions. Within the last ten years algebraic methods have become successful in solving problems in mechanism analysis and synthesis [8]. One of the main reasons is the advances in solving systems of polynomial equations. In addition to this, it seems to be advantageous to have a geometrical setting for the interpretation of the equations. The *kinematic image space*, introduced by W. Blaschke [9] and E. Study [10], provides such a setting.

Spherical parallel manipulators, also called orientation platforms, have been analyzed by several researchers. There exist different formulations to determine the orientation of a rigid body [11]. In [12], the kinematics of a 3-S$\underline{\text{P}}$S manipulator is studied by using the three Euler-angle representation (in their ZXZ version). Following an analytic procedure an eighth-degree characteristic polynomial is obtained for the spherical 3-S$\underline{\text{P}}$S manipulator studied in [12], demonstrating that the direct kinematics of the orientation platform has at most eight feasible postures. However, one of the disadvantages of the three Euler-angle representation is that a given orientation can be represented by at least two triplets of angles. To avoid this situation, the authors in [13,14] use the three-angle orientation representation proposed in [15], called the *Tilt-and-Torsion* (T&T) angles, which enables representing any orientation in a cylindrical coordinate system through a one-to-one mapping. In [13, 14], a methodology for computing analytically the workspace and singularity loci of symmetric spherical parallel mechanisms is presented. In [16], a novel approach for representing the workspace, singularities and dexterity evaluation is presented. This approach expresses the rotation matrix by using the Euler parameters which avoids the parameterization singularities that appear for certain angles of rotation when using Euler angles.

In this paper, the spherical 3-R$\underline{\text{P}}$R manipulator is analyzed regarding its capacity for assembly mode changing. The kinematics of this manipulator will be studied by establishing a geometric interpretation of the moving platform's motion based on the kinematic mapping approach. This approach was also formulated in [17] so as to analyze the assembly mode defect in spherical four-bar platforms and in [5] to demonstrate the existence of two aspects for a general planar 3-R$\underline{\text{P}}$R platform. Following the methodology developed in [18], the direct kinematics of the spherical 3-R$\underline{\text{P}}$R will be solved, showing that, for a general design, performing non-singular transitions between different solutions is feasible.

The paper is organized as follows: in Section 2 we recall basic concepts of kinematic mapping and introduce the algorithms that translate the motion behavior of a mechanism into algebraic equations. In Sections 3 and 4, the direct kinematics of a general design will be solved, analyzing the possibility of assembly mode change. Section 5 introduces the general expression of the direct kinematic singularity surface. In Section 6, we analyze several designs of the robot with congruent platforms, emphasizing two specific cases in which the singularity surface splits the kinematic image space in such a way that the solutions lie separated from one another.

2 KINEMATIC IMAGE OF SPHERICAL 3-R<u>P</u>R

2.1 Preliminaries

Study's kinematic mapping relates kinematic features to the field of algebraic geometry. This mapping associates to every Euclidean displacement γ a point $\mathbf{c}$ in real projective space P^7 of dimension seven or, more precisely, a point on the Study quadric $S \subset P^7$ [10].

Euclidean three space is the three dimensional real vector space $\Re^3$ together with the usual scalar product $\boldsymbol{x}^{\boldsymbol{T}}\boldsymbol{y} = \sum_{i=1}^{3} x_i y_i$. A Euclidean displacement is a mapping

$$\gamma\colon \Re^3 \to \Re^3, \qquad \boldsymbol{x} \mapsto \boldsymbol{A}\boldsymbol{x} + \boldsymbol{a} \tag{1}$$

where $\boldsymbol{A}$ is a proper orthogonal three by three matrix and $\boldsymbol{a} \in \Re^3$ is a vector.

The group of all Euclidean displacements is denoted by SE(3). It is convenient to write Eq. (1) as a product of a four by four matrix and a four dimensional vector according to

$$\begin{bmatrix} 1 \\ \boldsymbol{x} \end{bmatrix} \mapsto \begin{bmatrix} 1 & \boldsymbol{o}^T \\ \boldsymbol{a} & \boldsymbol{A} \end{bmatrix} \tag{2}$$

Study's kinematic mapping κ maps an element α of SE(3) to a point $\boldsymbol{x} \in P^7$. The point in P^7 is established by the homogeneous coordinate vector $\boldsymbol{x} = [x_0 : x_1 : x_2 : x_3 : y_0 : y_1 : y_2 : y_3]^T$, and the kinematic pre-image of $\boldsymbol{x}$ is the displacement α described by the following transformation matrix

$$\frac{1}{\Delta}\begin{bmatrix} \Delta & 0 & 0 & 0 \\ p & x_0^2 + x_1^2 - x_2^2 - x_3^2 & 2(x_1x_2 - x_0x_3) & 2(x_1x_3 + x_0x_2) \\ q & 2(x_1x_2 + x_0x_3) & x_0^2 - x_1^2 + x_2^2 - x_3^2 & 2(x_2x_3 - x_0x_1) \\ r & 2(x_1x_3 - x_0x_2) & 2(x_2x_3 + x_0x_1) & x_0^2 - x_1^2 - x_2^2 + x_3^2 \end{bmatrix} \tag{3}$$

where

$$\begin{aligned} p &= 2(-x_0y_1 + x_1y_0 - x_2y_3 + x_3y_2) \\ q &= 2(-x_0y_2 + x_1y_3 + x_2y_0 - x_3y_1) \\ r &= 2(-x_0y_3 - x_1y_2 + x_2y_1 + x_3y_0) \end{aligned} \tag{4}$$

and $\Delta = x_0^2 + x_1^2 + x_2^2 + x_3^2$.

As the Study's mapping describes a six degrees-of-freedom general displacement by using eight homogeneous parameters, two constraint equations must be added [19]. The first fundamental relation that must be fulfilled is the following:

$$x_0y_0 + x_1y_1 + x_2y_2 + x_3y_3 = 0 \tag{5}$$

The second constraint establishes that not all coordinates x_i can be zero. If these conditions are fulfilled we call $[x_0 : \dots : y_3]^T$ the *Study parameters* of the displacement α. The important relation given by Eq. (5) defines a quadric $S \subset P^7$ and the range of κ is this quadric minus the three-dimensional subspace defined by

$$E\colon\ x_0 = x_1 = x_2 = x_3 = 0 \tag{6}$$

We call S the *Study quadric* and E the *exceptional* or *absolute generator*. Points belonging to E do not correspond to valid transformations in the pre-image space.

2.2 Spherical kinematic mapping

In this paper the authors analyze the spherical 3-R<u>P</u>R parallel manipulator. The motion of this platform belongs to a specific three-space on the Study quadric which is the kinematic image of all elements of the special orthogonal group SO(3). The elements of this group are pure rotations without any translational component. This way, the translational components of the homogeneous coordinate vector are zero: $y_0 = y_1 = y_2 = y_3 = 0$, and the corresponding transformation matrix is given by

$$\boldsymbol{A} = \frac{1}{\Delta}\begin{bmatrix} x_0^2 + x_1^2 - x_2^2 - x_3^2 & 2(x_1x_2 - x_0x_3) & 2(x_1x_3 + x_0x_2) \\ 2(x_1x_2 + x_0x_3) & x_0^2 - x_1^2 + x_2^2 - x_3^2 & 2(x_2x_3 - x_0x_1) \\ 2(x_1x_3 - x_0x_2) & 2(x_2x_3 + x_0x_1) & x_0^2 - x_1^2 - x_2^2 + x_3^2 \end{bmatrix} \tag{7}$$

Spherical Euclidean displacements γ can be described by

$$\boldsymbol{X} = \boldsymbol{A} \cdot \boldsymbol{x} \tag{8}$$

where $\boldsymbol{X}$ and $\boldsymbol{x}$ represent a point in the fixed and moving frame, respectively, and $\boldsymbol{A} \in SO(3)$ is a 3×3 proper orthogonal matrix.

The mapping

$$\kappa\colon \gamma \to \boldsymbol{p} \in P^3,$$
$$\boldsymbol{A} = \boldsymbol{A}(x_i) \mapsto [x_0\colon x_1\colon x_2\colon x_3]^T \neq [0\colon 0\colon 0\colon 0]^T$$

is called the *spherical kinematic mapping* and maps each spherical Euclidean displacement γ to a point $\boldsymbol{p}$ in P^3. It constitutes the restriction of the general spatial kinematic mapping to the orientation part of the Euclidean displacement group. The space P^3 is called the *spherical kinematic image space*.

2.3 Constraint equation

A spherical 3-R<u>P</u>R platform is depicted in Fig. (1). The manipulator consists of a fixed base connected by three prismatic limbs to a moving platform, both platforms lying on the unit sphere. The fixed platform constitutes a spherical triangle defined by three revolute joints located at the three vertices P_1, P_2 and P_3. Each of these joints is linked via a prismatic leg to the corresponding revolute joint of the spherical moving platform, named M_i, for $i = 1,2,3$. The rotational axes of all the revolute joints intersect at the same point which is the center of the unit sphere.

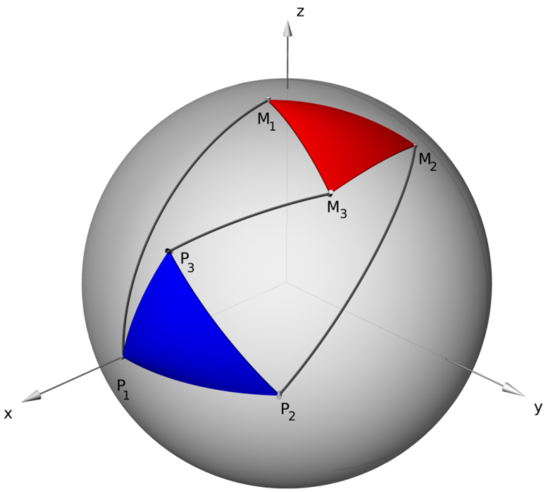

Figure 1: Spherical 3-R$\underline{P}$R parallel manipulator

The moving joints M_i are bound to move on circles over the sphere in such a way that, for each leg i, the corresponding circle is the one that arises when intersecting the unit sphere with the sphere centered at the fixed joint P_i and radius $r = \overline{P_i M_i}$. Thus, we can state that each point M_i is constrained to be on two spheres. Let the vector of the fixed revolute axis be $[A, B, C]^T$ and let the corresponding vector of the moving revolute axis in the coupler system be $[a, b, c]^T$. The endpoints of these vectors will be P_i resp. M_i when we have the side conditions

$$A^2 + B^2 + C^2 = 1 \quad and \quad a^2 + b^2 + c^2 = 1 \tag{9}$$

The path of M_i is now modeled as the intersection curve of the two aforementioned spheres:

$$X_1^2 + X_2^2 + X_3^2 - X_0^2 = 0 \tag{10}$$

$$X_1^2 + X_2^2 + X_3^2 - 2X_0(AX_1 + BX_2 + CX_3) + RX_0^2 = 0 \tag{11}$$

being $R = A^2 + B^2 + C^2 - r^2$ where r is the radius of the sphere $r = \overline{P_i M_i}$, and coordinates A, B, C are the components of the vector defining the location of the sphere's center. X_i are the coordinates of the moving pivot $[a, b, c]^T$ expressed in the fixed frame which can be computed via Eq. (8).

By substituting $[X_0, X_1, X_2, X_3]^T = \boldsymbol{A} \cdot [a, b, c]^T$ into Eq. (11) and simplifying the result using Eq. (10) yields the following quadratic surface:

$$\begin{aligned}
&2Cc(x_1^2 + x_2^2 - x_3^2 - x_0^2) + 2Aa(x_2^2 + x_3^2 - x_0^2 - x_1^2)\\
&+2Bb(x_1^2 + x_3^2 - x_2^2 - x_0^2) - 4Ab(x_1x_2 - x_0x_3)\\
&-4Ac(x_1x_3 + x_0x_2) - 4Ba(x_1x_2 + x_0x_3)\\
&-4Bc(x_2x_3 - x_0x_1) - 4Ca(x_1x_3 - x_0x_2)\\
&-4Cb(x_2x_3 + x_0x_1) + RR(x_0^2 + x_1^2 + x_2^2 + x_3^2) = 0
\end{aligned} \tag{12}$$

where the term $RR = A^2 + B^2 + C^2 + a^2 + b^2 + c^2 - r^2$.

Equation (12) constitutes the general expression of a point M_i bound to move on a circle. Hence it is the constraint equation for each leg i of the spherical 3-R<u>P</u>R platform.

3 DIRECT KINEMATICS AND SINGULARITY SURFACE

In this section the Direct Kinematic Problem (DKP) for a general case of the spherical 3-R<u>P</u>R will be studied. The polynomials representing the three constraint equations form an ideal $I = (g_1, \dots, g_n)$, and the zero set of the three polynomials determine an algebraic variety belonging to the ideal I (see [20]). On the other hand, each constraint equation determines also an algebraic variety. The zero set we are looking for corresponds to the intersection of these three varieties.

The constraint equation for each leg i, given by Eq. (12), depends on the homogeneous coordinates $[x_0 : \dots : x_3]^T$, the coordinates of vectors that define the fixed and moving joints P_i and M_i, these being $[A, B, C]^T$ and $[a, b, c]^T$ respectively, and the radius $r = \overline{P_i M_i}$ which corresponds to the input variable of each leg and is encoded in the term RR.

The elimination in this setting can be done completely general. The final result is an eight order univariate polynomial having coefficients which are functions of the design parameters (A, B, C, a, b, c) and the radius r. This univariate polynomial contains hundreds of thousand terms and it is only of academic value. Therefore we explain the algorithm with an example which is used in this study. For that, the following numeric values will be established:

- Leg 1: $A = 1, B = 0, C = 0, a = 1, b = 0, c = 0, RR = -\frac{1}{3}$
- Leg 2: $A = \frac{1}{2}, B = \frac{1}{3}, C = \frac{\sqrt{23}}{6}, a = \frac{1}{2}, b = -\frac{1}{2}, c = \sqrt{\frac{1}{2}}, RR = -\frac{1}{5}$
- Leg 3: $A = \frac{1}{\sqrt{10}}, B = 0, C = -\frac{3}{\sqrt{10}}, a = \frac{1}{3}, b = \frac{1}{2}, c = \frac{\sqrt{23}}{6}, RR = -\frac{1}{9}$

Note that the coordinates of the vectors $[A, B, C]^T$ and $[a, b, c]^T$ satisfy the conditions given by Eq. (9).

Introducing the corresponding parameters' values for each leg into Eq. (12), yields the three constraint equations:

$$g_1:\ \frac{5}{3}(x_2^2 + x_3^2) - \frac{7}{3}(x_0^2 + x_1^2) = 0 \tag{13}$$

$$\begin{aligned} g_2:\ &\frac{\sqrt{46}}{6}(x_1^2 + x_2^2 - x_3^2 - x_0^2) - \frac{1}{30}(31x_1^2 + 11x_0^2 + x_3^2 - 19x_2^2) \\ &-\sqrt{2}\left(x_1x_3 + x_0x_2 + \frac{2}{3}(x_2x_3 - x_0x_1)\right) \\ &+\frac{1}{3}\left(\sqrt{23}(x_0x_2 + x_2x_3 + x_0x_1 - x_1x_3) + x_1x_2 - 5x_0x_3\right) = 0 \end{aligned} \tag{14}$$

$$\begin{aligned} g_3:\ &\frac{\sqrt{230}}{10}(x_0^2 + x_3^2 - x_1^2 - x_2^2) - \frac{1}{9}(x_0^2 + x_1^2 + x_2^2 + x_3^2) \\ &+\frac{\sqrt{10}}{15}(x_2^2 + x_3^2 - x_0^2 - x_1^2) \\ &+\frac{\sqrt{10}}{5}\left(2(x_1x_3 - x_0x_2) + 3(x_2x_3 + x_0x_1) - x_1x_2 + x_0x_3 - \frac{\sqrt{23}}{3}(x_1x_3 + x_0x_2)\right) = 0 \end{aligned} \tag{15}$$

As previously mentioned, adding a normalizing condition is necessary so as to ensure the exceptional generator E is removed from the ideal. For example, the following normalizing conditions can be used:

$$n_1:\ x_0^2 + x_1^2 + x_2^2 + x_3^2 = 1 \tag{16}$$

$$n_2:\ x_0 = 1 \tag{17}$$

Without loss of generality, in our work, the second normalizing condition n_2 will be used. Thus, so as to solve the DKP, a system F of polynomial equations is established, which is formed by the three constraint equations g_i and the normalizing condition n_2.

Computing the Gröbner basis of this system, using lexicographic term order, a univariate a univariate polynomial of 8th degree into variable x_3 is obtained, and can be solved numerically. This means that this manipulator has a maximum of eight real solutions of the DKP. For the established design parameters and inputs, eight different real DKP solutions are obtained, which are given in Table 1.

DKP solutions	x_1	x_2	x_3
$s1$	0.1455934659	0.5058908986	-1.083158926
$s2$	-0.7586040489	-1.395011793	-0.5121514075
$s3$	-0.4307312688	-1.278552670	0.1754496214
$s4$	0.5470469063	1.112511306	0.7434360257
$s5$	1.464273504	-1.916959858	0.8944956997
$s6$	0.8904566163	1.317559845	0.9440331511
$s7$	-1.519697964	1.220102599	1.774898338
$s8$	-2.599564052	-0.2003248069	3.287058217

Table 1: Eight real solutions of the DKP

The direct kinematic singularity surface is computed by performing the determinant of the Jacobian matrix. This matrix is the following:

$$\boldsymbol{J}(f_j) = \frac{\partial f_j}{\partial x_i} \tag{18}$$

where f_j are the polynomials of the system F, and x_i are the homogeneous coordinates $[x_0: \ldots : x_3]^T$.

By computing the determinant of $\boldsymbol{J}$ a cubic surface in the variables x_i is obtained. Setting $x_0 = 1$, according to the normalizing condition n_2, this singularity surface can be represented in the kinematic image space which is depicted, together with the location of the eight DKP solutions, in Fig. (2). Two different views of the surface are shown in Fig. (2). Visualizing only the view represented in Fig. (2a) it seems that the surface divides the space into four separated volumes, but however, analyzing the view depicted in Fig. (2b) it can be observed that there exist some 'holes' that connect these volumes in such a way that the surface divides the kinematic image space into only two separated volumes, i.e. two aspects.

The DKP solutions are distributed four by four, four solutions associated with the positive sign of $\det(\boldsymbol{J}) > 0$ lie inside one aspect (which are $s1, s3, s6, s7$) and the remaining solutions with $\det(\boldsymbol{J}) < 0$ in another aspect ($s2, s4, s5, s8$). Thus we can connect between either the four solutions associated with one sign of $\det(\boldsymbol{J})$ or the remaining four associated with the opposite sign.

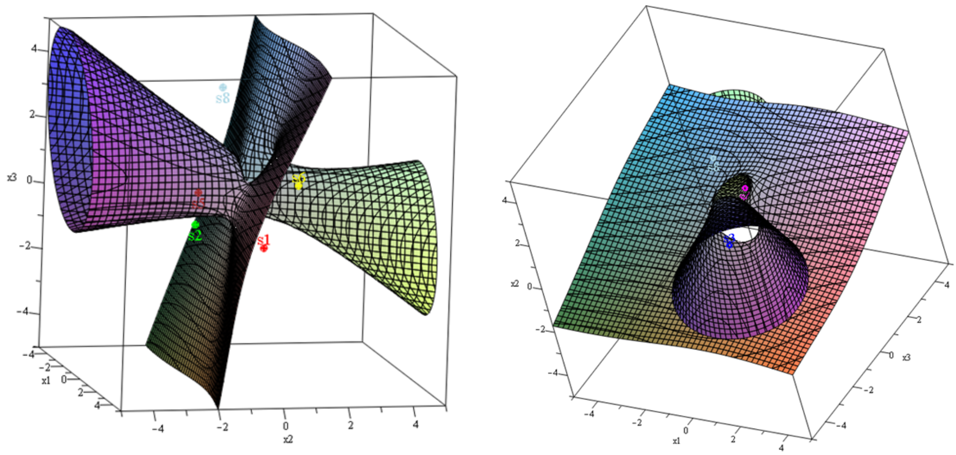

(a) (b)

Figure 2: Direct kinematic singularity surface

4 ASSEMBLY MODE CHANGE

Our main purpose is to show that a general spherical 3-RPR can perform non-singular transitions between its assembly modes so that the manipulator's range of motion is enlarged. In Section 3, it has been shown that, for a general design of the manipulator, the direct kinematic singularity surface splits the kinematic image space into two aspects, meaning that assembly mode changing is feasible.

Let's perform a path between two different assembly modes by carrying out a non-singular transition, i.e. a trajectory that avoids the singularity surface. The following parametric curve, which corresponds to a quadratic B ezier curve, constitutes a non-singular transition connecting solutions $s5$ and $s8$:

$$\begin{aligned} x_1 &= 1.464234898(1-t)^2 + 1.2t(1-t) - 2.599571150t^2 \\ x_2 &= -1.916718185(1-t)^2 - 5t(1-t) - 0.2002550213t^2 \\ x_3 &= 0.8945016211(1-t)^2 + 10t(1-t) + 3.287058223t^2 \end{aligned} \tag{19}$$

which for $\mathrm{t} = 0$ the manipulator is posed in $s5$ and for $t = 1$ yields $s8$. A close up view of this curve is represented in Fig. (3), observing that it goes around the singularity surface without crossing it.

The value of $det(\boldsymbol{J})$ all along the trajectory given by Eq. (19) is plotted in Fig. (4), showing that at any moment a non-zero value of the Jacobian is obtained. This demonstrates that the path corresponding to the curve in Eq. (19) yields a non-singular transition between both assembly modes.

It is well-known that reaching a direct kinematic singular pose implies losing the control of the manipulator. For the 3-RPR planar case, there is a geometric interpretation of the manipulator being in a singular configuration. It corresponds to a pose in which the fixed and moving platforms are located such that the extension of the three leg lines intersects at one point. Similarly, for the spherical case under study, the geometric meaning of reaching a singular pose is that the great circles associated with the three legs intersect at two points, as in the spherical case, every point on the sphere has a diametrically opposite point, called the *antipodal* point.

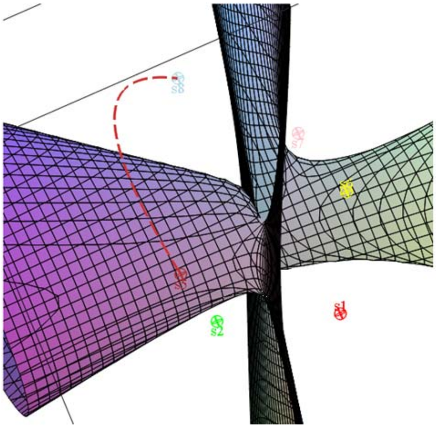

Figure 3: Non-singular transition between $s5$ and $s8$

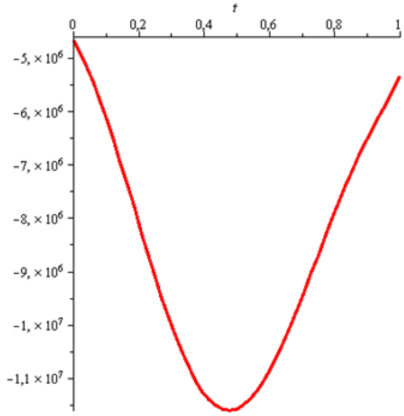

Figure 4: Value of $det(\boldsymbol{J})$ along the path

In Fig. (5), four different poses of the manipulator along the transition between $s5$ and $s8$, given by the quadratic curve in Eq. (19), are represented. The great circles associated with each of the three legs have been plotted, observing that, for all the poses, these circles do not intersect at any point. Hence, as it was already known, this trajectory corresponds to a non-singular transition.

Due to limitation of space only four poses have been depicted, but of course the authors have verified that all along the trajectory there is no pose in which the manipulator is in a singular configuration.

4.1 Direct kinematic singular configuration

In order to show an example of a singular configuration of the manipulator, the following trajectory will be made. It constitutes in the kinematic image space a straight line joining $s5$ and $s8$, its expression given by:

$$\begin{aligned} x_1 &= -2.59904429p + 1.464196522(1-p) \\ x_2 &= -0.2028714158p - 1.916478044(1-p) \\ x_3 &= 3.287058164p + 0.8945075101(1-p) \end{aligned} \tag{20}$$

where the parameter p varies from $p = 0$, in which case the manipulator is in its assembly mode $s5$, to the value $p = 1$, the manipulator then being in $s8$.

This path crosses the singularity surface twice, as it can be observed in Fig. (6). Hence this trajectory constitutes a singular transition between the two assembly modes. In Fig. (7), a pose in which the manipulator is singular is represented, that pose corresponding to the first intersection point of the straight line with the singularity surface. It can be observed in Fig. (7) that the three great circles of the legs intersect at two points, namely point P and its antipodal point P'.

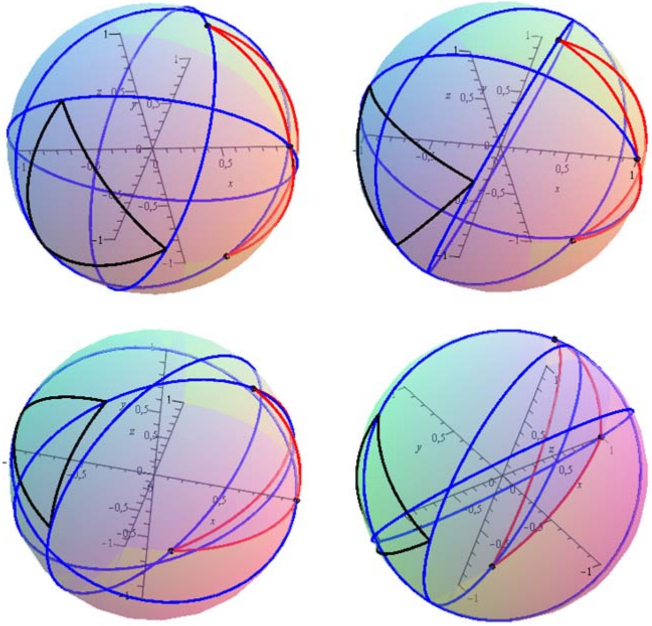

Figure 5: Different poses along the non-singular transition

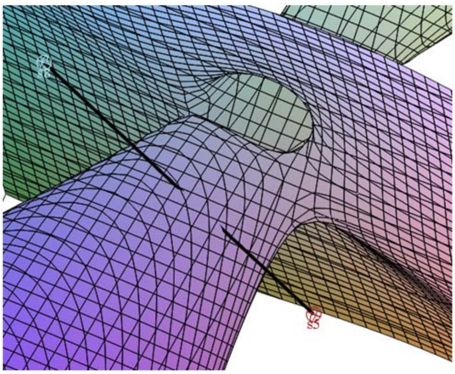

Figure 6: Singular transition from $s5$ to $s8$

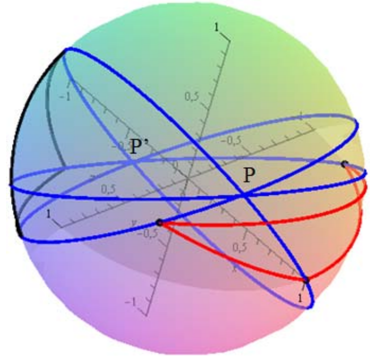

Figure 7: Singular configuration of the manipulator

5 GENERAL SINGULARITY SURFACE

The aim of this section is to obtain the expression of the direct kinematic singularity surface in a complete general form, that is, without specifying the numeric values of the design parameters.

Without loss of generality, the coordinate system in base and platform can be chosen such that the constraint equations for each leg will depend on the following parameters:

- Leg 1: $A = A_1, B = 0, C = 0, a = a_1, b = 0, c = 0, RR = RR_1$
- Leg 2: $A = A_2, B = B_2, C = C_2, a = a_2, b = b_2, c = c_2, RR = RR_2$
- Leg 3: $A = A_3, B = B_3, C = C_3, a = a_3, b = b_3, c = c_3, RR = RR_3$

Geometrically this choice of coordinate systems means that the vectors that define the first revolute joint of the base resp. moving platform lie on the x-axis of the fixed resp. moving frame.

The system F of polynomial equations is formed by the three constraint equations depending on the above parameters and the normalizing condition n_2. Computing the determinant of the Jacobian of this system, the equation of the singularity surface S turns out to be a cubic surface that can be written in the form:

$$\begin{aligned} S\colon\ & Ax_1^3 + Bx_2^3 + Cx_3^3 + x_0^2(Dx_1 + Ex_2 + Fx_3) \\ & + x_1^2(Gx_0 + Hx_2 + Ix_3) + x_2^2(Jx_0 + Kx_1 + Lx_3) \\ & + x_3^2(Mx_0 + Nx_1 + Ox_2) + x_0(Px_3x_2 + Qx_2x_1 + Rx_3x_1) \\ & + Sx_3x_2x_1 = 0 \end{aligned} \tag{21}$$

where $A, B, C, D, E, F, G, H, I, J, K, L, M, N, O, P, Q, R, S$ are functions of the design parameters and of the terms RR_i in which the radius $r = \overline{P_iM_i}$ of each leg i is encoded. These coefficients can be computed completely general, without specifying the design parameters, but they are too large to be listed here.

6 CONGRUENT PLATFORMS

In this section, the case in which the base and moving platforms are formed by congruent spherical triangles will be studied. First, it will be analyzed the special case in which the three revolute joints of the base resp. moving platform lie on the axes of the fixed resp. moving frame. It will be shown that establishing this shape of the spherical triangles yields a special singularity surface that splits up the kinematic image space into eight separated volumes. Hence each DKP solution will lie inside each volume so that performing non-singular transitions will not be feasible.

Secondly, a more general condition related to the geometric shape of the spherical triangles that achieve a *splitting singularity surface* will be stated. Finally, a general case of congruent platforms will be analyzed showing that, for this case, the singularity surface does not split into three planes.

6.1 Congruent platforms: joints on the principal axes

Both congruent platforms are formed by a spherical triangle in which the three vertices lie on the principal axes (x, y, z) of the fixed frame, for the base platform, and on the principal axes of the attached moving frame in the case of the moving platform. Then they constitute a equilateral spherical triangle with angle $\alpha = \pi/2$ in each vertex, as it is shown in Fig. (8) where the spherical triangle of the fixed platform is depicted.

This way, for each leg the coordinates of the joints given by the vectors $[A, B, C]^T$ and $[a, b, c]^T$ are specified as follows, and the term RR is left as a design parameter bearing in mind that this term depends on the radius $r = \overline{P_iM_i}$:

- Leg 1: $A = 1, B = 0, C = 0, a = 1, b = 0, c = 0, RR = RR_1$
- Leg 2: $A = 0, B = 1, C = 0, a = 0, b = 1, c = 0, RR = RR_2$
- Leg 3: $A = 0, B = 0, C = 1, a = 0, b = 0, c = 1, RR = RR_3$

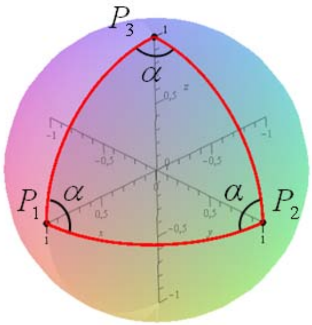

Figure 8: Spherical triangle with vertices on the principal axes

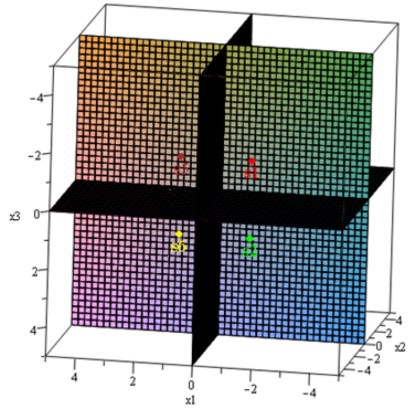

Figure 9: Kinematic image space for congruent triangles with joints on the principal axes

Introducing the design parameters into the constraint equations and computing the $det(\boldsymbol{J}) = 0$ of the corresponding system F, yields the general expression of the singularity surface for the case under study:

$$(RR_3 + RR_2 + RR_1 + 2)x_1x_2x_3 = 0 \qquad (22)$$

From Eq. (22) it can be easily observed that the direct kinematic singularity surface is formed by three planes associated with the nullity of the three homogeneous coordinates x_1, x_2 and x_3. The expression inside the brackets: $(RR_3 + RR_2 + RR_1 + 2)$ is a constant that never vanishes and the value of this constant will depend on the radius $r = \overline{P_iM_i}$ of each leg. The three planes $x_1 = 0$, $x_2 = 0$ and $x_3 = 0$ split the kinematic image space into eight separated volumes (eight aspects) in such a way that each solution lies inside one volume. For example, assigning $RR_1 = -1/3$, $RR_2 = -1/5$ and $RR_3 = -1/9$ yields the eight DKP solutions given in Table 2. Note that due to the symmetry of the spherical case only four solutions are different, i.e. si for $i = 1, \ldots, 4$, as the solutions corresponding to $i = 5, \ldots, 8$ are the antipodal points of the previous ones.

The singularity surface together with the location of the DKP solutions is represented in the kinematic image space in Fig. (9). It can be concluded that, for this particular case, performing non-singular transitions is not feasible, as moving from one solution to another would obligatorily imply crossing the singularity surface.

DKP solutions	x_1	x_2	x_3
$s1$	-1.207897509	-1.286754718	-1.336744271
$s2$	-1.207897509	-1.286754718	1.336744271
$s3$	-1.207897509	1.286754718	-1.336744271
$s4$	-1.207897509	1.286754718	1.336744271
$s5$	1.207897509	-1.286754718	-1.336744271
$s6$	1.207897509	-1.286754718	1.336744271
$s7$	1.207897509	1.286754718	-1.336744271
$s8$	1.207897509	1.286754718	1.336744271

Table 2: DKP solutions for congruent triangles with joints on the principal axes

6.2 Congruent platforms: meridian triangles

In this section we will show that there is a more general condition so as to get a singularity surface that splits into three planes in such a way that the kinematic image space will be divided into eight separated aspects. The authors will refer to this special singularity surface as the *splitting singularity surface*.

Yet again the fixed and moving platforms must be congruent, but the difference with the previous case analyzed in **6.1**, is that only two of the angles of the spherical triangle will be equal to $\pi/2$. The platforms are formed by a spherical triangle as the one shown in Fig. (10). Let P_1, P_2 and P_3 be the three joints that define the fixed platform. Bear in mind that the moving triangle will be congruent to the base, therefore the same design conditions are applied to the moving triangle. Joint P_1 lies on the x-axis, joint P_2 is an arbitrary point on the xy-plane, and the third joint P_3 is located on the z-axis. As points P_1 and P_2 lie on the equator of the unit sphere, and the great circles through P_1 and P_2 subtending an angle of $\pi/2$ with the equator intersect at the poles, one of which is the point P_3, we will call this triangle the *meridian triangle*. The angle α of the two vertices at points P_1 and P_2 is equal to $/2$, and the angle of the third vertex, β, depends on the location of point P_2 (as β is equal to the length P_1P_2).

Then the parameters defining each leg are:

- Leg 1: $A = 1, B = 0, C = 0, a = 1, b = 0, c = 0, RR = RR_1$
- Leg 2: $A = A_2, B = B_2, C = 0, a = A_2, b = B_2, c = 0, RR = RR_2$
- Leg 3: $A = 0, B = 0, C = 1, a = 0, b = 0, c = 1, RR = RR_3$

The expression of the singularity surface for this case yields:

$$\begin{aligned} x_3(&-RR_2x_1x_2 - 2x_1x_2 + 2A_2^2x_1x_2 + 2A_2B_2x_2^2 \\ &-RR_1A_2B_2x_1^2 - RR_1x_1x_2 + 2RR_1A_2^2x_1x_2 \\ &+A_2B_2RR_1x_2^2 - A_2B_2RR_3x_1^2 \\ &-RR_3x_1x_2 + RR_3A_2^2x_1x_2) = 0 \end{aligned} \tag{23}$$

where according to the side conditions in Eq. (9): $B_2 = \sqrt{1 - A_2^2}$.

It can be observed in Eq. (23) that the singularity surface is formed by the multiplication of two terms. On the one hand, the plane $x_3 = 0$, and, on the other hand, the expression inside the brackets which constitutes a quadratic equation into variables x_1 and x_2. This aforementioned expression can be factorized as the product of two planes that intersect at the origin in the following form:

$$(Lx_1 + Mx_2)(Nx_1 + Ox_2) \tag{24}$$

where L, M, N, O are expressions that depend on the design parameters and the terms RR_i.

For example, by assigning the following numeric values: $A_2 = 1/3$, $RR_1 = -1/2$, $RR_2 = -1/3$ and $RR_3 = -1/7$, the expression of the splitting singularity surface yields:

$$x_3\left(-24x_1 + \sqrt{2}x_2\left(39 + \sqrt{849}\right)\right)\left(-24x_1 - \sqrt{2}x_2\left(39 - \sqrt{849}\right)\right) = 0 \tag{25}$$

The singularity surface for this case is represented in Fig. (11), together with the location of the eight DKP solutions.

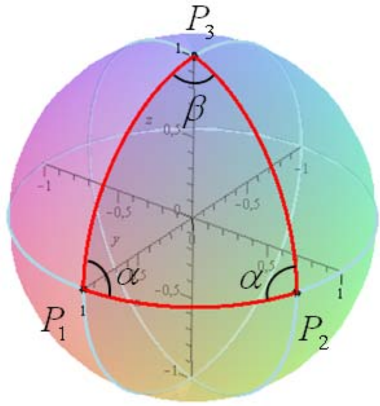

Figure 10: Meridian triangle

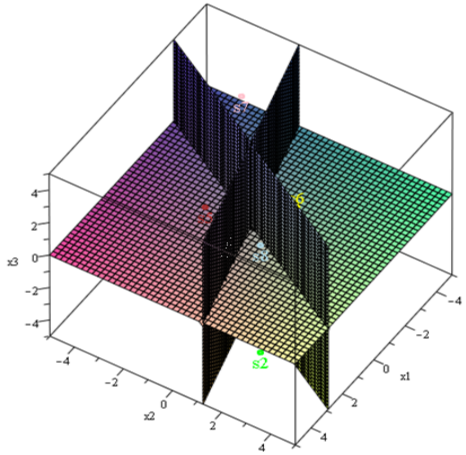

Figure 11: Splitting singularity surface and DKP solutions

6.3 Congruent platforms: general case

Now, we analyze a general case of congruent platforms, meaning that the three angles (α, β, γ) of the spherical triangle are different (see Fig. (12)). For this case, it will be shown that the direct kinematic singularity surface is a cubic surface which, contrary to the previous cases studied in **6.1** and **6.2**, does not split into three planes.

The spherical triangle depicted in Fig. (12) has joint P_1 located on the x-axis, joint P_2 on the xy-plane and joint P_3 on the xz -plane. The values given to the design parameters and inputs are:

- Leg 1: $A = 1, B = 0, C = 0, a = 1, b = 0, c = 0, RR = -\frac{1}{2}$
- Leg 2: $A = \frac{1}{3}, B = \frac{2\sqrt{2}}{3}, C = 0, a = \frac{1}{3}, b = \frac{2\sqrt{2}}{3}, c = 0, RR = -\frac{1}{3}$
- Leg 3: $A = \frac{1}{2}, B = 0, C = \frac{\sqrt{3}}{2}, a = \frac{1}{2}, b = 0, c = \frac{\sqrt{3}}{2}, RR = -\frac{1}{7}$

The expression of the singularity surface yields:

$$\begin{aligned} \frac{\sqrt{6}}{3024}(&-252x_1(x_2^2 + x_3^2) + 391\sqrt{6}x_1x_2x_3 - 252\sqrt{3}x_2^2x_3 \\ &-504\sqrt{2}x_3^2x_2 - 420x_1^3 - 88\sqrt{3}x_1^2x_3 - 273\sqrt{2}x_2x_1^2) = 0 \end{aligned} \tag{26}$$

which is represented in the kinematic image space in Fig. (13). This surface splits the image space into two separated volumes, meaning that assembly mode change is feasible.

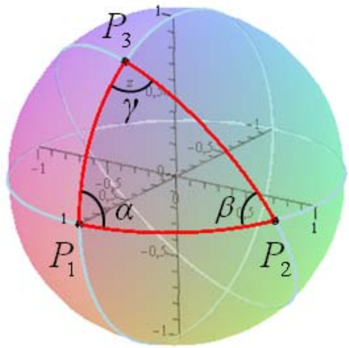

Figure 12: Congruent triangles with three different angles

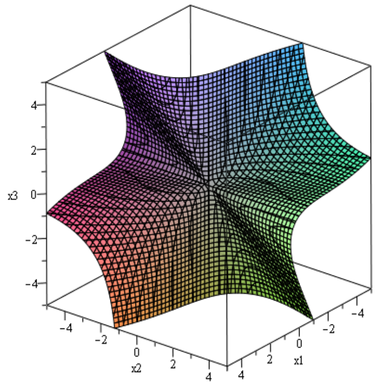

Figure 13: Singularity surface for congruent triangles with three different angles

7 CONCLUSIONS

The spherical 3-R<u>P</u>R parallel manipulator has been analyzed regarding the feasibility of assembly mode change. The direct kinematics based on the kinematic mapping approach has been solved in a complete general form. In order to analyze different designs, numeric examples have been given, concluding that a general design of this manipulator allows transitioning between different direct kinematic solutions by following a path that avoids the singularity surface. Finally, two specific designs which yield a particular shape of the singularity surface in such a way that assembly mode change is not possible have been presented.

ACKNOWLEDGEMENTS

The authors wish to acknowledge the financial support received from the Spanish Government through the Ministerio de Educación y Ciencia (Project DPI2008-00159), the European Union (Project FP7-CIP-ICT-PSP-209-3) and the Basque Government through the Dpto. Educ., Univ. e Investig. (Project IT445-10). Mónica Urízar would also like to thank the members of the Unit Geometry and CAD (University Innsbruck) for their support and contribution to this work.

REFERENCES

[1] C. Innocenti and V. Parenti-Castelli. Singularity free evolution from one configuration to another in serial and fully-parallel manipulators. *Journal of Mechanical Design*, vol. 120, nº 1, 73-79, 1998.

[2] P. McAree and R. Daniel. An explanation of never-special assembly changing motions for 3-3 parallel manipulators. *The International Journal of Robotics Research*, vol. 18, nº 6, 556-575, 1999.

[3] H. Bamberger, A. Wolf and M. Shoham. Assembly mode changing in parallel mechanisms. *IEEE Transactions on Robotics*, vol. 24, nº 4, 765-772, 2008.

[4] M. Zein, P. Wenger and D. Chablat. Non-singular assembly mode changing motions for 3-R<u>P</u>R parallel manipulators. *Mechanism and Machine Theory*, vol. 43, nº 4, 480-490, 2008.

[5] M.L. Husty. Non-singular assembly mode change in 3-RP_R-parallel manipulators. In *Proceedings of the 5th International Workshop on Computational Kinematics*, pp. 51-60, A. Keckskeméthy and A. Müller (Eds.), Springer, 2009.

[6] M. Urízar, V. Petuya, O. Altuzarra and A. Hernández. Researching into non-singular transitions in the joint space. In *Advances in Robot Kinematics: Motion in Man and Machine*, pp. 45-52, J. Lenarcic and M. Stanisic (Eds.), Springer, 2010.

[7] J. Angeles. *Fundamentals of Robotic Mechanical Systems. Theory, Methods and Algorithms*. Springer, New York, 1997.

[8] M.L. Husty, M. Pfurner, H.-P. Schröcker and K. Brunnthaler. Algebraic methods in mechanism analysis and synthesis. *Robotica*, vol. 25, nº 6, 661-675, 2007.

[9] W. Blaschke. *Kinematik und Quaternionen*. Wolfenbüttler Verlagsanstalt, 1960.

[10] E. Study. *Geometrie der Dynamen*. B.G. Teubner, Leipzing, 1903.

[11] R.N. Jazar, *Theory of Applied Robotics: Kinematics, Dynamics and Control (2nd Edition)*. Springer, New York, 2010.

[12] L.-W. Tsai. *ROBOT ANALYSIS: The mechanics of serial and parallel manipulators*. John Wiley & Sons, Inc., 1999.

[13] I.A. Bonev and C.M. Gosselin. Singularity Loci of Spherical Parallel Mechanisms. In *Proceedings of the 2005 IEEE, Int. Conf. on Robotics and Automation*, Barcelona, Spain, 2005.

[14] I.A. Bonev and C.M. Gosselin. Analytical Determination of the Workspace of Symmetrical Spherical Parallel Mechanisms. *IEEE Transactions on Robotics*, vol. 22, nº 5, 1011-1017, 2006.

[15] I.A. Bonev and J. Ryu. Orientation workspace analysis of 6-DOF parallel manipulators. In *Proceedings of the ASME 1999 Design Engineering Technical Conferences*, Las Vegas, NV, 1999.

[16] S. Bai, M.R. Hansen and T.O. Andersen. Modelling of a special class of spherical parallel manipulators with Euler parameters. *Robotica*, vol.27, 161-170, 2010.

[17] H.-P. Schröcker, M.L. Husty and J.M. McCarthy. Kinematic mapping based assembly mode evaluation of planar four-bar mechanisms. *Journal of Mechanical Design*, vol. 129, nº 9, 924-929, 2007.

[18] F. Bulca and M.L. Husty. Kinematic mapping of spherical three-legged platforms. In *Proc. 15th Canadian Congress of Applied Mechanics (CANCAM)*, vol. 2, pp. 874-875, Victoria, Br. Columbia, Canada, 1995.

[19] O. Bottema and B. Roth. *Theoretical Kinematics*. North-Holland Publishing Company, Amsterdam, 1979.

[20] D. Cox, J. Little and D. O'Shea. *Ideals, Varieties and Algorithms: An Introduction to Computational Algebraic Geometry and Commutative Algebra (Undergraduate texts in Mathematics)*. Springer, 2007.

Proceedings of MUSME 2011, the International Symposium
On Multibody Systems and Mechatronics
Valencia, Spain, 25-28 October 2011

FAILURE IN FRONT SUSPENSION MECHANISM. MITSUBISHI L-200 CASE

Carlos César Munares Tapia

Mechanical Engineer, with Peruvian Engineers' Association (CIP) Number 38973, member of the Expert Analysis Center of the Lima Departmental Council of the Peruvian Engineers' Association, senior professor at the Mechanical Engineering Faculty of the National University of Engineering (UNI)

1. - BACKGROUND

According to the preliminary report given by the driver, Antonio VALENCIA VARGAS, identified by National Identity Card (DNI) 40381022, on August 18th, 2010, approximately at 2:00 pm, the Mitsubishi pick-up, model L200, with license plate No. A8K-867 and with approximately 8000 km. of route suffered a sudden rollover, at the speed of 80 km/h, in a straight and flat roadway in the Department of Ica.

The requesting party needs a Technical Comparative Expert Analysis Report so that the causes of the fault on the upper ball joint of the left wheel (driver's side) can be revealed.

Photo Nº 1: Place of the occurrence

2. - OBJECTIVE OF THE REPORT

The objective of this report is to give an opinion about the causes of the fault on the upper ball joint of the left wheel of the pick-up with license plate No. A8K-867, through a Technical Comparative Expert Analysis Report on the ball joint of the vehicle, which was damaged on its left part and undamaged on its right part.

3. - General features of the broken ball joint:

Concept:

Brand name : Factory original

Material of the cup : Steel

4. - USED METHOD

4.1 Inspection of the ball joint handbooks.

4.2 Technical inspection of the damaged parts.

4.3 Metallographic analysis and hardness tests.

4.4 Interview to the driver of the vehicle.

4.5 Review of the bibliography material about analysis about failures and breakages of vehicle parts.

4.6 Technical inspection of the damaged ball joint of the vehicle with license plate A8K-867 and the undamaged upper right ball joint, which were delivered to the expert by the requesting party.

4.7 Analysis and conclusions.

5. - INFORMATION SOURCES

5.1 Technical handbooks:

5.1.1 ASM Metals Hand Book "Failure Analysis".
5.1.2 ASM Metals Hand Book "Fractography".
5.1.3 ASM Metals Hand Book "Metallography".
5.1.4 ASM Metals Hand Book "Atlas of Microstructures".
5.1.4.1.1 Technical Standards
5.1.5 Photographs taken at the place of the occurrence and at the facility where the damaged car is currently kept.
5.1.6 BOSCH's Technical Vehicle Handbook.
Shafts - Applied Failure Analysis/1991 Caterpillar Inc.

6. Auto parts delivered to the expert:

6.1 An upper ball joint out of its cup, deformed on the left side of the vehicle.

6.2 An upper ball joint of the right side, in good condition.

7. – MAIN CONCEPTS USED IN THIS REPORT:

- Martensite, ferrite, perlite.

- Hardness.

8. - VEHICLE OPERATING CONDITIONS:

- Roadways in bad condition.

We can appreciate the cup of the damaged upper ball joint in the following photos:

Photo No. 2 – Cup of the upper ball joint cup on the driver’s side.

Photo No. 3 - in this photo you can see the ball joint covered by its poncho out of the cup.

9. - SUMMARY OF CONCEPTS USED IN THIS REPORT:

9.1 Martensite, perlite and ferrite: The steel used in the cups of the ball joints are subject to a series of thermal treatments to improve the homogeneity of the material, increase their resistance, improve their resistance to fatigue and increase their hardness. As a result of Standardized, Quenched and Tempered, the steel gets a Martensite matrix. Perlite and ferrite components are relatively softer than martensite. In the studied case, ferrite can be seen in both cups but in different proportions.

9.2 Surface hardness: The outer surface of some parts reaches a hardness of 65 HRC, due to the surface hardening to which they are subject to, such as gears. The most used method in the automobile industry is the Quenched with a high frequency electric current. In this studied case, the parts have not been subject to thermal treatment for their surface hardening.

9.3 Hardness: Technically, hardness is the ability of the material of a piece to endure the scratches resulting from another body.

10. - ANALYSIS

10.1 Visual inspection: the visual inspection was concretely performed on both ball joints, having the following results:

10.1.1 The cup of the damaged ball joint shows the open mouth uniformly in its entire diameter and an area deformed by crushing. See Photos No. 4 and 5.

Photo No. 4 Photo No. 5

10.1.2 The ball joint was removed from its place, but this did not deform its geometry.

10.1.3 The cup of the damaged ball joint shows signs of distorting of its mouth (ovalization and widening) and plastic deformation by compression caused by the mobile part of the ball joint shown in Photo No. 3.

10.1.4 The plastic deformation was caused nearly at the end of the exhaust of the mobile part of the ball joint regarding its housing.

See Photo No. 6.

10.1.5 Evidence has not been found of a heavy blow in the inner part of the cup.

10.1.6 The right ball joint in good condition has the following appearance:

Photo No. 7.

10.2 Four (4) test tubes were provided for the metallographic and hardness tests.

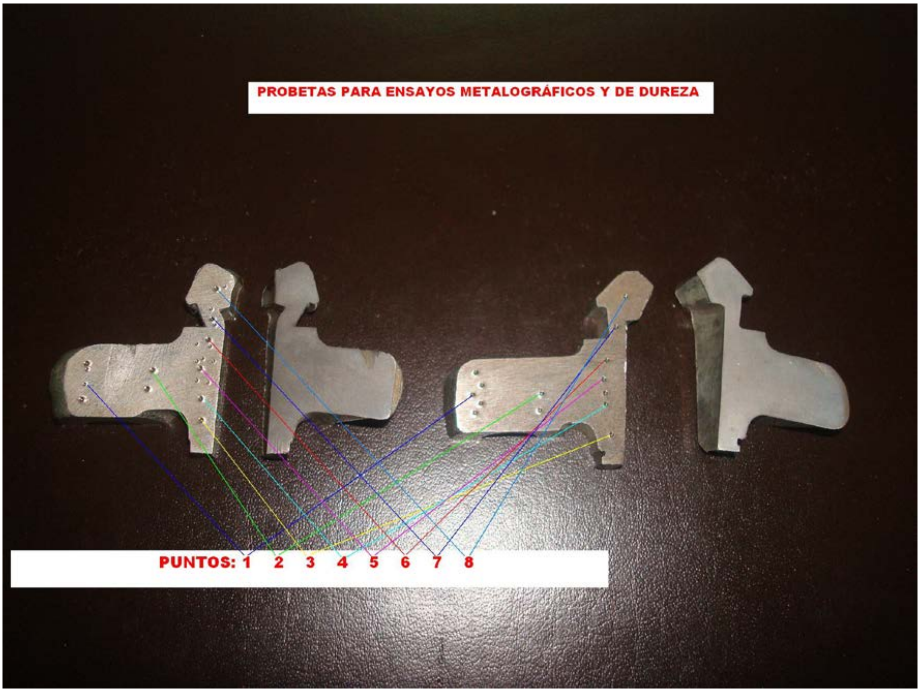

Photo No. 8 - The test tubes showed in the left side of the picture belong to the damaged ball joint and the test tubes in the right side belong to the ball joint in good condition. Items mentioned from 1 to 8 have been used for the comparison of hardness in similar areas of both ball joints.

10.3 The metallographic analysis was performed on a transversal section of the cups of both ball joints. The mentioned items correspond to those on Photo No. 4:

COMPONENT	ITEMS	MICROSTRUCTURAL STATUS	GRAIN SIZE

Damaged cup	1 and 2	Quenched martensite matrix of a fine glass-like grain	10
Normal cup	1 and 2	Quenched martensite matrix of a fine glass-like grain	10
Damaged cup	5, 6 and 7	Heterogeneous martensite matrix Ferrite in a greater percentage	8, 9 and 10
Normal cup	5, 6 and 7	Heterogeneous martensite matrix Ferrite in a smaller percentage	8, 9 and 10

See the comparative photos:

Damaged cup Normal cup

First row of photos taken to the top sides of the cups from 50x, near the sixth reference point.

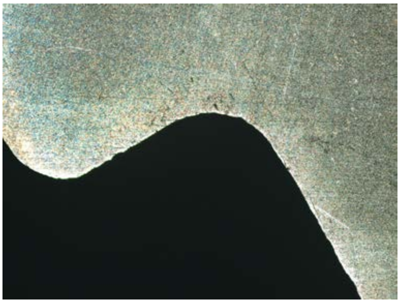

Photo No. 9

Photo No. 10

Second row of photos taken from 1000x, near the fifth reference point.

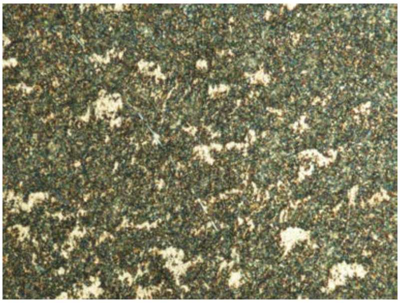

Photo No. 11

Photo No. 12

The white spots confirm the presence of ferrite in the cup of the damaged ball joint, while the other cup, which has martensite in it and is ferrite-free quenched, has greater resistance than the first one.

10.4 Results of the Hardening Test: Measures in Rockwell HRC:

ITEM	HARDENING – DAMAGED CUP	HARDENING – NORMAL CUP	DELTA %
1	17.5	22.0	29.4
2	15.5	21.0	35.8
3	12.0	16.0	33.3
4	12.5	16.0	28
5	10.5	15.0	42.8
6	12.0	18.0	50
7	12.5	13.0	4
8	15.5	19.0	22.5

We can see that the normal cup with regard to the damaged cup has greater hardening values in 30.7% as an average value, taken from the last column of the chart shown in item 10.4.

10.5 ANALYSIS OF HOW THE FAULT WAS CAUSED

10.5.1 According to the information received by the driver, the vehicle turned over abruptly.
10.5.2 The roadways are not flat, in some areas. It is worth mentioning that the driver saw that some station wagons had better speed levels, that is, many station wagons passed him.
10.5.3 During the accident, the driver realized that the vehicle tilted to the left and then turned over once. The vehicle was found wheels up as shown in Photo No. 1.
10.5.4 The status of the inner part of the damaged cup does not show signs of a strong blow, so it can be affirmed that the mobile part of the ball joint was starting to gradually open to the mouth of the ball joint cup until it was removed from its housing.
10.5.5 The temperature of the front brakes equally affects both the damaged and the normal ball joints. The difference is that the ball joints of this vehicle have different resistance levels; the left ball joint has a smaller resistance level than the right ball joint.
10.5.6 The hardening values measured in the previous eighth items in Photo No. 6 in the test tubes of each ball joint confirms the mentioned in the previous item.
10.5.7 The average hardening difference between the test tubes of each ball joint is greater than 30%, which shows that the fault was caused by the scarce resistance of the material of the left upper ball joint of the vehicle.

This Expert Analysis resolves:

That the fault on the upper ball joint of the left side of the vehicle, with License Plate No. A8K-867, was caused by the scarce resistance of the material of the cup of the mentioned ball joint.

That the presence of ferrite has weakened the resistance level of the left ball joint cup and, therefore, it is a manufacturing defect.

It is dismissed that the investigated fault has something to do with the inadequate use of the vehicle by the driver.

12. – FINAL RESULT

Mitsubishi Japan Motor Corporation talked to its representative in the city of Lima, in an urgent way, and ordered him to lend an L-200 pick-up to Yarthum RODRIGUEZ, while a new vehicle is given to him, which shall replace the damaged vehicle under the responsibility of the manufacturing company.

MODELING AND CONTROL OF A BIPED ROBOT BASED ON THE CAPTURE OF HUMAN MOVEMENT PATTERNS

Elvis O. Jara[*], Cristian Cisneros[*], Edison Alfaro[*] and José Oliden[†]

[*] School of Mechatronics Engineering
Universidad Nacional de Ingeniería, Av. Túpac Amaru 210 - Rímac/ Lima 25 - Perú
e-mail: `ejaraa@ uni.pe`
`web page: http://www.uni.edu.pe`

† Center for Information and Communications Technologies - CTIC
Universidad Nacional de Ingeniería, Av. Túpac Amaru 210 - Rímac/ Lima 25 - Perú

Keywords: Biped robot, Fuzzy control, Human movement patterns, Multibody Systems.

Abstract. *This work focused on a 6-DOF biped robot; where, a control algorithm was designed to achieve independent leg path control, given into considering the robot's kinematic and dynamic model. The control was based on fuzzy logic algorithms, directly applied to each DC motors located at every joint. Furthermore, an image processing based method was used to determine human's walking patterns. This served as the system's desired path. Finally, development of a first prototype is also shown. This prototype's goal was to validate kinematic equations only. The prototype's main electronic boards were a DSP, as the responsible device for all the system's calculations, and a microcontroller HCS08, to command servo motors. For sensors, the information given by a three-axis accelerometer was used to check the robot's stability.*

1 INTRODUCTION

The humanoid robot is one of the main paradigms of anthropomorphic robotics, among other reasons, because it enables the creation of a fully robotic body. This idea may have multiple implications: the creation of robots with capabilities similar to human driving, so that these robots can serve as a direct replacement for humans in jobs in which appearance is important and human qualities implicit to it. Therefore, in this paper we focus on the development of a biped robot prototype that can emulate human walking with the future vision of using this technology, not only in more advanced prototype, but also as support for medical devices such as exoskeletons rehabilitation and prosthetic legs.

We are also interested in developing this prototype as a scientific and academic exercise in an effort to keep pace with global research and contribute to the development of the science and technology of robotics. In that sense, the main objective of the first prototype presented in this paper is to serve as an experimental module which can validate different control techniques in the field of monitoring of human walking patterns. Additionally, the development of this project strengthens a significant number of important areas related to mechatronics, such as multibody systems analysis, control theory, design and programming of embedded systems, mechanical and electronic design.

2 PROCEDURE

The project begun by finding the robots mathematical models and designing control blocks, so that the robot's end effector could be controlled at will, making it follow any desired trajectory. Later, human walking patterns were obtained, so they could be used as desired trajectories; for this, a simple image processing algorithm was used to obtain the paths of our own joints - hip, knee and ankle, when walking. For simulations, a biped mechanical structure was designed, similar to human's physiognomy and modeled into matlab software. Furthermore, control blocks to simulate each dc motor located in the robot's joints were added to the model; where each motor had a PID–Fuzzy control implemented. The system's input was the desired ankle's path, and the output was the simulated path; feedback control used joint's angular rates measured by gyro sensors to determine states.

After verifying the robot's proper operation in the simulation, a first prototype of the biped robot was built, with the intent to test our kinematic equations only. For this prototype six servo motors and one DSP were used; the last one being in charge of all the calculations. A microcontroller was also used, to serve as a driver for the servo motors. To monitor, by means of a PC, the robot's equilibrium; an accelerometer was used.

2.1 Biped robot's mechanism design

Solidworks [17] was used for this design, where the robot's limbs consisted of aluminum 1x1 inch^2 AA-1060/8 frames. Part's names and dimensions were defined based on an analogy to the standard structure of a person, taking into account the called "divine proportion" that exists in nature [6].

DC motors were conveniently placed robot's joints to facilitate mechanical design; also, there is a gap between feet, so when both feet aligned there is no contact between them. Mechanical design should also consider where to place all the circuitry needed for the robot's control. All these features, mentioned above are shown in Fig. (1). This structure was also based on BARt robot [10, 13].

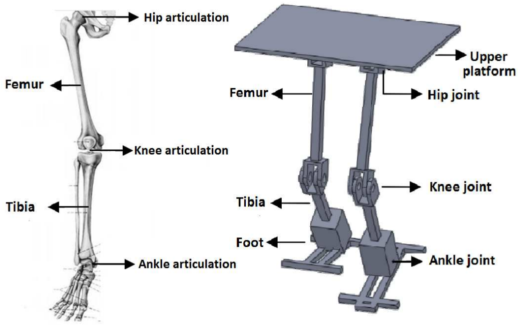

Figure 1: Design of biped robot mechanism similar to the human physiognomy and description of its parts [6].

Table 1 summarizes dimensional characteristics of the biped robot, it also shows approximate weight of each element that were taken from the CAD software.

	Dimensions (mm)	Weight (g)	Quantity	Total weight (g)
Foot	200 x 130	685	1	685
Tibia	400	700	1	700
Femur	450	745	1	745
Motor DC	150 – 254	820	3	2460
Upper platform	400x200	350	1	530
Total Leg Weight				**5120**

Table 1. Dimensional characteristics of the mechanism of the biped robot

Within the construction process of the fore mentioned biped robot, it became necessary to firstly develop a prototype, which would allow visualizing mechanical aspects not too evident in the CAD software. This prototype was developed in a 1:2 scale and used 6 servo motors as joint actuators. This prototype also served to test electronics and correct its design where needed.

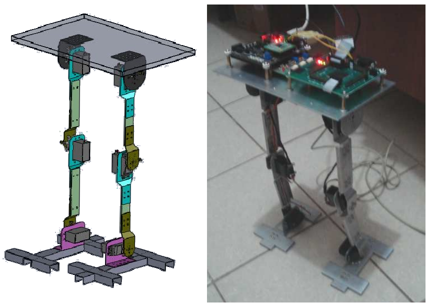

(a) (b)

Figure 2: (a) Prototype designed in solidworks, (b) implementation including the robot's circuitry.

2.2 Electronic's interface design

Electronic boards design is another important point in the development of this project. The selected electronic interface includes a TMS320F2812 DSP as main device, and a microcontroller MC9S08QE128 as servo motors driver. To monitor stability a 3-axis accelerometer is used.

This electronic circuit was located in the upper platform of the robot, along with the battery. However, for the prototype no batteries are used, as the main power source is external to the robot, and power is supplied by wires. The electronic design is shown in a block diagram is in Fig. (3). A PC is used to send the desired path to the system, using the RS232 protocol, this path is received by the DSP, which performs the necessary calculations to determine the angle each joint needs to move, these results are sent towards the microcontroller by a SPI protocol, this uC sends PWM pulses to the servo motors. Signals from the low power digital processor enter a power driver with optocouplers, to isolate them from high power actuating ones, so damage to the controllers is avoided. A three-axis accelerometer used to determine the robot's equilibrium is also placed on board. This information is used so, when the robot loses its balance, it shuts down and restarts the test run.

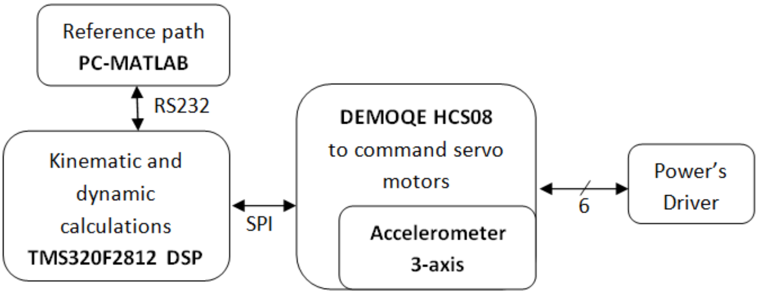

Figure 3: Electronic diagram block.

2.3 Modeling

For the dynamic model of the robot, Lagrange equations are used [1, 2, 3]. To do this, an inertial reference system must be selected. Primarily, this is addressed by assuming that each leg can move independently, so two independent end effectors with three degrees of freedom each one are considered; the objective of this method is to make each end effector follow its own desired path, with less computational effort that by considering a sole kinematic chain.

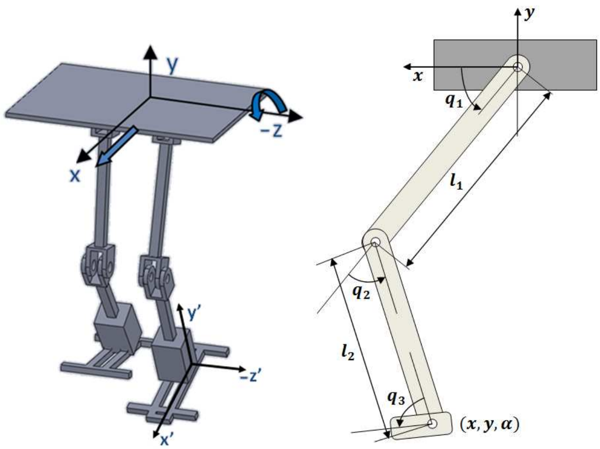

Figure 4: Biped robot with 6DOF, reference system on the top platform, with each ankle as end effector.

Below equations to model the biped robot are addressed [1].

*1) **Direct kinematics***

It defines the position of the end effector, according to the angular positions of the joints and considering the analysis of one leg only, this model is described in equation 2.1.

$$\begin{aligned} x &= l_1 \cos(q_1) + l_2 \cos(q_1 + q_2), \\ y &= -l_1 \sin(q_1) - l_2 \sin(q_1 + q_2), \\ \alpha &= q_1 + q_2 + q_3, \end{aligned} \tag{2.1}$$

where x, y are the end effector's position (base of the foot) on the hip; α is the end effector's orientation; q_1, q_2 and q_3 are the angular position of the joints located at the hip, knee and ankle, respectively; l_1 is the femur's link length; and l_2 is the tibia's link length; l_{c1} is the center femur's length and l_{c2} is the center tibia's length.

*2) **Inverse kinematics***

It is the angular position of each joint as a function of the desired trajectory. As mentioned before, each leg is considered as a 3DoF mechanism, so this robot needs one desired trajectory for each leg. The inverse kinematic are shown in equation 2.2, this was achieved by finding the angular positions using Equation 2.1, these are more complicated if the robot is considered as a sole mechanism with 6 DoF.

$$\begin{aligned} q_2 &= \cos^{-1}\left(\frac{x^2+y^2-l_1^2-l_2^2}{2l_1l_2}\right), \\ q_1 &= \tan^{-1}\left(\frac{x}{y}\right) - \tan^{-1}\left(\frac{l_2 \sin(q_2)}{l_1} + l_2 \cos(q_2)\right), \\ q_3 &= \alpha - (q_1 + q_2). \end{aligned} \tag{2.2}$$

3) Inverse jacobian

Inverse jacovian matrix is used to calculate the velocity of each joint; this matrix is shown in equation 2.3, robot's dimensions and desired trajectories are required to calculate this matrix.

$$J_i = \begin{bmatrix} \dfrac{\cos(q_1+q_2)}{l_1 \sin(q_2)} & \dfrac{-\sin(q_1+q_2)}{l_2 \sin(q_2)} & 0 \\ \dfrac{-l_1 \cos(q_1) - l_2 \cos(q_1+q_2)}{l_1 l_2 \sin(q_2)} & \dfrac{l_1 \sin(q_1) + l_2 \sin(q_1+q_2)}{l_1 l_2 \sin(q_2)} & 0 \\ \dfrac{\cos(q_1)}{l_2 \sin(q_2)} & \dfrac{-\sin(q_1)}{l_2 \sin(q_2)} & 1 \end{bmatrix}. \tag{2.3}$$

4) Static

This equation relates the forces and moments (F) applied by a load on each dc motor with the torques (τ) required to support such load and remain static.

$$\tau = J^T F,$$

$$\begin{bmatrix} \tau_1 \\ \tau_2 \\ \tau_3 \end{bmatrix} = \begin{bmatrix} -l_1 \sin(q_1) & l_1 \cos(q_1) & 0 \\ l_2 \sin(q_2) - l_1 \sin(q_1) & l_1 \cos(q_1) - l_2 \cos(q_2) & 1 \\ l_2 \sin(q_2) - l_1 \sin(q_1) & l_1 \cos(q_1) - l_2 \cos(q_2) & 0 \end{bmatrix} \begin{bmatrix} F_x \\ F_y \\ M \end{bmatrix}. \tag{2.4}$$

5) Dynamic

Equation 2.5 is the dynamic equation for robots of n DoF, which is a nonlinear vectorial differential equation of the state $\left[q^T \dot{q}^T \right]^T$, $H(q)$ is a matrix reffered to as the inertia matrix, which is symmetric and positive definite , $C(q,\dot{q})\dot{q}$ is a vector of dimension n called the vector of centrifugal and Coriolis forces, $G_{(q)}$ is a vector of dimension n of gravitational forces or torques and τ is a vector of dimension n called the vector of external forces, which in general corresponds to the torques and forces applied by the actuators at the joints [1].

$$H(q)\ddot{q} + C(q,\dot{q}) + G(q) = T.u, \tag{2.5}$$

calculation of the Inertia matrix:

$$h = m_2 l_1 l_{c2} C_{1-2} + m_3 l_1 l_2 C_{1-2}, \tag{2.6}$$

$$H = \begin{bmatrix} -l_{c1}^2 m_1 + m_2 l_1^2 + m_3 l_1^2 + I_1 & h & 0 \\ h & m_2 l_{c2}^2 + m_3 l_2^2 + I_2 & 0 \\ 0 & 0 & I_3 \end{bmatrix}, \tag{2.7}$$

calculation of the coriolis matrix:

$$C(q,\dot{q})\dot{q} = \dot{H}_{(q)}\dot{q} - \frac{1}{2}\frac{\partial}{\partial q}\left[\dot{q}^T H(q)\dot{q} \right], \tag{2.8}$$

$$C(q,\dot{q}) = \begin{bmatrix} -\frac{1}{2} l_1 (m_2 l_{c2} + m_3 l_2) sin(q_1 - q_2)\dot{q}_2 & l_1 (m_2 l_{c2} + m_3 l_2)(\frac{1}{2} sin(q_1 - q_2)\dot{q}_1 + sin(q_1 - q_2)\dot{q}_2) & 0 \\ -l_1 (m_2 l_{c2} + m_3 l_2)(sin(q_1 - q_2)\dot{q}_1 + \frac{1}{2} sin(q_1 - q_2)\dot{q}_2) & \frac{1}{2} l_1 (m_2 l_{c2} + m_3 l_2) sin(q_1 - q_2)\dot{q}_1 & 0 \\ 0 & 0 & 0 \end{bmatrix}. \tag{2.9}$$

For simulation, the previous equations can be coded in a matlab/simulink environment and used as the kinematic/dynamic model; however, another useful alternative is to employ simmechanics' blocks (which are part of a simulink toolbox [16]) and obtain the robot's dynamics directly from them. To do so, one can import the designs made in solidwork to simulink and use them. Fig. (1) showed both legs of our biped robot using simmechanics' blocks. Fig. (5) graphically shows the results of this model, left leg model is only shown as symmetrical results are obtained for the right one; moreover, this blocks also enables the representation of sensors and actuators. Different joints can also be selected, in this diagram a welded joint of the hip to a fixed point as an absolute reference is shown.

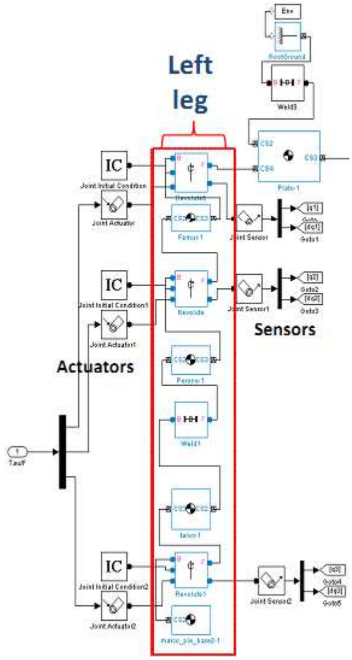

Figure 5: Simmechanics' blocks for modeling a robot's leg.

3 CONTROL

As gravity was added for a more realistic analysis, and because the effect generated by the weight of each link in our mechanism is always changing as the position of the centers of gravity, the gravity compensation should be considered. This factor must be added to the output signal of Fuzzy-PD control [4]. Gravity compensation also includes white noise that serves as an additional disruption to the controller, Fig. (6) shows the simulink model of the system including such features using simmechanics' blocks, while Fig. (7) shows the same implementation but with standard simulink blocks.

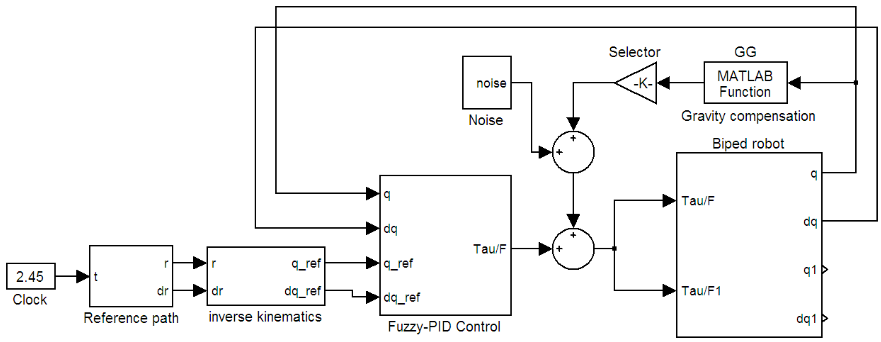

Figure 6: System model in simulink

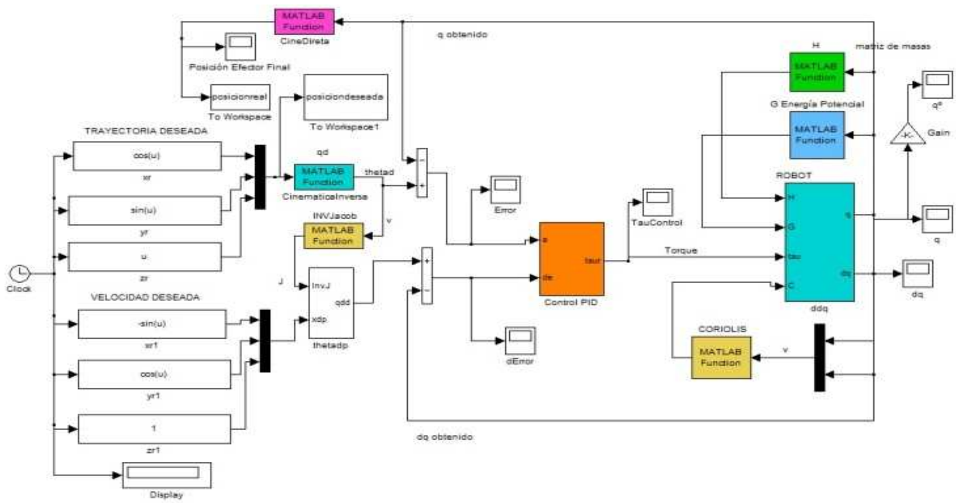

Figure 7: Simulation of the system in script code

3.1 Optimization of PID control by fuzzy logic

The common problem of PID control is the tuning of its parameters, Kp, Kd and Ki; the robot would have 18 parameters to tune, considering both legs, fuzzy logic algorithms can overcome this problem, because the parameters are automatically tuned using PID-Fuzzy control; membership functions to denote the error are triangular and trapezoidal types as shown in Fig. (8)

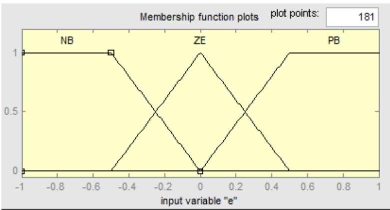

Figure 8: Membership functions

Mandani as fuzzy system is used, in addition to possible membership rules. Once designed our controller, change the initial PID for the new Fuzzy-PID [13]. Control blocks for the left leg are shown in Fig. (9), for each joint there is a PID control whose parameters are optimized with a fuzzy controller.

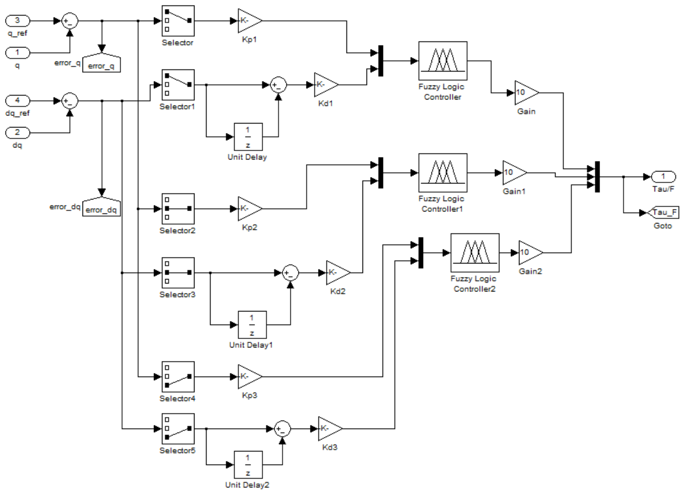

Figure 9: Fuzzy-PID control for each of the actuators

4 CAPTURE OF HUMAN MOVEMENT PATTERNS

4.1 Capture Data

After designing the robot, the end effector must follow the desired trajectory, in this case that trajectory should allow controlled movement of the robot at all times, so balance can be maintained during movement [7, 8, 9]. This reference trajectory can be obtained by observing the characteristics of human walk. To get accurate data, a LED diode can be placed at each joint and then record the walk on video [7]. For ease of image post processing, each LED must be of a different color. The video is then color filtered, and to further simplify this, basic RGB (red, green, blue) colors are used; located in the ankle, knee and hip respectively. Fig. (10) shows an example of this procedure.

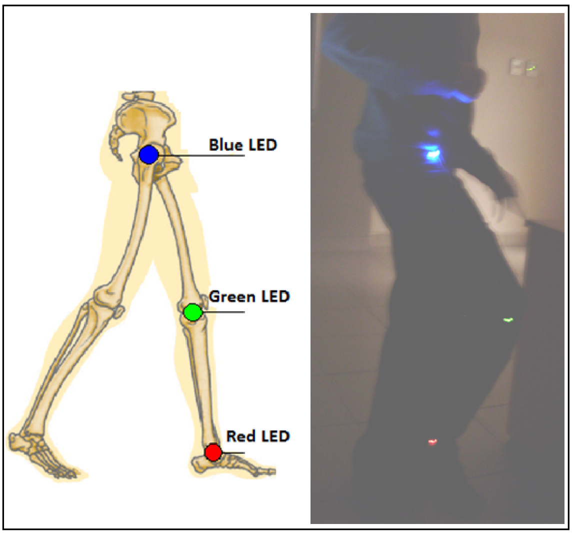

Figure 10: Location of LEDs diodes in joints to determine the reference trajectory

Because the robot size does not necessarily match the person's height used to define the reference trajectory; the curves of the Fig. (11), that are the result of the experiment described before, need be scaled in the same ratio than the robot's and the model person's size.

The method presented has as main advantage the ease to obtain, fairly easily, a wide range of trajectories, like the ones required to go up and down a staircase, to kneel down or even to jump. Nevertheless, it also presents disadvantages, as the mismatch between the positions of the LEDs and real joints, and the need for the camera to always lie perpendicular to the direction of the walk. In order to validate the curves obtained despite these problems, mathematical prove of the stability of these ones, as seen on several biped trajectory generation papers, is presented.

Separate graphs for each joint are:

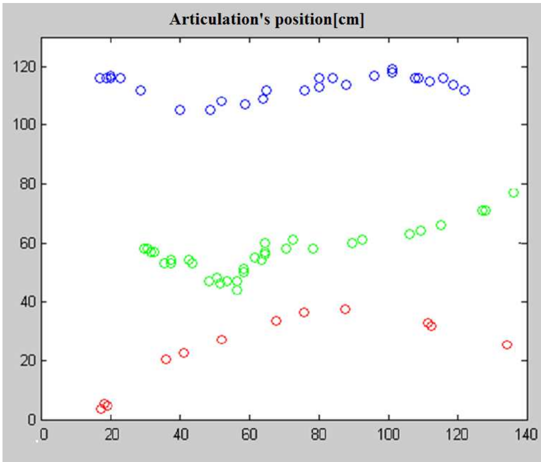

Figure 11: Reference trajectory for the robot's joints, hip (blue), knee (green) and ankle (red).

The trajectories shown in Fig. (11) are relative to a fixed point on earth; however, these should be replaced by others where the fixed point is the hip. To do so, each position vector of the ankle's trajectory must be subtracted from respective position of the hip; these points are shown in Fig. (12).

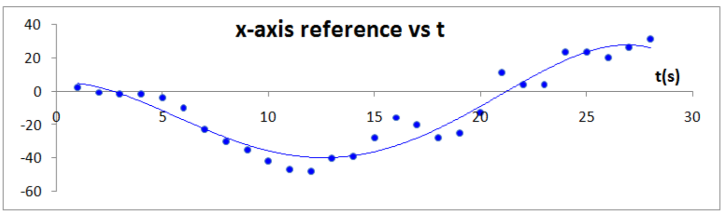

(a)

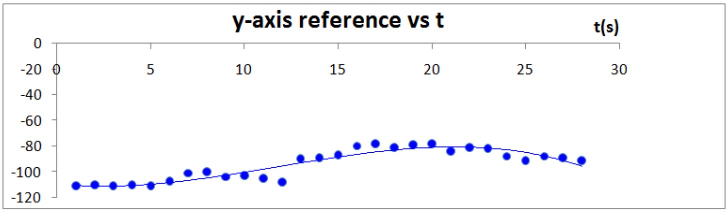

(b)
Figure12: Reference path for biped based on capture of human movement patterns (a) x-axis reference and (b) y-axis reference.

The corresponding parametric equations shown in Equation 4.1

$$x_{reference} = -0.001t^4 + 0.094t^3 - 1.247t^2 + 0.77t + 4.965,$$
$$y_{reference} = -0.009t^3 + 0.33t^2 - 1.476t - 10. \tag{4.1}$$

The polynomial curve described on Equation 4.1 was obtained by fitting the data from Fig. (12). A polynomial function was used as its derivate is easy to calculate, and it is required for Equation 2.5. This parametric equation relates to the ankle's trajectory with respect to the hip, for human walking.

5 THE FIRST PROTOTYPE'S IMPLEMENTATION

To test this work's results, a first prototype was implemented. This prototype is shown in Fig. (13), this 1:2 scale robot has as actuators servo motors, and includes all the electronic mentioned before, as all the mechanical design considerations for the structure described for the original model.

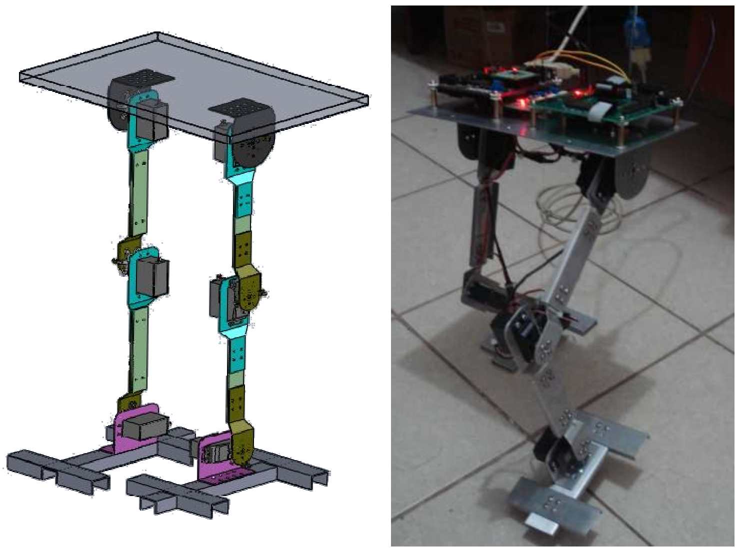

Figure 13: Implementation of the first prototype

5.1 Prototype's characteristics

- HCS08 freescale: servo motor controller.
- Processor: TMS320F2812 de TI [15]
- 3-axis accelerometer
- Size: 50x25cm
- Weight: 800g
- Power driver
- Servo motors tower Pro(2 in the hip 15Kg.cm, 2 in the knee 6Kg.cm)
- Servo motors Futaba: 2 in the ankle 3Kg.cm

5.2 Functional diagram of the prototype

The following diagram represents the input and output signals of our first prototype. Input signals are the reference trajectories obtained from the human walk (explained on section 4.1), and outputs PWM signals to the servo motors, previously passed through a power driver with optocouplers protection.

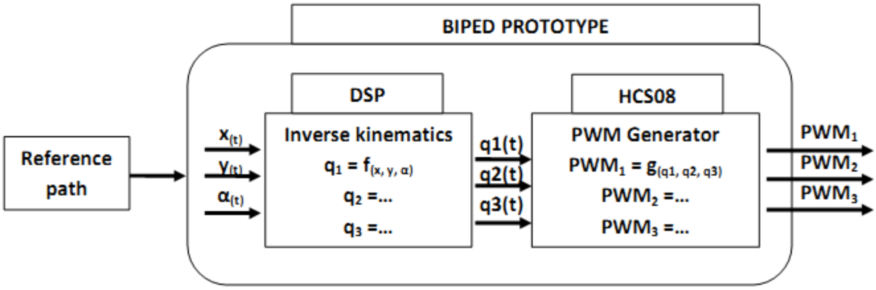

Figure 14: Prototype's functional diagram

5.3 Embedded system prototype

Fig. (15) shows the electrical circuit to implement our algorithms; it uses two independent power sources, one of 3.3VDC, which feeds the digital circuits, and a 15VDC power, which feeds the power circuits. Figure also shows the DSP in charge of making all the system's calculations. The DSP sends its results by SPI protocol to the PWM driver, which sends them to the power driver to generate movement in the servo motors. There is always monitoring from the PC by UART communication, and an accelerometer shuts down the system when it detects that the robot has lost its balance.

To implement the program, we must convert our system equation from matlab scripts [16] to C language code that is used to program the TMS320F2812-DSP. The required tasks to be implemented are shown in Table 2, and were implemented on a simple RTOS [5]. There are three important tasks that must be done by the uC. The first one is the kinematic calculations, which must be performed and fed to each motor. Then, another task is to control each motor by using an inner PID-Fuzzy loop; however, for the prototype this task is not required, as servomotors are used, which already come with an inner control loop for its position. Lastly, the uC must also supervise the 3-axis accelerometer, placed on top of the robot's hip, and communicate this information to a PC; this information is related to the robot's stability.

Task	Initialization	Main function
Calculations_task	Calculations_init	Calculations_run
Sensor_acell_task	Sensor_acell_init	Sensor_acell_run
Motor_hip_left_task	Motor_hip_left_init	Motor_hip_left_run
Motor_knee_left_task	Motor_knee_left_init	Motor_knee_left_run
Motor_ankle_left_task	Motor_ankle_left_init	Motor_ankle_left_run
Motor_hip_right_task	Motor_hip_right_init	Motor_hip_right_run
Motor_knee_right_task	Motor_knee_right_init	Motor_knee_right_run
Motor_ankle_right_task	Motor_ankle_right_init	Motor_ankle_right_run

Table 2: Tasks of embedded systems.

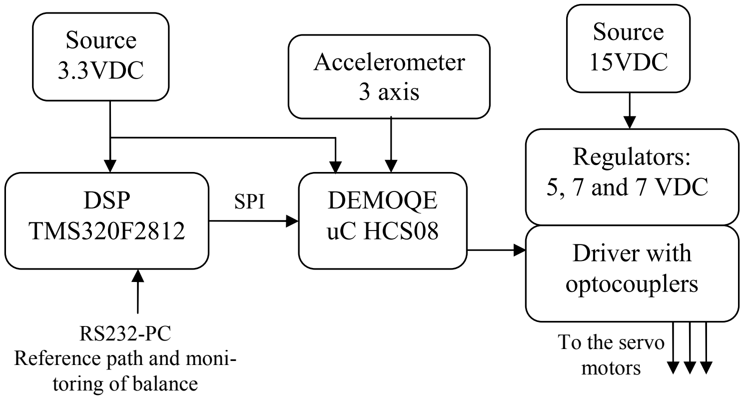

Figure 15: Electrical block diagram of biped prototype.

Below are the three cards installed on the upper platform of the robot.

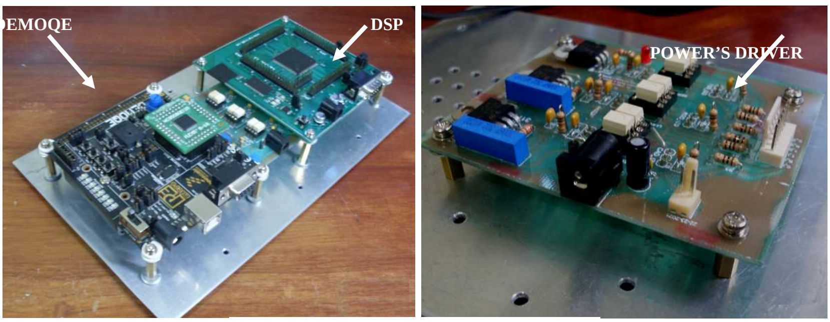

Figure 16: seating plans electronic circuits.

6 RESULTS

A straight line was used as reference trajectory to test the performance of our simulated system. The parameters chosen for the controller - proportional (Kp), derivative (Kd) and integral (Ki); are corrected by the Fuzzy-PID control.

Joint 1: Kp1=10, Ki1=2, Kd1=1
Joint 2: Kp2=10, Ki2=2, Kd2=1
Joint 3: Kp4=10, Ki4=2, Kd4=1

Fig. (17) shows the sequence of displacements obtained for a straight line as reference trajectory.

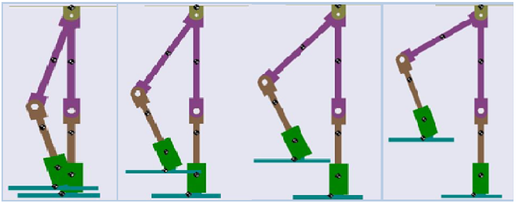

Figure 17: Sequence of states of the biped robot to follow a straight line as reference trajectory

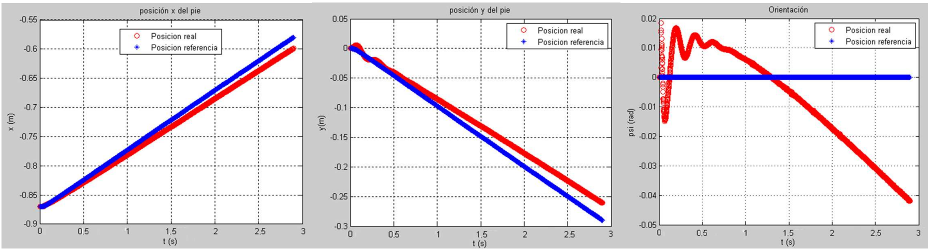

(a) (c) (b)

Figure 18. Diagrams of the reference and real trajectory for (a) hip, (b) knee and (c) ankle.

To show the proper behavior of the controller designed, errors from the obtained data and angular position of the motors are plotted in Fig. (18). From it can be noticed that the controller arrives to an stable output quite fast, this is better seen in Fig. (19) where end effector errors are shown.

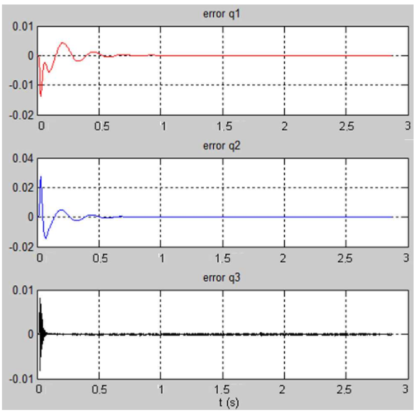

Figure 19: Good performance of the PID-Fuzzy, minimum error in each actuator.

7 CONCLUSIONS

- Desired trajectory modeled and controlled using the robot's ankle as effector, and considering each leg as an independent 3 DoF chain fixed over the upper platform, enabled the development of human walking, in an easy manner.
- Fuzzy-PD control of each motor enabled a correct tracking of desired trajectories, which were determined by the identification of human walking parameters.
- Kinematic equations, mechanical and electronic design, validation and testing were achieved thanks to the robotic prototype described.

ACKNOWLEDGEMENTS

The authors are grateful to Ricardo Rodriguez, Nilton Anchayhua and David Achancaccaray, for their valuable comments and contributions to this project; all of them being faculty from the Universidad Nacional de Ingeniería. We also thank the Mechanical Engineering department and the Center of Information and Telecommunications Technologies CTIC-UNI for giving the working facilities for the development of this project.

REFERENCES

References to books and papers:

[1] R. Kelly, V.Santiváñes and A. Loría. Control of robots manipulators in Joint Space, Springer , UK 2005

[2] Yildirim Hurmuzlu, Frank Genot, Bernard Brogliato. Modeling, stability and control of biped robots—a general framework, ELSEIVER, France 2004.

[3] C. Chevallereau, G. Bessonnet G. Abba, Y. Aoustin, Bipedal Robots- Modeling, Design and Walking Synthesis, London 2007: chapter 2.

[4] R. Westervelt, W. Grizzle, C. Chevallereau, Jun Ho Choi, B. Morris, Feedback Control of Dynamic Bipedal Robot Locomotion Systems. France, 2007, chapter I, II, pag. 26.

[5] Gustabo Galeano A. "Programación de Sistemas Embebidos en tiempo en lenguaje C", Editorial Alpha Omega. México2009.

[6] Carmen Bonell. "La Divina Proporción-las formas geométricas", Ediciones de la Unversidad Politécnica de Cataluña. 1999.

[7] Rawichote Chalodhorn, David B. Grimes, Keith Grochow, and Rajesh P. N. Rao, Learning to Walk through Imitation, Washington 2007.

[8] Sven Wehner, Maren Bennewitz, Optimizing the Gait of a Humanoid Robot Towards Human-like Walking.

[9] Rawichote Chalodhorn and Rajesh P. N. Rao, Using Eigenposes for Lossless Periodic Human Motion Imitation. USA 2009.

[10] O. Höhn, W. Gerth, Probabilistic Balance Monitoring for Bipedal Robots, Germany 2009.

[11] Marco Antonio Meggiolaro, Controle de Sistemas Robóticos, Departamento de Engenharia Mecânica, Pontifícia Universidade Católica – Rio de Janeiro 2008.

[12] Rob Platt, Howie Choset, Inverting the Jacobian and Manipulability, Carnegie 2008.

[13] Jan Jantzen, Technical University of Denmark, Department of Automation,, Tuning Of Fuzzy PID Controllers, Denmark 1998.

Reference websites:

[14] Bipedal Autonomous Robot BARt, Hannover University, 2004-2007

http://www.irt.uni-hannover.de/forschung/asr/bart.html.

[15] Texas Instrument for TMS320F2812-DSP http://www.ti.com/.

[16] Matlab website, also Simmechanics and Simulink, www.mathworks.com

[17] http://www.solidworks.com/

Proceedings of MUSME 2011, the International Symposium
on Multibody Systems and Mechatronics
Valencia, Spain, 25-28 October 2011

UNIFIED THEORY OF FIELDS IN SWARM BASED OPTIMIZATION METHODS

Alexandr Stefek*

* University of Defence
Faculty of Military Technology, Kounicova 65, 46022 Brno, Czech republic
e-mail: alexandr.stefek@unob.cz,
web page: http://www.vojenskaskola.cz/school/ud/Pages/default.aspx

Keywords: Optimization methods, Heuristic optimization, Particle swarm optimization, Gravity search algorithm

Abstract. *This paper discusses some approach to use combination of two optimization methods based on swarms. The combination relies on reusing force fields from original methods and as a result of combination the hybrid methods are introduced. One hybrid method is tested and compared to Particle swarm optimization method (PSO) and Gravitational search algorithm (GSA).*

1 INTRODUCTION

The recent history proved that heuristic optimization methods are able to solve many problems which cannot be solved ordinarily. Heuristic methods have several advantages. The first method introduced in this area is Particle Swarm Optimization method (PSO). This method offers high performance with low costs – the results are (in many cases) close to global optimum and the implementation is easy.

PSO method was the leader of the set of other heuristic methods. Many of them use the principles of mass point – particle move. Particles explore the state space and they are attracted by different forces and their fields.

The differences between methods are so small that some methods can be interpreted as variation of already well known method. At first sight are those differences are based on different forces. This idea inspires next chapters.

2 HEURISTIC OPTIMIZATION METHODS

As mentioned above there exist many optimization methods which use heuristic approach. In this paper the PSO and GSA will be discussed and modified in some way. PSO and GSA methods were chosen because they are simple and easy to understand. Moreover they are using really different forces. But in generally presented principles they can be used also in other heuristic methods.

Firstly let's remember some facts about PSO and GSA.

2.1 PSO

PSO method (Particle Swarm Optimization method – for clarification) is defined by following equations: [1]

$$\begin{gathered} x_{n+1} = x_n + v_n \\ v_{n+1} = c_0 v_n + c_1 r(x_l - x_n) + c_2 r(x_s - x_n) \end{gathered} \tag{1}$$

where x_l is the best solution for particle and x_s is the best solution for whole swarm, c_i are setup coefficients, r represents random numbers from interval $\langle 0; 1)$, x_n, v_n define current state of particle and x_{n+1}, v_{n+1} define the next state of particle.

In process of state space exploration the particles ~~tends~~ tend to return back to the best known position (solution) and tend to visit the best known swarm solution. This process is controlled by coefficients c_1 and c_2. Coefficient c_0 defines the slowing speed. In fact these equations define (in general) the unstable system. The c_0 coefficient plays role of stabiliser. If this coefficient is $c_0 \geq 1$ then the kinetic energy in system is growing infinitely and this means that system is unstable and cannot produce the desired solution.

2.2 GSA

GSA method (Gravitational Search Algorithm – for clarification) is defined by equations (eq. 2 - 4) [2]

$$\begin{gathered} F_{ij} = G\frac{M_i M_j}{R}\left(x_i - x_j\right) \\ F_i = \sum_{\forall j} F_{ij} \end{gathered} \tag{2}$$

where G is substitution of gravity constant, M_i, M_j are particle masses, x_i and x_j are particle positions, F_{ij} and F_i are forces. Mass of particles (planets) is weighted by the value of fitness function at point where the planet is. The masses are normalized. The normalization of mass is based on the fitness function value. The particle with better fitness function value has bigger mass. Normalization process is described by next equation

$$
\begin{gathered}
m_i = \frac{(f(x_i) - min)}{(max - min)} \\
min = min\{f(x_1), f(x_2), \cdots, f(x_n)\} \\
max = max\{f(x_1), f(x_2), \cdots, f(x_n)\} \\
M_i = \frac{m_i}{\sum m_i}
\end{gathered}
\tag{3}
$$

where min is current minimum of fitness function, max is current maximum of fitness function, m_i are masses and M_i are normalized masses. The gravity coefficient is not constant and vary in time according to next equation

$$G = G_0 e^{a(t)} \tag{4}$$

where G_0 is base gravity constant, $a(t)$ can be a function but usually it is constant, G is gravity constant for current state of optimization process.

In the optimization process the set of particles which are acting as gravity source (according to eq. 2) is reducing. This process reduces the ability to find a better solution as time goes on.

3 NEW DEFINITION FOR PSO AND GSA

As mentioned in previous chapter, PSO and GSA (but also many other methods) use motion laws (see eq. 5, 6).

$$
\begin{gathered}
\acute{x} = v \\
\acute{v} = a \\
a = \frac{\sum F}{m}
\end{gathered}
\tag{5}
$$

$$
\begin{gathered}
x_{n+1} = x_n + hv \\
v_{n+1} = v_n + ha \\
a = \frac{\sum F}{m}
\end{gathered}
\tag{6}
$$

where x or x_n is position, v or v_n is velocity, a is acceleration, m is mass and F is force, x_{n+1} is future position, v_{n+1} is future velocity, h is step size in evaluation process (it usually has the value $h = 1$).

The sum $\sum F$ means that all sources of forces must be summed to get the acceleration. Individual parts of this sum can be evaluated by different ways but it is always a result of some force field. In PSO and GSA methods there can be recognized Slowdown field, Personal best field, Global best field, Repulsive field, Gravity field and many others (which depends on add-ons to “classic” methods).

Let's define the individual fields.

3.1 Slowdown Field

As mentioned in equation (PSO basic def.) $v_{n+1} = c_0 v_n + \cdots$ This can be defined as Slowdown field

$$\begin{gathered} v_{n+1} = v_n + (c_0 - 1)v_n + \cdots \\ a = (c_0 - 1)v \\ \frac{F}{m} = a = (c_0 - 1)v \\ F = (c_0 - 1)vm \end{gathered} \tag{7}$$

Where mass of particle is m, v is particle velocity, c_0 is coefficient and F is force generated by slowdown field on particle.

3.2 Personal Best Field

Personal best field attract particles to their best known solution. The mathematical model of Personal best field is very simple and it reflects the part of eq. 1.

$$\begin{gathered} \frac{F}{m} = a = c_1 r(x_l - x_n) \\ F = c_1 r(x_l - x_n)m \end{gathered} \tag{8}$$

Where mass of particle is m, r is random number, c_1 is coefficient, x_l is personal best value, x_n is current particle position and F is force generated by field on particle.

3.3 Global Best Field

Global best field attracts particles to the best solution that the swarm found. The mathematical model is nearly the same as mathematical model of Personal best field. This model just reflects part of eq. 2.

$$\begin{gathered} \frac{F}{m} = a = c_2 r(x_s - x_n) \\ F = c_2 r(x_s - x_n)m \end{gathered} \tag{9}$$

Where mass of particle is m, r is random number, c_2 is coefficient, x_s is swarm best value, x_n is current particle position and F is force generated by field on particle.

3.4 Repulsive Field

Repulsive field represents the "repulsive" behavior. It has to avoid stuck in local optimum and keeps the ability to explore wide space. Basic idea of repulsion is derived from random solution generation. This random solution has ability to attract particles.

There exist more mathematical models for this behavior. Eq. 10 represents the easiest model which (in fact) does not vary in time. It is based on random solution x_{RND}.

$$\frac{F}{m} = a = c_3 r(x_{RND} - x_n)$$
$$F = c_3 r(x_{RND} - x_n)m \tag{10}$$

Where mass of particle is m, r is random number, c_2 is coefficient, x_s is swarm best value, x_n is current particle position and F is force generated by field on particle.

3.5 Gravity Field

Gravity field is base field in GSA method. Base equations are described in chapter 2.2 with eq. 2, 3 and 4. Those equations define the mathematical model of gravity field very well. There are not needed any improvements.

4 FIELDS APPLICATION

Fields which were defined above allows implementation of some objects which are usable generally. This means that "old" methods can be implemented by nearly the same way as new methods. In a fact this approach can define the user which is preparing the solution process.

4.1 Fields Combination

As mentioned in equation (new definition) the acceleration is defined as fraction of sum of forces and mass.

$$a = \frac{\sum F}{m} \tag{11}$$

Every force F has it's own field. In real world ~~exists~~ many different force fields and they act on real things, peoples, items independently. This behaviour inspires to make the experiments where many different fields (from different methods) will be used. This process can be named as Hybrid methods.

4.2 Hybrid Methods

As one consequence of implementation of force fields the hybrid methods can be introduced. Those methods have both properties which are derived from parent methods (PSO and GSA in this case). This can lead to additional possibilities of tuning.

Let's imagine that we have already evaluated forces from basic methods F_{PSO} and F_{GSA}. Those forces can be combined into one as defined in next equation

$$F = (1 - q)F_{PSO} + qF_{GSA} \tag{12}$$

Where q can vary in interval $\langle 0; 1\rangle$. Limit value 0 denotes PSO method and 1 the GSA method. In some general case the another form can be used

$$F = q_1 F_{PSO} + q_2 F_{GSA} \tag{13}$$

q_1 and q_2 are now independent.

Generally for hybrid methods any of fields that are used in optimization methods based on particle swarms can be involved. This idea gains big potential to combine the best parts of optimization methods and improve the results by this way.

As an experiment which is introduced later the simplest combination of parameters q_1 and q_2 was used. Both parameters was set to $q_i = 0.5$. As mentioned in paragraph above there are more possibilities but this setting prove that basic idea can be used for improvement of optimization methods based on swarms.

4.3 Object Model for Hybrid Methods / Fields Implementation

Physical space where particles are moving – the state space represents a container for particles. Each particle is dynamic system with 2 state variables (position vector and velocity vector) and one force vector accumulator. Two of them are for position and two for velocity. Force accumulators are set to zero vectors in every step of computation. Every force source (fields) evaluates it's forces for all particles and adds those vectors to particle force accumulators. After this phase every particle knows their force vectors and it is possible to move them to new positions.

Most important part is the force field evaluation. Force fields have to be designed as system with unified interface which makes the computation of field forces transparent.

This approach gives the leader of optimization process possibility to choose subparts of optimization methods to get better results than can be retrieved by the original methods.

5 EXPERIMENTS

For the idea presented above the experiment with optimization process was chosen.

As a base fitness function the Schefel's function was chosen. For comparison the GSA, PSO and hybrid method (based on GSA and PSO) was used.

5.1 Schefel's function

This function is defined in two possible forms. First form produces $f(x) = 0$ in expected optimum but in most cases the second form is used, where no normalizations was used. Eq. 14 presents both versions of Schefel's function [2].

$$
\begin{gathered}
f(x) = 418.9829n - \sum_{i=1}^{n} x_i sin\sqrt{|x_i|} \\
f(x) = -\sum_{i=1}^{n} x_i sin\sqrt{|x_i|}
\end{gathered}
\tag{14}
$$

Schefel's function is artificially designed to get function with many local optimums. In fact this function has not any global optimum. The particles tend to stuck in local optimum. Schefel's function is one of the hardest artificial problems even in its basic form. It is often used for benchmarking of optimization methods.

In this experiment we will use the R^2 version of this function. The problem of no global optimum is solved via definition of starting area to $x \in \langle -500; 500\rangle \times \langle -500; 500\rangle$. In this area the optimum is at $x_i = [420.9687, 420.9687]$ with value $f(x) = -837.9658$. Because the optimization problem defined by this function is not constrained, there is some probability to cross the defined border. As mentioned above this function has not any global optimum if constrains are not defined. This feature leads to situation where always can be found a better value. In fact this is a good point of benchmarking / comparison of more optimization methods.

The visualization of state space is shown on figure 1.

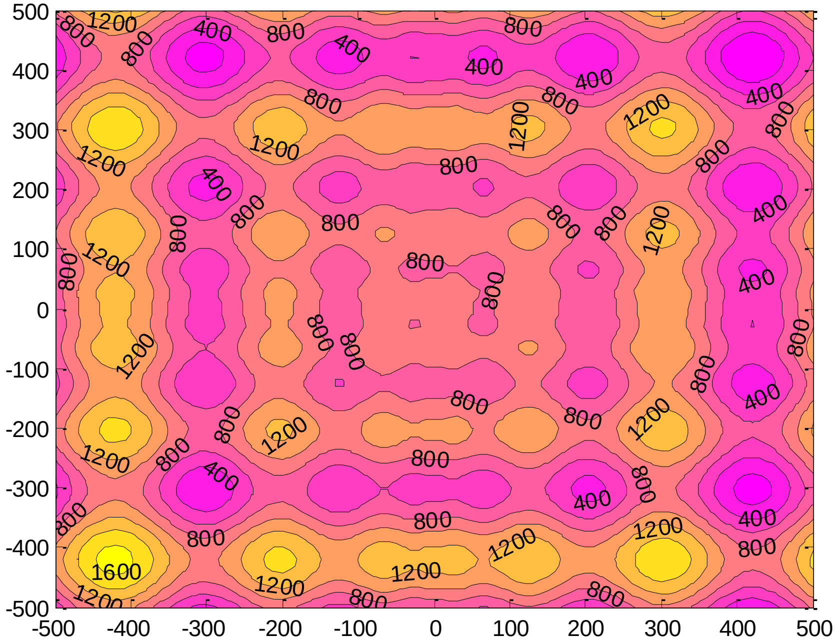

Figure 1: Schefel's function.

5.2 GSA, PSO and Hybrid method results

The experiments which have to found the best solution of fitness function must be normalized by some way. In this case any of individual experiment was limited to do 100000 calls of evaluation of fitness function.

Experiment No.	PSO	GSA	Hybrid A	Hybrid B	Hybrid C
1	-606.265	-382.586	-541.859	-501.455	-837.966
2	-469.272	-573.035	-601.089	-976.142	-719.527
3	-590.639	-541.512	-423.421	-502.388	-749.300
4	-686.458	-548.514	-916.917	-541.859	-482.618
5	-619.668	-473.806	-620.826	-324.628	-620.826
6	-423.446	-324.719	-1193.270	-364.180	-837.966
7	-613.892	-331.665	-976.142	-403.686	-541.859
8	-389.759	-420.13	-620.826	-620.826	-719.527
9	-484.163	-347.858	-837.966	-620.425	-364.180
10	-714.414	-492.766	-719.527	-482.618	-837.966
11	-680.083	-566.284	-620.826	-601.089	-719.527
12	-464.581	-399.933	-837.966	-719.527	-837.966
13	-499.172	-497.962	-620.826	-601.089	-423.421

Table 1: Results of individual experiments.

Fitness value	PSO	GSA	Hybrid A	Hybrid B	Hybrid C
Best	-714.414	-573.035	-1193.27	-976.142	-837.966
Worst	-389.759	-324.719	-423.421	-324.628	-364.180
Average	-557.062	-453.905	-733.189	-558.455	-668.665

Table 2: Experiment explanation.

As mentioned above the hybrid method use coefficients. Values are stored in next table.

Coefficient	Hybrid A	Hybrid B	Hybrid C
q_1	0.5	0.25	0.75
q_2	0.5	0.75	0.25

Table 3: Coefficient values.

GSA and PSO methods were unchanged. In some way the PSO method can be implemented as hybrid method with constants $q_1 = 1$, $q_2 = 0$ whereas GSA method uses $q_1 = 0$, $q_2 = 1$. Very important conclusion of experiments is that any tested hybrid method gets better results than pure method in average but best values were obtained with hybrid method where coefficients were equal (Hybrid A).

6 CONCLUSION

This paper decomposes "pure" methods to get force fields which are combined together with different impact on success in optimization process. As basement for decomposition the PSO and GSA methods was chosen. The tests which was performed with Schefel's function proved that new "hybrid" method offers better results in optimization methods that old ones. This approach can be generalized later when more fields from different methods will be combined to get better results.

REFERENCES

[1] J. Kennedy, R. Eberhart. Particle Swarm Optimization, In: Proc. *IEEE International Conference on Neural Networks*, Perth, Austria, 1995, URL: <http://www.engr.iupui.edu/~shi/Coference/psopap4.html>, [cit. 2011-02-27]

[2] E. Rashedi, H. Nezamabadi-pour, S. Saryazdi. GSA: A Gravitational Search Algorithm, In: *Information Sciences 179*, Elsevier 2002, ISSN 1935-3820, URL: <http://sci2s.ugr.es/eamhco/pdfs/formato07PIER.pdf>, [cit. 2011-01-18]

[3] Z. Krupka, A. Stefek. Method Cooperation in Optimization Process, In: Proceeding of International conference Mechatronika 2010, Trenčianske Teplice, Slovakia, ISBN 978-80-8075-394-8

[4] Z. Krupka, A. Stefek. Particle Swarm Optimization - Experiments and Results, In: Proceeding of AIM 09, International conference: Advances In Mechatronics 2009, Brno 2009, Czech republic, ISBN 978-80-7231-714-1

Proceedings of MUSME 2011, the International Symposium
on Multibody Systems and Mechatronics
Valencia, Spain, 25-28 October 2011

THE ORIGINAL DOUBLE-GOLDBERG 6*R* LINKAGE AND ITS BIFURCATION ANALYSIS

Chaoyang SONG, Yan CHEN

School of Mechanical and Aerospace Engineering
Nanyang Technological University, 50 Nanyang Avenue, 639798, Singapore
e-mail: song0068@ntu.edu.sg, chenyan@ntu.edu.sg

Keywords: Goldberg 5*R* linkage, original double-Goldberg 6*R* linkage, bifurcation analysis.

Abstract. *In this paper, the original double-Goldberg 6R linkage is obtained by merging two Goldberg 5R linkages on the commonly shared "roof-links" and then removing this connection to achieve the linkage. Two forms of the 6R linkage are obtained from this constructive method. Bifurcation analysis is performed to the original double-Goldberg 6R linkage to identify two other forms of the linkage in a full-circle movement. Transformation among these linkage forms reveals interesting morphing property of the linkage, which is worth attentions from related researchers.*

Notations:
z_i : coordinate axis along the revolute axis of joint i ;
x_i : coordinate axis along the common normal from z_{i-1} to z_i ;
$a_{(i-1)i}$: length of link $(i-1)i$, which is the common normal distance from z_{i-1} to z_i positively about x_i ;
$\alpha_{(i-1)i}$: twist of link $(i-1)i$, which is the rotation angle from z_{i-1} to z_i positively about x_i ;
R_i : offset of joint i , which is the common normal distance from x_i to x_{i+1} positively along z_i ;
θ_i : revolute variable of joint i , which is the rotation angle from x_i to x_{i+1} positively about z_i ;
a/α , b/β , c/γ , d/δ : the corresponding link length and twist of the same link are a and α , b and β , c and γ , or d and δ , respectively;
L, R: superscripts that denote different linkages during construction process.

1 INTRODUCTION

The study of overconstrained mechanisms has always been an interesting topic in mechanism design for over a century. Researchers such as Bennett [1, 2] and Bricard [3] have set the foundations and proposed their basic designs of overconstrained linkages. Most of the latter researchers are using existing linkages as the building block to create new overconstrained linkages. Goldberg [4] was the pioneer who used two or three Bennett linkages to build a series of 5*R* and 6*R* linkages by merging them on the common links or subtracting a linkage out of a primary loop. Later, Waldron [5] found a hybrid linkage by merging two Bennett linkages on a commonly shared joint axis to achieve a single-loop overconstrained 6*R* linkage. Wohlhart [6] further developed this concept by using two generalized Goldberg 5*R* linkages to be merged on the common “roof-links” to form an overconstrained 6*R* linkage. Chen & You [7] used similar method to combine two original Goldberg 5*R* linkages in a back-to-back configuration to form another overconstrained 6*R* linkage. Recently, Song and Chen [8] used one subtractive Goldberg 5*R* linkage and one original Goldberg 5*R* linkage to build a series of overconstrained linkages. In the area of kinematic analysis, Baker [9, 10] did the most work in studying linkages that using the Bennett linkages as the building block. However, little work has been done about linkages that are made of 5*R* linkages. In this paper, an original double-Goldberg 6*R* linkage, which is made of two original Goldberg 5*R* linkages, is studied at length. The bifurcation behavior of the linkage is investigated in detail to reveal the morphing nature of this particular linkage.

This paper is presented as follows. Section 2 introduces the kinematics of the original Goldberg 5*R* linkage. The two constructive forms of the original double-Goldberg 6*R* linkages are derived in section 3. In section 4, bifurcation analysis is performed to identify two non-constructive forms of the linkage. Conclusion is enclosed in section 5, which ends the paper.

2 KINEMATICS OF THE ORIGINAL GOLDBERG 5*R* LINKAGE

When two Bennett linkages are merged on a common link and two adjacent links are linearly posed, after removing the common link and joint, a Goldberg 5*R* linkage will be obtained as shown in Fig. (1).

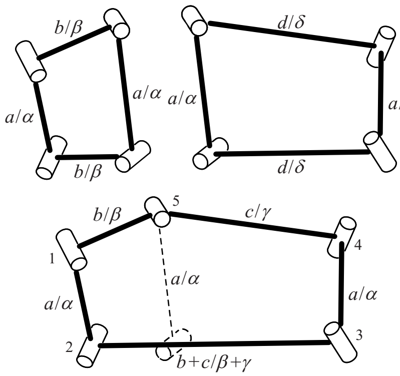

Figure 1: Construction of a Goldberg 5*R* linkage.

The geometry conditions and closure equations of the linkage are listed as

$$
\begin{gathered}
a_{12}=a_{34},\ a_{23}=a_{45}+a_{51}, \\
\alpha_{12}=\alpha_{34},\ \alpha_{23}=\alpha_{45}+\alpha_{51}, \\
\frac{\sin\alpha_{12}}{a_{12}}=\frac{\sin\alpha_{45}}{a_{45}}=\frac{\sin\alpha_{51}}{a_{51}}, \\
R_i=0\ (i=1,2,...,5);
\end{gathered} \tag{1}
$$

and

$$
\begin{gathered}
\tan\frac{\theta_2}{2}=\frac{\sin\frac{\alpha_{51}+\alpha_{12}}{2}}{\tan\frac{\theta_1}{2}\sin\frac{\alpha_{51}-\alpha_{12}}{2}},\ \tan\frac{\theta_3}{2}=\frac{\tan\frac{\theta_1}{2}\sin\frac{\alpha_{45}+\alpha_{12}}{2}}{\sin\frac{\alpha_{45}-\alpha_{12}}{2}},\ \theta_1+\theta_4=\pi, \\
\tan\frac{\theta_5}{2}=\frac{\left(1-\frac{\sin\frac{\alpha_{51}+\alpha_{12}}{2}}{\sin\frac{\alpha_{51}-\alpha_{12}}{2}}\frac{\sin\frac{\alpha_{45}+\alpha_{12}}{2}}{\sin\frac{\alpha_{45}-\alpha_{12}}{2}}\right)\tan\frac{\theta_1}{2}}{\frac{\sin\frac{\alpha_{51}+\alpha_{12}}{2}}{\sin\frac{\alpha_{51}-\alpha_{12}}{2}}+\frac{\sin\frac{\alpha_{45}+\alpha_{12}}{2}}{\sin\frac{\alpha_{45}-\alpha_{12}}{2}}\tan^2\frac{\theta_1}{2}}. \\
(\text{or } \theta_2+\theta_3+\theta_5=\pi)
\end{gathered} \tag{2}
$$

respectively. From the relationship between the revolute variables shown in Eq. (2), when we perform the algebraic substitution to make $x_i=\tan\frac{\theta_i}{2}\ (i=1,2,...,6)$, it is obvious that x_5 is quadratically related to x_1, while $x_{2,3,4}$ are linearly related to x_1. Therefore, for each value of θ_5, we can find two configurations of the linkage on the kinematic paths. For example, as shown in Fig. (2), when $\theta_5=5\pi/9$, we can locate configurations L1 and L2.

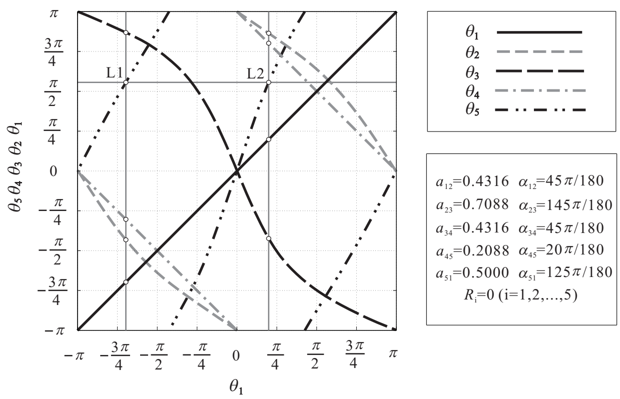

Figure 2: The input-output curves of the original Goldberg 5*R* linkage and the two configurations L1 and L2 when $\theta_5 = 5\pi/9$.

3 THE ORIGINAL DOUBLE-GOLDBERG 6*R* LINKAGE

In order to build the original double-Goldberg 6*R* linkage, two Goldberg 5 *R* linkages, namely linkages L and R, are such prepared so that they commonly share the same geometry conditions on the "roof-links", or link-pair 45-51. Therefore, we can have the geometry conditions of both linkages as

$$\begin{aligned}
&a_{12}^{\mathrm{L}} = a_{34}^{\mathrm{L}} = b,\ a_{23}^{\mathrm{L}} = a + c,\ a_{45}^{\mathrm{L}} = a,\ a_{51}^{\mathrm{L}} = c,\\
&\alpha_{12}^{\mathrm{L}} = \alpha_{34}^{\mathrm{L}} = \beta,\ \alpha_{23}^{\mathrm{L}} = \alpha + \gamma,\ \alpha_{45}^{\mathrm{L}} = \alpha,\ \alpha_{51}^{\mathrm{L}} = \gamma;\\
&a_{12}^{\mathrm{R}} = a_{34}^{\mathrm{R}} = d,\ a_{23}^{\mathrm{R}} = a + c,\ a_{45}^{\mathrm{R}} = a,\ a_{51}^{\mathrm{R}} = c,\\
&\alpha_{12}^{\mathrm{R}} = \alpha_{34}^{\mathrm{R}} = \delta,\ \alpha_{23}^{\mathrm{R}} = \alpha + \gamma,\ \alpha_{45}^{\mathrm{R}} = \alpha,\ \alpha_{51}^{\mathrm{R}} = \gamma.
\end{aligned} \tag{3}$$

From the results in previous section, take the configuration when $\theta_5^{\mathrm{L}} = 5\pi/9$ for example, we can find two layouts of linkage L, as shown in Fig. (3). Similarly, we can also find two layouts of linkage R when $\theta_5^{\mathrm{R}} = 5\pi/9$, as shown in Fig. (4). These configurations of linkages L and R will be used to build the original double-Goldberg 6*R* linkage.

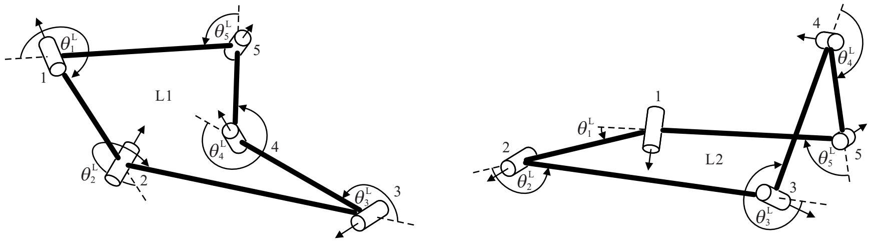

Figure 3: The spatial layout of L1 and L2 when $\theta_5^{\mathrm{L}} = 5\pi/9$.

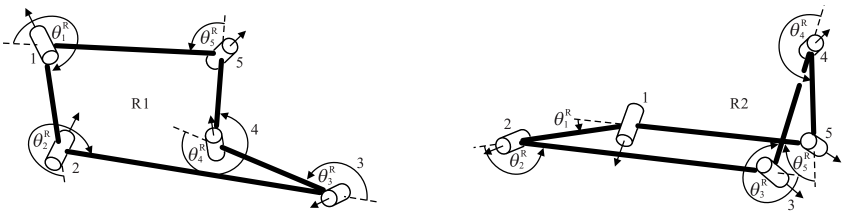

Figure 4: The spatial layout of R1 and R2 when $\theta_5^{\mathrm{R}} = 5\pi/9$.

3.1 Form I of the Original Double-Goldberg 6*R* Linkage

Linkages L1 and R2 will be used to build the Form I linkage. We first merge them on the commonly shared link-pair 45-51. Then, by removing this common link-pair, a single-loop overconstrained 6*R* linkage will be achieved as shown in Fig. (5). The geometry conditions of the Form I linkage are

$$\begin{gathered} a_{12} = a_{45} = a + c\,,\ a_{23} = a_{61} = b\,,\ a_{34} = a_{56} = d\,, \\ \alpha_{12} = \alpha_{45} = \alpha + \gamma\,,\ \alpha_{23} = \alpha_{61} = \beta\,,\ \alpha_{34} = \alpha_{56} = \delta\,, \\ \frac{\sin\alpha}{a} = \frac{\sin\beta}{b} = \frac{\sin\gamma}{c} = \frac{\sin\delta}{d}\,, \\ R_i = 0\ (i = 1, 2, \ldots, 6)\,. \end{gathered} \tag{4}$$

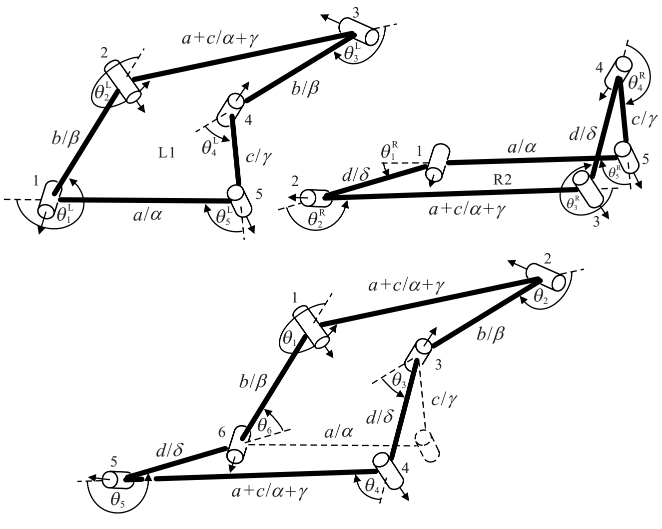

Figure 5: Construction of Form I original double-Goldberg 6*R* linkage by linkages L1 and R2.

According to Eq. (2), the closure equations of linkages L and R are

$$\tan\frac{\theta_2^{\mathrm{L}}}{2} = -\frac{m_1}{\tan\frac{\theta_1^{\mathrm{L}}}{2}},\ \tan\frac{\theta_3^{\mathrm{L}}}{2} = -m_2\tan\frac{\theta_1^{\mathrm{L}}}{2},$$
$$\theta_4^{\mathrm{L}} = \pi - \theta_1^{\mathrm{L}},\ \tan\frac{\theta_5^{\mathrm{L}}}{2} = \frac{(m_1m_2-1)\tan\frac{\theta_1^{\mathrm{L}}}{2}}{m_1 + m_2\tan^2\frac{\theta_1^{\mathrm{L}}}{2}}; \tag{5}$$

and

$$\tan\frac{\theta_2^{\mathrm{R}}}{2} = -\frac{m_3}{\tan\frac{\theta_1^{\mathrm{R}}}{2}},\ \tan\frac{\theta_3^{\mathrm{R}}}{2} = -m_4\tan\frac{\theta_1^{\mathrm{R}}}{2},$$
$$\theta_4^{\mathrm{R}} = \pi - \theta_1^{\mathrm{R}},\ \tan\frac{\theta_5^{\mathrm{R}}}{2} = \frac{(m_3m_4-1)\tan\frac{\theta_1^{\mathrm{R}}}{2}}{m_3 + m_4\tan^2\frac{\theta_1^{\mathrm{R}}}{2}}. \tag{6}$$

respectively. Here, $m_i\ (i = 1, 2, 3 \text{ and } 4)$ are used to simplify the following relationship.

$$m_1 = \frac{\sin\frac{\beta+\alpha}{2}}{\sin\frac{\beta-\alpha}{2}},\ m_2 = \frac{\sin\frac{\beta+\gamma}{2}}{\sin\frac{\beta-\gamma}{2}},\ m_3 = \frac{\sin\frac{\delta+\alpha}{2}}{\sin\frac{\delta-\alpha}{2}} \text{ and } m_4 = \frac{\sin\frac{\delta+\gamma}{2}}{\sin\frac{\delta-\gamma}{2}}. \tag{7}$$

The relationship between revolute variables of the resultant $6R$ linkage and linkages L and R are

$$\theta_1 = \theta_2^{\mathrm{L}},\ \theta_2 = \theta_3^{\mathrm{L}},\ \theta_3 = \pi - \theta_1^{\mathrm{L}} + \theta_1^{\mathrm{R}},$$
$$\theta_4 = 2\pi - \theta_3^{\mathrm{R}},\ \theta_5 = 2\pi - \theta_2^{\mathrm{R}},\ \theta_6 = \theta_1^{\mathrm{L}} - \theta_1^{\mathrm{R}} - \pi. \tag{8}$$

The compatibility relationship between linkages L and R is

$$\theta_5^{\mathrm{L}} = \theta_5^{\mathrm{R}}. \tag{9}$$

Therefore, we can subs titute Eqs. (5) and (6) into Eqs. (8) and (9) to derive the closure equations of the Form I linkage as

$$\tan\frac{\theta_2}{2} = \frac{m_1m_2}{\tan\frac{\theta_1}{2}},\ \theta_3 = \pi + 2\tan^{-1}\left(\frac{m_1}{\tan\frac{\theta_1}{2}}\right) + 2\tan^{-1}P_{\theta_1},$$
$$\tan\frac{\theta_4}{2} = m_4P_{\theta_1},\ \tan\frac{\theta_5}{2} = \frac{m_3}{P_{\theta_1}},\ \theta_6 = -\theta_3. \tag{10}$$

where

$$P_{\theta_1}=\frac{m_1m_2+\tan^2\frac{\theta_1}{2}}{2m_4(m_1m_2-1)\tan\frac{\theta_1}{2}}\left[(1-m_3m_4)\pm\sqrt{(1-m_3m_4)^2-\frac{4m_3m_4(m_1m_2-1)^2\tan^2\frac{\theta_1}{2}}{\left(m_1m_2+\tan^2\frac{\theta_1}{2}\right)^2}}\right].$$

Note that the above closure equations are in general form. When parameters of the geometry conditions changed, the value P_{θ_1} may apply to different domains to meet the condition of linkage closure. And the input-output curves of the Form I linkage are plotted in Fig. (6).

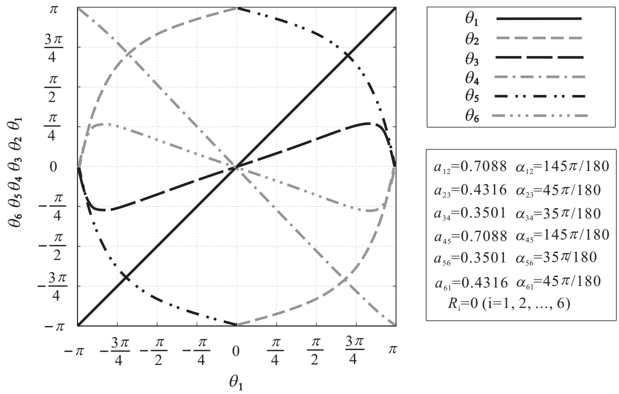

Figure 6: The input-output curves of Form I original double-Goldberg 6*R* linkage.

Similarly, we can achieve the Form I linkage by using linkages L2 and R1 as the construction bases, as shown in Fig. (7).

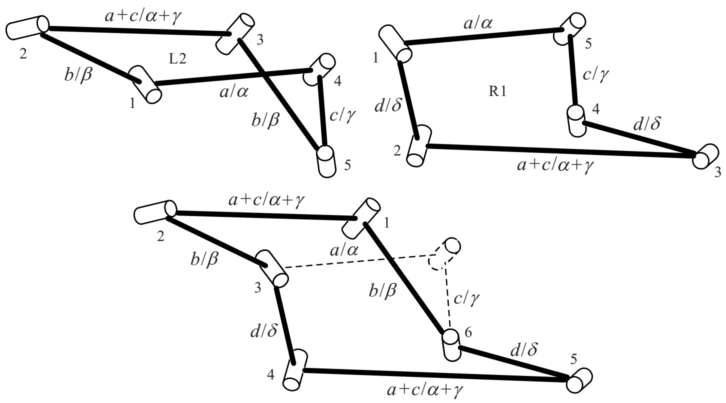

Figure 7: Construction of Form I original double-Goldberg 6*R* linkage by linkages L2 and R1.

3.2 Form II of the Original Double-Goldberg 6*R* Linkage

When using linkages L1 and R1 as the construction bases, through the same construction method as Form I linkage, a different form of the linkage, namely Form II linkage, will be obtained. As shown in Fig. (8), we can find that the geometry conditions of the Form II linkage are the same as the Form I linkage in Eq. (4). Even though they are derived from the same construction method, the Form II linkage has a different spatial layout as compared to the Form I linkage. Note that similar to the Form I linkage, when the parameters are changed, the value P_{θ_1} may apply to different domains to meet the condition of linkage closure.

$$\tan\frac{\theta_2}{2}=\frac{m_1 m_2}{\tan\frac{\theta_1}{2}},\ \theta_3=\pi+2\tan^{-1}\left(\frac{m_1}{\tan\frac{\theta_1}{2}}\right)+2\tan^{-1}P_{\theta_1},$$
$$\tan\frac{\theta_4}{2}=m_4 P_{\theta_1},\ \tan\frac{\theta_5}{2}=\frac{m_3}{P_{\theta_1}},\ \theta_6=-\theta_3, \tag{11}$$

where

$$P_{\theta_1}=\frac{m_1 m_2+\tan^2\frac{\theta_1}{2}}{2m_4(m_1 m_2-1)\tan\frac{\theta_1}{2}}\left[(1-m_3 m_4)\mp\sqrt{(1-m_3 m_4)^2-\frac{4m_3 m_4(m_1 m_2-1)^2\tan^2\frac{\theta_1}{2}}{\left(m_1 m_2+\tan^2\frac{\theta_1}{2}\right)^2}}\right].$$

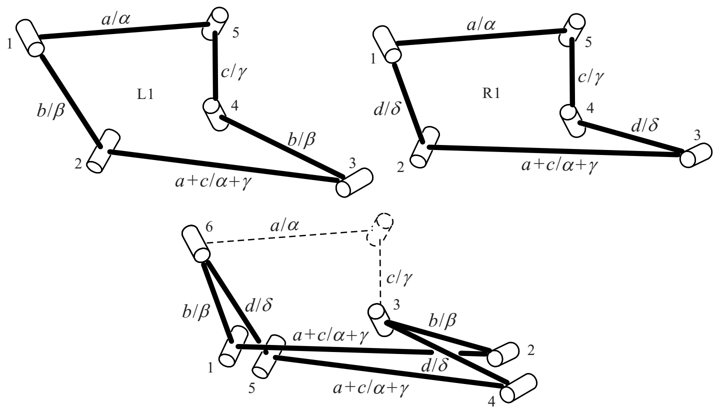

Figure 8: Construction of Form II original double-Goldberg 6*R* linkage by linkages L1 and R1.

The input-output curves of the Form II linkage are plotted in Fig. (9).

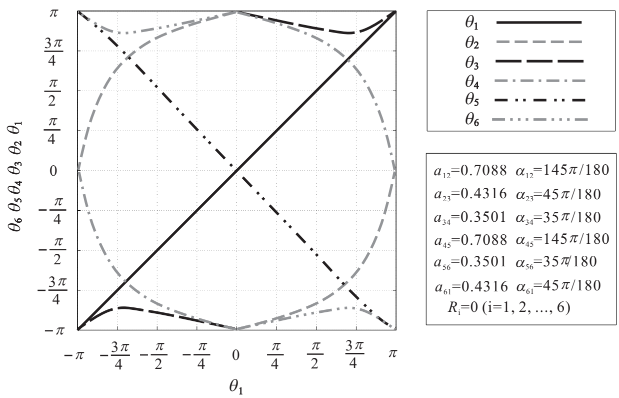

Figure 9: The input-output curves of Form II original double-Goldberg 6*R* linkage.

Alternatively, we can build the same linkage by using linkages L2 and R2 as the construction bases, as shown in Fig. (10).

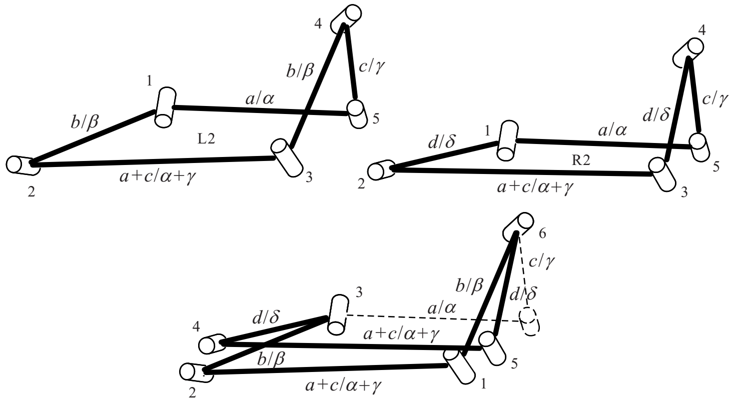

Figure 10: Construction of Form II original double-Goldberg 6*R* linkage by linkages L2 and R2.

4 BIFURCATION ANALYSIS OF THE ORIGINAL DOUBLE-GOLDBERG 6*R* LINKAGE

In order to take a further investigation into the kinematics of the original double-Goldberg 6*R* linkage, the method of Singular Value Decomposition (SVD) is used to examine the bifurcation behavior of the linkage. The SVD method is to solve the linkage's Jacobian matrix with a predictor and corrector step. Six singular values of the linkage's Jacobian matrix are monitored. When the sixth singular value remains zero, it indicates that the linkage has only one degree of freedom. When the fifth singular value falls to zero at some points, it indicates that the instantaneous mobility is increased in at these points. These points are the bifurcation points where the linkage might bifurcate into other kinematic paths. Plotted in Figs. (11) and (12) are the SVD results of the Forms I and II linkages. Bifurcation points are found in both figures when $\theta_1 = 0$ and $\theta_1 = \pm\pi$.

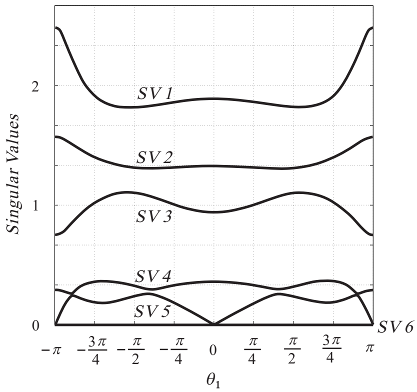

Figure 11: The SVD results of Form I original double-Goldberg 6R linkage.

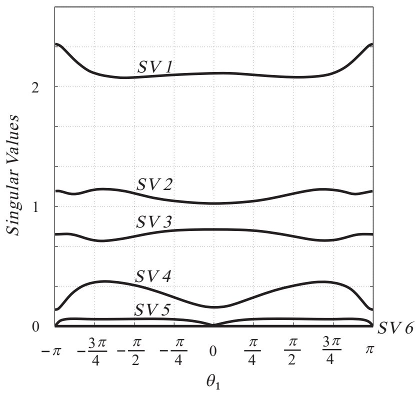

Figure 12: The SVD results of Form II original double-Goldberg 6R linkage.

4.1 Form III of the Original Double-Goldberg 6*R* Linkage

It is found that at the point $\theta_1 = 0$ in Fig. (11), the Form I linkage can bifurcate to another linkage form, namely the Form III linkage, as shown in Fig. (13). At the point $\theta_1 = \pm\pi$ in Fig. (12), the Form II linkage can bifurcate to the same linkage form.

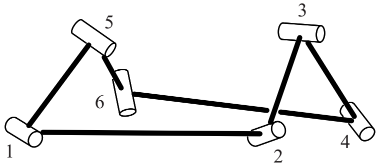

Figure 13: The Form III original double-Goldberg 6R linkage.

Different from Forms I and II linkages, the Form III linkage could not be decomposed into the combination between two Goldberg 5R linkages. By using the SVD method, we can plot the input-output curves of the linkage numerically, as shown in Fig. (14).

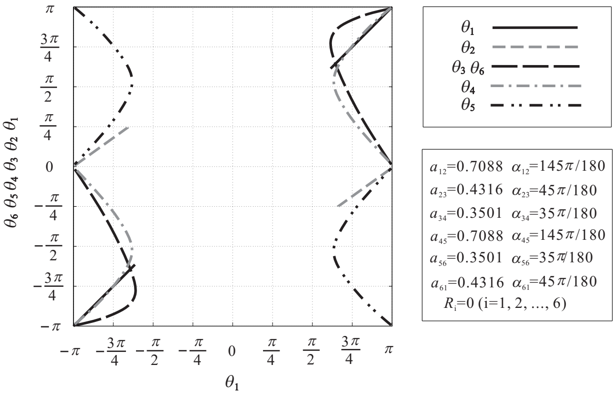

Figure 14: The input-output curves of Form III original double-Goldberg 6R linkage.

4.2 Form IV of the Original Double-Goldberg 6*R* Linkage

At the point $\theta_1 = \pm\pi$ in Fig. (11), the Form I linkage can bifurcate into the linkage form shown in Fig. (15), namely the Form IV linkage. At the point $\theta_1 = 0$ in Fig. (12), the Form II linkage can bifurcate to the same linkage form as well.

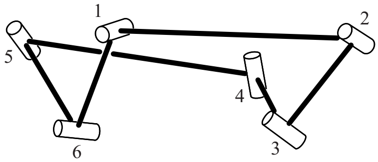

Figure 15: The Form IV original double-Goldberg 6R linkage.

The same as Form III linkage, the Form IV linkage cannot be decomposed into the combination between two Goldberg 5R linkages. By using the SVD method, we can plot the input-output curves of the linkage numerically, as shown in Fig. (16).

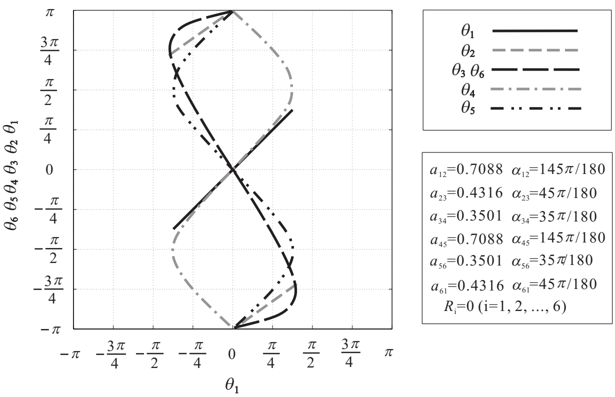

Figure 16: The input-output curves of Form IV original double-Goldberg 6R linkage.

θ and θ_1 as an example to demonstrate the transformation among these four forms of the original double-Goldberg 6*R* linkage. As shown in Fig. (17), (a)-(c) are the motion sequences of the Form I linkage; (d) is the bifurcation position B_{I} between the Forms I and III linkages; (e)-(g) are the motion sequences of Form III linkage; (h) is the bifurcation position $\mathrm{B}'_{\mathrm{II}}$ between the Forms III and II linkages; (i)-(k) are the motion sequences of Form II linkage; (l) is the bifurcation point B_{II} between the Forms II and IV linkages; (m)-(o) are the motion sequences of the Form IV linkage; (p) is the bifurcation position B'_{I} between the Forms IV and I linkages.

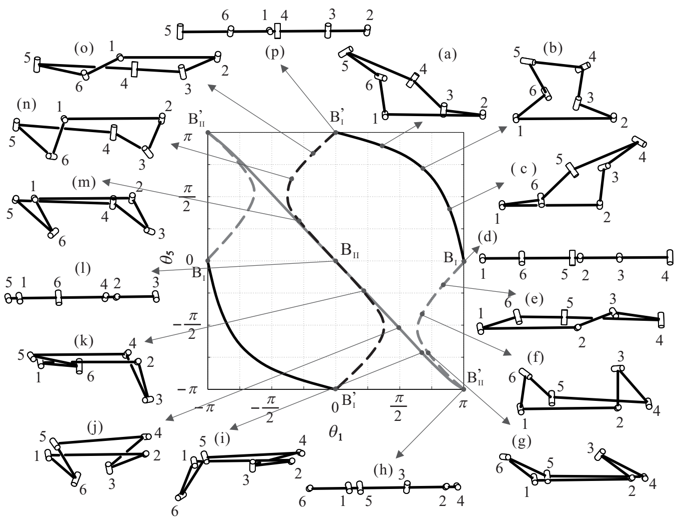

Figure 17: Transformation among different forms of the original double-Goldberg 6R linkage.

5 CONCLUSION

In this paper, the original double-Goldberg 6*R* linkage and its bifurcation behavior are studied at length. Because of the quadratic property of the revolute variable on the "roof-links" of the Goldberg 5*R* linkage, two different forms of the original double-Goldberg 6*R* linkages are achieved by merging two original Goldberg 5*R* linkages on the common "roof-links" and then removing this connection. By using the Singular Value Decomposition method, bifurcation points are located on both of the constructive forms of the linkage and two other forms of the linkage are found. The Forms I and II, which are derived from constructive method, are two different linkage forms; while the Forms III and IV, which are derived from numerical investigation, in fact share the same linkage layout. Moreover, Forms I and II cannot transform into each other directly, but they can only transform into each other by transform into either Forms III or IV first. Full transformation among these four forms of the original double-Goldberg 6*R* linkage makes it an interesting morphing structure to be studied.

ACKNOWLEDGEMENTS

Y. Chen would like to acknowledge the support from the Nanyang Technological University (NTU), Singapore, in the form of a research grant (RG 10/09). C. Y. Song would like to thank NTU for providing the University Graduate Scholarship during his PhD study.

REFERENCES

[1] G. T. Bennett. A new mechanism. *Engineering*, vol. 76, 777–778, 1903.

[2] G. T. Bennett. The skew isogram mechanism. *Proceedings of the London Mathematical Society*, vol. 2, 151, 1914.

[3] R. Bricard, Leçons de cinématique, *Tome II Cinématique Appliquée*, pp. 7-12, 1927.

[4] M. Goldberg, New five-bar and six-bar linkages in three dimensions, *Transactions of the ASME*, vol. 65, 649–663, 1943.

[5] K. J. Waldron, Hybrid overconstrained linkages, *Journal of Mechanisms*, vol. 3, no. 2, 73-78, 1968.

[6] K. Wohlhart, Merging two general Goldberg 5*R* linkages to obtain a new 6*R* space mechanism, *Mechanism and Machine Theory*, vol. 26, no. 7, 659-668, 1991.

[7] Y. Chen, and Z. You, Spatial 6*R* linkages based on the combination of two Goldberg 5*R* linkages, *Mechanism and Machine Theory*, vol. 42, no. 11, 1484-1498, 2007.

[8] C. Y. Song, and Y. Chen, A spatial 6*R* linkage derived from subtractive Goldberg 5*R* linkages, *Mechanism and Machine Theory*, vol. 46, no. 8, 1097-1106, 2011.

[9] J. E. Baker, The Bennett, Goldberg and Myard linkages--in perspective, *Mechanism and Machine Theory*, vol. 14, no. 4, 239-253, 1979.

[10] J. E. Baker, A comparative survey of the Bennett-based, 6-revolute kinematic loops, *Mechanism and Machine Theory*, vol. 28, no. 1, 83-96, 1993.

Proceedings of MUSME 2011, the International Symposium
on Multibody Systems and Mechatronics
Valencia, Spain, 25-28 October 2011

INVERSE AND DIRECT KINEMATICS OF AN UNDERWATER PARALLEL ROBOT

Hector A. Moreno, **Roque Saltaren**, **Eugenio Yime and Isela Carrera**

Center for Automation and Robotics, Technical University of Madrid-CSIC
Calle José Gutierrez Abascal, 2. 28006. Madrid. Spain
e-mail: hmoreno@etsii.upm.es

Keywords: Kinematics, Underwater Robot, Parallel Structure.

Abstract. *The kinematic analysis of a novel underwater robot with parallel mechanical structure, is presented. First, we introduce the design of this robot, named Remo II. Then the principal components of the robot (mechanical and electrical) are described. Due to its structure, this robot requires a smaller number of thrusters to navigate than other underwater vehicles. However, the kinematic analysis of this robot is more complex than conventional underwater robots. In this paper the position, velocity and acceleration kinematic analyzes of Remo II, are performed. The inverse kinematics formulation is easily parallelizable and can be implemented in multiple-core processors. On the other hand, the direct position kinematics is solved by constructing a kinematic constraints vector and using the Newton-Raphson numerical method.*

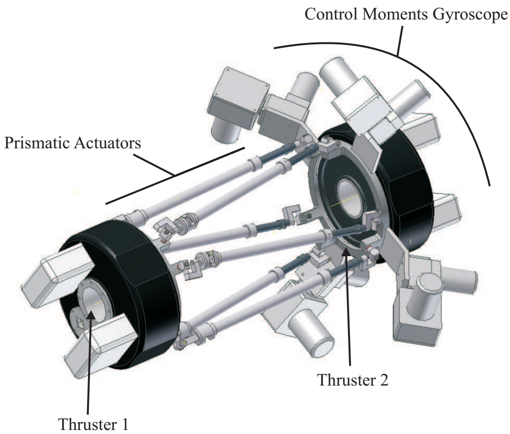

Figure 1. Underwater Robot Remo II.

1. INTRODUCTION

In the last decades, multiples architectures for underwater robots have been proposed. These architectures vary mainly in the number and disposition of the thrusters [19, 17]. In recent years there have been some efforts to equip submarines with vectored thrusters [12, 4, 14]. Thrust-vectoring has been used successfully for enhancing the maneuverability of aircraft, and different researchers believe this method must provide the same results in underwater environments.

More recently, a different concept of underwater robotics design, that provides thrust-vectoring, has appeared: underwater robots with parallel mechanical structure [3, 15]. In [15] an underwater robot, whose parallel structure allows controlling the position and orientation of a thruster, was presented. This type of mechanism provides higher maneuverability and thrust-vectoring by controlling the geometric configuration of the underwater vehicle.

However, modeling these robots is much more difficult than conventional underwater robots. The problem is mainly due to the complexity of modeling the parallel structure. Currently, the modeling of robots with parallel kinematic structure is an attractive research area because of its interesting features. In particular, several analytical and numerical formulation have been proposed for the kinematics modeling of different robotic architectures [9, 7, 18, 13].

Nevertheless, in all these works it is assumed that one of the platforms is fixed to the inertial frame. In this work we present the kinematic analysis of a parallel robot where neither of the platforms is fixed to the inertial frame. We also propose a strategy for computing the solutions of the inverse kinematic problems of position, velocity and acceleration, in multiple processors. For the direct kinematic problem a numerical method based on the Newton-Raphson formulation and a constraint function is presented.

The distribution of this paper is as follows: first, in the following section a description of Remo II is presented. After that, a brief introduction to underwater robotics kinematic modeling is summarized. Then, we present the kinematic modeling of the underwater robot REMO II. Finally, the last two sections discuss the results of a simulation and present the conclusions of this paper.

2. DESCRIPTION OF THE SYSTEM

REMO II is an underwater robot based on a Stewart-Gough (SG) parallel mechanism. This parallel structure is 6 DoF mechanism, composed of two platforms connected by six linear actuators using spherical and universal joints. This particular kinematics configuration has remarkable advantages compared to a serial 6 DoF mechanism, and has been proposed for several applications [13, 2, 11, 1, 16].

One of these advantages is its high rigidity, since the linear actuators are actively part of its mechanical structure and the load is distributed between the active legs. On the other hand, the parallel distribution of the actuators allows to withstand high forces and torques applied to the SG platform. Finally, the SG platform has low inertia, that consequently allows obtaining high velocities and accelerations.

The navigation system of the REMO II is composed by two thrusters and a control moments gyroscope (CMG). The thrusters are placed on each platforms respectively, and generate linear forces. Therefore, the control of the relative position and orientation of the platforms of the SG mechanism, allows the generation of a controlled resultant force.

The CMG system is composed of four controlled gyroscope with pyramidal configuration, mounted over one of the platform of the SG mechanism. The CMG can generate a resultant force (depending of the velocity and orientation of each gyroscope), that compensate the torque produced by the forces of navigation, thus improving the manoeuvrability of the robot.

The mechanical elements of the parallel structure of Remo II are made of stainless steel and aluminum. The SG platform that makes up the underwater vehicle weighs 15 kg and has a dimension of 550 x 300 x 300 mm with an aluminium structure. The CMG structure can be contained inside of a 800 mm-radius and 200 mm-height cylinder. Moreover, it adds 10 kg to the weight of the underwater vehicle.

The electronic components of the Remo II are allocated and distributed inside the hulls coupled at either ring of the SG platform. These hulls are made of PVC in one piece in order to improve its weight and sealing. They also have aluminium plates, which allows dissipating the heat generated by the electronics. These hulls add 400 mm to the SG platform length, therefore the UPR without the CMG is 950 x 300 x 300 mm in size.

Remo II has two embedded computers. The main computer controls the parallel structure and thrusters, and the CMG computer controls the gyroscopes. Both embedded systems are TS5600 computers of Technologic System, based on PC104 board. Both computers are connected through an ethernet port.

The main computer uses two analog outputs to control the velocity of the thrusters, and a CAN bus to communicate with the motor controllers of the SG platform linear actuators.

The embedded computer of the CMG controls the motion of the gimbal motors, and reads the data from the IMU. A PC104 CAN card is employed to carry out CAN communication with the EPOS 24/1. The TS5600 uses an analog output to command the speed of the gyroscopes flywheels through DEC 24/1 drivers. A RS-232 port is used for communication with the inertial unit. The ethernet port is used for communication with the main computer.

The six prismatic joints of the parallel structure are actuated by six 12 W Maxon Motors ECMax22. The selection of these actuators was done considering the continuous torque and the size of the electronic controller, which is EPOS24/1 controller. Each actuator is coupled to a

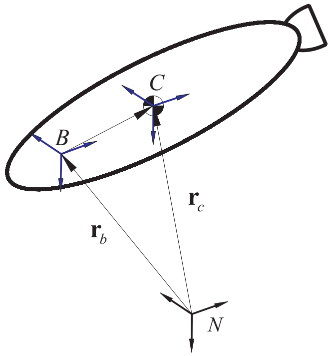

Figure 2. Scheme of an AUV

gearbox, and the gearbox is coupled to a ballscrew. The gearbox is Maxon GP22C with a 14:1 reduction. Altogether, the system motor-gearbox-ballscrew, is designed to provide a force of 15 N and a maximum velocity of 50 m/s, and 245 mm of maximum stroke.

Each gyroscope of the CMG is actuated by two electric motors, one of them controls the flywheel velocity and the other controls its orientation (gimbal). The flywheel of the gyroscope is directly coupled to a 25 W Maxon Motor ECMax-22 that reaches the 10000 rpm. The gimbal motor is a 16W Maxon Motor ECMax, coupled with a planetary gearbox of 231 : 1 reduction. The maximum velocity of the gimbal is 10 rpm, and can achieve a 360^o rotation.

Both thrusters can generate a force of 21.6 N. The robot has several sensors, such as the Iner-tial Measurement Unit (IMU), a depth sensor, a liquid lever sensor, etc.

3. MODELING OF UNDERWATER ROBOTS

When analyzing the motion of underwater robots two reference frames are defined to characterize their motion, named North-East-Down reference frame (denoted by *N*) and the Body reference frame (denoted by *B*) [6], see fig. 2.

The *N* reference frame is an inertial system defined on the surface of the Earth, where the *x* axis points towards North, the *y* axis points towards East, and the *z* axis points to the center of the Earth.

The location of the body's reference frame *B* with respect to the *N* reference frame is denoted by $\eta = \begin{bmatrix}\mathbf{r}_b^n & \Theta\end{bmatrix}^T$, where $\mathbf{r}_b^n$ is the position vector of the origin of the reference frame *B* with respect to the *N* frame, and Θ is the Euler angles vector that represents the relative orientation between the body and the *N* frame.

In navigation and control it is commonly used the *roll-pitch-yaw* convention to represent the orientation of the frame *N* to the frame *B* specified in terms of the Euler angles ψ, θ, and ϕ, respectively. The rotation matrix $\mathbf{R}_b^n$ is given by:

$$\mathbf{R}_b^n = \begin{bmatrix} c\psi c\theta & -s\psi c\phi + c\psi s\theta s\phi & s\psi s\phi + c\psi c\phi s\theta \\ s\psi c\theta & c\psi c\phi + s\phi s\theta s\psi & -c\psi s\phi + s\theta s\psi c\phi \\ -s\theta & c\theta s\phi & c\theta c\phi \end{bmatrix} \tag{1}$$

and $s\cdot = \sin(\cdot)$ and $c\cdot = \cos(\cdot)$.

Unlike a non-submerged rigid bodies, the convention used for underwater vehicles is to express the velocity as a function of the local reference system of the body. The vector $\nu = \begin{bmatrix}\mathbf{v}_b^b & \omega_b^b\end{bmatrix}^T$ is composed by the linear velocity $\mathbf{v}_b^b$ and the angular velocity ω_b^b of the body with respect to N frame decomposed in the body's reference frame. The vector $\dot{\eta} = \begin{bmatrix}\dot{\mathbf{r}}_b^n & \dot{\Theta}\end{bmatrix}^T$ is composed by the velocity of of the body's reference frame with respect to the N frame $\dot{\mathbf{r}}_b^n$, and $\dot{\Theta}$ is the time derivative of the Euler angles.

The angular velocity vector of the body ω_b^b and the Euler rate vector $\dot{\Theta}$ are related through a transformation matrix $\mathbf{T}_\Theta$ according to:

$$\dot{\Theta} = \mathbf{T}_\Theta \omega_b^b \tag{2}$$

where $\mathbf{T}_\Theta$ is given by:

$$\mathbf{T}_\Theta = \begin{bmatrix} 1 & s\phi t\theta & c\phi t\theta \\ 0 & c\phi & -s\phi \\ 0 & s\phi / c\theta & c\phi / c\theta \end{bmatrix} \tag{3}$$

and $t\cdot = \tan(\cdot)$. Summarizing the previous expressions, the kinematic model of the robot can be expressed as:

$$\dot{\eta} = \begin{bmatrix} \mathbf{R}_b^n & \mathbf{0} \\ \mathbf{0} & \mathbf{T}_\Theta \end{bmatrix} \nu \tag{4}$$

4. INVERSE KINEMATICS OF REMO II

In this section we solve the inverse kinematics problem. Therefore, given the time history of a desired trajectory for the underwater vehicle, the prismatic actuator and leg's bodies positions, velocities and acceleration must be determined. The time history of the robot can be expressed in terms of the position and orientation of both platforms, and their time derivatives.

For the analysis, we attach a reference frame P_1 to platform 1 and another reference frame P_2 to platform 2. The universal joints U_i are placed over platform 1, and the spherical joints S_i are placed over platform 2.

Additionally, we define two reference frames at the center of mass of each link of the ith-leg L_{1i} and L_{2i}. Since both reference frames L_{1i} and L_{2i} have the same orientation we define an auxiliary parallel reference frame L_i to each leg (with origin at U_i) in order to simplify the nomenclature of the equations. See Fig. 3.

4.1 Position Analysis

Consider Fig. 3, the vector associated to the ith-leg can be found according to:

$$\mathbf{d}_i^n = \mathbf{r}_{p2}^n + \mathbf{R}_{p2}^n \mathbf{s}_i - (\mathbf{r}_{p1}^n + \mathbf{R}_{p1}^n \mathbf{u}_i) \tag{5}$$

where $\mathbf{r}_{p1}$ is the position vector of frame P_1 with respect to the fixed frame, $\mathbf{r}_{p2}$ is the position vector of frame P_2 with respect to the fixed frame. $\mathbf{R}_{p1}$ and $\mathbf{R}_{p2}$ are the rotation matrices of platform 1 and platform 2 relative to the fixed frame, respectively. Vector $\mathbf{u}_i$ denotes the position of universal joint U_i in platform 1, and $\mathbf{s}_i$ represents the position vector of the spherical joint S_i in platform 2.

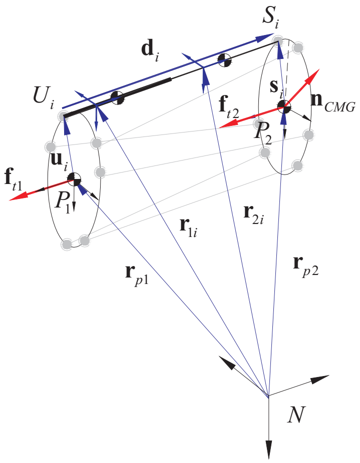

Figure 3. Remo II Scheme

The direction unit vector associated to the ith-leg is given by $\hat{\mathbf{d}}_i^n = \mathbf{d}_i^n / \|\mathbf{d}_i^n\|$

Given the position and orientation of both platforms, the position of the reference frames of the links is computed as follows:

$$\mathbf{r}_{1i}^n = \mathbf{r}_{p1}^n + \mathbf{R}_{p1}^n \mathbf{u}_i - \mathbf{r}_{ui}^n \tag{6}$$

and

$$\mathbf{r}_{2i}^n = \mathbf{r}_{p2}^n + \mathbf{R}_{p2}^n \mathbf{s}_i - \mathbf{r}_{si}^n \tag{7}$$

where $\mathbf{r}_{ui}^n = -l_u \hat{\mathbf{d}}_i^n$ and $\mathbf{r}_{si}^n = l_s \hat{\mathbf{d}}_i^n$. l_u is the distance between the center of mass of link 1 and the universal joint. l_s is the distance between the center of mass of link 2 and the spherical joint.

The reference frames attached to both bodies of the leg are defined considering that the $\hat{\mathbf{z}}_i^n$ axis is along the direction of vector $\hat{\mathbf{d}}_i^n$; the $\hat{\mathbf{y}}_i^n$ axis is normal to the plane given by $\hat{\mathbf{z}}_i^n$ and $\mathbf{s}_i$; finally $\hat{\mathbf{x}}_i^n$ is orthogonal to both $\hat{\mathbf{z}}_i^n$ and $\hat{\mathbf{y}}_i^n$.

Therefore, the orientation of the ith-leg referenced to the N frame can be expressed according to the rotation matrix given by:

$$\mathbf{R}_i^n = \begin{bmatrix} \hat{\mathbf{x}}_i^n & \hat{\mathbf{y}}_i^n & \hat{\mathbf{z}}_i^n \end{bmatrix} \tag{8}$$

where $\hat{\mathbf{z}}_i^n = \hat{\mathbf{d}}_i^n$, $\hat{\mathbf{y}}_i^n = (\mathbf{s}_i^n \times \hat{\mathbf{z}}_i^n)/\|\mathbf{s}_i^n \times \hat{\mathbf{z}}_i^n\|$ and $\hat{\mathbf{x}}_i^n = \hat{\mathbf{y}}_i^n \times \hat{\mathbf{z}}_i^n$. Since L_{1i} and L_{2i} have the same orientation of L_i we have $\mathbf{R}_{1i}^n = \mathbf{R}_{2i}^n = \mathbf{R}_i^n$.

The joint variable is obtained in the following way:

$$\rho_i = \|\mathbf{d}_i^n\| - l_m \tag{9}$$

where l_m is the dead length of the actuator.

4.2 Velocity Analysis

In order to obtain the velocity model of the robot, first we compute the time derivative of (5):

$$\mathbf{v}^n_{di} = \mathbf{v}^n_{p2} + \omega^n_{p2} \times \mathbf{s}^n_i - (\mathbf{v}^n_{p1} + \omega^n_{p1} \times \mathbf{u}^n_i) \tag{10}$$

where $\mathbf{v}^n_{p1}$ and ω^n_{p1} are the linear and angular velocity of reference frame P_1, respectively, and $\mathbf{v}^n_{p2}$ and ω^n_{p2} are the linear and angular velocity of reference frame P_2. At the same time vector $\mathbf{v}^n_{di}$ has two components:

$$\mathbf{v}^n_{di} = \rho_i \omega^n_{di} \times \hat{\mathbf{d}}^n_i + \dot{\mathbf{d}}^n_i \tag{11}$$

where ω^n_{di} is the angular velocity of the ith-leg and $\dot{\mathbf{d}}^n_i$ is the linear velocity along the ith-leg axis. The angular velocity is obtained as follows:

$$\omega^n_{di} = \frac{\mathbf{d}^n_i \times \mathbf{v}^n_{di}}{\|\mathbf{d}^n_i\|^2} \tag{12}$$

and $\dot{\mathbf{d}}^n_i$:

$$\dot{\mathbf{d}}^n_i = \dot{\rho} \hat{\mathbf{d}}^n_i \tag{13}$$

The velocity of the reference frames of the links can be found according to:

$$\mathbf{v}^n_{1i} = \mathbf{v}^n_{p1} + \omega^n_{p1} \times \mathbf{u}^n_i - \omega^n_{di} \times \mathbf{r}^n_u \tag{14}$$

and

$$\mathbf{v}^n_{2i} = \mathbf{v}^n_{p2} + \omega^n_{p2} \times \mathbf{s}^n_i - \omega^n_{di} \times \mathbf{r}^n_s \tag{15}$$

The joint velocity is computed by dot multiplying $\hat{\mathbf{d}}^n_i$ and (10):

$$\dot{\rho}_i = \mathbf{v}^n_{p2} \cdot \hat{\mathbf{d}}^n_i + (\mathbf{s}^n_i \times \hat{\mathbf{d}}^n_i) \cdot \omega^n_{p2} - (\mathbf{v}^n_{p1} \cdot \hat{\mathbf{d}}^n_i + (\mathbf{u}^n_i \times \hat{\mathbf{d}}^n_i) \cdot \omega^n_{p1}) \tag{16}$$

The previous equation obtains the velocity of the actuator given the linear and angular velocity of both platforms.

4.3 Acceleration Analysis

In order to obtain the acceleration model of the robot, we derive the equations of the previous subsection with respect to time. Deriving (10) we obtain:

$$\mathbf{a}^n_{di} = \mathbf{a}^n_{si} - \mathbf{a}^n_{ui} \tag{17}$$

where $\mathbf{a}^n_{di}$ is the acceleration of the leg vector,

$$\mathbf{a}^n_{di} = \ddot{\mathbf{d}}^n_i + 2\omega^n_{di} \times \dot{\mathbf{d}}^n_i + \dot{\omega}^n_{di} \times \mathbf{d}^n_i + \omega^n_{di} \times (\omega^n_{di} \times \mathbf{d}^n_i) \tag{18}$$

and, $\mathbf{a}_{ui}$ and $\mathbf{a}_{si}$ are the acceleration of points U_i and S_i,

$$\mathbf{a}^n_{ui} = \mathbf{a}^n_{p1} + \dot{\omega}^n_{p1} \times \mathbf{u}^n_i + \omega^n_{p1} \times (\omega^n_{p1} \times \mathbf{u}^n_i) \tag{19}$$

and

$$\mathbf{a}^n_{si} = \mathbf{a}^n_{p2} + \dot{\omega}^n_{p2} \times \mathbf{s}^n_i + \omega^n_{p2} \times (\omega^n_{p2} \times \mathbf{s}^n_i) \tag{20}$$

Vectors $\mathbf{a}^n_{p1}$ and $\dot{\omega}^n_{p1}$ represent the linear and angular accelerations of platform 1, $\mathbf{a}^n_{p2}$ and $\dot{\omega}^n_{p2}$ denotes the linear and angular accelerations of platform 2.

The angular acceleration of the *i-th* leg is:

$$\dot{\omega}^n_{di} = \hat{\mathbf{d}}^n_i \times (\mathbf{a}^n_{si} - \mathbf{a}^n_{ui}) - 2\dot{\rho}_i \omega^n_{di} \tag{21}$$

The acceleration of the frames attached to the links of the leg is obtained as follows:

$$\mathbf{a}^n_{1i} = \mathbf{a}^n_{ui} - (\dot{\omega}^n_{di} \times \mathbf{r}^n_{ui} + \omega^n_{di} \times (\omega^n_{di} \times \mathbf{r}^n_{ui})) \tag{22}$$

and

$$\mathbf{a}^n_{2i} = \mathbf{a}^n_{si} - (\dot{\omega}^n_{di} \times \mathbf{r}^n_{si} + \omega^n_{di} \times (\omega^n_{di} \times \mathbf{r}^n_{si})) \tag{23}$$

Generally, the equations of motion of underwater robots are expressed in terms of the linear velocity expressed in the body reference frame and its time derivative [5]. Therefore, for the links of the legs we have:

$$\dot{\mathbf{v}}^i_{1i} = \mathbf{R}^{nT}_i \mathbf{a}^n_{1i} - \omega^i_{di} \times \mathbf{v}^i_{1i} \tag{24}$$

and

$$\dot{\mathbf{v}}^i_{2i} = \mathbf{R}^{nT}_i \mathbf{a}^n_{2i} - \omega^i_{di} \times \mathbf{v}^i_{2i} \tag{25}$$

Finally we obtain the joint acceleration by dot multiplying $\hat{\mathbf{d}}^n_i$ and $\mathbf{a}^n_{di}$ from (17):

$$\ddot{\rho} = \hat{\mathbf{d}}^n_i \cdot (\mathbf{a}^n_{si} - \mathbf{a}^n_{ui}) \tag{26}$$

The inverse kinematics formulation is easily parallelizable and can be implemented in multiple-core processors. Fig. 4 shows a scheme of the implementation. First, in six different threads of execution, the computation of each vector $\mathbf{d}^n_i$ and matrix $\mathbf{R}^n_i$, and their time derivatives ($\dot{\mathbf{d}}^n_i$, $\ddot{\mathbf{d}}^n_i$, ω^n_{di} and $\dot{\omega}^n_{di}$), is performed. Subsequently, in the same threads, we compute the joint positions, velocities and accelerations, i.e. ρ_i, $\dot{\rho}_i$ and $\ddot{\rho}_i$. Then for computing the positions, velocities, and accelerations of each link of one leg ($\mathbf{r}^n_{ji}$, $\mathbf{v}^n_{ji}$ and $\mathbf{a}^n_{ji}$, for $j \in [1,2]$), two child threads are created. For the six legs, we have 12 concurrent threads. This scheme greatly reduces the computation time of the inverse kinematics.

4.4 Jacobian Analysis

Arranging (16) for each leg in matrix form, we obtain the following kinematic model of the robot:

$$\mathbf{J}_{\rho i}\dot{\rho} = \mathbf{J}_{p2}\mathbf{t}_{p2} - \mathbf{J}_{p1}\mathbf{t}_{p1} \tag{27}$$

where $\dot{\rho} = \begin{bmatrix}\dot{\rho}_1 & \dot{\rho}_2 & \dots & \dot{\rho}_6\end{bmatrix}^T$ is the joint velocity vector, $\mathbf{t}_{p1} = \begin{bmatrix}\mathbf{v}^T_{p1} & \omega^T_{p1}\end{bmatrix}^T$ and $\mathbf{t}_{p2} = \begin{bmatrix}\mathbf{v}^T_{p2} & \omega^T_{p2}\end{bmatrix}^T$ are the twists of platform 1 and platform 2, respectively, matrices $\mathbf{J}_{\rho i}$, $\mathbf{J}_{p1}$ and $\mathbf{J}_{p1}$ are the jacobian matrices of the robot. The Jacobian matrices have the following form:

$$\mathbf{J}_{\rho i} = \mathbf{I}_{6x6}, \tag{28}$$

where $\mathbf{I}_{6x6}$ is the identity matrix of size 6.

$$\mathbf{J}_{p1} = \begin{bmatrix} \hat{\mathbf{d}}^{nT}_1 & (\mathbf{u}^n_1 \times \hat{\mathbf{d}}^n_1)^T \\ \hat{\mathbf{d}}^{nT}_2 & (\mathbf{u}^n_2 \times \hat{\mathbf{d}}^n_2)^T \\ \vdots & \vdots \\ \hat{\mathbf{d}}^{nT}_6 & (\mathbf{u}^n_6 \times \hat{\mathbf{d}}^n_6)^T \end{bmatrix} \tag{29}$$

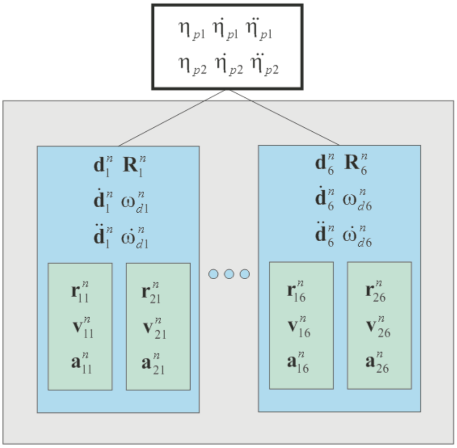

Figure 4. Parallel processes for calculating inverse kinematics

and

$$\mathbf{J}_{p2} = \begin{bmatrix} \hat{\mathbf{d}}_1^{nT} & (\mathbf{s}_1^n \times \hat{\mathbf{d}}_1^n)^T \\ \hat{\mathbf{d}}_2^{nT} & (\mathbf{s}_2^n \times \hat{\mathbf{d}}_2^n)^T \\ \vdots & \vdots \\ \hat{\mathbf{d}}_6^{nT} & (\mathbf{s}_6^n \times \hat{\mathbf{d}}_6^n)^T \end{bmatrix} \tag{30}$$

Furthermore, expanding (26) we can obtain the acceleration model in matrix form:

$$\mathbf{J}_\rho \ddot{\rho} = \mathbf{J}_{p2}\dot{\mathbf{t}}_{p2} - \mathbf{J}_{p1}\dot{\mathbf{t}}_{p1} + \mathbf{K} \tag{31}$$

where $\ddot{\rho} = \begin{bmatrix} \ddot{\rho}_1 & \ddot{\rho}_2 & \dots & \ddot{\rho}_6 \end{bmatrix}^T$ is the joint accelerations vector, $\dot{\mathbf{t}}_{p1} = \begin{bmatrix} \mathbf{a}_{p1}^{nT} & \dot{\omega}_{p1}^{nT} \end{bmatrix}^T$ and $\dot{\mathbf{t}}_{p2} = \begin{bmatrix} \mathbf{a}_{p2}^{nT} & \dot{\omega}_{p2}^{nT} \end{bmatrix}^T$ are the time derivatives of the twist vectors, and $\mathbf{K}$ is a vector that has the following form:

$$\mathbf{K} = \begin{bmatrix} \omega_1 d_1 + (\omega_{p1}^n \times \mathbf{u}_1^n \times \omega_{p1}^n - \omega_{p2}^n \times \mathbf{s}_1^n \times \omega_{p2}^n)^T \mathbf{d}_1^n \\ \omega_2 d_2 + (\omega_{p1}^n \times \mathbf{u}_2^n \times \omega_{p1}^n - \omega_{p2}^n \times \mathbf{s}_2^n \times \omega_{p2}^n)^T \mathbf{d}_2^n \\ \vdots \\ \omega_6 d_6 + (\omega_{p1}^n \times \mathbf{u}_6^n \times \omega_{p1}^n - \omega_{p2}^n \times \mathbf{s}_6^n \times \omega_{p2}^n)^T \mathbf{d}_6^n \end{bmatrix} \tag{32}$$

where $\omega_1 = \|\omega_{d1}^n\|$ and $d_i = \|\mathbf{d}_i^n\|$.

Matrices (29) and (30) have interesting properties which permit to evaluate the performance of the robot. When $\det(\mathbf{J}_{p1}) = 0$ or $\det(\mathbf{J}_{p2}) = 0$ the robot's parallel structure is at a singular configuration, and this can cause a loss of stiffness [8]. Therefore it is necessary to avoid configurations at which matrices (29) and (30) become singular.

5. DIRECT KINEMATICS OF REMO II

In this section we solve the direct kinematics of the parallel structure of the robot. For this, we consider that the position, velocity and acceleration of platform 1 are known. This information can be obtained trough the sensors system embedded on the platform. Additionally, from the sensor at the joint actuators we obtain the joints positions, velocities and accelerations.

5.1 Position Analysis

For the direct kinematic problem, the state of the actuators is known and the relative location of the platform must be obtained.

Finding the direct kinematic solution of a parallel mechanism is a complex task, and it is not always possible to find an analytic solution. In this work, the direct kinematic problem is solved by a numeric method based on the Newton-Raphson algorithm and a constraint function of the mechanism.

Considering the schematic diagram of the REMO II presented in Fig. 3, it can be seen that the vector of the leg i can be obtained in terms of the relative location of platform 2 with respect to platform 1 as follows:

$$\mathbf{d}_i^{p1} = \mathbf{r}_c + \mathbf{R}_{p2}^{p1}\mathbf{s}_i - \mathbf{u}_i \tag{33}$$

where $\mathbf{r}_c$ is the relative position of the origin of the reference frame of platform 2 with respect to the platform 1, and $\mathbf{R}_{p2}^{p1}$ is the rotation matrix that represents the relative orientation, from platform 2 to platform 1.

Considering that the state of the actuator of the leg i is given by L_{0_i}, a constraint function for leg i of the mechanism can be stated as follows:

$$\begin{aligned} f_i(\mathbf{r}_c, \mathbf{p}_c) &= 0 \\ &= \|\mathbf{d}_i^{p1}\| - L_{0_i} \end{aligned} \tag{34}$$

where $\mathbf{p}_c = \begin{bmatrix} e_0, & e_1, & e_2, & e_3 \end{bmatrix}^T$ defines the orientation of the moving platform expressed as unit quaternion (Euler's parameters). The generalized coordinate vector of platform 2 with respect to reference frame P_1 is thus $\mathbf{q} = \begin{bmatrix} \mathbf{r}_c^T, & \mathbf{p}_c^T \end{bmatrix}^T$.

The derivative of (34) is given by

$$f_{\mathbf{q}_i}(\mathbf{r}_c, \mathbf{p}_c) = \begin{bmatrix} \frac{d}{d\mathbf{r}_c}\left[f_i(\mathbf{r}_c, \mathbf{p}_c)\right] & \frac{d}{d\mathbf{p}_c}\left[f_i(\mathbf{r}_c, \mathbf{p}_c)\right] \end{bmatrix} \tag{35}$$

where the derivative of (34) with respect to the position of platform 2 is given by (36):

$$\frac{d}{d\mathbf{r}_c}\left[f_i(\mathbf{r}_c, \mathbf{p}_c)\right] = \hat{\mathbf{d}}_i^{p1} \tag{36}$$

where $\hat{\mathbf{d}}_i^{p1}$ is the unit vector of $\mathbf{d}_i^{p1}$. The derivative of (34) with respect to the orientation of platform 2 is given by (37).

$$\frac{d}{d\mathbf{p}_c}\left[f_i(\mathbf{r}_c, \mathbf{p}_c)\right] = -2\hat{\mathbf{d}}_i^{p1}\mathbf{R}_{p2}^{p1}\tilde{\mathbf{s}}_i\mathbf{G} \tag{37}$$

$\tilde{\mathbf{s}}_i$ is the skew antisymmetric matrix of $\mathbf{s}_i$ and G is the identity matrix of the Euler parameters given by (38), and satisfies $\mathbf{G}\mathbf{p}_c = \mathbf{0}$.

$$\mathbf{G} \equiv \begin{bmatrix} -e_1 & e_0 & e_3 & -e_2 \\ -e_2 & -e_3 & e_0 & e_1 \\ -e_3 & e_2 & -e_1 & e_0 \end{bmatrix} \tag{38}$$

Arranging the constraint functions for legs $i = 1, 2, \cdots, 6$ into matrix form as expressed in (39), a constraint vector $\Phi(\mathbf{r}_c, \mathbf{p}_c)$ for the mechanism is found.

$$\Phi(\mathbf{r}_c, \mathbf{p}_c) = \begin{bmatrix} f_1(\mathbf{r}_c, \mathbf{p}_c) \\ f_2(\mathbf{r}_c, \mathbf{p}_c) \\ \vdots \\ f_6(\mathbf{r}_c, \mathbf{p}_c) \end{bmatrix} = \mathbf{0} \tag{39}$$

Taking the derivative of the constraint vector of the mechanism with respect to the position and orientation of platform 2, a jacobian matrix can be defined as,

$$\Phi_{\mathbf{q}}(\mathbf{r}_c, \mathbf{p}_c) = \begin{bmatrix} \hat{\mathbf{d}}_1^{p1} & -2\hat{\mathbf{d}}_1^{p1}\mathbf{R}_{p2}^{p1}\tilde{\mathbf{s}}_2\mathbf{G} \\ \hat{\mathbf{d}}_2^{p1} & -2\hat{\mathbf{d}}_2^{p1}\mathbf{R}_{p2}^{p1}\tilde{\mathbf{s}}_2\mathbf{G} \\ \vdots & \vdots \\ \hat{\mathbf{d}}_6^{p1} & -2\hat{\mathbf{d}}_6^{p1}\mathbf{R}_{p2}^{p1}\tilde{\mathbf{s}}_6\mathbf{G} \end{bmatrix} \tag{40}$$

The Newton-Raphson algorithm makes possible to find a solution to (39), iterating (41) from an initial estimate $\mathbf{q}^{(0)}$ until (42) is satisfied [10].

$$\mathbf{q}^{(k+1)} = \mathbf{q}^{(k)} + \left[\Phi_{\mathbf{q}}^{(k)}\right]^{-1} \Phi^{(k)} \tag{41}$$

$$\|\Phi^{(k)}(\mathbf{q})\| < \sigma \tag{42}$$

Where σ is the accuracy of the numerical algorithm, and $k = 0, 1, 2, \dots$ is the iteration cycle.

It is important to recall that the method is highly dependent of the initial estimation ($\mathbf{q}^{(0)}$), thus the method may diverge if poor initial estimation is given. Another consideration that must be taken is that the numerical method depends on the evaluation of $\Phi_{\mathbf{q}}^{(k)}$, and it is possible to find no convergence for $\Phi_{\mathbf{q}}^{(k)} = \mathbf{0}$.

5.2 Velocity Analysis

Given the linear and angular velocities of platform 1, and the joint velocities, from (27) we can obtain the velocity of platform 2:

$$\mathbf{t}_{p2} = \mathbf{J}_{p2}^{-1}(\mathbf{J}_{\rho i}\dot{\rho} + \mathbf{J}_{p1}\mathbf{t}_{p1}) \tag{43}$$

5.3 Acceleration Analysis

Given the linear and angular accelerations of platform 1, and the joint acceleration, from (31) we can obtain the velocity of platform 2:

$$\dot{\mathbf{t}}_{p2} = \mathbf{J}_{p2}^{-1}(\mathbf{J}_{\rho}\ddot{\rho} + \mathbf{J}_{p1}\dot{\mathbf{t}}_{p1} - \mathbf{K}) \tag{44}$$

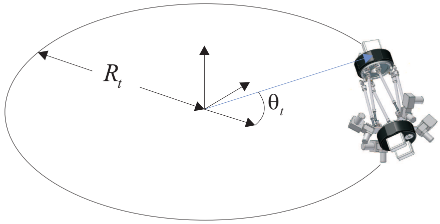

Figure 5. Trajectory of the robot

6. SIMULATION AND RESULTS

In this section, we present the results of a simulation of the robot using the formulation presented in the previous sections. For this, we consider a circular path that is parameterized by the angle ($\theta_t(t)$) between the position vector of platform 1 with respect to frame N in the plane xy, see Fig. 5. This angle is defined by a cycloidal motion function:

$$\theta_t(t) = \frac{\Delta\theta_t t}{T} - \frac{\Delta\theta_t}{2\pi}\sin\left(\frac{2\pi t}{T}\right) + \theta_t^{ini} \tag{45}$$

where t is the time and T is the period of time of the trajectory. Angle θ_t^{ini} is the initial value of $\theta_t(t)$ and $\Delta\theta_t$ is the difference between the initial and final value of $\theta_t(t)$.

The time derivatives of 45 are:

$$\dot{\theta}_t(t) = \frac{\Delta\theta_t}{T} - \frac{\Delta\theta_t}{T}\cos\left(\frac{2\pi t}{T}\right) \tag{46}$$

and

$$\ddot{\theta}_t(t) = \frac{2\pi\Delta\theta_t}{T^2}\sin\left(\frac{2\pi t}{T}\right) \tag{47}$$

The parameterized trajectory in function of $\theta_t(t)$ is given in the following way:

$$\eta_p = \begin{bmatrix} R_t\cos(\theta_t) \\ R_t\sin(\theta_t) \\ 0 \\ \pi/2 \\ \pi/2 \\ -\theta_t \end{bmatrix} \tag{48}$$

where R_t is the radius of the trajectory.

For the simulation we regard the real parameters of Remo II listed in table 1. Fig. 6 shows an image of the prototype of Remo II. The distribution of the joints in the platforms is given by vectors $\mathbf{u}_i = R_p\begin{bmatrix}\cos(\gamma_{1i}) & \sin(\gamma_{1i}) & 0\end{bmatrix}^T$ and $\mathbf{s}_i = R_p\begin{bmatrix}\cos(\gamma_{2i}) & \sin(\gamma_2 i) & 0\end{bmatrix}^T$, where γ_1 and γ_2 are defined in the following way:

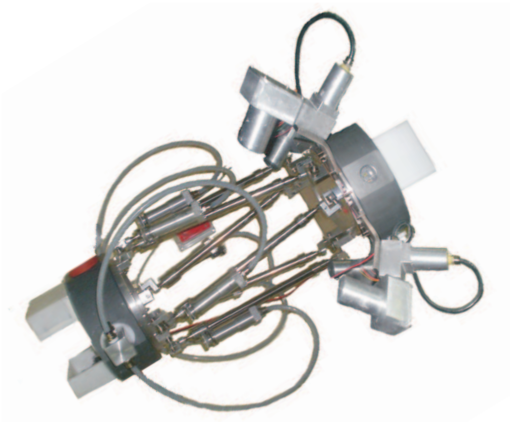

Figure 6. The Remo II underwater robot

Table 1. Geometric Parameters

Parameter		Value
Stroke length	l_{str}	243 mm
Dead length	l_m	437 mm
Distance between U_i and L_{1i}	l_u	140.8 mm
Distance between S_i and L_{2i}	l_s	126.6 mm
Platforms radius	R_p	145.5 mm
Angle between joints	λ	$\pi/6$

$$\gamma_1 = \begin{bmatrix} -\lambda/2 \\ \lambda/2 \\ 2\pi/3-\lambda/2 \\ 2\pi/3+\lambda/2 \\ 4\pi/3-\lambda/2 \\ 4\pi/3+\lambda/2 \end{bmatrix} \tag{49}$$

and

$$\gamma_2 = \begin{bmatrix} -\pi/3+\lambda/2 \\ \pi/3-\lambda/2 \\ \pi/3+\lambda/2 \\ \pi-\lambda/2 \\ \pi+\lambda/2 \\ -pi/3-\lambda/2 \end{bmatrix} \tag{50}$$

For the trajectory we considered $\theta_t^{ini} = \pi/6$, $\Delta\theta_t = 2\pi$ and $T = 10s$. Fig. 7, show the trajectory of $\theta_t(t)$ and its time derivatives. Cycloidal functions have the propriety that velocities and accelerations are zero at the beginning and end of the trajectory, and this fact makes them suitable for trajectory planning.

In Fig. 8 it is possible to observe the position of the reference frames attached to the links

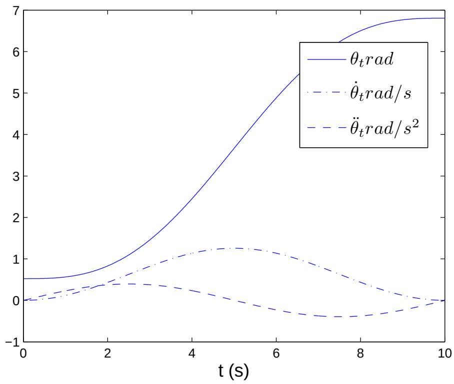

Figure 7. θ_t, $\dot{\theta}_t$ and $\ddot{\theta}_t$ vs t

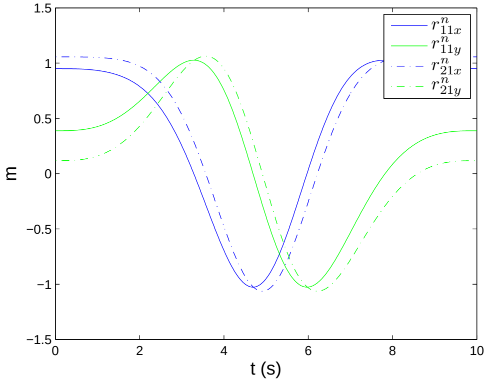

Figure 8. Position of leg 1

of leg 1, these are L_{11} and L_{21}. Since the trayectory followed by the robot is in the xy plane the position of the bodies in the z axis is zero (i.e. $r^n_{11z} = r^n_{21z} = 0$).

Fig. 9 shows the velocities of the origins of the reference frames L_{11} and L_{21}. It can be observed that the velocities at the beginning and end of the trajectory are zero, this is due to the used cycloidal function.

The accelerations of the links of leg 1 are shown in Fig. 10. The acceleration has a maximum at the middle of the trajectory and is zero at the beginning and end of the trajectory, in the same way that in the case of the velocities.

7. CONCLUSION

In this paper we presented the kinematic analysis of a novel underwater robot with parallel mechanical structure. First, we introduced the robot Remo II. The design of this robot is radically

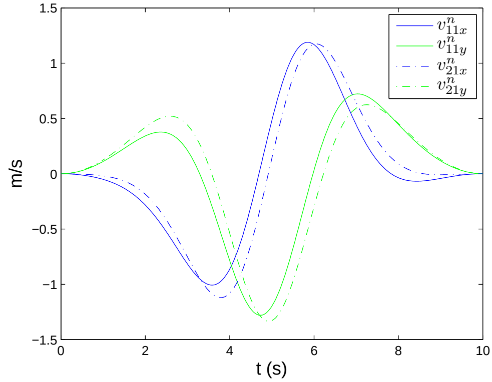

Figure 9. Velocities of leg 1

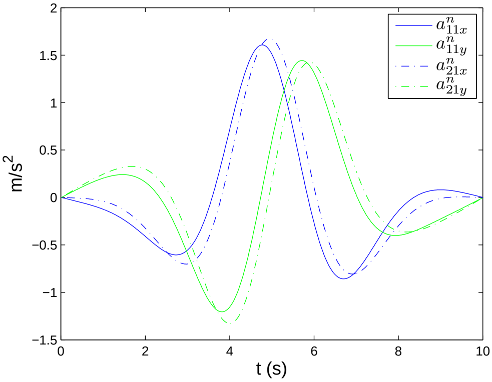

Figure 10. Accelerations of leg 1

different to that of conventional underwater robots. The parallel structure allows thrust vectoring, and this in turn, has the potential to provide the robot with high level of maneuverability, flexibility, and holonomic capabilities for navigation and positioning.

The resultant equations of the kinematic analysis are different to the case in which one of the platforms is fixed to the base. The obtained formulation is easily parallelizable and was implemented in a multiple-core processor. First, in six different threads of execution, the computation of each vector $\mathbf{d}_i^n$ and matrix $\mathbf{R}_i^n$, and their time derivatives, is performed. Then for computing the positions, velocities, and accelerations of each link of one leg, two child threads are created. For the six legs, we have 12 concurrent threads. On the other hand, the direct position kinematics is solved by constructing a kinematic constraints vector and using the Newton-Raphson numerical method. For simulation, we considered a circular path with cycloidal motion.

ACKNOWLEDGMENTS

This work is supported by project DPI2006-06493 of the Spanish Ministery of Science and Education.

REFERENCES

[1] R. Aracil, R. Saltaren, J.M. Sabater, and O. Reinoso, *Design, modeling and implementation of a 6 urs parallel haptic device*, Robot. Autonom. Syst **47** (2004), no. 1, 1–10.

[2] R. Aracil, R. Saltaren, J.M. Sabater, and O. Reinoso, *Robots paralelos: mquinas con pasado para una robtica de futuro*, RIAI. Revista Iberoamericana de Automtica e Informtica Industrial **3** (2006), no. 1, 16–28.

[3] E. Cavallo and R. Michelini, *A robotic equipment for the guidance of a vectored thrustor auv*, vol. 1, 2004, pp. 1–6.

[4] R. Damus, J. Manley, S. Desset, J. Morash, and C. Chryssostomidis, *Design of an inspection class autonomous underwater vehicle*, OCEANS '02 MTS/IEEE, vol. 1, 2002, pp. 180 – 185 vol.1.

[5] T. Fossen, *Nonlinear modeling and control of underwater vehicles*, Ph.D. thesis, Norwegian University of Science and Technology, Trondheim, 1991.

[6] T.I. Fossen, *Marine control systems. guidance, navigation, and control of ships, rigs and underwater vehicles*, Marine Cybernetics, 2002.

[7] J. Gallardo, C. Aguilar, L. Casique, J.M. Rico, and Md. Nazrul, *Kinematics and dynamics of 2(3-rps) manipulators by means of screw theory and the principle of virtual work*, Mechanism and Machine Theory **43** (2008), no. 10, 1281 – 1294.

[8] C. Gosselin and J. Angeles, *Singularity analysis of closed-loop kinematic chains*, Robotics and Automation, IEEE Transactions on **6** (1990), no. 3, 281 –290.

[9] C.M. Gosselin, *Parallel computational algorithms for the kinematics and dynamics of parallel manipulators*, Proceedings IEEE International Conference on Robotics and Automation, 1993., 1993, pp. 883–888 vol.1.

[10] Edward J. Haug, *Computer Aided Kinematics and Dynamics of Mechanical System*, Allyn & Bacon, Inc., Needham Heights, MA, USA, 1989.

[11] J. Lowe K. Liu, G. Lebret and F. Lewis, *Control of a stewart platform based robotic milling cell*, 1992, pp. 8–13.

[12] Y.G. Le Page and K.W. Holappa, *Simulation and control of an autonomous underwater vehicle equipped with a vectored thruster*, OCEANS 2000 MTS/IEEE Conference and Exhibition, 2000, pp. 2129 –2134 vol.3.

[13] J. P. Merlet, *Parallel robots*, Springer, 2006.

[14] Yannick Morel and Alexander Leonessa, *Adaptive Nonlinear Tracking Control of an Underactuated Non-minimum Phase Model of a Marine Vehicle Using Ultimate Boundedness*, 42nd IEEE Conference on Decision and Control, 2003.

[15] R. Saltaren, R. Aracil, C. Alvarez, E. Yime, and J.M. Sabater, *Field and service applications - exploring deep sea by teleoperated robot - an underwater parallel robot with high navigation capabilities*, Robotics Automation Magazine, IEEE **14** (2007), no. 3, 65–75.

[16] R. Saltaren, R. Aracil, and O. Reinoso, *Climbing parallel robot: A computational and experimental study of its performance around structural nodes*, IEEE Trans. Robot. **21** (2005), no. 6, 1056–1066.

[17] W.H. Wang, R.C. Engelaar, X.Q. Chen, and J.G. Chase, *The state-of-art of underwater vehicles - theories and applications*, Mobile Robots - State of the Art in Land, Sea, Air, and Collaborative Missions, X.Q. Chen, Y.Q. Chen and J.G. Chase (Ed.), InTech.

[18] Yu-Xin Wang and Yi-Ming Wang, *Inverse kinematics of variable geometry parallel manipulator*, Mechanism and Machine Theory **40** (2005), no. 2, 141 – 155.

[19] J. Yuh, *Design and control of autonomous underwater robots: A survey*, Auton. Robots **8** (2000), no. 1, 7–24.

Proceedings of MUSME 2011, the International Symposium
on Multibody Systems and Mechatronics
Valencia, Spain, 25-28 October 2011

ON THE INFLUENCE OF ANTI-ROLL STIFFNESS ON VEHICLE STABILITY AND PROPOSAL OF AN INNOVATIVE SEMI-ACTIVE MAGNETORHEOLOGICAL FLUID ANTI-ROLL BAR

Flavio Farroni, Daniele Giordano, Michele Russo, Mario Terzo and Francesco Timpone

Department of Mechanics and Energetics, University of Naples "Federico II",
Via Claudio 21, 80125 Napoli, Italy
e-mail: flavio.farroni@gmail.com

Keywords: Vehicle Dynamics, Local Stability, Anti-Roll Stiffness, Magnetorheological Fluid.

Abstract. *Modern vehicles are equipped with several active and passive devices whose function is to increase active safety. This paper is focused on the anti-roll stiffness influence on vehicle handling, and follows a theoretical approach.*

The work firstly develops a quadricycle theoretical model, useful to study the influence of anti-roll stiffness on the vehicle local stability. The model, involving non-linear phenomena, is simplified by proper linearizations.

This procedure allows local stability analysis with low computational load. At the same time, the linearized model takes into account the dynamic effects induced by load transfers through a tyre-road interaction model sensitive to the vertical load. The study is conducted considering the anti-roll stiffnesses of the two axles as parameters. The proposed model defines the relationship between the anti-roll bars stiffness and the system state.

In order to realize an adaptive system able to provide a variable roll stiffness, a semi-active anti-roll bar prototype, employing magnetorheological fluid, is described. Such device gives the possibility to quickly change the roll stiffness, according to the system state, to preserve its stability.

1 INTRODUCTION

In recent years, the interest for vehicle stability control systems has been increasing, and consequently the study of the local stability has become a fundamental discipline in the field of vehicle dynamics.

Loss of stability of a road vehicle in the lateral direction may result from unexpected lateral disturbances like side wind force, tyre pressure loss, or μ-split braking due to different road pavements such as icy, wet, and dry pavement. During short-term emergency situations, the average driver may exhibit panic reaction and control authority failure, and he may not generate adequate steering, braking/throttle commands in very short time periods.

Vehicle lateral stability control systems may compensate the driver during panic reaction time by generating the necessary corrective yaw moments.

The main idea of this paper is to approach the local stability analysis in a simplified way, taking into account all the phenomena involved in the lateral vehicle dynamics. In particular, the adopted tyre model is the Pacejka magic formula, which has been linearized around a steady-state vehicle equilibrium point, expressing the lateral force as a function of both slip angle and vertical load. This kind of linearization allows to take also into consideration the tyre saturation behaviour with respect to the vertical load.

The adopted vehicle model is an 8-DOF quadrycicle planar model performing a reference manoeuvre chosen with the aim to consider the lateral vehicle dynamics.

The study of local stability has been addressed by analyzing the state matrix of the linearized motion equations in matrix form.

This analysis shows the influence of anti-roll stiffness on local vehicle stability and the importance of a proper variation of its value to preserve vehicle safety conditions.

At the end of the work an innovative semi-active anti-roll bar is described. In particular, it is able to vary axle anti-roll stiffness according to vehicle dynamics conditions in order to guarantee stability and handling.

2 VEHICLE MODEL

The vehicle has been modelled using an 8 degree-of-freedom quadricycle planar model. In particular, 3 DOF refer to in plane vehicle body motions (longitudinal, lateral and jaw motions), 4 DOF to wheel rotations and the last DOF to the steering angle. To describe the vehicle motions two coordinate systems have been introduced: one earth-fixed (X' ; Y'), the other (x ; y) integral to the vehicle as shown in Fig. (1).

With reference to the same figure, v is the centre of gravity absolute velocity referred to the earth-fixed axis system and U (longitudinal velocity) and V (lateral velocity) are its components in the vehicle axis system; r is the jaw rate evaluated in the earth fixed system, β is the vehicle sideslip angle, F_{xi} and F_{yi} are respectively longitudinal and lateral components of the tyre-road interaction forces.

The wheel track is indicated with t and it is supposed to be the same for front and rear axle; the distances from front and rear axle to the centre of gravity are represented by a and b, respectively. The steer angle of the front tyres is denoted by δ, while the rear tyres are supposed non-steering.

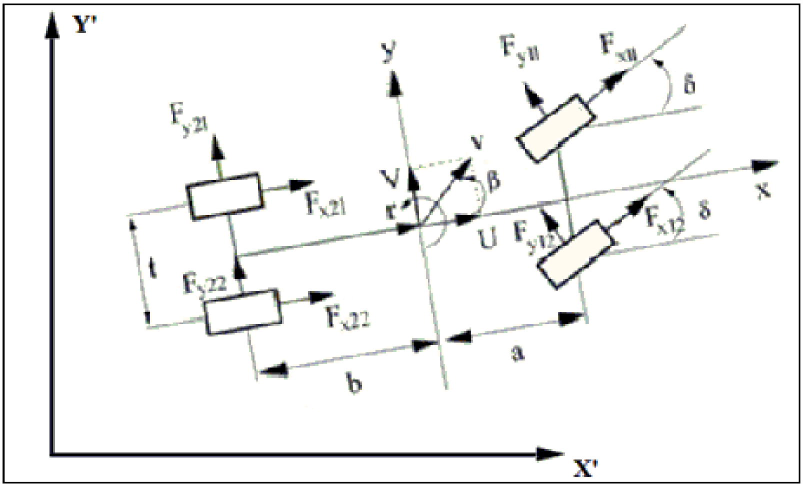

Figure 1: Coordinate systems.

In hypothesis of negligible aerodynamic interactions, little steer angles (<15°) and rear wheel drive, the motion equations of in plane vehicle dynamics, Ref. [1], are:

$$
\begin{gathered}
m(\dot{U} - Vr) = (F_{x_{21}} + F_{x_{22}}) - (F_{y_{11}} + F_{y_{12}})\delta \\
m(\dot{V} + Ur) = F_{y_{11}} + F_{y_{12}} + F_{y_{21}} + F_{y_{22}} \\
J_z\dot{r} = (F_{y_{11}} + F_{y_{12}})a - (F_{y_{21}} + F_{y_{22}})b - (F_{x_{21}} - F_{x_{22}})\frac{t}{2} + (F_{y_{11}} - F_{y_{12}})\,\delta\frac{t}{2}
\end{gathered}
\tag{1}
$$

where m is the vehicle total mass and J_z is its moment of inertia with respect to z axis.

2.1 Manoeuvre

The simulation scenario is described as a curve to the left, approached with an increasing steering law, described by a sinusoid between 0 and π/2; the torque M_m, transmitted to the rear wheels, increases with the same kind of function. This kind of input-laws have been chosen with the aim of not generating irregularities in the simulation; it allows to reach the steady state with a signal that shows null derivative values in the origin and at the end of the transient state.

At the end of the described manoeuvre, defined henceforth as "*reference manoeuvre*", the vehicle reaches an equilibrium condition, characterized by constant values of the physical quantities. This equilibrium state, once determined, represents the point in whose neighbourhood will be analyzed the system in the space state.

2.2 Wheel motion dynamics

Angular velocities are calculated integrating the angular accelerations $\dot{\omega}_{ij}$, obtained thanks to wheel dynamics equation:

$$I_{w_{ij}}\dot{\omega}_{ij} = M_{m_{ij}} - F_{x_{ij}}R \tag{2}$$

where I_w is wheel moment of inertia with reference to its revolution axis, $\dot{\omega}_{ij}$ are the tyre angular accelerations and R is the tyre effective radius.

The longitudinal wheel slip ratios are given by:

$$
\begin{aligned}
s_{11} &= \frac{\left(U - r\frac{t}{2}\right)\cos(\delta) + (V + ra)\sin(\delta) - \omega_{11}R}{\omega_{11}R} \\
s_{12} &= \frac{\left(U + r\frac{t}{2}\right)\cos(\delta) + (V + ra)\sin(\delta) - \omega_{12}R}{\omega_{12}R} \\
s_{21} &= \frac{\left(U - r\frac{t}{2}\right)\cos(0) - (V - rb)\sin(0) - \omega_{21}R}{\omega_{21}R} \\
s_{22} &= \frac{\left(U + r\frac{t}{2}\right)\cos(0) - (V - rb)\sin(0) - \omega_{22}R}{\omega_{22}R}
\end{aligned}
\tag{3}
$$

in which ω_{ij} are the tyre angular velocities. For little steering angles and not-steering rear tyres, last equations become:

$$
\begin{aligned}
s_{11} &= \frac{\left(U - r\frac{t}{2}\right) + (V + ra)\delta - \omega_{11}R}{\omega_{11}R} \\
s_{12} &= \frac{\left(U + r\frac{t}{2}\right) + (V + ra)\delta - \omega_{12}R}{\omega_{12}R} \\
s_{21} &= \frac{\left(U - r\frac{t}{2}\right) - \omega_{21}R}{\omega_{21}R} \\
s_{22} &= \frac{\left(U + r\frac{t}{2}\right) - \omega_{22}R}{\omega_{22}R}
\end{aligned}
\tag{4}
$$

2.3 Tyre model

One of the most critical aspects in modelling the dynamics of a vehicle is the determination of the lateral force generated by the interaction between tyre and road. The underlying physical phenomenon is rather complex and, for its description, is often necessary referring to empirical models, the most renowned of which is undoubtedly the Pacejka's magic formula, Ref. [2] [3].

This allows the expression of the lateral force as a function of the slip angle α and of the vertical load F_z by means of a non-linear function. The formula contains a number of parameters, the value of which has to be tuned in order to distinguish between different kinds of tyres, with their own characteristics in terms of size, constitutive material, inflation pressure, etc.

In the Pacejka's magic formula, parameters have no clear physical meaning, and usually they are estimated from experimental data. In the present work the parameters are referred to a common passenger tyre.

With reference to the described quadricycle model, Ref. [1], the slip angles are:

$$\alpha_{11} = \delta - tan^{-1}\left(\frac{V + ra}{U - r\frac{t}{2}}\right)$$
$$\alpha_{12} = \delta - tan^{-1}\left(\frac{V + ra}{U + r\frac{t}{2}}\right)$$
$$\alpha_{21} = -tan^{-1}\left(\frac{V - rb}{U - r\frac{t}{2}}\right)$$
$$\alpha_{22} = -tan^{-1}\left(\frac{V - rb}{U + r\frac{t}{2}}\right) \tag{5}$$

With reference to the reached steady state conditions of a curving manoeuvre, it is possible to neglect the low longitudinal load transfers due to the lateral interaction forces and so the attention can be focused on these last and on the lateral load transfers.

The non-linear tyre Pacejka model, coupled with the vehicle model, is employed to determine the steady-state conditions in the neighborhood of which the analysis of the influence of the anti-roll stiffness on vehicle stability is carried out.

In order to execute the local stability analysis and to evaluate the influence of the anti-roll stiffness, it is necessary to take into account the saturation of the lateral interaction with respect to vertical load. At the same time, vehicle and interaction models have to be as simple as possible in order to express them in a state space form. In this way, the local stability analysis can be executed via state matrix eigenvalues calculus.

To this aim, the proposed model is characterized by a linearization of lateral force with respect to slip angle α and vertical load F_z around the reached steady state conditions. In fact, once determined the steady state conditions (i.e. known the equilibrium point) for each tyre, a linearization of the lateral force is executed with respect to slip angle and vertical load. Consequently, tyre-road interaction will consist in a linear relation for each tyre.

The linearization process of the lateral forces modeled by Pacejka in the neighborhood of the working point consists of the identification of three parameters (m_{1ij}, m_{2ij}, q_{ij}, different for each tyre), necessary to set a linear relationship expressing the lateral force as a function of vertical load and slip angle.

So, the proposed generic lateral force F_{yij} expression will be:

$$F_{y_{ij}} = (m_{1_{ij}}F_{z_{ij}} + q_{ij}) + m_{2_{ij}}\alpha_{ij} \tag{6}$$

where the term in parenthesis, dependent on the vertical load, can be seen as the bias of the expression related to the slip angle.

As an example, in Fig. (2) and (3) the results of the double linearization are shown as concerns the left front tyre. Particularly, Fig. (2) illustrates, for the steady state vertical load (F_{zss}), Pacejka relationship between F_y and α (continuous curve) and its linearization (dotted curve) around the steady-state point. Fig. (3) shows linearization with respect to vertical load for the steady-state α value (α_{ss}).

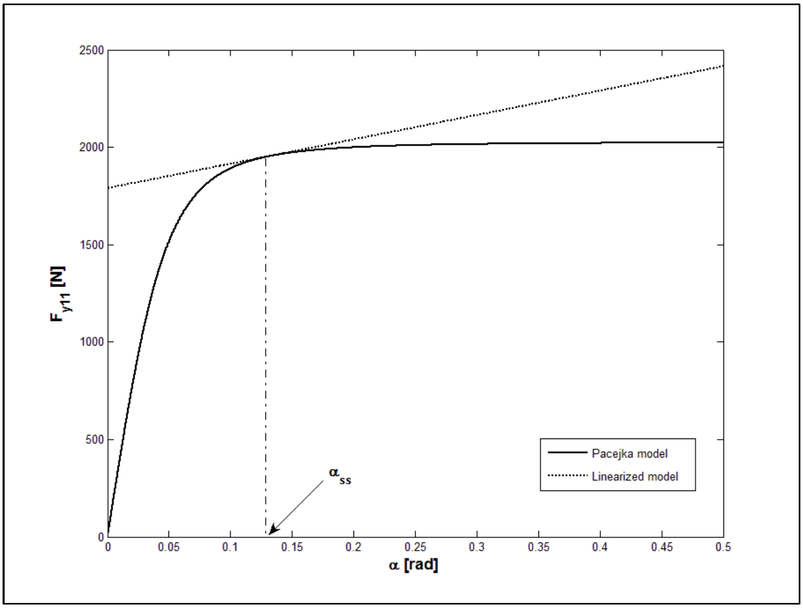

Figure 2: Result of the linearization of Pacejka model in an α - F_y plane for $F_z = F_{zss}$

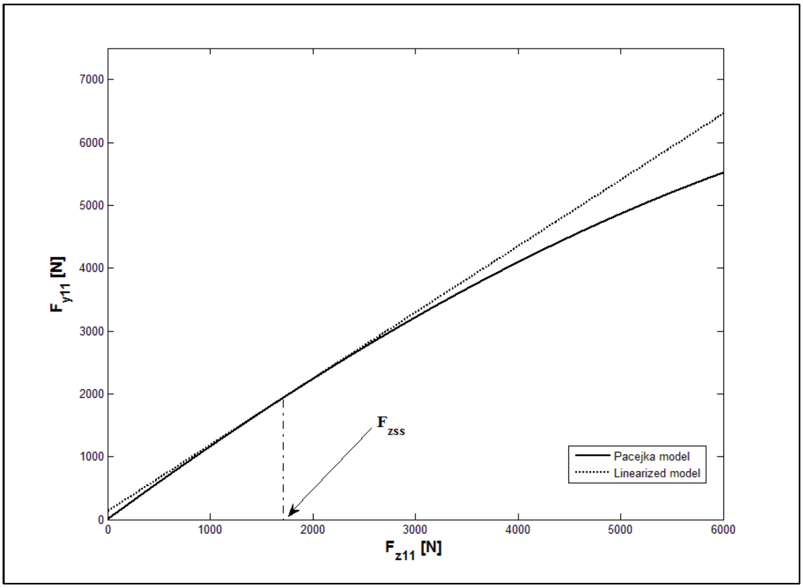

Figure 3: Result of the linearization of Pacejka model in an F_z - F_y plane for $\alpha = \alpha_{ss}$

The proposed linearized model allows to take into account the effects of the lateral forces with respect to the vertical load saturation due to the lateral load transfers. The different angular coefficients characterizing each tangent to the F_z – F_y curve in the working point allows to well approximate this phenomenon.

Ignoring camber angles and aligning moments, the normal forces take into account the lateral load transfers as follows, Ref. [1]:

$$
\begin{aligned}
F_{z_{11}} &= \frac{mGb}{2(a+b)} - \frac{1}{t}\left[d\left(F_{y_{11}} + F_{y_{12}}\right) + \frac{k_{\phi_1}}{k_\phi}(h-d)\left(F_{y_{11}} + F_{y_{12}} + F_{y_{21}} + F_{y_{22}}\right)\right] \\
F_{z_{12}} &= \frac{mGb}{2(a+b)} + \frac{1}{t}\left[d\left(F_{y_{11}} + F_{y_{12}}\right) + \frac{k_{\phi_1}}{k_\phi}(h-d)\left(F_{y_{11}} + F_{y_{12}} + F_{y_{21}} + F_{y_{22}}\right)\right] \\
F_{z_{21}} &= \frac{mGa}{2(a+b)} - \frac{1}{t}\left[d\left(F_{y_{21}} + F_{y_{22}}\right) + \frac{k_{\phi_2}}{k_\phi}(h-d)\left(F_{y_{11}} + F_{y_{12}} + F_{y_{21}} + F_{y_{22}}\right)\right] \\
F_{z_{22}} &= \frac{mGa}{2(a+b)} + \frac{1}{t}\left[d\left(F_{y_{21}} + F_{y_{22}}\right) + \frac{k_{\phi_2}}{k_\phi}(h-d)\left(F_{y_{11}} + F_{y_{12}} + F_{y_{21}} + F_{y_{22}}\right)\right]
\end{aligned}
\tag{7}
$$

where G is the gravity acceleration, d is the height of the intersection point between the roll-axis and the vertical plane passing by y-axis, h is the height of the centre of gravity, k_{ϕ_1} and k_{ϕ_2} are, respectively, front and rear axle anti-roll stiffnesses and their sum is indicated with $k_\phi = k_{\phi_1} + k_{\phi_2}$.

3 MOTION EQUATIONS AND LOCAL STABILITY ANALYSIS

According to the theory of dynamic systems, the steady motion of a vehicle constitutes an equilibrium point for the state variables. The local stability analysis of a dynamic system around an equilibrium point involves the eigenvalue analysis of the corresponding linearized equations of motion.

For a rear wheel drive vehicle with no steering rear wheels, the motion system of equations simplifies to an extreme degree, being composed by only two differential equations in *V(t)* and *r(t)*, in which the forces F_z and F_y have been calculated in Eq. (6) and (7), Ref. [1].

The terms $\left(F_{x_{21}} - F_{x_{22}}\right)\frac{t}{2}$ and $\left(F_{y_{11}} - F_{y_{12}}\right)\delta\frac{t}{2}$, appearing in motion equations (Eq. (1)), can be neglected; the first one is null for vehicles equipped with an ordinary open differential, the second one is neglectable for its low value:

$$
\begin{aligned}
m\left(\dot{V} + Ur\right) &= F_{y_{11}} + F_{y_{12}} + F_{y_{21}} + F_{y_{22}} \\
J_z\dot{r} &= \left(F_{y_{11}} + F_{y_{12}}\right)a - \left(F_{y_{21}} + F_{y_{22}}\right)b
\end{aligned}
\tag{8}
$$

that, expliciting the derivatives of the state variables, become:

$$
\begin{aligned}
\dot{V} &= \frac{F_{y_{11}} + F_{y_{12}} + F_{y_{21}} + F_{y_{22}}}{m} - Ur \\
\dot{r} &= \frac{\left(F_{y_{11}} + F_{y_{12}}\right)a - \left(F_{y_{21}} + F_{y_{22}}\right)b}{J_z}
\end{aligned}
\tag{9}
$$

Solving the system in function of r and V allows to obtain the equilibrium values of these variables (r_p, V_p). The validity of the linearization process previously described is confirmed by the correspondence between the values of r_p and V_p and the values of the same variables

(r^* and V^*) calculated at the steady state conditions reached below for the reference manoeuvre with the complete vehicle model.

The calculation of the values of the state variables in the equilibrium conditions (r_p, V_p) is necessary for the expression of the motion equations as a Taylor series. Arresting the calculation at the first order, the system of equations of motion can be written in matrix notation and its solution needs to be evaluated numerically, Ref. [4]:

$$\dot{w} = Aw + k \tag{10}$$

where $w(t)=(V(t),r(t))$ is the state variables vector, A is the state matrix and k is the constant terms vector.

If U=constant (and this condition is satisfied by the reached steady state) the system becomes a constant coefficients linear system. It allows to solve analytically the homogeneous system:

$$\dot{w}_0 = Aw_0 \tag{11}$$

The eigenvalues λ_1 and λ_2 can be calculated thanks to the equation:

$$\det(A - \lambda I) = 0 \tag{12}$$

and are linked with tr(A) and det(A) with the following relations:

$$\begin{gathered} tr(A) = \lambda_1 + \lambda_2 \\ \det(A) = \lambda_1 \lambda_2 \end{gathered} \tag{13}$$

Vehicle stability is determined by λ_1 and λ_2, and, more precisely, by their real parts Re(λ_1) and Re(λ_2). The system is asymptotically stable around its equilibrium point if its eigenvalues have negative real part:

$$stability \Leftrightarrow Re(\lambda_1) < 0 \; and \; Re(\lambda_2) < 0 \tag{14}$$

The just defined real parts are called Lyapunov exponents, but stability can be studied directly referring to the trace and to the determinant of the state matrix. The conditions to satisfy are:

$$stability \Leftrightarrow tr(A) < 0 \; and \; det(A) > 0 \tag{15}$$

The linearizations operated in the model allow to decrease the computational loads required to solve the motion equations expliciting $\dot{V}$ and $\dot{r}$ and consequentially make possible the study of the trace and of the determinant of the state matrix.

4 RESULTS

The vehicle model simulations results are presented in this section, highlighting the influence of anti-roll stiffness on vehicle stability. In particular, the simulations have been carried on varying the anti-roll stiffness of the only front axle.

Fig. (4) illustrates det(A) with respect to tr(A) variations for different constant values of front anti-roll stiffness, for a constant-steering curving manoeuvre, performed at increasing U. It shows how, varying properly the bar stiffness, it is possible to reach more stable equilibrium configurations, expressed by higher values of det(A). Moreover, it can be noticed that the manoeuvres characterized by the same values of steering angle and longitudinal velocity, (indicated in the plot by the marked points), represent more stable equilibrium configurations for higher values of the anti-roll stiffness, showing the relevance of this parameter on the stability conditions.

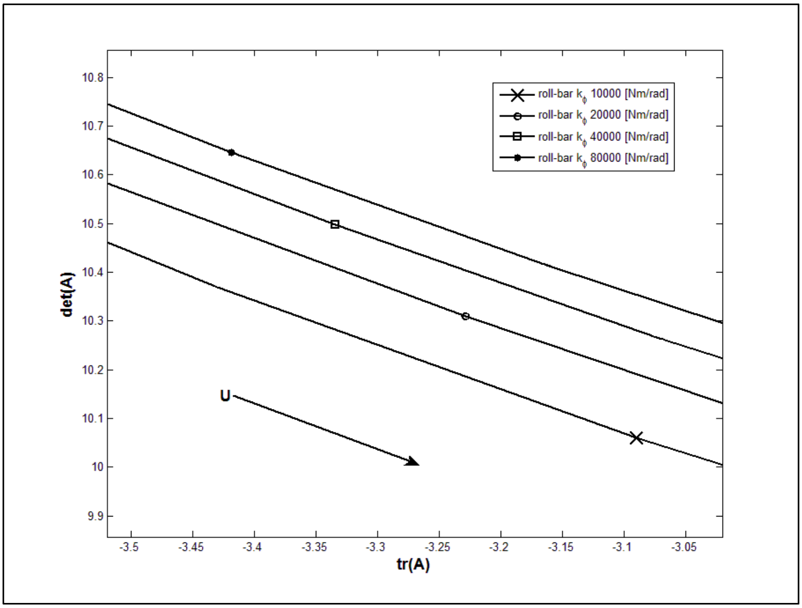

Figure 4: Variations of the eigenvalues, expressed in terms of tr(A) and det(A), for a constant-steering curving manoeuvre, performed at increasing U, in conditions of stable equilibrium and for different values of the anti-roll stiffness.

It is possible to notice how, increasing longitudinal speed, the values of $\det(A)$ and of $\mathrm{tr}(A)$ tend to zero, thus approaching to unstable configuration. Employment of an adequately variable anti-roll stiffness sets the vehicle on more stable conditions, confirmed by higher values of $\det(A)$.

This last annotation could suggest the development of a controlled system, able to vary its anti-roll stiffness as a function of variables such as the longitudinal velocity or the lateral acceleration, with the purpose of increasing the stability of the vehicle.

As it concerns the vehicle handling behaviour, it can be interesting to examine the variations induced by different values of front anti-roll stiffness on the tyre slip angle, Ref [5].

Equipping an axle with an anti-roll bar influences the vehicle dynamics showing a decreasing roadholding of the axle for increasing values of the stiffness. Reducing the lateral force performed by the front axle can be useful, for an over-steering vehicle, to contrast this tendency, reducing, as a consequence, the rear axle slip angle.

Fig. (5) shows, using the same anti-roll stiffness adopted in Fig. (4), the left rear slip angle trend during the reference manoeuvre.

The different values of anti-roll stiffness employed in the simulations allow to evaluate its influence on vehicle stability and on rear slip angles: considering the reference manoeuvre, increasing the front anti-roll stiffness, the rear steady state slip angle values decrease; it means that controlling opportunely the anti-roll stiffness can contribute to reach a more stable configuration in comparison with the configuration obtained keeping constant values of stiffness.

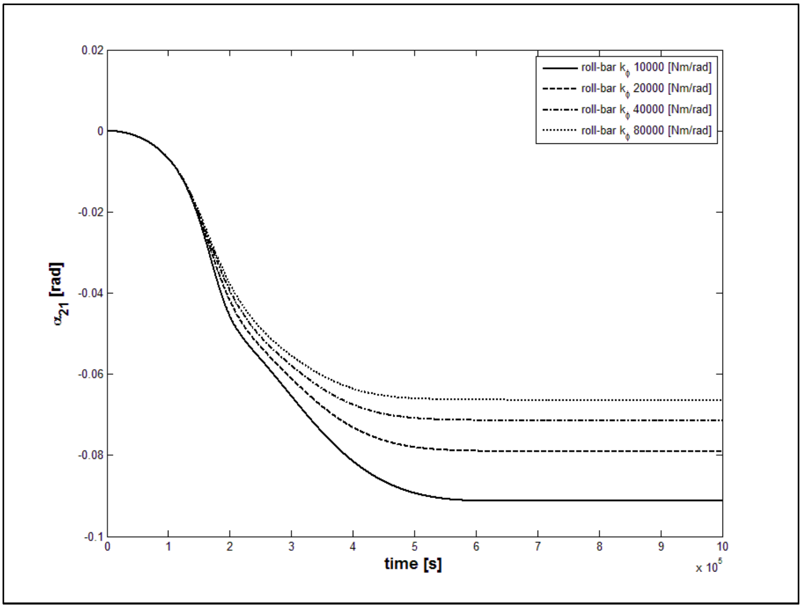

Figure 5: Variations induced by different values of front axle anti-roll stiffness on the left rear slip angle.

5 THE MAGNETORHEOLOGICAL FLUID ANTI-ROLL BAR

The described results highlight that acting properly on the anti-roll stiffness of an axle it is possible to confer to the entire vehicle a more stable equilibrium configuration.

To this purpose, an innovative semi-active anti-roll bar, based on the properties of the magnetorheological fluids, will be now presented. The proposed idea allows to control the anti-roll stiffness of the axle on which it is installed, adopting the well known properties of the magnetorheological fluids, which are suitable for control-based applications.

The system is constituted by two parts: a passive one (A in Fig. (6)), represented by a traditional torsional steel bar and a semi-active device B linked in parallel. The device B is characterized by the employment of magnetorheological fluid, thanks to which it is possible to regulate the stiffness.

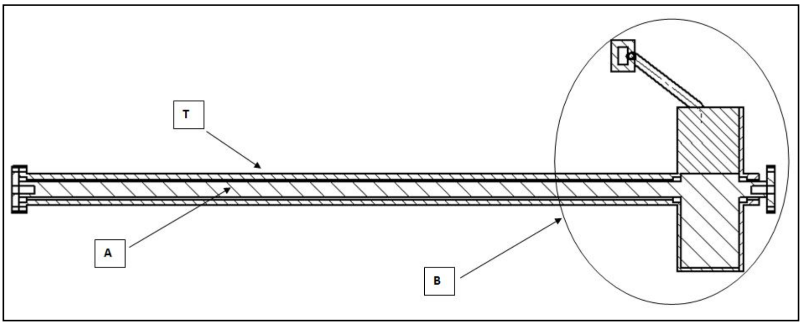

Figure 6: Section view of the magnetorheological fluid anti-roll bar. The passive part of the system, constituted by a high stiffness bar, is evidenced.

The device is constituted by an external cylindrical surface (C in Fig. (7)) in which two elements (D1 and D2) are contained. The element D1 is integral with the classical anti-roll bar (A in Fig. (6)), while element D2 is integral to the surface C. The surface C is made integral with the classical anti-roll bar by means of a coaxial pipe T characterized by a high value of torsional stiffness, so as to consider it as perfectly rigid.

Elements D1 and D2 are respectively integral with the two extreme sections of the classical anti-roll bar A. The elements D1 and D2, in relative motion, create two chambers E containing the magnetorheological fluid. The two chambers of the cylinder are connected by an external by-pass circuit (F in Fig. (7)), characterized by a "virtual valve" G, that allows to control the equivalent torsional stiffness of the system. Particularly, by means of variation of the fluid magnetization, and then of its rheological properties, a regulation of the anti-roll stiffness can be produced. As an example, an increase in the magnetic field generates, as a consequence, an increase in fluid viscosity and an additional anti-roll torque acting on vehicle body.

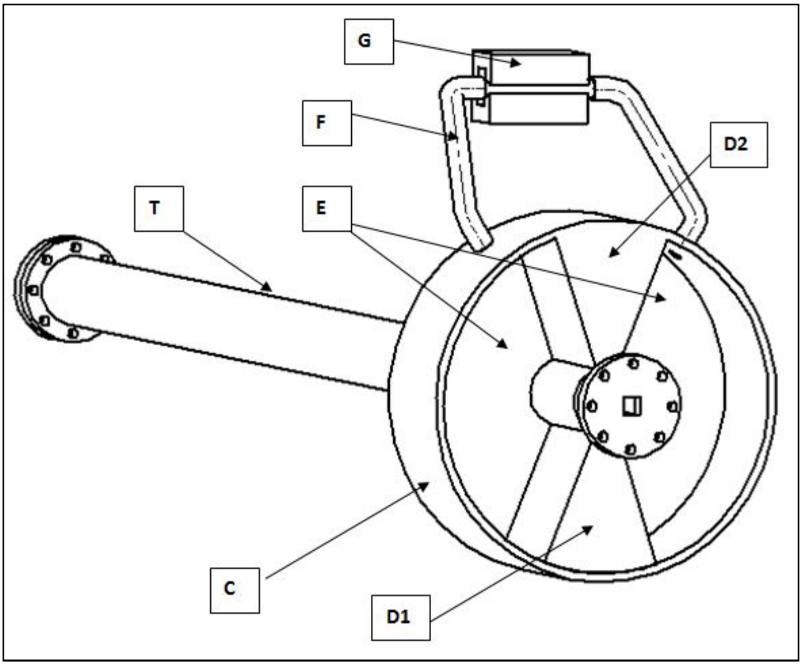

Figure 7: General scheme of the anti-roll bar. It is possible to distinguish the passive part, the chambers in which the fluid evolves and the external by-pass circuit.

In Fig. (8) it is showed the internal geometry of the virtual valve. It constrains the fluid, alternatively moving among the chambers through the pipes, to move across a circular-ring shaped section. The copper-coloured element represents the electric coils generating the magnetic field, able to magnetize the fluid.

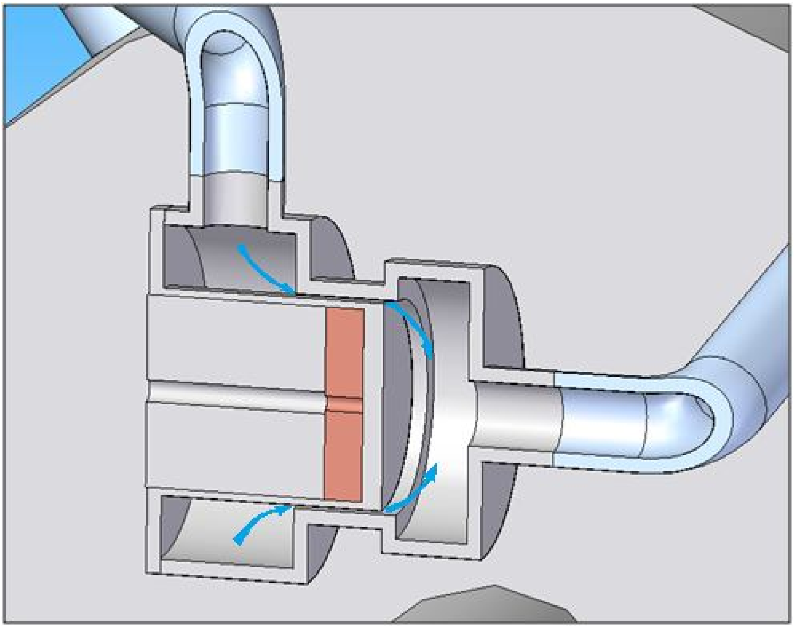

Figure 8: Scheme of the valve constituting the by-pass circuit. The fluid, passing through the coils following the blue arrows, is magnetized, changing its rheological properties.

6 CONCLUSIONS

The purpose of the present paper is the study of the influence of the anti-roll stiffness on the local vehicle stability. To this aim, an 8 degrees-of-freedom quadricycle planar vehicle model has been employed. A reference manoeuvre has been chosen for this analysis: it is a curve approached with steering angle and longitudinal velocity both increasing to saturation values. The manoeuvre lasts until the steady state motion conditions are reached.

Tyre lateral forces, expressed by Pacejka's model, have been linearized for each tyre in the neighborhood of its equilibrium steady state point, to study local vehicle stability in the state space. This kind of analysis is characterized by a heavy computational load, so it has been necessary to adopt simpler expressions of the lateral interaction forces, able, at the same time, to take into account the saturation phenomena due to lateral load transfers. The proposed linearized tyre model has been developed with the aim to satisfy these requirements.

The local stability analysis has been carried out, studying the eigenvalues of the motion equations system in the state space.

The results have been presented, highlighting the influence of the anti-roll stiffness of the axles on the local stability conditions, expressed by means of the state matrix A determinant and trace. It has been possible to notice how, varying adequately the anti-roll stiffness, a more stable equilibrium configuration is reachable.

As a consequence of this result, an innovative semi-active anti-roll bar has been described. This device is based on the properties of the magnetorheological fluids and is able to control the anti-roll stiffness of the axle on which it is installed, driving the vehicle to conditions of increased stability.

REFERENCES

[1] M. Guiggiani. *Dinamica del veicolo*. Città Studi Edizioni, 2007.

[2] H. B. Pacejka. *Tire and Vehicle Dynamics*. SAE International, 2005.

[3] S. Garatti, S. Bittanti. Parameter Estimation in the Pacejka's Tyre Model through the TS Method. 15th IFAC Symposium on System Identification, 2009.

[4] J. L. Escalona, R. Chamorro. Stability analysis of vehicles on circular motions using multibody dynamics. *Nonlinear Dynamics*, vol 53, 237-250, 2007

[5] W. F. Milliken, D. L. Milliken. *Race Car Vehicle Dynamics*. SAE International, 1995.

Proceedings of MUSME 2011, the international Symposium
on Multibody Systems and Mechatronics
Valencia, Spain, 25-28 October 2011

A HISTORY OF ARTIFICIAL HANDS

Ettore D'Aliesio and Marco Ceccarelli

LARM: Laboratory of Robotics and Mechatronics,
University of Cassino, Via Di Basio 43, 03043 Cassino, Italy
ceccarelli@unicas.it

Keywords: Student Paper, History of Robotics, Artificial Hands, Anthropomorphic Grippers, Prosthesis

Abstract. *In this paper a historical survey is reported on the evolution of mechanical design and its actuation for artificial hands with the aim to point out both main historical changes and design problems for efficient solutions. The historical survey is presented by discussing the mechanical design of significant examples of used systems, such as prostheses and robotic hands. Main focus of those examples reveals a strong aim of mimicking and even replicating human hand and its grasping performance with even human shape. The specific case of LARM Hand is also analyzed as an example of how an historical background can help for a modern user-oriented solution of a robotic hand.*

1. BIOMECHANICS OF HUMAN HAND

The human hand is the body part that is used to interact with the surrounding world. Its weight is about 0.4 kg and it can exert a maximum force larger than 500 N in general grasps, and 100 N in configurations for two-fingers grasp [1].The hand has the double function of tool element and data acquisition system. It can exerts a very high resolution control on force, position and velocity and can perform a large variety of configurations to grasp and manipulate objects that are different for shape and size. The high density of nervous centers makes it the main locus of the sense of touch.

As shown in Fig.1, a human hand consists of 5 fingers, a palm (composed of the metacarpal bones) and a wrist (carpus). Each finger has three phalanges, but the thumb has only two ones. Metacarpophalangeal joints have two d.o.f.s and can perform flexion/extension (pitch) and abduction/adduction (yaw) movements; interphalangeal joints have only one d.o.f. for the pitch movement. The thumb has two more d.o.f.s at the intercarpal joint and another d.o.f. is due to the palm with the aim to permit the thumb to be brought in opposition to all the other fingers.

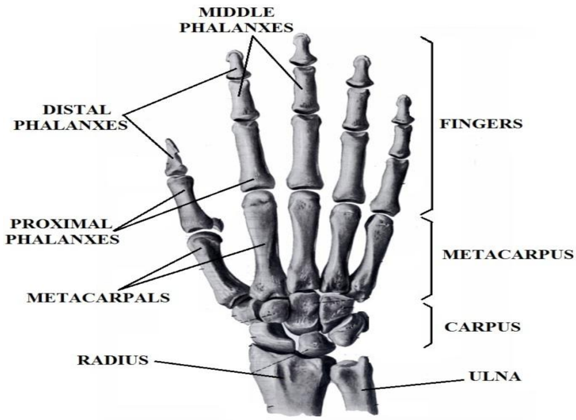

Fig. 1. Dorsal view of a human hand bone structure,

The muscles of the hand are located partially in the hand itself (intrinsic muscles) and partially in the forearm (extrinsic muscles). The intrinsic muscles are responsible of the palm's movements, opposition of the thumb, and generally dexterity of the hand. The extrinsic muscles control the fingers flexion/extension movement and wrist's movements [2].

A hand can perform a high number of power and precision grasps, that are classified by Napier depending on manipulative task in [3]. Power grasps are used for heavy and voluminous objects or when a stable prehension is required as in this case there is a large contact area or the contact is continuous, even under the effect of disturbs. Precision grasps are needed for dexterous manipulations of small objects, in which little movements and orientation changes occur and the contact takes place on the fingertips. There is a high resolution control of force and position so that the fingers are able to respond to small vibrations and grasp condition variations. A partial taxonomy of human grasps is reported in Fig.2, [3]. The different grasps are arranged from top to bottom by increasing the specificity of tasks, and from left to right by increasing the dexterity and precision and by decreasing power and objects size.

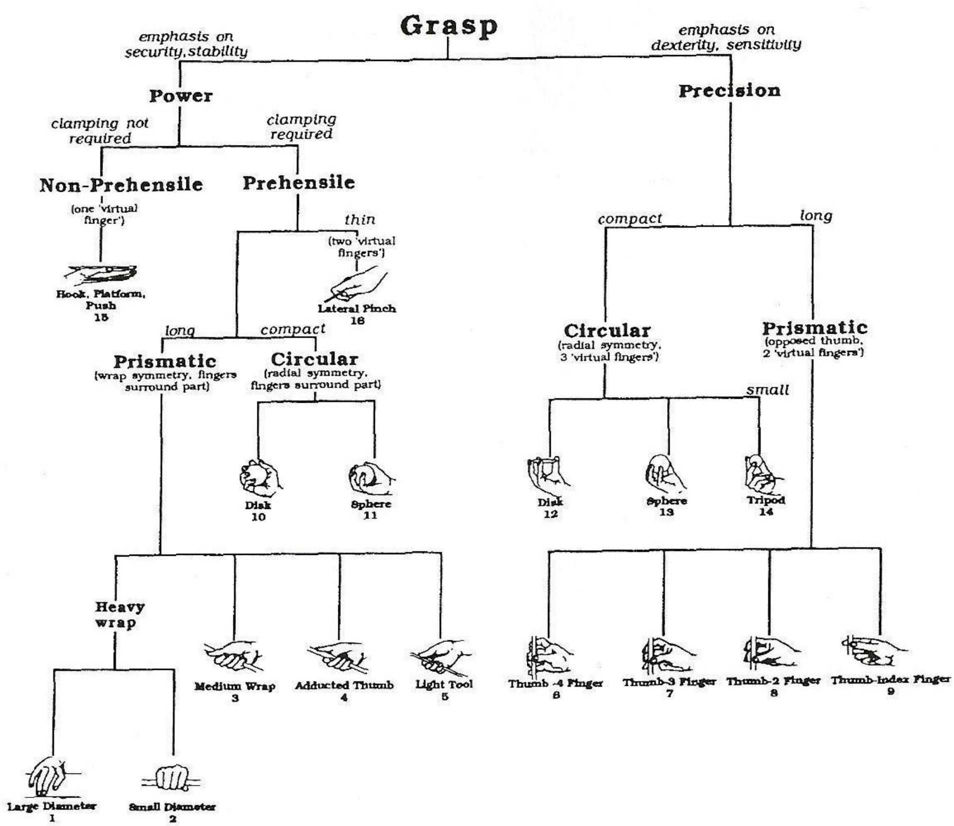

Fig. 2. Human grasping configurations according to [3]

1.1 A two-fingers grip analysis

Through analysis and modeling of a two-fingers grip is possible to emphasize important characteristics, also for three-dimensional case [4]. The phases of a generic two-fingers grip are reported Fig.3.a), [5]: a) one finger impacts the object and starts the grasping; b) the finger pushes the object against the other finger while the motion continues; c) second and final impacts of the fingers to the object; d) the object is grasped at a static equilibrium between the fingers; e) dynamic force may change the equilibrium but still the object is statically grasped by the fingers; f) an external disturbance may change the equilibrium and the object may move to another static equilibrium configuration. A reference system can be identified through three particular lines, [4], namely the contact line joining the two contact points A and B; the squeezing line, which is orthogonal to the contact line and passes across the centre of mass; and the slipping line, which is orthogonal respect to grasping the plane determined by the other lines.

In Fig.3.b) F_1 and F_2 are the grasping forces, which are exerted by the fingers; μ_1 and μ_2 are the friction coefficients that can be assumed with a common value μ; the grasping configuration of the object with respect to the fingers gives the angles ψ_1 and ψ_2 which strongly depend on the orientation of the fingers, position of the contact points, shape of the object and fingers. Vectors r_A and r_B represent the distances of A and B from the squeezing line; W is the weight of the object and it is oriented with an angle Φ_W with respect to the squeezing line. T is an external torque acting on the object and it includes the inertial actions due to the manipulator movement.

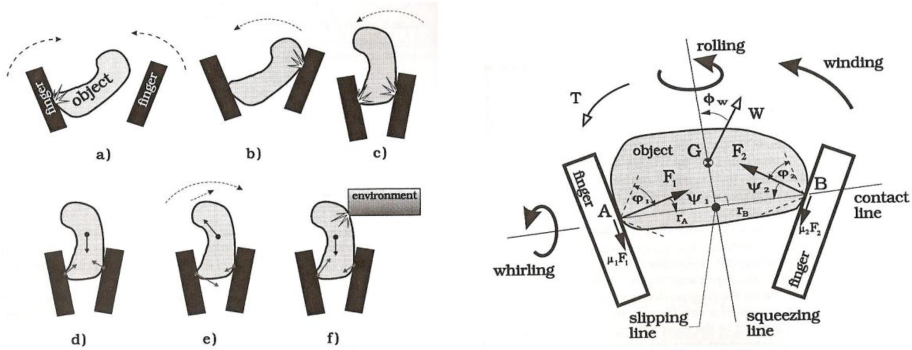

a) b)

Fig. 3. Two-fingers grip: a) grip phases; b) a summary model of the grip [5]

Under the hypothesis of negligible friction forces, the static equilibrium of an object gripped between two fingers can be formulated as

$$F_1\cos\psi_1 - F_2\cos\psi_2 + \mu_1F_1\sin\psi_1 - \mu_2F_2\sin\psi_2 + W\cos\Phi_W = 0 \quad (1)$$
$$F_1\sin\psi_1 + F_2\sin\psi_2 - \mu_1F_1\cos\psi_1 - \mu_2F_2\cos\psi_2 + W\sin\Phi_W = 0 \quad (2)$$
$$T - r_G W\sin\Phi_W - r_A F_1(\sin\psi_1 - \mu_1\cos\psi_1) + r_B F_2(\sin\psi_2 - \mu_2\cos\psi_2) = 0 \quad (3)$$
$$F_G \geq S \quad (4)$$
$$T_G \geq N \quad (5)$$

in which equations (4) and (5) define the stability conditions.

F_G e T_G represent grasping force and torque, S and N represent the disturbing forces. If T and W are assumed dependent to the motion of the gripper and object, a dynamic model is

$$F_G = F_1\tan\varphi_1\cos\psi_1 + F_2\tan\varphi_2\cos\psi_2 \quad (6)$$
$$S = W\cos\Phi_W + F_1\sin\psi_1 + F_2\sin\psi_2 \quad (7)$$
$$T_G = F_1r_A\tan\varphi_1\cos\psi_1 - F_2r_B\tan\varphi_2\cos\psi_2 \quad (8)$$
$$N = T + F_2r_B\sin\psi_2 - F_1r_A\sin\psi_1 \quad (9)$$

A three-dimensional case can be deduced accordingly by considering the equilibrium along the three axes, including the slipping line [6].

2. GRASPING DEVICES IN ANTIQUITY

Documents and archeological finds testify that artificial arms and hands were used as prostheses even in ancient times. An iron hand was found attached to an Egyptian mummy's arm and upper limbs are mentioned into the holy book of Talmud. In a section of the Shabbath treatise that provides Hebraic laws about prosthesis the word "lukitmin", literally "(tool) to carry loads", can be translated as "artificial arm" [7]. It can be supposed that this kind of prosthesis was merely intended for cosmetic purposes. A very first documented case of functional use of ancient upper limbs goes back to the roman period. Plinius the Older rports in his "Naturalis Historiae" that the praetorian Marcus Sergius Silus during the second

Punic War (218 – 202 B.C.) lose his right hand and continued fighting with an artificial one:

"*Sinistra manu sola quater pugnavit, duobusequi sin sident eosuffossis. Dexteram sibi ferream fecit, eaquer eligata prœliatus, Cremonam obsidionem exemit, Placentiam tutatus est.*" [8]

"He fought four times with his left hand only, two times this lead to a fall from the horse. He made for himself an iron right hand, he went in battle with it laced, set free the city of Cremona, protected the city of Piacenza."

Probably the roman general was able to efficiently use the artificial hand in battle, unfortunately a detailed description of the device is missed.

3. EARLY MODEL MECHANICAL HANDS AS PROSTHESIS

At the end of 15^{th} century a wide diffusion of functional mechanical prostheses begins. There are several reports similar to the story told by Plinius and several inventories in modern historical museums count many devices of that period. The artificial hands of the 15^{th} – 17^{th} centuries were iron passive devices with the shape of an armor gauntlet, furnished of levers, springs and gears return mechanisms.

3.1 The Eisern Hand

The Iron (Fig.4) Hand of Götz von Berlichingen is a good example of these efficient prostheses. Berlichingen was born around 1480 from an aristocratic family of the German region of Wurttenberg. He lost the right arm in the Landshut siege in 1508 and replaced it with an iron limb. The device is composed of a forearm and a hand and has a weight of 1.4 kg. All the fingers are full articulated and independent each other; each phalanx moves by means of small partially toothed cylinder that engages a ratchet cut; release buttons free the mechanism and linear springs bring the phalanx to the full extended position. The thumb is opposable and the wrist allows a little pitch movement of the hand [9]. The knight's long life as mercenary prove the effective efficiency of the device that was actively used to hold a sword or a pike.

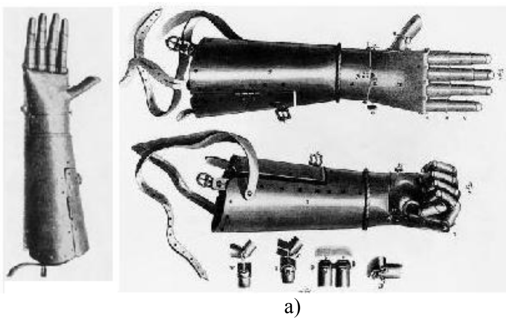
a)

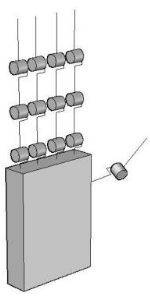
b)

Fig. 4. Götz von Berlichingen's Eisern Hand: a) Museum remains; b) a kinematic model

3.2 Petit Lorrain's Hand

An artificial hand with relevant historic worth was created by the father of modern surgery, Paré Ambroise (Fig.5). He served for years as military surgeon by developing new amputation's techniques and gun wound's treatments. This prosthesis was created around

1550 by a craftsman named "le Petit Lorrain" and was used by a French high rank soldier. In his work [10] Paré included a detailed drawing of the device. The hand has 4 lightly flexed fingers that all are independent and articulated at the metacarpophalangeal joint, with a fixed thumb, not opposed to the fingers. Fingers are kept in extension by linear springs. In each knuckle there is a small gear and a trigger that engages the space between the teeth, with the aim to make possible to close the fingers in several stop positions. A bigger trigger, that is actuated by a release button from the dorsal surface of the hand, disengages all the other triggers, and the linear springs can bring the fingers to the initial position.

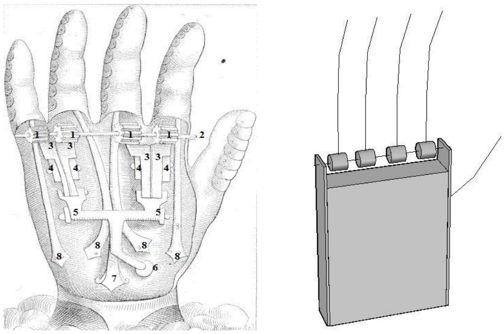

a) b)

Fig. 5. Petit Lorraine's hand: a) prosthesis [10]; b) a kinematic scheme

3.3 Stibbert Arm

This is an iron device of 15th-16th century, the weight is 1.8 kg and it is designed for a right arm. It is composed of an arm, a forearm and a hand [11]. The arm is a tubular piece that is linked to a bracelet to which was inserted a stump by means of a ring that allows the rotation. The forearm is formed by two semi-cylindrical iron pieces and it is linked to the arm by three metal plates that look like an armor's elbow protection. An inner mechanism is used to extend the arm by pushing the external button to bring the arm from the full flexed position to the full extension, in one, two or three phases (Fig.6.a). The hand is linked to the forearm in full supination with metallic screws.

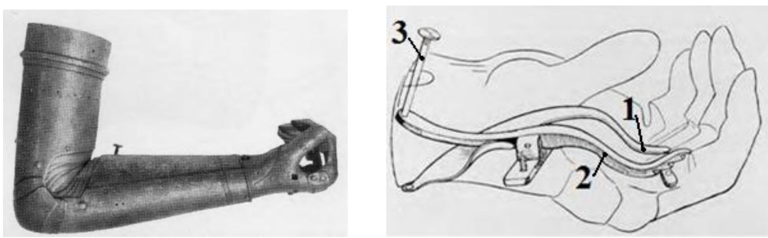

a) b)

Fig. 6. Stibbert arm: a) Museum remains; b) detail of hand's mechanism [11]

The hand is composed of a metacarpus piece, that includes a fixed thumb and fingers that are each other coupled and semi-flexed. Each finger is a semi-cylinder, linked at the metacarpophalangeal joint to the semi-cylindrical palm. A spring attached to the internal side of the back keeps the fingers in extension. A mechanism that is composed of a lever (n. 1) and a ratchet (n. 2) is linked near the middle finger. By pushing the button from the wrist (n. 3) it is possible to extend the fingers in one, two or three phases (Fig.6.b). The range of movement appear very limited and there is no contact between palm and fingers even in the full flexed position.

3.4 Poldi-Pezzoli Arm

This is an iron right arm prostheses, probably of the 16th century. It is composed of an arm, a forearm and a hand [11]. The arm is formed by two semi-cylindrical pieces that were closed around the stump with a lateral buckle and a belt should have been attached to it but it is missed (Fig.7.a).

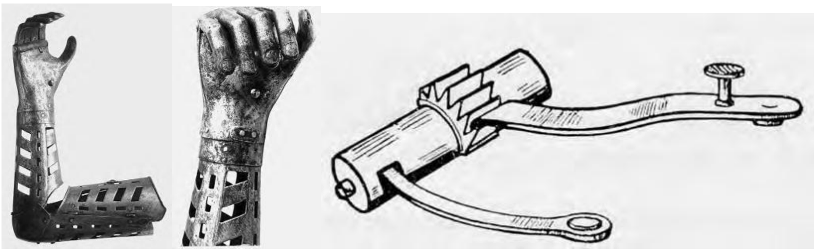

a) b)

Fig. 7. Poldi-Pezzoli arm: a) Museum remains; b) detail of hand's mechanism [11]

The arm is linked to the elbow that is linked to the forearm. In order to obtain a full extension of the device it is necessary to operate on both the arm and the forearm by means of two buttons that free a start/stop ratchet mechanism. The whole arm is pierced with a reticule of rectangular holes. The hand is linked to the forearm by a rigid wrist in semi-supination. Thumb and fingers are flexed at the interphalangeal joints and have a smoothed surface that offers a flat contact area. The mechanisms consists of a toothed segment coupled to a horizontal cylinder where the fingers are hinged with two iron leaf springs (Fig.7.b). A spring is attached to the internal side of the palm and its free end engages the toothed segment. The other spring is attached to the internal side of the back and its free end insisted on a slot on the horizontal cylinder. By pushing a release button from the palm, near the wrist, is possible to extend the fingers in 7 phases. This device is certainly well manufactured and the design respects the natural orientation of the forearm, with a good architecture and a good profile of grasp (a triangular section). Mechanisms are functional and require small spaces. However the hand in supination and the strong flexed fingers make this prosthesis useful to only hold the reins of a horse [11].

3.5 Stibbert Museum's Hand A

This is a left hand prosthesis of 15th century with a weight of 0.58 kg [11]. There are 4 fingers that can be moved on the metacarpophalangeal joint and a fixed thumb (Fig.8.a). All the fingers are rigidly flexed at the interphalangeal joints and the surfaces are flattened for a secure grasp. The shape of the fingers offers a grasp of cylindrical objects. The fingers are attached to a cylinder linked to a ratchet wheel (Fig.8.c).A lever from the back of the hand is engaged to the teeth of the ratchet (Fig.8.b). When the fingers are closed, a lateral button can be pushed to disengage the lever to give a quick opening of the fingers, maybe by the action of a spiral spring situated into the hinge. The mechanism is however inside the device and it is impossible to see. The movement can be performed to obtain six stop positions. The hand is roughly assembled and there are prominent rivets and only small nails as decoration [11].

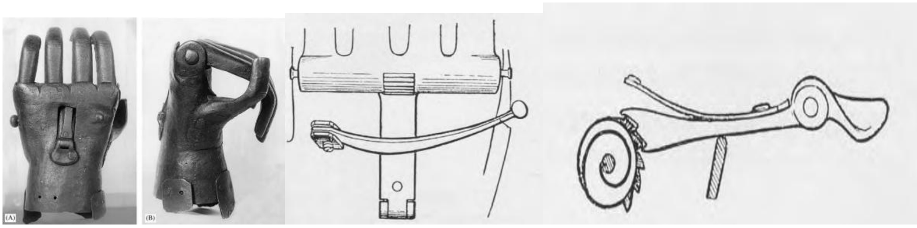

a) b) c)

Fig. 8. a) Stibbert Museum's Hand A; b) control lever; c) spiral spring mechanism [11]

3.6 Stibbert Museum's Hand B and C

The hand in Fig.9 is another right hand prosthesis of the 15th century, it is stubby and quite heavy (g. 840). The design is essentially mediocre, but the craftsman wished to preserve the natural slope of the fingers and the styloid process of ulna. The mechanism is composed by two springs and a ratchet linked to the hinge and it is controlled by a release button placed on the back. The worn look prove the frequent use of this prosthesis [11].

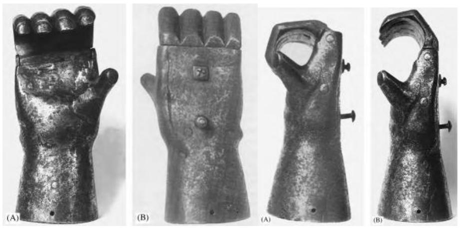

Fig. 9. Stibbert Museum's Hand B [11]

Fig. 10. Stibbert Museum's Hand C [11]

The Stibbert Museum's Hand C in Fig.10 is a right hand prosthesis. The decorative holes on the palm and the back enhance the aesthetic value and reduce the weight, that is about 0.6 kg. The fingers are tubular, flexed at the interphalangeal joints and coupled to a pin linked to the metacarpus; the distal phalanx is missed in the ring finger. All the fingers are articulated on the metacarpophalangeal joints and independent each other. The thumb is hinged to the palm and it has an interphalangeal joint also, maybe with another hinge. Unfortunately the device is rusty and broken in some points, so that is possible to only imagine how it really worked. It seems that the craftsman wished to keep independent the two couple of fingers. The mechanism of this prosthesis has been designed to keep the fingers closed and the fingers can be free by the control button, that can be locked with a small hook.

All the above prostheses have commons features as follows. The mechanical design was almost the same, with ratchet wheels or racks mechanisms, return springs and lock/unlock buttons. The efficiency of the grasp's system was strictly connected to the talent of the manufacturer. The movement was passive, so that the functionality of these device was very limited and sometimes these prostheses had a merely esthetic function; however the smoothed surfaces of some of them demonstrate that they were used frequently and efficiently.

4. MODERN PROSTHESES

A development of medical and mechanical knowledge lead to improve the efficiency and the comfort of the upper prosthesis with the introduction of new materials and actuation systems. The progress was mainly pulled by the need to rehabilitate the great number of people subjected of amputation, because of both war wounds and daily life accidents, that sensibly increased with the advent of industrial machinery.

At the beginning of the industrial age the efficient emulation of the lost limbs work capability became the principle aim. A prosthetic device was supposed to be robust and able to interact with the most common tools. They were generally composed of an arm articulated by steel tutors and firmly attached to the stump and a metallic extremity that could be screwed to a hook, a fork, a hammer or other tools (Fig.11.a). This kind of prosthesis was used mainly by machinists or farmers who lost one limb on work [12]. In 19th century there was a great evolution of the mechanical systems, with the production of the first devices with direct mechanical actuation. The mechanician Van Peterson thought to take mechanical power from the shoulder and stump of an amputee and to deliver it to the artificial limb by using a wires and pulleys system to flex or extend the elbow and the fingers, dependently by the range of the shoulder's movements (Fig.11.b). The system was improved later by Mathieu, but its diffusion was quite limited since it was very expensive as for aristocratic or highborn people only. Moreover, in most of the cases, amputees easy learn to do activity with one hand rather than properly use prosthesis.

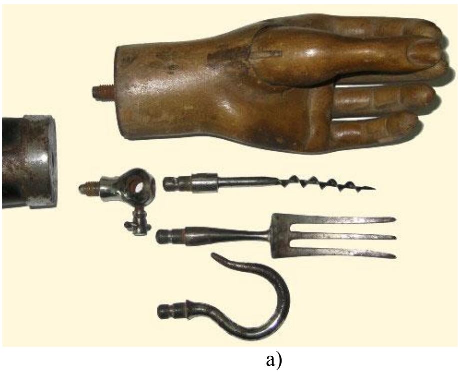

a)

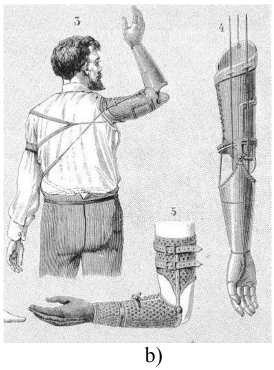

b)

Fig. 11. Early modern prostheses: a) artificial cosmetic hand and tools; b) Van Peterson's actuation system [12]

At the very end of 19th the orthopedist Giuliano Vanghetti invented a completely different system by using muscular canals. His prosthesis was directly actuated by the residual muscles of the stump [9]. This idea was developed by other doctors, especially by the surgery Ferdinand Sauerbruch, who mainly operated in World War I. He surgically modified the muscles to obtain some loop knots, where could be inserted little ivory pins linked to the mechanism of the hand. This prosthesis made possible to open and close the hand by using the extensor and flexor muscles, but the functionality degenerated with time, because of the progressive extension of the body parts involved and the frequently inflammations of the muscular canals.

After the two World Wars the great growth of amputees, especially in USA, drove further ahead the research of different external type of power supply. In 1957 Heidelberg, Hoefner e Marquard invented a 6 d.o.f.s device actuated with carbon dioxide cylinders and at the same time first electric and hydraulic systems appeared. Unfortunately these prostheses could be operated and controlled with the healthy hand, so that they could be used by monolateral amputees only. Moreover there were several weak points, such as noise and heavy weight of the pneumatic prostheses and frequent leaks of the hydraulic ones.

From the 40's the research focused on the variations in electrical potential coupled with the muscle's contraction that are also detectable on the skin for the depolarization of the fibers [9]. The first myoelectric hand actuated by an electromagnet was built by Reiter and the manufacture rights were bought by England and Canada; thanks to the studies carried out also by other nation in 60's began a wide commercialization of the myoelectric prostheses: the Viennatone's hand in 1967 and the Otto Bock's hand in 1969 (Fig.12).

Fig. 12. Otto Bock's upper limb prosthesis [12]

The first Italian myoelectric prosthesis was developed in 1965 at the Vigorso INAIL Center. It had three fingers, a maximum grasping force of 50 N and a fair velocity compared with other models [9]. Researches have leaded to develop more sophisticated and functional components, providing upper limb prostheses with high reliability and light weight, low power consumption and, last but not least, a good cosmetic look. The functionality has been improved so that the myoelectric signals are proportional to the contraction applied by the patient.

There is a significant gap between the progress of the research and the commercial diffusion of these devices. Advanced prototypes are able to emulate the human hand's high dexterity and versatility, but there are several limitations in terms of portability and direct control by the user. Sometimes patients prefer even more simple solutions that allows the only pinch grip. Moreover the prosthesis market is actually quite small and this causes a stagnation of both costs and innovation. To give an example, modern hook prostheses, as shown in Fig. 13, have the same hook design and scapular actuation system patented by dr. Dorrance in 1912 [13].

An interesting commercial solution is offered by Touch Bionics (Fig.14), [14]. The I-Limb Hand costs about 18.000 USD and has a myoelectric control by means of two electrodes placed on the skin; all the fingers are independent each other, the thumb can oppose to them both frontally and laterally and the wrist allows a roll movement; the patient receives a feedback on the outlet pressure and is possible to perform operations often impossible for an artificial hand, like opening a rink can; the mechanical structure is provided with a cosmetic cover.

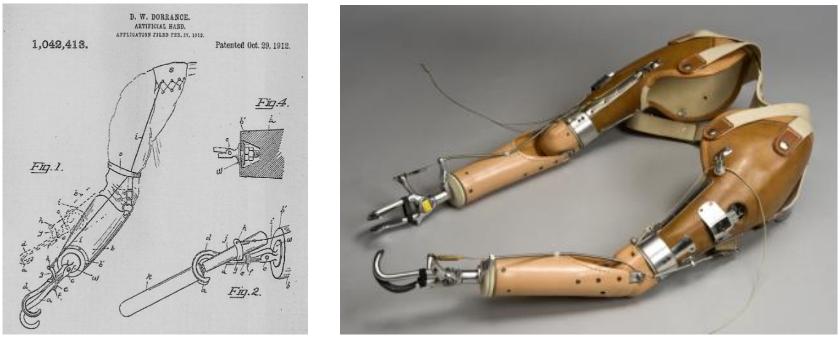

a) b)

Fig. 13. Hook hand prostheses: a) Dorrance’s Hook patent drawing [12]; b) modern prostheses

Fig. 14. I-Limb Hand: a) structure; b) cosmetic cover [14]

The main problem with myoelectric implants is the high specialization of manufacturers on single components and the consequent dependence on the components providers. Another limitation is the lack of universal standards for control software and hardware interfaces. This often prevents the dialogue between components made by different companies, which tend to protect programming languages and encoding made by their research laboratories.

5. MODERN ROBOTIC HANDS

In the 1980’s there was a considerable development of new technologies, and at the same time a growth of demand of more accurate and versatile systems, mostly for industrial and aerospace applications [15]. This led to a very first significant development of robotic hands, from two-fingers grippers for teleoperation towards more advanced task-oriented systems. Significant prototypes and solutions are examined in the following.

5.1 Stanford/JPL Hand

The prototype has been designed and built around the middle 80’s at the NASA Jet Propulsion Laboratory by Kenneth J. Salisbury of the Stanford University department for Computer, Science and Surgery (Fig.15). The hand has a weight of 1.1 kg and is composed of three modular fingers connected to a fixed base, without a wrist or a palm. Each fingers has two articulated phalanxes. The first phalanx is linked to the base with two separate joints, that causes a reduction of anthropomorphism and potential dexterity. The first joint allows a yaw movement of ± 90°, the second joint a pitch movement of ± 90°; the interphalangeal joint have a pitch range of ± 135°. Twelve DC actuators LO-COG give the motion to the joints by means of four Teflon coated wires, with a maximum grasping force of about 44 N.

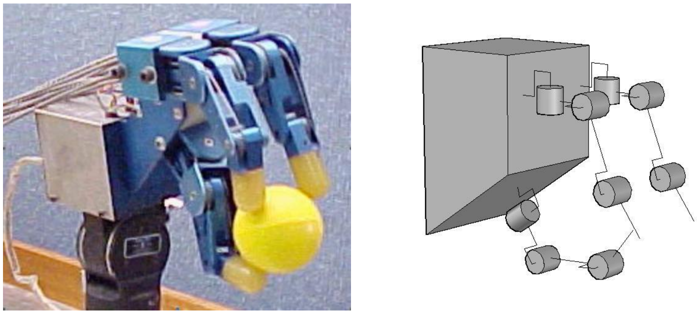

a) b)

Fig. 15. Stanford/JPL Hand: a) prototype; b) a kinematic scheme

The control is based on input signals provided by tactile and force sensors placed inside the fingertips and by strain gauges and encoders, placed in each proximal joint. Despite of its modularity and low cost components, this prototype is not suitable for industrial use, due to the characteristics of the transmission system difficult to maintain and repair [15].

5.2 Utah/MIT Hand

The Utah/MIT Dexterous Robotic Hand (Fig.16) has been conceived at the Artificial Intelligence Laboratory of the Massachusetts Institute of Technology, with the collaboration of the Center for Biomedical Design of Utah, [15].

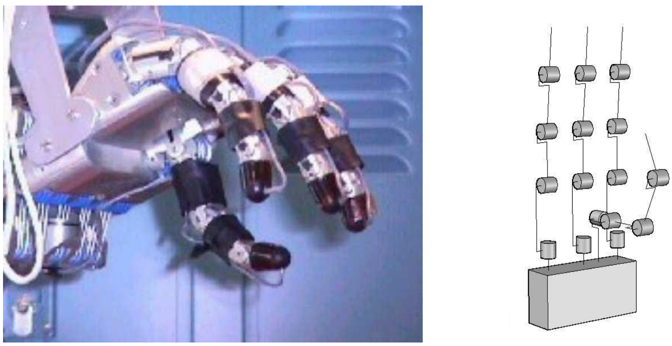

a) b)

Fig. 16. Utah/MIT Hand: a) prototype; b) a kinematic scheme

The hand has four modular fingers, consisting of three articulated phalanxes and the thumb is identical to the other fingers. Each finger has four degrees of freedom: two are located in the metacarpophalangeal joints and allow movement of pitch and roll, creating a non-anthropomorphic circling motion; the remaining two d.o.f.s correspond with the interphalangeal joints, that allow the movement of pitch. The fingers are controlled by pairs of wires that act as antagonistic tendons, a couple for each d.o.f. The actuators are 32 double effect pneumatic cylinders that generate a force of about 31 N at the fingertips, with a frequency response of over 20 Hz. Linear Hall effect sensors are used for position control. The device has a high number of d.o.f.s, high dexterity and good dynamic performance, but the flexible transmission is a weakness point since it limits the movement range of the wrist, makes difficult the assembling on different robot arms and requires an elaborate system of pulleys for correct control [15].

5.3 TUAT/Karlsruhe Humanoid Hand

The prototype has been designed in 2000 to equip the anthropomorphic robot ARMAR, that was developed at the Forschungs zentrum Informatik Karlsruhe of Karlsruhe University in Germany for human daily help and cooperation (Fig.17.a).

The TUAT/Karlsruhe Humanoid Hand has been designed to emulate the ability of human hand to adapt the grasp to a grasped object [16]. The hand has only one degree of mobility and the motions is transmitted to the individual parts by means of a mechanism consisting of bars, plates, revolution joints and spherical joints. The prototype has the size of a human hand and, excluding the external actuator, a weight of only 0.125 kg. The hand consists of 5 articulated fingers mounted on a wooden base. The index and the middle finger metacarpals are fixed to the base, while the ring and the little finger metacarpals have two d.o.f.s by spherical joints. The 4 fingers are linked by means of a complicated mechanism that allows to share forces. The angle of the index and the little finger produces also a lateral contact force (Fig.17.b). The hand can hold small objects and reproduce the main strategies of the human grasp, but the manipulation of the objects is impossible because of the interdependence the fingers movements.

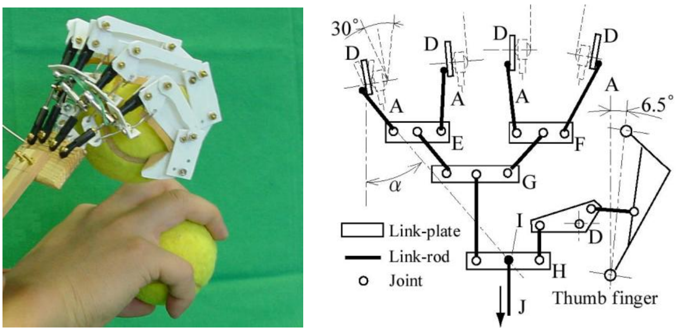

a) b)

Fig. 17. TUAT/Karlsruhe Hand, [16]: a) prototype; b) a kinemtic scheme

5.4 DLR Hand II

The DLR Hand was developed by Deutsches Zentrum für Luft- und Raumfahrt with a first version in 1997 and a second one in 2001 with a lighter structure and more advanced actuation and sensors. In 2003 a collaboration between DLR and Harbin Institute of Technology started with the aim to make the hand suitable for commercialization. The DLR Hand II weighs about 1.8 kg and has a modular open structure (Fig.18.a). Each finger is coated with polymer protective shells, that act as fingertips. A differential bevel gear mechanism at the metacarpophalangeal joint provides two d.o.f.s and controls the pitch and yaw movements by means of brushless motors even simultaneously (Fig.18.c). Another brushless motor moves the two interphalangeal joints, which are directly coupled with one d.o.f. The transmission consists of harmonic drive gear and timing belts. The three motors exert a maximum force of 30 N at fingertips [17]. An additional degree of freedom (for a total of thirteen) is supplied by a DC motor that drive the fourth finger in order to better oppose the thumb. The fingers are equipped with a strain gauge in each joint and a small six-axes sensors in the fingertips, for torque and force measurement. The position is measured using high resolution potentiometer and the measurement of velocity is done by derivation of position by using Hall effect linear sensors that provide a relative position and must be calibrated at each start [18]. The necessary electronics are integrated in the palm and the fingers, so that it is possible to install the hand on any robotic arm with minimum cables.

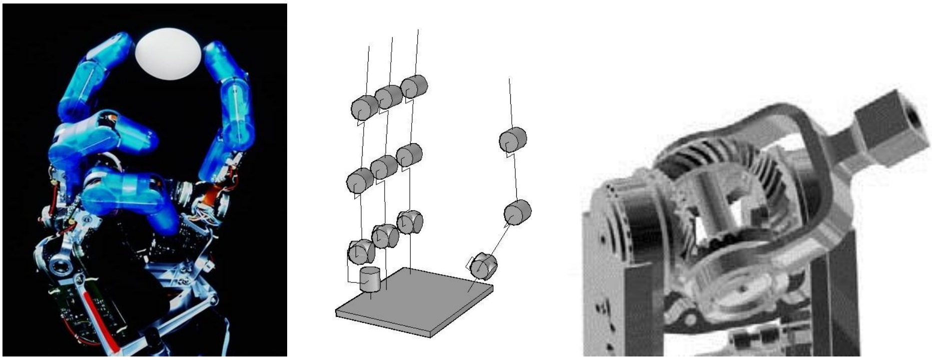

a) b) c)

Fig. 18. DLR Hand II, [17]: a) prototype; b) a kinematic scheme; c) differential joint

5.5 Gifu Hand III

Gifu Hand has been designed at Gifu University in Japan in 2002 with the collaboration of Dainichi Company Ltd. There are both a right and a left hand prototype (Fig.19.a).

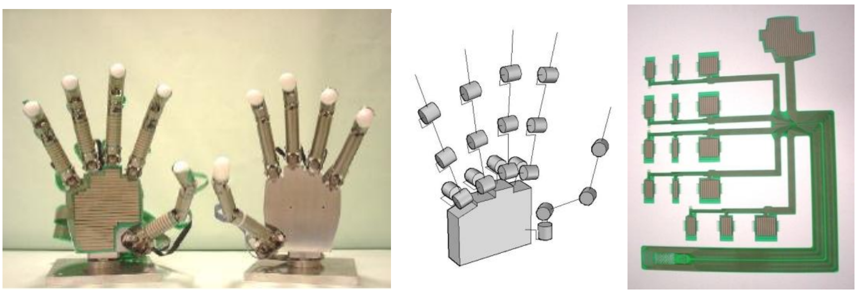

a) b) c)

Fig. 19. Gifu Hand III, [19]: a) prototype; b) a kinematic scheme; c) tactile sensor

Each hand has a weight of about 1.4 kg and is made of a hard metacarpus to which are attached four articulated fingers and a thumb, that are composed of three phalanxes. The four fingers have three d.o.f.s by means of two metacarpohalangeal joints and two interphalangeal joints that are coupled by a four-bar mechanism and each phalanx can effectuate a small retroflection. The thumb has another d.o.f. due to the independence of the third phalanx and a wider yaw range. Each d.o.f. is controlled by a compact DC servomotor integrated in the hand and equipped with encoder. The transmission system consists of satellite and face gears to increase the compactness and a secondary gears system, which is symmetric with respect to the axis of yaw, provides force balance and reduces backlash effects [19]. Gifu Hand can exert a maximum force of less than 4 N at the fingertips, with a frequency response of 7.4 Hz. The hand is equipped with six-axes force sensors on each fingertip and a tactile sensor placed on the surface of the palm and fingers (Fig.19.c). A touch sensor has been developed in collaboration with Nitta Corporation to produce a network of electrodes that are arranged in a grid and thin film of conductive ink, whose electrical resistance changes proportionally with the applied pressure. The tactile sensor occupies one-half of the hand's surface, with 859 points total for a maximum load of 2.2 x 10-3 N/mm^2.

5.6 UB Hand III

The UB Hand III is the third version, completed in 2004, of the robotic hand that was developed at the Laboratory of Automation and Robotics of the Bologna University (Fig.20.a). The hand has five modular fingers, mounted on a small carpus. Each finger has four plastic phalanxes and four flexible joints, made of three steel coil springs and activated by a cable (Fig.20.c). The thumb has a spherical joint with a coil spring and three cables, placed at 120° to each other; index and little fingers have a joint for yaw motion. Sixteen of the twenty d.o.f.s are actuated by low cost DC motors that are installed externally and equipped with position and force sensors for current/torque control. Each tendon is attached to the actuator by means of a sprocket and a pulley to give maximum force of 70 N with a frequency response of about 3 Hz, [20]. Position and force sensors are also installed placed in the fingers as half-bridge strain gauges that detect the force exerted by the springs of the flexible joints by means of an integrated mini-load cell. The actuation system is however quite heavy and requires a large and stiff forearm to accommodate the motors.

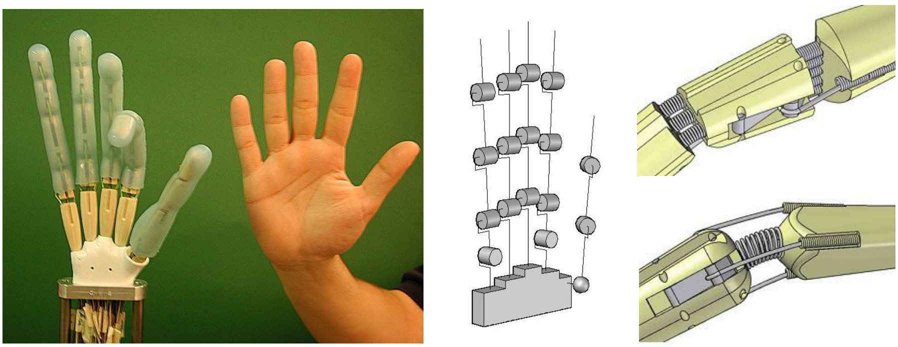

a) b) c)

Fig. 20. UB Hand III, [20]: a) prototype; b) kinematic scheme; c) spring joints

5.7 CyberHand

The CyberHand has been built in 2005 within a collaboration project between the INAIL RTR Center in Viareggio and the ARTS lab of the Sant'Anna School of Advanced Studies [21]. The hand consists of 5 modular fingers and a palm and weighs 320 grams, excluding the external actuators for the fingers flexion (Fig.21.a). Each finger is composed of three phalanxes made of an aluminum alloy and is underactuated by one DC motor. The opposable thumb has an extra degree of mobility that allows a rotation of 120°. The palm is composed of three parts: an outer shell made of carbon fiber, an aluminum inner structure and a soft cover. The hand can perform lateral, cylindrical, spherical and tripod grasps. The actuators placed in the forearm are DC motors equipped with magnetic encoders; a screw drive systems connected to motors tight the wires that transmit the movement to the fingers. The maximum force at the fingertips is 15 N, but in the cylindrical grasp configuration it rises up to 40 N. However the dynamics is rather slow and the closure minimum time is about 6 seconds [21]. In addition, the forearm structure that hosts the actuators is very heavy (Fig.21.a). Six incremental encoders mounted on each motors and 15 Hall effect position sensors, one for each joint, are used for position and velocity control. The measure of the force is done through three-axes force sensors, one in each fingertip, and voltage sensors, one for each tendon. All phalanxes are equipped with a touch sensor. A suitable neural interface and algorithms are scheduled to allow a direct transmission of the artificial sensor signals to the nerves of an amputee.

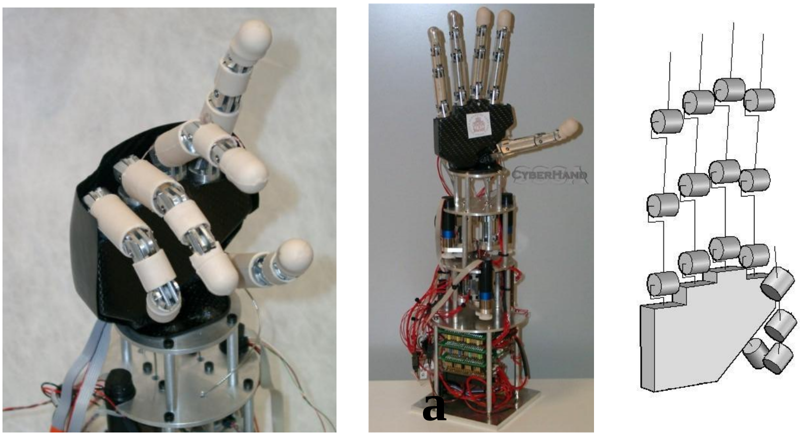

a) b)

Fig. 21. Cyber Hand: a) prototype; b) a kinematic scheme

5.8 Barret Hand

The Barrett Hand (Fig.22) is produced by Barrett Technology Inc. and it has been commercialized since 1999. It has been designed for industrial applications, [22].

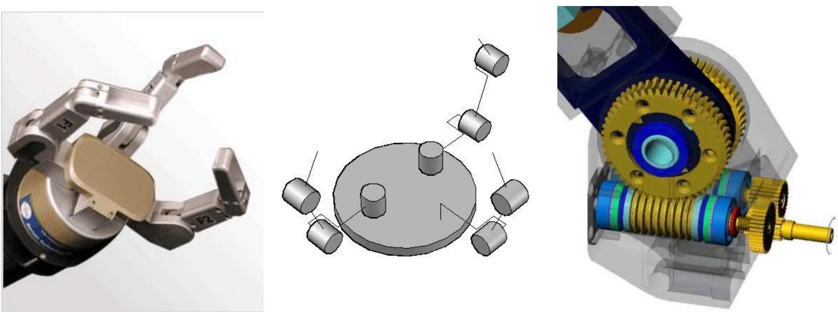

a) b) c)

Fig. 22. Barrett Hand: a) prototype; b) kinematic scheme; c) worm screw system [22]

The hand consists of a palm and three underactuated fingers with a compact structure of 1.18 kg weight. Each finger has two d.o.f.s, one for each phalanxes; the first and the second fingers have another d.o.f. that allow a symmetric rotation (Fig.22.a). The hand is actuated by four DC servomotors: three for the pitch movement of each finger, one for the roll movement of the first and second finger. The underactuation is obtained by means of a worm screw system that redirects the torque from proximal to distal phalanxes and operates automatically (Fig.22.c). When the grasping force is sufficient, the fingers are locked so that is possible to shut down the motors and save energy. The fingers are controlled in position, velocity and acceleration through incremental optical encoder. The minimum time for complete closure of the fingers on the palm is of the order of seconds, while the full lateral rotation takes about half a second. The maximum payload is 6 kg. The hand is controlled by an integrated microprocessor that interacts with other four dedicated microprocessors, one for each joint. A standard RS232 serial interface is used for PC control in both supervisory and real time mode. The cost of the Barrett Hand is 30.000 USD and has been purchased and used primarily by automotive industries, such as Yamaha, Honda, Fanuc Robotics and NGK [22].

5.9 MARS e SARAH Hand

MARS (Main Articulé Robuste Sous-actionnée) and SARAH (Self Adaptive Robotic Auxiliary Hand) Hands were developed at the Laval University, in Canada, Fig 23.

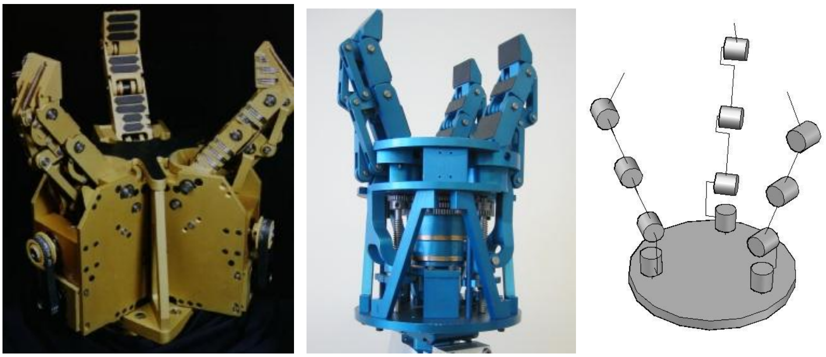

a) b) c)

Fig. 23. Hands at Laval University: a) MARS Hand; b) SARAH Hand; c) a kinematic scheme

They are designed for applications in hazardous environments [23]. The structure of the two hands is almost the same since it consists of three fingers orthogonally mounted to a base that acts as palm. The fingers are articulated by means of a differential mechanism, which also allows the passive flexion. The MARS model (Fig.23.a) has been built in 1996 with a weight of 9 kg and a size approximately twice as the human hand; it has 12 d.o.f.s, one in each interphalangeal joint one at the base of the proximal phalanxes, for the rotation of the fingers on the palm. The actuation includes six brushless motors, three for the roll and three for the pitch movements of the fingers. The hand can make both power and precision grasps, for a maximum payload of 70 kg. The hand is equipped with potentiometers to control finger position and force sensors, placed on the knuckles [24]. SARAH model (Fig.23.b) is smaller than MARS, it has been built in 1999 and has 10 d.o.f.s that are actuated by only two motors: one motor controls the simultaneous closure of all three fingers, the second motor controls their orientation. The hand has a maximum payload of 25 kg and it is designed to be mounted on the Canadarm, the robotic arm used by the shuttle, but it can be used for other applications.

5.10 Shadow Hand

The Shadow Hand is produced by Shadow Robot Company Ltd. since 2006. The hand has high anthropomorphism and dexterity and is designed to have all the human hand's d.o.f.s (Fig.24.a). It consists of 5 articulated fingers, a palm, a wrist and a forearm, that hosts the actuators.

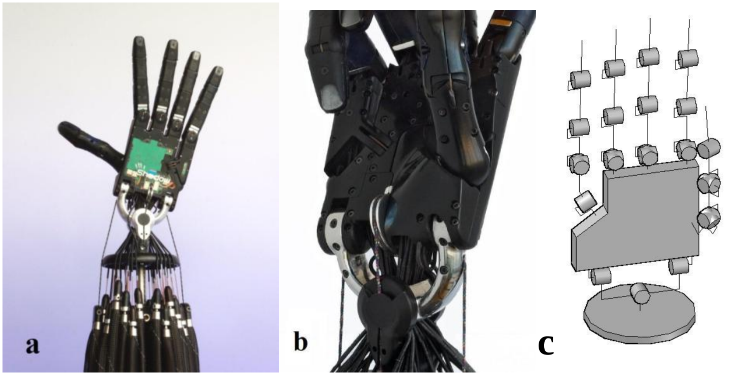

Fig. 24. The Shadow Hand: a) prototype; b) wrist detail; c) a kinematic scheme

Each finger has 4 joints and 3 d.o.f.s, because the two interphalangeal joints are coupled. Each pitch movement is controlled by pairs of antagonist actuators, the yaw movement, owned by knuckles, is controlled by single actuators and return springs. The thumb has 5 d.o.f.s, and another is owned by the palm to allow the opposition of the thumb to all the fingers. The wrist is mobile respect to the pitch and yaw directions. The actuators are both electric and pneumatic (Fig.24.b). Pneumatic actuators are designed to be similar to human muscles: a deformable rubber tube is wrapped around a high resistant texture of carbon fibers; the compressed air in the tubes causes a contraction of the fibers which generates a traction force transmitted to the fingers by wires. The muscle works with few bars of pressure and exert a force that decreases with the increasing of deformation [26]. The maximum force at the middle fingertip is about 10 N, with a time for complete closure of 0.2 seconds. The sensory system consists of Hall-effect position sensors; pressure sensors and touch sensors will be added in future times.

6. A HISTORY OF LARM HAND

For the design of an anthropomorphic hand a suitable knowledge of the human grasp can be very useful. Dimensions of fingers, grasping forces and contact points have been investigated in human grasping for designing LARM Hand [28].

6.1 First prototypes

The natural motion of the finger has been studied by the observation of filmed human grasp's acts. The analysis highlighted the relation between the interphalangeal joints angles during the grasping phases, thus a 1 d.o.f. kinematic model has been developed to mimic the finger's movement [29]. In 2001 a first prototype of articulated finger with gears transmission has been built at LARM (Fig.25.a); in 2002 a second model based on 4-bar mechanism has been designed (Fig.25.b) [30].

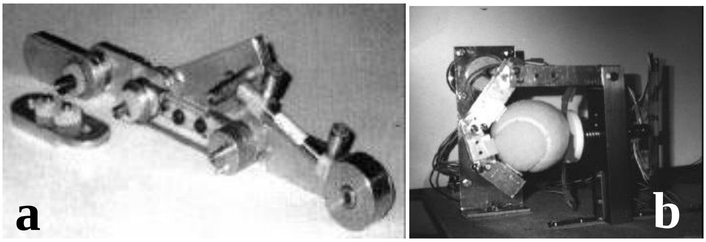

Fig. 25. Early designs: a) first articulated finger of LARM [29]; b) dynamic test on second finger [30]

Kinematics and dynamics tests on this second prototype leaded to the design and in 2003 of the first LARM Hand. The LARM Hand I (Fig.26.a) consists of three articulated fingers and a mobile palm of aluminum alloy, with dimensions of 1.5 times of the human average scale. Each phalanx is composed of aluminum plates connected with screws. The fingers are actuated simultaneously by three DC motors with planetary gears and universal joints that exert a maximum force of 10 N. The hand is controlled by a commercial PLC and there is no closed loop control [31].

The LARM Hand II is similar to the previous version, except for the smaller dimension and more compact structure, by means of the conic gears transmission (Fig.26.b). The LARM Hand III (Fig.23.c) has been designed with a multi-objective optimization process, in order to achieve optimal human-like motion of the phalanxes, and minimal power consumption under several design constraints, [31]. The motors are independent and there is a closed loop force control, by means of a user-friendly interface in LabVIEW virtual environment [32].

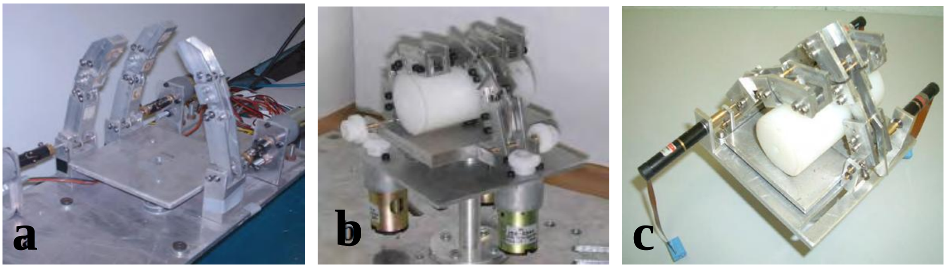

Fig. 26. Versions of LARM Hand: a) LARM Hand I, 2003; b) LARM Hand II, 2004; c) LARM Hand III, 2006 [31]

6.2 LARM Hand IV

The fourth and last version of LARM Hand (Fig.27.a) has been built in 2007 and it represents an economic, light weight and easy operational solution, with underactuated fingers able to emulate the cylindrical human grasp, [32]. It has been designed with multi-objective optimization process, [33]. The hand is 1.2 times the human hand and it consists of 3 modular fingers, a mobile palm and a standard base for the assembling on a robotic arm. Each fingers is composed of 3 phalanxes with a rectangular section. Each finger is actuate by a DC motor with conic gears and a maximum force of 15 N. A closed loop control of the current is implemented, so that the grasping force is always controlled. The hand is provided of piezoresistive force sensors for grasp regulation. The motion is provided by a double 4-bar mechanism, integrated in each finger (Fig.27.b). The design is optimized for the grasp of cylindrical objects, with a diameter between 20 and 60 mm, but it can stably grasp object with different size and shape as indicated in Fig.28,with 4 possible contact forces.

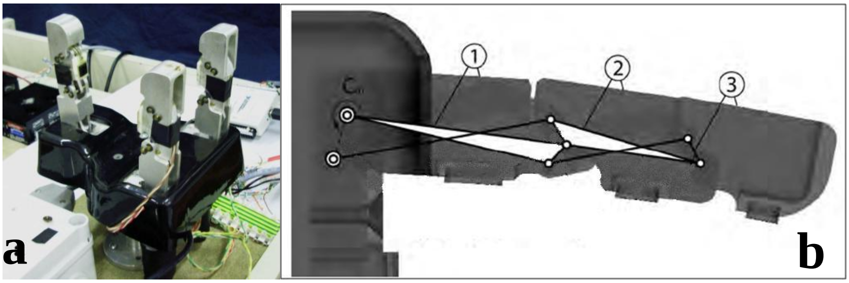

Fig. 27. LARM Hand IV: a) prototype [27]; b) finger mechanism [33]

Referring to Fig. 28, the static equilibrium can be described by the expression

$$F_4 = W + F_{1z} + F_{2z} + F_{3z} \tag{10}$$

where F_4 is the grasping force measured on the palm; W is the weight of the grasped object; F_{1z}, F_{2z}, F_{3z}, are the components along Z direction of F_1, F_2, F_3. The larger is the size of the object to be grasped, the closer is the finger that will be to the vertical configuration and the value of the grasping force F_4 will increase with the size of the object to be grasped [28].

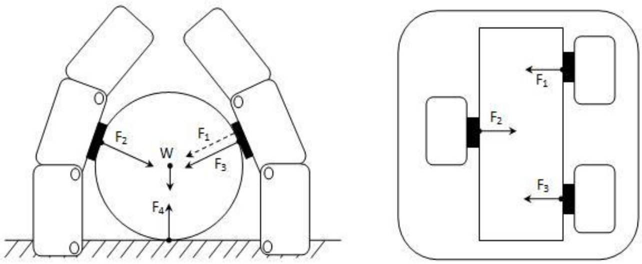

Fig. 28. Schemes of the grasps by LARM Hand [27]

7. CONCLUSIONS

The paper gives an overview of the history of artificial hands with the aim to illustrate peculiarities of the mechanical designs and implementation of successful prototypes. Such a historical study has been also useful to focus on the evolution of LARM Hand to better emphasize the trends and achievements in the specific fields of robotic hands.

REFERENCES

[1] De Nicola M., "Ottimizzazione del progetto biomeccatronico di una protesi di mano per la regolazione della forza di presa", Master degree Thesis, Libera Università Campus Bio-medico, Rome, 2007

[2] AA. VV., "Anatomia umana", Edi.Ermes, Milan, 2000, vol. 1, pp. 203-270

[3] Cutkosky M. R., "On grasp choice, grasp models and the design of hands for manufacturing tasks", IEEE Transactions on Robotics and Automation, 1989, vol. 5, n. 3, pp. 269-279

[4] Ceccarelli M., "Fundamentals of Mechanics of Robotic Manipulation", Springer, Dordrecth, 2004
[5] Ceccarelli M., "Grippers as Mechatronic Devices", Advances in Multibody Systems and Mechatronics, Contribution dedicated to prof. Manfred Hiller on the occasion of his sixtieth birthday, Gerhard-Mercator-Universitat Duisburg, 1999
[6] Ceccarelli M., "Design Problems for Industrial Robot Two-Finger Grippers", 3rd International Workshop on Robotics in Alpe-Adria Region, Bled, July 1994, pp.117-120.
[7] "Come and Hear" website: http://come-and-hear.com/shabbath/shabbath_66.html
[8] Plinio G. S., "Naturalis Historiæ", libro VII, Bibliotheca Classica Latina sive Collectio Auctorum Classicorum Latinorum cum notis et indicibus, Lemaire, 1827, vol. 3, p. 121
[9] A. Davalli, R. Sacchetti, "Protesi di arto superiore – Terapia occupazionale, metodologie riabilitative e ausili", Editrice SOLEI Press, 1996
[10] Paré A., "Dix Livres de Chirurgie avec le Magasin des Instruments Nécessaires à icelles", Jean de Royer, Paris, 1564, pp. 121-124
[11] Putti V., "Protesi Storiche", La Chirurgia degli Organi di Movimento, 1925, vol. 9, nn. 4-5
[12] Cartaz A., "La Prothèse chirurgicale", La Nature: revue de sciences et de leurs applications aux artes et a l'industrie, Year VI, Semester I, Masson Editeur, Paris, 1888
[13] Kuniholm J., "Open arms – What a prosthetic-arm engineering is learning from open source, crowd sourcing and the video-game industry", IEEE Spectrum, March 2009, pp. 37-41
[14] Touch Bionics website: http://www.touchbionics.com/professionals.php?section=5
[15] Rosheim M. E., "Robot Evolution: the Developments of Anthrobotics", Wiley, New York, 1994, pp. 189-225
[16] Fukaya N., Toyama S., Asfour T., Dillmann R, "Design of the TUAT/Karlsruhe humanoid hand", Proceedings on 2000 IEEE/RSJ, International Conference on Intelligent Robots and Systems IROS 2000, Takamatsu, 2000, vol. 3, pp. 1754-1759
[17] Butterfass J., Liu H., Hirzinger G., Grebenstein M., "Next generation of a dexterous robot hand", Proceedings of the 2001 IEEE, International Conference on Robotics and Automation ICRA '01, Seoul, 2001, pp. 109-114
[18] DLR Hand, Deutsches Zentrum für Luft- und Raumfahrt website: http://www.dlr.de/rm-neu/en/desktopdefault.aspx/tabid-3802/
[19] Mouri T., Kawasaki H., Yoshikawa K., Takai J., Ito S., "Anthropomorphic Robot Hand: Gifu Hand III", International Conference on Control and Automation Systems ICCAS '02, Jeanbuk, 2002, pp. 1288-12937
[20] F. Lotti, P. Tiezzi, G. Vassura, L. Biagiotti, C. Melchiorri, G. Palli, "Development of the UB Hand 3: Early Results", IEEE International Conference on Robotics and Automation, ICRA'05, Barcelona, 2005, pp. 4488-4493
[21] Carrozza M. C., Zollo L., Roccella S., Guglielmelli E., Dario P., "Biomechatronic Design and Control of an Anthropomorphic Artificial Hand for Prosthetic and Robotic Applications", IEEE/ASME Transactions on Mechatronics, 2007, vol. 12, n. 4
[22] Townsend W. T., "The Barret Hand grasper, programmably flexible part handling and assembly", Industrial Robot: an Internal Journal, MCB University Press, 2000, vol. 27, n. 3, pp. 181-188
[23] MARS Hand - SARAH Hand, Laboratoire de robotique de l'Université Laval website: http://robot.gmc.ulaval.ca/en/research/themes.html
[24] Gosselin C. M., Laliberte T., "Underactuated mechanical finger with return actuation", United States Patent, 1998 (US 5,762,390), 1998

[25] Gosselin C. M., Laliberte T., "Actuation system for highly underactuated gripping mechanism", United States Patent, 1998 (US 6,505,870), 2003
[26] Walker R., "Shadow finger test unit (C3) – Technical specification", Shadow Robot Company Ltd. Technical data sheets, March 2006
[27] D'Aliesio E., "Evoluzione storico-tecnicadi mani artificiali", Bachelor degree Thesis, LARM: LAboratorio di Robotica e Meccatronica, University of Cassino, Cassino, 2009
[28] Nardelli A., Carbone G., "An Experimental Characterization of LARM Hand IV", CD Proceedings of IFToMM-FeIbIM Int. Symposium on Mechatronics and Multibody Systems MUSME08, San Juan, 2008, paper n.27
[29] Figliolini G., Ceccarelli M., "A novel articulated mechanism mimicking the motion of index fingers", International Journal Robotica, 2002, vol. 20, pp. 13-22
[30] Carbone G., Civitillo R., Ceccarelli M., "Design and test of an articulated mechanism for 1 d.o.f. anthropomorphic finger", Proceedings of DETC '02 ASME 2002 Design Engineering Technical Conferences and Computers and Information in Engineering Conference, Montreal, 2002, paper DETC2002/MECH-34300
[31] Carbone G., Ceccarelli M., "Experimental Tests on Feasible Operation of a Finger Mechanism in the LARM Hand", Mechanics Based Design of Structures and Machines An International Journal, 2008, vol. 36, n. 1, pp. 1-13
[32] Iannone S., "Regolazione della presa della LARM Hand", Bachelor degree Thesis, LARM: LAboratorio di Robotica e Meccatronica, University of Cassino, Cassino, 2006
[33] Ceccarelli M., Carbone G., "Design of LARM Hand: problems and solutions", 2008 IEEE-TTTC International Conference on Automation, Quality and Testing, Robotics, AQTR 2008, Cluj-Napoca, 2008, pp. 298-303; (best paper award): in Journal of Control Engineering and Applied Informatics, vol. 10, n.2, pp. 39-46.

Proceedings of MUSME 2011, the International Symposium
on Multibody Systems and Mechatronics
Valencia, Spain, 25-28 October 2011

A DYNAMIC ANALYSIS OF THE ROBOT CAPAMAN (CASSINO PARALLEL MANIPULATOR) AS SOLAR TRACKER

Elisabet Jiménez[1], Marco Ceccarelli[2] and Giuseppe Carbone[2]

1 School of Industrial Engineering
Technical University of Almería, Carretera de Sacramento s/n 04120, Almería, Spain
e-mail: ejo1988@hotmail.com,

2 LARM, Laboratory of Robotics and Mechatronics
University of Cassino, Via G. Di Biasio 43, 03043 Cassino, Italy
e-mails: ceccarelli@unicas.it, carbone@unicas.it

Keywords: Bachelor student paper, Parallel Manipulators, Dynamics Analysis, Solar Trackers.

Abstract. *This paper reports work for a bachelor thesis that has been focused on a study of feasibility of CaPaMan (Cassino Parallel Manipulator) as solar tracker. An analysis is proposed both in motion simulations and dynamic response in order to check the operation of CaPaMan as solar tracker. The study includes modeling of the prototype mechanical CaPa-Man (Cassino Parallel Manipulator), taking into account the size of the laboratory prototype and its features. A suitable modeling of the solar tracking operation has been applied to Ca-PaMan with the aim to simulate properly its operation as solar tracker by considering its platform as solar panel. simulations results are obtained with suitable performance expect for the limited workspace that will be not able to cover the full range for tracking the sun. then laboratory test have been carried out both to check the validity of simulation a results and practical feasibility of CaPaMan as solar tracker.*

1. INTRODUCTION

Parallel manipulators have attracted great interest since a couple of decades both as new robot structure and for new applications. Thus, beside several theoretical developments have been developed and presented in a very riche literature, even several new designs have been proposed both for old and new applications. One of these novel designs is CaPaMan (Cassino Parallel Manipulator), [1]. Furthermore, new applications of robots have been possible because of better performance with respect to traditional serial manipulators mainly in terms of motion acceleration, stiffness, and accuracy. In fact also CaPaMan prototype at LARM in Cassino has been experienced in novel applications such as earthquake simulator. Previous works have reported those experience with results, [2-6].

In this paper, CaPaMan is investigated as solar tracker having a solar panel to be guided to face the solar during the day. Although the limited workspace of CaPaMan cannot give a full operation as solar tracker, the study has been aimed to simulate operation efficiency in terms of motion and force transmission under dynamic conditions.

2. CAPAMAN

CaPaMan is a parallel manipulator with 3 degrees of freedom, Fig. 1, that has been designed and built at LARM (Laboratory of Robotics and Mechatronics of Cassino), in order to obtain simple and economic parallel manipulators, [1].

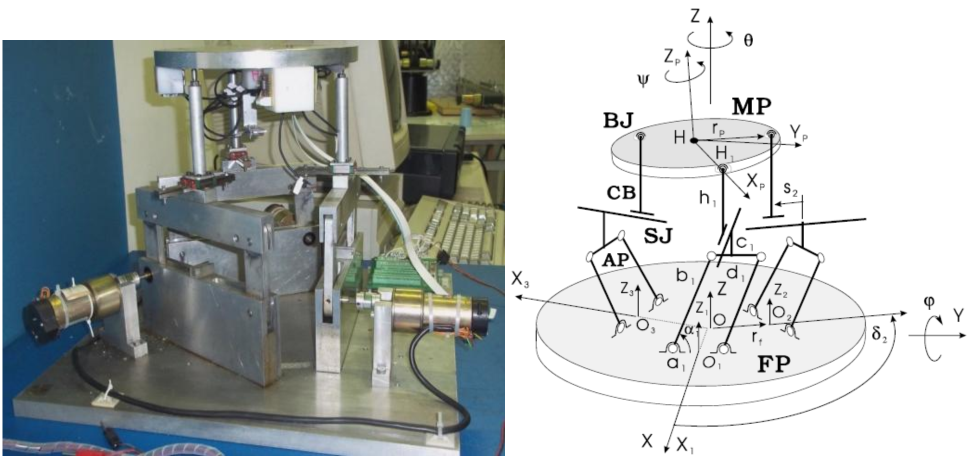

a) b)

Fig. 1. CaPaMan Cassino Parallel Manipulator: a) prototype; b) a kinematic scheme.

Table 1. Sizes and motion parameters of the built prototype for CaPaMan, Fig. 1.

$a_j = c_j (mm)$	$b_j = d_j (mm)$	$h_j (mm)$	$r_p = r_f (mm)$	α_j	$s_j (mm)$
200	**80**	**100**	**250**	**32:148**	**50:50**

It is composed of a movable plate MP that is connected to a fixed plate FP by means of three leg mechanisms. Each leg mechanism is composed of an articulated parallelogram AP whose coupler carries a prismatic joint SJ, a connecting bar CB which transmits the motion from AP to MP through SJ, and a spherical joint BJ, which is installed on MP. CB may translate along the prismatic guide of SJ keeping its vertical posture while the BJ allows the MP to rotate in the space. Each AP plane is rotated of π=3 with respect to the neighbor one so that it lies along the vertices of an equilateral triangle geometry to give symmetry properties to the mechanism. Particularly, links of a k leg mechanism are identified through: a_k, which is the length of the frame link; b_k, which is the length of the input crank; c_k, which is the length of the coupler link; d_k, which is the length of the follower crank; h_k, which is the length of the connecting bar (see Table 1). The kinematic variables are: α_k, which is the input crank angle and s_k, which is the stroke of the prismatic joint. The size of MP and FP are given by r_p and r_j , respectively, where H is the centre point of MP, O is the centre point of FP, H_k is the centre point of the k BJ and Ok is the middle point of the frame link a_k, Fig. 1a). Indeed MP is driven by the three leg mechanisms through the corresponding articulation points H_1, H_2, H_3. Each leg mechanism can be actuated by a motor on the input crank shaft so that the device is a 3 d.o.f. spatial mechanism. By using this solution the revolute actuators can be conveniently installed on the fixed plate, as shown in Fig. 1 for the built prototype. In order to describe the motion of MP with respect to FP a world frame O-XYZ has been assumed as fixed to FP and a moving frame $H - X_p Y_p Z_p$ has been fixed to MP, Fig. 1. O-XYZ has been fixed with Z axis orthogonal to the FP plane, X axis as coincident with the line joining O to O1, and Y axis to give a Cartesian frame. The moving frame $H - X_p Y_p Z_p$ has been fixed in an analogous way to the movable plane MP with ZP orthogonal to the MP plane, XP axis as coincident to the line joining H to H1 and YP to give a Cartesian frame. Useful expressions have been deduced for the direct kinematics by using a suitable analysis procedure with a vector and matrix formulation to give, [1], the coordinates of the centre point H of MP as

$$H_X = \frac{y_3 - y_2}{\sqrt{3}} - \frac{r_p}{2}(1-\sin\varphi)\cos(\psi-\theta) \tag{1}$$

$$H_Y = y_1 - r_p(\sin\psi\cos\theta + \cos\psi\sin\varphi\,\sin\theta) \tag{2}$$

$$H_Z = \frac{z_1 + z_2 + z_3}{3} \tag{3}$$

and the orientation Euler angles of MP, Fig. 1b), as

$$\theta = \sin^{-1}\left[2\frac{y_1 + y_2 + y_3}{3r_p(1+\sin\varphi)}\right] - \psi \tag{4}$$

$$\psi = \tan^{-1}\left(\sqrt{3}\frac{z_3 - z_2}{2z_1 - z_2 - z_3}\right) \tag{5}$$

$$\varphi = \cos^{-1}\left(\pm\frac{2}{3r_p}\sqrt{z_1^2+z_2^2+z_3^2-z_1z_2-z_2z_3-z_1z_3}\right) \quad (z \geq z_1 \Rightarrow "+";\ z < z_1 \Rightarrow "-") \tag{6}$$

where the coordinates y_k y z_k are

$$y_k = b_k\cos\alpha_k \tag{7}$$

$$z_k = b_k\sin\alpha_k + h_k \tag{8}$$

so that they can be considered the input coordinates for the platform motion.

3. SOLAR TRACKING

Euler angles of CaPaMan can be adjusted to correspond to solar angles according to the scheme in Fig.2 as

- The elevation angle α, corresponds to the angle φ of CaPaMan
- The azimuth angle ψ, corresponds to the angle θ of CaPaMan
- The zenith angle θ_z, corresponds to the angle ψ of CaPaMan

Because there are many unknowns and equations it is necessary to establish boundary conditions.

Since the angle to the vertical has no influence, it can be assumed as

$$\psi = 0 \tag{9}$$

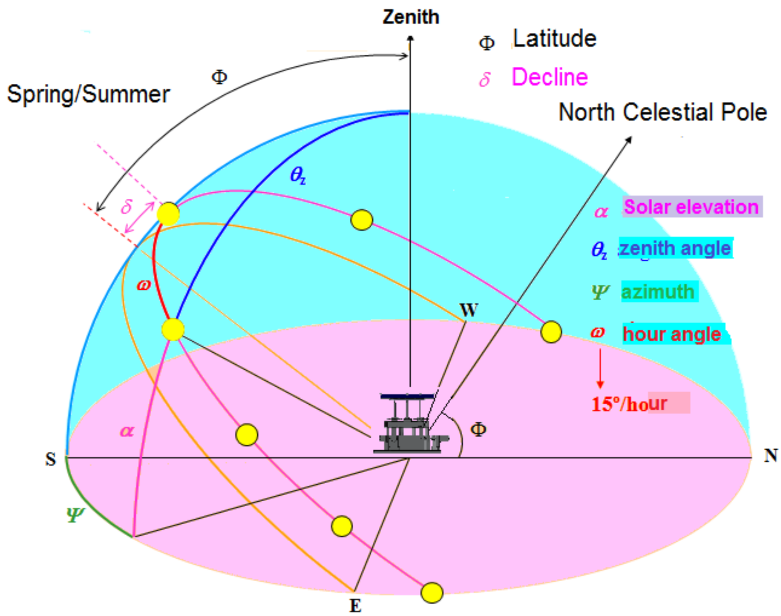

Fig. 2. Solar angles.

Therefore,

$$\tan(\psi) = 0 \tag{10}$$

If the tangent of ψ is 0, this gives

$$z_2 = z_3 \tag{11}$$

$$\alpha_2 = \alpha_3 \tag{12}$$

$$y_2 = y_3 \tag{13}$$

In order too simplify calculations, a value for $y_1 + y_2$ can be conveniently assumed within the workspace, like for example

$$Y = y_1 + y_2 = 150 \tag{14}$$

Then, substituting (14) in (4) and solving y_1, it gives

$$y_1 = \frac{3 r_p (1+\sin\phi)(\sin\theta)}{2} - Y \tag{15}$$

Solving α_1 from (7) gives

$$\alpha_1 = \arccos \frac{y_1}{b_1} \tag{16}$$

It is to note that y_1 must be less than b_1 so that it can operate in real space, and therefore the value of Y is assumed for (15) to give a number less than 80. then, substituting y_1 in (16) we obtain the value of α_1.

Using (6) and replacing the values in (8) give a quadratic equation whose solution calculate z_2.

These equations are calculated into a spreadsheet for easy and accurate resolution of position of CaPaMan's platform.

an example has been computed as referring to the town of Almería (latitude: 36, 50°; Longitude: 2, 28°) at the date of February 21, 2011, in the time range of 13:54 and 13:55 hours. Entering data into the Excel spreadsheet to calculate solar angles, following results are obtained

For the 13:54,

$$\theta = 16{,}16^{\circ} \tag{17}$$

$$\varphi = 41{,}20^{\circ} \tag{18}$$

For the 13:55,

$$\theta = 16{,}48^{\circ} \tag{19}$$

$$\varphi = 41{,}38^{\circ} \tag{20}$$

Since φ is computed as outside the workspace, we add 50° and a simulation can be performed with the platform tilted 50° from the horizontal.

4. SIMULATIONS

4.1 First simulation

For this simulation, the angles α_1, α_2 y α_3 are chosen for the 13:54 time and subtracting the angles referring to the case of 13:55 time. This gives the space that the platform travels in one minute of time and gives the corresponding input degrees in one second. This rate is assigned to each of the actuators of CaPaMan and it is used to perform the first simulation. Results of the simulation give , the graphs are drawn for the completion of necessary data.

Table 2. Dates for first simulation

time	***13:54***	***13:55***	$\Delta\alpha(°)$	$\Delta\alpha(°)/60s$
$\alpha_1(°)$	*42,82*	*38,36*	*4,46*	*0,0743*
$\alpha_2 = \alpha_3$ *(°)*	*56,97*	*47,18*	*9,79*	*0,16316*

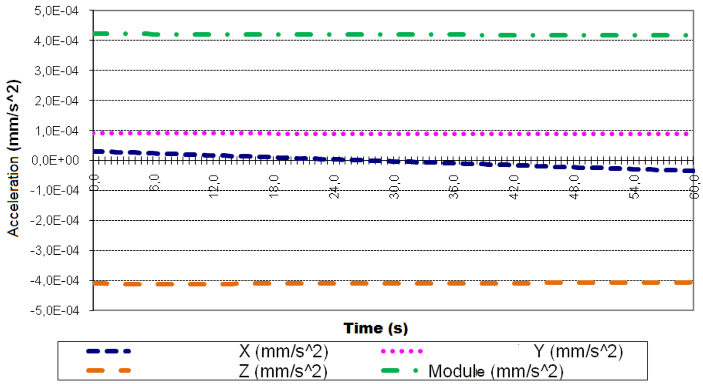

Fig. 3. Acceleration of the platform for the first simulation with data in Table 2.

4.2 Second simulation

For this simulation the speed is increased by 10 times and the simulation time is reduced from 60 to 30 seconds, so that results can be better analyzed as given in the computed plot of Fig.4.

Table 3. Dates for second simulation

time	***13:54***	***13:5 5***	$\Delta\alpha(°)$	$\Delta\alpha(°)/60s$

$\alpha_1(°)$	*42,82*	*38,36*	*4,46*	*0,743*
$\alpha_2 = \alpha_3(°)$	*56,97*	*47,18*	*9,79*	*1,6316*

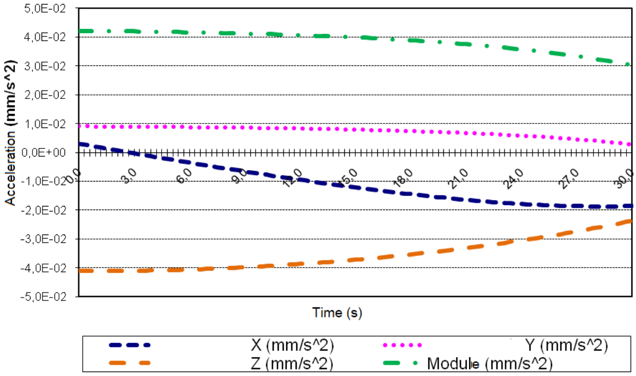

Fig. 4. Acceleration of the platform for the second simulation with data in Table 3.

4.3 Third simulation

For this simulation speed is increased by 100 times and the simulation time is reduced to 4 seconds. This simulation will be conducted with the laboratory prototype, as it is with the best displayed the prismatic guides movements during the experiment.

Table 4. Data for third simulation

Test	***1***	***2***	$\Delta\alpha(°)$	$\Delta\alpha(°)/60s$
$\alpha_1(°)$	*42,82*	*38,36*	*4,46*	*7,43*
$\alpha_2 = \alpha_3(°)$	*56,97*	*47,18*	*9,79*	*16,316*

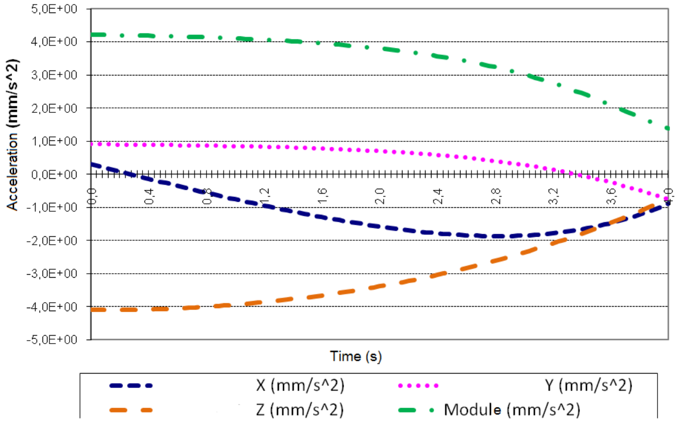

Fig. 5. Acceleration of the platform for the third simulation with data in Table 4.

The actuator number 1 is assigned with a speed of 1,24 rpm and the actuators 2 and 3 with a speed of 2,72 rpm. While watching from time 2 to 3 seconds, the maximum acceleration of the platform is 3.5 mm / s ² in the Z component, while the minimum is about 0.5 mm / s ² in the component Y.

5. EXPERIMENTAL VALIDATION

The prototype CaPaMan consist of a manipulator, a data acquisition card, which is connected to the computer and controller, to acquire the components of accelerations that occur along the axes of the system reference belonging to the mobile platform. Accelerometers have been successfully installed on the faces of three bins made of plastic at the point H (Hx, Hy, Hz), as shown in Figure 6. The robot is programmed with ACL language. Virtual instruments LabVIEW are used to acquire data to verify that the simulation results.

Fig. 6. Accelerometers of the platform.

In the block diagram in Fig. 7 the flow of the acquired data are outlined that travel over virtual files and go through several blocks, which represent various functions, down to the indicators that display the results on the front panel.

In fig. 8 the lay-out for experimental test is shown as referring to the hardware. For the software and motion programming the following is the adopted procedure. When the control system of the robot (white older computer) is activated , typing ATS begins the programming for the platform motion.

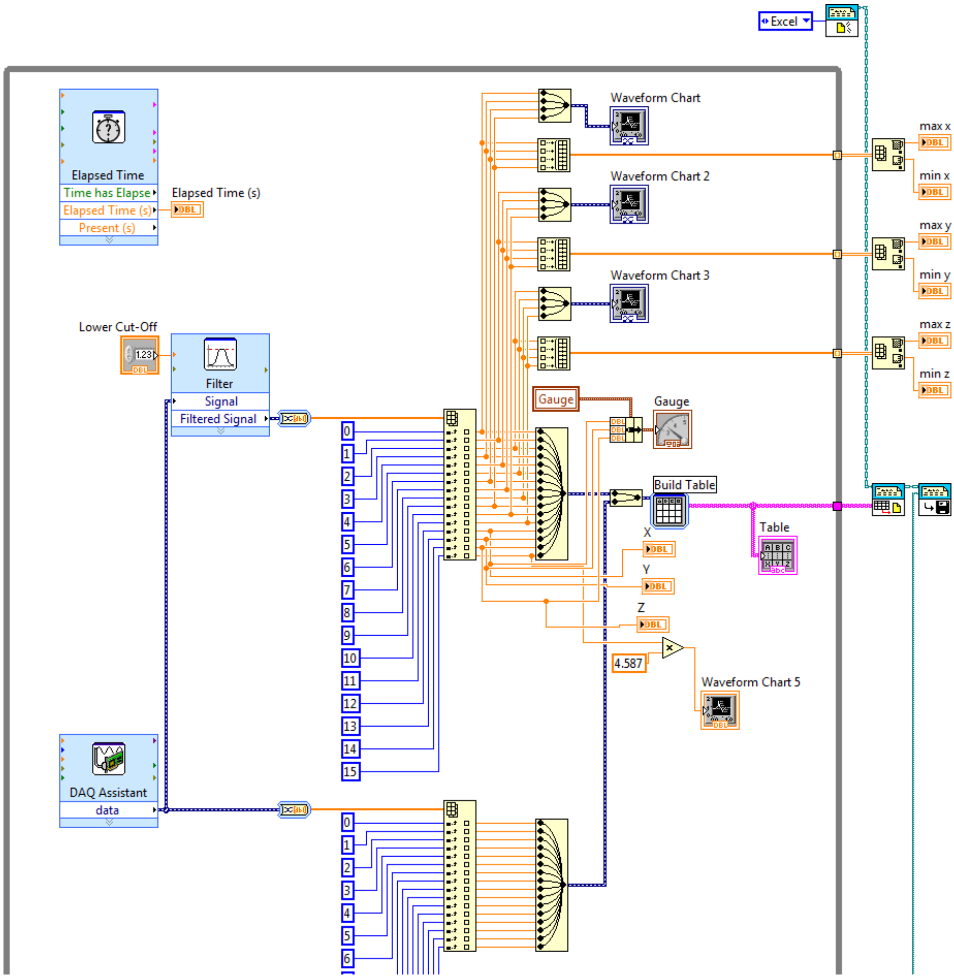

Figure 7. Software scheme in LabVIEW environment.

EDIT ELI1 is written, and gives the option of creating a new program. Here we begin to write operations. To finish, EXIT is used. To test the validity of the program, press F1 to enable the prototype. ELI1 RUN is written and executed. To stop you type A ELI1. Once the experiment, press F2 to disable the prototype. At this point the prototype can be manipulated directly by hand. If you want to change some parameter of the sequence of instructions will have to write EDIT ELI1, and enable the window that was written above. To clear written DEL, and the top line will be canceled.

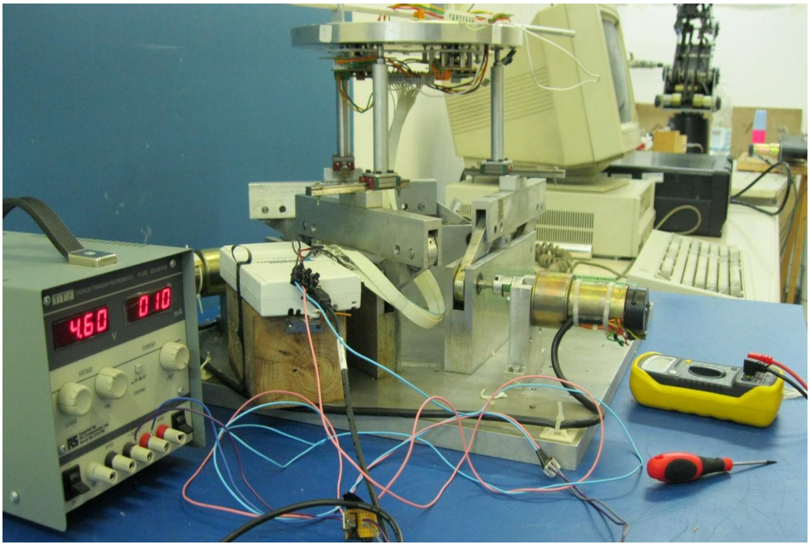

Figure 8. test-bed lay-out at LARM.

5.1 First test

For the first test data are used from the third simulation.

When the robot is in a position lying to the left, you activate the program ELI1 [A.2.1. in Table 5] to raise it to vertical position. If you lie to the right activates the program ELI2 [A.2.2. in Table 5] to raise it to vertical position. From this position ELI3 program is activated [A.2.3. in Table 5], where the angles are told that you must move each leg to the desired position.

Table 5. List of instructions for the programmed test with layout in Fig.8

A.2.1.	*A.2.2.*	*A.2.3.*
ELI1 HERE START SHIFT POSI BY 7 -128 SHIFT POSI BY 8 -128 SHIFT POSI BY 9 -128 MOVED POSI 300 EXIT	**ELI2** HERE START SHIFT POSI BY 7 128 SHIFT POSI BY 8 128 SHIFT POSI BY 9 128 MOVED POSI 300 EXIT	**ELI3** HERE START HERE POSI SHIFT POSI BY 7 16 SHIFT POSI BY 8 35 SHIFT POSI BY 9 35 MOVED POSI 300 EXIT

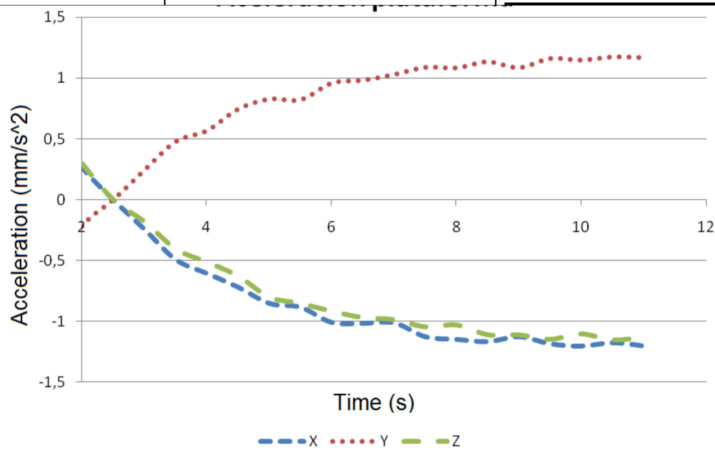

Fig. 9. Acceleration of the platform during the first test.

5.2 Second test

The test has been performed with doubled speed of the first test.

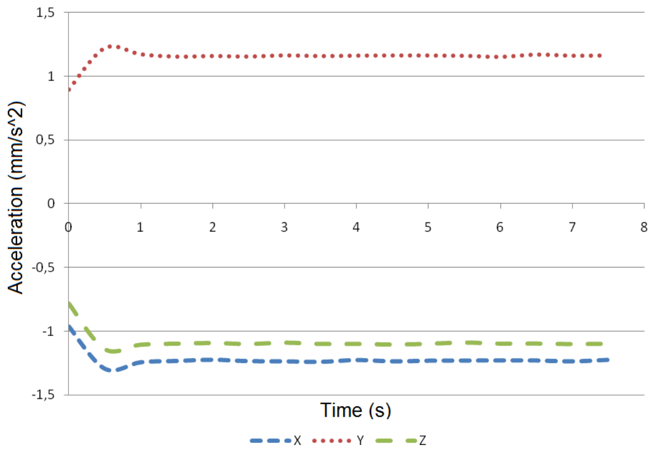

Fig. 10. Acceleration 2 of the platform.

5.3 Third test

To perform this experiment was twice the value of viewing angles for the experiment better.

In the first experiment is found that the curves of the acceleration in X, Y and Z of the platform keep the same meaning as in the simulation. You can see the proportional increase in the value of the acceleration as it passes the time until the point between 1 and 1.5 mm / s ² which is constant. These graphs do not change by doubling the speed (second experiment) or by doubling the value of the angles (third experiment).

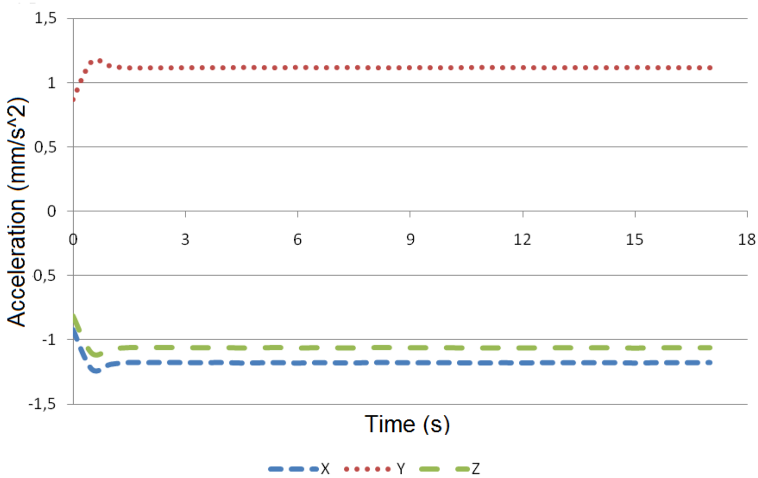

Fig. 11. Acceleration 3 of the platform.

6. CONCLUSIONS

The paper presents a work for a bachelor thesis dealing with operation analysis of CaPaMan whose mobile platform is assumed carrying a solar panel. Simulation has been carried out in Solidworks Cosmos Motion environment whose results have been checked with laboratory tests. However, the lab test results are quite different to the numerical results, mainly because of simple CAD modeling including few real characteristics. Because of this experience, it has been noted that CaPaMan cannot be a good solar tracker as a unique unit, since it has not enough motion capability to track the whole sun motion. Nevertheless, it can be very convenient as complementary unit for high-load solar panels with high-accuracy motion requirements.

The study includes modeling of the prototype mechanical CaPaMan (Cassino Parallel Manipulator), taking into account the size of the laboratory prototype and its features.

As general remark, a properly designed parallel manipulator can be used as solar tracker with a high number of degrees of freedom to cover the necessary work space. But in our case, CaPaMan workspace is not large enough for application. However, this prototype it is accurate enough to be attached to another tracking system and thus assisting it in positioning accuracy.

ACKNOWLEDGEMENTS

The first author wishes to thank the support of University of Almería for Erasmus grant that has permitted her to spend a period of study at LARM in the year 2011.

REFERENCES

1. Ceccarelli, M. 1997. A New 3 D.O.F. Parallel Spatial Mechanism, Mechanism and Machine Theory, Vol. 32, No. 8, pp.. 895-902.
2. Carbone, G.; Ceccarelli, M. 2002. A stiffness analysis for CaPaMan. Mechanism and Machine Theory. Pergamon, Vol.37, No.5, pp. 427–439.
3. Carbone, G.; Carvalho J.C.M.; Ceccarelli, M.; Oliveira P.; Saramago S.F.P. 2008. An Optimum Path Planning of CaPaMan (Cassino Parallel Manipulator) by Using Inverse Dynamics, Robotica: An International Journal, Vol.26, No.2, pp. 229-239.
4. Ceccarelli, M.; Lanni, C.; Mende, J.; Pugliese, F. 1999. CaPaMan (Cassino Parallel Manipulator) as sensored earthquake simulator, In Proceedings of the 1999 IEEE/RSJ International Conference on Intelligent Robots and Systems, Vol.3, pp. 1501-1506.
5. Ceccarelli M.; Ottaviano E. 2002. Optimal Design of CaPaMaN (Cassino Parallel Ma-

nipulator) with Prescribed Orientation Workspace, International Journal Robotica, 2002, Vol. 20, pp. 159-166.

6. Ceccarelli, M.; Florea, C.; Itul, T.P.; Ottaviano, E.; Pisla, A. 2007. An Experimental Characterization of Earthquake Effects on Mechanism Operation. International Conference on Automation, Quality and Testing, Robotics.